GROUND- AND EXCITED-STATE CHEMISTRY OF [BIS(2,2'-BIPYRIDINE)(2-(2-PYRIDYL)PYRAZINE) RUTHENIUM(II)]: PROTONATION AND COORDINATION

by

Elena Ferloni

A dissertation submitted to the Graduate Faculty in Chemistry in partial fulfillment of the requirements for the degree of Doctor of Philosophy, The City University of New York

2012

This manuscript has been read and accepted by the Graduate Faculty in Chemistry in satisfaction of the dissertation requirement for the degree of Doctor of Philosophy.

Harry D. Gafney

_____ _____

Date Chair of Examining Committee

Maria Tamargo

_____ _____

Date Executive Officer

John Lombardi

Richard Magliozzo

Thomas C. Strekas

Supervision Committee

City University of New York

To the FERLONI family

Abstract

GROUND- AND EXCITED-STATE CHEMISTRY OF [BIS(2,2'-BIPYRIDINE)(2-(2-PYRIDYL)PYRAZINE) RUTHENIUM(II)]: PROTONATION AND COORDINATION

by

Elena Ferloni

Supervisor: Harry D. Gafney

Ruthenium(II) diimines have been extensively studied for their notable photo physical properties. Of particular interest are compounds with ligands with peripheral base sites, where the metal-to-ligand charge transfer shifts electron density onto the ligand yielding an emissive state of increased in basicity. One well known example of such complexes, (bis(2,2'-bipyridine) (2-3-bis(2-pyridyl) pyrazine) ruthenium(II), $[Ru(bpy)_2dpp]^{2+}$, has been studied extensively, yet questions remained regarding the sequence of protonation steps at the two peripheral dpp nitrogens in the ground and excited states and the magnitude of the photo-induced change in acid-base properties at each site. In order to reach a deeper understanding of the kinetic and thermodynamic steps involved in its protonation and coordination, a similar complex was synthesized and studied, (bis(2,2'-bipyridine) (2-(2-pyridyl) pyrazine) ruthenium(II), $[(bpy)_2Ru(pypz)]^{2+}$. The alternative ligand is identical in almost every respect to dpp except for the absence of the free pyridyl ring and the fact that it has only one possible protonation site instead of two. The pypz ligand, thus, represents an ideal candidate to elucidate how the pyrazinyl nitrogen on the coordinated dpp would behave if the additional pyridyl ring on dpp was

not present. The differences and similarities in the properties of $[(bpy)_2Ru(pypz)]^{2+}$ and $[Ru(bpy)_2dpp]^{2+}$ in the same environment are highlighted here, describing the peculiar behavior of the acid-base sites of each complex upon excitation and their role in protonation reactions and coordination reactions to d^{10} metals, namely zinc.

Acknowledgments

Writing this manuscript was a monumental task that took years and the help and support of many people that I would like to acknowledge here.

Of course, life got in the way, but mostly, it was the sight of what still needed to be accomplished that was scaring me into inaction and self-doubt. I could not have persevered without the encouragement of my family, my parents, Paolo and Lidia, my brothers and sister, Maria, Marco and Andrea, and my uncle and aunt, Zio Valerio and Zia Marilisa. They knew the value and sacrifice needed and reminded me it was worth it. Worth more than any other task I would rather engage in. They have been a living example of what they preached to me: “education is important”. And when I tried to forget that fundamental truth, they wouldn’t hesitate to remind me. Thank you for grounding me, for loving me and for the example of life that you all are.

Many thanks are due to the Executive Officers of the Chemistry Department, Professor Koeppl, who encouraged me to enroll in the program and saw potential in me and Professor Tamargo, who generously and patiently allowed me to stay in it long enough to finish. And, of course, the wonderful and efficient secretaries, Mrs Adebowale and Mrs Mason, who guided me through the bureaucratic maze of forms and applications, year after year, whether I was on time or very last minute, with the patience of Buddhist monks.

My research mentor, Professor Gafney deserves my utmost gratitude for everything from trips to Ikea to last minute Friday afternoon n^{th} revisions to the same paragraph and everything in between. He was, from day one, more than a scientific advisor to me: he was like a father while mine was across the ocean. He has always cared about every aspect of his students’ life, from coursework and research to the quality of coffee, home renovation projects and life’s big or little events. He has been supportive, helpful, insightful, non-judgmental and all with his ever-present sense of humor that helped lighten the darkest hours. He would like me to only say that he helped in “crystallizing” the ideas that I had research-wise into well thought out concepts. But he did so much more than that! This may be my only chance to let him know how amazing his presence has been in my life without risking bursting into tears right in front of him! Thank you!!

Thank you to my Thesis Committee members, Professor Lombardi and Professor Magliozzo for their insightful comments at committee meetings and patience in scheduling. Thank you to Dr. Karimi for his help in synthesizing the pypz ligand and for teaching me about radial-chromatography, yet another way to separate mixtures, especially the ones as tricky as diimine ligands!

All my lab mates, past and present, and my fellow Ph.D students have been instrumental in providing support and making the research campus a “home” in the many years of research and writing. First and foremost, I must mention my one and only true peer mentor, Dr. José Zambrana Jr., (if only because he is the most cited author in this

manuscript!!). He taught me everything I know about Nd-YAG lasers and so much more. He was an unparalleled companion and guide in the first few years of research, when I still wasn't sure what direction my research project was going to take. Like Prof. Gafney, José did not limit his personal interaction with me and our fellow lab mates to the scientific realm. He cared to make his interpersonal relationships go beyond the surface and enjoyed sharing hikes at Bear Mountain, backyard BBQs and even Sunday masses. José, it was a pleasure getting to know you and this thesis could not have been conceived without your help and wisdom and all the hours spent discussing with you ruthenium dpp's chemistry.

My other lab mates over the years, Dr. Edward Look, Jim Dimitrikopolous, Martha Kowalczyk, Parbatee Jagassar, Dr. Rolande Hodel, Dr. Shanta Amarasinghe, Tony Perry, all contributed in their unique ways either by brainstorming ideas with me, by sharing their research experience or comparing notes at conferences and before key presentations. Francois was the first fellow graduate student I met on our first day at the Graduate Center. He was a wonderful friend and classmate during the first few years of courses and exams. Incredibly talented and smart, he held the bar high and inspired me to use my own talents to the best of my abilities. Thank you also for your help in the electrochemistry experiments described herein and insights on their interpretation. And finally, Dr. Julie Colis: a lab mate by chance and a best friend by choice. Wonderfully unassuming in everything she does, yet the most thoughtful member of our lab crew. Thank you for helping me sort and review my references, for ALWAYS being there for me over the years, for your help and critical eye in designing and formatting scientific posters, for the unforgettable conferences we went to, and the many pictures to document our adventures! I can't list all that I owe you for. This Thesis is already long enough. But know that every little gesture you have done, though maybe not immediately acknowledged, has been appreciated beyond words. You are the sweetest, most generous friend I have.

Lastly, but certainly no less important, I would like to thank Marcus Johnson, my pillar of strength. Without you, I could not have accomplished it. You made it possible by reminding me there was no rest until this was done. You joined my fight in the last years, when I had lost momentum and faith that it could be done and you brought me new enthusiasm and contagious energy. You helped me by carrying my load at home so that I could focus on writing. You allowed me to make my deadline by driving me to each campus. You corrected countless page numbers, graph numbers, superscripts, and subscripts … through it all, you were there to hand support and push me forward. Standing still or giving up was not an option in your book and you believed in me more than I did. You knew that I could do it, but I couldn't have done it… without you. Thanks to you, I have more than just a wonderful and loving family to be proud of. I have my education and myself.

Table of Contents

List of Figures

List of Schemes

List of Tables

Symbol Key

Δ	Change
ΔE	Energy difference
ΔG	Change in Gibbs free energy
ΔH	Enthalpy change
ΔS	Change in spin multiplicity
A	Ground-state form of compound under study
A^*	Excited-state form of compound under study
A_1	First set of pre-exponential values for a bi-exponential fit
A_2	Second set of pre-exponential values for a bi-exponential fit
bpm	2,2'-bipyrimidine
bpy	2,2'-bipyridine
bpz	2,2'-bipyrazine
c	speed of light
dpp	2,2'-pyridyl-3-pyrazine
E_a	Activation energy
f	Mean activity coefficient
h	Planck's constant
H_o	Hammett acidity constant
I	Rate of production of A^* or emission intensity at an analytical wavelength
I_0	Emission intensity at zero quencher concentration
k	Boltzmann's constant or generic rate constant for any relaxation event or total rate constant for deactivation
$k_{0,}$	Rate constant for deactivation for the base form
k_0"	Rate constant for deactivation for the acid form
k_{2a}	Electron-transfer rate constant
k_{2b}	Energy-transfer rate constant
k_d	Diffusion rate constant
k_{de}	Rate constant for deactivation of the encounter complex
K_{eq}	Equilibrium constant
k_{Fl}	Fluorescence rate
k_{nr}	Non-radiative decay rate
k_p	Intra-molecular reaction rate
k_{p2}	Inter-molecular reaction rate
k_{Ph}	Phosphorescence rate
k_q	Quenching rate constant
k_r	Radiative decay rate
K_a	Acid dissociation constant
K_{SV}	Stern-Volmer constant
M	Molarity
N_A	Avogadro's number
pK	negative log of the equilibrium constant K
pK_a	Ground state equilibrium constant for protonation
pK_a^*	Excited state equilibrium constant for protonation

pypz	2-(2-pyridyl)pyrazine
Q	Quencher
R	gas constant
γ	Differential ratio of intensity between two forms
ε	Molar extinction coefficient or absorptivity
λ_{em}	Emission wavelength
λ_{exc}	Excitation wavelength
λ_{max}	Maximum emission wavelength
ν	frequency, usually in cm^{-1}
τ	Lifetime
φ	Emission efficiency
Φ	Quantum yield
χ	Fraction of light absorbed by a molecule

1. Introduction

1.A. Inorganic Photochemistry

The action of visible and ultraviolet light in promoting chemical changes such as bleaching of fabrics or plant growth has been common knowledge for centuries. The early observation of photoreactions more than likely developed from accidental or intentional exposure of materials to sun. The oldest known written evidence about luminescent phenomena from fireflies and glow-worms was found in China roughly dating from 1500 to 1000 B.C. The luminescence of inorganic materials was known at least as far back as 400 years ago with the first recorded observation of inorganic phosphorescence made in Europe in 1602, when the "Bolognian Phosphorus" was discovered[1]. Mr. Vincenzo Casciarolo, a cobbler by trade and alchemist by avocation, found the natural stone on Monte Paderno, just outside of Bologna and observed that it had the mysterious and magical ability to "accumulate" light when exposed to the sun and to emit it in the darkness. The Renaissance, with the development of the scientific method, had brought about a more rational and systematic approach to the study of natural phenomena and that stone, actually made of barium sulfate, became the first object of scientific study of luminescent phenomena, although in the spirit of times, this approach was tinged with a magical quality and applied to finding or making the Philosopher's Stone. Throughout the 18th century, many new solid luminescent materials were discovered[2] and at the beginning of the 19th century luminescence in solution became known as well. By the 1830 the photochemistry of ferrocyanide ion, ferrioxalate, and uranyl oxalate had been studied[3]. During the same period, Grotthus (1817) and Draper (1843) recognized that “only that light which is absorbed by a system can cause

chemical change". However the quantitative examination of processes taking place after absorption of light and the understanding of the underlying principles actually developed at the beginning of the 20th century, when the study of the photochemistry and photophysics of many metal complexes was complemented by increasing understanding of electromagnetism and the quantum mechanical description of the electronic structure of molecules. The discovery of the dual nature of radiation and the understanding of the quantum distribution of energy levels set the theoretical framework for exploratory photochemistry, initially applied mainly to organic molecules[4]. In the 1950's the field of inorganic photochemistry, as the study of the interaction of visible and ultraviolet light with inorganic materials, began to evolve and expand. Together with the advances being made in organic photochemistry, these studies provided a deeper theoretical understanding of spectroscopy and the nature of excited states of metal complexes and organometallic compounds. The introduction by R. G. Norrish and G. Porter of "flash photolysis" was a significant breakthrough as it allowed for the study of extremely fast chemical reactions, which before that time could only be studied under steady-state conditions where short-lived intermediates could not be detected[5]. The development of fast kinetic instrumentation with improved resolution and more powerful pulsed-lasers, and the use of computers for experimental control and data management dramatically empowered time-resolved techniques allowing for experiments testing faster and faster processes. Concurrently, a clearer grasp of the structure of nuclei shifted the inquiries from the general observation of light-induced processes to a more specific examination of the mechanistic details of such processes. The field of photochemistry progressed from an interest in function and structure of luminescent compounds to the elucidation of the

molecules' excited states and excited state reactions, the detailed kinetics of electron-, energy- and charge-transfer steps, and competing radiative and radiationless processes. It is now common practice, for example, to measure and use excited state properties such as lifetimes, in the spectroscopic assignment of excited state types, or to highlight existing competing processes, including quenching and radiative decay and excited state inversions.

The advances in photochemistry in general have led to a wide range of diverse, yet inter-related areas of research, and the measurement of quantities characteristic of excited states, such as lifetime and quantum efficiency, have been used in physics, chemistry, biology, solar energy storage and conversion and laser technology. For example, in analytical chemistry, the combined luminescence and excitation spectra provide a valuable identification tool, because they supply information about the chemical composition of the emitting system, but do not require much of the material under examination. In addition, excitation and emission wavelength can be varied to discriminate against other luminescent components in a mixture. The sensitivity of ions' luminescent lifetime to their chemical surroundings is a useful probe of the structure of binding sites, solvent environments, and the extent and nature of interactions with ligands and metals.

On a more practical level, if a chemical compound readily undergoes photo-excitation and can transfer its energy or electrons to other molecules, it has the potential to be integrated in homogeneous or heterogeneous systems and function as photon-harvesting antenna for conversion of solar energy to electric energy. Indeed, several attempts have already been made and continue to be made to find the optimum

photosensitizer and substrate for the purpose. Luminescent compounds can also be used as cryogenic thermometers, given the temperature-dependence of lifetime changes, or as molecular yardsticks, to identify the distances between specific sites by attaching a luminescent probe or monitoring an intrinsic luminescent component at one site with a quencher attached at another site[6].

The aspect of most interest here is the study of the dynamics of the interactions of optically excited metal complexes with surrounding molecules, based on their decay characteristics. Many chromophores do not show appreciable interaction with each other or with other molecules in the ground state, but upon light excitation, they might form an *exci*ted state com*plex,* called an exciplex, having luminescence characteristics that differ from those of the excited individual molecules. Others may greatly change their acid-base or redox properties in the excited state and undergo inter- or intra-molecular proton or electron transfer as a consequence of it. The fact that the chemistry of the excited state differs from that in the ground state, and that interactions between molecules are altered by the absorption of radiation opens the possibility of finding alternative pathways for synthetic reactions that are not viable thermally, and not thermodynamically favored in the ground state. In addition, “turning on” the chemistry with light when coupled to the phenomenal advances in time and power of pulsed lasers, provides the means to “time-resolve the process” thereby supplying new insights on the rates and mechanisms of these interactions[7].

1.B. Basic principles

1.B.1. Excitation and deactivation pathways

When a photon is absorbed, a short-lived excited molecule forms as a result. If the wavelength of the exciting light falls in the ultra violet or visible range, the photon has enough energy to excite an electron and change the electronic configuration of the molecule. The Born-Oppenheimer approximation states that electronic motion is far more rapid compared to inter-nuclear motion and that each electronic configuration can be treated as a separate potential energy surface (Figure 1)[8].

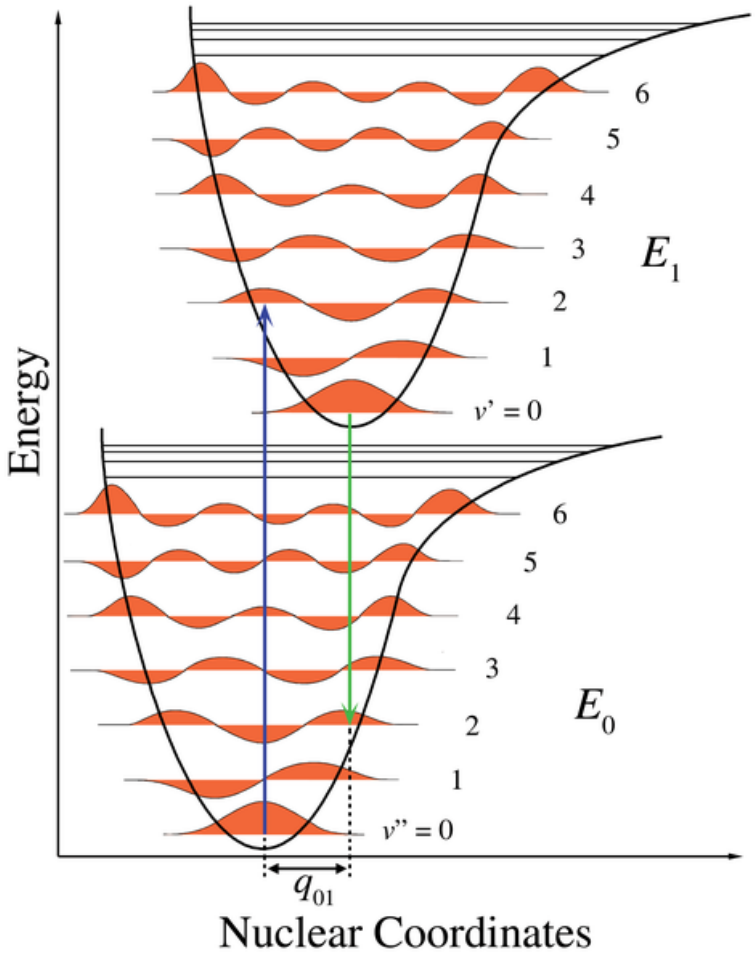

Figure 1: Ground and first excited state electronic and vibrational levels.

Photon absorption is instantaneous (~10^{-16}s) and according to the Franck-Condon principle the molecule formed in the excited state is most likely to undergo an electronic rearrangement without undergoing appreciable nuclear motion. As a consequence the excited state reached upon vertical transition, called a Franck–Condon state, is not thermally equilibrated and the excited molecule possesses vibrational excitation as well as the electronic excitation. Polyatomic inorganic complexes have several vibrational and rotational states for each electronic state, which translates into absorption spectra composed of broad bands instead of the sharp lines characteristic of the electronic spectra of atoms.

The properties and reactivity of excited species are fundamentally related to the type of state reached after light absorption, so it is important to elucidate the nature of the first few excited states of complexes, how efficiently they are populated, and how they contribute to the photochemical and photophysical processes.

Absorption spectra provide information about the energy and electron distribution within the excited states relative to that in the ground state. Depending on the position and intensity of the absorption bands in the spectrum, the energy and allowedness, or probability, of the transition can be determined, respectively. Emission spectra on the other hand, carry information about competing photochemical processes. According to Kasha's rule "…*In condensed phases the emitting level of a given multiplicity is the lowest excited level of that multiplicity*"[9]. The *lowest* excited states of molecules are also the ones predominantly involved in photochemical reactions. Therefore the emission of light, in competition with other deactivation pathways, becomes a probe by which the energy degradation pathways can be studied.

Complexes can be viewed as charged central metal ions electrostatically and covalently bonded to negatively charged ions or the negative ends of the dipoles of neutral ligands. It is sometimes convenient, when trying to establish the electronic structure of a complex, to treat the electrons localized on the ligand system as a separate set from the electrons localized on the metal ion. This is conceptually possible because most ligand electrons, except for the ones in orbitals directed toward the charged metal ion, are located in ligand bonding orbitals far from the central metal ion, and are thus relatively unaffected by complexation. After considering the details of each set of electrons separately, recombining the two sets may provide insight into the new features of the combined structure that are not present in the constituent parts.

A d^6-transition metal octahedral complex in a strong ligand field, like ruthenium complexes that are the subject of this study, has a $(t_{2g})^6$ configuration, a unique diamagnetic state with all electrons spin paired as confirmed by measurements of magnetic susceptibilities. The highest occupied orbitals are t_{2g} d-orbitals and the lowest unoccupied orbitals are e_g d-orbitals.

The valence electrons of the ligands are also important, having excitation energies comparable to those of metal electrons. Many free ligands possess nonbonding electrons that are easily excited. Pyridine-type molecules for instance, possess a nonbonding electron pair (n^2) on the N atom that can be promoted into antibonding orbitals (π^*) on the aromatic ring. When such ligands coordinate with a metal ion, the n-electrons form a sigma-bond with the ion, thus lowering the energy of the n-electrons to levels not accessible to low energy photons. As a generalization, $\pi \rightarrow \pi^*$ transitions of coordinated moieties are not shifted greatly upon complexation, whereas $n \rightarrow \pi^*$ transitions are

usually shifted substantially to higher energies. In complexes possessing at least one π-conjugated ligand in the coordination sphere, the highest filled set of bonding orbitals consist of the π-bonding orbitals on the ligand(s) and the lowest antibonding orbitals on the ligand comprise an unfilled π^* set.

Considering both sets of electrons together, three orbital dispositions ensue for strong-field $(nd)^6$ transition metal complexes coordinated to pyridine-type ligands: intraligand (ligand centered), ligand field (metal centered, d-d) and charge transfer (metal-to-ligand) (Figure 2)[10].

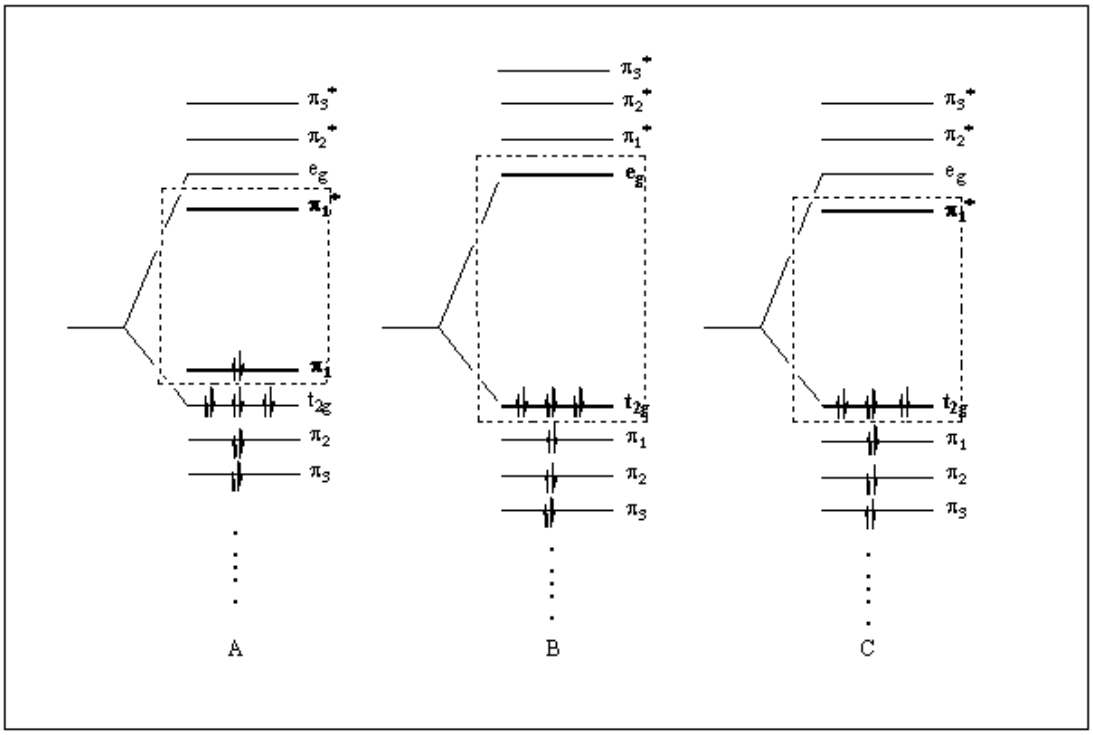

Figure 2: Schematic representation of orbitals for strong-field $(nd)^6$ complexes: ligand-centered (A), metal-centered (B) and charge transfer (C).

In the first case (A), the metal orbitals play a negligible role in the excitation process and the lowest energy transitions are essentially ligand localized. Photochemical processes for complexes with this kind of configuration will be expected to involve mainly the ligand and if radiative decay to the ground state is observed, it is expected to be due to a $\pi^* \rightarrow \pi$ transition. In the second case (B), excitation of the low-lying electronic states of the complex leads to distinctive ligand field photochemistry, where the lowest-energy transition is centered on the metal and is d $\rightarrow$ d in character. Substitutional photochemistry is typical for this configuration since formally electron density increases in the antibonding e_g orbitals, which are thought to enhance ligand loss. Ruthenium diimine complexes are part of the third group (C). In this case, the lowest energy transition promotes an electron from a metal d orbital to a low-lying anti-bonding π^* level of the organic ligand. As a result, the excited molecule will have increased electron density localized over the ligand system, and an electron deficiency over the metal. Emission from such state results in a $\pi^* \rightarrow$ d transition. Alternatively, a complex with this type of charge transfer configuration can, in the excited state, transfer its energy to another molecule through interactions involving the ligand portion of the complex, or transfer the promoted electron to another species and undergo oxidation. The transfer of charge upon excitation may also be ligand-to-metal or complex-to-solvent and consequently the excited complex may have other reactive channels open to it. Charge-transfer bands often dominate the visible region of the spectrum, and thus the d - π^* excited states are those initially reached during the primary act of light absorption after which the photochemically important processes occur in sequence. Depending on the coordination complex involved and the excitation wavelength used, the efficiency of the

absorption may change and lead to a transition of different nature, but in all three cases the low-lying electronic states of complexes are the ones controlling, to a large extent, the photochemistry of the system.

In addition to the states populated following excitation, the properties and reactivity of the excited species also depend on the efficiency of the competing pathways by which the molecule returns to the ground state. The extra electronic energy gathered by the molecule can be dissipated either chemically or physically via the following pathways (Scheme 1):

Scheme 1: Possible deactivation pathways of a species following excitation.

$A + h\nu \xrightarrow{I} A^*$	Excitation	(1)
$A^* \xrightarrow{Knr} A + \Delta$	Non-radiative decay	(2)
$A^* \xrightarrow{Kr} A + h\nu$	Radiative decay	(3)
$A^* \xrightarrow{Kp}$ products	Intra-molecular reaction	(4)
$A^* + B \xrightarrow{Kp2}$ products	Inter-molecular reaction	(5)
$A^* + Q \xrightarrow{Kq} A + Q + \Delta$	Quenching	(6)
$A^* + B \xrightarrow{K2a} A^{\pm} + B^{\mp}$	Electron-transfer	(7)
$A^* + B \xrightarrow{K2b} A + B^*$	Energy-transfer	(8)

The symbols A and A^* are the ground and excited state form of the species under study and the rate constant for each process are indicated above each equation. A molecule may revert spontaneously from upper excited states to lower excited states or to

the ground state through interactions with neighboring molecules and the surrounding solvent cage, the excess energy being converted into vibrational energy, i.e., heat (equation (2)). Transitions between states of the same spin are called internal conversion, whereas transitions between states of different spin multiplicity are called intersystem crossing. Collisions between vibronically excited molecules and solvent typically occur at rates of about 10^{12} s^{-1}. Unless there is some extremely rapid competing process, internal conversions leading to equilibration of the vibrational energy down to the lowest excited state will commonly follow absorption of light. Further deactivation from the thermally equilibrated excited state occurs more slowly or is slow enough for other relatively fast processes, such as intersystem crossing, to compete. Although technically considered intra-molecular, the rates of these processes depend on the solvent medium and the extent of the solvation, which may delay the relaxation of the excited molecule to different degrees.

Another way a molecule may return to the ground state without undergoing changes in composition is by losing only some energy to reach the lowest excited state and from there emitting the remaining extra energy in the form of radiation (equation (3)). Two emission processes can be distinguished: Phosphorescence, a transition between an excited state and the ground state, associated with a change in spin multiplicity ($\Delta S \neq 0$), and fluorescence, which occurs with no corresponding change in spin multiplicity ($\Delta S = 0$). In either case, the transition leading to emission of a photon must occur from a thermally equilibrated state. A change of spin makes the transition less allowed, so the phosphorescence natural lifetime is longer than it would otherwise be. Even if there is spin-orbit coupling, as is the case in ruthenium complexes, the

forbiddeness still applies. The Franck-Condon effect indicates that transitions from thermally equilibrated excited states will form excited vibrational levels of the ground state (Figure 1). Thus, the energy available in the excited state is in fact smaller than that needed for vertical excitation of the ground state. Provided that the emission and absorption bands correspond to the same transition, the difference in energy, referred to as Stokes' shift, explains why the emission occurs on the red side of absorption.

Inorganic complexes in excited states may also return to a different ground state than the one they came from. By virtue of the electronic excitation, they have acquired excess of free energy that may be sufficient to cause excited species to undergo bond breaking or a strong interaction with another ground state species even though an interaction between the two species in their ground states may be very weak or completely absent[11]. These are sometimes the counterparts of thermal reactions, but in many cases the photochemical pathway is distinctly different from that of the thermal reaction.

In the absence of quenchers, excited molecules can undergo intra-molecular photo-induced chemical changes, equation (4), such as reorganization/isomerization, excited-state decomposition, or intra-molecular proton and electron transfers. In the presence of other species, bimolecular relaxation processes such as substitution/exchange reactions or addition/complex formation may take place through excited state intermediates and leading to possible product formation, as in equation (5). A common photoreaction is the replacement of one ligand by the solvent, particularly water. Thermally and photochemically induced ligand substitutions give different products and different stereochemistry. In fact, it is this difference that established that photochemical

reactions are from different electronic states and are not accelerated ground-state thermal reactions.

If the excited species has vacant orbitals or unpaired electrons, it may accept or donate an electron to the quencher and undergo electron transfer instead (equation (7)). The limitation of this process is that usually the electron transfer is reversible and the back reaction is very fast, so overall no net reaction occurs.

If the reacting specie (quencher) has low-lying unfilled excited state orbitals and there is significant overlap between the emission spectrum of the excited species and the absorption spectrum of the quencher, energy transfer may occur (equation (8)). Energy transfer is a physical process in which an excited state molecule transfers its excitation energy to a different molecule. The lifetime of the donor molecule has to be long enough for it to come in contact with the acceptor but once that happens, the donor and acceptor usually interact rapidly so that energy transfer is diffusion-controlled. From the standpoint of the absorbing molecule, energy transfer leads to a quenching of the excited state, proportional to the concentration of the quenching species. From the point of view of the quenching species, the process allows it to reach an excited state and undergo photochemical reactions in a region of wavelengths in which it does not absorb.

Excited state interaction of an excited species with a quencher (equation (6)), ultimately causes the deactivation of the excited species, but may occur following all the primary deactivation pathways described so far, which are rarely completely independent and depending on how the system is organized, it may or may not involve diffusional motion of A^* and Q. The interaction between two excited state molecules have not been mentioned because they generally occur only under conditions of extremely intense

illumination or very long excited state lifetimes, and require very high concentrations, which is not our case.

1.B.2. Criteria to study photochemical reactions

Three main criteria, kinetics, energetics and structure, are useful when trying to establish the plausibility of a proposed excited state mechanism. A full understanding of the processes involved implies knowing the identity of molecules interacting, the significant structures, how they are connected through transitions or chemical transformations and the relative probabilities that a specific configuration or pathway will be followed.

The detailed molecular structure of the ground-state reactants and products can be fully established by conventional spectroscopic techniques (NMR, IR, UV, X-Ray, Mass spectrometry) and/or chemical methods (method of synthesis), while transient structures or excited state intermediates are often inferred from spectroscopic data. When a stable product is not available, conjectures are made on the basis of the initial reactants and transient structures.

Although the most definitive information concerning photochemical events is the knowledge of the structure of reactants, products and intermediates, the assessment of the rates for all photophysical processes, radiative and non-radiative, as well as the energy inherent in each excited species and involved in each transition has to be established to obtain a complete picture of the situation.

From an energetic perspective, a simplified energy level diagram, the so-called Förster cycle, highlights the connection between molar enthalpies and activation energies

(Figure 3)[12]. The cycle represents ground and first electronic excited state for two molecular species, A and A′, involved in a chemical equilibrium in both electronic states.

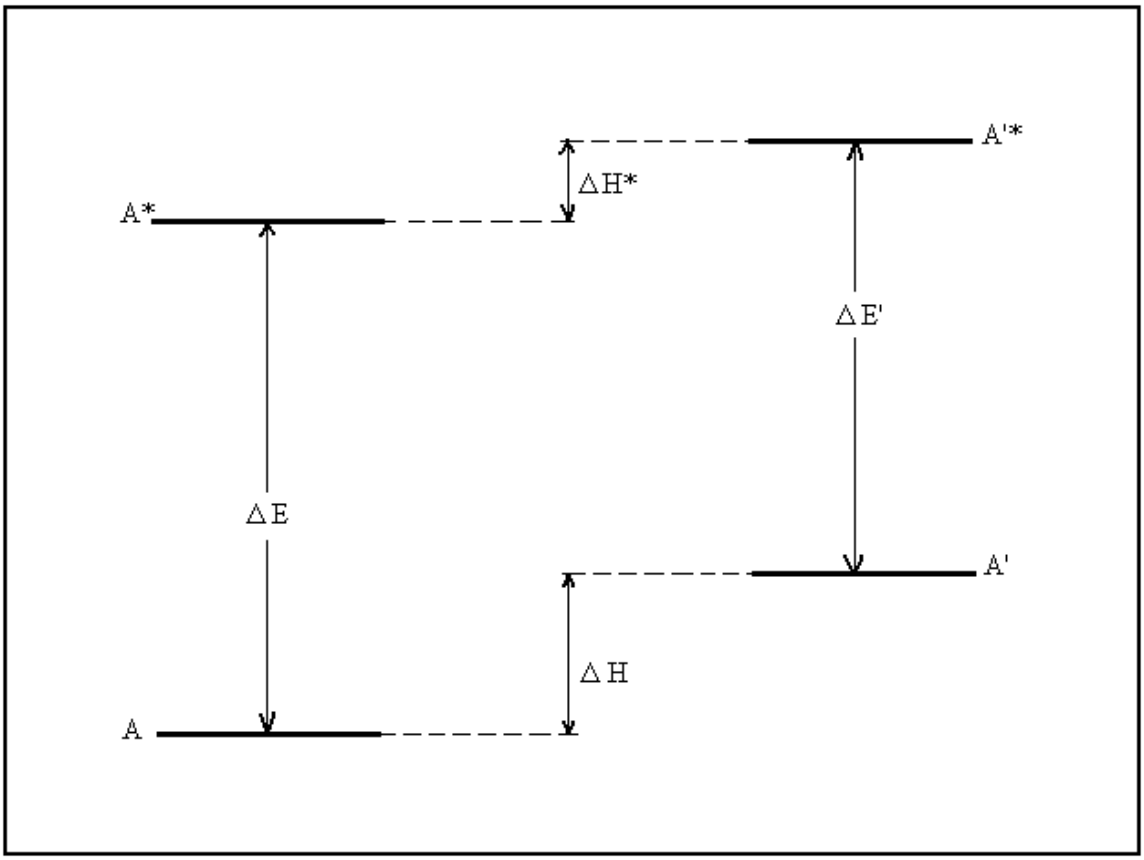

Figure 3: Schematic representation of relationship between enthalpy changes and electronic transitions for species A and A′ in equilibrium with each other.

The difference in energy, ΔE, is the energy required to reach the excited state and can be established experimentally from the long wavelength absorption band of A, while the molar enthalpy refers to the equilibrium in equation (9), which may involve other non-absorbing molecules indicated by B:

$$A\ (+\ B)\ \leftrightarrows\ A'\ (+\ B') \qquad (9)$$

The diagram shows that

$$\Delta H - \Delta H^{*} = \Delta E - \Delta E' \propto h(\tilde{\nu}_A - \tilde{\nu}_{A'}) = h\,\Delta\tilde{\nu} \qquad (10)$$

The difference in molar enthalpy of the reaction in the ground and excited state is analogous to the difference in energy which corresponds to the frequency shift in the absorption bands of A and A′, associated with the reaction. Assuming that excited and ground states have equal reaction entropies, the following equation is obtained:

$$\ln \frac{K^{*}}{K^{0}} = \frac{\Delta E - \Delta E'}{RT} = \frac{hc}{Tk}\Delta\tilde{\nu} \qquad (11)$$

where R is the gas constant, h is Planck's constant, c is the speed of light, k is Boltzmann's constant and T is the temperature. K^{*} and K^{0} are the constant of the equilibrium in equation (9), in the excited state and ground state respectively. Equation (11) provides a criterion to establish the thermodynamic possibility of the reaction in the excited state.

For the reaction to be observable by luminescence techniques there is an additional requirement that the reaction time be comparable to or shorter than the mean lifetime of the excited molecules and to establish that criterion, knowledge of the kinetic rate constants for each process is essential. From a kinetic and energetic perspective, the excited molecule undergoing a photochemical reaction is generally assumed to have acquired sufficient energy during its lifetime to overcome the activation energy required to react at a rate competitive with other modes of excited-state deactivation. The Arrhenius expression (equation (12)) relates the rate constant, k, for the reaction to the activation energy and the probability factor, A, which take into account energy and lifetime.

$$k\ (sec^{-1}) = A \exp -E_a / RT \qquad (12)$$

When compared with unimolecular reactions, the probability factor, A, for bimolecular reactions is smaller by a factor of ~10^4 due to the energy required for such encounters and for structural organization in the transition state[13]. This also means that rate constants for a first-order processes are, in general, much larger than bimolecular rate constants. Bimolecular processes start to assume relevance when intramolecular processes are slow or the concentration of quencher is high.

Rate constants depend on both energetic ($\Delta H^{\ddagger}$ or E_a) and entropic ($\Delta S^{\ddagger}$ or A) factors. Restrictions of conformational freedom in reactants can increase the rate of reaction if the restriction also favors the formation of the reaction transition state. This is an entropic enhancement of the rate constant for the reaction since less ordering is required to achieve the transition state. Other times the entropic factor may be more or less constant, but a reaction may happen faster than another because the energetic factor, E_a differs in the series.

Kinetic rate constants, together with quantum yields provide a quantitative measure, respectively of the probability and efficiency of a photochemical reaction. Knowledge of those quantities offers convincing evidence in support of a mechanistic hypothesis. Reaction rate constants of photochemical processes can be determined experimentally by two methods, the time-resolved method and the steady-state method. The *time-resolved* method perturbs the system using a very short pulse of light and monitors spectroscopically the rate of return of the system to equilibrium. After a pulsed excitation, the excited state, A^*, decays via a unimolecular process corresponding to the rate law:

$$[A^*]_t = [A^*]_0 \exp(-t/\tau_A) \equiv [A^*]_0 \exp(-k_A \cdot t) \qquad (13)$$

where $[A^*]_t$ and $[A^*]_0$ represent the concentrations of A^* respectively at time t and 0, τ_A is the experimental lifetime of A^* and k_A is the rate constant, also equivalent to the inverse of the lifetime. Typically, the absorption or emission of A^* are monitored to track the concentration of A^* as a function of time.

The *steady-state* method depends on establishing a fixed time-independent concentration of reactive intermediates and from knowledge of the rate of one pathway and the ratio of partitioning between pathways, evaluating the rate of the other pathway. In a system under constant-intensity excitation the rate of production of A^* is constant, expressed by I (equation (1)), while the loss depends on the lifetime of the excited species and is proportional to $[A^*]$ (equation (13)). Over time, the concentration of the excited species becomes large enough so that the losses equal the gains, and a steady state or constant value of $[A^*]$ is established. If the lifetime of excited molecules is very long or if the excitation source is very intense, a constant excited state population may not be achieved, because the rate of generating A^*, I, is no longer constant. If a large fraction of A is excited, the concentration of molecules in the ground state decreases, reducing the absorbance, and consequently reducing I. With a very strong excited state pumping, population inversion can arise. Alternatively, A^* may compete with A for the available photons, also affecting the absorbance, and reducing I.

The efficiency of a photochemical reaction expressed in terms of quantum yield, Φ, represents the number of molecules undergoing a transition or change per photon absorbed:

$$\Phi = \frac{\text{moles of given species formed or changed}}{\text{moles of photons absorbed by the system}} \qquad (14)$$

The quantum yield is often dependent on the excitation wavelength and it relates the effectiveness with which absorbed photons can form products. Values of quantum yield can range from zero to a very large number ($>10^4$). Since one photon excites only one molecule, a Φ more than one is indicative of a chain reaction. On the other hand if Φ is less than one, a pathway must exist that degrades energy competitively with the reaction.

Several methods allow the determination of quantum yields, but all require measuring the light intensity absorbed and the rate of product/reactant change. If the photoreaction is irreversible and stable products are formed as a result, the amount of reactant consumed or product formed can be measured using the following techniques: spectrophotometric, pH, EMF, HPLC. Systems exhibiting fully reversible photochemistry or formation of unstable and extremely reactive products present special problems. In these cases, the rapidity of the back reaction and the time required to apply the techniques precludes their application to monitor excited states. Whenever possible, pulsed techniques with flash lamps or lasers are used to overcome the problems, and monitor transient absorption on a microsecond or nanosecond time scale and many of the interconversions that are taking place. Alternatively, quantum yields are often measured by relative techniques. For example, when exploring the extent of quenching of an emission as a function of the concentration of the quencher; then only the ratio of the unquenched to quenched quantum yields, Φ^0/Φ, is required (*vide infra*).

The state efficiency, defined as the number of moles of molecules in a given state, per mole of photon absorbed, relates to *individual steps* from states along the reaction pathway, while the quantum efficiency is an *overall* quantity of a reaction. For the reaction of reactant A to form product P,

$$A \xrightarrow{\phi_{A^*}} A^* \xrightarrow{\phi_R} I \xrightarrow{\phi_I} P \qquad (15)$$

the quantum yield is the product of the state efficiency of each step in the reaction sequence, i.e., the step to produce the excited species (A^*); the step involved in formation of the intermediate (I); and eventually, the step that converts I to the product (P):

$$\Phi_R = \phi_{A^*}\, \phi_R\, \phi_I \qquad (16)$$

In direct excitation experiments in solution, ϕ_{A^*} is generally equal to one because the thermally equilibrated excited state is thought to be reached so fast that no other process can compete with it. The product $\phi_R\phi_I$ is crucial in determining photochemical reactivities, and depends on the decay rate constant and the rate constant for reaction to form I and P. Once a set of elementary reactions is postulated to occur in the system, the rate constant expressions for each reaction can be combined based on the mechanism suggested, to provide overall rates and quantum yield expressions which may be compared with experimental results to test the validity of the proposed mechanism.

Keeping in mind the above considerations it is possible to propose a mechanism for a photochemical reaction after careful evaluation of some or all of the following experimental quantities:

- Amount and identity of the reaction products and intermediates;
- Wavelength and intensity of absorbed light correlated with the assignment of the electronic spectrum;
- Quantum yields of combined steps or when possible, of each individual process;
- Rates of decay of emission or excited state absorption;
- Lifetimes of the excited species.

When the data are incomplete, parts or all of the mechanism may be ambiguous or even completely incorrect. The goal of a complete mechanism remains always somewhat elusive because ever-increasing levels of sophistication and understanding are called for.

1.B.3. First and pseudo first-order systems

The majority of lifetime measurements involve first-order or pseudo first-order kinetic processes, which arise in situations where the probability of decay of the excited species under investigation is unaffected by the presence of like neighbors. Since $[A^*]$ is usually too low to affect the decay of another A^*, many excited state relaxation processes fall in this category. A first-order system is one that, in the absence of external perturbations such as addition of more material, undergoes first-order decay:

$$d[A^*]/dt = -k[A^*] \qquad (17)$$

with first-order rate constant for loss of A^* expressed by k. The solution of the differential equation above is expressed by equation (13) and represents the behavior of a sample after a pulse of excitation much shorter than the excited state lifetime, so that formation of A^* is complete before appreciable loss of A^* can occur.

Scheme 2: Reaction steps involving excitation and first order decay.

$A + h\nu \xrightarrow{I} A^*$	Rate = I	(1)
$A^* \xrightarrow{Knr} A + \Delta$	Rate = $k_{nr}[A^*]$	(2)
$A^* \xrightarrow{Kr} A + h\nu$	Rate = $k_r[A^*]$	(3)
$A^* \xrightarrow{Kp}$ products	Rate = $k_p[A^*]$	(4)

In scheme 2, I represents the rate of excited state production (usually in units of moles of excited state per liter per second, M sec^{-1}). k_r is the radiative rate constant for emission of a photon from the excited state, either by fluorescence, phosphorescence or both.

$$k_r = k_{Fl} + k_{Ph} \tag{18}$$

k_{nr} is the rate constant for radiationless decay, including intersystem crossing and interconversion; and k_p is the rate constant for excited-state decomposition or other intra-molecular process. Non-radiative pathways (equations (2) and (4)) reduce the probability of emission of a photon and are all accounted for in the rate constant k, expressed as the sum of all rate constants for both emissive and non-emissive processes:

$$k = k_r + k_{nr} + k_p \tag{19}$$

When equation (17) is written in the logarithmic form,

$$\ln([A^*]) = \ln([A^*]_0) - kt \tag{20}$$

the rate law for first-order systems can be displayed in a plot of $\ln([A^*])$ versus time, and yields a straight line with slope (- k) and intercept of $\ln([A^*]_0)$. As previously mentioned, the overall rate constant of an exponential decay is the inverse of the *observed* lifetime of the excited species.

$$k = \frac{1}{\tau} \tag{21}$$

The *radiative* lifetime, on the other hand, is the inverse of the radiative constant alone ($\tau_r = 1/ k_r$). If the observed lifetime and the concentration of the excited species can be determined experimentally, the rate constant for the process can be established as well. Radiative lifetimes are not observable, but can be calculated when the other constants are known. The same system under constant-intensity excitation (steady state) is still a first

or pseudo-first order system. Given that the excited state population does not change overtime, the rate law becomes:

$$\frac{d[A^*]}{dt} = 0 = I - k[A^*] \qquad (22)$$

The concentration of the excited state in steady-state conditions and is given by:

$$[A^*]_{ss} = \frac{(\text{rate of formation of } A^*)}{(\text{rate of disappearance of } A^*)} = \frac{I}{k} \qquad (23)$$

The rate of formation, I, may vary during the course of an experiment, but during a single excited state measurement remains virtually constant and can be treated as such. If I is constant, the rate constant k is also assumed to be time independent.

Monitoring the decay curve does not provide direct information about the relative magnitude of each rate constant (k_r, k_{nr}…etc), or even the number of processes involved, only the overall rate of decay. To obtain k_r, k_{nr}, and k_p in addition to the lifetime, the luminescence photon or quantum yield is required. The photon yield, Φ_{em}, with values ranging from zero to near unity, is the probability that an excited molecule will emit and equals the ratio of the rate of photon emission to the total rate of excited state loss. In this case,

$$\Phi_{em} = k_r /(k_r + k_{nr} + k_p) = k_r \tau \qquad (24)$$

The photon yield and the lifetime are experimentally observable, and from their value, the rate constant is calculated:

$$k_r = \Phi_{em} / \tau \qquad (25)$$

Similarly, the yields for non-radiative processes are:

$$\Phi_{nr} = k_{nr}/(k_r + k_{nr} + k_p) \qquad \Phi_p = k_p/(k_r + k_{nr} + k_p)$$

(26)

Together they account for the total energy lost,

$$\Phi_{em} + \Phi_{nr} + \Phi_p = 1 \tag{27}$$

In the absence of photochemistry, excited state decomposition ($k_p = 0$), and bimolecular quenching, the overall k_{nr} is also readily obtained from τ and Φ:

$$k_{nr} = (1 - \Phi)/\tau \tag{28}$$

Direct measurements of rates of interconversion or intersystem crossing are possible in principle, but in practice such measurements are not easily done because relaxation rates are very high and each individual process lacks a well-characterized spectroscopic signature associated with it. Many upper excited states emit too weakly for detection and except for rare cases, only the first singlet and triplet state of most molecules emit measurably. One way to establish if "upper excited states" are involved in photoreactions is to determine if the reaction is wavelength-independent or not. If it is independent, then a common structure is responsible for the result. Lack of wavelength-dependence however, only eliminates upper singlet levels, while leaving open the possibility that a triplet derived from the S_1 state might be the reactive state. The invariance of the photon yield on excitation usually establishes that the rate constants for the photophysical processes of interconversion and intersystem crossing are so large that they happen with a quantum efficiency of unity.

Now, if a bimolecular deactivation process does take place (equation (5)-(8)), and if the concentration of the quencher remains constant during the course of the experiment, the system is referred to as pseudo-first order. Second-order terms need to be considered

in establishing the kinetics of the system, but are assumed not to vary with time. Many substances efficiently quench excited states by a bimolecular collisional process. A notoriously good one is oxygen, which explains why solutions for photochemical experiments are frequently deoxygenated before being tested.

A *Stern-Volmer analysis*[14,15] can be performed to obtain quantitative information about the kinetics of a pseudo-first order system arising from the competition between a bimolecular process and unimolecular decay pathways of the excited molecule. This type of analysis consists in tracking variations of quantum yields or lifetimes of photophysical (fluorescence, phosphorescence) or photochemical (redox, exciplex formation…) processes or decays as a function of the concentration of a given reagent or quencher. The simplest situation that can be envisioned is a reaction mechanism which involves a competition between a unimolecular decay of A^* and a bimolecular quenching by a deactivator or quencher Q (Scheme 3).

Scheme 3: Reaction steps involving competition between decay and quenching.

$$A + h\nu \xrightarrow{I} A^* \qquad \text{Rate} = I \qquad (1)$$

$$A^* \xrightarrow{Knr} A + \Delta \qquad \text{Rate} = k_{nr}[A^*] \qquad (2)$$

$$A^* + Q \xrightarrow{Kq} A + Q + \Delta \qquad \text{Rate} = k_q[Q][A^*] \qquad (6)$$

where k_q is the rate constant for bimolecular quenching. The rate constants for other non-radiative decay processes, such as intramolecular excited state deactivation and direct excited state decomposition have been omitted but are considered to be part of k_{nr}. The lifetime and radiative rate constant associated with the unimolecular decay of A^* in

the absence of Q are τ_0 and k_{nr} respectively. In the presence of the quencher the overall rate constant is defined using the theoretical rate law expressions as:

$$k = k_{nr} + k_q[Q] = \frac{1}{\tau_0} + k_q[Q] \quad (29)$$

and the shortened (quenched) lifetime of A^*, τ, in accordance with equation (21) is:

$$\tau = \frac{1}{k} = \frac{1}{k_{nr} + k_q[Q]} \quad (30)$$

When both lifetimes are measurable, and [Q] is known, k_q can be determine graphically by plotting the values of k as a function of [Q]: the slope of the graph corresponds to k_q.

If the excited state undergoes emission as well, the system is described by the set of reactions in Scheme 3 plus equation (3). The rate constant again incorporates all the rate constants for deactivation and can still be expressed as in equation (29), keeping in mind that the lifetime in the absence of quencher now includes the radiative rate constant:

$$k = k_r + k_{nr} + k_q[Q] = \frac{1}{\tau_0} + k_q[Q] \quad (31)$$

with

$$\tau_0 = \frac{1}{k_r + k_{nr}} \quad (32)$$

and

$$\tau = \frac{1}{k} = \frac{1}{k_r + k_{nr} + k_q[Q]} \quad (33)$$

The Stern-Volmer equation for lifetime quenching can be derived combining eqns. (32) and (33):

$$\frac{\tau_0}{\tau} = 1 + k_q \tau_0 [Q] \qquad (34)$$

The system is said to follow Stern-Volmer kinetics if a plot of lifetimes versus the concentration of the quencher [Q] yields a straight line with an intercept of 1.0 and a slope equal to the Stern-Volmer constant, K_{SV} or $k_q \tau_0$.

Experimental observation of Stern-Volmer quenching is in itself evidence for an intermediate being intercepted by the quencher, with larger values of K_{SV} corresponding to more efficient quenchers. The constant $k_q \tau$ is characteristic of that intermediate for a given solvent and temperature. Because k_q is limited by the rate of diffusion, the *minimum lifetime* of the species quenched can be calculated if $k_q = k_{Dif}$. If only one state is quenched, and if the species is non-emissive the lifetime can be derived from the plot, provided that k_q is known for similar systems in the same solvent.

Under steady-state excitation:

$$\frac{d[A^*]}{dt} = 0 = I - (k_r + k_{nr} + k_q[Q])[A^*] \qquad (35)$$

and the concentration of the excited state in steady state conditions is given by:

$$[A^*]_{ss} = \frac{(\text{rate of formation of A*})}{(\text{rate of disappearance of A*})} = \frac{I}{k_r + k_{nr} + k_q[Q]} \qquad (36)$$

As defined by equation (24), the emission efficiency in the absence of quencher can be mathematically expressed by:

$$\Phi_r^0 = \frac{k_r[A^*]}{I} = \frac{k_r}{k_r + k_{nr}} = k_r \tau_0 \qquad (37)$$

However, because of the lifetime quenching, all the unimolecular pathways of A^* become less efficient in the presence of Q according to:

$$\Phi_r = \frac{k_r[A^*]}{I} = \frac{k_r}{k_r + k_{nr} + k_q[Q]} = k_r\,\tau \qquad (38)$$

and a Stern-Volmer equation for emission quenching can be derived combining equations (37) and (38):

$$\frac{\Phi_r^0}{\Phi_r} = 1 + k_q\tau_0[Q] = 1 + K_{SV}[Q] \qquad (39)$$

Since quantum yield values are proportional to the emission intensity observed experimentally at a given wavelength, $I_r(\lambda)$, a similar relationship between k_q and the intensity of the emission exists,

$$\frac{I_r^0}{I_r} = 1 + k_q\tau_0[Q] = 1 + K_{SV}[Q] \qquad (40)$$

If the quencher inhibits either a photochemical reaction or a photophysical process by a single reaction, the mechanism written predicts that quantum yields, emission intensities and lifetimes will vary with quencher concentration according to the Stern-Volmer equations. In principle, both intensity and lifetime data can yield the same results if a simple diffusional quenching model holds. Typical Stern-Volmer plots offer a straightforward way to obtain the bimolecular rate constant of the quenching process and establish its efficiency. Similar equations can be written for quenching of photochemical reactions, or when the competing bimolecular process involved is energy or electron transfer.

For several reasons including the presence of competing quenching mechanisms, multiple emitting states or the so-called static quenching, experimental complications may arise. If additional bimolecular quenching mechanisms are present, equations (34) and (39) are still valid, provided that k_q is replaced by the sum of the rate constants of the

various bimolecular processes. When several excited states are involved, the mechanism becomes more complex and, at the same time, more ambiguous. In such cases, there are often more parameters -such as rate constants- than there are independent data sets to determine them. In the presence of static quenching, deviations from linearity in the Stern-Volmer plots for emission and photoreaction quenching are expected.

1.B.4. Static quenching

Discrepancies between the ϕ and τ Stern-Volmer plots can supply useful chemical information and be an indication that alternative quenching mechanisms are at play. When an interaction between a photochemically active species and a quencher takes place both in the ground state and in the excited state, as is the case for ion-pairs between ions of different sign, two kinds of quenching are said to be happening at the same time: “static” and “dynamic”. Static quenching refers to bimolecular processes that occur prior to excitation, whereas dynamic quenching refers to diffusional processes that occur after excitation.

Scheme 4: Static and dynamic quenching.

$$\begin{array}{l} A + Q \xrightarrow{h\nu} A^* \xrightarrow{+Q} \text{dynamic quenching} \\ \uparrow\downarrow K_{eq} \\ A\text{-}Q \xrightarrow{h\nu} (A^*\,Q) \longrightarrow \text{static quenching} \end{array}$$

K_{eq}, the ground-state association constant for the equilibrium, gives an indication of the extent of adduct formation:

$$A + Q \underset{k_{-d}}{\overset{k_d}{\rightleftarrows}} A\text{-}Q \qquad K_{eq} = \frac{[AQ]}{[A][Q]} = \frac{k_d}{k_{-d}} \qquad (41)$$

k_d is the bimolecular rate constant for association and k_{-d} is the unimolecular rate constant for dissociation. As shown in Scheme 4, the incident light is absorbed not only by A but also by A-Q. If A and A-Q have the same molar absorptivity at the exciting wavelength, the fraction of light absorbed by uncomplexed A molecules, χ, is given by:

$$\chi = (1 + K_{eq}[Q])^{-1} \qquad (42)$$

and the fraction of light absorbed by A-Q is $(1 - \chi)$ of I (defined in equation (1)). Consequently, the labile adducts formed in the ground state reduce the intensity of the absorbed light that can lead to emission.

Furthermore, each A-Q species that gets excited, (A*-Q), may undergo deactivation before having had the chance to dissociate, and before A^* had the chance to emit. Thus, static quenching alone decreases the emission intensity from A^*, while it does not affect the emission lifetime since the latter is an intrinsic property of the A^* molecules, regardless of their concentration. Under such conditions, equations (34) and (39) no longer yield coincidental plots of the quantum yield of emission and the luminescence lifetime *vs* the quencher concentration. Static quenching is postulated to occur simultaneously with dynamic quenching if the ground-state association affects both quantum yields and lifetimes. The direct proportionality between quenching and concentration of quencher no longer holds and Stern-Volmer data will not yield a straight line, since the rate of quenching is faster than would otherwise be if the quencher were diffusing up to the excited donor. For such situation, it was shown[16] that the following relation holds:

$$(\phi_0/\phi)(\tau/\tau_0) = 1 + K_{eq}[Q] \qquad (43)$$

and the association constant can be evaluated by combining static and dynamic quenching experiments. For equilibria with large values of K_{eq} the chromophores can be thought as irreversibly "pre-quenched" and the Stern-Volmer plot will show positive deviations from linearity. Equilibria with small K_{eq} show negative deviations in their Stern-Volmer plot and a tendency to reach a limiting value at high [Q]. Hoffman, Bolletta, Moggi and Hug[17] have reported a detailed steady-state treatment of static quenching for reversible and irreversible quenching reactions. In this review, the expressions for positive and negative deviations from Stern-Volmer are discussed.

When association takes place between counter ions in an ion pair, several parameters of the medium (such as, e.g., viscosity, dielectric constant and ionic strength) must be kept constant during the quenching experiments or otherwise taken into consideration in order to interpret correctly a quenching process.

1.B.5. Protonation & Acid-Base reactions

Protolytic equilibria constitute an important group of reactions and a particular kind of static and dynamic quenching, relevant to the ruthenium systems studied here. As previously mentioned, chemical compounds in an electronically excited state may take part in reversible reactions analogous to those undergone in the ground state. Since excited molecules may be regarded as distinct from the molecules in the ground state, the equilibrium constants in the excited state may also differ from those in the ground state. Due to the relocation of charge, excited states may be stronger Brønsted acids or bases. Alternatively, protonation (or deprotonation) in the excited state may lead to radiationless

relaxation of the chromophores or formation of new species that relax radiatively, either way, causing repercussions on the equilibrium (equation (44)).

$$[HA \cdot H_2O]^* \underset{k_{-a}}{\overset{k_a}{\rightleftharpoons}} [A^-]^* + H_3O^+ \qquad K_a{}^* = \frac{[A^-]^*[H_3O^+]}{[HA \cdot H_2O]^*} \qquad (44)$$

Considering the short lifetimes of the species under investigation and the low concentration in solution, the equilibrium in the ground state is not affected by the changes happening in the excited state and if changes in the ground state do happen they are sufficiently small to be neglected without loss of integrity in the results.

Assuming that both species in the ground state, HA and A^-, absorb at different wavelength and have distinct emissions, it is possible to differentiate spectroscopically the regions of the pH scale, where only HA or A^- are present and luminesce. At intermediate pH values, one species may be predominant in the ground state, but upon excitation it may undergo a protolytic reaction and the emission band may be due to a different species than the one responsible for the absorption band in the UV-Vis spectrum.

Förster distinguished two categories of compounds that exhibit excited state equilibria: the ones reaching equilibrium in the excited state before luminescence occurs, and the ones that do not achieve equilibrium before emitting. The change over from the basic to the acidic spectrum with changing pH observed by Förster for naphthylamines in water is quite steep (i.e. within 4 pH units), indicating that the equilibrium in the excited state is almost completely established before the two forms fluoresce. Phenols are also more strongly acidic in the excited state, but the protonation is generally not sufficiently rapid to achieve equilibrium before radiative and radiationless depopulation of the excited states occurrs. If protonation in the excited state is slow compared to the back

reaction or other deactivation processes, excited molecules may start to ionize, but before deprotonation can be completed, the remainder of the excited molecules would have returned to the ground state through any of the other more efficient pathways, thus allowing fluorescence emissions of both forms to be present over a wide range of pH values. Accordingly, the pH-dependence of emission spectra is affected both by the pK_a^* of the excited state equilibrium, and the rates of reaction.

In general, two conditions must be satisfied in order to observe appreciable emission in intermediate situations when both protonated and unprotonated form are present in solution and both are capable of emitting. First, protonation must occur "adiabatically", without loss of electronic excitation energy, meaning that the bimolecular encounter must be fast enough to compete with non-radiative deactivation of $[A^-]^*$ and direct formation of ground state molecules:

$$k_{-a}^* [H_3O^+] \gg k_{nr} \qquad (45)$$

This may frequently *not* be the case, since H^+ is light and the bond formed is a facile oscillator that can efficiently dissipate energy to the surroundings. Transfer of a proton to an excited base may result in loss of excitation due to reorganization and subsequent production of the ground state protonated species. From a practical point of view, the proportion of excited molecules undergoing adiabatic proton transfers, would count as being quenched either by protons or by solvent and the effect included in k_q or k_{nr}.

Second, the reaction must be fast enough to compete with first order radiative and non-radiative conversions to the ground state hence the dissociation constant must be larger or equal to the inverse of the lifetime of the excited species:

$$k_{-a}^* \geq \frac{1}{\tau_o} \qquad (46)$$

Both of these conditions are satisfied for many luminescent systems, although oftentimes the equilibrium in the excited state is not completely established before emission occurs.

The first observation of luminescence due to protolytic dissociation was reported by Weber[18], who observed a shift in emission in an organic molecule not correlated with a change in absorption spectrum. The effect was later interpreted by Förster[19-20], who demonstrated the occurrence of excited state dissociation in similar organic systems. For compounds that are stronger acids in the excited state, Förster showed by fluorescence spectroscopy that in aqueous solutions of organic compounds, the acid dissociation equilibrium in the excited state is at least partially established at pH values six or more units lower than the pK_a value of the ground state equilibrium. This is indicated by the appearance of the fluorescence of the dissociated form at pH lower than usual. Similar results have been obtained for acids that are weaker in the excited state. This time a much lower acidity is sufficient to observe the protonated form of the analyte.

The Förster cycle discussed in paragraph 1.B.2 can be applied to the specific equilibrium of protonation and deprotonation, assuming once again that the entropy change is not significant between ground and excited state. The Förster cycle combines information about the ground and excited state and relates them to each other by suggesting that, if equilibrium conditions can be established in both ground and excited state, the change in enthalpy (and hence in Gibbs free energy) is proportional to the difference observed between emissions (or absorptions) and is also proportional to the change in pK_a value. Adapting equation (10) to a Brønsted acid-base equilibrium (equation (44)):

$$\Delta H - \Delta H^* \approx \Delta G - \Delta G^* = N_A h \left(\tilde{\nu}_{A^-} - \tilde{\nu}_{HA} \right) \qquad (47)$$

where N_A is Avogadro's number, and the form with an absorption band at longer wavelength is the more stable in the excited state. Also:

$$\Delta G - \Delta G^* = 2.303\ RT\ (pK_a^* - pK_a) \qquad (48)$$

Acids may be stronger ($pK_a^* < pK_a$) or weaker ($pK_a^* > pK_a$) in the excited state. From both equations, (47) and (48), it follows that in order to calculate the pK_a values in the excited state for a particular molecule (pK_a^*), it is necessary to know the ground state equilibrium constant for the reaction in question and to have some measure of the energy difference between the lowest vibrational level of the ground and excited state, the 0-0 transition, in both the HA and A^- forms:

$$pK_a^* = pK_a - \frac{0.625}{T}\ \Delta\tilde{\nu}\ (cm^{-1}) \qquad (49)$$

If the molecules of interest absorb at substantially different wavelengths in the HA and A^- forms, the ground state pK_a for the acid dissociation equilibrium is commonly determined following variations of a ground state property of the system, such as electronic absorption as a function of pH. The energy difference between the 0-0 transitions for compounds that emit can, in principle, be obtained following one of three approaches: the use of absorption maxima, the use of luminescence maxima and the averaging of the absorption and emission maxima of each form. In practice, with the exception of those cases in which molecules shows vibrational fine structure in the absorption or emission spectrum, a good value for the energy of the 0-0 transition is not easy to obtain. For most substituted aromatic compounds or transition metal complexes containing aromatic portions, the absorption and emission spectra in solution are characterized by broad, structureless bands. If the position of the 0-0 transition cannot be

located, the best estimate for the energy is obtained from the mean of the two maxima of the longest wavelength feature for absorption and emission:

$$E = ½ (h\nu_{abs} + h\nu_{em}) \quad (50)$$

provided that it can be established without doubt that they both refer to the same transition. For organic molecules such as the ones studied by Weller and Förster[19-20], and reviewed by Ireland and Wyatt[21], absorption and emission involve the same singlet states and the entropy assumption is valid. For transition-metal complexes where spin-orbit coupling may be extensive, the absorption and emission bands may not engage the same states, as the emitting states may have a different spin character. Furthermore, it is often found experimentally that the acidic (or basic) form is non-emissive; hence it is sometimes necessary to estimate the 0-0 transition energy differently for the acid or base forms.

If the compound does not fluoresce, an approximation for $\Delta\tilde{\nu}$ can be obtained from the difference in the absorption maxima and the pK_a^* value can be estimated from absorption measurements alone. The pK_a^* values calculated this way are mainly of theoretical interest since the lifetime of the S_1 state is likely to be too short to allow the protolytic reaction to reach equilibrium. Another drawback of using this approach is that absorption measurements monitor the singlet states associated with the absorption, and do not necessarily provide the same information that could have been obtained from emission measurements which may arise from excited singlet state, triplet state or a combination of both. Clearly the Förster cycle gives precise pK_a^* values only in special cases but it does indicate the direction of the pK_a shift and often can offer a good approximation to the magnitude of the change.

Though helpful from a thermodynamic perspective, the Förster cycle does not indicate whether or not proton transfer in the excited state is kinetically feasible and gives no account of the relevant rates of the particular processes involved. The kinetics of fast reactions in the excited state, including protolytic equilibria, have been worked out by Weller[22-23] in the 60s and still constitute an important theoretical basis for the analysis of a wide range of reactions in the nanosecond to microsecond time-scales.

Assuming that an aqueous solution contains a luminescent acid HA and its conjugate base A^-, upon light excitation the following reactions may take place to various extents:

Scheme 5: Protolytic reactions of HA and its conjugate base in the excited state.

$$HA^* + H_2O \underset{[H_3O^+]\,k_{-a}^*}{\overset{k_a^*}{\rightleftarrows}} A^{-*} + H_3O^+ \quad (51)$$

$$HA^* \xrightarrow{k_r} HA + h\nu \quad (52)$$

$$HA^* \xrightarrow{k_o} HA \quad (53)$$

$$A^{-*} \xrightarrow{k_r'} A^- + h\nu' \quad (54)$$

$$A^{-*} \xrightarrow{k_o'} A^- \quad (55)$$

If the solution contains a buffer acid HB and its conjugate base, an additional protolytic reaction should be included:

$$HA^* + B^- \underset{[HB]\,k_{-b}^*}{\overset{k_b^*[B^-]}{\rightleftarrows}} A^{-*} + HB \quad (56)$$

At very low and very high pH values where emission from only one species is observed the efficiencies of luminescence from HA^* and A^{-*} are ϕ_o and ϕ_o' respectively.

$$\phi_o = k_r/(k_r + k_o) = k_r\tau \quad (57)$$

$$\phi_o' = k_r'/(k_r' + k_o') = k_r'\tau' \quad (58)$$

where τ and τ' are the lifetimes of HA^* and A^*, respectively.

If the emission spectra of the acid-base pair overlaps, at intermediate pH values the emission efficiency measured for each form, φ and φ', contains a component due to the other form. The true efficiencies (ϕ) are related to the measured emission efficiencies, according to the equations:

$$\varphi = \phi + k'\phi' \qquad \varphi' = \phi' + k\phi \quad (59)$$

which, upon rearrangement, become:

$$\phi = (\varphi - k'\varphi')/(1 - kk') \qquad \phi' = (\varphi' - k\varphi)/(1 - kk') \quad (60)$$

The overlap ratios, k and k' of the HA and A^- forms, are obtained from solutions containing only one luminescent species at a time in the excited state. In a solution where only HA emits, k is calculated from the ratio between the emission intensity at the analytical wavelength of A^- and the emission intensity at the wavelength where HA emission is measured:

$$k = \frac{I(\lambda_{A^-})}{I(\lambda_{HA})} \quad (61)$$

so that in the case limit where $I(\lambda_{A^-}) \rightarrow 0$, eqn. (59) reduces to $\varphi' = \Phi'$. Similarly k' can be determined from the emission spectrum of a solution where only A^- emits. If ϕ_o or ϕ_o' is not directly measurable, it can be determined from the relationship derived by combining the efficiencies from both forms of the acid-base pair:

$$\phi/\phi_o + \phi'/\phi_o' = 1 \quad (62)$$

The inflection point of the curve constructed by plotting relative efficiencies (ϕ/ϕ_o and ϕ'/ϕ_o') against acidity, gives a first approximation to the pK_a^*, assuming that the protolytic equilibrium is established within the lifetime of the excited state and that the lifetimes of the acid base forms are equal. However, more often than not, such assumptions do not hold true, particularly, when one of the two species is non emissive. If τ_o and τ_o' are the lifetimes of HA and A^- respectively, it can be shown that for excited state equilibrium to be achieved, the rates of decay for the excited base or acid must be much lower than the rate of protonation or deprotonation:

$$\frac{1}{\tau_o'} \ll k_{-a}^* [H_3O^+] \qquad \text{or} \qquad \frac{1}{\tau_o} \ll k_a \tag{63}$$

If, on the other hand, one form is short-lived the equilibrium will be shifted in the direction of formation of the shorter-lived species, in accord with Le Chatelier's Principle. Experimentally the compound will appear to be a weaker acid than it really is if HA is the shorter lived form (and vice versa it will appear as a stronger acid if A^- is shorter lived), since the equilibrium will shift towards formation of more HA and it will seem that more HA is present. So a correction must be made that takes into account the lifetime of the species involved in the excited state reaction:

$$pH = pK_a^* - \log(\tau_o/\tau_o') \tag{64}$$

Whenever possible, the direct measurement of excited state lifetimes and the study of the changes in lifetime with changes in experimental conditions can lead to the determination of rates of reactions and equilibrium constants. For instance, when a steady state is established for HA^* and A^{-*} in the absence of a buffer, it has been demonstrated[24] that the

following equation can be applied to obtain rate constants for the forward and reverse reactions if the lifetimes τ_o and τ_o' are known:

$$\phi/\phi_o = \frac{1 + k_{-a}\tau_o'[H_3O^+]}{1 + k_a\tau_o + k_{-a}\tau_o'[H_3O^+]} \tag{65}$$

$$\phi'/\phi_o' = \frac{k_a\tau_o}{1 + k_a\tau_o + k_{-a}\tau_o'[H_3O^+]} \tag{66}$$

Equation (65) (or (66)) can be re-written in a form that allows a more immediate graphical determination of the thermodynamic constant and yields a linear plot as a function of acidity:

$$\frac{1}{\phi_o/\phi - 1} = \frac{1}{K_a^*} + \frac{\tau_o'[H_3O^+]}{\tau_o(K_a')^*} \tag{67}$$

where

$$(K_a')^* = k_a^*/k_{-a}^* = K_a^*/f^2 \tag{68}$$

K_a^* is the thermodynamic equilibrium constant in the excited state and f is the mean activity coefficient. Weller found that plots of $(\phi_o/\phi - 1)^{-1}$ against $f^2[H_3O^+]$ deviated from linearity at high acidity. This deviation is due to the fact that eqn. (67) is strictly valid only when a steady state is established. To eliminate the effect of transient reaction rates, it is necessary to quantify the fraction W of excited molecules that obey equation (56). The residual fraction, (1-W), emits without having reacted and represents the probability of finding at least one proton (or hydroxyl ion) within the volume of diffusion around the excited molecules. It is possible by successive approximation to obtain a value for W, and thus obtain satisfactory linear plots from which values of $\tau_o k_a^*$ and $\tau_o'/\tau_o(K')^*$, can be

derived and consequently also K^* and the rate constants k_a^*, k_{-a}^*. The values obtained will still depend on the ionic strength of the solution if the reaction takes place between charged particles.

In the presence of a buffer, similar equations can be derived. The assumption that a steady-state concentration is fully established in the excited state leads to negligible errors in organic systems and the data treatment outlined by Weller can be used. The presence of other acids or bases will affect the equilibrium concentrations only to the extent it affects the pH value and activity coefficients. However it can produce profound changes in the rates of the reactions involved in the equilibrium, and hence alters the intensities of emission if radiative decay occurs before equilibrium is established. Using Weller's method it is possible to work out kinetic expressions for the reactions taking part in an aqueous solution of buffer and chromophores.

1.B.6. Energetics and Kinetics of Transition Metal Exciplexes

The first studies of inorganic exciplexes began to be published in the 70s, stemming from the interest in their potential role as light sensitizers on solar energy storage and conversion. Many research groups focused their efforts in trying to gain a better knowledge of the nature of exciplexes and a deeper understanding of their role in the mechanisms of light-induced chemical processes. After more than a decade, Horvath and Stevenson reviewed the progress made and gave a summary of photophysical and photochemical properties of exciplexes, considering the electronic structure and the role of energetics and kinetics in their formation and stabilization[25]. This paragraph briefly touches upon some fundamental notions regarding exciplexes and outlines a kinetic

treatment of interest for application to excited state processes involving ruthenium diimines.

When an excited molecule comes in contact with a quencher (anything other than solvent), the two species often relax back to the original ground state species or diffuse apart. Charge, size and polarizability are some of the important factors affecting the diffusion of each species, and the outcome of the contact. In some instances, however, the interaction of the quencher and the excited chromophore may lead to the formation of an *exci*ted-state com*plex* (exciplex). Exciplexes are generally characterized by a strong binding energy (20-80 kJ mol^{-1}), a charge-transfer nature, a relatively long lifetime and moderate stability in the excited state. They are more frequently found in organic photochemical systems, and only rarely in inorganic systems involving transition metal complexes. The general quantum mechanical description of organic and inorganic exciplexes is the same, but transition metal complexes have additional excited states with d orbital character and because of spin orbit coupling, they do not have a clear singlet or triplet state. Exciplexes involving inorganic coordination compounds are often classified into two main groups based on the nature of the reactive site and the properties of the ground state reactant: Ligand-Centered, (LC) and Metal-Centered, (MC).

Ligand-centered exciplexes form when one of the species is a coordinatively saturated complex and the source of the interaction forming the exciplex is the ligand. Metal-centered exciplexes form from coordinatively unsaturated metal complexes and the metal is the interacting entity. In the LC type, favored in non-polar solvents, ligands possessing extended delocalized π electron systems tend to produce exciplexes with properties very similar to those of organic exciplexes. In the MC type of exciplexes, the

orbitals of the metal play a dominant role in the interaction. Most of the metal centers that are part of this group have a d^{10} electron configuration in the ground state (example Ag(I)) and their excitation leads to population of the diffuse ns orbital, providing an efficient overlap with an appropriate orbital of the molecular entity of the ground state, and stabilizing the exciplex.

The solvent plays an important role in the formation of an exciplex and its ability to luminesce, especially when there is a substantial change in electronic distribution between reactants and exciplex. The solvent molecules' response to changes in electron density can cause dramatic shifts in absorption or emission and thus alter the exciplexes' energetics and dynamics to a large extent. The dynamic interconversion between encounter pairs such as the exciplex and solvent-separated ion-pairs is also strongly influenced by interactions with the solvent molecules. For inorganic exciplexes, with constituents having similar electric charges, an increase in solvent polarity favors the formation of the exciplex as opposed to an ion pair, due to a considerable decrease in solvation energy in the exciplex case. In the case of constituents of opposite sign, the solvation term may actually stabilize more ion pairs, favoring dissociation of exciplexes and consequently exciplex emission may not be observed. From a kinetic point of view, rate constants for exciplex formation increase at high ionic strength, where shielding of charged species is increased. As for the ability to emit, it may decrease if the transition from excited state to ground state is accompanied by a significant change in molecular geometry, which may or may not be assisted by reorganization of solvent molecules. Indeed, changing the medium and the coordination sphere is used, in some cases, to fine

tune the potential barriers and enhance or reduce the processes leading to exciplex formation.

The In(III)-porphyrin exciplex studied in 1985 by Hoshino and coworkers[26] represents the first example of inorganic exciplex formation between two species of positive charge in a polar solvent. Laser flash photolysis experiments revealed an interaction between the excited triplet state of the complex $InTPP^{+}$ (Indium(III)tetraphenylporphyrin) and methylviologen (MV^{2+}) and based on the quenching kinetics suggested a mechanism involving an excited state equilibrium reaction with triplet exciplex formation. For ruthenium, the first example was reported a few years later, when Ayala et al.[27] and Tsobomura et al.[28] investigated in more detail the luminescent behavior of the $Ru(bpy)_3^{2+}$ - Ag^{+} system originally studied by Whitten and coworkers[29] in the early 1980s. They found that the lowest energy MLCT absorption band of the ruthenium complex in aqueous solution exhibited a small red shift in the presence of Ag^{+} ions. Luminescence studies also revealed a dramatic red shift in emission peak and a decrease in the peak intensity with Stern-Volmer plots showing strong negative deviations from the linear behavior. The evidence suggested that there was at least one new excited luminescent species and Tsobomura confirmed the formation of $[Ru(bpy)_3^{2+}\cdots Ag^{+}]^{*}$ and $[Ru(bpy)_3^{2+}\cdots Ag_2^{2+}]^{*}$ exciplexes by circularly polarized luminescence spectroscopy, probably involving the association of silver with the aromatic π system of the ligands.

The excited state reaction can be regarded as exciplex formation when the interaction between the two ground-state molecules is negligible or when the excited state equilibrium constant is larger than that of the corresponding ground state process:

$$K_e = \frac{k_e}{k_{-e}} \ll 1 \tag{69}$$

$$K_e^* = \frac{k_e^*}{k_{-e}^*} \gg K_e = \frac{k_e}{k_{-e}} \tag{70}$$

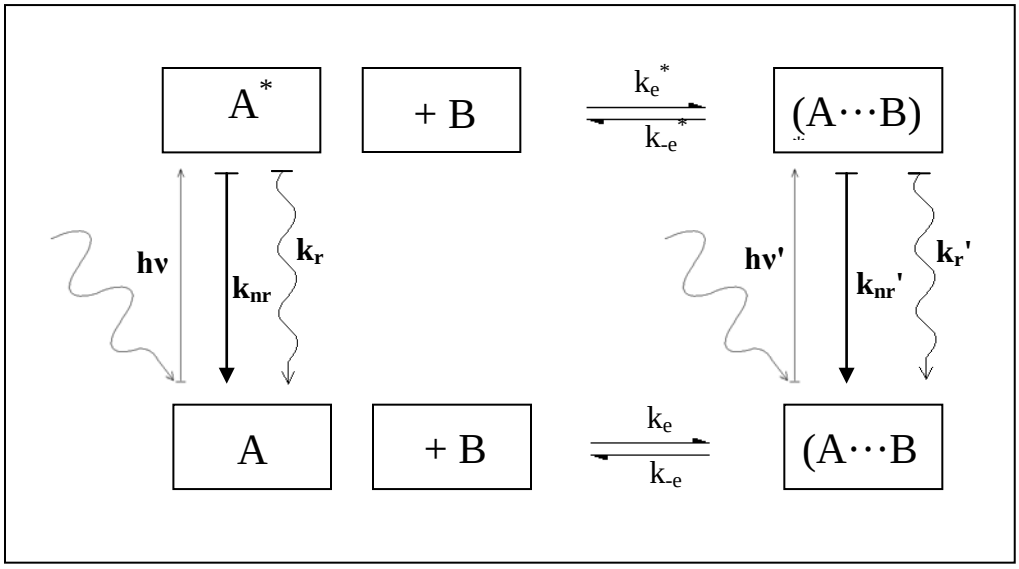

Figure 4: Ground and excited state interactions between A and B.

The decay rates of the two excited species, A^* and $(A\cdots B)^*$, are given by:

$$d[A^*]/dt = -(k_{nr} + k_r + k_e^*[B])[A^*] + k_{-e}^*[(A\ldots B)^*] \tag{71}$$

$$d[(A\ldots B)^*]/dt = k_e^*[B][A^*] - (k_{nr}' + k_r' + k_{-e}^*)[(A\ldots B)^*] \tag{72}$$

The general solution of equations (71) and (72) has been derived and results in fairly complicated expressions of the dependences of the concentration of the excited species with time. Simpler, more convenient expressions have been obtained in the 'equilibrium limit' case and for the steady-state approximation.

If the excited reaction has time to come to equilibrium:

$$k_e^*[B] \gg k_{nr} + k_r \tag{73}$$

$$k_{-e}^{*} >> k_{nr}' + k_r' \quad (74)$$

the ratio of populations of A^* and $(A\cdots B)^*$ is described by the equilibrium constant $K_e^* = k_e^* [B]/k_{-e}^*$. The lifetimes of the excited species are:

$$\tau_A = 1/(k_{nr} + k_r) \quad (75)$$

$$\tau_{(A\ldots B)} = 1/(k_{nr}' + k_r') \quad (76)$$

and the observed lifetime for the exciplex is given by:

$$1/\tau_{obs} = (1/\tau_A)\,(1 + K_e^*[B]) + (1/\tau_{(A\ldots B)})\,(K_e^*[B])/(1 + K_e^*[B]) \quad (77)$$

In the steady-state approximation, $[A^*] << [(A\ldots B)^*]$ and the lifetime observed experimentally is given by:

$$1/\tau_{obs} = [(1/\tau_A)\,(k_{-e}^* + 1/\tau_{(A\ldots B)}) + k_e^*[B]/\tau_{(A\ldots B)}] / [(1/\tau_A) + k_e^*[B]]$$

(78)

In both cases, if the lifetimes of the excited species A^* and $(A\cdots B)^*$ can be measured separately, quantitative data regarding the excited state equilibrium can be gathered knowing the observed lifetime at different concentrations of B.

1.C. Ruthenium diimines

The luminescent complexes of transition metals, such as Rh(III), Co(III), Ru(II), and other d^6 systems are of intense photochemical and spectroscopic interest, due to the fact that a variety of these complexes can be designed to possess radically different types of excited states lowest in energy and accessible with visible and near-UV radiation. There is an extensive excited state and redox chemistry based on the second and third row transition metals utilizing bi- or tri-dentate aromatic heterocyclic ligands. Ruthenium(II)-diimine complexes in particular possess rich and varied photophysical

properties. Probably the most studied among these metal complexes is $Ru(bpy)_3^{2+}$, tris(2,2'-bipyridine)ruthenium(II), with its highly desirable properties, including microsecond lifetimes in solution, intense visible absorption and emission, well defined redox chemistry, and high stability under many conditions (Figure 5).

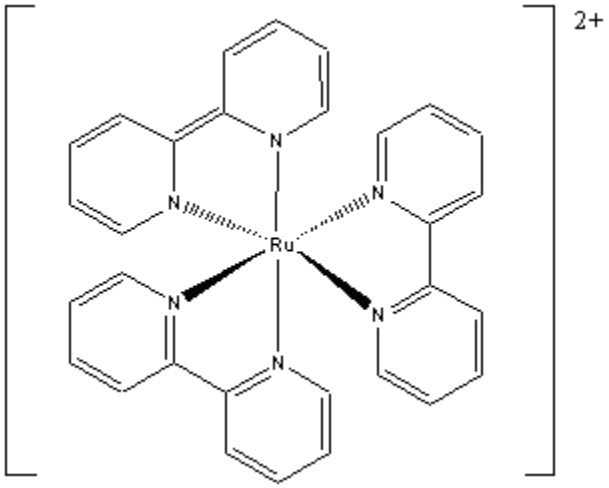

Figure 5: Schematic representation of $Ru(bpy)_3^{2+}$ complex ion.

The luminescence properties of the $Ru(bpy)_3^{2+}$ complex were first characterized by Crosby and coworkers[30,31] in the late 1960s and in 1972, Gafney and Adamson gathered evidence of electron-transfer quenching[32] from the excited state of $Ru(bpy)_3^{2+}$, at the time a rare occurrence in organic photochemistry and even more so among transition metal exciplexes. The discovery prompted other laboratories to investigate further the complex's reactivity. In the years that followed, several research groups[33,34,35,36] came to recognize that $Ru(bpy)_3^{2+}$ had interesting photoredox properties and suggested it could potentially be used as a photocatalyst[37] in practical devices for decomposition of water, as a sensor[38] for O_2, CO_2, pH and temperature and as a photon-

harvesting antenna[39,40] in solar energy conversion schemes. Today, in the face of rising fuel prices, global warming and environmental concerns, the need to find alternative ways to produce storable energy from readily available and fairly inexpensive raw materials is still very pressing. Likewise, after the latest attack on US soil and in the context of the war on terrorism, the demand for reliable and quick luminescent sensors for the detection of potentially harmful compounds such as amine-based explosives has become a priority. Now, while practical systems have yet to be developed, the progress achieved in this area over the years has been impressive and continued studies of Ruthenium-based systems are worth the effort because they increase the fundamental understanding of basic photochemical and catalytic processes and they suggest new research directions, which are likely to lead to improvements in system performance.

1.C.1 Spectral features

At least four major requirements need to be satisfied in order for a reactant to be considered a suitable component for applications based upon photochemical reactions.

First and foremost, the compound must absorb light with high efficiency over a wide range of wavelength in the solar spectral region. Many complexes or complex ions, especially those of metals in their lower valence states with π-conjugated ligands, such as $Ru^{II}(L)_3^{2+}$ (L = 2,2'-bipyridine, 1,10-phenanthroline, or other substituted derivatives), satisfy this requirement. Absorption of these complexes throughout the near UV and part of the visible range ($\lambda \leq 600$ nm) gives, independent of wavelength, intense and broad metal-to-ligand charge-transfer absorption bands around 400nm that span hundreds of nanometers and extend well into the visible region. The intense colors manifested by

these compounds are dramatic evidence of the occurrence of absorption bands that are neither $d \rightarrow d$ nor $\pi \rightarrow \pi^*$ in character. Indeed, following light absorption, an electron is promoted from a metal-based d orbital to a low lying π^* level on the polypyridyl ligand or other aromatic ring system and the lowest excited state is reached rapidly with near-unity interconversion efficiency from higher vibronic states. For the complex $Ru(bpy)_3^{2+}$, the efficiencies of populating the emitting level by internal conversion (IC) and intersystem crossing (ISC) is independent of the orbital parentage of the state initially excited (Φ_{IC} = 1 and Φ_{ISC} = 1). Evidence of the wavelength independence of the emission yield was recorded at low and room temperature for a variety of Ru(II) photosensitizers and is one of the many attractive features that qualifies Ru(II) complexes as photosensitizers. Bands arising from a series of MLCT transitions appear because low molecular symmetries lift the degeneracy of the $d\pi$ levels and the polypyridyl ligands have a series of π^* acceptor levels. Each individual MLCT transition has vibronic components and spin-orbit coupling "mixes" states that are singlet and triplet in character. The combination of multiple MLCT transitions, vibronic progressions and solvent broadening is what allows the $(d\pi)^6$ polypyridyl complexes to absorb light over a wide energy range. In addition, the range can be extended from the near infrared to the ultraviolet, or tuned systematically by adjusting the relative energies of the $d\pi$ and π^* levels through chemical changes in the metal or the surrounding ligands[41].

The other two requirements for compounds to be considered useful photosensitizers are closely related to the nature of the excited state populated upon light absorption: they must have sufficiently long excited state lifetimes to allow for bimolecular reactions to compete with other deactivation processes, and they should be

stable under the reaction conditions. The lowest excited states of Ru(II) with bidentate N-heterocyclic ligands do possess considerably long lifetimes on the order of hundreds of nanoseconds at room temperature in aqueous solution. Moreover, polypyridine-type ligands are often inert to photosubstitution in room temperature aqueous solution and therefore contribute to the overall stability. Like absorption, emitting-state energies and excited-state redox properties of the sensitizers also respond to variations in the metal, coordinating ligands and solvent, so changes in any of those areas provides the means to shift the relative positions of different excited states, and to "tune" photophysical and photochemical properties.

1.C.2 Redox properties

The stable and long lifetime of the excited state allows Ru(II) complexes with polypiridine-type ligands to undergo bimolecular processes such as electron-transfer. For the $Ru(bpy)_3^{2+}$ complex, both reductive quenching and oxidative quenching have been observed with a variety of oxidants or reductants. After the charge transfer transition, the complex can be simplistically visualized as possessing a hole in the t_{2g} orbital set with the excited electron residing on the ligand system. The creation of a separated electron-hole pair within the complex transforms $^{*}Ru(bpy)_3^{2+}$ into both a stronger reductant and a stronger oxidant than the ground state by the excitation energy of 2.1 eV. Reductive quenching of $^{*}Ru(bpy)_3^{2+}$ produces the powerful reductant, $Ru(bpy)_3^{+}$, while oxidative quenching generates the potent oxidant, $Ru(bpy)_3^{3+}$. Electron transfer is rapid because the differences in structure that exist between $^{*}Ru(bpy)_3^{2+}$ and $Ru(bpy)_3^{+}$ or $Ru(bpy)_3^{3+}$ are small. This minimizes the barrier to electron transfer that arises from intramolecular

structural changes, while the barrier arising from the reorientation of solvent dipoles is thought to be small because the complexes are relatively large.

For $Ru(bpy)_3^{2+}$ in water, the potentials (vs NHE) are shown in Figure 6 and equations (79) and (80).

$$^{*}Ru(bpy)_3^{2+} + e^- \rightarrow Ru(bpy)_3^{+} \qquad E^{\circ\prime}_{ox} = 0.72\ V \qquad (79)$$

$$Ru(bpy)_3^{3+} + e^- \rightarrow {}^{*}Ru(bpy)_3^{2+} \qquad E^{\circ\prime}_{red} = -0.74\ V \qquad (80)$$

From an energetic perspective, the equations above show that both pathways for bimolecular electron transfer are a viable option in the excited state, but if there is no spatial separation between the photoproduced oxidant/reductant pair, as soon as they return to the ground state, the recombination by back electron transfer is inevitable and too fast to be intercepted by another reaction.

$$Ru(bpy)_3^{2+} + e^- \rightarrow Ru(bpy)_3^{+} \qquad E^{\circ\prime}_{ox} = -1.28\ V \qquad (81)$$

$$Ru(bpy)_3^{3+} + e^- \rightarrow Ru(bpy)_3^{2+} \qquad E^{\circ\prime}_{red} = 1.26\ V$$

(82)

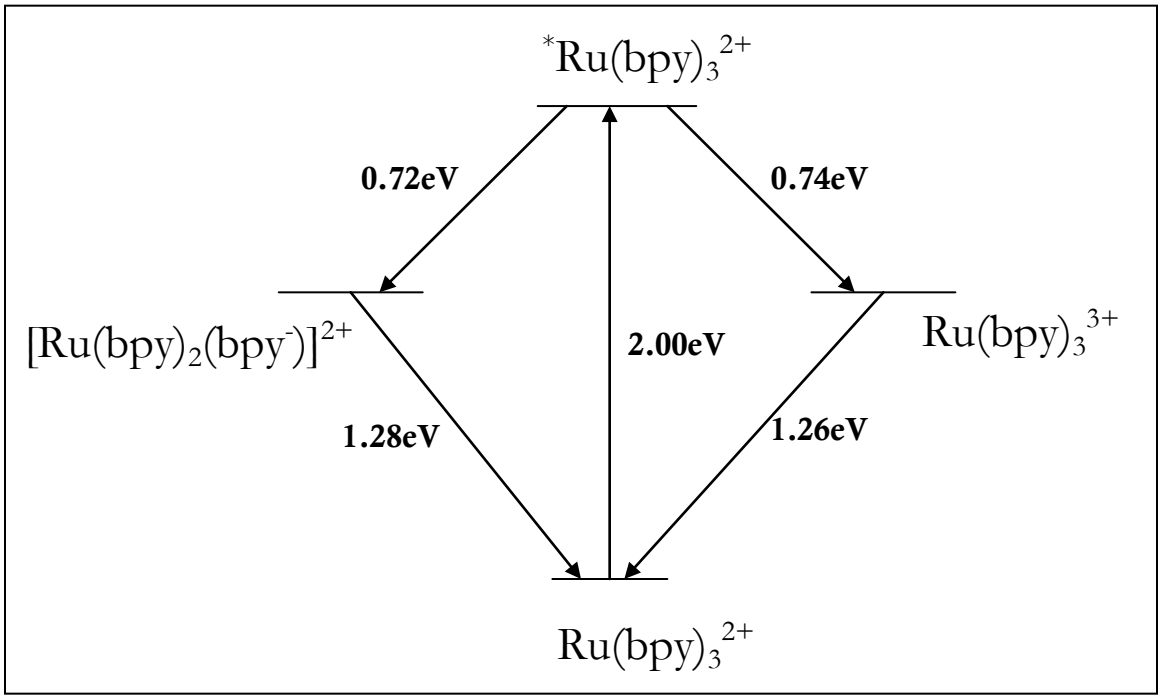

Figure 6: Redox potential for $Ru(bpy)_3^{2+}$ and its excited state form.

In an attempt to convert the incident photon energy into transiently stored potential energy, several researchers sought out a mean to direct the oxidative and reductive equivalents toward spatially separated catalysts. On a molecular level, this implied trying to build a directional charge-transfer character into the system by spatially separating the oxidized and reduced parts of the molecule with a molecular connector or by creating a gradient that could render the back reaction unfavorable. In his article[7], Dr Meyer describes examples of synthetic molecules in which the separation of oxidative and reductive equivalents induced by light absorption is accomplished by placing the chromophore and the electron-transfer donors and acceptors in appropriate spatial arrays so that they are chemically attached to each other but at separate sites. One approach takes advantage of the multiple sites on a polymer and explores the possibility to add chromophores-quencher assemblies to it. Variations of the same theme involve addition of chromophores and quenchers to different polymeric strands, inclusion in micelles or vesicles, and deposition on polymeric films covering conducting electrodes. Another approach, synthetically challenging but that could potentially produce more compact and manageable systems, involves the construction of a single large molecule in which chromophores and quencher are chemically attached to the oxidative or reductive catalyst via a bridging ligand. For this purpose, a series of interesting chromophores based on pyridines and polypyridines have been prepared, such as $[Ru(bpyCH_2OCH_2An)_3]^{2+}$, where visible light absorption by the Ru-bpy moiety is followed by intramolecular electron transfer and formation of a triplet state on the anthracene end of the bridging

ligand. The complexes studied here fall into a third category which partly combines the ideas behind both approaches. While trying to take advantage of the interesting luminescent properties characteristic of $Ru(bpy)_3^{2+}$, efforts were made to synthesize molecules possessing a bridging ligand with free coordination sites that would enable the complex as a whole to function as a ligand and coordinate to other units, including polymers, according to the specific system requirements. At least in principle, the technical tools and knowledge of the synthetic chemistry of these systems are available to construct a complex electron-transfer apparatus of this kind, and having the option to connect the chromophore to different oxidative or reductive catalysts increases the versatility and broadens the applicability of a light-harvesting center. Interesting examples of complexes tested in this role include $[Ru(bpy)_2(dpp)]^{2+}$ (dpp = 2,2'-pyridyl-3-pyrazine)[42], $[Ru(bpy)_2(pypz)]^{2+}$ (pypz = 2-(2-pyridyl)pyrazine), and $Ru(bpz)_3^{2+}$ (bpz = 2,2'-bipyrazine)[43] .

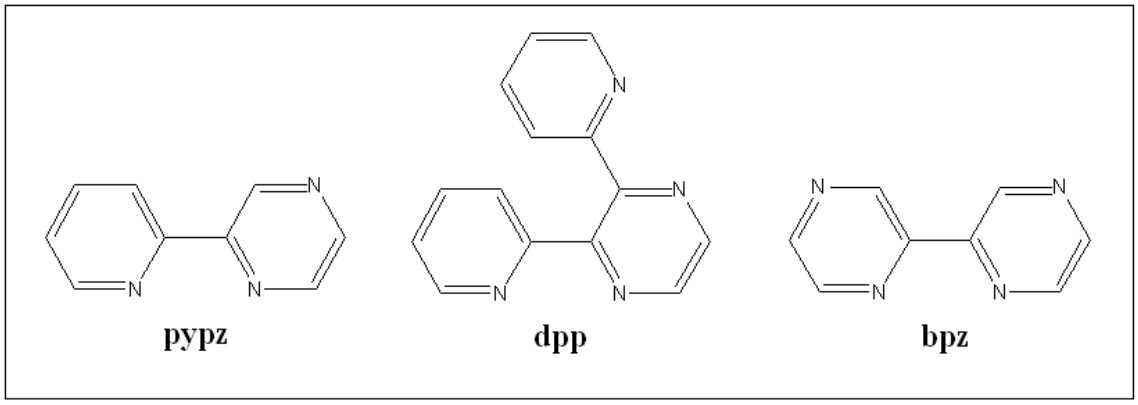

Figure 7: Structure of the polypyridine ligands, pypz, dpp, bpz.

This work does not delve into every aspect of the making of artificial photosynthetic machines, but takes a first step to understand the ground and excited state chemistry of one such molecule, $[Ru(bpy)_2(dpp)]^{2+}$, by synthesizing and studying its analogue, $[Ru(bpy)_2(pypz)]^{2+}$.

1.C.3 Background research on dpp and $[Ru(bpy)_2(dpp)]^{2+}$

From the point of view of structure, bridging ligands are appealing since they allow great flexibility in the design of molecular systems and potentially give rise to oligonuclear metal complexes and other complex supramolecular species. However, from the standpoint of the excited state properties, unsubstituted pyridine-based ligands such as 2,2'-bipyridine, bpy, and 1,10-phenanthroline, phen, coordinate more strongly with Ru(II) and their complexes in solution exhibit more intense and longer-lived luminescence than most Ru(II) complexes containing one or more bridging ligands. The ligand 2,3-bis(pyridyl)-pyrazine, abbreviated as dpp, having two chelation sites analogous to the bpy bidentate site seemed a promising candidate to fulfill the need for ligands with the electronic properties of bpy and phen and, at the same time, the structural properties of bridging units.

The dpp ligand, was first synthesized by Goodwin and Lions from 2,2'-pyridil and ethylenediamine in alcoholic solution[44]. Their study of the coordination chemistry of dpp with copper(II) chloride and iron(II) chloride in aqueous solution initially led to the disappointing observation that coordination at one bidentate site would prevent coordination at the second chelating site, due to spatial distortion of the third ring being pushed out of the plane by the first coordination interaction. Experiments seemed to

confirm that only one of the pyrazine nitrogens at a time had the capacity to function as a donor nitrogen atom. These results continued along the line of previous observations by Elderfield a couple of years earlier regarding pyrazine and the fact that coordination bonding of a pyrazine nitrogen atom to a metal atom seemed to markedly reduce any tendency of the second nitrogen atom of the pyrazine ring to indulge in coordination bonding[45].

Interestingly though, when Braunstein *et al.* utilized the ligand in the synthesis of asymmetrically substituted ruthenium(II)-bipyridine complexes, they observed that bimetallic species with dpp coordinated simultaneously to two metals do occur[46]. The flexibility of the free rotating pyridyl ligand turned out to be, in some respects, an advantage, as it can twist to accommodate chelation to a number of other metals[41,43,47,48]. In fact, complexes of ruthenium and other metals with three dpp bridging ligands, i.e. $Ru(dpp)_3^{2+}$, were afterwards used as building blocks to synthesize polynuclear compounds[49] of desired nuclearity containing many chromophoric and redox centers. More importantly, mono- and bi-metallic complexes with one bpy substituted by dpp, proved to be luminescent at room temperature. In general, deviations from a bipyridine-like structure in the bridging ligand would cause a loss of the d-π* luminescence characteristic of $Ru(bpy)_3^{2+}$ and its homologues, as slight differences in structure are sufficient to prevent luminescence. Conveniently however, the dpp ligand resembles closely enough 2,2'-bipyridine so that the dimmer $(bpy)_2Ru(dpp)Ru(bpy)_2^{4+}$ satisfies the criteria of field strength and coordination about each Ru(II) ion necessary for luminescence, which is helpful to provide information regarding excited state thermodynamics and kinetics.

Curiosity in the monometallic complex, $[Ru(bpy)_2dpp]^{2+}$ grew even more when attention was directed toward its excited-state coordination chemistry. Evidence showed that the complex's ability to function as a ligand is enhanced by light excitation because the MLCT transitions increase the electron density at the peripheral nitrogens and ultimately their basicity[50]. Increased basicity in the presence of a variety of transition metal salts in turn leads to coordination to a second metal and studies proved that there is a direct proportionality between increased basicity of the peripheral nitrogens and their ability to coordinate. This is not always the case, but researchers have observed in ruthenium diimines patterns of behavior consistent with increased excited state nucleophilicity[51]. The measurement of equilibrium constants for coordination reactions within a series of similar ligands[39] further substantiated the claim that nucleophilicity parallels basicity in pyridine-type ligands.

It follows that optical excitation may lead to a coordination chemistry unseen in the ground state or to formation of products at a faster rate. The reaction between $[Ru(bpy)_2dpp]^{2+}$ and $PtCl_6^{2-}$ resulting in formation of the bimetallic species, $[Ru(bpy)_2dppPtCl_4]^{2+}$, provides a good example. The reaction occurs thermally in refluxing ethanol over a relatively long period of time, but it may also be performed photochemically in a matter of minutes by exposing the reaction mixture to 457-nm light[47]. The absorption spectra taken at different time intervals reveal, in both cases, a red-shift of the MLCT transition to dpp due to coordination to platinum and increase in the metal content of the Ru(II) molecular entity.

This example and result is remarkable for several reasons. First because it shows how, unlike most photochemical reactions that tend to be dissociative in nature, reactions

with $^{*}[Ru(bpy)_2dpp]^{2+}$ result in an “associative” excited state coordination chemistry. Second, in contrast with what generally happens with monodentate ligands, the product is thermodynamically stable, thanks to the chelate, effect and does not dissociate back into the original reactants. Due to the difference between the energy provided by thermal and photochemical reactions, the former usually yields thermodynamically stable products, whereas the latter yields products that are stable only relative to the excited state. And transient products may not be detectable or quantitatively gathered, which explains why excited state coordination chemistry may have previously gone unnoticed. Third because, looking at it from a different perspective, the reaction is an example of a kind of quenching mechanism where a metal, the platinum complex, acts as a luminescence quencher. Contrasting with the case of electron- or energy-transfer, here changes in coordination are the cause of the reduced emission intensity and shorter lifetime. Finally, the most important reason why the example mentioned is relevant and innovative in its own way, is because it is a testimony of a photochemical reaction, where the interaction between reactants is the result of the increased electron density on the dpp moiety of the Ru(II) complex which exists only in the excited state, hence the interaction itself is more appropriately described as “exciplex” to emphasize the point that excitation facilitates the formation of the bimetallic relative to the ground state. Experiments confirm that the production of the bimetallic involves the excited $^{*}[Ru(bpy)_2dpp]^{2+}$ complex and formation of an exciplex with the platinum ion and that photolysis of platinum hexachloride, although possible, cannot alone be responsible for the observed changes. The photochemical synthesis of a bimetallic does not often occur among transition-metal complexes, since it has to compete with other more efficient excited-state processes, such

as electron- or energy-transfer. However in this case bimetallic formation is favored because the energy absorbed by $[Ru(bpy)_2dpp]^{2+}$ is not sufficient to render energy-transfer feasible and electron-transfer is likewise energetically implausible.

Examples like the one just described, are promising in the quest for systems mimicking the photosynthetic centers in plants and capable of performing multi-electron processes as they show new pathways to connect light-harvesting units to molecules capable of transient electron storage. However, the magnitude and mechanistic details of the basicity enhancement and interaction to other metals are not unequivocally established. In an attempt to exclude competitive processes such as electron- and energy-transfer from the system under study and focus on the affinity of peripheral imine nitrogens to metals, the work presented here considers solely the coordination chemistry that arises from the interaction with ^{10}d metals, specifically Zn^{2+}, Cd^{2+}, and Ag^{+}. Salts of these metals are soluble in water so that high concentrations of the quencher can be reached. But more importantly they do not possess d states at energies accessible for energy transfer and have unfavorable redox potentials for electron-transfer. Still, a competition that cannot be avoided is the one with protons as aqueous solutions of metals are often acidic. Hence a review of the acid-base chemistry of $[Ru(bpy)_2dpp]^{2+}$ is at the same time necessary and instructive in the discussion of the application of the MLCT states of Ru(II) diimine complexes in the formation of polymetallic complexes.

1.C.4 Excited-state Acid-Base Chemistry of $[Ru(bpy)_2(dpp)]^{2+}$

As previously mentioned, population of the emissive MLCT state of a complex possessing uncoordinated acid-base sites can, depending on the specifics of the charge

transfer, increase or decrease the basicity of the sites by several orders of magnitude. The more common situation, reported for several Ru(II) diimine complexes and one that applies to the research reported here, is the apparent increase in Brønsted basicity that occurs on excitation of $[Ru(bpy)_2(dpp)]^{2+}$. In mixed-ligand complexes such as this, excitation increases the charge density of the ligand containing peripheral electronegative atoms or substituents that can be easily reduced. As expected then, excitation of $[Ru(bpy)_2(dpp)]^{2+}$ leads to an MLCT state localized on the bridging ligand, dpp, and Resonance Raman spectra indicate, by the enhancement of the normal modes resonant with the MLCT $d\rightarrow\pi^*$ absorption at 470 nm assigned to dpp, that the majority of the electron density resides on or near the peripheral nitrogens[43].

The increased electron density at the peripheral nitrogen increases their basicity, a phenomenon that is reflected in the change in pK_a of the peripheral acid-base functionality, and is substantiated by the reported pH dependence of the emission lifetime and intensity. The pK_a values in the excited state are not necessarily the *actual* equilibrium values; they represent a thermodynamic value only if the excited state has time to reach equilibrium (equilibrate). The term "equilibrium" is used to describe a situation where the ratio of the protonated and deprotonated forms of a complex present under a given set of experimental conditions is not changing with time beyond what can be attributed to the excited-state lifetime of said forms. A published plot of the pK_a^* values versus the lifetimes of the deprotonated form for a series of Ru(II) diimines shows a curve that seems to reach a plateau above 300 ns with higher pK_a^* values obtained for complexes with longer lifetime[39]. It is only speculation, but it seems reasonable to expect that complexes with MLCT state lifetimes less than 200 ns will NOT achieve a time-

invariant ratio of protonated and deprotonated forms of the complex while complexes with lifetimes higher than 300ns might. If the excited state does not achieve a time-invariant ratio, then the measured pK_a^* is expected to depend on the excited state lifetime. When both protonated and unprotonated (or coordinated and uncoordinated) forms emit corrections can be made to account for the differences in lifetimes (equation (64)). However, many protonated forms are not emissive, as are many bimetallic species and the ΔpK_a calculated from the absorption spectra *via* the Förster cycle are often approximate due to the drawbacks associated with that approach (paragraph 1.B.5.). In general, for Ru complexes, the reported pK_a^* values are most likely high estimates of the actual values because of the short lifetime of the protonated species: protonated species with much shorter lifetimes than unprotonated ones are prone to shift the excited state equilibrium toward the protonated form, giving the impression that the excited unprotonated species is a stronger base than it would actually be if it had time to equilibrate.

The excited state chemistry of $[Ru(bpy)_2dpp]^{2+}$ is further complicated by the availability of two basic sites in close proximity with different acid-base properties in the ground and excited state. The peripheral pyridyl and pyrazinyl nitrogens on the dpp ligand are electronically and chemically distinct. In the ground state, the site that responds first to changes in pH is the peripheral pyridyl nitrogen, as expected by the comparison of the basicity of the unsubstituted analogues, pyridine (pK_a= 5.23) and pyrazine (pK_{a1}= 0.80). The basicity of the coordinated pyrazinyl nitrogen is lower than that of uncoordinated pyrazine as a result of the inductive effect of the positively charged ruthenium in the para position. The peripheral pyridyl nitrogen of dpp is less susceptible

to the inductive effect of the metal, because the pyridyl ring is twisted out of the plane by steric forces and is not as strongly coupled electronically to the rest of the molecule.

In the excited state, according to Strekas and coworkers[52], the relative basicity of the two sites is inverted because the charge transfer shifts the majority of the charge on the peripheral pyrazinyl nitrogen, thus increasing its basicity relative to that in the ground state as well as to that of the other nitrogen. The nature of the most enhanced normal modes in resonance Raman spectra confirms that the pyrazyl ring is the site of more electron density in the excited state and that charge is not transferred symmetrically to both nitrogens, as would be the case for bpz.

The inversion of acid-base properties of the two sites in ground and excited state introduces a source of uncertainty when trying to assign the change in pK_a calculated from the $[H^+]$ dependence of the absorption and emission to a specific imine nitrogen. The change is unlikely to follow the acid-base change of a single site or specific donor atom and measuring the magnitude of the basicity enhancement for each site becomes problematic as a result of it.

Recent attempts to fully resolve the matters of controversy concerning the $[Ru(bpy)_2dpp]^{2+}$ complex's properties in pH ranges where coordination to other units may take place have benefited from the technological advances in systems' detection. Thanks to the successful integration of the ICCD camera system with both pulsed and continuous wave lasers, experiments have revealed emissions that could not be previously detected, one of which was assigned to the monoprotonated complex[53]. Moreover NMR spectra reveal pH dependent changes intermediate between those evident in the absorption and emission spectra that can be reasonably considered evidence of a

ground state protonation step in the 1-3 pH range. Both discoveries have potential implications in the current understanding of the dynamics of the protonation events. These changes reveal that protonation or coordination may occur in the 1 to 3 pH range and that optically induced coordination may involve the pyridyl nitrogen more than it was originally anticipated and possibly also involve an intra-molecular transfer from one acid-base functionality to the other. Energetically, the changes in the absorption and in the emission spectra, from which the ΔpK_a value is estimated, may not reflect protonation of the same site.

The research presented here continues in an effort to identify the sequence of protonation steps at the peripheral dpp nitrogens in the ground and excited states, and to quantify the magnitude of the photoinduced change in acid-base properties at each of the sites. The usefulness of the measured ΔpK_a as a thermodynamic parameter rests on a clear understanding of the effect of $[H^+]$ on *both* the ground and excited states, and on a quantitative discernment of the extent of the equilibria established. Especially when the equilibrium constant for coordination is a linear function of the basicity of the diimine, distinguishing the acid-base properties of the individual donor atoms comprising the chelation site is crucial to gather insights into the sequence of coordination steps leading to chelate formation.

To minimize the ambiguity arising from the presence of two basic sites, the pypz analogue of the dpp ligand was synthesized, and used to prepare a mixed ligand complex of ruthenium(II). The pypz ligand was chosen because it is identical in almost every respect to $[Ru(bpy)_2dpp]^{2+}$ except for the absence of the free pyridyl ring (Figure 8).

This thesis describes the redox and structural properties of both the pypz ligand and its corresponding Ru(II) complex, $[Ru(bpy)_2pypz]^{2+}$. The dynamics of protonation and of exciplex formation with a d^{10} transition metal ion have also been determined to establish a solid base for comparison. The differences and similarities in the properties of $[(bpy)_2Ru(pypz)]^{2+}$ and $[Ru(bpy)_2dpp]^{2+}$ in the same environment can highlight the peculiar behavior of each acid-base site upon excitation and their role in coordination and protonation reactions.

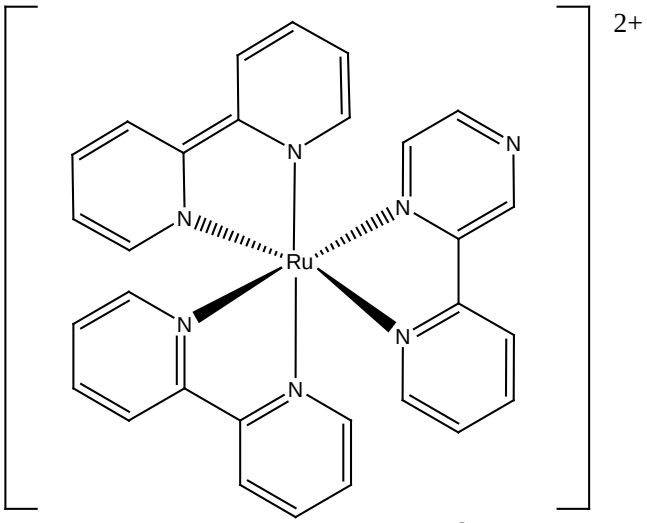

Figure 8: Schematic representation of $[(bpy)_2Ru(pypz)]^{2+}$ ion.

Suppositions have been made as to the importance of a concerted action of both bases in possible equilibria and deactivation pathways of $[(bpy)_2Ru(dpp)]^{2+}$ in aqueous solutions, including intra-molecular proton transfer and bimolecular exciplex formation with d^{10} transition metal complexes. The absence of a second peripheral basic site in $(bpy)_2Ru(pypz)]^{2+}$ allows said propositions to be tested and possibly to gather definitive evidence in support of one mechanism over another.

2. Experimental

2.A. Synthesis and Characterization

All reagents purchased commercially were used without further purification, unless otherwise noted. Water was deionized in a glass-distillation system.

The synthetic strategies adopted in the preparation of ruthenium polypyridine complexes follow a common protocol previously outlined in the literature. Published purification procedures, on the other hand, are generally specific to each complex or series of complexes and less widely applicable. The purification step is crucial in the isolation of pure products owing to the presence of several impurities similar in size and sometimes charge, such as unreacted reagents, bimetallic side-products, stereoisomers and more. Considerable effort was devoted to finding an effective purification method and the route developed here for [bis(2,2'-bipyridine)(2-(2-pyridyl)pyrazine) ruthenium(II)]nitrate was later successfully employed in the purification of other diimine ruthenium and rhodium complexes.

2.A.1. [Bis(2,2'-bipyridine)(2,3-bis(pyridyl)pyrazine)ruthenium(II)]nitrate

The water-soluble nitrate salt of bis(2,2'-bipyridine)(2,3-bis(pyridyl)pyrazine) ruthenium(II), $[(bpy)_2Ru(dpp)]^{2+}$, was synthesized according to literature methods[43], with slight modifications in the purification step. The crude complex was initially precipited as hexafluorophosphate salt by addition of an aqueous, saturated solution of NH_4PF_6 (Aldrich 10121HE Ammonium hexafluorophosphate, 95+%). The solution was filtered and washed repeatedly with small amounts of cold water and diethyl ether. The precipitate that was obtained was re-dissolved in a small amount of acetonitrile and

charged onto a chromatography column loaded with Sephadex (Sigma-Aldrich G10120 Sephadex G-10).

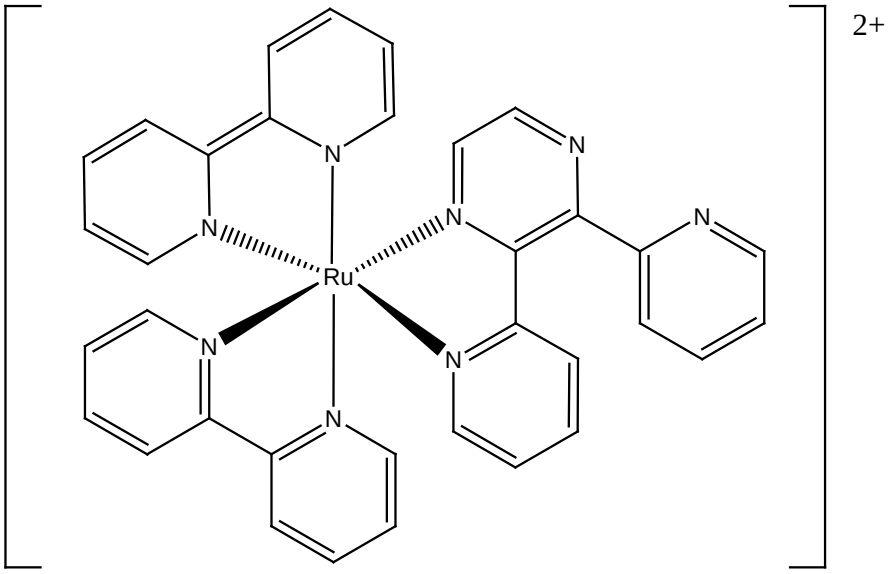

Figure 9. Structure of the ion $[(bpy)_2Ru(dpp)]^{2+}$.

The light orange band containing the product separated from the initially loaded complex and was eluted with acetonitrile. The desired product eluted first, and was collected and the eluent removed by rotary-evaporation under vacuum at 50°C. An ion-exchange resin (J. T. Baker Chemical Co., Dowex 1-X8) saturated with 6M sodium nitrate was used to convert $[(bpy)_2Ru(dpp)](PF_6)_2$ to the nitrate salt, $[(bpy)_2Ru(dpp)](NO_3)_2$, which was eluted with a 25% solution of acetonitrile and water (v/v) and evaporated to dryness. The product was tested for purity and characterized using NMR, UV-Vis, luminescence and lifetime measurements.

2.A.2. Tris(2,2'-bipyridine)osmium(II)hexafluorophosphate

The complex (Figure 10) was synthesized by reacting $(NH_4)_2[OsBr_6]$ (Strem Chemicals 76-0080 Ammonium hexabromoosmate(IV), 99%) with bipyridine (Aldrich D216305 2,2'-Dipyridyl, 99%) in a 1:3 ratio following the procedure of Nakabayashi and coworkers[54].

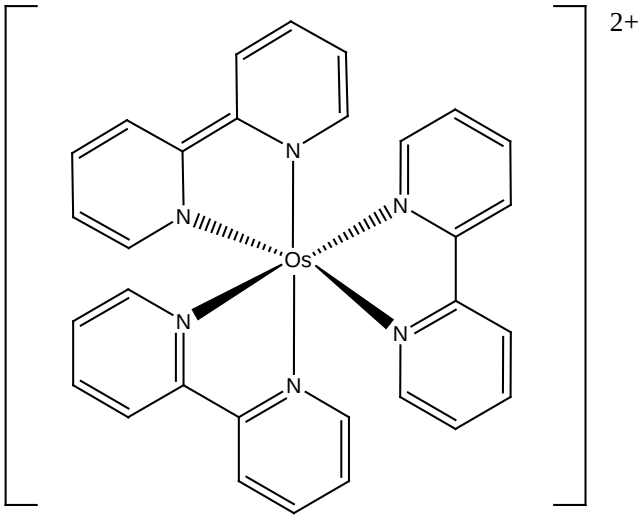

Figure 10. Structure of the ion $[Os(bpy)_3]^{2+}$.

The reaction was carried out under a nitrogen atmosphere as oxygen may prevent the reduction of osmium and as a safety precaution against release of toxic osmium compounds. The crude microcrystalline product was collected on a fritted Hirsch funnel and washed three times with ice water and ethyl ether. To purify the complex, column chromatography was performed using alumina as the stationary phase and acetonitrile as eluent. The deep-green-colored band due to the complex eluted first and was dried by rotary evaporation. An acetonitrile solution of the fine green precipitate was characterized by absorption and emission spectroscopy and lifetime measurements.

2.A.3. 2-(2-pyridyl)pyrazine

The ligand 2-(2-pyridyl)pyrazine was prepared using the Stille cross-coupling reaction outlined in a previously published synthesis by Berghian *et al.*[55] (Figure 11).

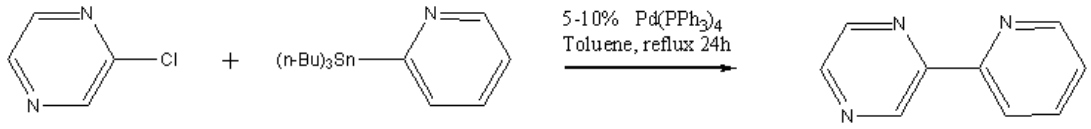

Figure 11. Synthetic scheme of 2-(2-pyridyl)pyrazine.

Anhydrous 2-chloropyrazine was obtained upon distillation of commercial 2-chloropyrazine (Aldrich 132489 chloropyrazine 97%) under constant flux of nitrogen, and stored in the refrigerator under nitrogen until needed. All other reagents were used as received from the chemical suppliers. In a nitrogen glove bag, the palladium catalyst $Pd(PPh_3)_4$ (Aldrich 216666 Tetrakis(triphenyl-phosphine)palladium(0) 99%) was weighed and transferred to a three-neck flask with a condenser. The apparatus was assembled in the glove bag in order to avoid the possibility of the chemical being exposed to air while being transferred to the flask. A solution of tributylstannylpyridine (Frontier Scientific T3254 2-(Tributylstannyl) pyridine, 85-95%) in degassed toluene was injected into the flask through a septum. The mixture was refluxed (~110°C) overnight under a nitrogen atmosphere.

After the reaction was stopped and brought to room temperature, dichloromethane was added. The solution was transferred to a separatory funnel and washed with aqueous ammonia (15%). However, it was difficult to distinguish the organic and aqueous layers. To improve the separation sodium chloride was added. The organic phase was collected

and washed twice with water until the water tested neutral on pH paper. The last wash was done with a saturated solution of NaCl. The orange organic solution was dried by addition of $MgSO_4$. Radial chromatography was used to purify the crude product. The eluent was initially a 10% solution of ethyl acetate in hexane. As the bands started to separate, the concentration of ethyl acetate was gradually increased to 35%. The fractions collected were analyzed by NMR and the ones containing the ligand were gathered in the same petri dish. The product was recrystallized in methylene chloride by the addition of hexane. The yellowish crystals that precipitated were washed three times with hexane, then dried at room temperature under a gentle flow of nitrogen. Purity of the ligand was confermed by ^{1}H-NMR, ^{13}C-NMR and melting point (58-60°C).

2.A.4. [Bis(2,2'-bipyridine)(2-(2-pyridyl)pyrazine)ruthenium(II)]chloride

The complex was obtained using a modified version of the synthetic procedure described earlier for $[(bpy)_2Ru(dpp)](NO_3)_2$.

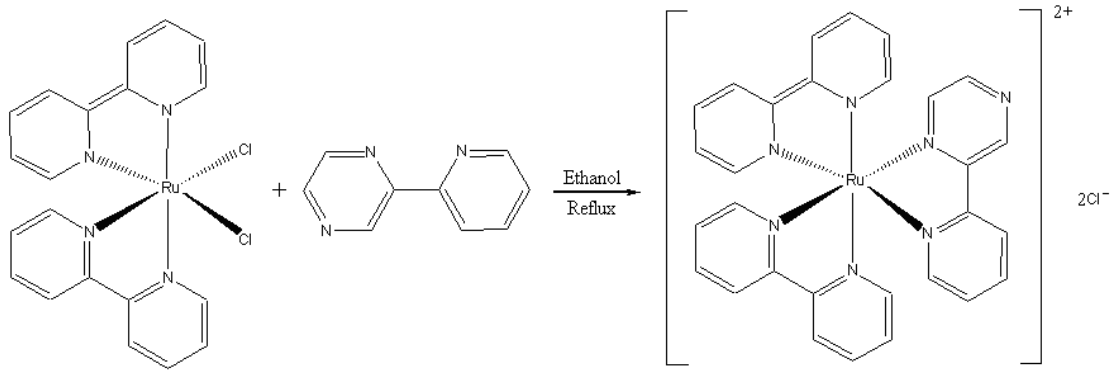

Figure 12. Synthetic scheme of $[(bpy)_2Ru(pypz)]^{2+}$.

A two-fold excess of the pypz ligand, 2-(2-pyridyl)pyrazine, was added, under flowing nitrogen, to a solution of $[(bpy)_2RuCl_2]$ (Aldrich 28,812-8 cis-Dichlorobis(2,2'-bipyridine)-ruthenium(II)hydrate) in absolute ethanol (Aaper Alcohol Ethyl Alcohol 200 Proof). After refluxing for 24 hours at 78°C, the color of the solution changed from purple to orange. The reaction mixture was monitored periodically by UV-Vis spectroscopy (Figure 13).

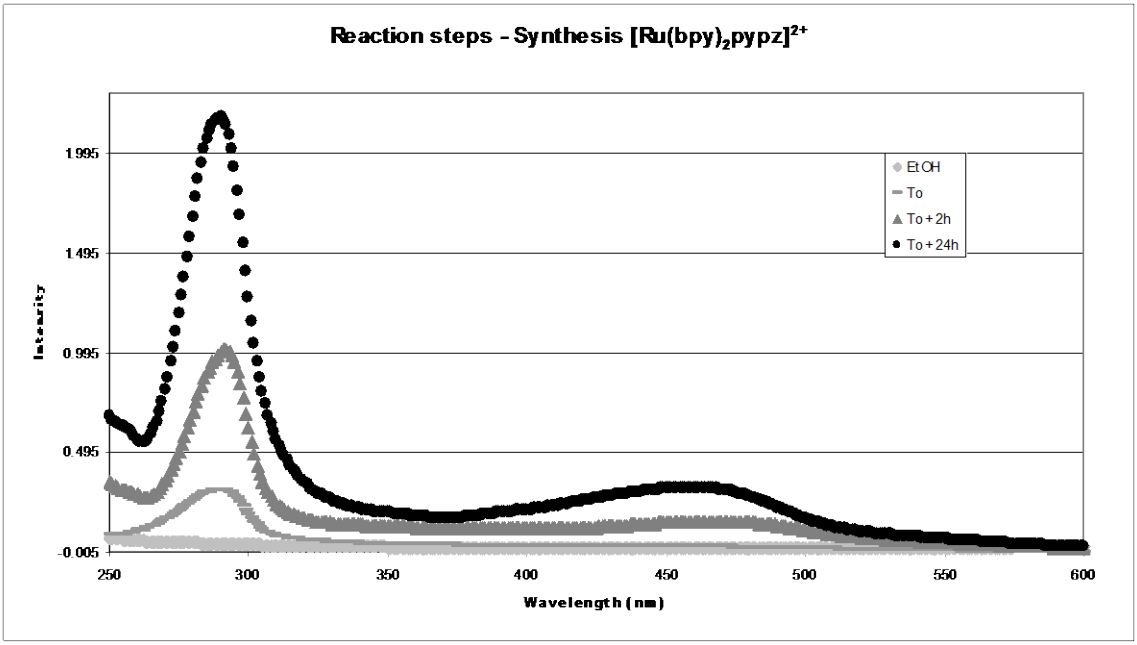

Figure 13. UV-Vis spectra of solvent and reaction mixture at T_o and after 2 and 24 hours.

When the UV-Vis profile stopped changing, the reflux was halted and the solution allowed cooling to room temperature. Most of the solvent was removed via rotary-evaporation. The crude product was re-dissolved in a minimum volume of a water-acetone solution in a 5:3 ratio (v/v) and the solution was loaded onto a Sephadex column (Sigma-Aldrich G10120 Sephadex G-10). Before use, the Sephadex material was washed twice with 0.2M NaOH (two column volumes) and allowed to re-equilibrate with three

column volumes of 0.05M NaCl, until the eluting solution tested neutral on pH paper. The charged column was then eluted with a 0.05M aqueous solution of NaCl. A light yellow band, attributed to the unreacted ligand that had been added in excess to facilitate the synthesis, eluted first. The second band was orange and contained the complex and a third purple band eluted last and was likely due to some form of dimetallic ruthenium complex. The concentration of the eluent had to be gradually increased from 0.05M NaCl to 0.1M NaCl, in order to elute the second and third fractions completely. The orange band was collected and examined by UV-Vis and NMR spectroscopy. A broadening of the visible band in the 400-500nm region of the absorption spectrum, in addition to the presence of extra peaks in the NMR spectrum, suggested the fraction still contained impurities. Furthermore, it contained a high concentration of NaCl from the eluent. Dissolving the dried orange fraction in ethanol and filtering out the salt that precipitated, allowed some sodium chloride to be separated out. To eliminate the remaining NaCl and other impurities, an alumina column (Aldrich cat # 19,944-3 Aluminum oxide, activated, basic, Brockmann I, standard grade, 150 mesh) was then set up, charged with the impure complex, and eluted with acetonitrile. Again three bands appeared (orange, yellow and purple). UV-Vis spectroscopy confirmed that the yellow band contained the desired complex (Figure 14). The orange band eluted quickly with acetonitrile, and was tested and discarded. Acetonitrile was gradually diluted with increasing volumes of ethanol and water, to separate the other two bands. The yellow band eluted, while the purple band stayed on the column and was discarded with the alumina. The acetonitrile-water-ethanol solution containing the yellow band was evaporated to dryness.

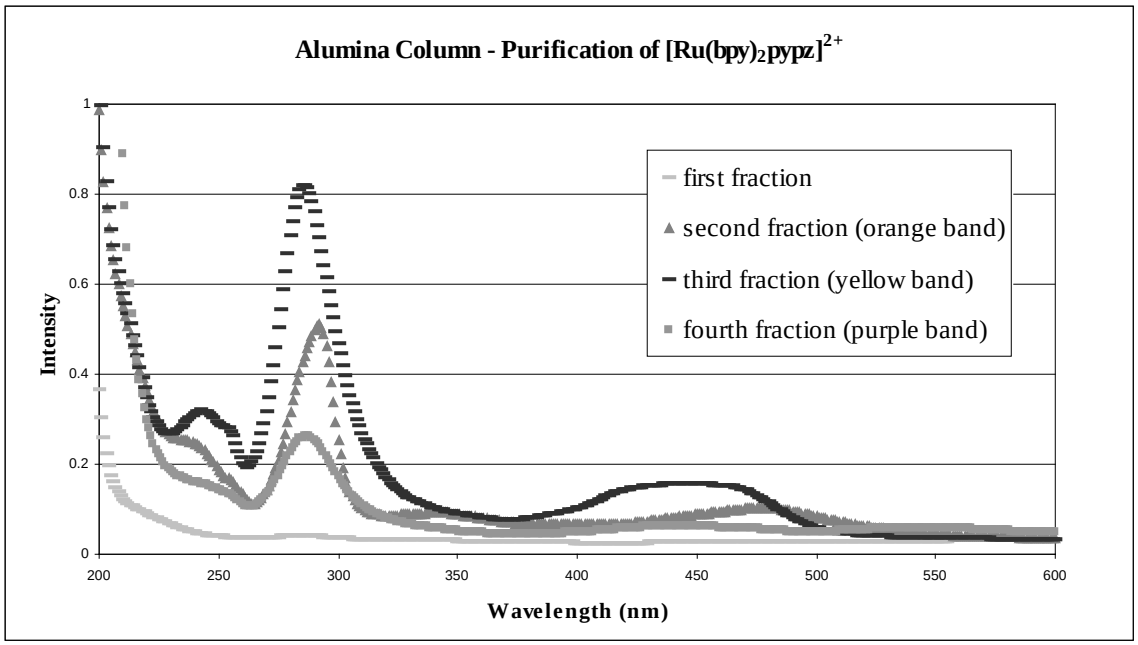

Figure 14. UV-Vis spectra of chromatography fractions from alumina column.

A portion of the pure product was dissolved in a minimal amount of acetone and stored in the freezer for several days, until bright orange crystals appeared. The crystals were kept in the mother liquor until ready to be tested by X-ray diffraction because prolonged exposure to the air would remove the acetone molecules from the crystals rendering them unsuitable for analysis. The product was also characterized by one- and two-dimensional NMR techniques, absorption and emission spectroscopy, lifetime measurement and elemental analysis (calcd (%) for $RuC_{29}H_{23}N_7 \cdot 6H_2O$: C 43.26, H 4.71, N 13.08; found: C 43.01, H 4.70, N 12.03).

2.B. Titrations

2.B.1. Acid Titration of $[(bpy)_2Ru(dpp)](NO_3)_2$

A concentrated stock solution of $[(bpy)_2Ru(dpp)](NO_3)_2$ in distilled water was diluted to a concentration of 10^{-5} M with buffer solutions (Fisher Scientific Chemical

Company) ranging from pH 1 to 8, and with 1M nitric acid (Pharmco Products Inc.) to obtain a pH 0 solution. Five samples with negative Hammet acidity function were prepared using concentrated sulfuric acid (Pharmco Products Inc. 18.0 M). The value of H_o and amounts of acids used for each sample are listed in Table 1. The values of molarity for acid solutions A2 dpp and A3 dpp were taken from published data[56]. To cover a broader range of acidities beyond those listed by Paul and Long[56], molarities for samples A4 dpp, A5 dpp, and A6 dpp were calculated from the density values of each sulfuric acid-water mixture along with data published by Hammett and Deyrup[57], which correlate the percent by mass of acid to the acidity of the resulting solution.

Table 1: Sulfuric acid sample molarities and volumes at selected H_0.

Sample code	Ho	Molarity Acid*	mMoles Acid	Vol Acid (mL)	Tot sample Vol (mL)
A1 dpp	0.13	0.50	2.5	0.139	5.00
A2 dpp	-2.06	4.50	22.5	1.250	5.00
A3 dpp	-4.14	8.50	42.5	2.361	5.00
A4 dpp	-5.11	10.70	53.5	2.973	5.00
A5 dpp	-6.08	11.95	59.8	3.319	5.00
A6 dpp	-10.59	18.00	87.3	4.850	5.00

*** From published data (Ref 56 & 57).**

Absorption and emission spectra of each sample were recorded, using 10 mm quartz cuvettes sealed with rubber septa, degassed by bubbling with Ar gas for five minutes and mantained under an argon atmosphere.

Furthermore, 0.05 M solutions of the $[(bpy)_2Ru(dpp)](NO_3)_2$ complex both in D_2O (with DSS as an internal reference) and D_2SO_4, were prepared separately in order to record ^{1}H-NMR spectra as a function of $[D^+]$. The deuterated sulfuric acid solution of the

complex was added dropwise to the D_2O solution directly in the NMR tube, to obtain increasingly acidic samples while keeping constant the concentration of the metal.

2.B.2. Acid Titration of $[(bpy)_2Ru(pypz)]Cl_2$

The electronic absorption and emission spectra and lifetime of aqueous 10^{-5} M $[(bpy)_2Ru(pypz)]Cl_2$ solutions were obtained over a wide range of proton concentrations to characterize the acid-base properties of the complex. Samples with pH values ranging from 1 to 12 were prepared by diluting a fixed amount of ruthenium stock solution with buffers of the appropriate acidity (Fisher Scientific Chemical Company). The electronic spectra of the pure buffer solutions were recorded as reference solutions and their spectra subtracted from the sample spectra to ensure that they would not modify the spectrum of the complex. The pH 0 sample was prepared using 1 M nitric acid (Pharmco Products Inc.) measured against the 1 M solution of acid, without the Ruthenium complex.

Samples of much higher acidity, corresponding to negative values of the Hammet acidity function (H_0), were prepared using concentrated sulfuric (Pharmco Products Inc. 18.0 M) and perchloric acid (Pharmco Products Inc. 11.65 M). The spectroscopic behavior of the complex in these acids was compared to determine whether the acid used and consequently the ionic strength of the solution would have an effect on the titration. Paul and Long[56] established experimentally using indicators, the correlation between the molarity of a particular acid and the acidity of the resulting solution and tabulated the values of H_0 for several acids at room temperature. The volumes of concentrated acid needed for each sample were established from the tabulated data, the molarity of the concentrated acid and the total volume of the final sample (5ml), and are listed in Table

2. Paul and Long's values of H_0 as a function of acid concentration were obtained using spectrophotometric measurement and were considered to be more reliable and therefore were the preferential choice over the slightly different values obtained by Hammett and Deyrup[57] using colorimetric methods. A limitation in the use of such sets of data (ref. Table 2) is the fact that sulfuric acid samples can be prepared only up to a level of acidity corresponding to H_0 = -4.89, because data at higher concentrations of acid were not reported.

Table 2: Perchloric and Sulfuric acid sample molarities and volumes at selected H_0.

Sample code	Ho	Molarity Acid*	mMoles Acid	Vol Acid (mL)
P1	-0.04	0.75	3.75	0.322
P2	-1.01	2.50	12.50	1.073
P3	-1.97	4.50	22.50	1.931
P4	-2.84	6.00	30.00	2.575
P5	-3.98	7.50	37.50	3.219
P6	-4.69	8.50	42.50	3.648
P7	-5.05	9.00	45.00	3.863
P8	-5.79	10.00	50.00	4.292

Sample code	Ho	Molarity Acid*	mMoles Acid	Vol Acid (mL)
S1	0.83	0.10	0.50	0.028
S2	0.13	0.50	2.50	0.139
S3	-0.07	0.75	3.75	0.208
S4	-0.84	2.00	10.00	0.556
S5	-1.85	4.00	20.00	1.111
S6	-2.06	4.50	22.50	1.250
S7	-2.76	6.00	30.00	1.667
S8	-3.03	6.50	32.50	1.806
S9	-3.87	8.00	40.00	2.222
S10	-4.14	8.50	42.50	2.361
S11	-4.89	10.00	50.00	2.778

*** From published data (Reference 56).**

Reference solutions containing the same volume of acid, but no ruthenium complex were prepared for each sample and brought to volume with distilled water. All samples to be tested were transferred to quartz cuvettes, sealed with rubber septa, and argon gas was bubbled through each solution for 5 minutes prior to spectroscopic analysis.

2.C. Association with d^{10} metals

2.C.1. Association of $[(bpy)_2Ru(dpp)](NO_3)_2$ with Zinc and Cadmium

A detailed examination of the association dynamics between $[(bpy)_2Ru(dpp)]^{2+}$ and zinc and cadmium salts in solution was carried out with steady-state and time-resolved methods. Absorption and emission spectra of 2.5 x 10^{-5} M solutions of $[(bpy)_2Ru(dpp)]^{2+}$ with increasing concentrations of zinc nitrate or cadmium nitrate were recorded in a pH 5 buffer for optimum solubility. Emission lifetimes were measured in room temperature solutions containing 3 M Zn^{2+} or Cd^{2+}.

2.C.2. Association of $[(bpy)_2Ru(pypz)]Cl_2$ with Zinc

The dependence of absorption and steady-state emission of the $[(bpy)_2Ru(pypz)]Cl)_2$ complex on the concentration of Zn^{2+} in aqueous solution was measured. A 5 M aqueous solution of Zinc chloride, $ZnCl_2$, (Fluka Chemika, cat. # 96470) was initially prepared and used as stock solution to make samples with increasing zinc molarity from 0 to 5.0 M and a constant, 10^{-5} M, concentration of $[(bpy)_2Ru(pypz)]^{2+}$. However, at zinc concentrations higher than 0.1 M, a white fluffy precipitate started to form so the sample preparation was interrupted and revised. To

avoid formation of insoluble zinc by-products, increasingly large aliquots of the zinc stock solution were added to a pH 3 buffer solution. A list of the volumes and concentrations of each chemical making up each sample is presented in Table 3.

Table 3: Sample composition for Zinc titration of $[(bpy)_2Ru(pypz)]^{2+}$.

Sample code	Zinc Molarity	ml Zn stock	ml Ru stock	ml Buffer 3
Zn3buf0	0.00	0	0.150	4.850
Zn3buf3	0.05	0.050	0.150	4.800
Zn3buf4	0.10	0.100	0.150	4.750
Zn3buf5	0.25	0.250	0.150	4.600
Zn3buf6	0.50	0.500	0.150	4.350
Zn3buf8	1.00	1.000	0.150	3.850
Zn3buf9	1.50	1.500	0.150	3.350
Zn3buf11	2.50	2.500	0.150	2.350
5M Zn	5.00	4.850	0.150	0

Reference solutions containing a corresponding volume of zinc, but no ruthenium complex were prepared for each sample and brought to volume with the pH 3 buffer. All samples were transferred to quartz cuvettes, sealed with rubber septa, and argon gas was bubbled through each solution for 5 minutes. Emission spectra were recorded on a FluoroMax spectrometer using 5 mm slits and excitation set at 400 or 420 nm. The time-resolved emission spectra of $[(bpy)_2Ru(pypz)]^{2+}$ at room temperature were also obtained for all samples and used to calculate the emission lifetimes, whenever possible.

2.D. Quantum Yield Determinations

Luminescence quantum yields, defined as the ratio of photons absorbed to photon emitted through luminescence, were determined using the comparative method of

Williams and co-workers[58]. This method assumes that solutions of the standard and the test samples that have identical absorbance at the same excitation wavelength will also be absorbing the same number of photons. The method involves the use of well-characterized standard samples with known quantum yields at the temperature of interest. Along with being well characterized, the optimal standard has to absorb at the excitation wavelength of choice for the test sample, and if possible, emit in a similar region with comparable emission lifetimes. This is necessary so that the settings of the ICCD camera can be kept constant during both data collections. The validity of the standard plays such an important role in the soundness of the final quantum yield value that a second standard was chosen for cross-calibration and to confirm the applicability/reproducibility of the experimental method used. For the measurement to be reliable, another major factor to be considered is the possibility of concentration effects. In order to minimize the likelihood that the signal intensity might be affected by re-adsorption or self-quenching, measurements were taken using sample solutions that had optical densities ranging from 0.02 to 0.1 at the wavelength of interest (usually 458 and 488 nm, the same wavelengths as the ones used for excitation by steady state laser). To maximize accuracy, sufficient data were acquired while keeping operational parameters (slit width, excitation intensity, camera gain, monochromator grating…etc) constant so that linearity of the integrated emission across the range of concentrations could be ensured (gradient method[58]). For the same reason, emission and absorption spectra for reference samples were recorded on the same day as the spectra for analytes and were recorded again each time the quantum yield determination experiment had to be performed. The use of different solvents for standard

and test samples was accounted for by including the solvent refractive indices, η, in the calculation of quantum yield ratios:

$$\Phi_{unknown} / \Phi_{standard} = (Grad_{unknown} / Grad_{standard}) \times (\eta^2_{unknown} / \eta^2_{standard}) \qquad (83)$$

where Φ represents the quantum yield and Grad is the gradient or slope obtained from the graph of absorbance versus emission.

All glassware was cleaned and dried scrupulously prior to filling with solution to be measured, samples were degassed by argon bubbling and solvents were checked for background fluorescence.

2.D.1. Quantum Yield of $[Os(bpy)_3]^{2+}$

The relative quantum yield of emission from $[Os(bpy)_3]^{2+}$ was investigated with the intention of using it as a reference for the determination of the quantum yield of $[(bpy)_2Ru(dpp)]^{2+}$ emission since both complexes have similar quantum yields and their emission maxima, 722 and 700nm respectively, are not far apart. When measured relative to $[Ru(bpy)_3]^{2+}$ however, $[Os(bpy)_3]^{2+}$ solutions gave a value of quantum yield much smaller than the published value of 0.005[59] so the complex $[(bpy)_2Ru(dpp)]^{2+}$ at pH 7 was used instead as a reference to establish the quantum yield of $[Os(bpy)_3]^{2+}$, and the $[Os(bpy)_3]^{2+}$ was in turn used as a reference for $[(bpy)_2Ru(dpp)]^{2+}$ at pH=5, and for $[(bpy)_2Ru(dpp)Zn]^{4+}$ in water . The same operational parameters used for the quantum yield determination of $[(bpy)_2Ru(dpp)]^{2+}$ were adopted (vide infra). In fact, both

experiments were performed on the same day so as to maintain constant other parameters such as room temperature, instrument alignment and laser power.

2.D.2. Quantum Yield of $[(bpy)_2Ru(dpp)]^{2+}$

The quantum yield of emission of $[(bpy)_2Ru(dpp)]^{2+}$ was determined in a pH=7 buffer solution, so as to avoid issues arising from its pH dependence. The chloride salt of $[Ru(bpy)_3]^{2+}$ dissolved in water and previously cross-standardized against an aqueous solution of $[Ru(phen)_3]^{2+}$ was used as the reference[59], although its range of emission is slightly shifted and its lifetime longer than the complex under investigation. The steady-state emission spectra were recorded both on the Fluorolog spectrometer and with the ICCD camera, to compare values and standardize the method. The Fluorolog's operational parameters were 8 mm slit widths, 0.5 seconds acquisition times and 436-nm excitation. The ICCD system was set to a much narrower slit width of 250 μm, 1.0 second exposure time, 255 camera gain and the 150/800 grating of the monochromator. Emission areas were integrated from 510-865 nm for spectra recorded on the Fluorolog, and from 500-900 nm for spectra recorded with the ICCD camera. Deviations from near Gaussian-shaped emissions on the higher energy side of $[(bpy)_2Ru(dpp)]^{2+}$ emission due to the water raman signal were smoothed out by fitting the signal to a template of the emission of $[(bpy)_2Ru(dpp)]^{2+}$ with the same maximum intensity (Figure 15).

2.D.3. Quantum Yield of $[(bpy)_2Ru(dppH)]^{3+}$

The quantum yield of emission of $[(bpy)_2Ru(dppH_{py})]^{3+}$ was established relative to the quantum yield of $[(bpy)_2Ru(dpp)]^{2+}$. The monoprotonated form of $[(bpy)_2Ru(dpp)]^{2+}$ with the proton attached to the peripheral pyridyl nitrogen of the dpp

ligand, has very low emission intensity. For this reason, the quantum yield determination required different parameters for the ICCD-coupled instrument than those used while recording the gradient of the standard. In particular, the gain of the camera had to be increased when recording the emission of the protonated complex. In order to correlate the emission areas measured with different camera gains, the gain settings were calibrated by measuring the steady-state quantum yield of emission (area under the curve) of $[(bpy)_2Ru(dpp)]^{2+}$ independently at several gain values[60]. The ratio of the emission areas at two gain settings was used to extrapolate the emission area of the emissive species under investigation. The slit width was kept at 250 μm to maintain the monochromicity of the light, and the exposure time was also kept constant to avoid saturating the camera.

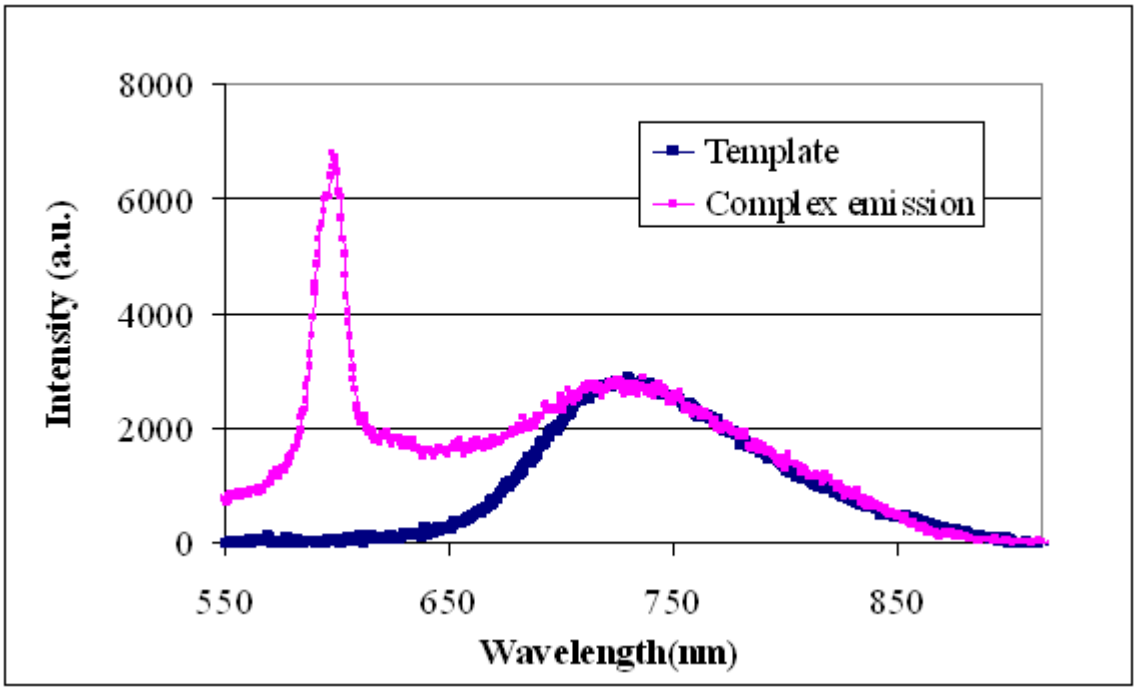

Figure 15. Anomalies smoothing using a template.

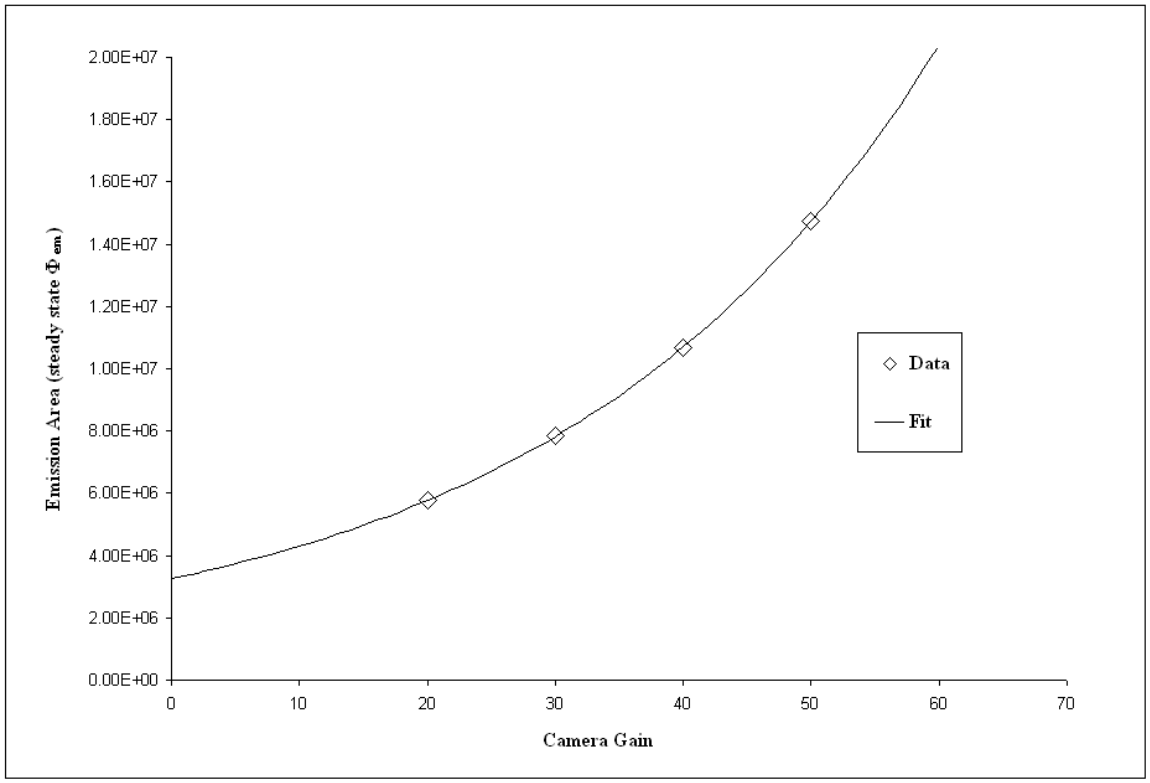

Figure 16. Camera gains calibration.

2.D.4. Quantum Yield of $[(bpy)_2Ru(dpp)]^{2+}$ with Zn^{2+} and Cd^{2+}

To prepare solutions containing the same relative concentrations of the Ru(II) complex and Zn^{2+} and Cd^{2+} ions, two stock solutions were prepared in pH 5 buffer. Five increasingly dilute samples for each metal were prepared from the corresponding stock solution upon addition of appropriate amounts of pH 5 buffer solution, in order to obtain samples with optical density values ranging from 0.02 to 0.1 in the 400- to 500- nm spectral region. The quantum yield of the bimetallics were measured relative to pH 7 buffer solutions of $[(bpy)_2Ru(dpp)]^{2+}$. Given the low luminescence intensity, the samples were excited with the 532-nm NdYag laser line and the ICCD camera centered at 710 nm for zinc and 720nm for cadmium. All spectra were recorded using 250 μm slit width,

150/800 monochromator grating and 1.0 second exposure time, while camera gain was set at 150 for $[(bpy)_2Ru(dpp)Zn]^{4+}$ and 80 for $[(bpy)_2Ru(dpp)Cd]^{4+}$. Emission areas were integrated in the 600-900 nm range for the Ru-Zn^{2+} complex and the 565-915 nm range for the Ru-Cd^{2+} complex.

2.D.5. Quantum Yield of $[(bpy)_2Ru(pypz)]^{2+}$

To determine the quantum yield of emission of $[(bpy)_2Ru(pypz)]^{2+}$ in water, aqueous solutions of $[(bpy)_2Ru(dpp)]^{2+}$ and $[Ru(bpy)_3]^{2+}$ were used as references and cross-references, respectively. The steady-state emission spectra were recorded on the Fluoromax-P spectrometer with 2-μm slit widths and using two excitation wavelengths for comparison, 436 nm and 450 nm. Emission areas were integrated from 550-840 nm.

2.D.6. Quantum Yield of $[(bpy)_2Ru(pypz)]^{2+}$ protonated

The quantum yield of emission of protonated $[(bpy)_2Ru(pypz)]^{2+}$ was determined in 5M sulfuric acid solutions with increasing concentrations of the ruthenium complex ranging from 0.02 to 0.1 in optical density. The gradient of the integrated emission across this range of concentrations was compared to the gradients obtained for aqueous solutions of $[(bpy)_2Ru(pypz)]^{2+}$, $[Ru(bpy)_3]^{2+}$ and $[(bpy)_2Ru(dpp)]^{2+}$. The steady-state emission spectra were recorded on the Fluoromax-P spectrometer with 2 μm slit, and 436-nm and 450-nm excitation. Emission areas were integrated from 545-830 nm.

2.E. Instrumental

2.E.1. Melting Point and Elemental Analysis

Melting points were determined on a Thermo Scientific EW-03011 apparatus. C, H, N microanalyses were performed by Schwarzkopf Microanalytical Laboratory, Inc.

2.E.2. Radial Chromatography

Radial chromatography was conducted using a Harrison Research Co. Chromatotron with Merck TLC grade silica gel as the adsorbant (Aldrich #7749). The extent of the separation was monitored by shining UV-light onto the silica disk with a portable lamp.

2.E.3. UV-Vis Spectroscopy

Absorption spectra in the ultraviolet-visible and near-infrared regions were obtained with three different instruments. Initially data were collected using either an AVIV Model 14DS Spectrophotometer, or a Hewlett-Packard Model 8452A Photodiode Array UV-VIS Spectrometer with a deuterium lamp source. More recent measurements were performed on a Varian Cary 5000 UV-VIS-NIR spectrophotometer equipped with a D_2-Hg lamp and a Vis QI lamp. All spectra were recorded at room temperature, using 10-mm optical path length quartz cells and the liquid samples were de-aerated with nitrogen or argon gas. A reference spectrum for the solvent was always acquired and subtracted from the sample spectrum, either during the data collection (with Cary double beam instrument) or using the instrument software (for single beam instruments).

2.E.4. Steady-State Emission Spectroscopy

Emission spectra were recorded on three different instruments: (1) a Spectraphysics Model 1692T (Fluorolog-2 emission spectrometer, Jobin Yvex) with two Model 1681 0.22m monochromators, a 450W Xenon lamp (Model 1909 housing), and red-sensitive Hamamatsu photomultiplier detector (R928); (2) a FluoroMax instrument by Horiba, Jobin Yvon, with a Xenon Arc lamp; (3) or a SpectraPro Model SP-308 Acton Research Corporation spectrograph with a Princeton Instruments PI Max ICCD Camera equipped with Generation II Intensifier (Roper Scientific). With the ICCD detection, the samples were excited with a Coherent Innova 100-20 Argon ion laser tuned to a specific wavelength, usually 488 nm. Different slit width were used according to the intensity of the emission and need for wavelength accuracy. All 3D spectra (excitation wavelength *vs* emission wavelength *vs* emission intensity) were recorded using the FluoroMax spectrometer (2). Sample preparation protocol for room temperature measurements was the same as that for UV-Vis spectroscopy. Low temperature, 77K, measurements were obtained with instrument setup (3). The samples, contained in 3mm quartz EPR tubes were immersed in a quartz finger Dewar filled with liquid N_2 (Figure 17). To minimize condensation, the outer surface of the Dewar was cleaned with ethanol at regular intervals.

2.E.5. Time-resolved Emission Spectroscopy

All time-resolved data were obtained with the excitation/detection system described by Zambrana[61]. The excitation source was a Quanta Ray DCR-2A Pulsed Nd:YAG (neodymium doped yttrium aluminum garnet) laser fitted with a HG-2

harmonic generator and an amplifier, giving optimum output at 10Hz. The samples were generally excited with the 532-nm second harmonic from the laser. The light emitted by the sample was sent through a 532-nm holographic notch filter to remove scattered excitation and into a SpectraPro Model SP-308 spectrograph (Acton Research Corporation). The emission spectrum was recorded with the Princeton Instruments PI Max ICCD Camera (Roper Scientific), digitized and processed by the supplied software.

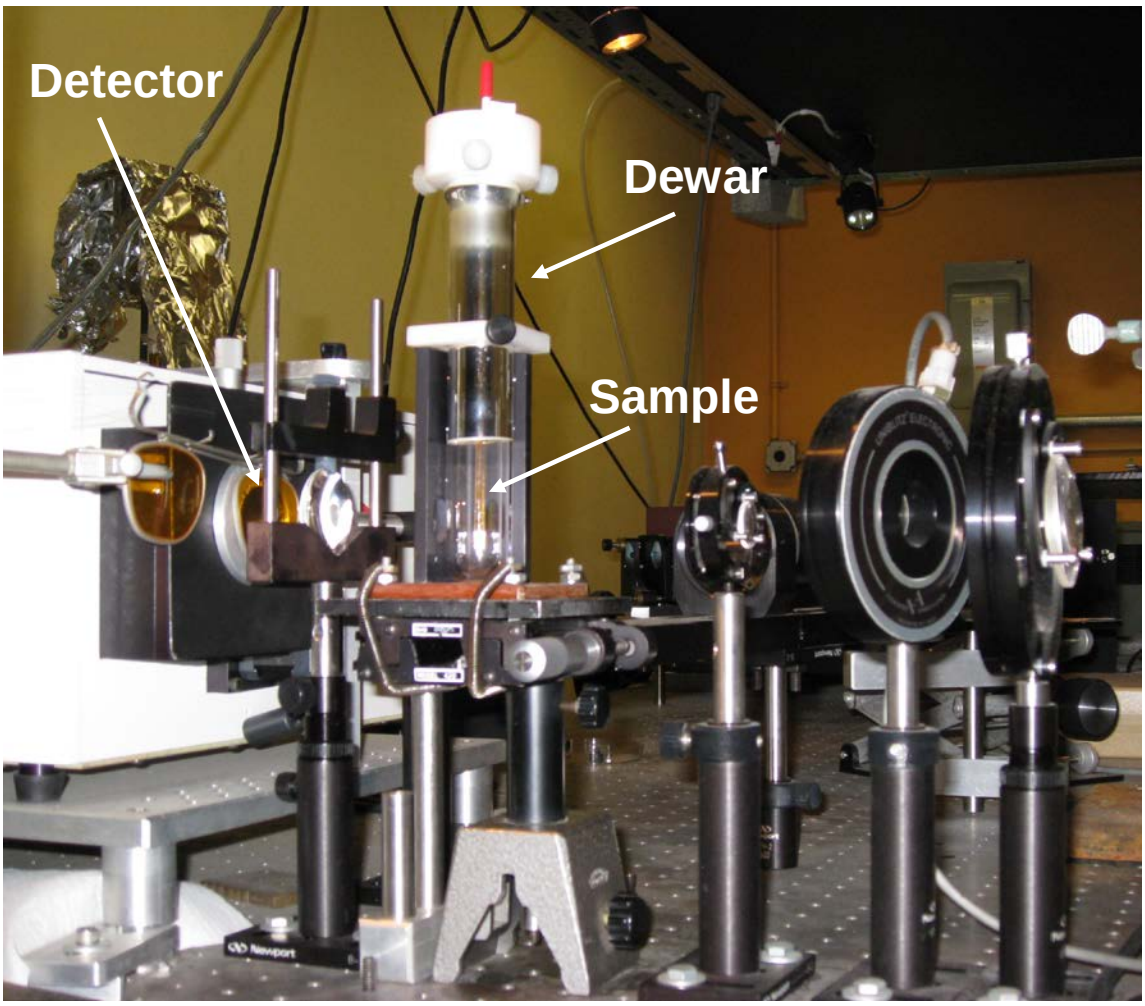

Figure 17. Low temperature set up for steady state emission experiments.

2.E.6. NMR Spectroscopy

One-dimensional proton and carbon spectra, and the two-dimensional correlation spectra (COSY45SW, COSY90SW, COSW) were recorded on a Bruker Avance DPX400 FT-NMR instrument at room temperature. Data were aquired using 400.13MHz proton frequency, 2s relaxation delay, and DSS as reference. The main acquisition parameters are listed in Table 4. All deuterated solvents were purchased from Aldrich Chem Co. or Cambridge Isotope Laboratories, Inc. and used as received.

Table 4: Acquisition parameters for NMR spectra.

		1-H	13-C	COSY
AQ: Acquisition time	**AQ**	3.96 s	1.37 s	0.22 s
TE: Temperature (kelvin)	**TE**	297.2 K	295.2 K	295.2 K
SWH: Spectral width (Hz)	**SWH**	8278 Hz	23980 Hz	4630 Hz
NS: Number of scans	**NS**	16	512	8
FIDres: FID resolution	**FIDres**	0.126 Hz	0.366 Hz	2.260 Hz
D1: Relaxation delay	**D1**	2 s	2 s	2 s
DE: Pre-scan delay	**DE**	6 us	6 us	6 us
DW: Dwell time	**DW**	60.400 us	20.850 us	108.00 us
SFO1: Irradiation frequency 1	**SFO1**	400.13 MHz	100.62 MHz	400.13 MHz
SFO2: Irradiation frequency 2	**SFO2**	--	400.13 MHz	--
TD: Data points	**TD**	65536	65536	2048

2.E.7. X-ray Crystallography

X-Ray diffraction data on single crystal of $[(bpy)_2Ru(pypz)]^{2+}$ grown in acetone were measured on an Bruker-Nonius KappaCCD diffractometer (graphite-monochromated Mo *K*α radiation, λ = 0.71073 Å, ϕ-ω scans) at 100 K. The data were corrected for absorption. The structure of the crystals was solved with SHELXS-97 and

refined by full-matrix least squares on F^2 with SHELXL-97 by Dr L. Todaro at Hunter College, CUNY. The hydrogen atoms were included in the structure-factor calculations but their parameters were not refined.

2.E.8. Cyclic Voltammetry

Cyclic voltammograms of 10^{-3} M acetonitrile solutions of $[(bpy)_2Ru(pypz)](NO_3)_2$ were recorded with a BAS100 (Bioanalytical Systems Inc., USA), using a platinum working electrode and a platinum wire as the counter electrode. The working electrode was polished with 50nm alumina powder, rinsed with distilled water and dried before use. The supporting electrolyte was tetraethylammonium perchlorate (TEAP) present at a concentration of 0.1 M. The measurements were made *vs* a Ag/AgCl (saturated KCl) aqueous reference electrode. The 5-ml sample solution was degassed by Argon bubbling for 5 minutes prior to CV measurements and the electrodes were rinsed in distilled water after each run. Each run consisted of 4 scans in the potential range between + 0.7 and +1.2V, starting with a positive sweep. Cyclic voltammograms were recorded at five different scan rates: 5, 10, 20, 100 and 200 mV/sec.

3. Results

3.A. Characterization

3.A.1. $[(bpy)_2Ru(dpp)](NO_3)_2$

The complex had been previously characterized by absorption and emission spectroscopy[43,62], resonance Raman, NMR[63] and electrochemical measurements[43,64]. As new batches of the complex were synthesized, the identity of the pure product was confirmed by electronic spectroscopy (Figure 18) and NMR.

In the UV-Vis spectrum of transition metal complexes, the occurrence of charge transfer or $d \rightarrow \pi^*$ transitions at low energies is expected whenever the ligand system contains appropriate acceptor orbitals, such as the π^* orbitals on bipyridine, and the central ion is in a low oxidation state. In the spectrum of this complex, the MLCT bands characteristic of the $d \rightarrow \pi^*$ transition to the bpy ligand and to the dpp ligand are found respectively at 432 nm and at 487 nm. A Gaussian fit shows the individual contributions of the two transitions in the visible region (Figure 19) and yields molar extinction coefficients of 9600 M^{-1} cm^{-1} and 4600 M^{-1} cm^{-1} and full width at half maximum of 5000 cm^{-1} and 2000 cm^{-1} respectively. The high-intensity bands in the UV range (248 and 286 nm) are intraligand $\pi \rightarrow \pi^*$ transitions of the bpy and dpp ligands.

The luminescence spectrum (Figure 18) obtained by exciting the complex at 470 nm yields a broad emission with wavelength maximum at 700 ± 5 nm that appears red-shifted by approximately 10 nm compared to previously published values[61]. The shift to lower energy is attributed to the enhanced red sensitivity of the detection system. The emission follows a single-exponential decay and occurs invariably from the lowest energy MLCT state, independent of the excitation wavelength used.

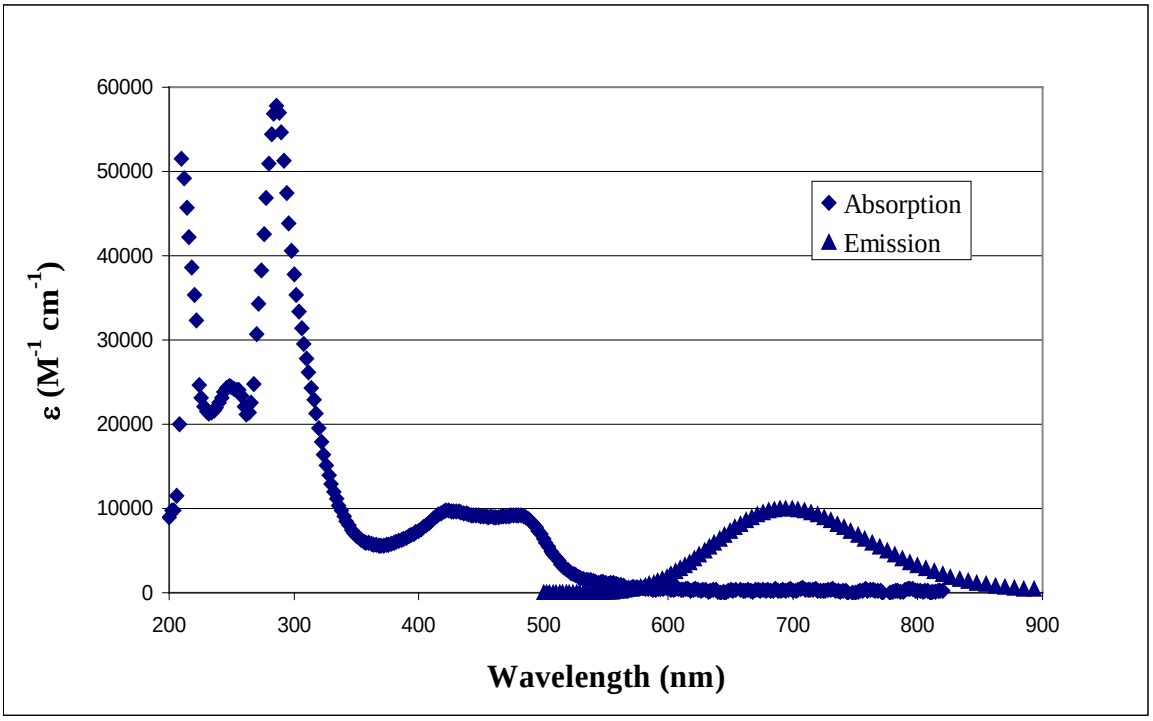

Figure 18. UV-Vis absorption and emission spectra of $[(bpy)_2Ru(dpp)](NO_3)_2$ in H_2O at room temperature.

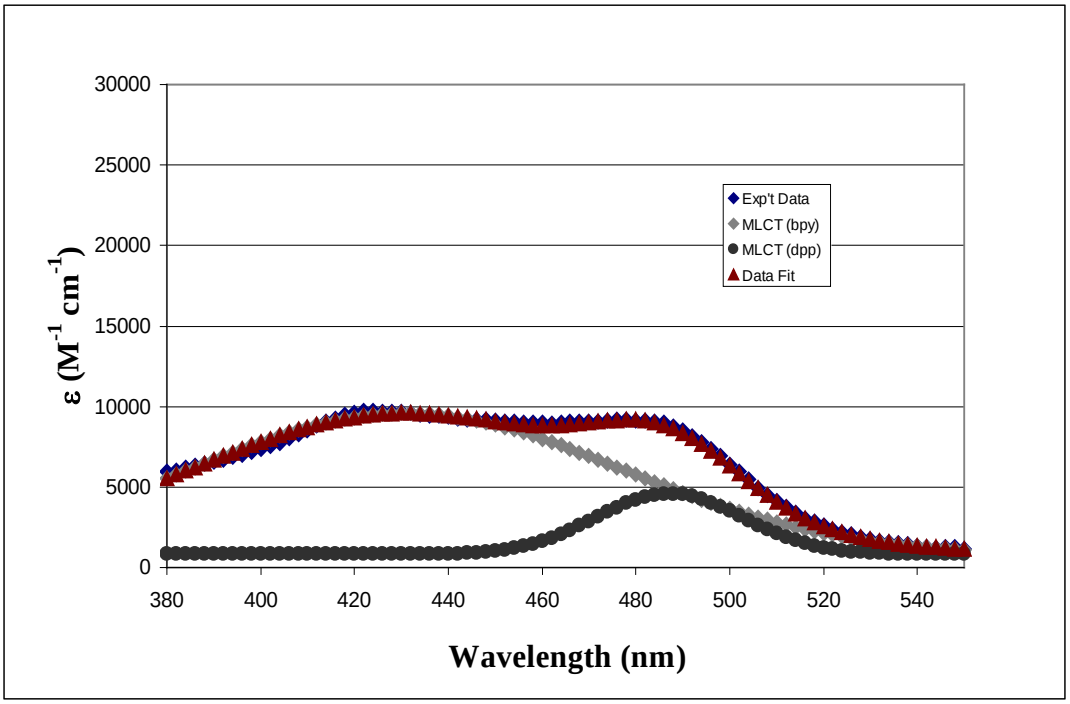

Figure 19. Gaussian fit of $[(bpy)_2Ru(dpp)](NO_3)_2$ MLCT transitions.

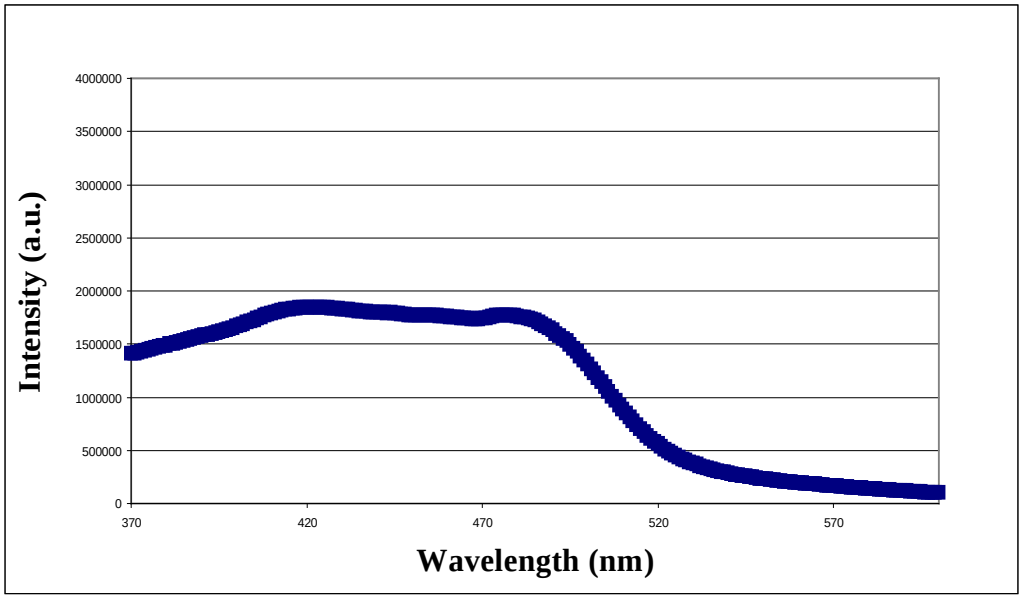

Figure 20. Excitation spectrum of $[(bpy)_2Ru(dpp)]^{2+}$ at pH 7 monitored at 700 nm.

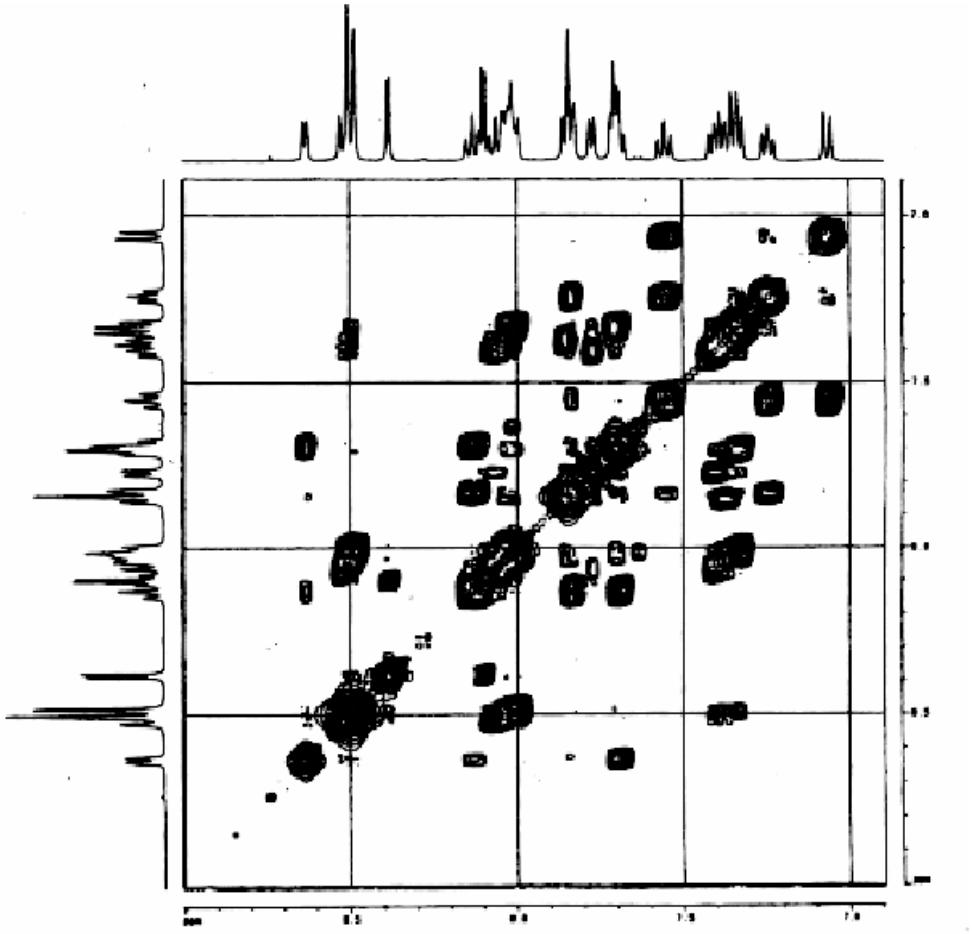

Figure 21. ^1H-^1H COSY-NMR of 0.01 M $[(bpy)_2Ru(dpp)]^{2+}$ in D_2O[65].

The excitation spectrum (Figure 20) confirms that both MLCT contribute to the emission as the contour mirrors the absorption spectrum. Time-resolved analysis yields a lifetime of 128 ± 2 nsec in distilled water and of 200 ± 10 nsec in ethanol, in agreement with values reported by other researchers[61].

The ^{1}H-NMR of the nitrate form of the complex dissolved in D_2O is shown in Figure 22. All signals fall in the aromatic region and integration confirms the presence of 26 protons belonging to 7 ring systems. The electron density on the ligands is diminished upon coordination causing a slight downfield shift in the position of the peaks relative to that of the free ligands. The third ring of the dpp ligand introduces an asymmetry in the complex that affects the bipyridine ligands differently. The signals for the protons of each bpy ring can be broadly grouped in four clusters according to their position in the ring. Attributing each peak to a specific ring however, is complicated by the fact that the chemical shifts for a specific position on the ring may overlap but do not always coincide.

Table 5. ^{1}H-NMR chemical shifts of $[(bpy)_2Ru(dpp)](NO_3)_2$.

Position	H-NMR (ppm) bpy protons	H-NMR (ppm) dpp protons
3	8.66 (d)	--
4	8.1 - 8.3 (t)	--
5	7.5 - 7.6 (t)	8.54
6	7.7 - 7.9 (d)	8.24
3’	--	7.22
4’	--	7.71
5’	--	7.40
6’	--	8.00
3’’	--	8.00
4’’	--	8.29
5’’	--	7.85
6’’	--	8.78

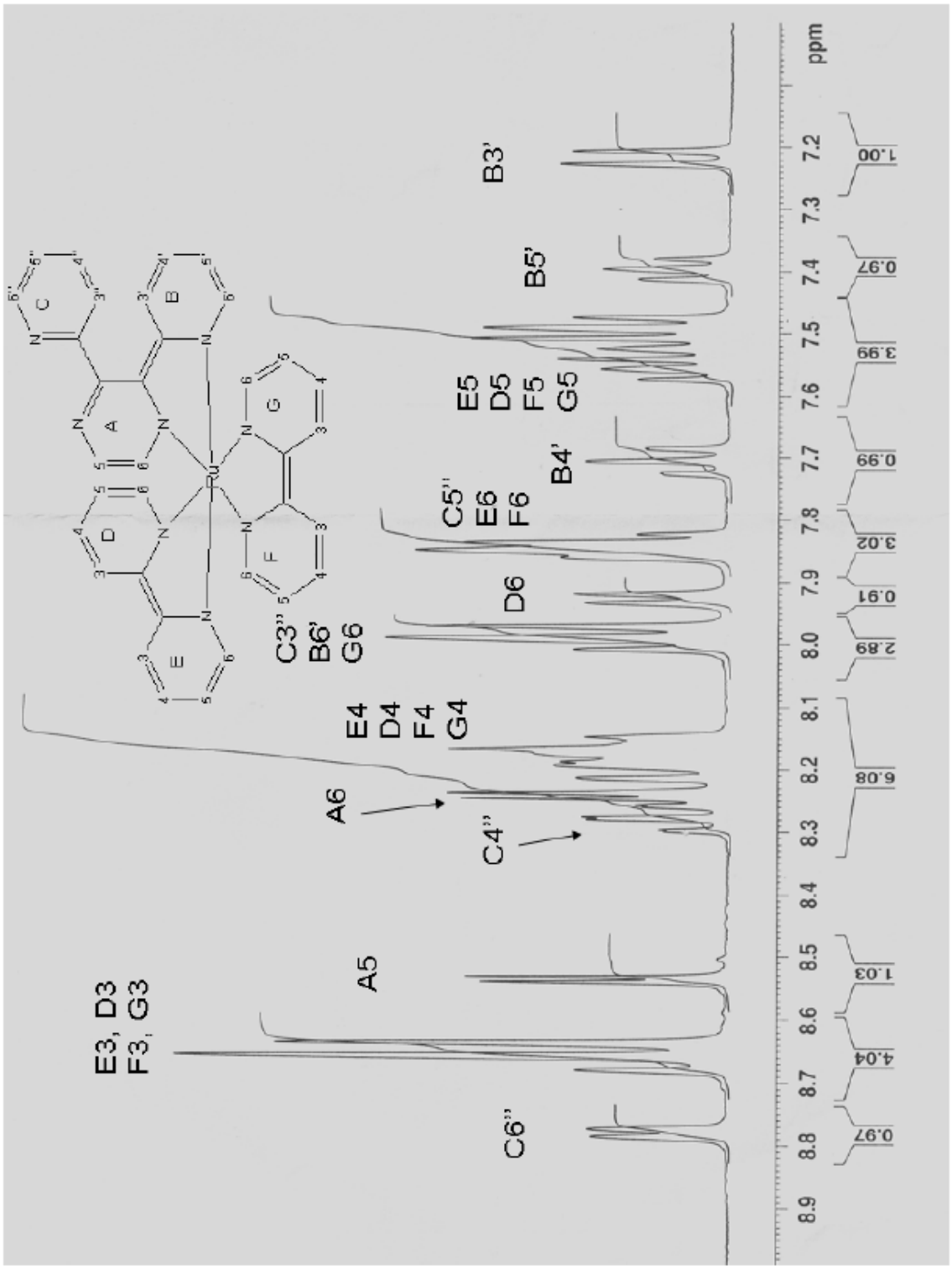

Figure 22. ^{1}H-NMR of 0.01 M $[(bpy)_2Ru(dpp)]^{2+}$ in D_2O[65].

The ^{1}H-^{1}H COSY NMR and the comparison to chemical shifts reported for the same complex in acetonitrile[62] helped in the assignement of the peaks belonging to the dpp ring system.

3.A.2. $[Os(bpy)_3](PF_6)_2$

The complex was synthesized as a spectroscopic standard to quantitate the emission properties of $[Ru(bpy)_2dpp]^{2+}$. The UV-vis absorption spectrum of $[Os(bpy)_3](PF_6)_2$ recorded in acetonitrile (Figure 23) consists of three series of bands with varying energies and intensities. The ligand-localized π-π^* transitions appear at high energies with wavelengths characteristic of complexed bipyridines (248 and 289 nm). Because of significant spin-orbit coupling, the MLCT bands responsible for the deep green brown colors of the material include transitions to states largely singlet in character in the near-UV and visible regions, and to states largely triplet in character on the low-energy side of the spectrum. The intense set of transitions mainly singlet in character spans the region from 360 to 530 nm ($\varepsilon_{max} > 10^4$) while the bands with diminished intensity ($\varepsilon_{max} \sim 5 \times 10^3$) covering the region from 530 to 700 nm are due to spin forbidden singlet-triplet MLCT transitions. The results described are in agreement with values reported in the literature[66,67,68].

The emission spectrum of a sample of the complex in acetonitrile, degassed with Argon, shows a single broad luminescence peak with maximum at 722 nm ± 5 nm upon excitation at 436nm (Figure 24). Emission occurs from a lower energy, largely triplet state with lifetime in acetonitrile of 60 ± 2 nsec and exhibits a single-exponential decay. In contrast to $[Ru(bpy)_3]^{2+}$ and $[(bpy)_2Ru(dpp)]^{2+}$, the emission from $[Os(bpy)_3](PF_6)_2$

occurs in a spectral region that partially overlaps the lower energy MLCT absorption range of the Os(II) complex.

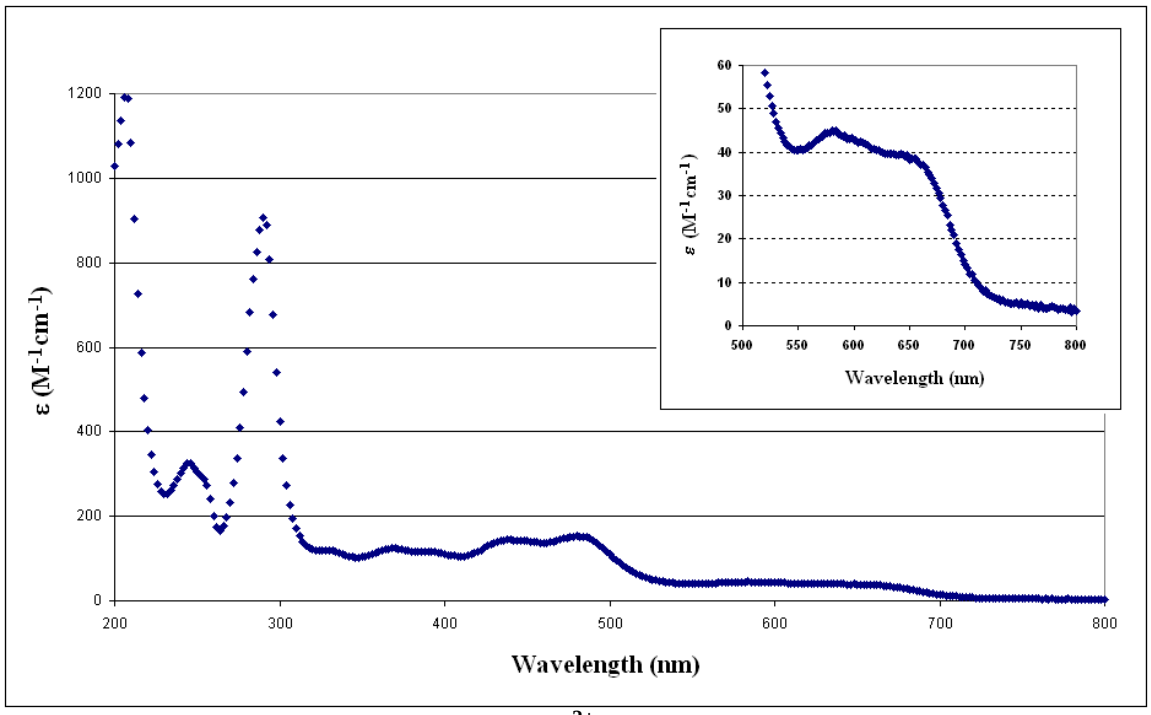

Figure 23. UV-Vis spectrum of $[Os(bpy)_3]^{2+}$ in acetonitrile at room temperature.

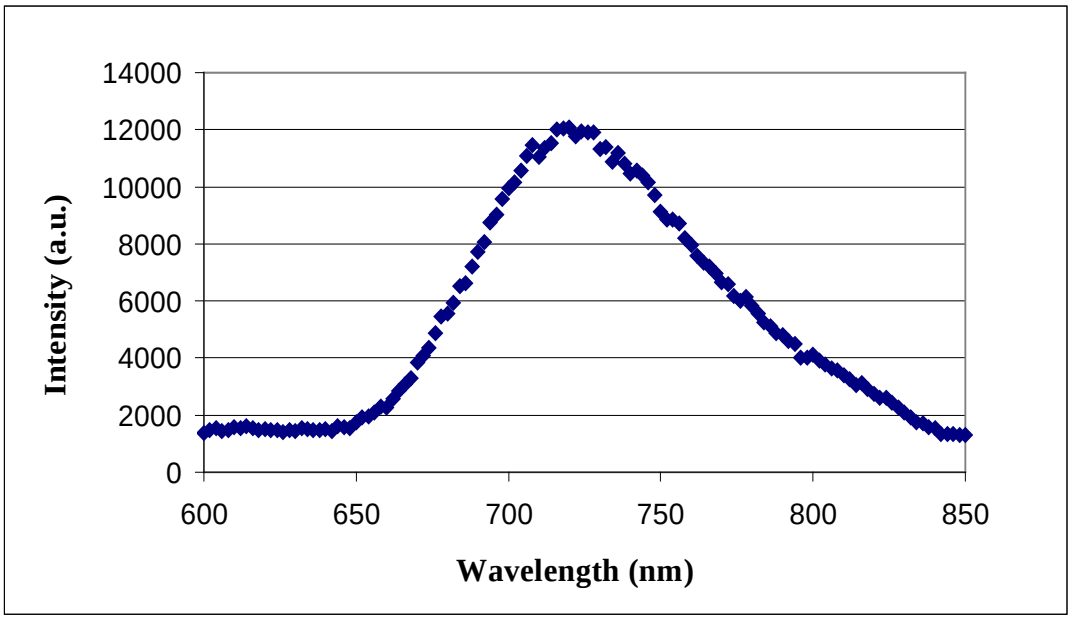

Figure 24. The steady-state emission spectrum of $[Os(bpy)_3]^{2+}$ in acetonitrile at room temperature.

3.A.3. 2-(2-Pyridyl) Pyrazine

The pypz ligand was characterized by proton and carbon NMR spectroscopy in deuterated chloroform (Figure 25-27) and the experimental values of chemical shifts found were compared with values in the literature[55]. The signal at 7.28 ppm is the solvent peak of $CDCl_3$.

Table 6. ^{1}H-NMR and ^{13}C-NMR chemical shifts of free pypz.

Position	H-NMR (ppm) exp	H-NMR (ppm) lit	C-NMR (ppm) exp	C-NMR (ppm) lit
6’	8.75 (d)	8.69	149.5	149.9
5’	7.39 (t)	7.34	124.5	124.8
4’	7.88 (t)	7.82	137.2	137.5
3’	8.39 (d)	8.33	121.5	121.8
2’	--	--	154.2	154.6
2	--	--	151.1	151.5
3	9.66 (s)	9.61	143.4	143.7
5	8.64 (d)	8.60	144.5	144.8
6	8.64 (d)	8.57	143.6	143.9

The UV-Vis spectrum of pypz in water, Figure 28, shows two intense bands in the UV region at 229 and 284 nm due to $\pi^* \leftarrow \pi$ transitions of the conjugate system. As expected, no bands are evident in the visible and near-IR regions. Emission in water was not observed.

3.A.4. $[(bpy)_2Ru(pypz)]Cl_2$

The complex was originally prepared by Kincaid and coworkers and characterized by resonance Raman and time-resolved resonance Raman[69]. NMR and electronic properties are presented here for the first time, together with electrochemical data and a preliminary attempt to identify the crystal structure of the chloride complex.

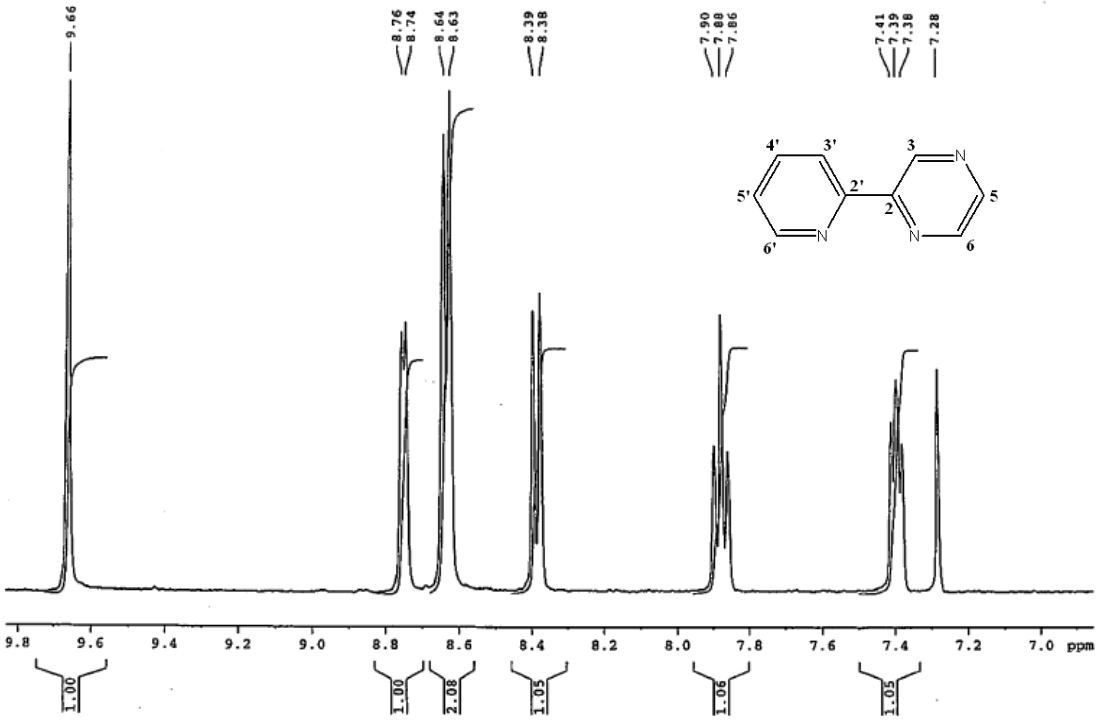

Figure 25. ^{1}H-NMR spectrum of 2-(2-pyridyl)pyrazine.

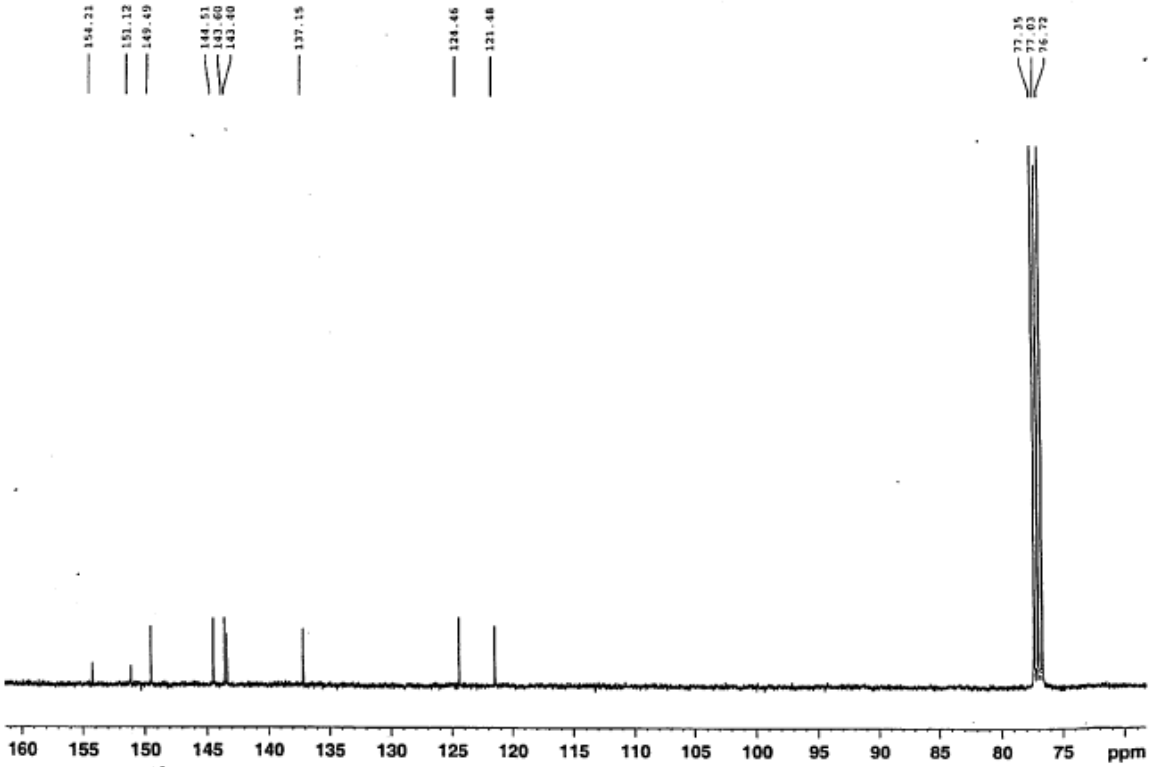

Figure 26. ^{13}C-NMR spectrum of 2-(2-pyridyl)pyrazine.

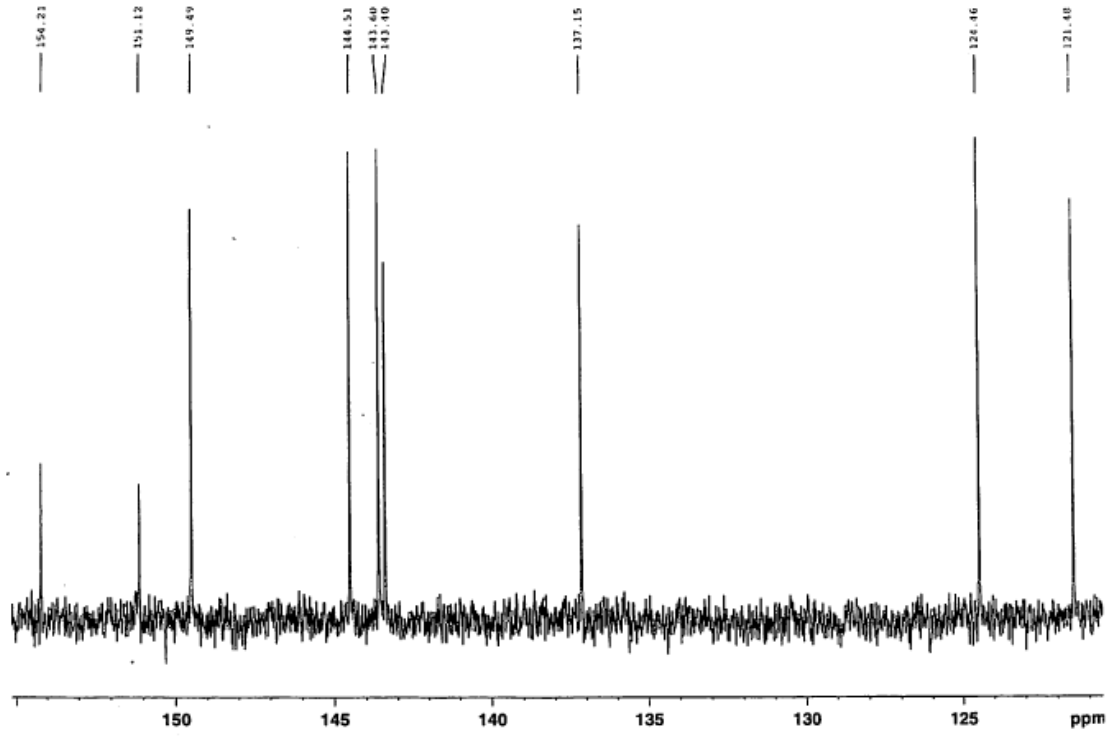

Figure 27. Blown-up portion of the ^{13}C-NMR spectrum of 2-(2-pyridyl)pyrazine.

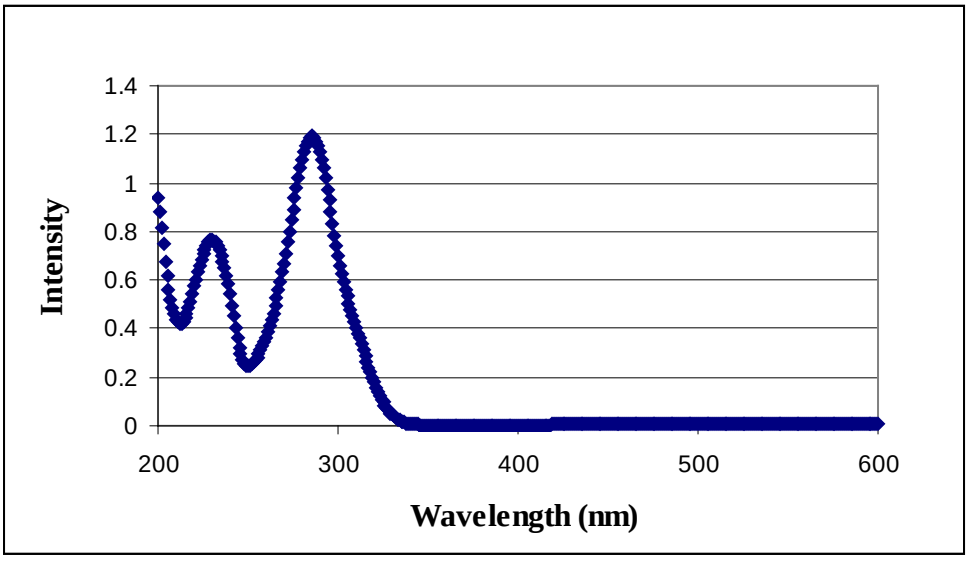

Figure 28. UV-Vis spectrum of 2-(2-pyridyl)pyrazine in water at room temperature.

3.A.4.a. Absorption, Emission, Excitation

The spectrum of $[(bpy)_2Ru(pypz)]Cl_2$ in water at room temperature is shown in Figure 29. Strong spin-allowed intraligand absorptions appear in the UV region at 284 and 243 nm with a shoulder at 250 nm. The broad charge-transfer band in the visible region responsible for the bright orange color arises from two $d\rightarrow\pi^*$ transitions, from the metal to the bpy and pypz ligands. Using resonance Raman spectroscopy, Kincaid and coworkers[69] studied in detail the charge distribution of the MLCT states and assigned the ligand termination of each transfer. Here, a gaussian fit shows the contribution of each transition to the overall absorption (Figure 30). The transition to the bpy ligand exhibits a maximum at 435 nm, has a 4440 cm^{-1} FWHM (full width at half maximum) and an extinction coefficient of 10900 M^{-1} cm^{-1}. The transition to the pypz ligand is centered at 476 nm, has a narrower width, 1640 cm^{-1}, and the extinction coefficient taken from the mathematical data fit is 5250 M^{-1} cm^{-1}. No additional absorption is observed at lower energies.The luminescence spectrum obtained at room temperature yields a broad emission with wavelength maximum at 675 ± 5 nm (Figure 32) and lifetime of 150 ± 16 ns. In water, the emission follows a single-exponential decay (Figure 33) and occurs invariably from the lowest energy MLCT state, independent of the excitation wavelength used. The excitation spectrum (Figure 31) taken in buffer solution at pH 8 confirms that both MLCT absorptions contribute to the emission as the contour mirrors the absorption spectrum. The complexes' emission was also recorded in acetonitrile and proved to be solvent-dependent. The wavelength max, 697 nm, is red-shifted in acetonitrile if compared to water, 675nm, and the excited state has longer lifetime (345 ± 5 ns).

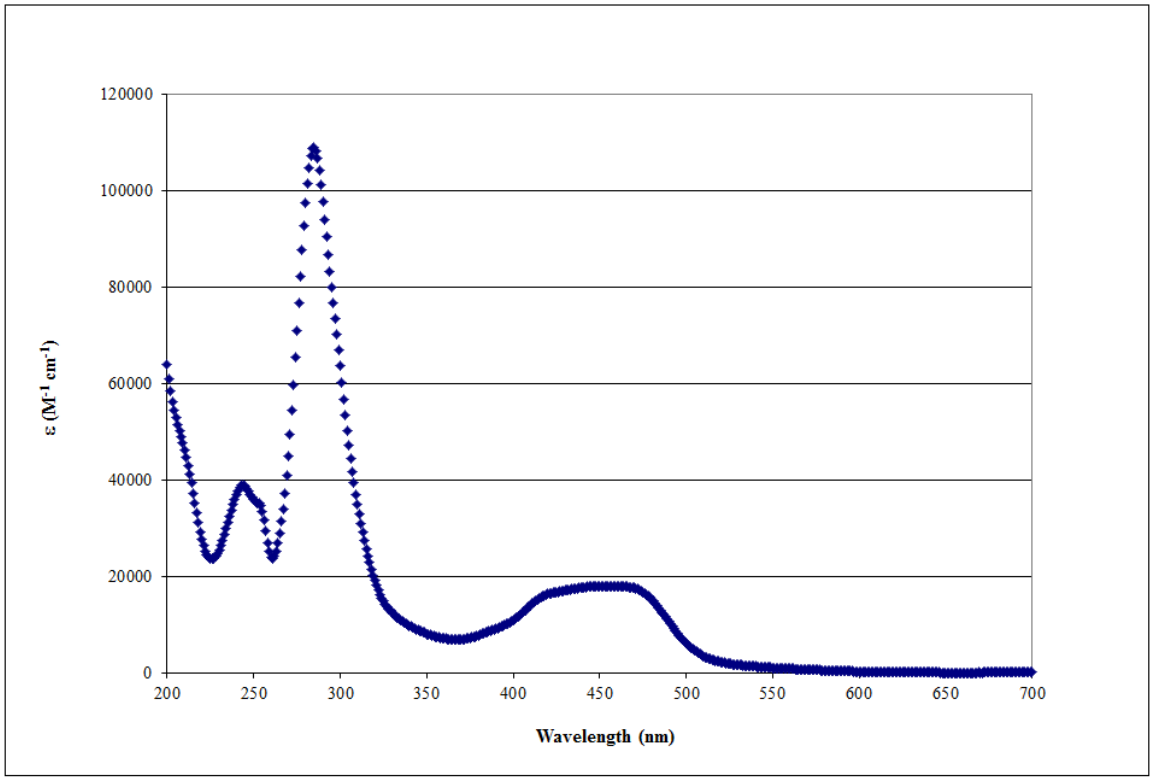

Figure 29. UV-Vis spectrum of $[(bpy)_2Ru(pypz)]Cl_2$ in H_2O.

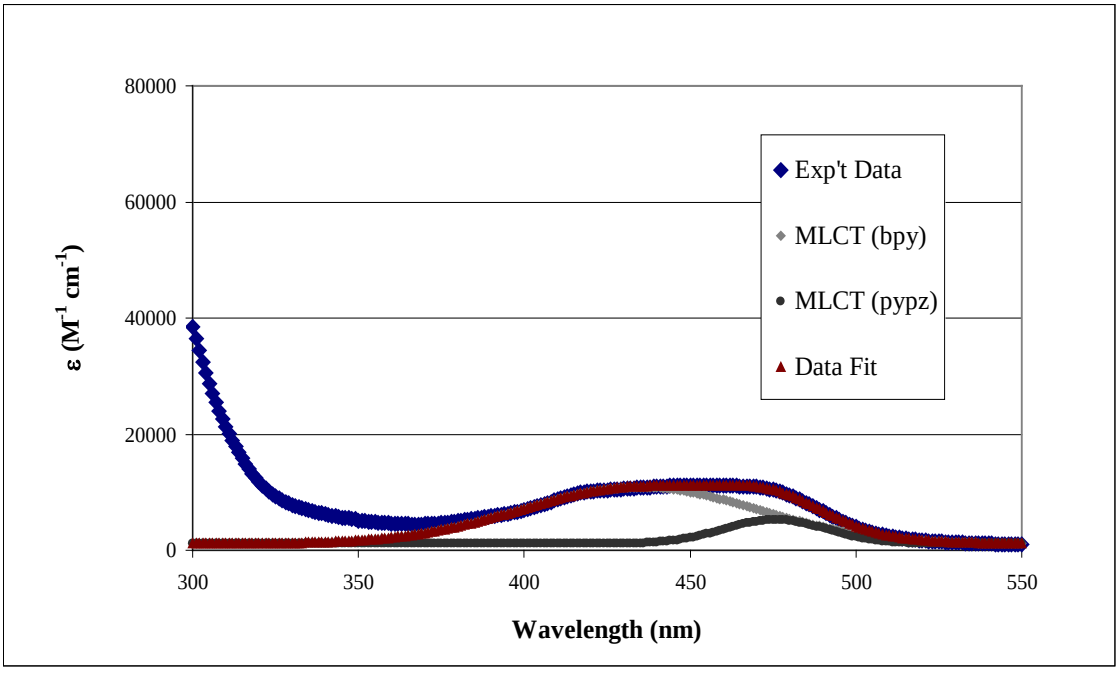

Figure 30. Gaussian fit of $[(bpy)_2Ru(pypz)]Cl_2$ MLCT transitions.

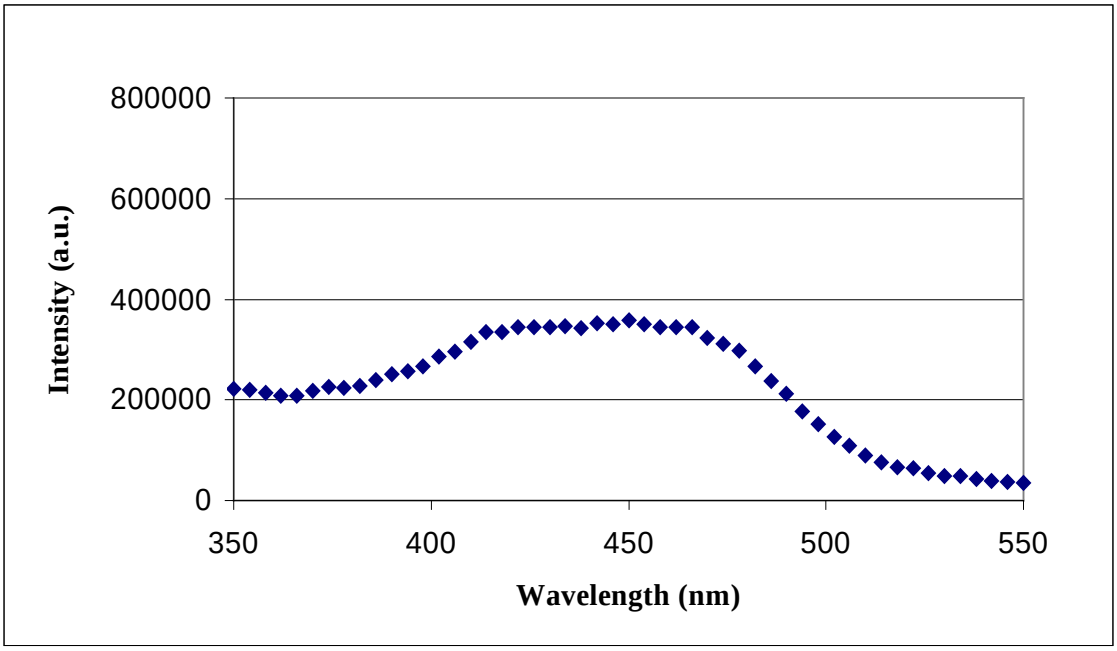

Figure 31. Excitation spectrum of $[(bpy)_2Ru(pypz)]^{2+}$ monitored at 670 nm.

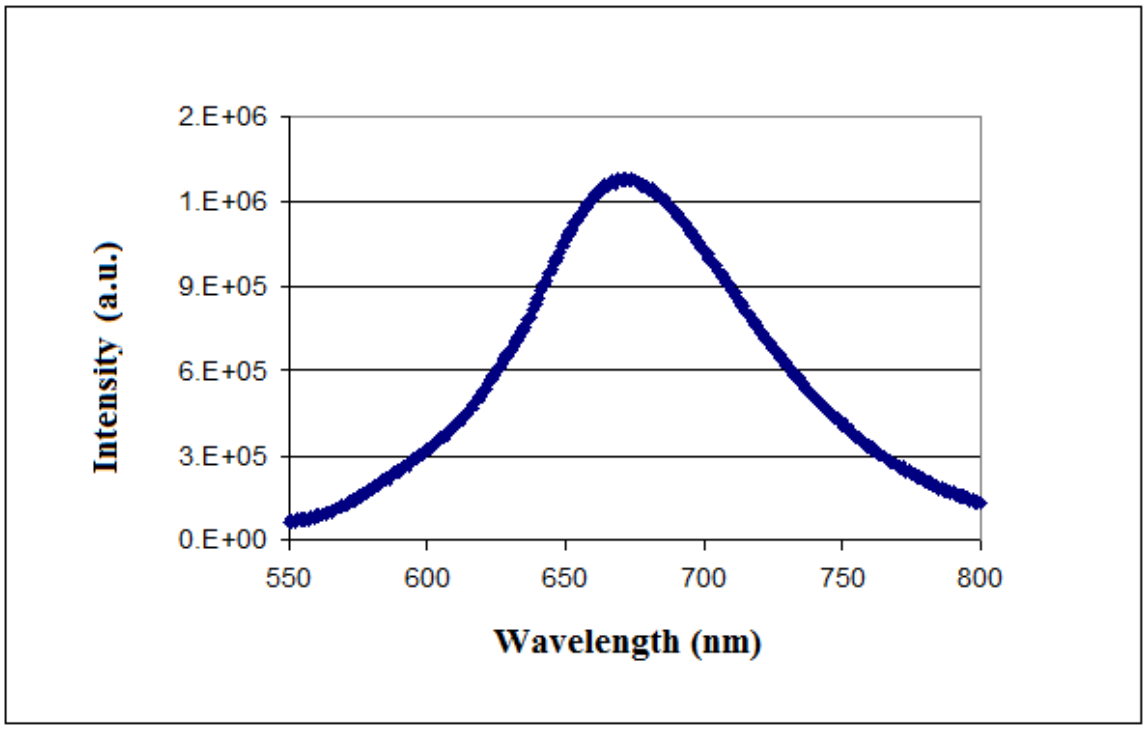

Figure 32. Emission spectrum of $[(bpy)_2Ru(pypz)]Cl_2$ in H_2O (λ_{exc} = 470 nm).

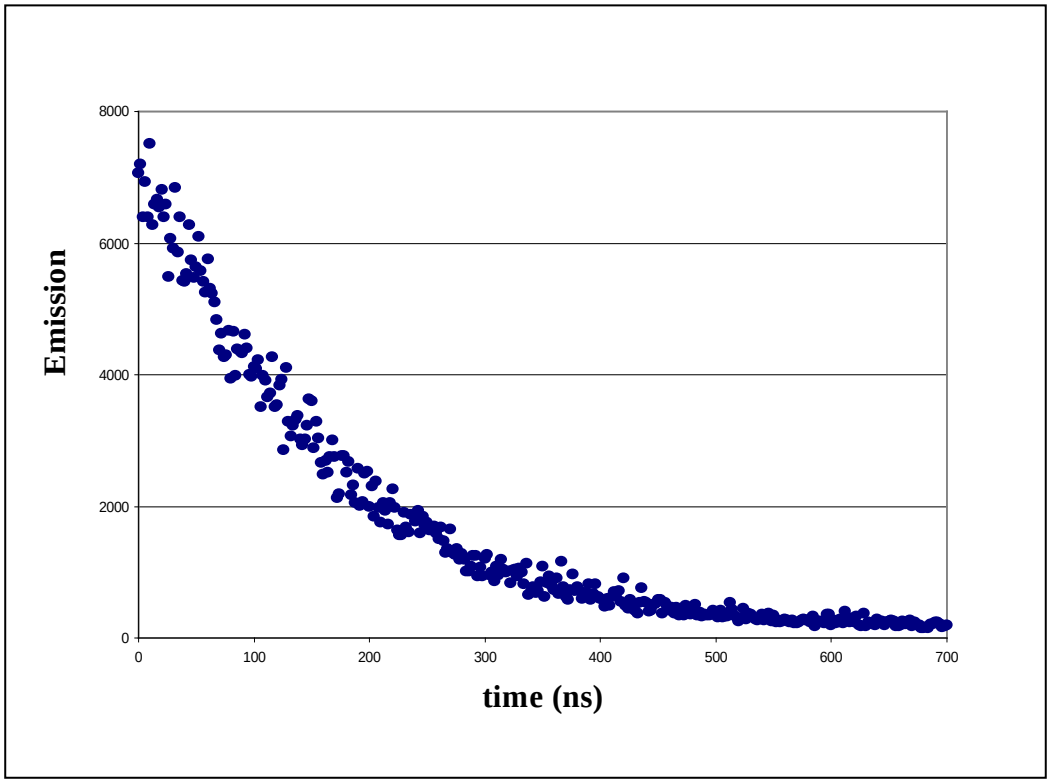

Figure 33. Decay profile of $[(bpy)_2Ru(pypz)]Cl_2$ in H_2O.

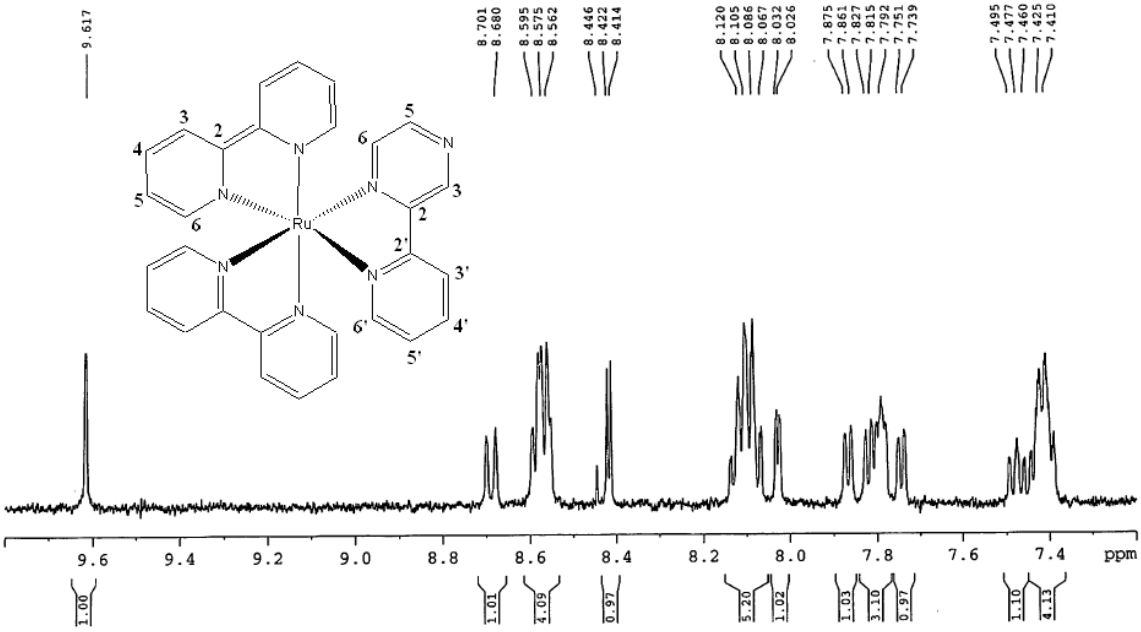

Figure 34. ^{1}H-NMR spectrum of $[(bpy)_2Ru(pypz)]Cl$ in D_2O.

3.A.4.b. NMR

The proton, carbon and 2D NMR spectra of $[(bpy)_2Ru(pypz)]^{2+}$ in D_2O were recorded, integrated and studied in detail to assign unambiguously the chemical shift of each nucleus. The values obtained are reported in Table 7. The numbering of each position is consistent with the convention adopted earlier for the free ligand (Figure 34).

Table 7. ^{1}H-NMR and ^{13}C-NMR chemical shifts of $[(bpy)_2Ru(pypz)]Cl_2$.

Position	H-NMR (ppm) bpy protons	H-NMR (ppm) pypz protons	C-NMR (ppm) bpy protons	C-NMR (ppm) pypz protons
2	--	--	155.5-156.0	153.28
3	8.57	9.62 (s)	123.40	143.25
4	8.08	--	137.35	--
5	7.45	8.03 (m)	126.56	145.75
6	7.7-7.8	8.42 (d)	150.43	144.94
2’	--	--	--	154.08
3’	--	8.7 (d)	--	124.07
4’	--	8.1	--	137.11
5’	--	7.48 (t)	--	127.28
6’	--	7.87 (d)	--	150.84

The integration of the ^{1}H-NMR accounts for 23 protons signals, assuming the integration of the singlet at 9.62 ppm represents 1 proton. All signals of the 6-ring system fall in the aromatic region. The bpy protons appear in 4 clusters of signals, according to their position in the ligand. The asymmetry introduced by the presence of the pypz ligand is not enough to allow the distinction between the protons on each ring. In fact, the overlap limits the level of detail that can be gathered for each, hence the mutiplicity and coupling constant of each signals cannot be established. Protons H-5 and H-6 on pypz form a doublet because of each other’s presence and they have a coupling constant of 3.2 Hz. Higher coupling constants are recorded on the pyridyl moiety, with J(5’-6’) = 5.6 Hz

and J(3'-4') = 8.4 Hz. The coupling constant for H-4' and H-5' could not be established because their signals partly overlap with bpy signals.

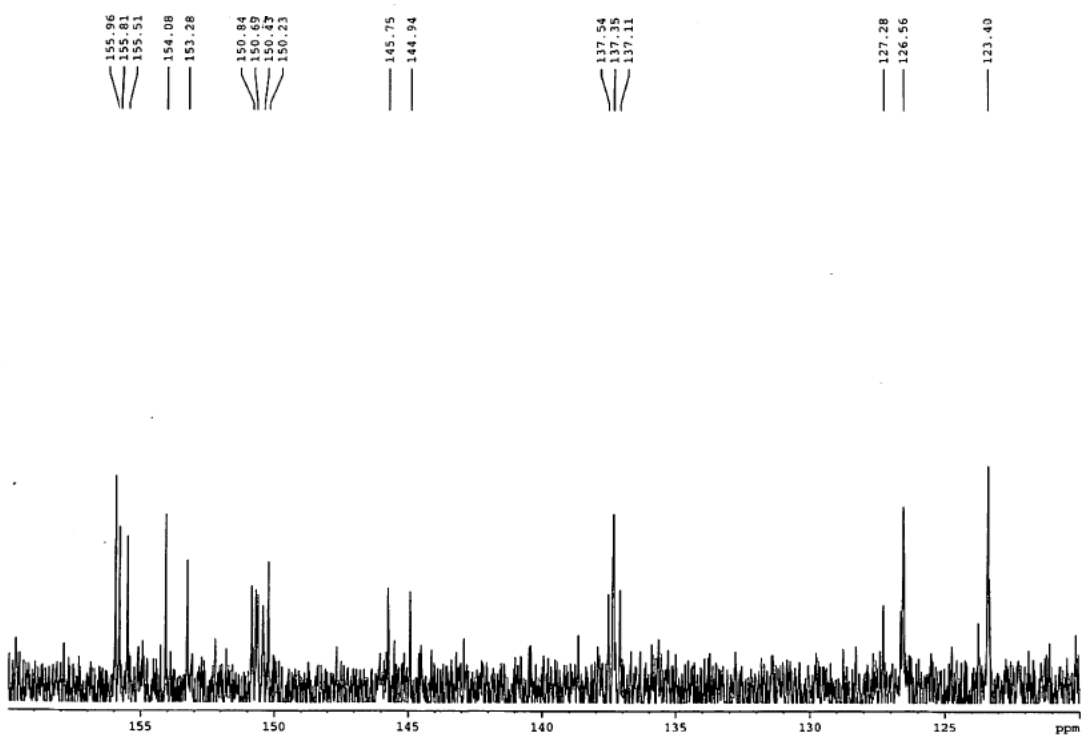

Figure 35. ^{13}C-NMR spectrum of [(bpy)$_2$Ru(pypz)]Cl$_2$ in D$_2$O.

The signals from the bpy and pypz carbons are all accounted for in the ^{13}C-NMR spectrum and fall either close to their position in the uncoordinated ligands or slightly downfield due to the deshielding presence of the positively-charged metal.

The two-dimensional ^{1}H-^{13}C COSY spectrum (Figure 38), although faint, was crucial in the assignment of the protons of the pypz system as it correlated the well-established position of the carbon nuclei with the more ambiguous proton chemical shifts. The ^{1}H-^{1}H correlation spectra, Figures 36 and 37, provided the final confirmation necessary when the assignment was complicated by the overlap with bpy signals.

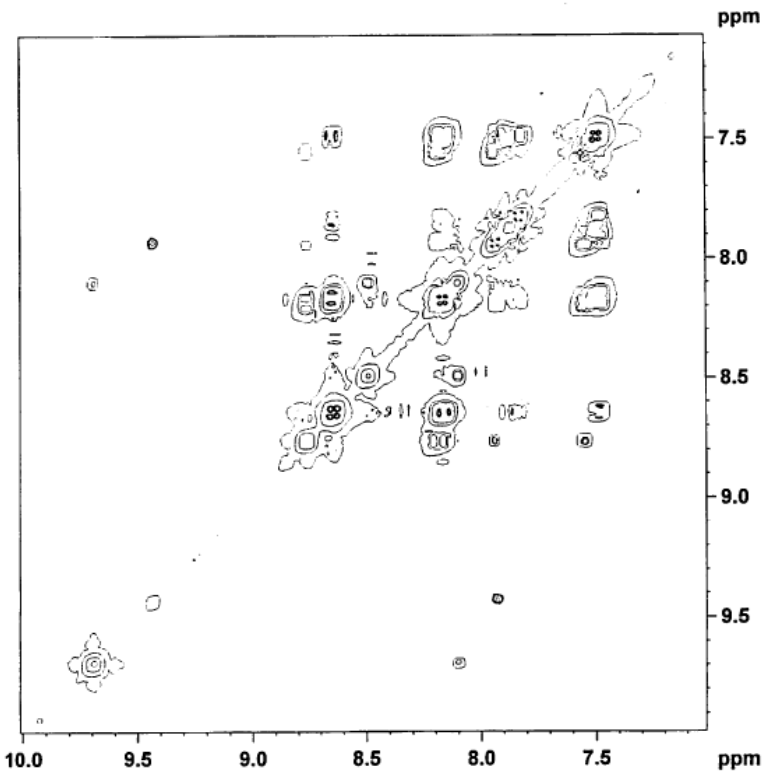

Figure 36. COSY 90SW NMR spectrum of $[(bpy)_2Ru(pypz)]Cl_2$ in D_2O.

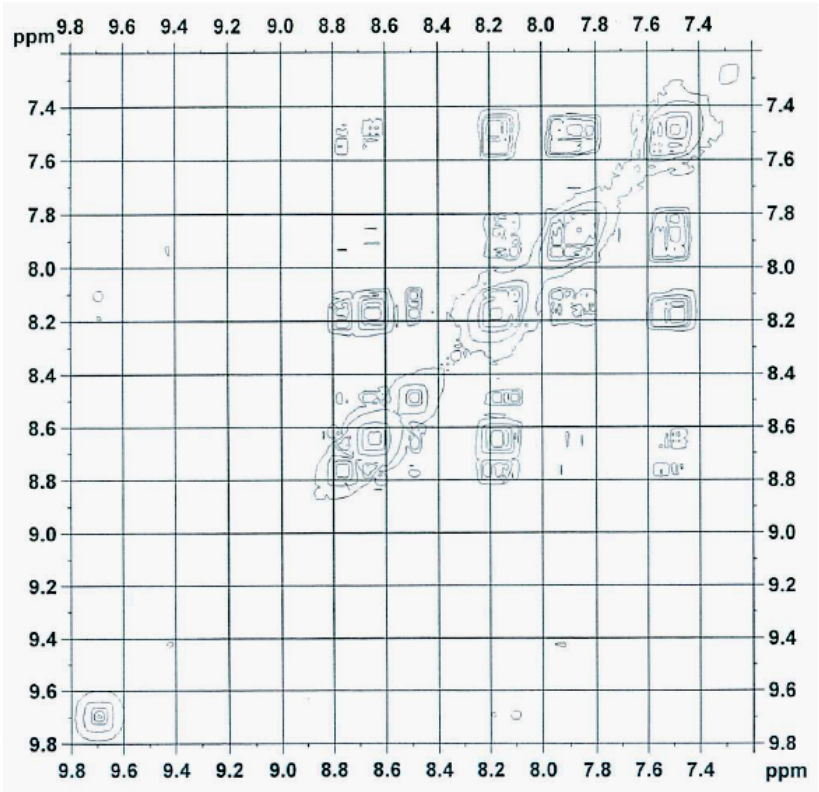

Figure 37. COSY 45SW NMR spectrum of $[(bpy)_2Ru(pypz)]Cl_2$ in D_2O.

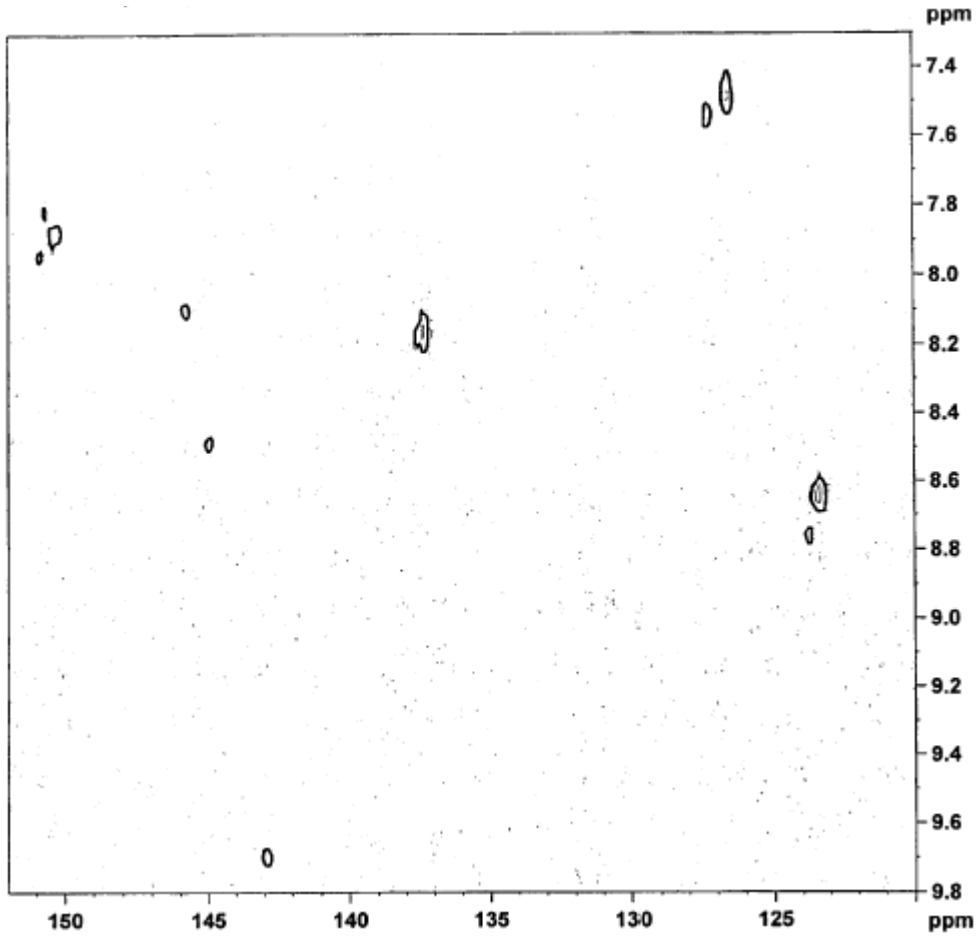

Figure 38. ^{1}H-^{13}C COSW NMR spectrum of $[(bpy)_2Ru(pypz)]Cl_2$ in D_2O.

3.A.4.c. Electrochemistry

Cyclic voltammetry experiments on $[(bpy)_2Ru(pypz)]^{2+}$ were performed in acetonitrile with 0.1M TEAP as supporting electrolyte. Water could not be used as a medium, since the potential necessary for the reaction is high enough to cause its oxidation. For the same reason, highly acidic solutions could not be tested. The results are reported in Table 8 and Figure 39 shows the values of potential in millivolts (mV) *vs* the current generated as a result of the potential applied. Each run consisted of 4 scans

starting with a positive sweep and recorded the oxidation of the metal (Ru(II)/Ru(III)) in the potential range between + 0.7 and +1.2V.

The two parameters of interest on the cyclic voltammograms are the separation of peak potentials, E_{pa} –E_{pc}, and the ratio of peak currents, i_{pc}/i_{pa}. The difference in potential between anodic and cathodic peak currents declined from 180 to 90 mV as the scan rate

Table 8. Electrochemical data from cyclic voltammetry of $[(bpy)_2Ru(pypz)]^{2+}$.

Experiment	E_{pc} (mV)	E_{pa} (mV)	$E_{1/2}$ (ox) (V)	ΔE_p (mV)	Scan Rate (mV/sec)
#1	858	1038	0.95	180	200
#2	875	1021	0.95	146	100
#3	891	1000	0.95	109	20
#4	901	999	0.95	98	10
#5	905	995	0.95	90	5

is reduced (Figure 40). This suggests the kinetics of the reaction is 'slow' and thus the equilibria at the electrode surface are not established rapidly competitively with the voltage scan rate. Such behavior indicates that the current takes more time to respond to the applied voltage than in the case of reversible systems and the voltage applied does not result in the generation of the concentrations at the electrode surface predicted by the Nernst equation. At lower scan rates, the system tends toward the reversible case (ΔE_p = 58 mV). The $E_{1/2}$ values for the oxidation potential were calculated from the average of the anodic and cathodic peak potentials:

$$E_{1/2} = (E_{pa} + E_{pc})/2 \qquad (84)$$

The ratio of peak currents for a Nernstian (reversible) wave with stable product should equal unity regardless of scan rate and diffusion coefficients. When, as is the case here,

the actual baseline for measuring i_{pc} cannot be determined without ambiguity, the ratio can be calculated from the expression suggested by Nicholson[70]:

$$\frac{i_{pc}}{i_{pa}} = \frac{(i_{pc})_0}{i_{pa}} + \frac{0.485\,(i_{sp})_0}{i_{pa}} + 0.086 \qquad (85)$$

where $(i_{pc})_0$, is the uncorrected cathodic peak current with respect to the zero current baseline and $(i_{sp})_0$ is the current at the switching potential (Figure 39).

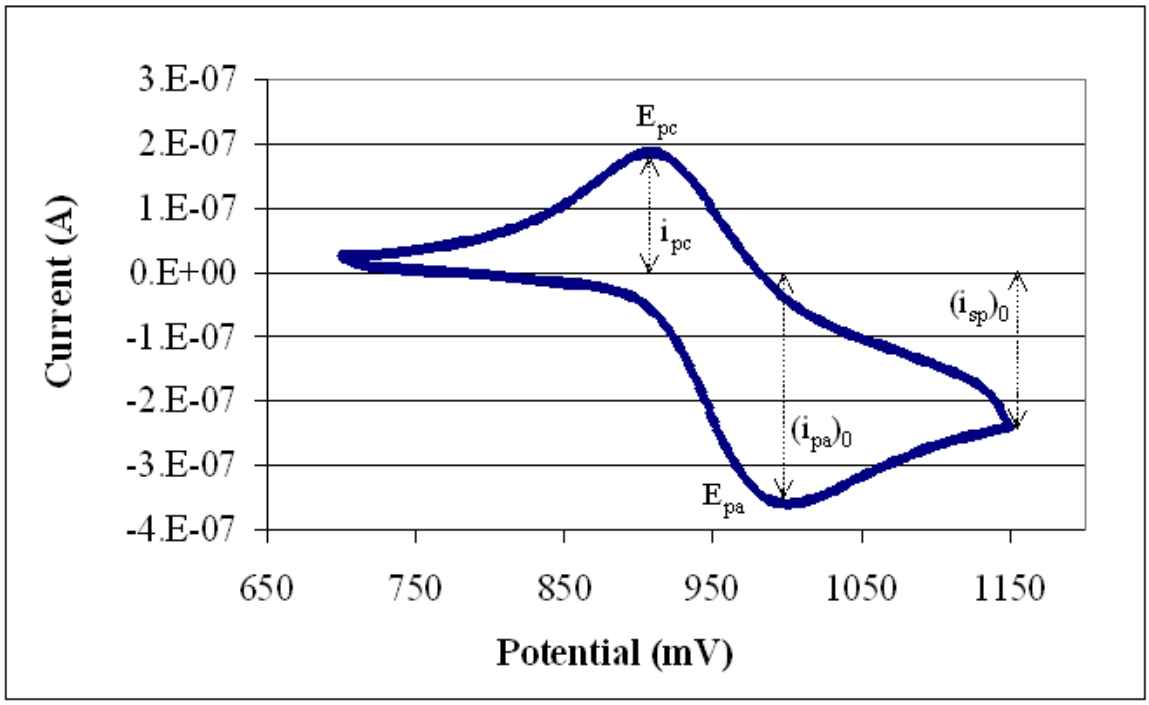

Figure 39. Cyclic voltammogram of $[(bpy)_2Ru(pypz)]^{2+}$ in ACN at 20 mV/sec.

The experimental current values obtained from the voltammogram recorded at the lowest scan rate are 0.186 microamps (μA) for $(i_{pc})_0$, 0.361 μA for i_{pa} and 0.240 μA for $(i_{sp})_0$. The ratio of currents calculated from equation 85 using the above-mentioned values is 0.93. A slight deviation of the ratio from unity is not uncommon[71] and is unlikely due to complications in the electrode process. There was no evidence of precipitate formation

during scans and the sample retained its emissivity after the experiment, indicating that the ruthenium had returned to its original oxidation state. Dissociation of one of the ligands would have also caused loss of luminescence and was therefore excluded.

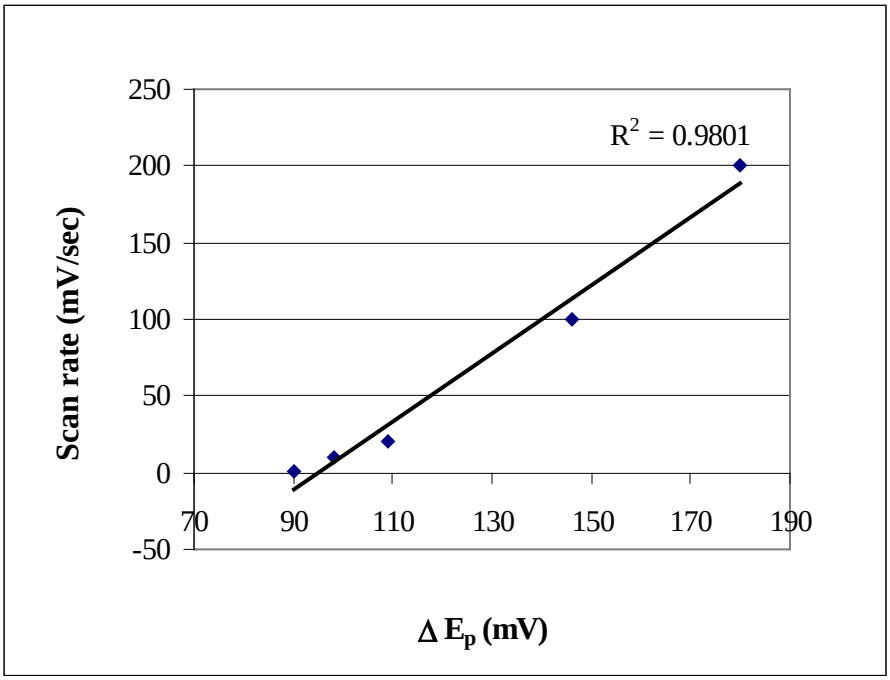

Figure 40. Difference in anodic and cathodic peak potentials at decreasing scan rates.

3.A.4.d. X-ray Crystallography

The crystals (labeled X1638L) of $[(bpy)_2Ru(pypz)]^{2+}$ grown in acetone were analyzed by X-Ray diffraction to try to obtain more information about the molecular structure of the complex. Two data sets were collected. The approximate formula of the crystals is $C_{29}H_{23}N_7RuCl{\cdot}4(CH_3COCH_3)$. Crystals X1638L were found to have approximate dimensions 0.12 x 0.34 x 0.34 mm and resulted hexagonal with space group *P*6/*mcc*. The final unit-cell constants of X1638L were *a* = 13.106(2) Å, b = 13.106(2) Å,

c = 20.916(4) Å, V = 3111.4(9) Å^3, Z = 4, approximate ρ = 1.590 g cm^{-1}, μ = 0.64 mm^{-1}, formula weight = 2978.74. The reported formula and density are approximate since the disordered solvent could not be identified with certainty. The solvent of crystallization used was acetone hence it is probable that the disordered solvent in the crystals is also acetone. The final discrepancy indices for the 1226 unique reflections (θ < 27.51˚) were R = 0.0283 (calculated on F) and R_w = 0.0766 (calculated on F^2) with 106 parameters varied. The major peaks (< 0.44 e Å^{-3}) of the final difference map are near the ruthenium atom. The crystallographic data (bond distances and angles) and parameters at 100 K are summarized in Table 9 and 10.

Table 9. Basic crystal data for X1638L at 100K

```
 TITL x1638l C29H23N7RuCl2.CH3C0CH3 P6/mcc Gafney/Ferloni 29-Jan-2008 100 K
 CELL 0.71073  13.1060  13.1060  20.9160  90.000  90.000 120.000
 ZERR    6.00   0.0019   0.0019   0.0042   0.000   0.000   0.000
 LATT  1
 SYMM -Y, X-Y, Z
 SYMM -X+Y, -X, Z
 SYMM -X, -Y, Z
 SYMM Y, -X+Y, Z
 SYMM X-Y, X, Z
 SYMM Y, X, 0.5-Z
 SYMM X-Y, -Y, 0.5-Z
 SYMM -X, -X+Y, 0.5-Z
 SYMM -Y, -X, 0.5-Z
 SYMM -X+Y, Y, 0.5-Z
 SYMM X, X-Y, 0.5-Z
 SFAC   C   H   N   O  CL  RU  NA
 UNIT 192 174  42   6  12   6   6

V = 3111.35     F(000) = 2202.0     Mu = 1.09 mm-1      Cell Wt = 4335.49
Rho = 2.314
TEMP -173
SIZE 0.12 0.34 0.34
```

Table 10. Bond distances and bond angles for X1638L at 100 K

Bond	Distance	Bond	Angle
Ru - N1	2.061 Å	N1 - Ru - N1	94.6°
Ru - N1	2.062 Å	N1 - Ru - N1	94.5°
Ru - N1	2.062 Å	N1 - Ru - N1	78.9°
Ru - N1	2.061 Å	N1 - Ru - N1	92.7°
Ru - N1	2.062 Å	N1 - Ru - N1	170.6°
Ru - N1	2.062 Å	N1 - Ru - N1	94.5°
		N1 - Ru - N1	92.7°
		N1 - Ru - N1	170.6°
		N1 - Ru - N1	78.9°
		N1 - Ru - N1	170.6°
		N1 - Ru - N1	78.9°
		N1 - Ru - N1	92.7°
		N1 - Ru - N1	94.6°
		N1 - Ru - N1	94.5°
		N1 - Ru - N1	94.5°
N1 - Ru	2.061 Å	Ru - N1 - C2	126.2°
N1 - C2	1.352(3) Å	Ru - N1 - C6	115.6°
N1 - C6	1.362(2) Å	C2 - N1 - C6	118.0(1)°
N4 - C3	1.380(3) Å	C3 - N4 - C5	118.9(2)°
N4 - C5	1.385(3) Å		
C2 - N1	1.352(3) Å	N1 - C2 - H2A	118.8°
C2 - H2A	0.950 Å	N1 - C2 - C3	122.5(2)°
C2 - C3	1.384(2) Å	H2A - C2 - C3	118.7°
C3 - N4	1.380(3) Å	N4 - C3 - C2	119.3(2)°
C3 - C2	1.384(2) Å	N4 - C3 - H3A	120.3°
C3 - H3A	0.950 Å	C2 - C3 - H3A	120.4°
C5 - N4	1.385(3) Å	N4 - C5 - H5A	120.3°
C5 - H5A	0.950 Å	N4 - C5 - C6	119.4(2)°
C5 - C6	1.388(2) Å	H5A - C5 - C6	120.2°
C6 - N1	1.362(2) Å	N1 - C6 - C5	121.8(2)°
C6 - C5	1.388(2) Å	N1 - C6 - C6	114.9(1)°
C6 - C6	1.474(3) Å	C5 - C6 - C6	123.4(2)°

The distance between Ru-N is 2.061 Å, shorter than the value of 2.104 Å found in $[Ru(NH_3)_6]^{2+}$, indicating some degree of π-backbonding between Ru(II) and the π^* orbitals of the ligands[72]. The Ru-N distance of $[(bpy)_2Ru(pypz)]^{2+}$ is comparable, albeit slightly larger, to 2.05 Å, the distance reported for analogous Ru-diimine complexes[73, 74]. For example, the distance measured for $[Ru(bpy)_3]^{2+}$ is 2.056 Å and the distances in $[Ru(bpy)_2dpp]^{2+}$ range from 2.040 to 2.059 Å (Table 11), with the shortest distance assigned to the bond between Ru and the pyrazine nitrogen. This observation could

suggest that the additional nitrogen at the periphery of the pypz ligand reduces marginally the π-backbonding with the orbitals of said ligand. However, more probably, the value obtained is an average of the different distances within the crystal that could not be resolved due to the reason discussed below.

Table 11. Selected bond lengths (Å) of $[Ru(bpy)_2dpp]^{2+}$.[63]

Ru – N1	2.049 Å
Ru – N2	2.058 Å
Ru – N3	2.056 Å
Ru – N4	2.059 Å
Ru – N5	2.046 Å
Ru – N6	2.040 Å

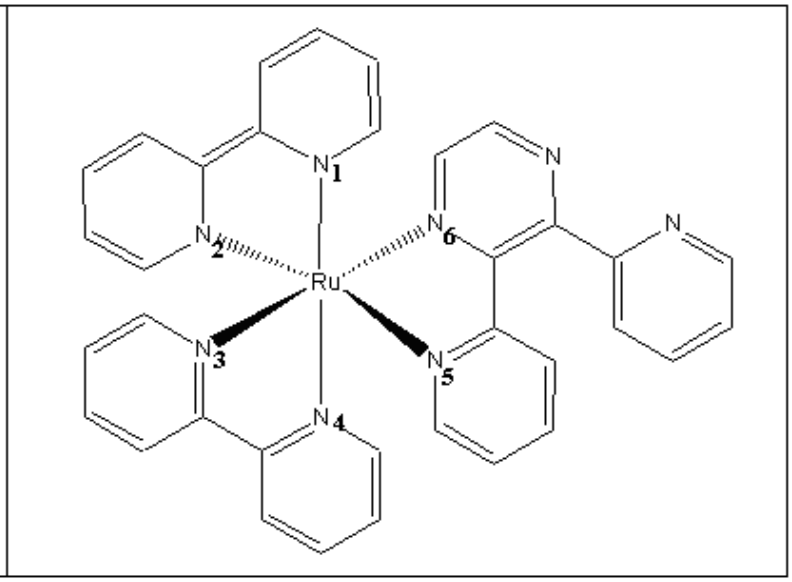

The N1-C2 and N1-C6 distances (see Figure 41B) are approximately 1.35 Å, instead of 1.90 Å as is the C-C distance in benzene. The shorter distance is indicative of the presence of the nitrogen and attributed to its higher electronegativity. The assignment of the symmetry group, however, was not simple since the location of the additional nitrogen, that we expect to be present on one of the bipyridine-like ligands, could not be univocally assigned. The distance of the carbons to the ambiguous nitrogen, 1.38Å, is higher than 1.35 Å, but still lower than 1.90 Å.

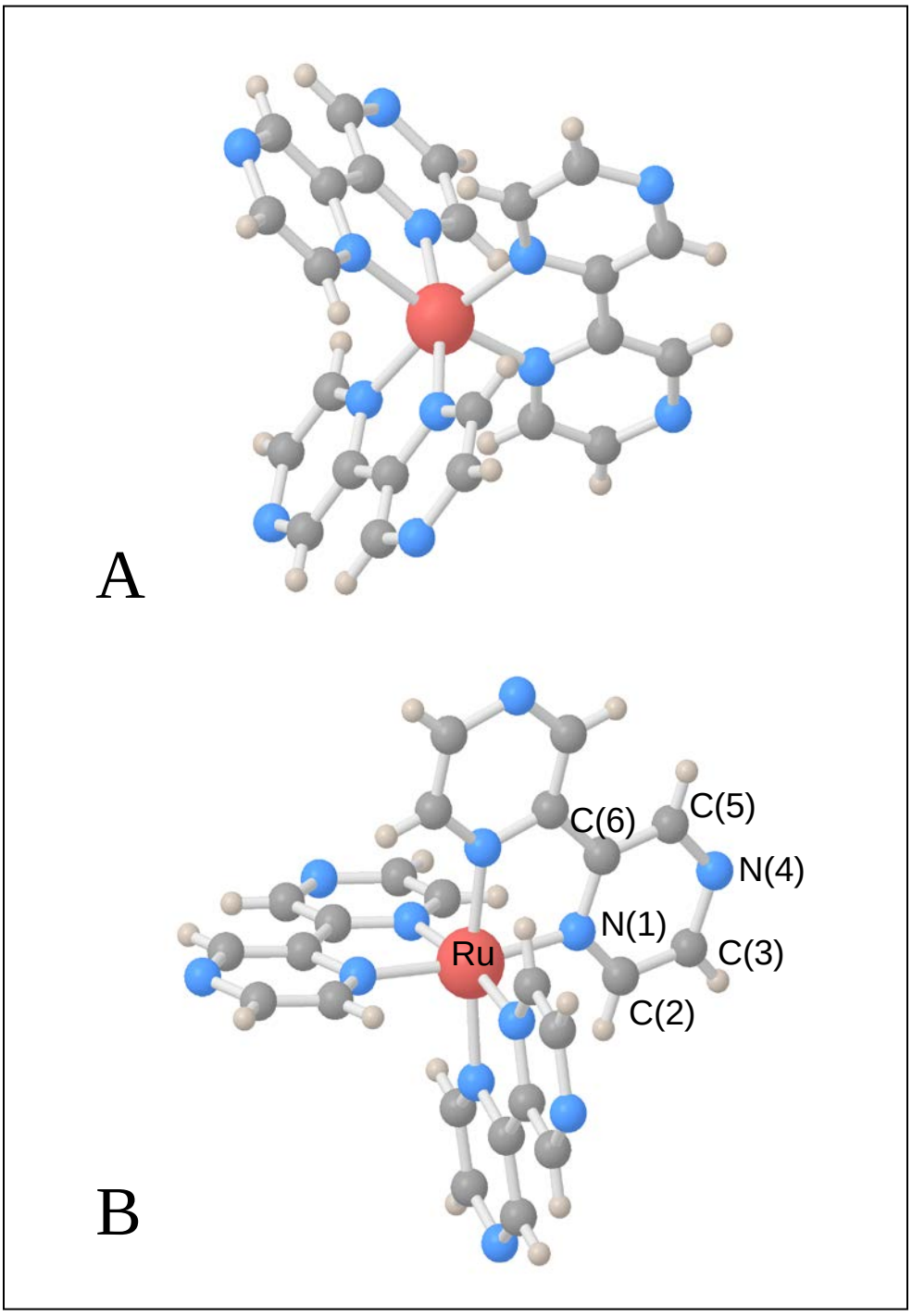

Figure 41. Ball-and-stick representations of the X-ray structure of the cationic $[Ru(bpy)_2pypz]^{2+}$ octahedral complex. Top view (A) shows the planes of the three coordinating ligands pointing along different orientations. Bottom view (B) highlights the planarity of each ligand system.

This distance resembles closely the C(2)-C(3) and C(5)-C(6) distances, hence based on the value of bond distance alone, it is hard to say if a second nitrogen is present. Given the proximity in atomic mass between carbon and nitrogen and the fact that the bpy and pypz ligands only differ by that one element, diffraction yields a structure where the nitrogen appears alternatively at position (4) of either ring in any of the three bidentate ligands. The pictures below show two additional nitrogens on each ligands but they are meant to be alternatively carbons OR nitrogens (meaning if one atom is assigned as nitrogen all the other atoms in position (4) are carbons and *vice versa* if the nitrogen is at another position that previous position with N is instead occupied by C). Figure (41A) shows the different orientation of the ligands relative to each other while Figure (41B) highlights the planarity of each ligand, both rings in the ligand laying on the same plane.

From the diffraction data it can be inferred that the molecule is highly symmetrical. According to the proposed structure, the crystals exhibit the 6-fold and mirror symmetry present in the space group *P*6/*mcc*. The crystallographic unique portion is roughly 1/6 of the molecule with formula $C_{29}H_{23}N_7Ru$. The parent complex, $[Ru(bpy)_3]^{2+}$, is expected to possess high symmetry and from X-ray crystallographic studies[72] conducted on the PF_6 salts of the cation in 1979 it was established to have D_3 symmetry. This study's conclusion suggests that the crystals of $[(bpy)_2Ru(pypz)]^{2+}$ that were analyzed have even higher symmetry than ruthenium(II) trisbipyridine. The conclusion is surprising and considered unlikely. More studies on crystals obtained with different techniques or from other solvent matrices are required to determine with confidence the exact structure of the complex cation.

3.B. Acid Titrations

Absorption and emission spectra of $[(bpy)_2Ru(dpp)](NO_3)_2$ and $[(bpy)_2Ru(pypz)]Cl_2$ were recorded at periodic intervals within a range of acidity from pH 12 to Hammett acidity constant (H_0) of –11 and the changes observed were quantitatively assessed. $[(bpy)_2Ru(dpp)](NO_3)_2$ was also titrated between pH 7 and 0 and NMR spectra recorded as a function of pH. All spectral transformations proved to be reversible upon addition of a strong base and the systems were cycled between the protonated and unprotonated complexes at least three times without significant decomposition.

3.B.1. Ground-state Titration of $[(bpy)_2Ru(dpp)](NO_3)_2$

3.B.1.a. UV-Vis

Acid-base variations in the UV-Vis spectrum for this complex have been previously published[49,62] and the observations reported here agree in all major aspects. The changes observed are minor going from alkaline solutions down to pH zero and then drastically increase in magnitude at negative Hammett acidity values. The intense UV absorptions exhibit some dependence on pH; however, given that both ligands have $\pi \rightarrow \pi^*$ transitions in this region, it would be hard to distinguish which ligand is the one causing the change and the experimental observations would not directly provide information about the emissive excited state, so these changes were not plotted and studied in further detail. The contour modifications in the MLCT absorption maxima are reported in Figure 42. In the pH 7 to 0 range, a 14-nm shift to the red from 476 nm to 490 nm for the MLCT transition to dpp is accompanied by a 20% decrease in intensity

while the high-energy MLCT transition to bpy increases slightly in intensity (10%) and remains nearly constant at 422 nm. When the solution becomes highly acidic, a clear color change from orange to purple is observable to the naked eye. At intermediate negative Hammett acidity levels, three bands are simultaneously present in the visible region, at 410, 510 and 560 nm, respectively. The 422-nm band ultimately blue-shifts and decreases in intensity leaving behind a slight shoulder around 380 nm. The dpp MLCT band at 480 nm continues to decreases in intensity and is replaced by a band with maximum at 578 nm skewed to shorter wavelengths. A gaussian fit obtained using the Origin Pro 7.0 software reveales two maxima at 527 and 583 nm with FWHM ratio in cm^{-1} of 2:1 (Figure 43).

A plot of the decrease in absorbance of the 480-nm dpp MLCT band as a function of the Hammett acidity function tracked at three wavelength, 450, 460 and 470 nm, (Figure 44) reveals two trends: a larger change in the region of acidity corresponding to negative Hammett acidity values and a substantially smaller change above pH 0. Each data set can be fitted mathematically using the Boltzmann equation:

$$y = A_2 + (A_1 - A_2) / (1 + e^{((x - xo)/dx)}) \qquad (86)$$

where A_2 indicates the bottom of the sigmoidal curve and $(A_1 - A_2)$ the top. x_o is the pH at half maximum and corresponds to the pK_a of the protonation step that the sigmoidal curve refers to, while dx represents the rate of change of absorbance.

Spectral changes in the pH range from 7 to Ho = -2 were originally attributed to ion pairing effects. If, however, they are due to protonation, the equilibrium constant for the reaction obtained from the fitting of the first data set (Figure 45) is $pK_{a_1} = 2.7 \pm 0.1$.

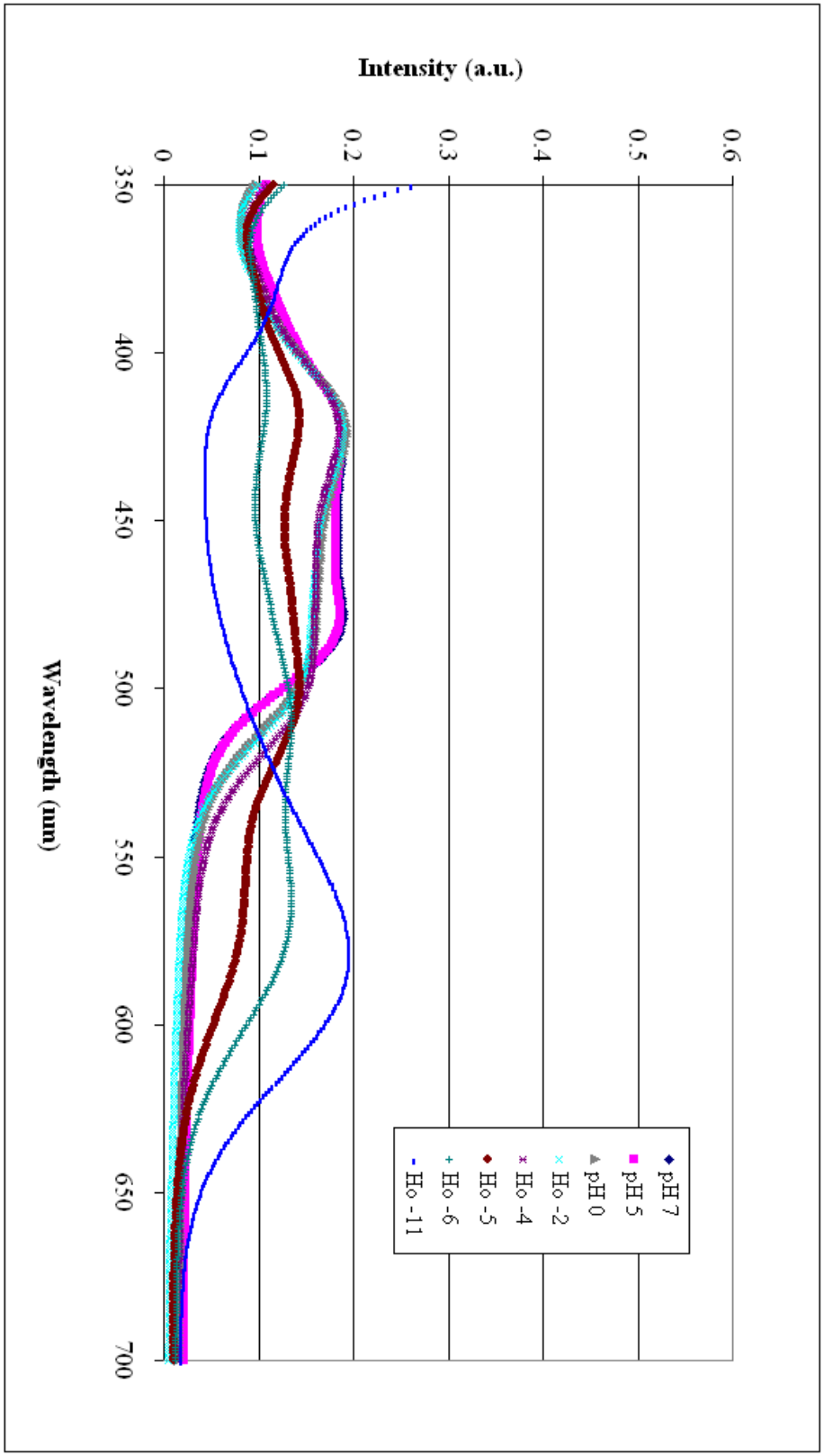

Figure 42. UV-Visible spectra of room temperature, aqueous solutions of $[(bpy)_2Ru(dpp)](NO_3)_2$ as a function of pH.

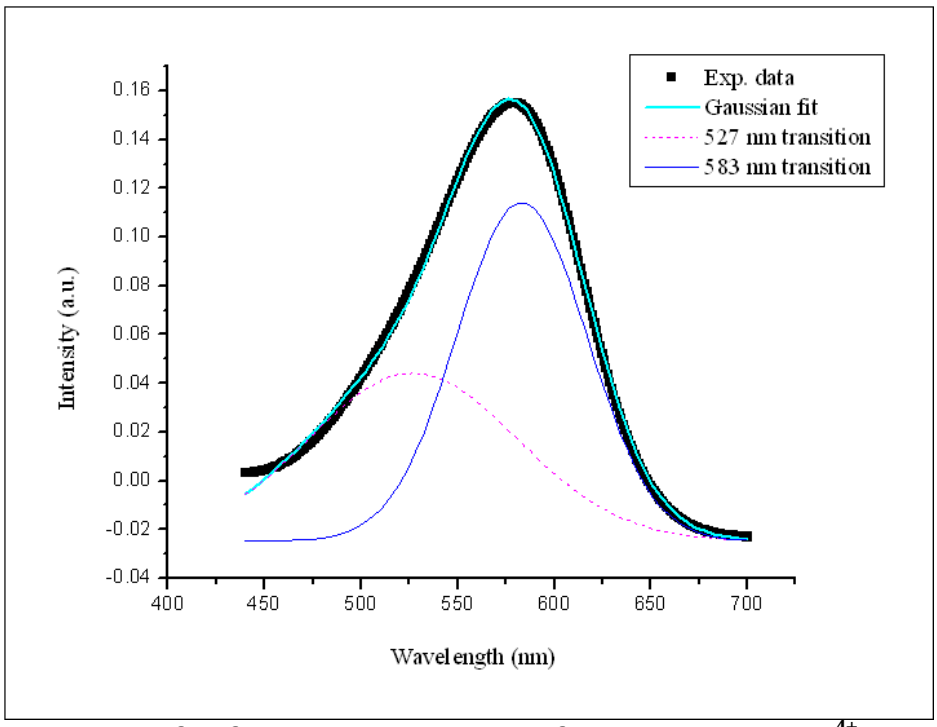

Figure 43. Gaussian fit of 578-nm MLCT band of $[(bpy)_2Ru(dppH_2)]^{4+}$ in H_2O.

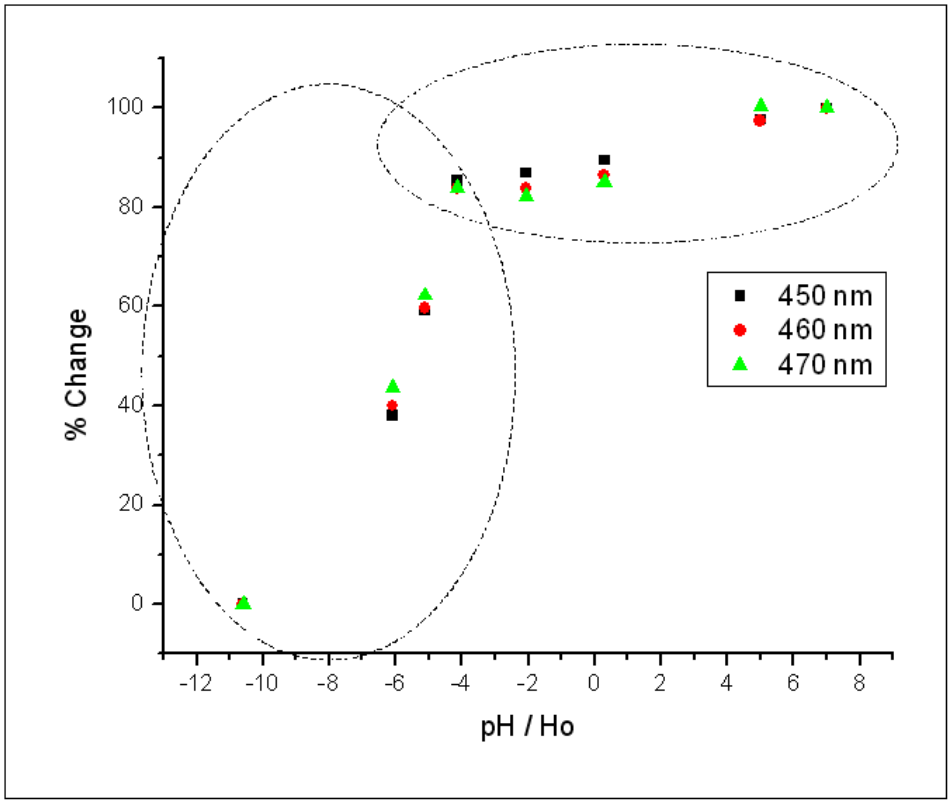

Figure 44. Percent of intensity changes observed in UV-Vis spectra of $[(bpy)_2Ru(dpp)](NO_3)_2$ as a function of pH at wavelength 450, 460 and 470 nm. The ovals designate the different rates of change in the two regions of pH.

The 476-nm wavelength was considered in particular because it directly corresponds to the maximum of the MLCT absorption band localized on the dpp ligand, which is the one undergoing the biggest change and is characteristic of the unprotonated complex.

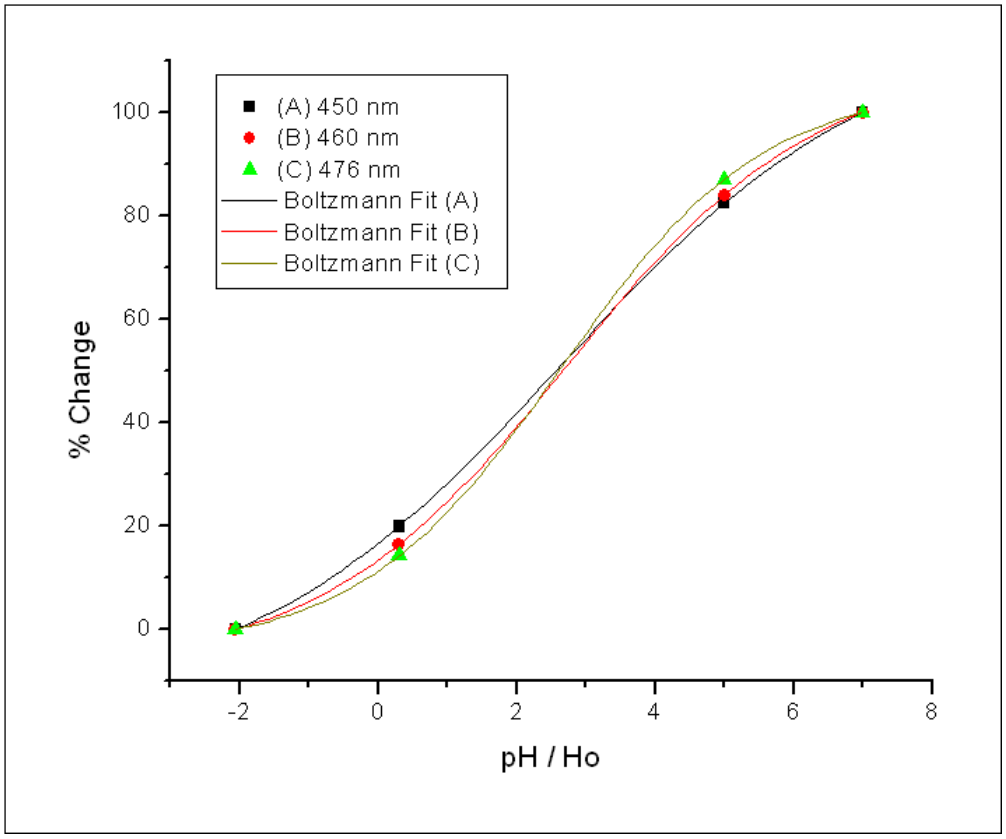

Figure 45. Intensity changes observed as a function of pH in UV-Vis spectra of $[(bpy)_2Ru(dpp)](NO_3)_2$ at wavelength 450, 460 and 476 nm.

The second protonation is observed at much higher acidity. Considering only the range Ho –2 to –11 for the fit (Figure 46), the equilibrium constant obtained is pKa_2 = -5.9 ± 0.1. If the entire range of acidities is included (Figure 47) the value of the constant remains within experimental error, –5.7 ± 0.1, of the value obtained from the more

limited set of data. The curve that provides the least accurate result is the one obtained by following the changes at an intermediate wavelength and that includes the changes from the first protonation.

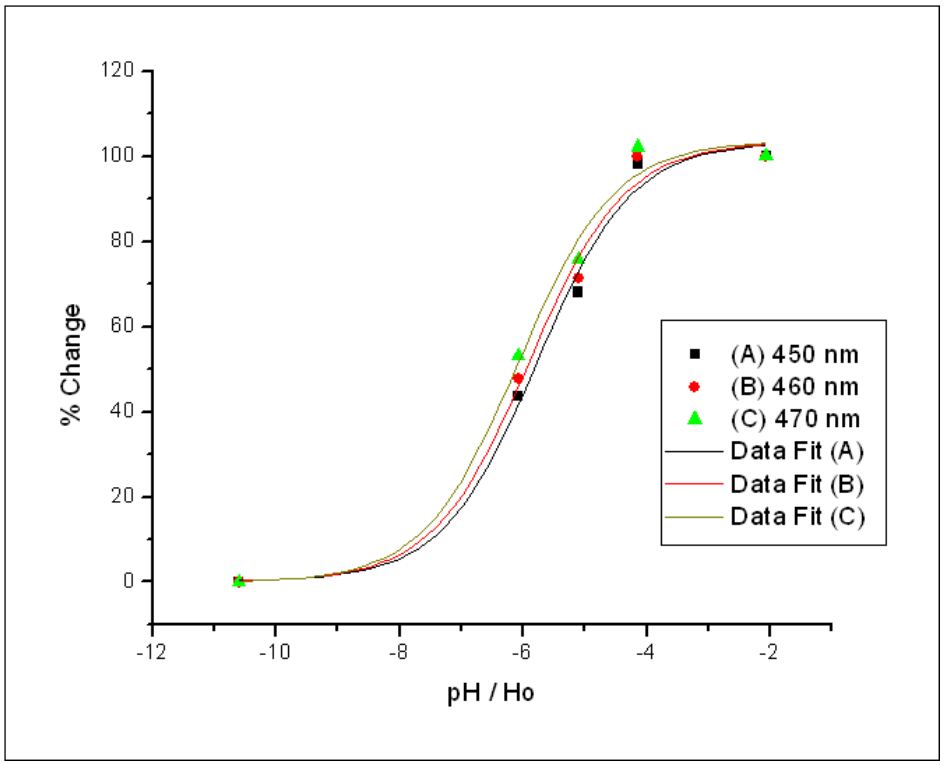

Figure 46. pH–dependent UV-Vis intensity changes of $[(bpy)_2Ru(dpp)](NO_3)_2$.

The changes observed at the 420-nm MLCT band centered on the bpy ligand and the changes measured where the new band appears (578 nm) are both at least partially independent from the first protonation step (if we exclude possible tails of other gaussian bands) and consequently may be more reliable.

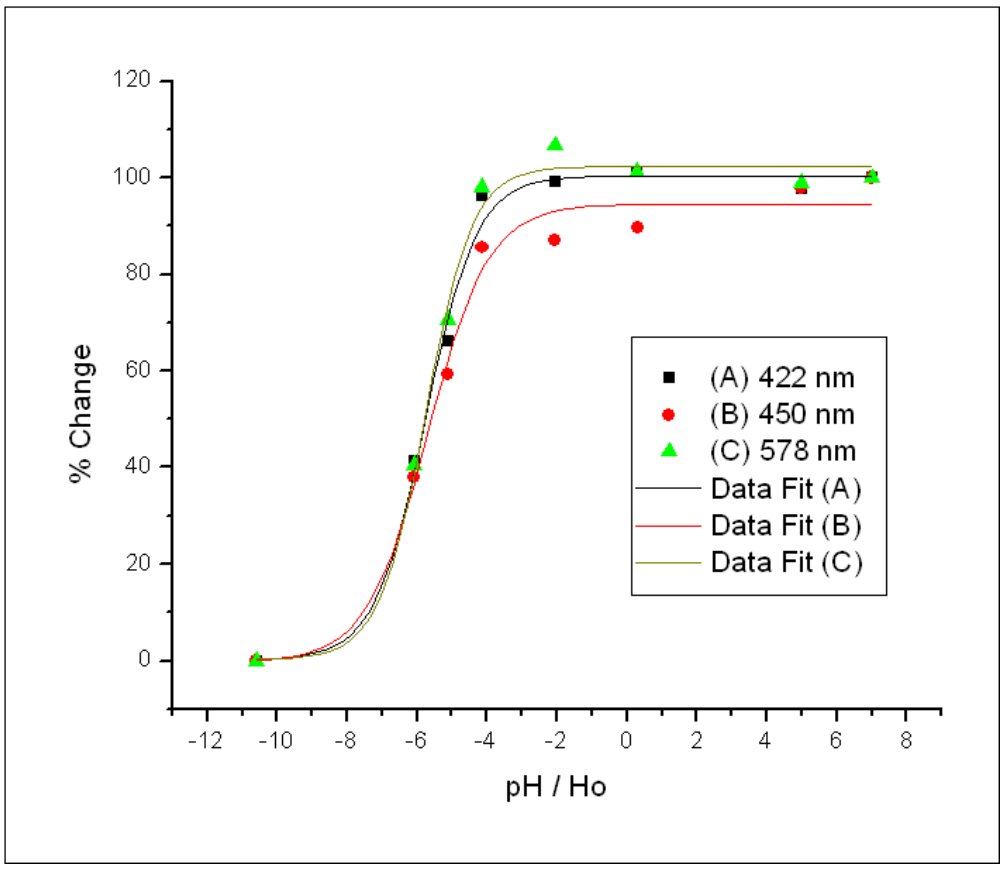

Figure 47. pH-dependence of I over the entire range of acidity.

3.B.1.b NMR

An alternative method was used to titrate solutions of $[(bpy)_2Ru(dpp)](NO_3)_2$ in the 7-0 pH range. Concentrated, deuterated solutions of analyte were acidified with deuterated sulfuric acid, and the changes of chemical shift of several peaks were detected by NMR spectroscopy (Figure 48). Spectra revealed that the nuclei most affected by the decrease in pH were the ones on the free pyridyl ring of the dpp ligand and one proton on the coordinated pyridyl ring (B3'). The theoretical chemical shifts at 100% protonation, δ_{bound}, calculated by Zambrana[65] for all five shifting protons are listed in Table 12 together with the observed experimental changes: both sets of values agree closely, as can

be seen from Figure 49, which refers to the nucleus C4''. An average value of 1.52 ± 0.03 for the equilibrium constant was obtained by plotting the changes in chemical shift as a function of the acid concentration (pD) and assuming a single protonation step (Figure 50).

Table 12. Chemical shifts at 100% protonation and pKa values from NMR data fit.

H-position	δ (exp)	δ (calc)[71]	pKa (fit)
B3'	7.17	7.68	1.515
C3''	7.97	7.84	1.491
C4''	8.27	8.86	1.522
C5''	7.82	8.44	1.512
C6''	8.76	9.18	1.563

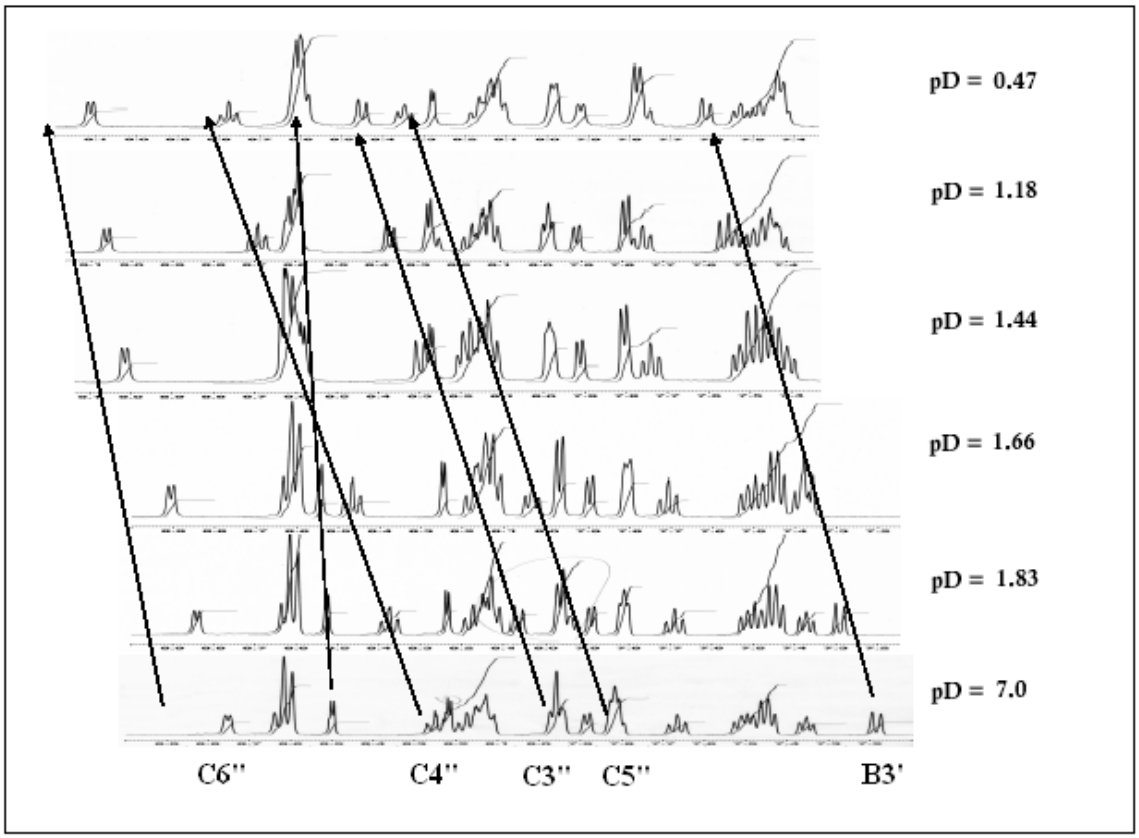

Figure 48. NMR spectra of $[(bpy)_2Ru(dpp)](NO_3)_2$ as a function of pH. Only the aromatic region is shown since change is limited to protons in this region[65].

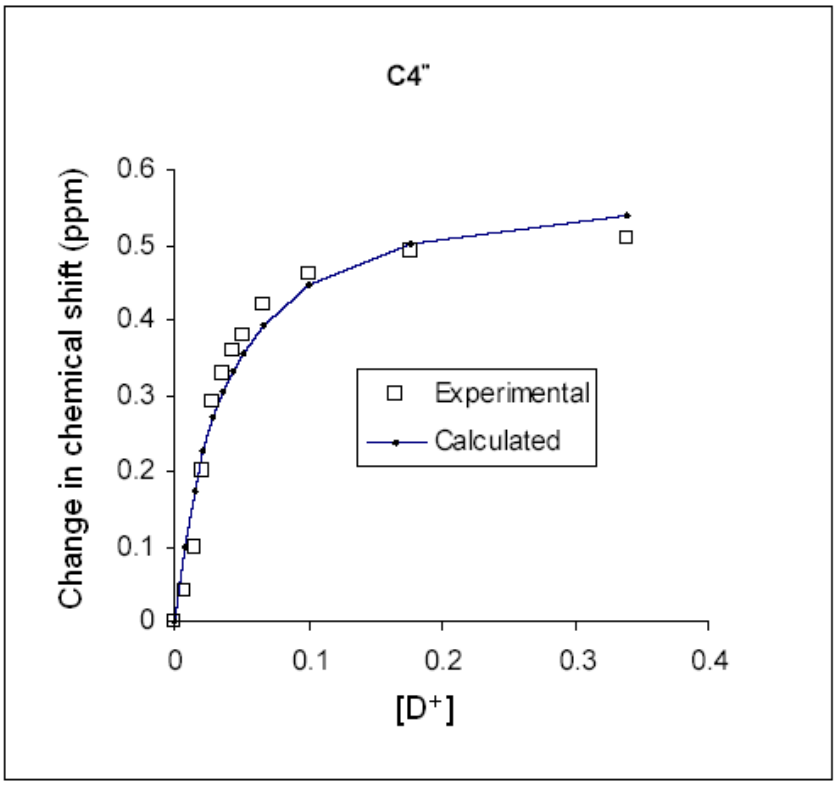

Figure 49. Mathematical fit of the changes in chemical shift undergone by the dpp C4'' proton in $[(bpy)_2Ru(dpp)](NO_3)_2$ as a function of $[D^+]$[65].

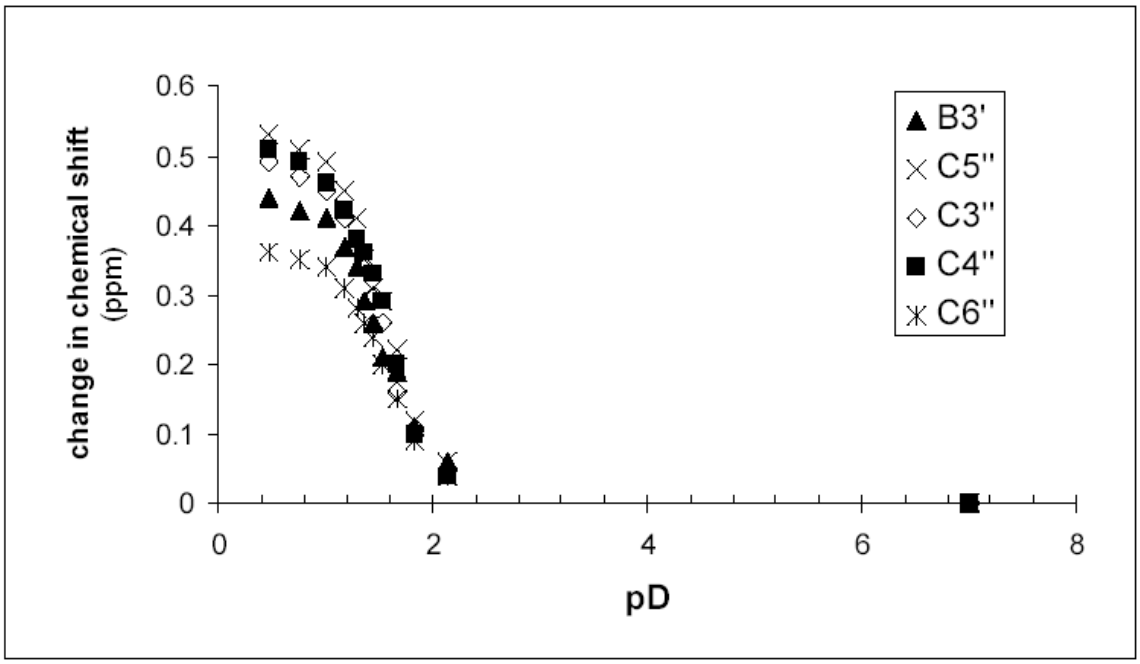

Figure 50. Sigmoidal plots[65] for the NMR titration of $[(bpy)_2Ru(dpp)]^{2+}$.

3.B.2. Excited-State Titration of $[(bpy)_2Ru(dpp)](NO_3)_2$

The complex in aqueous solution at pH 7 has a broad emission centered at 700 ± 5 nm. Increasing the solution's pH above 8 does not show emission-related variations. However, increasing the acidity produces a sharp decrease in the lifetime (τ) and emission intensity (I) of the luminescent state of $[(bpy)_2Ru(dpp)](NO_3)_2$. Consistent with similar previously reported experiments[49,62], the emission in the 8-1 pH range remains centered at 700 ± 5 nm (Figure 51), decaying as a single-exponential and no other emission appears.

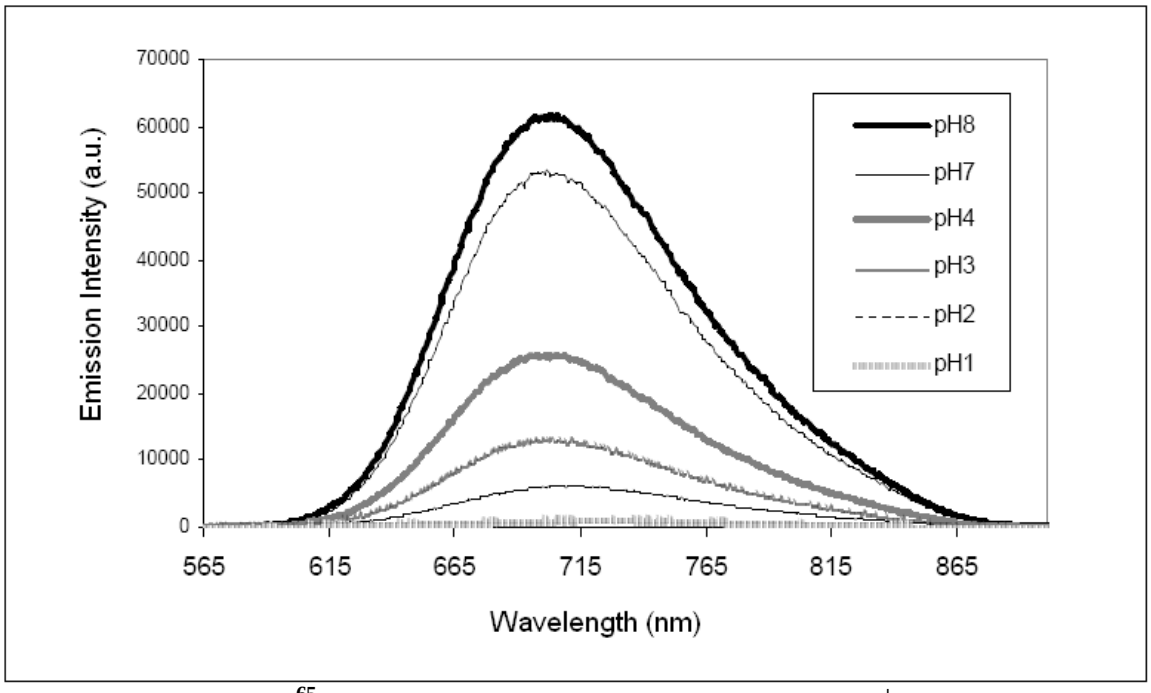

Figure 51. Quenching[65] of the 700-nm emission with increasing $[H^+]$.

At pH 1 and below, however, the emission profile becomes broader and reveals the presence of two much weaker emission peaks, one centered at 620 nm and one at 730 nm (Figure 52), which may have gone undetected in previous studies because of the huge difference in emissivity when compared to that of the 700-nm emission. These emissions

reach a maximum intensity at pH=1 at which the K_a derived from the UV-Vis data, shows that 98% of the complex exists in the mono-protonated form, $[Ru(bpy)_2dppH]^{3+}$, with the proton attached to the peripheral pyridine nitrogen of dpp as confirmed by NMR spectra.

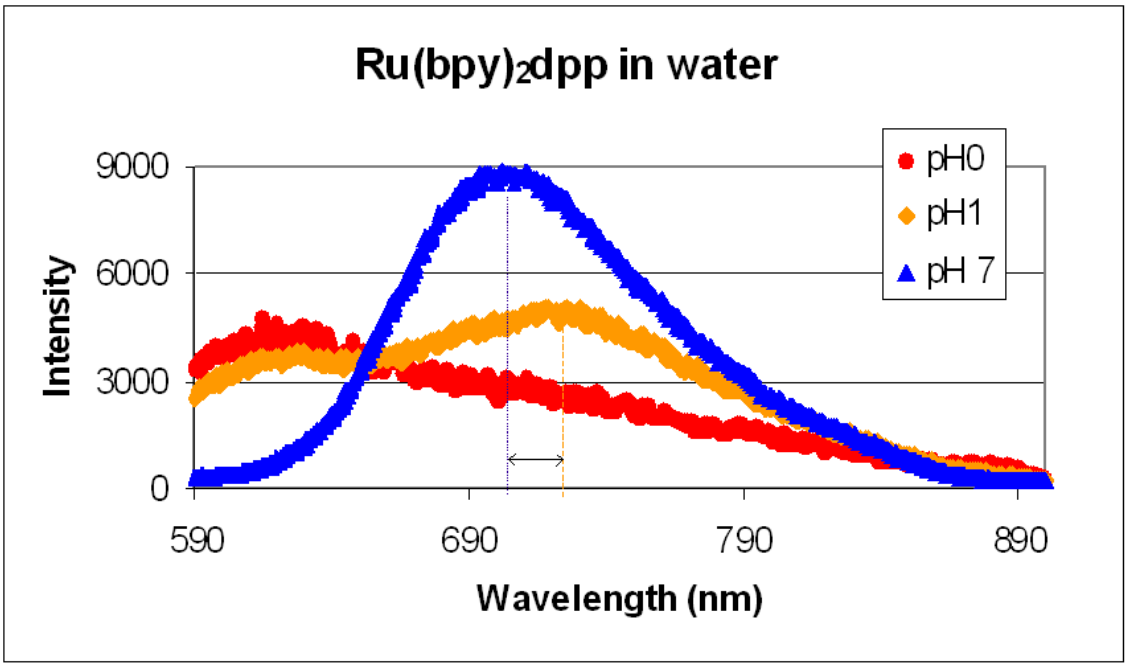

Figure 52. Single and multiple emission from $[(bpy)_2Ru(dpp)]^{2+}$ at different pH (the intensities are not on scale).

The multiple emission can be resolved into two single-exponential curves with lifetimes in the sub-nanosecond domain, less than 16 picoseconds, and quantum efficiencies of $3 \pm 1 \times 10^{-8}$ and $4 \pm 1 \times 10^{-9}$ for the 620- and 735-nm emissions, respectively.

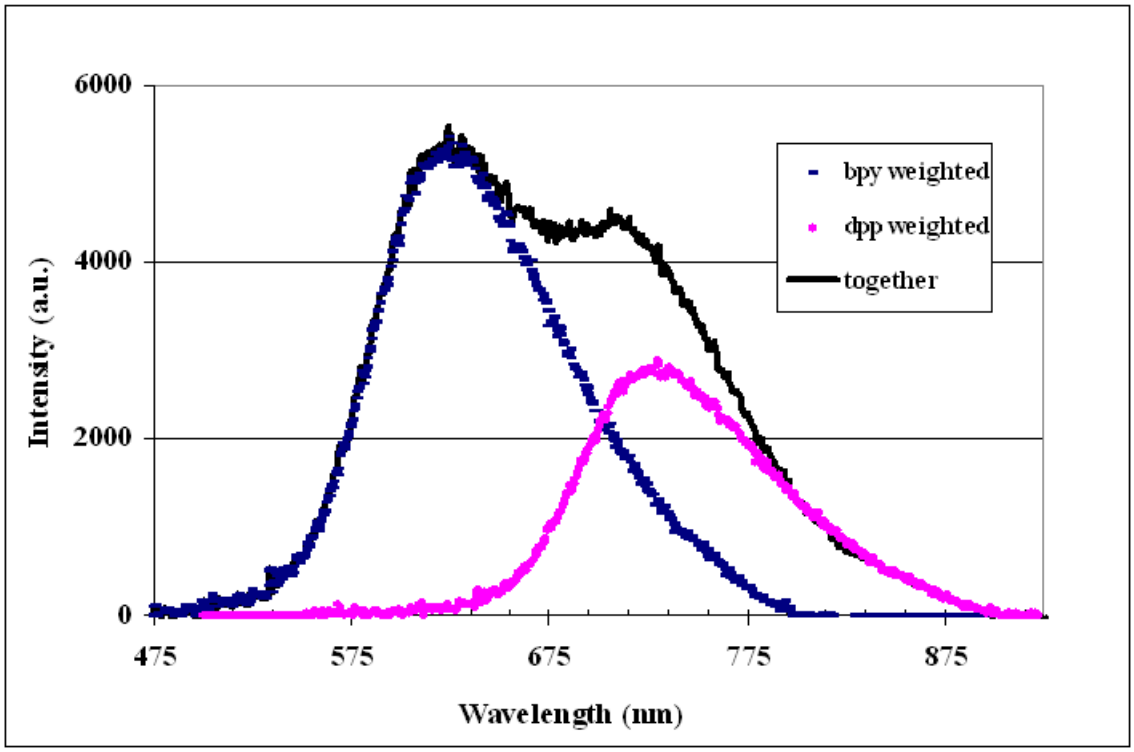

Figure 53. Mathematical fit[65] of the double emission of $[(bpy)_2Ru(dpp)]^{2+}$ at pH 0.

In contrast to the single broad emission observed at pH 7, the double emission is dependent on the excitation wavelength. The relative intensity of the two peaks observed at pH 0 varies when excited with 458, 488 and 514nm laser light: the 620-nm peak becomes more intense when the excitation wavelength is shorter, while the 730-nm emission becomes dominant when 514-nm excitation light is used (Figure 54). Furthermore, the 735-nm emission intensity declines as $[H^+]$ increases from 0.1M to 2M, whereas the 620-nm emission intensity is unchanged over the same $[H^+]$. Increasing $[H^+]$ beyond 2M eliminates both emissions. No set of experimental conditions examined in these experiments gave any indication that the di-protonated complex is luminescent.

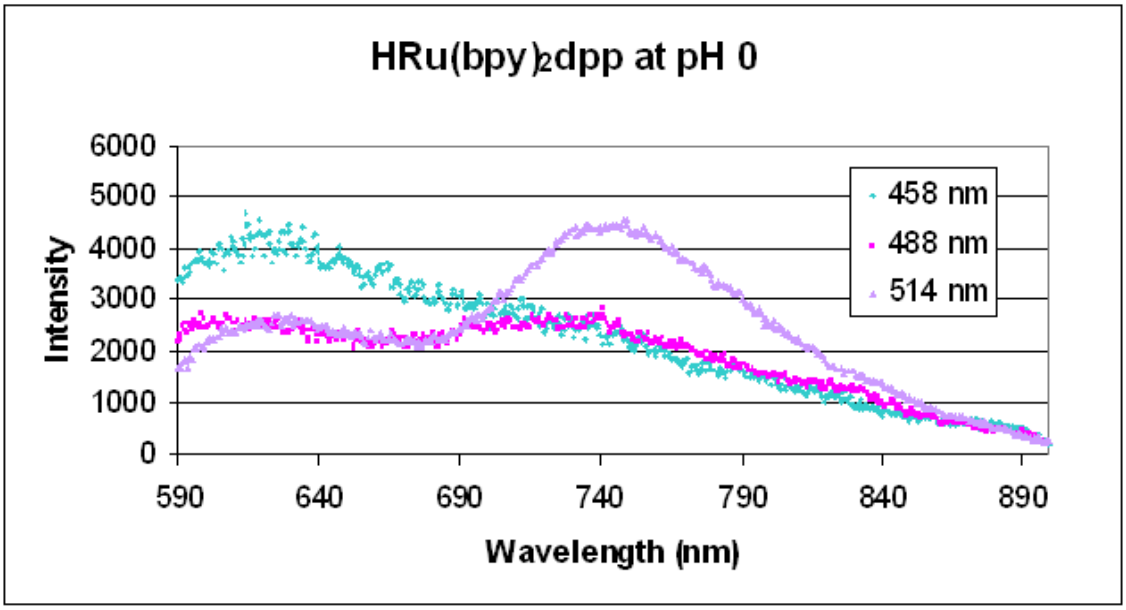

Figure 54. Wavelength dependence of the multiple emission of $[(bpy)_2Ru(dpp)]^{2+}$ at pH 0.

The changes in lifetime, quantum yield, area under the emission spectra, and intensity as a function of pH are plotted in Figure 55 where τ_0, Φ_0, A_0, and I_0 are the values of the parameters in the pH 8 sample. The graphs show that variations of those quantities between pH 8 and 0 closely parallel each other and can be nicely fitted mathematically as demonstrated by the plot of the decrease in intensity as a function of pH tracked at the emission maximum (Figure 56). From the midpoint of the breaks in these curves, pK_a^*(app) were estimated within ± 0.2 units (Table 13) and the average value obtained was 4.5 ± 0.2.

Table 13. Excited-state protonation constants derived from the emission pH titration of $[(bpy)_2Ru(dpp)]^{2+}$.

Parameter	pKa^* (app.)
Lifetime	4.4 ± 0.1
Time-resolved Quantum Yield	4.2 ± 0.1
Steady-state Quantum Yield	4.8 ± 0.2
Intensity	4.7 ± 0.2

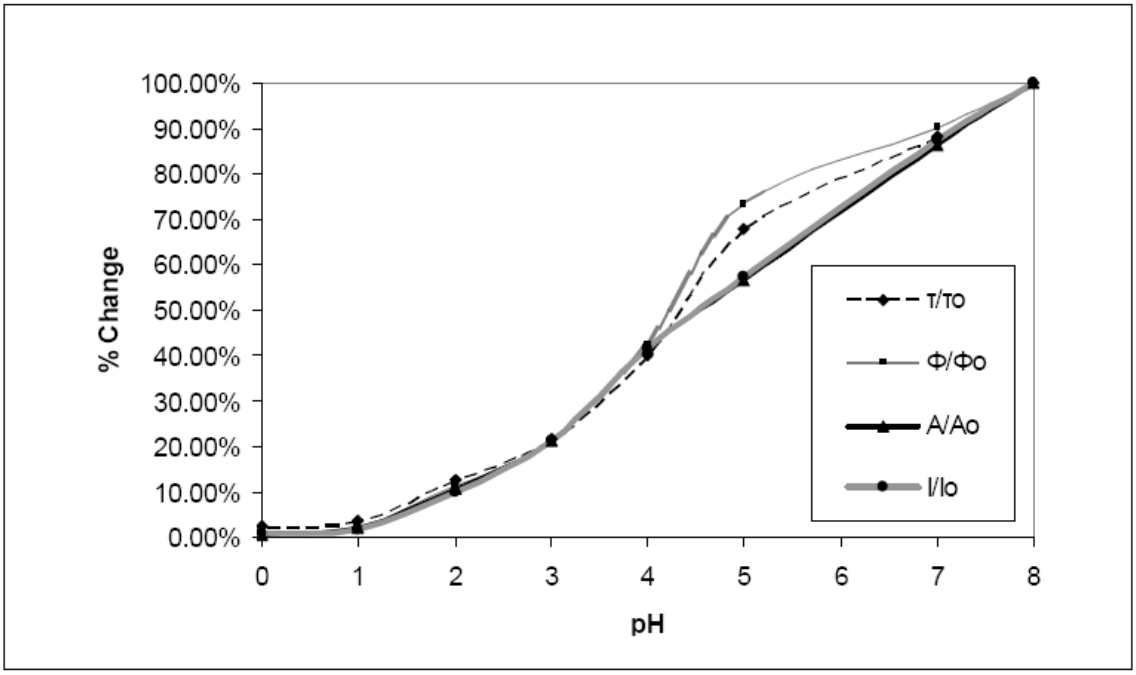

Figure 55. pH dependence of lifetime, quantum yield, area under the curve and intensitiy of $[(bpy)_2Ru(dpp)]^{2+}$ in the 7-0 pH range[65].

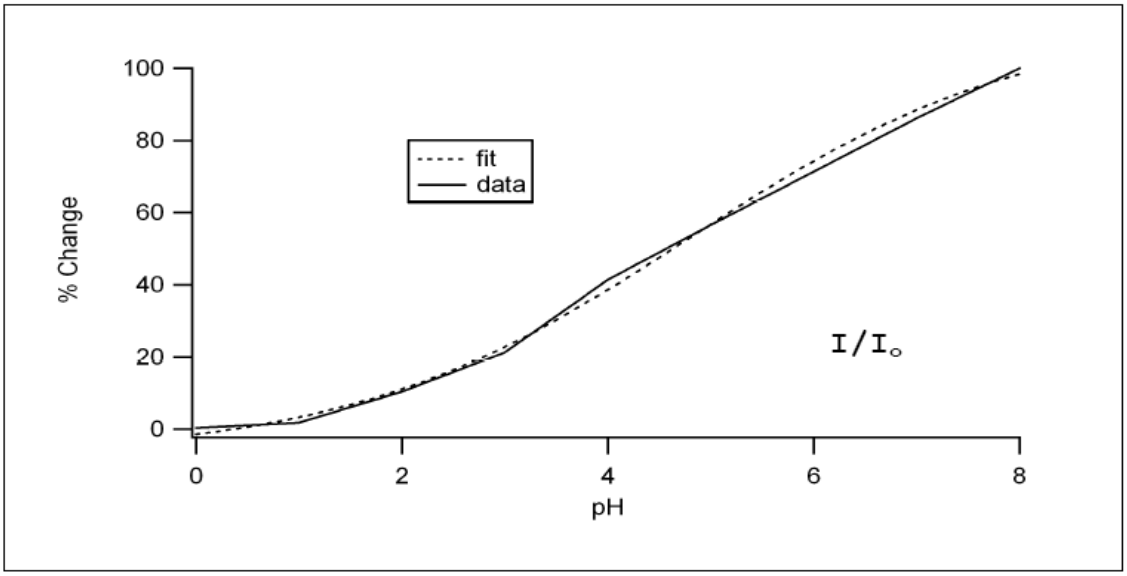

Figure 56. Intensity titration plot[65] and mathematical fit for $[(bpy)_2Ru(dpp)]^{2+}$.

The Stern-Volmer plot of the proton quenching displays strong negative deviations from linearity and the plots of quantum yield and lifetime, Φ_0/Φ and τ_0/τ respectively, are not coincident. No single equation fits adequately all points.

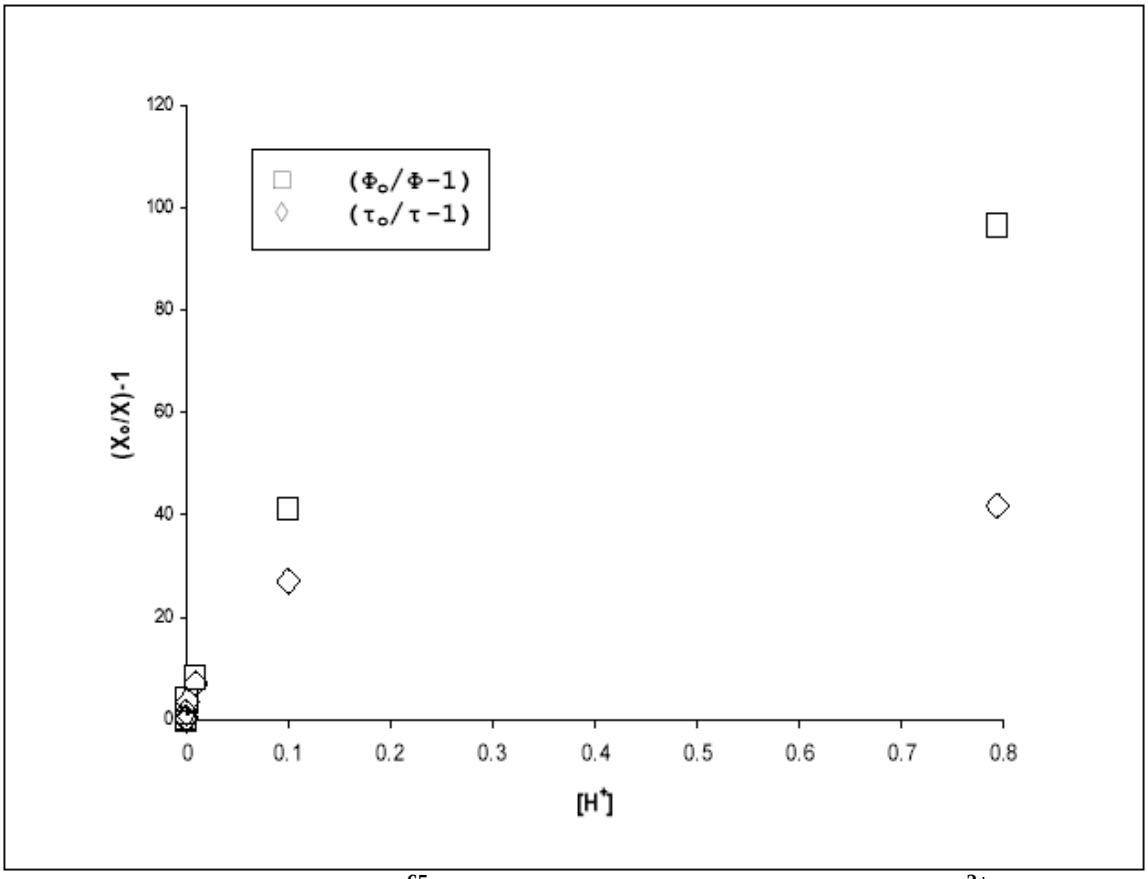

Figure 57. Stern-Volmer plots[65] of the acid titration of $[(bpy)_2Ru(dpp)]^{2+}$.

According to Hoffman and associates, if the excited state is emissive and is treated as an exciplex[17], under steady-state conditions the intensity curve can be fitted to equation (87).

$$\frac{I_1^0}{I_1} = \frac{1 + \dfrac{k_q\,[H^+]}{k_o}}{1 + \gamma\left(\dfrac{k_q[H^+]}{k_0^{"}}\right)} \qquad (87)$$

where k_0 and $k_0^{"}$ are the rate constants for deactivation for the base and acid form, k_q is the quenching constant and γ represents the differential ratios of intensity between the two forms. Figures 58 and 59 show how the equation fits the beginning and the end of the intensity curve and the values of the constants are listed in Table 14. However, attempts to fit the complete dependence on $[H^+]$ failed.

Table 14. Photophysical constants derived from the fit of pH titration emission data of $[(bpy)_2Ru(dpp)]^{2+}$.

	k_0 (s^{-1})	$k_0^{"}$ (s^{-1})	K_{SV} (M^{-1})	γ	k_q (s^{-1} M^{-1})
High pH	8.0×10^5	3.9×10^6	3.4×10^6	2500	2.7×10^{12}
Low pH	8.5×10^6	5.9×10^{10}	1174	44	1.0×10^{10}

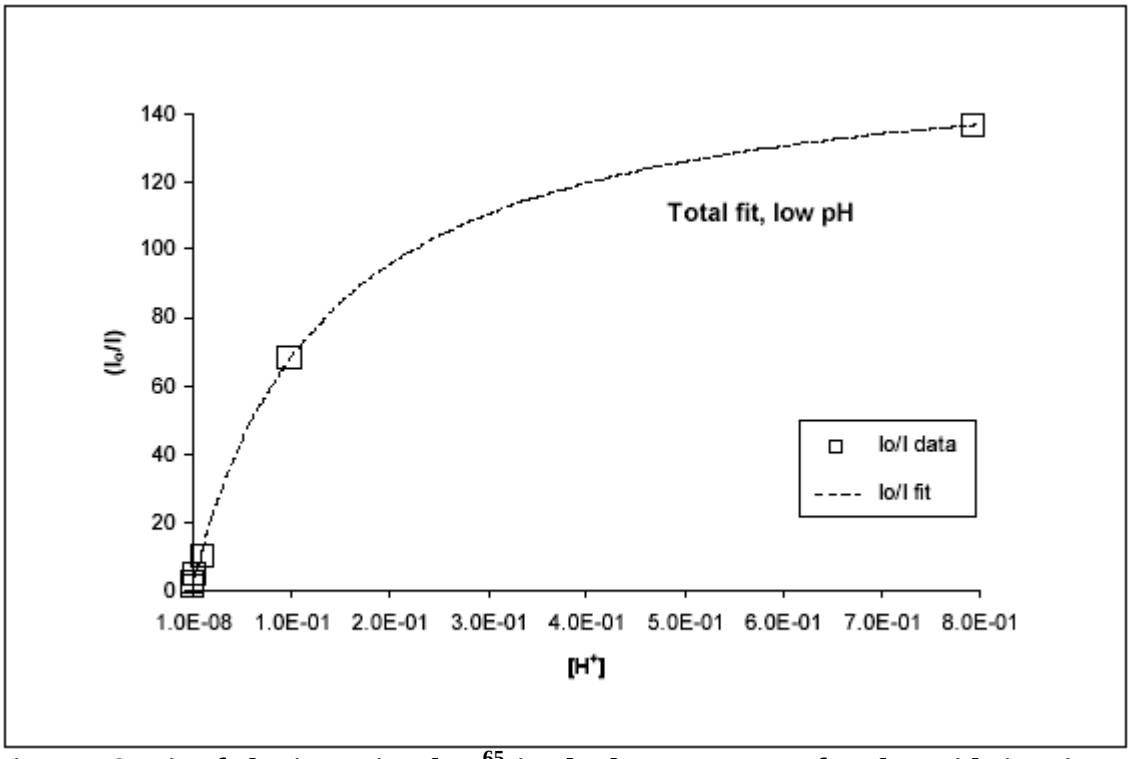

Figure 58. Fit of the intensity data[65] in the low pH range for the acid titration of $[(bpy)_2Ru(dpp)]^{2+}$.

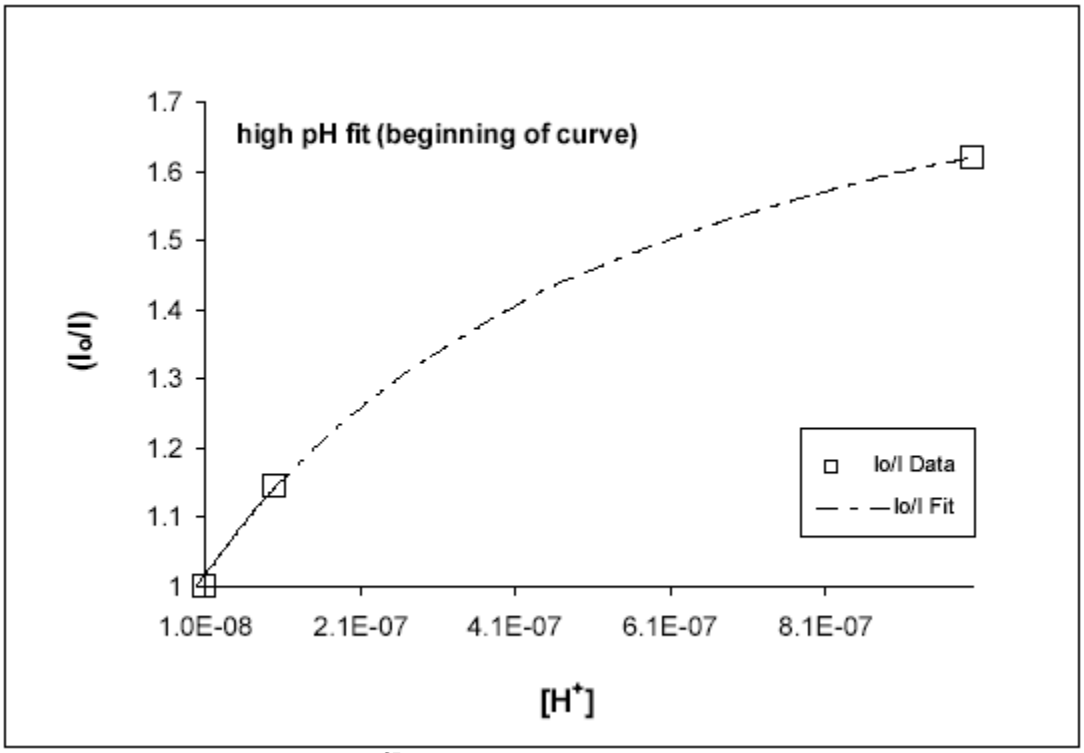

Figure 59. Intensity data fit[65] in the high pH range for the acid titration of $[(bpy)_2Ru(dpp)]^{2+}$.

3.B.3. Ground-state Titration of $[(bpy)_2Ru(pypz)]Cl_2$

The complex was titrated over the range from pH 8 to H_0 -6 using buffer solutions for pH 1 and above, and concentrated perchloric and sulfuric acids at negative Hammett acidity values. Contrary to what was observed in the case of $[(bpy)_2Ru(dpp)]^{2+}$, no change in absorbance was recorded going from pH 8 to pH 1. In that range, the MLCT band remains unaffected both in intensity of the peaks and band position (Figure 60). Increasing the acidity further with either acid (Figures 61 and 63) changes the color of the solution from orange to pink/purple and yields two isosbestic points in the MLCT region, at 402 and 495 nm (Figure 62). The most significant changes in the spectra happen between pH 0 and H_0 –2: the MLCT transitions in the 400 to 500 nm region decrease in

intensity by about 60% and shift in opposite directions: the 430-nm MLCT transition to the bpy ligand blue-shifts to 396 nm, while the 476-nm MLCT transition to the pypz ligand moves to lower energy and is replaced by a band centered at 550 nm in the most acidic solution (H_0 = -6). Mathematical fits of the UV-Vis spectra in the pH range from 0 to H_0 –6 obtained using Origin pro 7.0 software, resolved the changes affecting each peak that contribute to the broad MLCT band. The trends in peak position for three transitions are presented in Figure 64. From the mathematical fit it appears that the 476-nm transition decreases in intensity and shifts to a final position centered at 528 nm in the most acidic solution, while a new band starts growing in at pH 0 at 525 nm and shifts to the red to a final position of 558 nm. Hence, the final band at 551 nm is due to the contribution of two bands, at 528 and 558 nm, respectively, whose FWHM ratio in cm^{-1} is 1.5:1.

In order to establish the equilibrium constant for the protonation of the complex in the ground state, the relative changes in optical density were plotted as a function of pH or H_0. The changes were monitored at five wavelengths for both titrations, i.e., the titration with perchloric acid and the titration with sulfuric acid (Figures 65 and 66). The graph in Figure 65, indicative of a single protonation step, has an inflection point at –1.3 ± 0.2. Using Igor Pro 5.00, the titration data from each acid titration were plotted and fitted separately, revealing an inflection point for perchloric samples at Ho –1.22 ± 0.1 (K_a = 17) and -1.59 ± 0.08 (K_a = 39) for the sulfuric ones (Figures 66). Individual inflection points were also derived for each monitored wavelength and reported in Table 15. The constants determined using the sulfuric acid data set are slightly more negative than the ones determined using the perchloric acid data set and within the same titration

series, the values vary as a function of the wavelengths used: the shorter the monitoring wavelength, the lower the equilibrium constants.

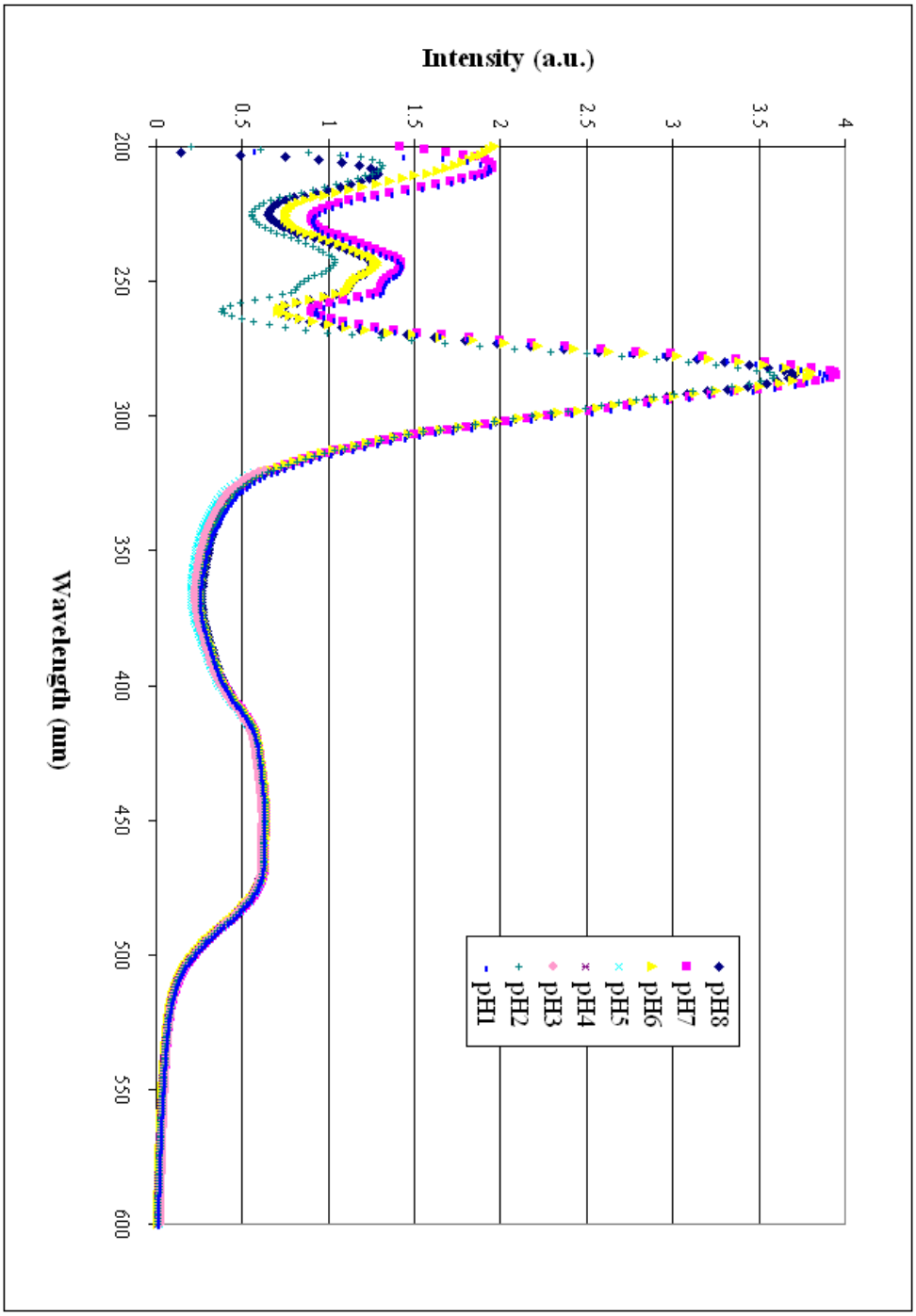

Figure 60. UV-Visible spectra of room temperature, aqueous solutions of $[(bpy)_2Ru(pypz)]^{2+}$ in the 1-8 pH range.

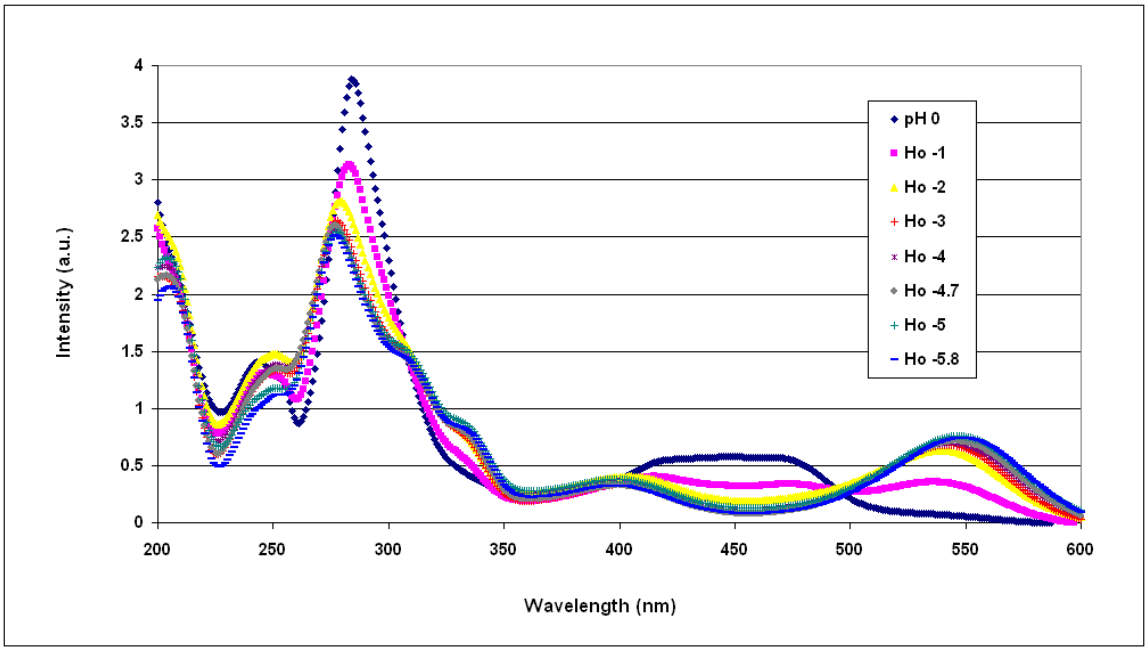

Figure 61. UV-Visible spectra of room temperature, aqueous perchloric acid solutions of $[(bpy)_2Ru(pypz)]^{2+}$ in the 0 to -6 H_0 range.

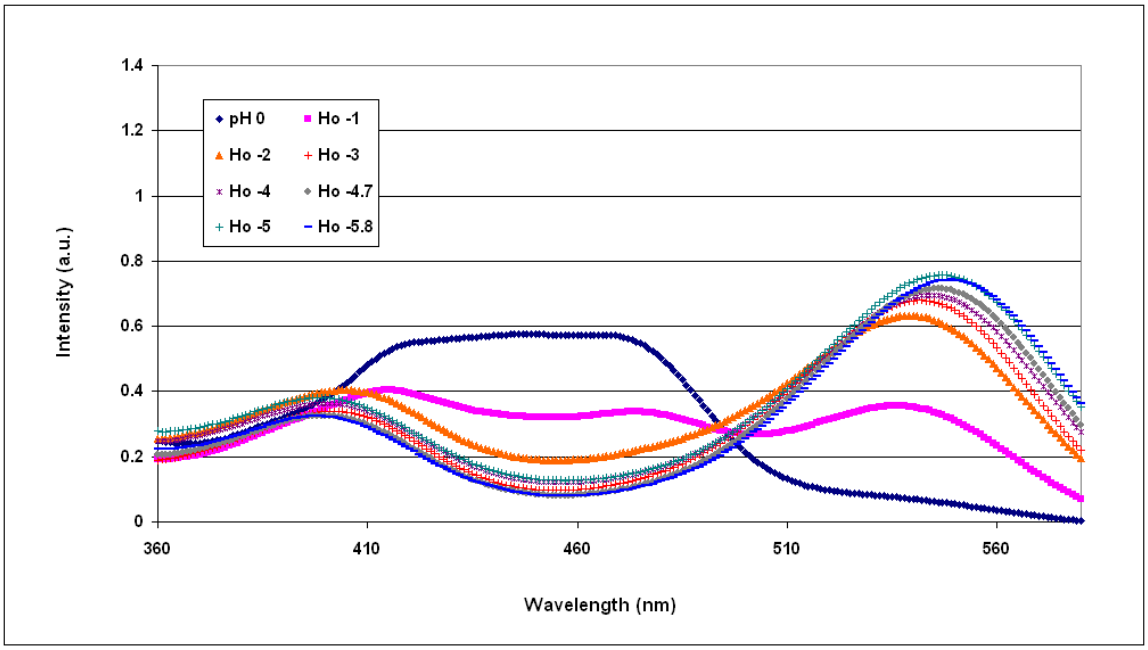

Figure 62. Expanded UV-Visible spectra of RT aqueous perchloric acid solutions of $[(bpy)_2Ru(pypz)]^{2+}$ in the 0 to -6 H_0 range, between 360 and 580 nm.

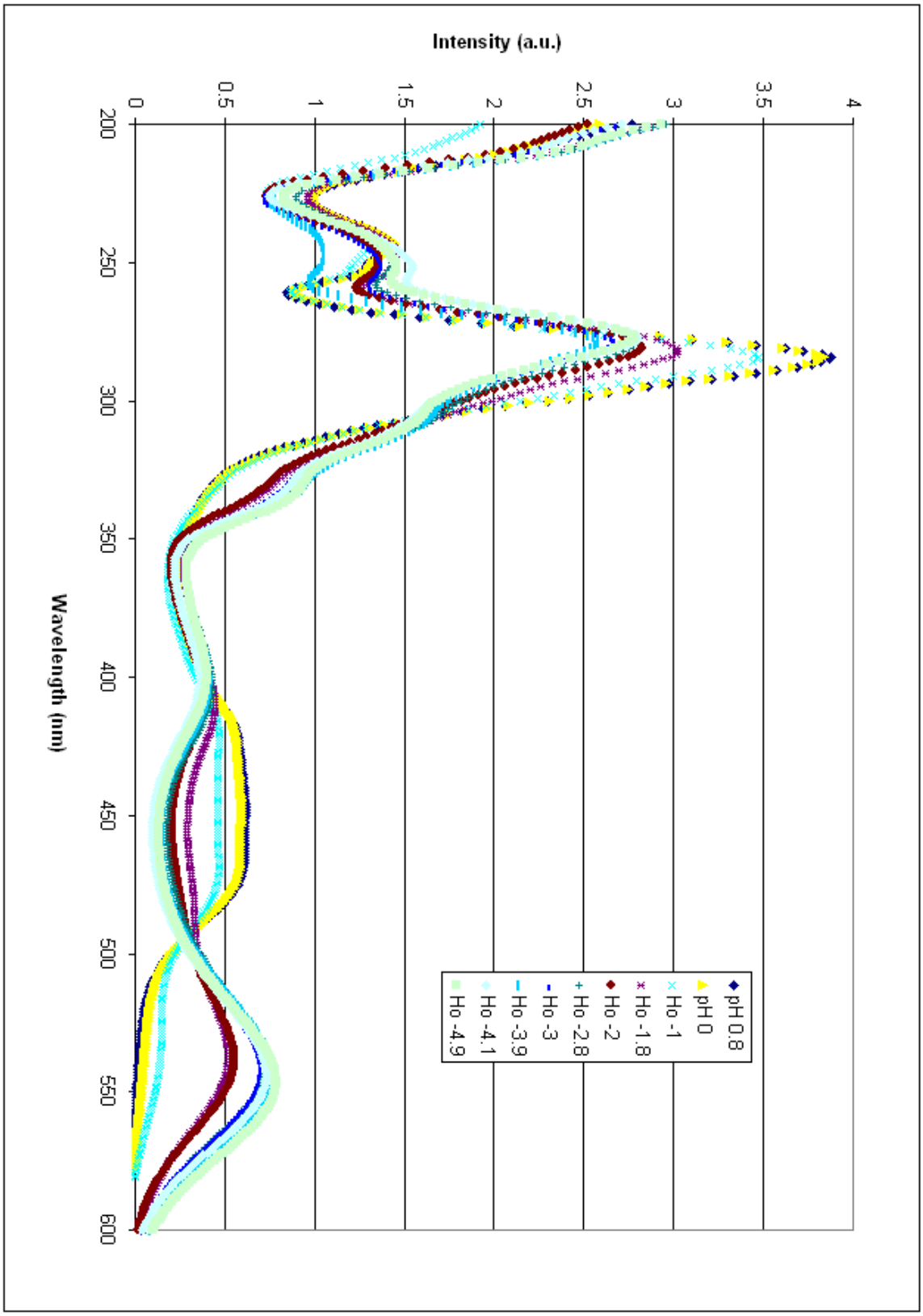

Figure 63. UV-Visible spectra of room temperature, aqueous sulfuric acid solutions of $[(bpy)_2Ru(pypz)]^{2+}$ in the 0 to -5 H_0 range.

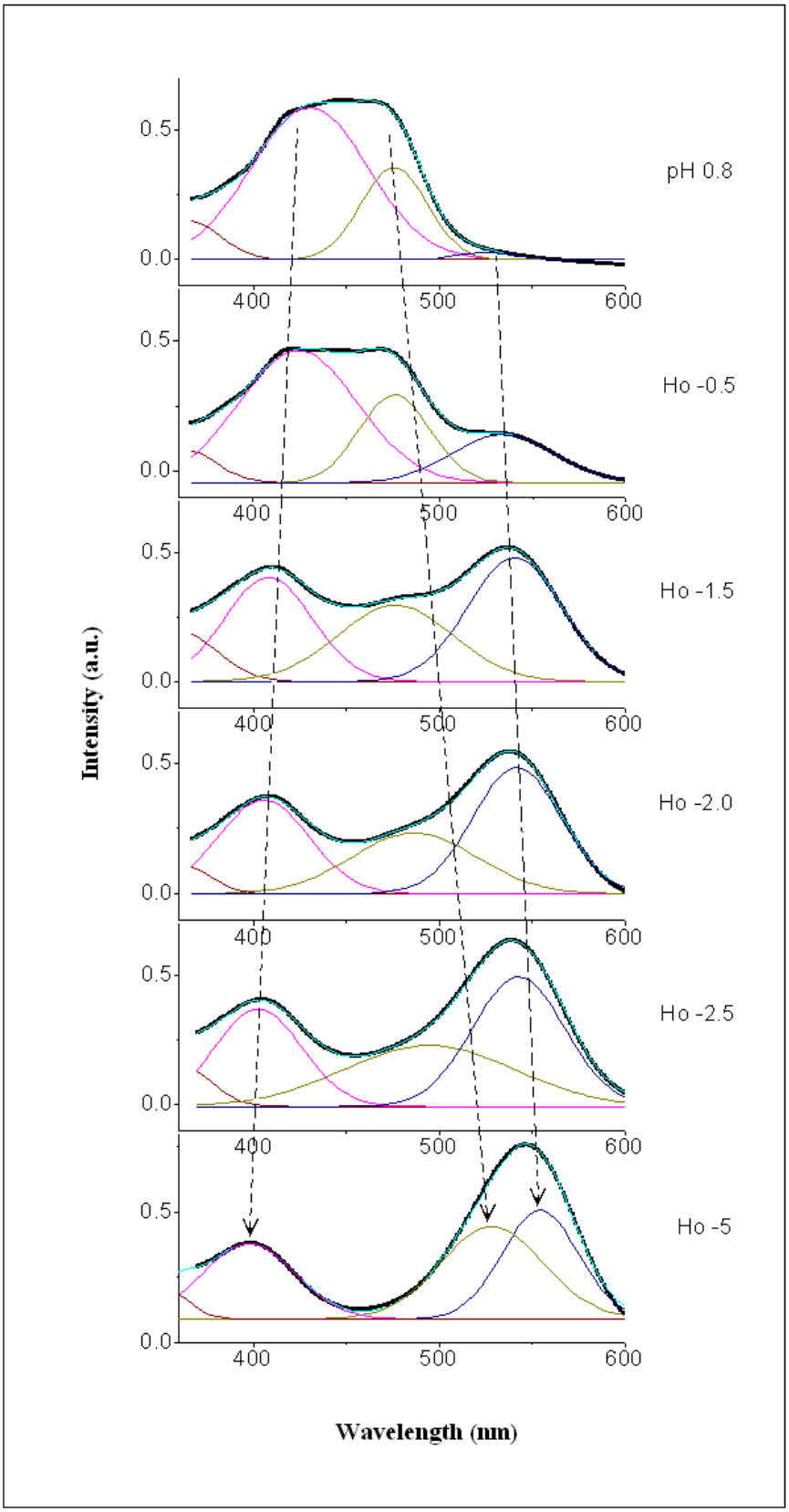

Figure 64. Mathematical fit and peak shift in the MLCT bands of $[Ru(bpy)_2pypz]^{2+}$.

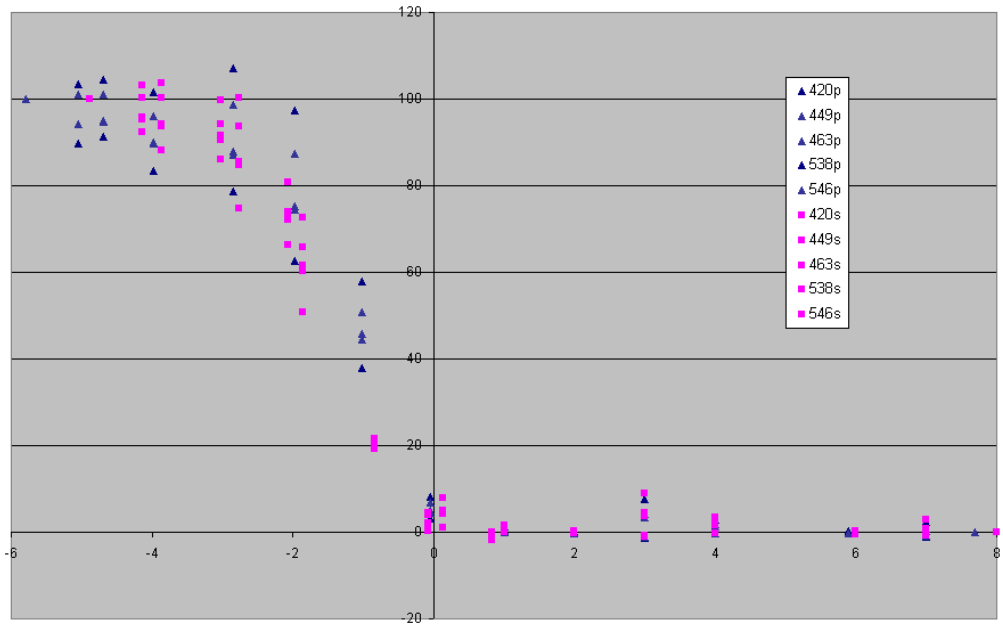

Figure 65. Percent of absorbance change as a function of [H^+] obtained from the UV-Vis spectra of $[(bpy)_2Ru(pypz)]^{2+}$ and monitored at five different wavelengths: ▲ Perchloric titration; ■ Sulfuric titration.

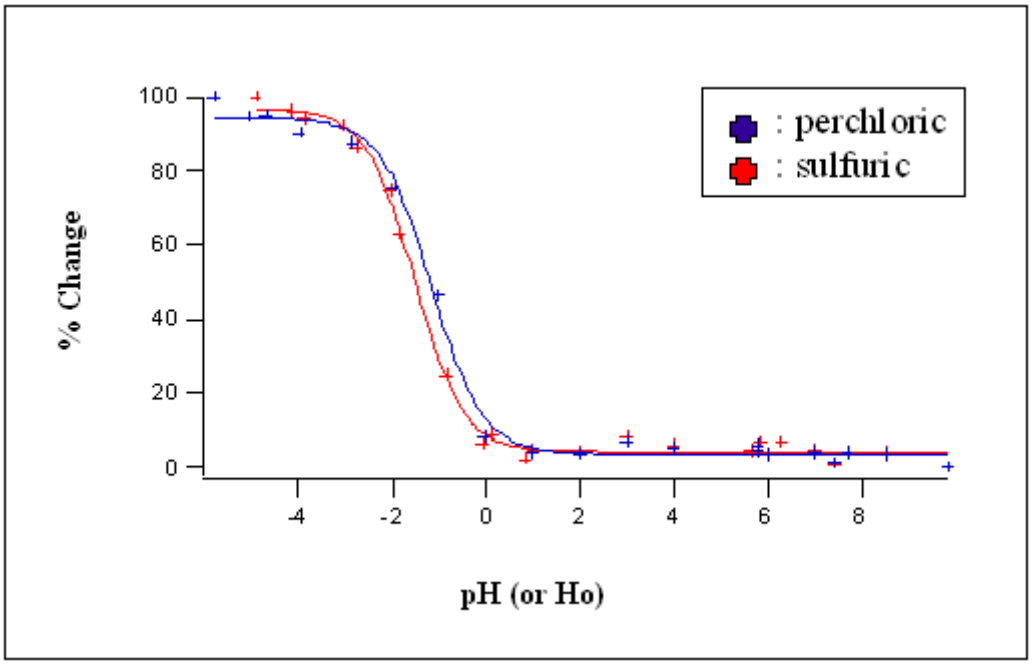

Figure 66. Percent of intensity changes observed at 463 nm in UV-Vis spectra of $[(bpy)_2Ru(pypz)]^{2+}$ as a function of pH for perchloric and sulfuric samples.

Table 15. Inflection points from perchloric and sulfuric samples obtained by plotting the absorbance changes at several wavelengths as a function of pH or H_0.

Wavelength (nm)	Perchloric titration	Sulfuric titration
420	-1.56	-1.78
449	-1.22	-1.59
463	-1.22	-1.59
538	-0.9	-1.42
546	-1.01	-1.54

A more in depth analysis of the trend was carried out by plotting the changes in peak max position and in absorbance intensity obtained from the mathematical fits of the UV-Vis spectra for perchloric and sulfuric samples. The values of the inflection points that could be determined (meaning with error < 20%) are reported in Table 16. Figure 67 shows the changes in peak max position using the sulfuric acid data set. The data pertaining to the 430-nm band best fit a sigmoidal curve and the 50% change occurs at H_0 –1.52 ± 0.05. The inflection point of the sigmoidal curve obtained monitoring the position of the 366-nm peak max has a larger error associated with it, while no reliable value of pK_a can be derived from the other curves.

Table 16. Inflection points from perchloric and sulfuric samples obtained by plotting the changes in peak max position and absorbance calculated from the mathematical fits of the MLCT transitions as a function of pH or H_0.

Wavelength (nm)	Peak max Perchloric titration	Peak max Sulfuric titration	Absorbance Perchloric titration	Absorbance Sulfuric titration
366	n/a	-1.35	n/a	n/a
430	-1.37	-1.52	n/a	-0.95
476	-1.30	n/a	-1.50	-1.38
525	-0.80	n/a	-0.90	-1.41

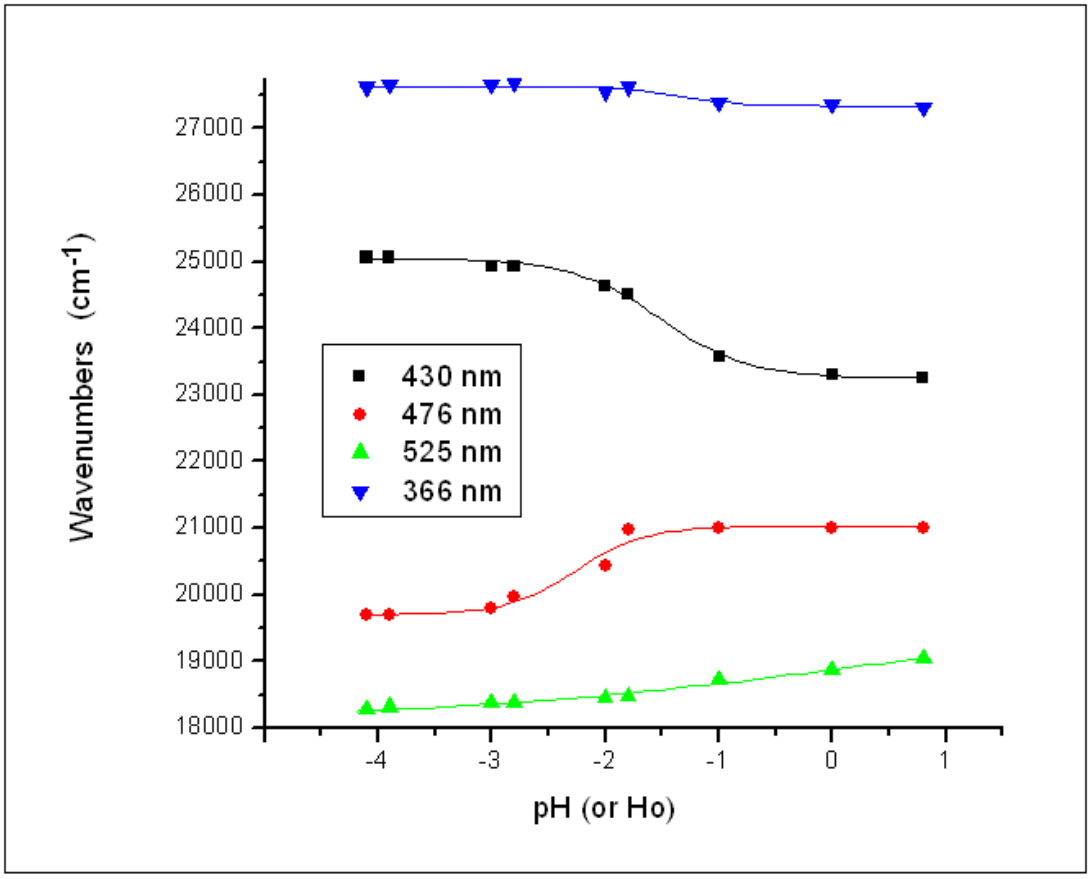

Figure 67. Changes in peak max position observed in the UV-Vis spectra of $[(bpy)_2Ru(pypz)]^{2+}$ as a function of pH (sulfuric titration).

3.B.4. Excited-state Titration of $[(bpy)_2Ru(pypz)]Cl_2$

At neutral pH the $[(bpy)_2Ru(pypz)]Cl_2$ complex emits at 675 ± 5 nm following a single-exponential decay with lifetime of 52 ± 1.6 ns. As pH increases to 11, the lifetime increases to 180 ± 10 ns with an accompanying 180% increase in intensity, but no change in the position of the emission maximum. Changes in the opposite direction occur as pH is lowered and the acidity of the medium increases. In the pH range from 6 to 2, protonation quenches the luminescence intensity and reduces the emission lifetime with no variation of the emission maximum position (Figure 68). Unlike $[(bpy)_2Ru(dpp)]^{2+}$, at

high acidity no new emission is observed at higher wavelength, which indicates that the protonated species in not emissive.

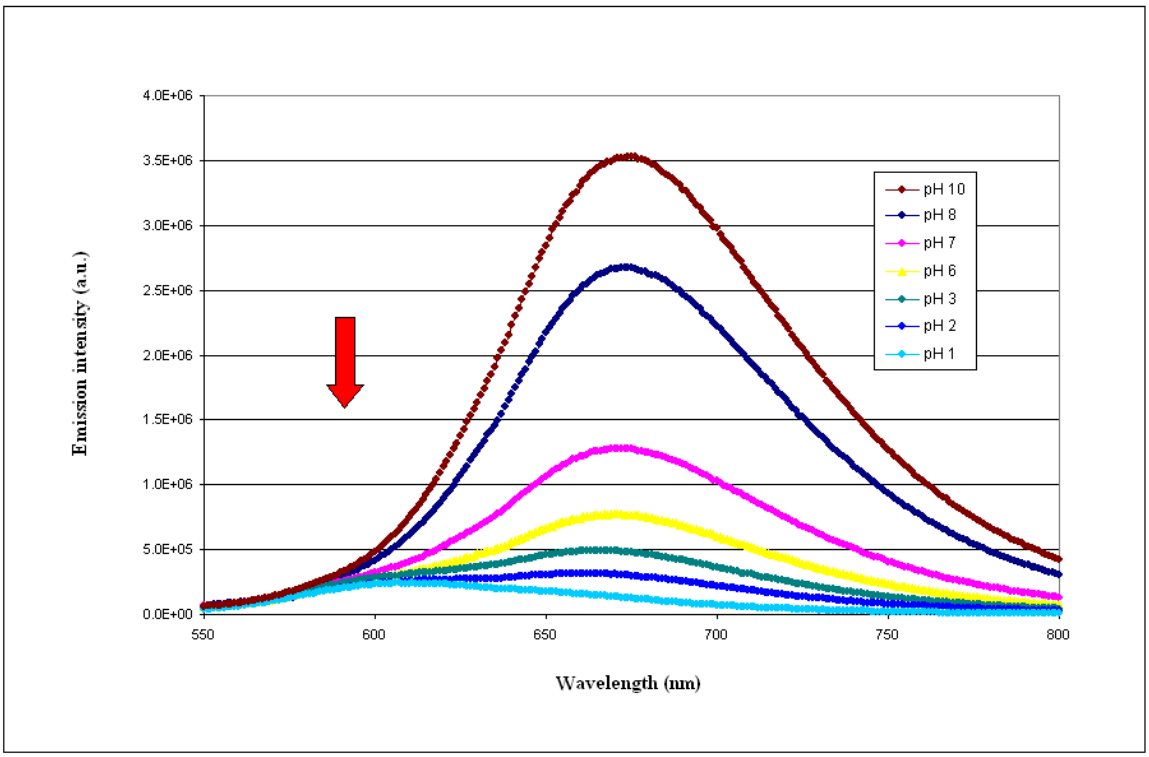

Figure 68. Quenching of the 675-nm emission at increasing [H^+].

The intensity of the 675-nm emission reaches a minimum at approximately pH 1. At pH 2 and lower, a new emission maximum starts to grow in at shorter wavelength and continues to grow and blue-shifts gradually (Figure 69), until the limits of highest achievable acidity are reached (H_0 = -5). The new emission is centered at 610 ± 5 nm and has a lifetime greater than 500ns at H_0 –3. The emissions observed throughout the entire pH range are independent of the excitation wavelength. The excitation spectrum of the unprotonated complex mirrors its absorption spectrum while the excitation spectrum at high acidity shows a maximum localized around 450 nm (Figure 70).

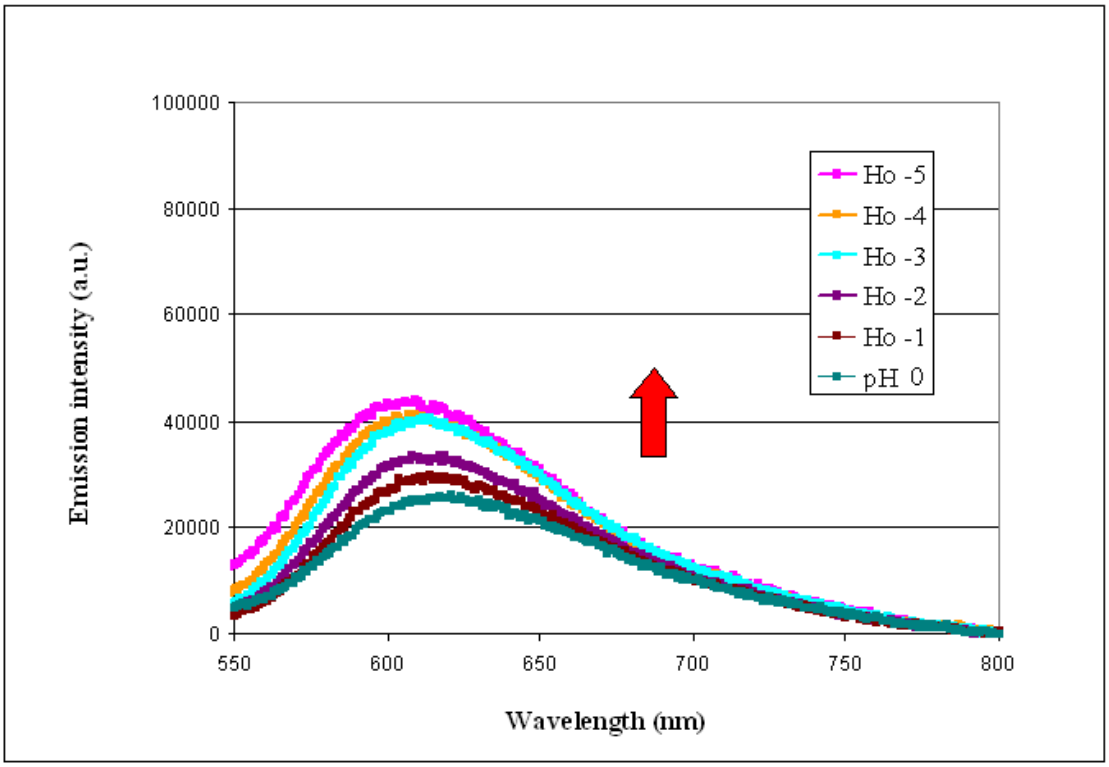

Figure 69. Spectral changes of the 610-nm emission at increasing [H^+] below pH 0.

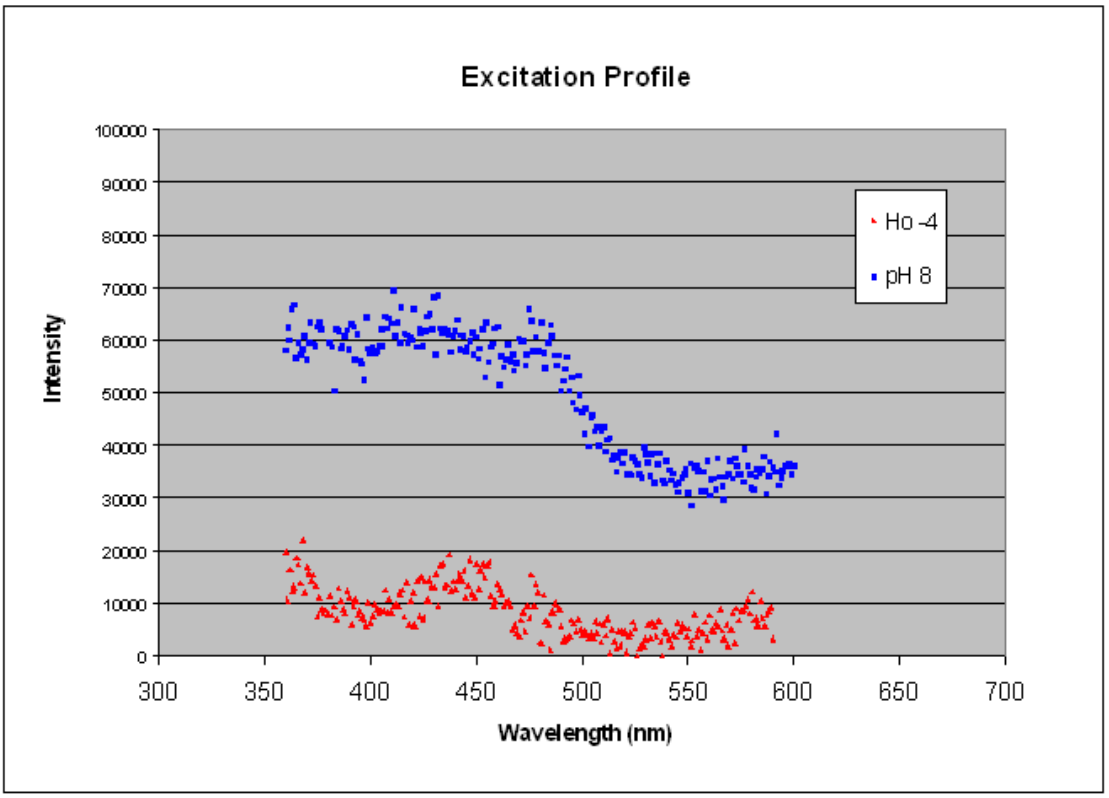

Figure 70. Excitation spectra of $[(bpy)_2Ru(pypz)](NO_3)_2$ at pH 8 and H_0 –4 monitored at 670 nm.

The parameters monitored during the titration as a function of pH are: emission intensity at 675 and 725 nm, lifetimes, and area under the emission curve between 550 and 750 nm (Figures 71-78). Only the emission curves between pH 10 and 0 were integrated in the spectral range between 550 nm and 750 nm. The curves in the negative Hammett acidity range were not integrated and used in plotting the titration curve because of the interfering 610-nm emission that starts growing at acidity higher than pH 0. The graphs in Figure 71 show that, contrary to what was observed in the ground state titration, the variations recorded in the excited state titration with perchloric acid closely parallel the ones observed in the titration with sulfuric acid.

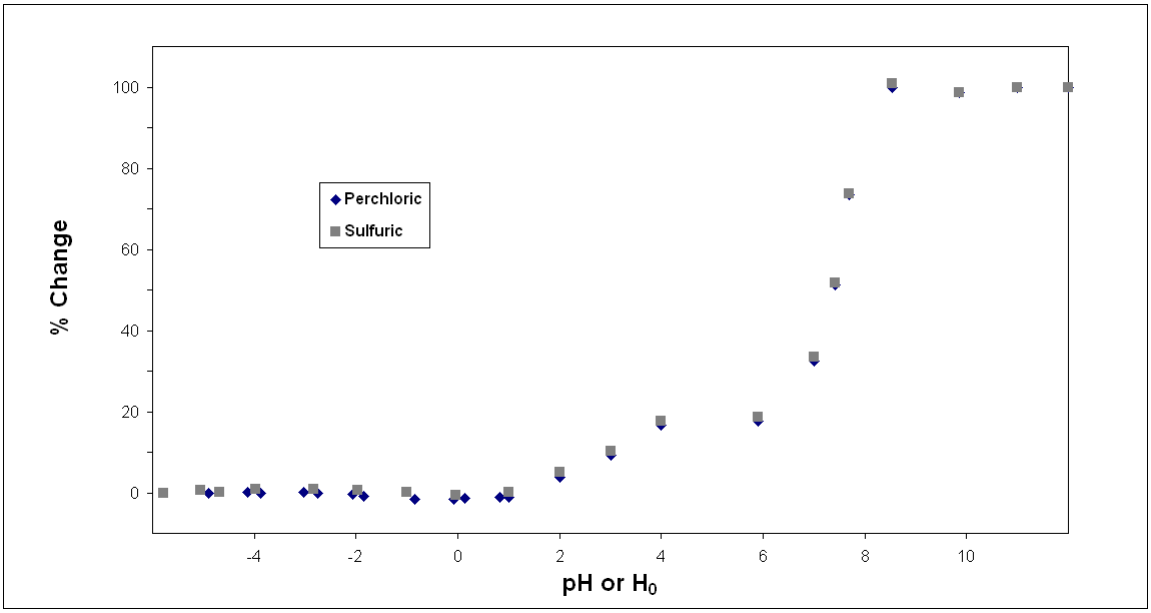

Figure 71. Luminescence titrations of $[(bpy)_2Ru(pypz)](NO_3)_2$ using sulfuric and perchloric acid. Intensity changes monitored at 674 nm.

All graphs reveal similar patterns of change in two distinct regions, the 12 to 7 pH range and the 6 to 0 pH range. For each range, the change in the plotted parameter can be

fitted mathematically using a sigmoidal curve. The pH values extrapolated from the fit at the midpoint of the breaks in the fitted curves are listed in Table 17.

Table 17. Inflection points from excited-state acid titrations obtained by plotting the parameters' changes as a function of pH.

pH range	0 - 6	6 - 10
Emission Intensity at 675 nm	2.73 ± 0.2	7.70 ± 0.1
Emission Intensity at 725 nm	2.76 ± 0.2	7.65 ± 0.01
Lifetime	2.47 ± 0.1	7.51 ± 0.01
Area under the curve (550-750nm)	2.69 ± 0.2	7.64 ± 0.01

The sigmoidal fits of the emission intensity titration monitored at 675 nm for the two pH ranges, 0-6 and 6-10 are presented in Figure 72 and 73, while Figure 74 reports the sigmoidal fit of the emission intensity titration monitored at 725 nm over the entire range. Similarly, the emission lifetime titration over the full range of pH, from 0 to 10, is plotted in Figure 75 and the individual regions are highlighted in Figure 76 and 77. Every graph has an R-squared value of 0.99 or above and the fit is very good in both regions for every parameter plotted.

The apparent pKa for protonation in the 0 to 6 pH range was estimated from the midpoint of the breaks in the four titration curves and the average value is 2.6 ± 0.1, which corresponds to a Ka^{*} (app.) = 2.51 x 10^{-3}. The average pH value for the midpoint of the breaks in the titration curves of the second occurrence at higher pH is 7.6 ± 0.1.

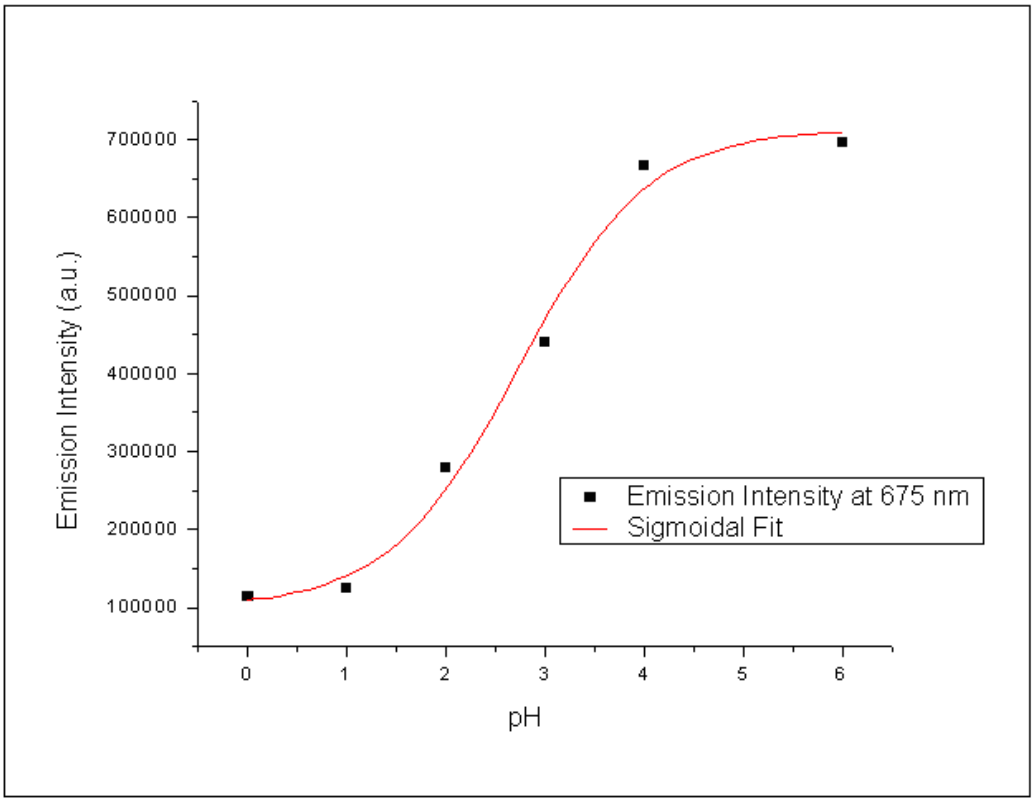

Figure 72. Sigmoidal fit of the emission titration of $[(bpy)_2Ru(pypz)](NO_3)_2$ monitored at 675 nm in the 0 to 6 pH range.

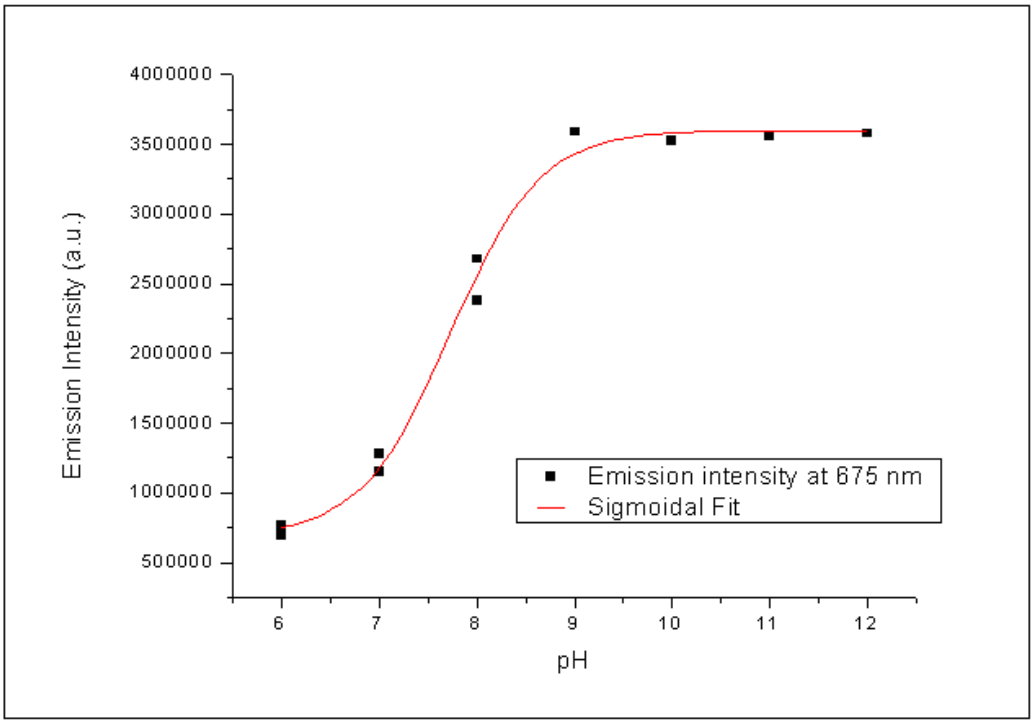

Figure 73. Sigmoidal fit of the emission titration of $[(bpy)_2Ru(pypz)](NO_3)_2$ monitored at 675 nm in the 6 to 10 pH range.

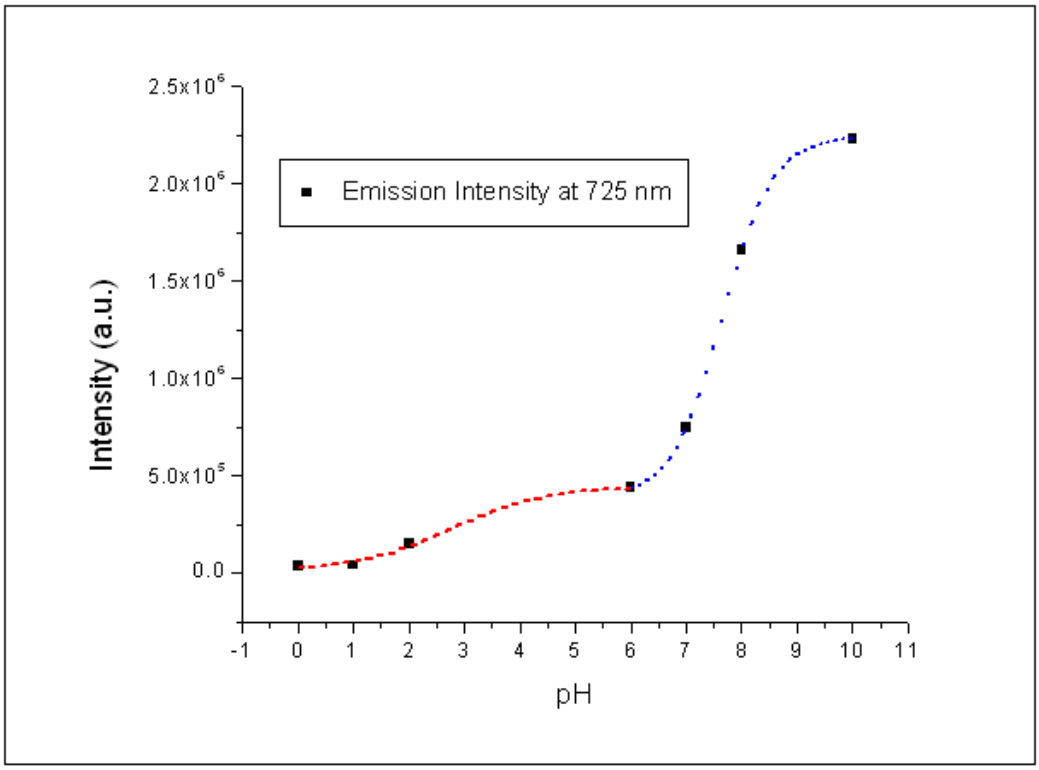

Figure 74. Emission titration and sigmoidal fit of $[(bpy)_2Ru(pypz)](NO_3)_2$ monitored at 725 nm in the 0 to 10 pH range.

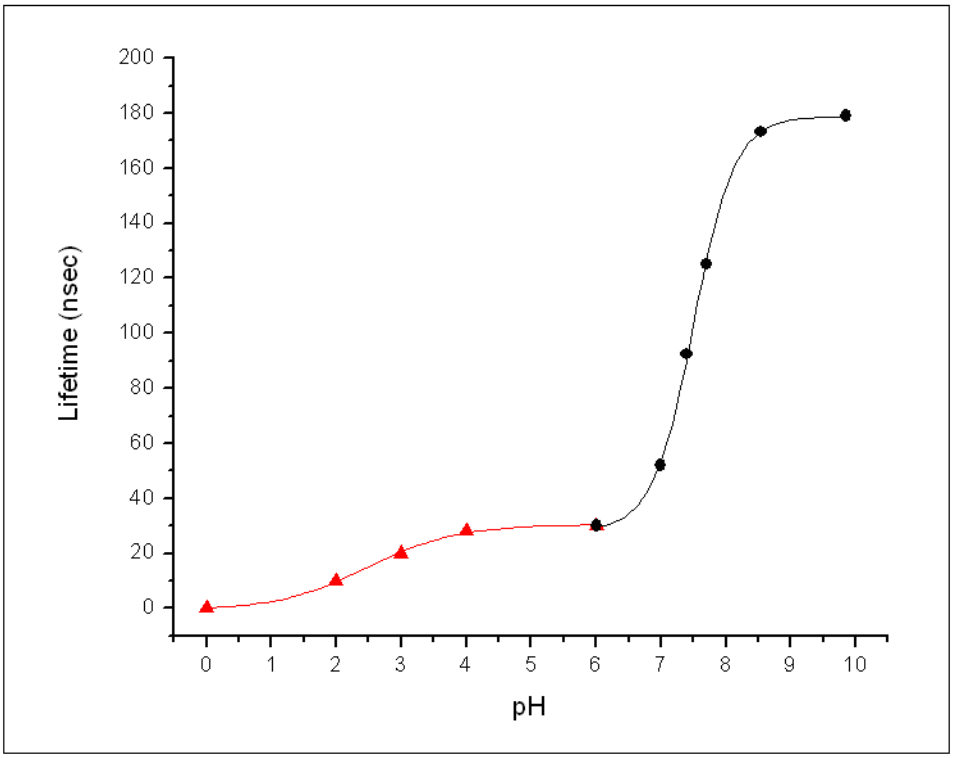

Figure 75. Lifetime titration & sigmoidal fit of $[(bpy)_2Ru(pypz)](NO_3)_2$ in the 0 to 10 pH range.

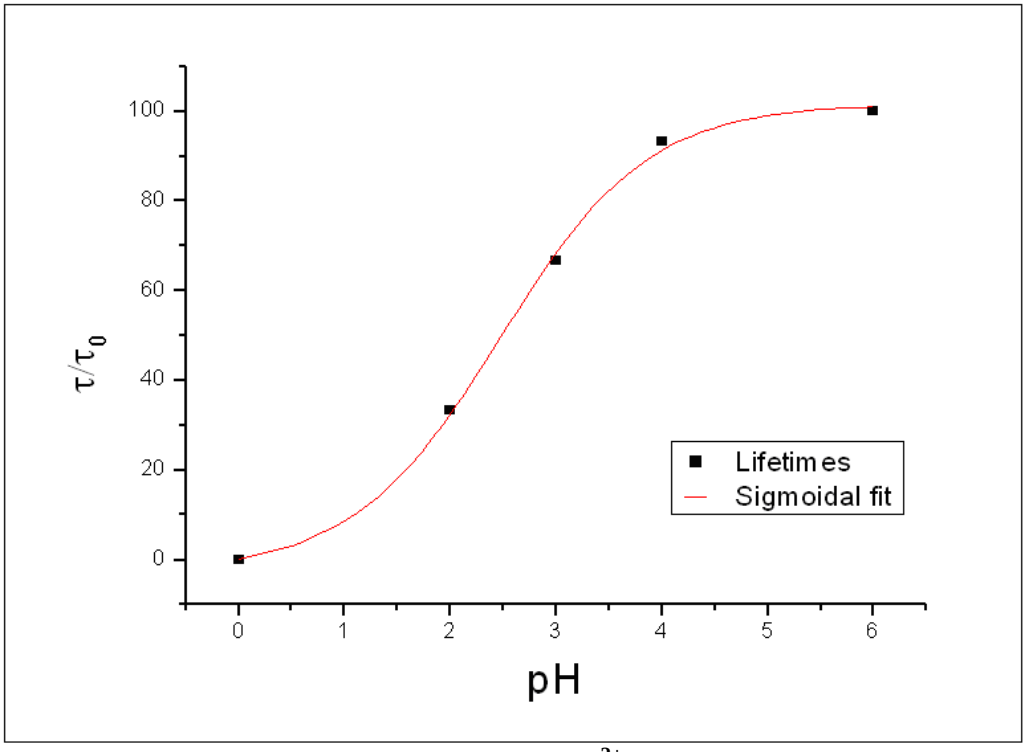

Figure 76. Lifetime titration of $[(bpy)_2Ru(pypz)]^{2+}$ in the 0 to 6 pH range.

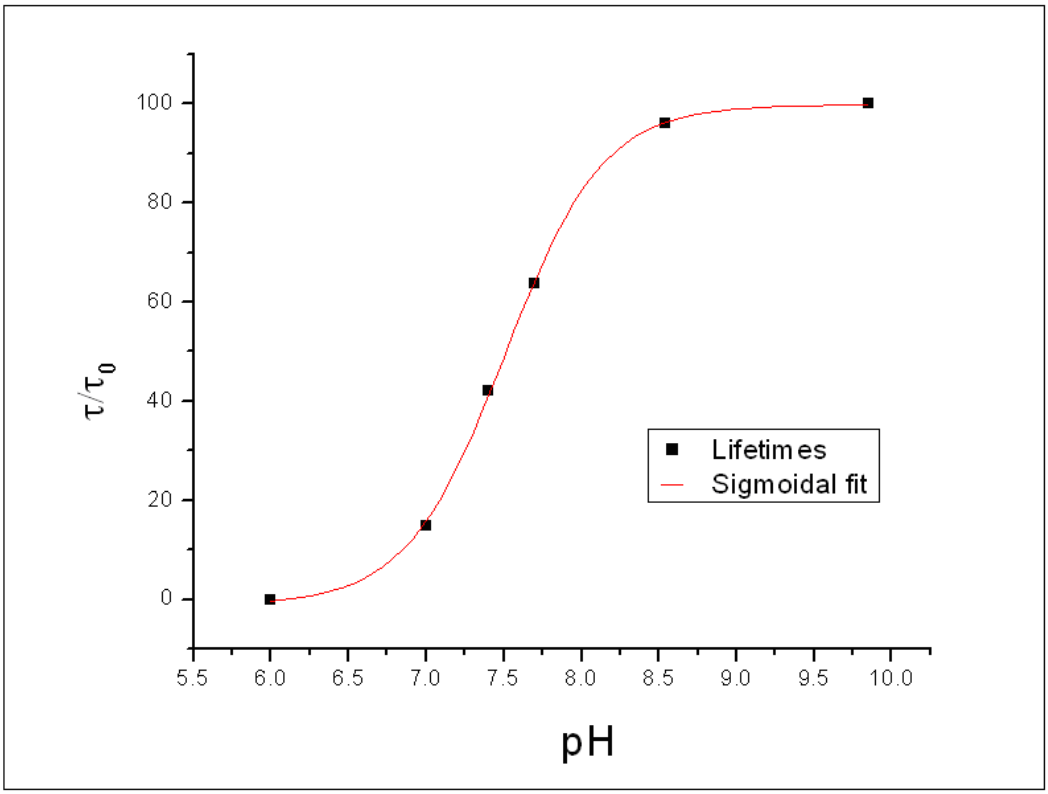

Figure 77. Lifetime titration of $[(bpy)_2Ru(pypz)]^{2+}$ in the 6 to 10 pH range.

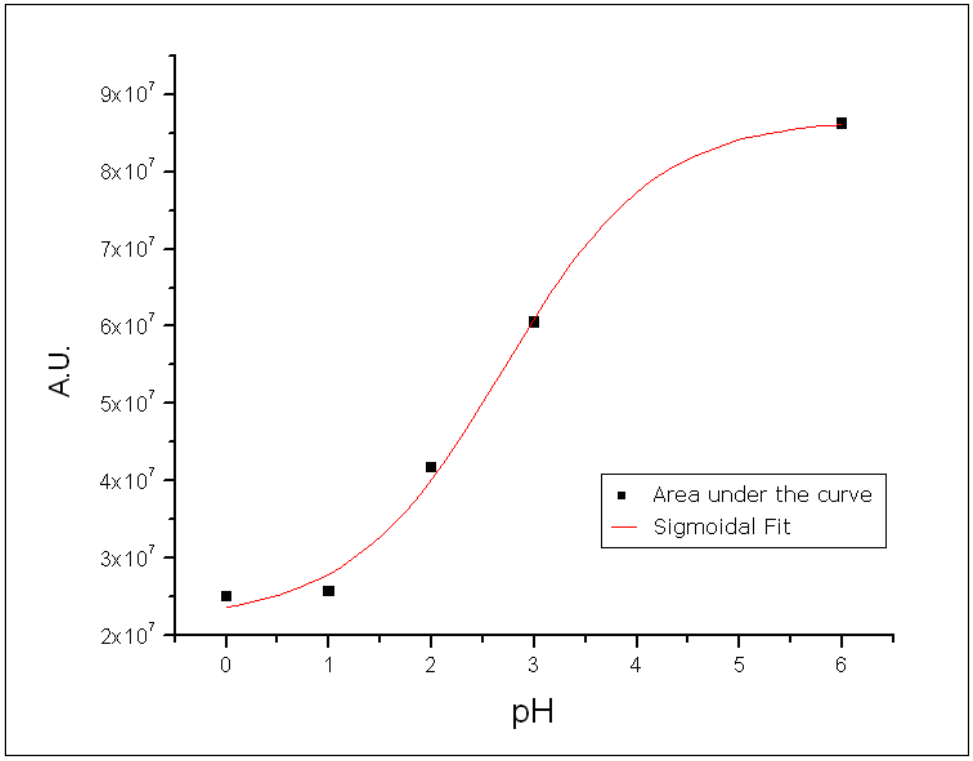

Figure 78. Luminescence titrations of $[(bpy)_2Ru(pypz)](NO_3)_2$ in the 0 to 6 pH range. Emission curves were integrated between 550 and 750 nm.

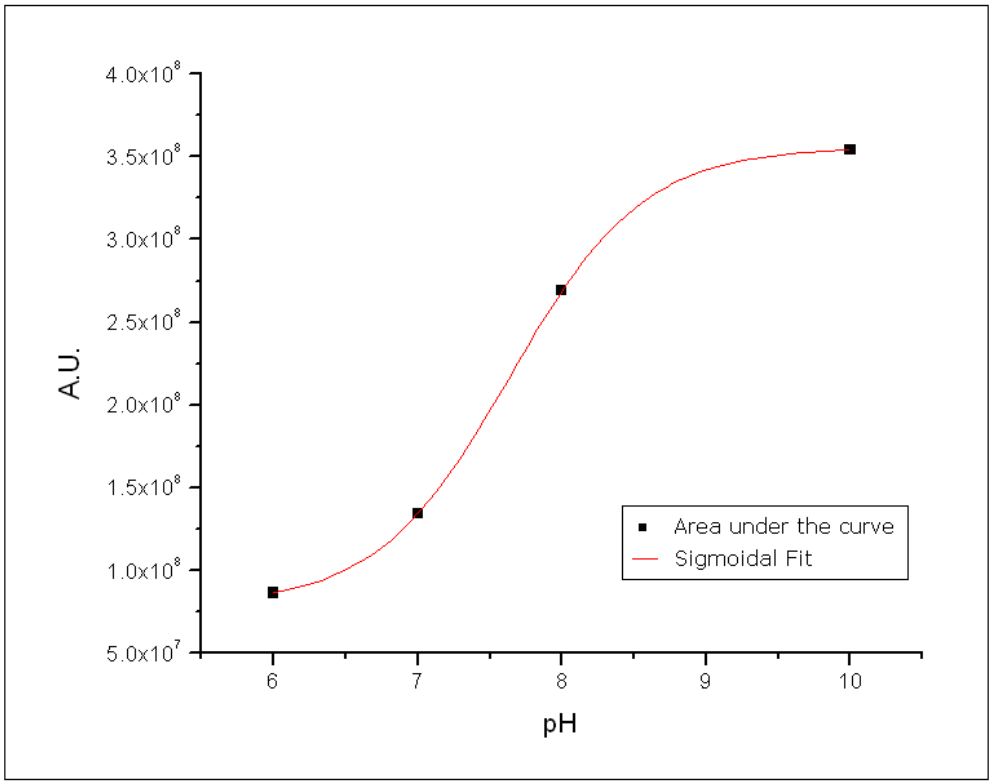

Figure 79. Luminescence titrations of $[(bpy)_2Ru(pypz)](NO_3)_2$ in the 6 to 10 pH range. Emission curves were integrated between 550 and 750 nm.

Stern-Volmer plots of I_0/I and τ_0/τ are shown in Figure 80. The curves are linear only at high pH and do not overlap over the entire titration acidity range. The Stern-Volmer plot of the decrease in lifetime at high pH is presented in Figure 81. Above pH 7 the curve can be fitted to the classic Stern-Volmer equation and the constant derived is $K_{SV} = 2.3 \times 10^7\ M^{-1}$ or $k_q = 1.3 \times 10^{14}\ s^{-1}\ M^{-1}$. The second part of the curve, below pH 7, shows a negative deviation from linearity similar to the one observed in the acid quenching of $[(bpy)_2Ru(dpp)]^{2+}$ and could not be fitted by any equation (Figure 82). Similarly, the Stern-Volmer plot of the decrease in emission intensity is linear only at high pH (Figure 83) with constants in that range $K_{SV} = 1.8 \times 10^7\ M^{-1}$ and $k_q = 1.0 \times 10^{14}\ s^{-1}\ M^{-1}$ and displays negative deviations from linearity in the 7 to 1 pH range (Figure 84).

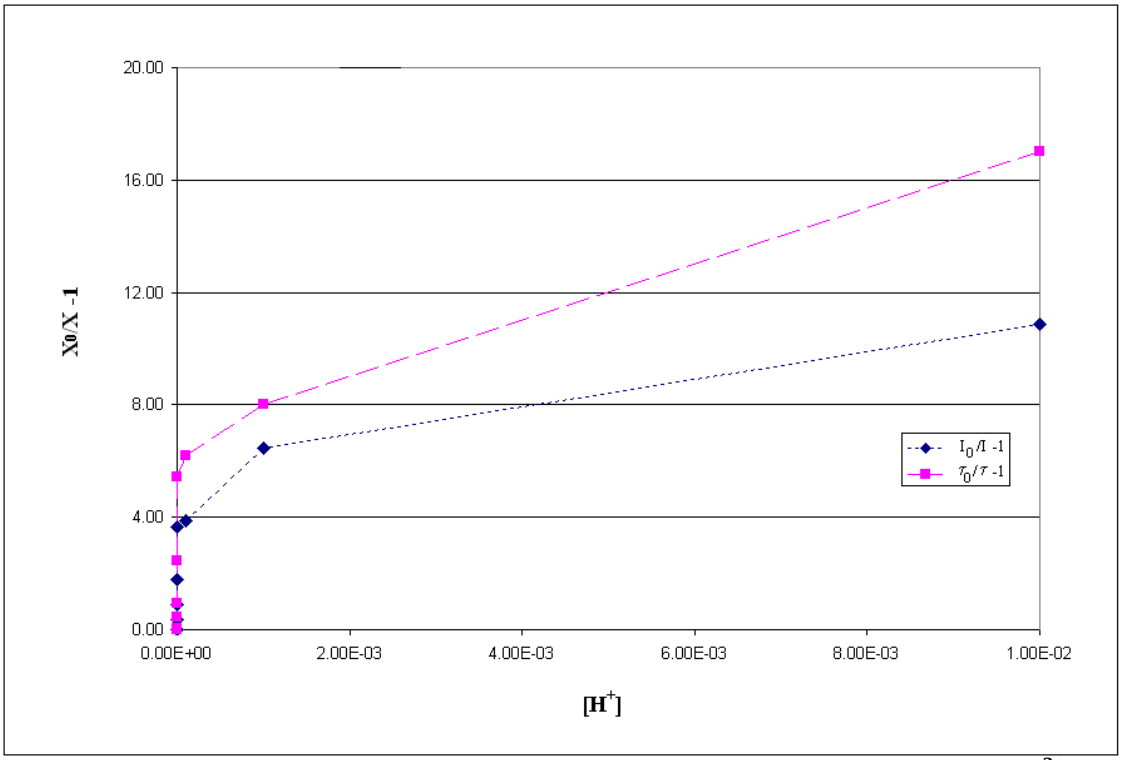

Figure 80. Stern-Volmer plots of lifetimes and intensities $[(bpy)_2Ru(pypz)]^{2+}$ as a function of acidity.

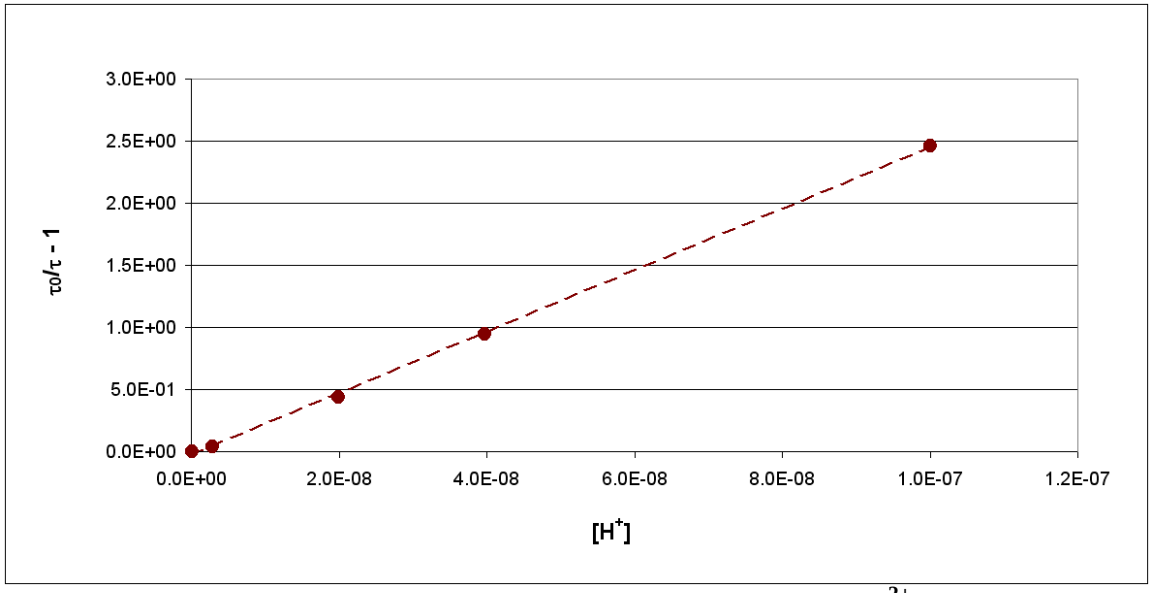

Figure 81. Stern-Volmer plots of lifetimes of $[(bpy)_2Ru(pypz)]^{2+}$ as a function of acidity in the 7 to 10 pH range.

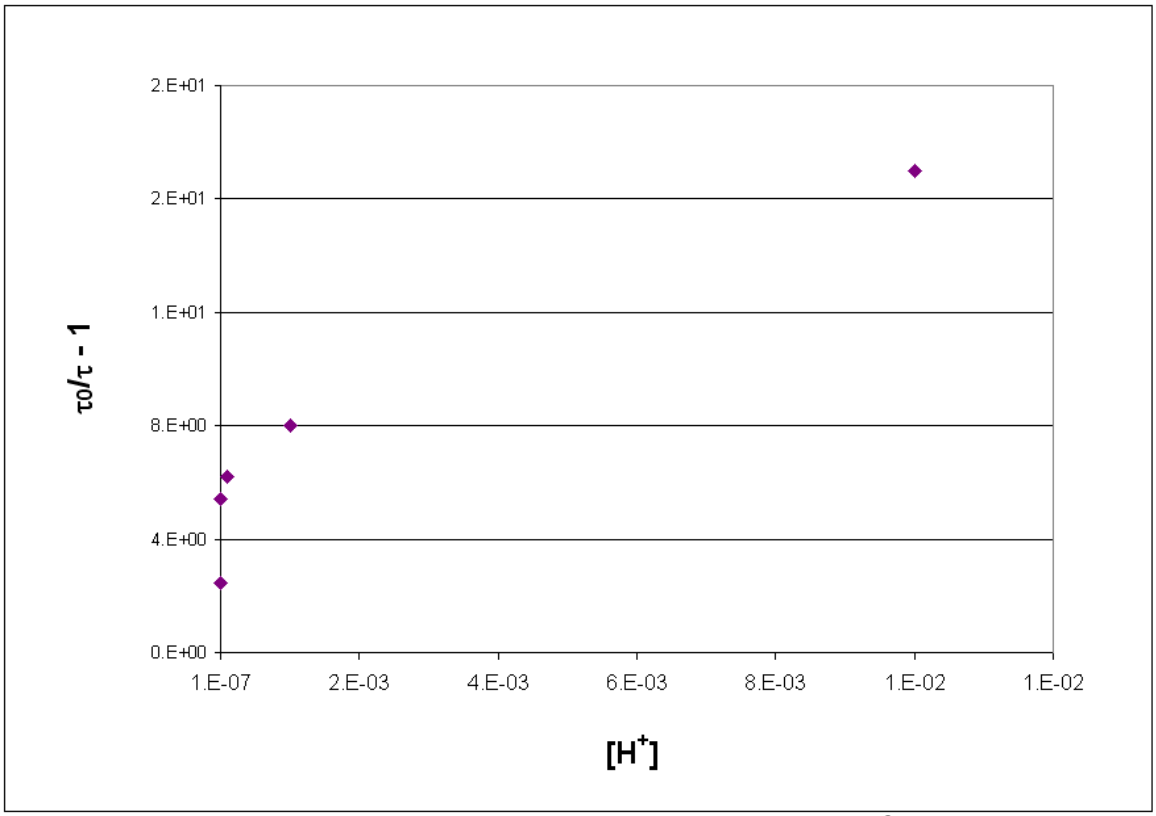

Figure 82. Stern-Volmer plot of lifetimes of $[(bpy)_2Ru(pypz)]^{2+}$ as a function of hydronium ion concentration in the 2 to 7 pH range

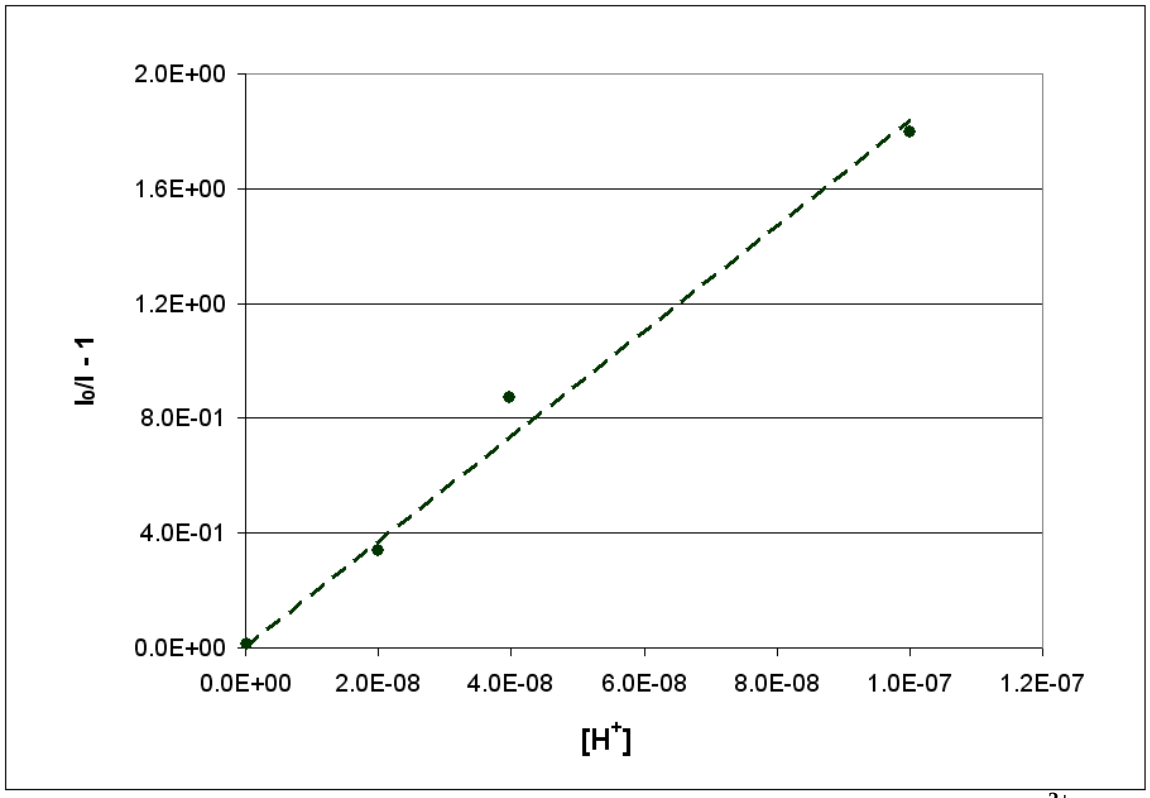

Figure 83. Stern-Volmer plot of 674-nm intensities of $[(bpy)_2Ru(pypz)]^{2+}$ as a function of acidity in the 7 to 10 pH range.

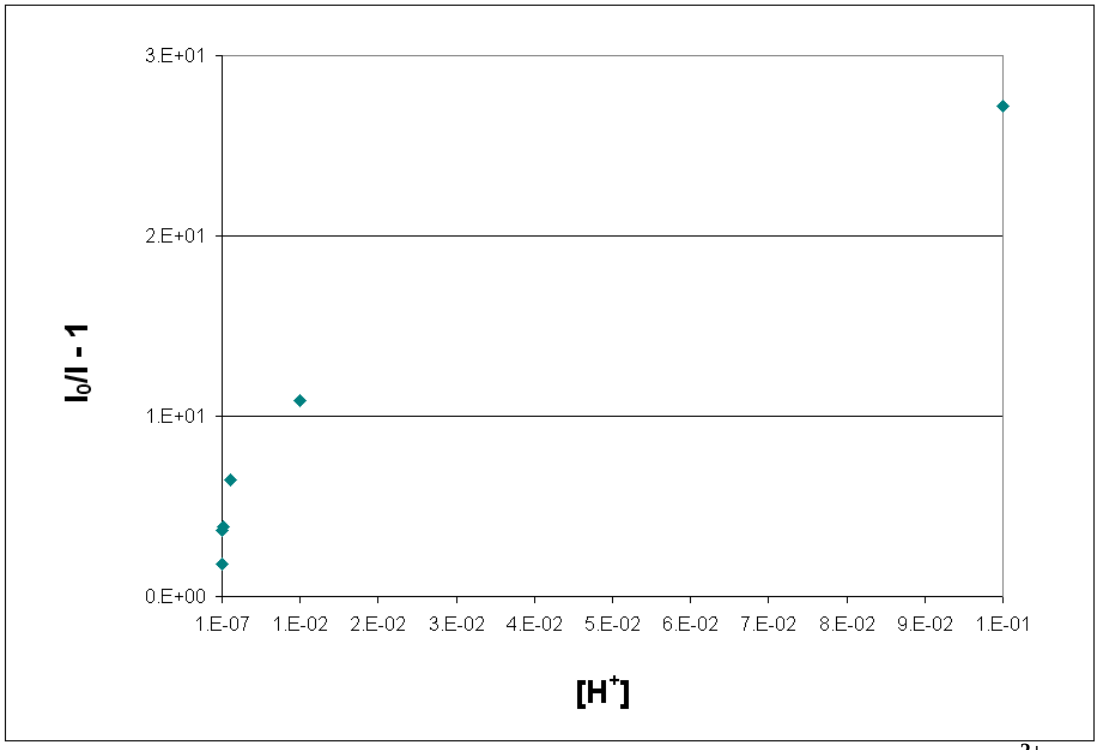

Figure 84. Stern-Volmer plot of 674-nm intensities of $[(bpy)_2Ru(pypz)]^{2+}$ as a function of hydronium ion concentration in the 1 to 7 pH range.

In the negative Hammett acidity domain, the new emission at 610 nm grows in and the Stern-Volmer plot of intensities as a function of acidity is not linear (Figure 85). The emission intensity at peak maximum increases as hydronium ion concentration increases (Figure 86), corresponding in a Stern Volmer trend opposite to the trend observed between pH 1 and 7, during quenching of the 675 nm emission.

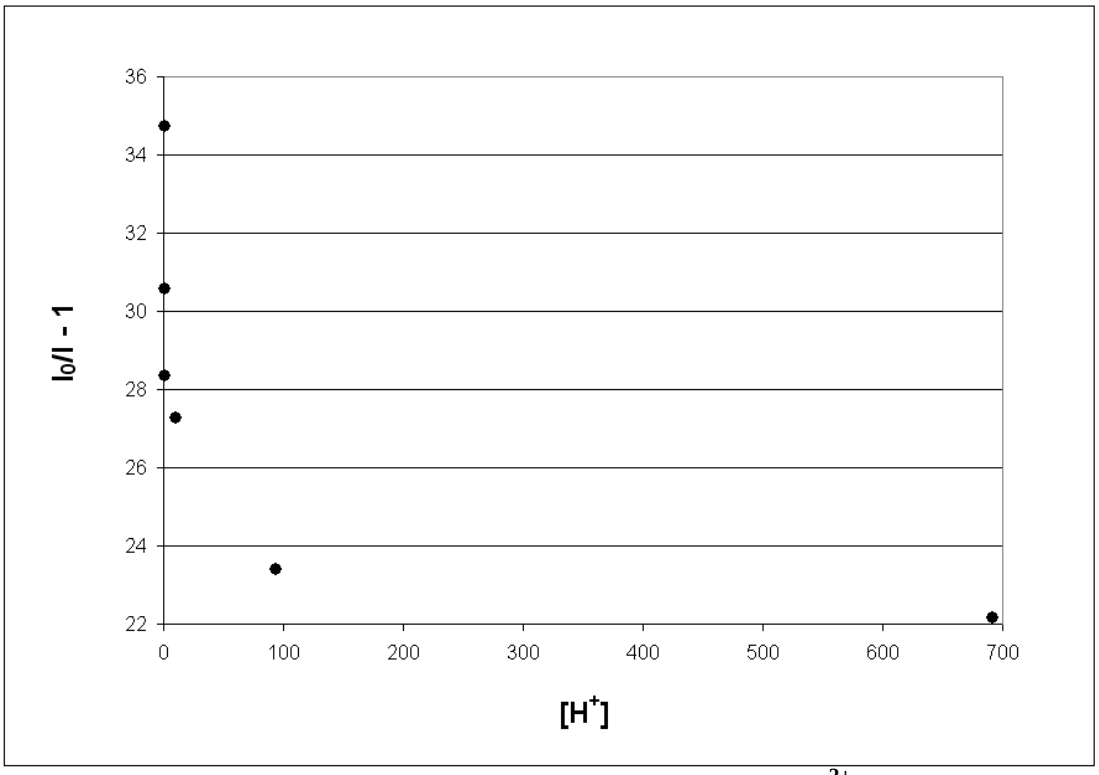

Figure 85. Stern-Volmer plot of intensities of $[(bpy)_2Ru(pypz)]^{2+}$ as a function of hydronium ion concentration from pH 0 to H_0 –3.

3.C. Association of ruthenium(II) diimine complexes with d^{10} metals

The behavior of Ru-diimine complexes in the presence of d^{10} metals was studied both in the ground and in the excited state via titrations and time-resolved measurements. The mathematical equations applied in order to interpret the data gathered from each set of experiments are described and reported below.

In the ground state, assuming the following one-to-one interaction is established between complex and metal cation:

$$[Ru(bpy)_2L]^{2+} + M^{2+} \leftrightarrows [Ru(bpy)_2L\cdots M]^{4+} \quad (88)$$

the constant of association, K_{eq}, can be obtained by following the changes in the concentrations of each species at increasing concentrations of the d^{10} metal:

$$K_{eq} = \frac{[Ru(bpy)_2L\cdots M^{4+}]}{[Ru(bpy)_2L^{2+}][M^{2+}]} \quad (89)$$

When the electronic absorption due to the metal cation, M^{2+}, is negligible in the spectral range under investigation, the absorption spectrum of the two-component homogeneous solution, can be considered at each moment in time as due to the contributions to the absorption of both species and expressed mathematically by the linear combination of the two spectra:

$$A(\lambda) = \varepsilon_{Ru}[Ru] + \varepsilon_{Ru\text{-}M}[Ru\text{-}M] \quad (90)$$

where $A(\lambda)$ is the absorbance value at wavelength λ, ε_{Ru} and $\varepsilon_{Ru\text{-}M}$ are the extinction coefficients of the free ruthenium complex and the associated complex, respectively, and [Ru] and [Ru-M] are the concentrations of the free and associated species. If the concentrations of the intermediates cannot be established by other means, the values of [Ru] and [Ru-M] can be expressed as a funtion of the initial concentrations of ruthenium complex and metal, respectively:

$$[Ru] = [Ru]_0 - X \quad (91)$$

$$[M] = [M]_0 - X \quad (92)$$

$$[Ru\text{-}M] = X \quad (93)$$

Hence:

$$A(\lambda) = \varepsilon_{Ru}([Ru]_0 - X) + \varepsilon_{Ru\text{-}M}X$$

$$= (\varepsilon_{Ru\text{-}M} - \varepsilon_{Ru})\, X + \varepsilon_{Ru}\, [Ru]_0 \qquad (94)$$

and

$$K_{eq} = \frac{X}{([Ru]_0 - X)\,([M]_0 - X)} \qquad (95)$$

Solving equation (95) for X gives equation (96) below:

$$X = \left[\frac{1}{2}\left(\frac{1}{K_{eq}} + [M]_0 + [Ru]_0 \right) \pm \sqrt{\left[\frac{1}{2}\left(\frac{1}{K_{eq}} + [M]_0 + [Ru]_0 \right) \right]^2 - \quad ([Ru]_0[M]_0)} \right] \qquad (96)$$

and combining equation (94) and (96), a relationship is found between the absorbance of the recorded spectrum $A(\lambda)$ and the initial concentrations:

$$A(\lambda) = \varepsilon_{Ru}\, [Ru]_0 + \ldots \qquad (97)$$

$$(\varepsilon_{Ru\text{-}M} - \varepsilon_{Ru}) \left[\frac{1}{2}\left(\frac{1}{K_{eq}} + [M]_0 + [Ru]_0 \right) - \sqrt{\left[\frac{1}{2}\left(\frac{1}{K_{eq}} + [M]_0 + [Ru]_0 \right) \right]^2 - \quad ([Ru]_0[M]_0)} \right]$$

where ε_{Ru} is known and $\varepsilon_{Ru\text{-}M}$ and K_{eq} can be extrapolated from the two-parameter non-linear fit of the titration data. A similar fit, equation (98), was used to derive the association constant in the ground state from NMR titration data. In this case, the change in the chemical shift, $\Delta\delta$, and not the absorbance, was plotted as a function of the initial reactant concentrations[75]:

$$\Delta\delta_{observed} = (\delta_{bound} - \delta_{free})\ x\ \ldots \qquad (98)$$

$$\ldots\ x \left[\frac{1}{2}\left(\frac{1}{K_{eq}} + [M]_0 + [Ru]_0 \right) - \sqrt{\left[\frac{1}{2}\left(\frac{1}{K_{eq}} + [M]_0 + [Ru]_0 \right) \right]^2 - \quad ([Ru]_0[M]_0)} \right]$$

In the excited state, the analysis of steady-state luminescence data was complicated by several factors. Assuming the free ruthenium complex and the associated complex were to emit at wavelength far enough from each other so that each contribution to the spectrum could be distinguished, the apparent association constant in the excited-state could, in theory, be found by plotting the emission intensities or quantum yields as a function of pM. In the case where the emission maxima were to only partially overlap, the intensities for the overlap ratios could be corrected using the method suggested by Wyatt and Ireland for protonation equilibria (equations (56) to (68)). If, on the other hand, the emissions happened to overlap more completely, as is observed in the results presented below, the determination of the association constant would depend on the ability to resolve the individual components of the luminescence signal. An attempt to resolve steady-state spectra was made by Zambrana[65]. However, it turned out to be extremely difficult to minimize the sources of uncertainty associated with the mathematical manipulations and consequently with the values found.

The method used by Zambrana[65] to resolve the spectral contributions from each emission, was based on several assumptions or approximations. For instance:

1. The limiting emission spectra were attributed to the free and associated $[Ru(bpy)_2dpp]^{2+}$ species, thus assuming that at high concentrations of the metal, the complex is 100% coordinated and no free complex remains and/or its contribution to the total emission is negligible;
2. Since the absorption spectra of Ru and Ru-M are similar, the fraction of the excitation light absorbed by each was assumed to be equal to the concentration of each, no correction was made for the fractions of light absorbed;

3. A linear regression was used to fit the “in-between” spectra, although it is not self-evident that the emission intensity varies linearly;
4. The relative proportion of each emitting species was assumed to provide an estimate of the concentration of the free and associated species: this assumption implies that both species have equal quantum yield.

Finally, as discussed by Zambrana, the values of K^* found are meaningful only assuming that both species have comparable lifetimes. It could not be established unequivocally whether the species could achieve equilibrium within their lifetime and it could not be ignored that other reactions or pathways may simultaneously be at play in the overall system.

In the excited-state titration of $[Ru(bpy)_2pypz]^{2+}$ with Zn^{2+}, a limiting emission spectrum assigned to associated $[Ru(bpy)_2pypz]^{2+}$-Zn^{2+} cannot be obtained. Furthermore, the presence of emissions overlapping the main 655-nm emission from $[Ru(bpy)_2pypz]^{2+}$ namely, the 610-nm emission in the blue and the rising multiple emission from the Zn-adduct in the red region of the spectrum, does not allow to individually and unambiguously follow the quenching of the 655-nm band. Therefore, the excited-state titration profiles from the $[Ru(bpy)_2pypz]^{2+}$ titration were studied here in their entirety and compared with similarly treated data from the corresponding $[Ru(bpy)_2dpp]^{2+}$ titrations.

The time-resolved data, according to what was appropriate in each specific situation, were alternatively fit to a single-exponential decay equation:

$$y = y_0 + Ae^{-t/\tau} \tag{99}$$

or a double-exponential decay equation:

$$y = y_0 + A_1 e^{-t/\tau_1} + A_2 e^{-t/\tau_2} \quad (100)$$

where y_0 represents the signal baseline, A, A_1, A_2, are the pre-exponential factors at a given wavelength, and τ_1 and τ_2 are the corresponding lifetimes. The pre-exponential factor represents the emission intensity and theoretically, for each emitting species, a plot of pre-exponential factors as a function of wavelength should match the emission spectrum. Likewise, the double-exponential fit provides two sets of pre-exponential factors and lifetime for each emitting species. If, however, the emitting species interact either through static or dynamic quenching, the lifetime values may be affected by the time-dependent interactions and do not correspond to the "actual" lifetimes of each species. The ability of the analysis to distinguish between two emitting species is in part dependent on how similar the lifetimes are, how close their emission maxima are, and in part, on the signal to noise ratio that can be achieved by the instrument. In all the double-exponential fits, the lifetimes are reported to one standard deviation, as a means to distinguish between lifetimes, and establish if it is in fact even possible to make that distinction.

3.C.1. Association of $[(bpy)_2Ru(dpp)](NO_3)_2$ with Zinc and Cadmium

The visible region of the absorption spectra for 10^{-5} $[(bpy)_2Ru(dpp)]^{2+}$ in 3 M $Cd(NO_3)_2$ and in 3 M $Zn(NO_3)_2$ are shown in Figure 86. The MLCT bands characteristic of the $d\rightarrow\pi^*$ transition to the bpy ligand and to the dpp ligand in solutions of the complex with d^{10} metals are centered at 422 and 491 nm for Cd^{2+} and at 421 and 495 nm for Zn^{2+}. Gaussian fits revealing the individual contributions of the two transitions for each metal solution are presented in Figure 87.

In the sample solution containing zinc, the two bands have approximately the same absorbance; whereas in the spectrum of $[(bpy)_2Ru(dpp)]^{2+}$ with cadmium, the absorbance of the higher energy transition is slightly larger than the absorbance of the lower energy band.

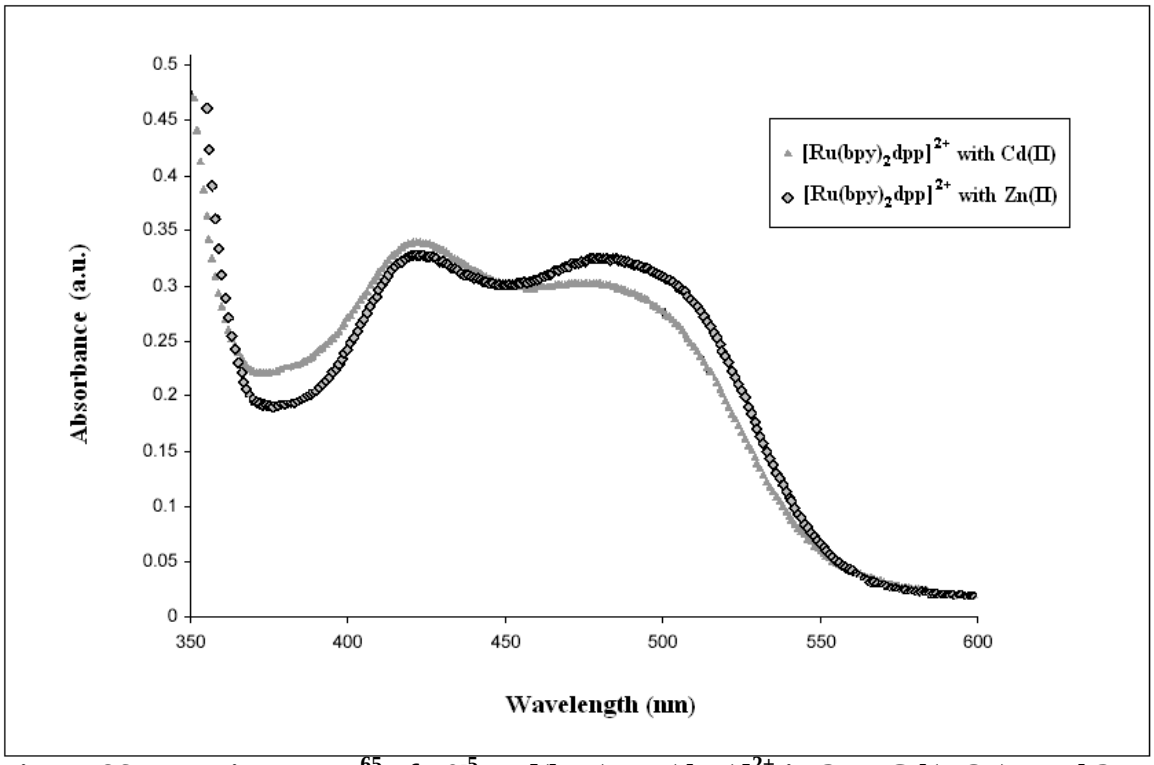

Figure 86. UV-Vis spectra[65] of 10^{-5} M $[(bpy)_2Ru(dpp)]^{2+}$ in 3 M $Cd(NO_3)_2$ and 3 M $Zn(NO_3)_2$, respectively.

The emission spectrum of $[(bpy)_2Ru(dpp)]^{2+}$ with Cd^{2+}, shown in Figure 88, consists of a broad luminescence peak centered at 760 nm and slightly skewed at longer wavelength, which can be resolved by gaussian fit into two emissions, centered at 745 nm and 816 nm, respectively.

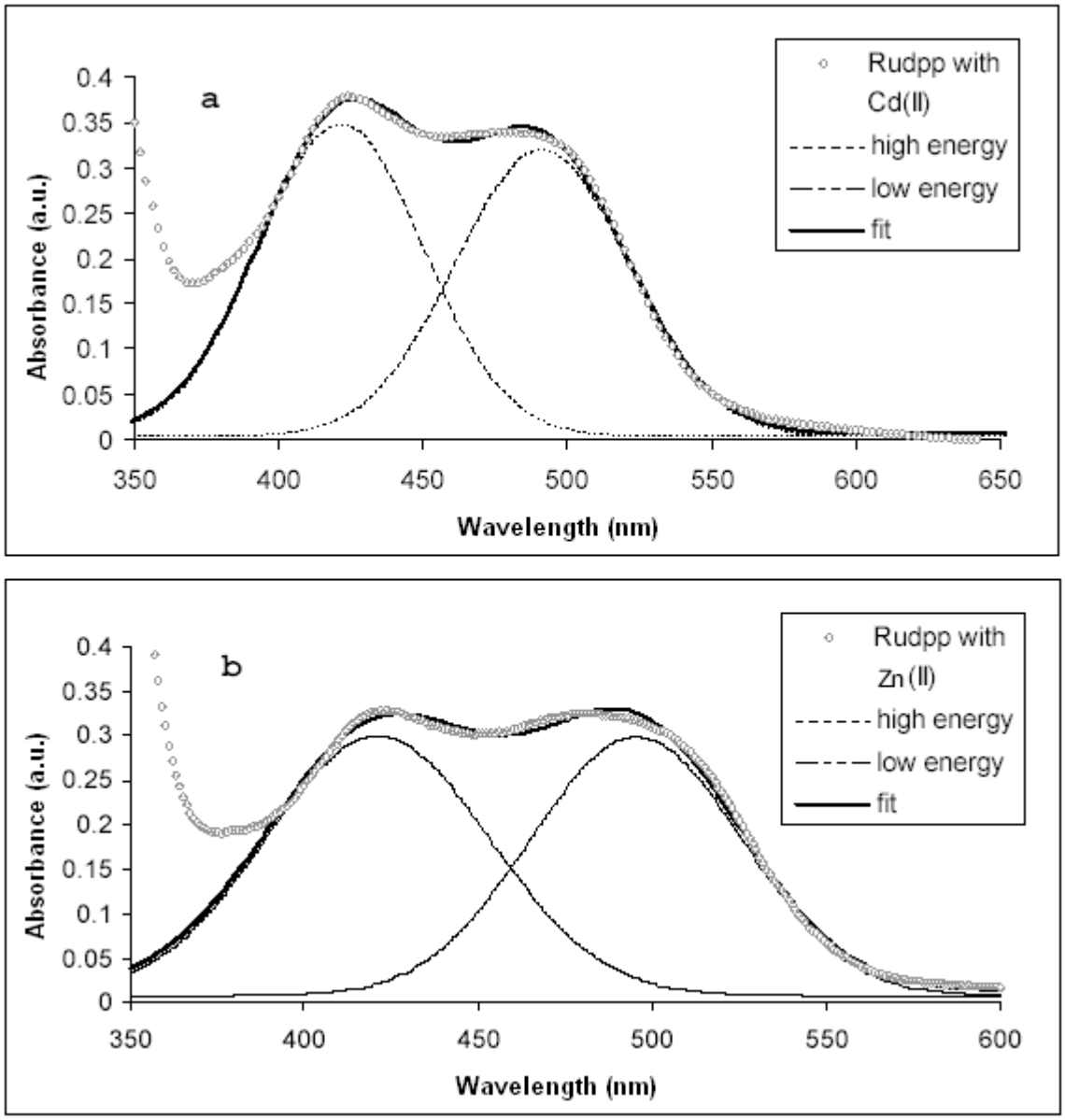

Figure 87. Gaussian fits of the MLCT Regions of the UV-Vis spectra of: a) Rudpp-Cd and b) Rudpp-Zn bimetallics[65].

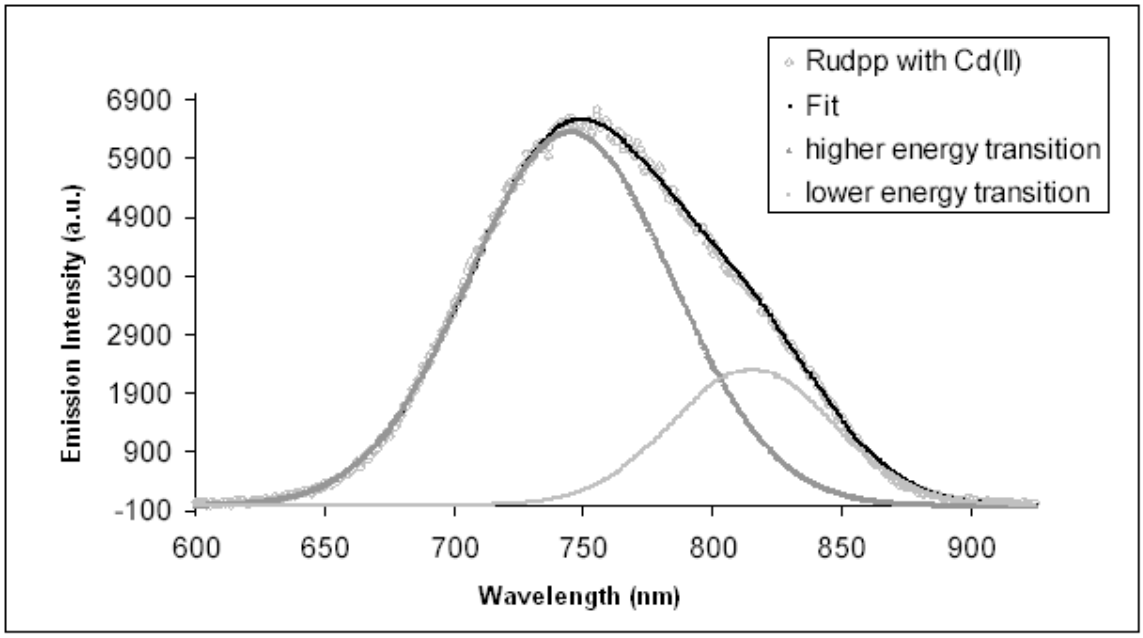

Figure 88. Emission spectrum and gaussian fits[65] of $[(bpy)_2Ru(dpp)]^{2+}$ in 3 M $Cd(NO_3)_2$.

The average lifetime of the 760-nm emission is 32 ± 3 ns. However, time-resolved data modeled assuming a double-exponential decay (Figure 89a) establish two emission lifetimes to one standard deviation of 63 ± 16 ns and 20 ± 4 ns. Since the gaussian fits to the profiles of the pre-exponential factors (Figure 89b) place the emission maximum at 760 nm for both signals, the lifetime measurement does not allow the assignment of each lifetime to a specific emission maximum. However, since at the short-wavelength edge of the emission the lifetime measured as a single-exponential is shorter than at the higher-wavelength one, it is plausible to deduce that the longer-lived emission is the one centered at 816 nm.

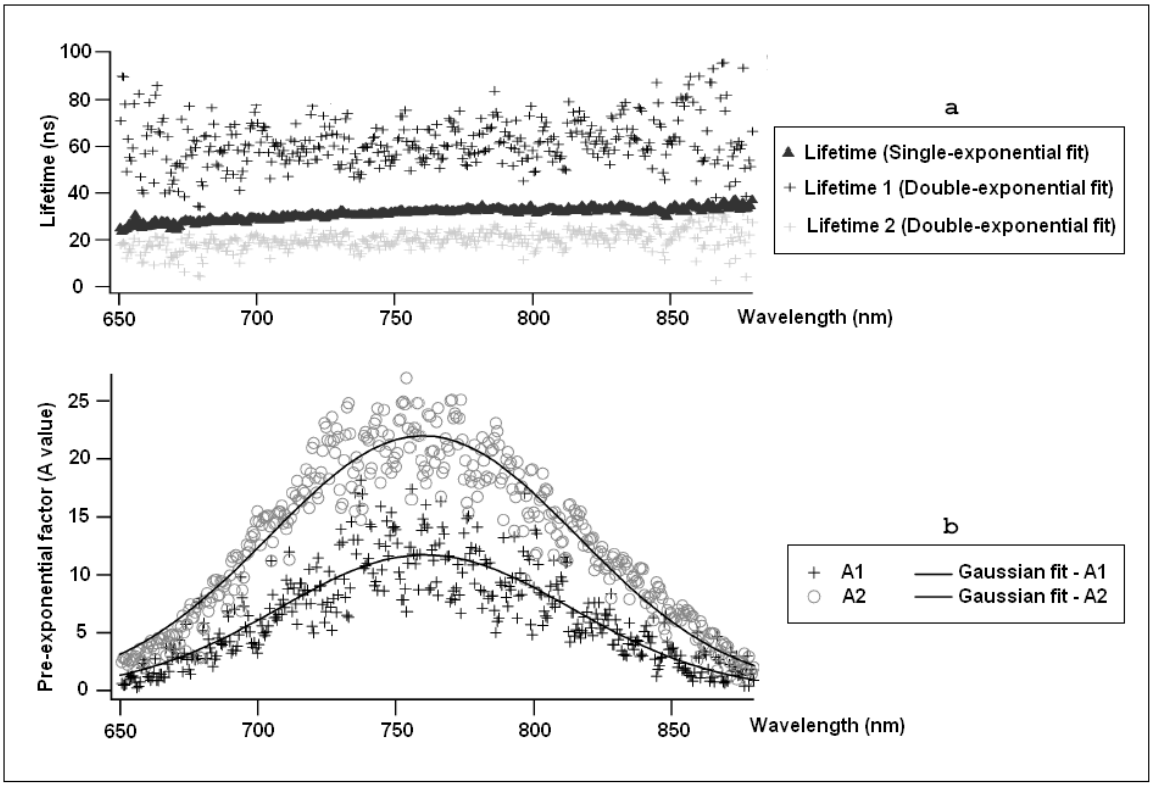

Figure 89. Single-exponential and double-exponential fits of: a) lifetimes and b) pre-exponential factors[65] of the emission of $[(bpy)_2Ru(dpp)]^{2+}$ in 3 M $Cd(NO_3)_2$.

The emission of $[(bpy)_2Ru(dpp)]^{2+}$ with Zn^{2+} parallels that with Cd^{2+}. The luminescence peak for zinc(II), Figure 90, is centered at 773 nm and is also slightly skewed at longer wavelength. The double Gaussian fit reveals two possible emissions, with maxima at 752 nm and 815 nm. The average lifetime from single exponential fits is 33 ± 1 ns, whereas from the double exponential analysis (Figure 91) the two average lifetimes over the 700 to 850-nm range are 54 ± 6 ns and 17 ± 4 ns. Again, the assignment of each lifetime to a specific emission maximum could not be made.

Results suggest that $[(bpy)_2Ru(dpp)]^{2+}$ does form emissive bimetallics with d^{10} metal cations via the imine nitrogens of the dpp ligand. The bimetallic compounds can be observed spectroscopically but are not stable enough thermodynamically to be isolated.

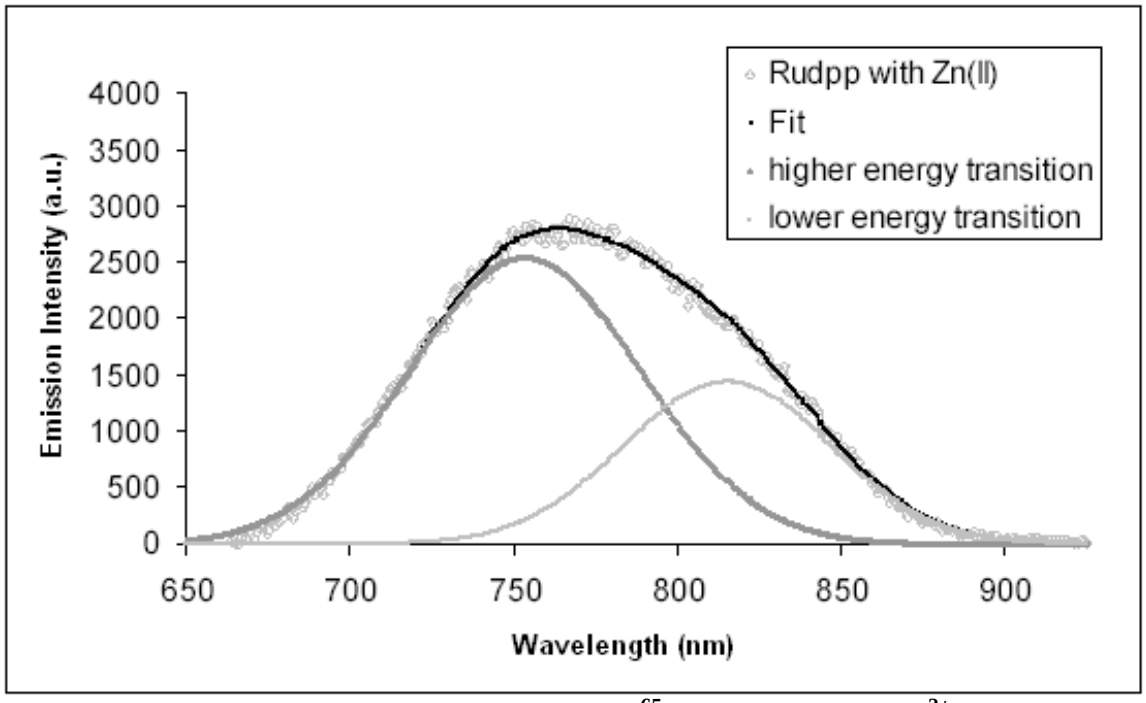

Figure 90. Emission spectrum and gaussian fits[65] of $[(bpy)_2Ru(dpp)]^{2+}$ in 3 M $Zn(NO_3)_2$.

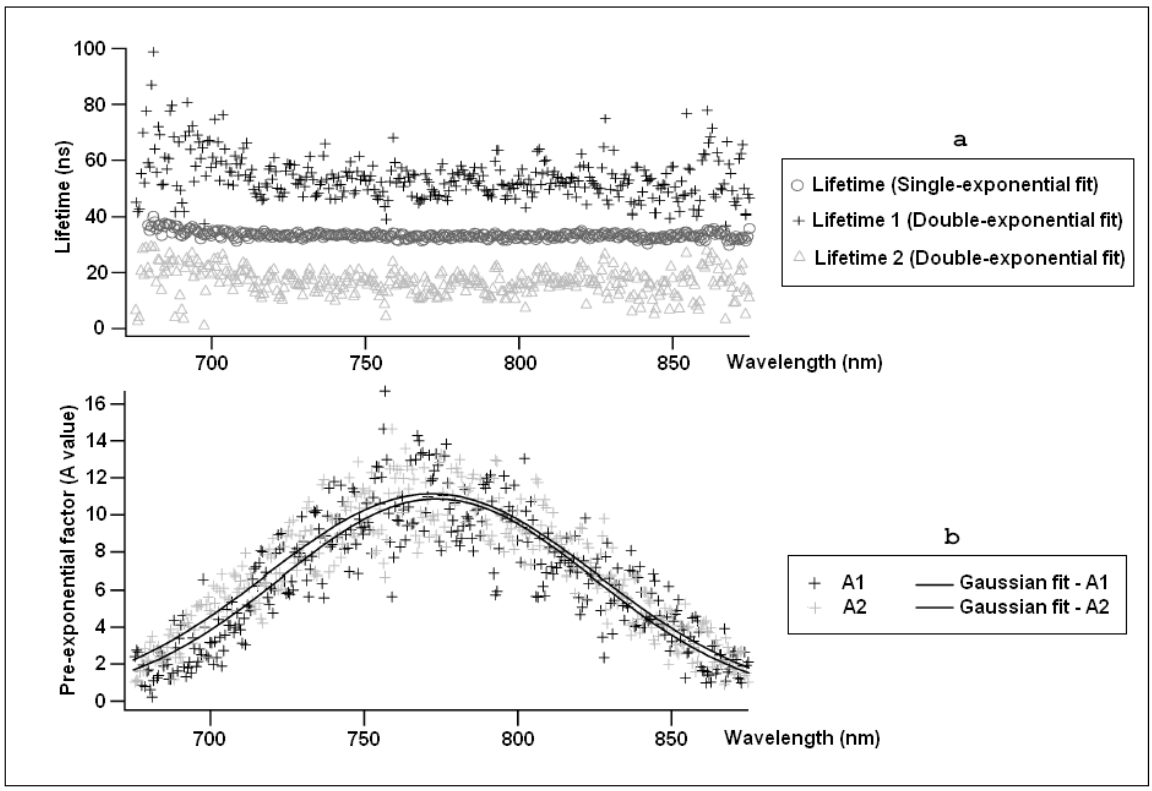

Figure 91. Single-exponential and double-exponential fits of: a) lifetimes and b) pre-exponential factors[65] of the emission of $[(bpy)_2Ru(dpp)]^{2+}$ in 3 M $Zn(NO_3)_2$.

3.C.1.a. Ground-State Titration

The absorption spectra from the UV-Vis titration of 3.17 x 10^{-5} M $[(bpy)_2Ru(dpp)]^{2+}$ with increasing concentration of cadmium ions is shown in Figure 92. One isosbestic point is observed at 491 nm. The values of absorbance monitored at the wavelength that exhibited maximum change, 520 nm, were plotted as a function of $[Cd^{2+}]$ (Figure 93) and the equilibrium constant for association obtained from fitting the data to equation (97) is 9 ± 2 M^{-1}.

The ground-state titration of $[(bpy)_2Ru(dpp)]^{2+}$ with zinc gives analogous results (Figure 94 and 95). The isosbestic point is also observed at 491 nm and the fit of absorbance values at 520 nm versus $[Zn^{2+}]$ yields an equilibrium constant of 15 ± 3 M^{-1}.

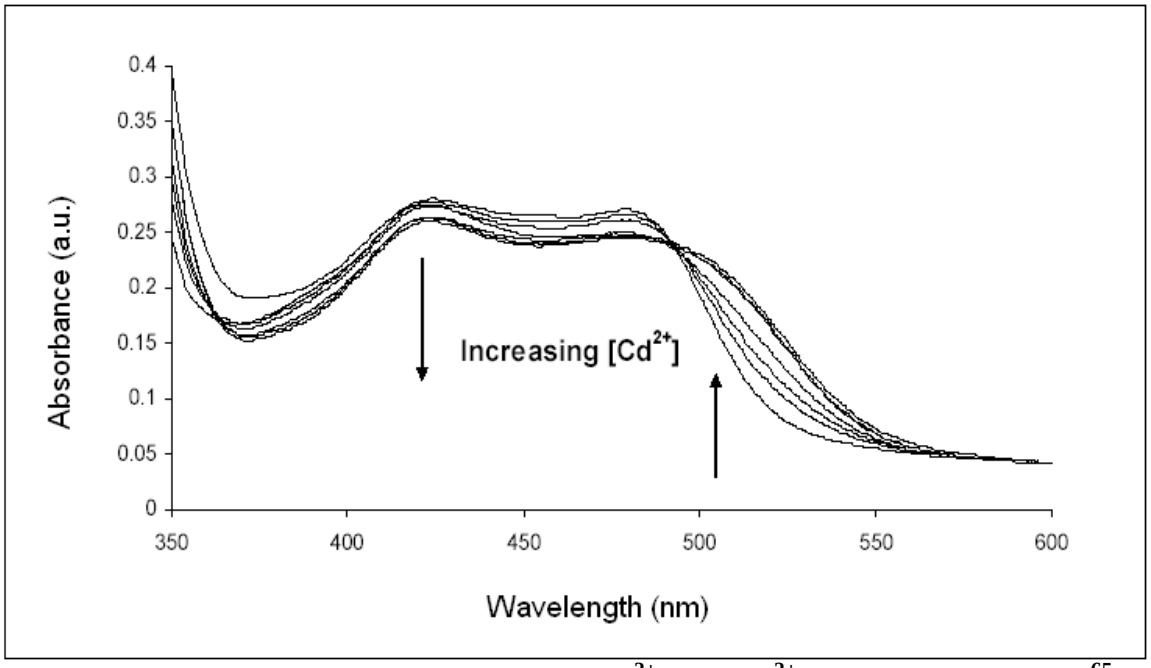

Figure 92. UV-Vis titration of $[(bpy)_2Ru(dpp)]^{2+}$ with Cd^{2+} at room temperature[65].

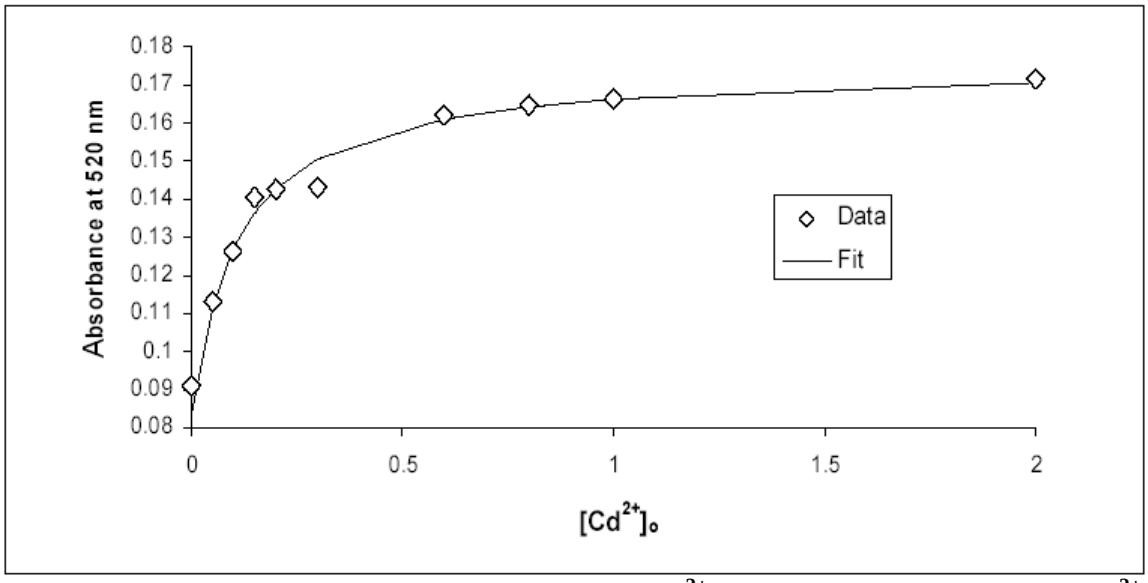

Figure 93. UV-Vis absorbance of $[(bpy)_2Ru(dpp)]^{2+}$ solutions with increasing $[Cd^{2+}]$ monitored at 520 nm at room temperature[65].

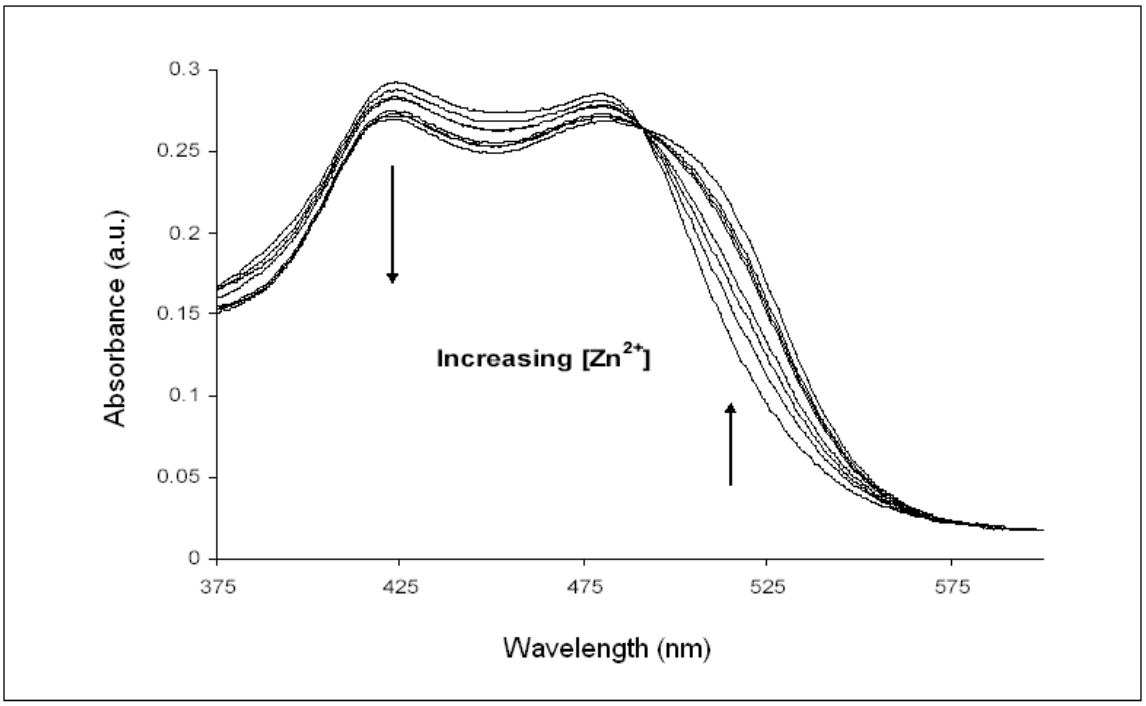

Figure 94. UV-Vis titration of $[(bpy)_2Ru(dpp)]^{2+}$ with Zn^{2+} at room temperature[65].

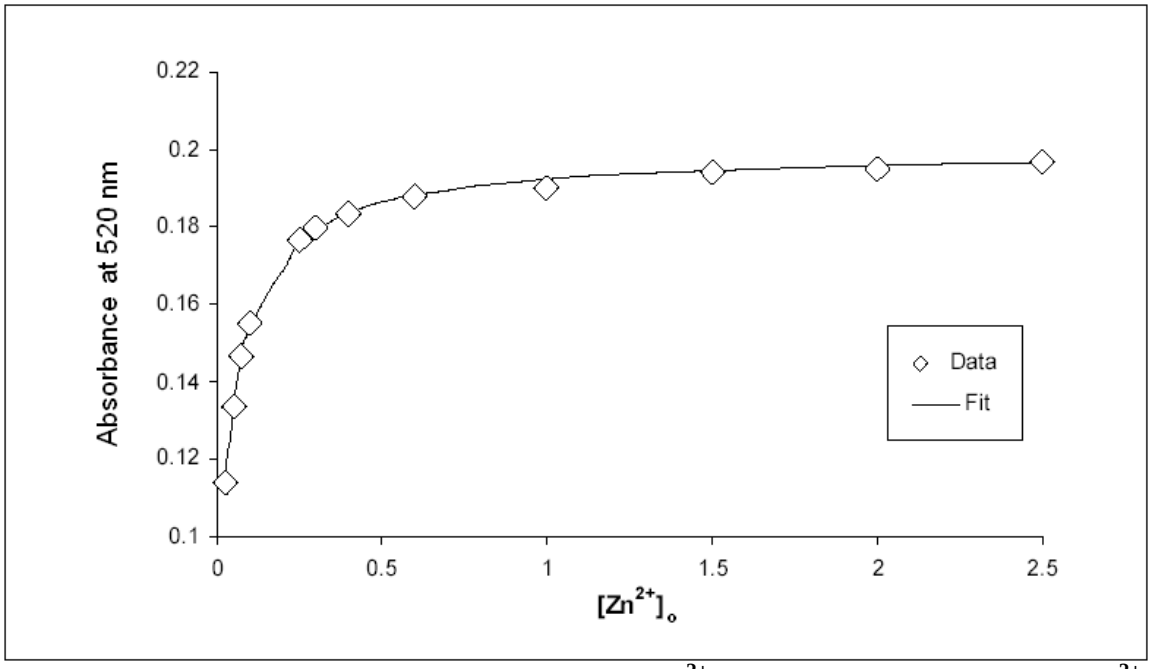

Figure 95. UV-Vis absorbance of $[(bpy)_2Ru(dpp)]^{2+}$ solutions with increasing $[Zn^{2+}]$ monitored at 520 nm at room temperature[65].

The ground state titration of $[(bpy)_2Ru(dpp)]^{2+}$ with Cd^{2+} and Zn^{2+} was also performed using ^{1}H-NMR spectroscopy. Figures 96 and 98 show how the NMR spectrum of $[(bpy)_2Ru(dpp)]^{2+}$ changes when the complex interacts with either of the d^{10} metals. Both titrations displayed similar chemical shift changes in direction and magnitude, involving protons occupying the same relative positions. For instance, in both cases, the protons belonging to the bpy rings (rings D, E, F, G in Figure 97) remain mostly unaffected while the A5 proton associated with the pyrazyl ring shifts downfield at high metal concentrations. The protons on the dpp ligand shift downfield, however not all by the same amount. The nuclei changing the most are B3' and C6". Other downfield shifts are seen in C5", C3", B5' and B4'.

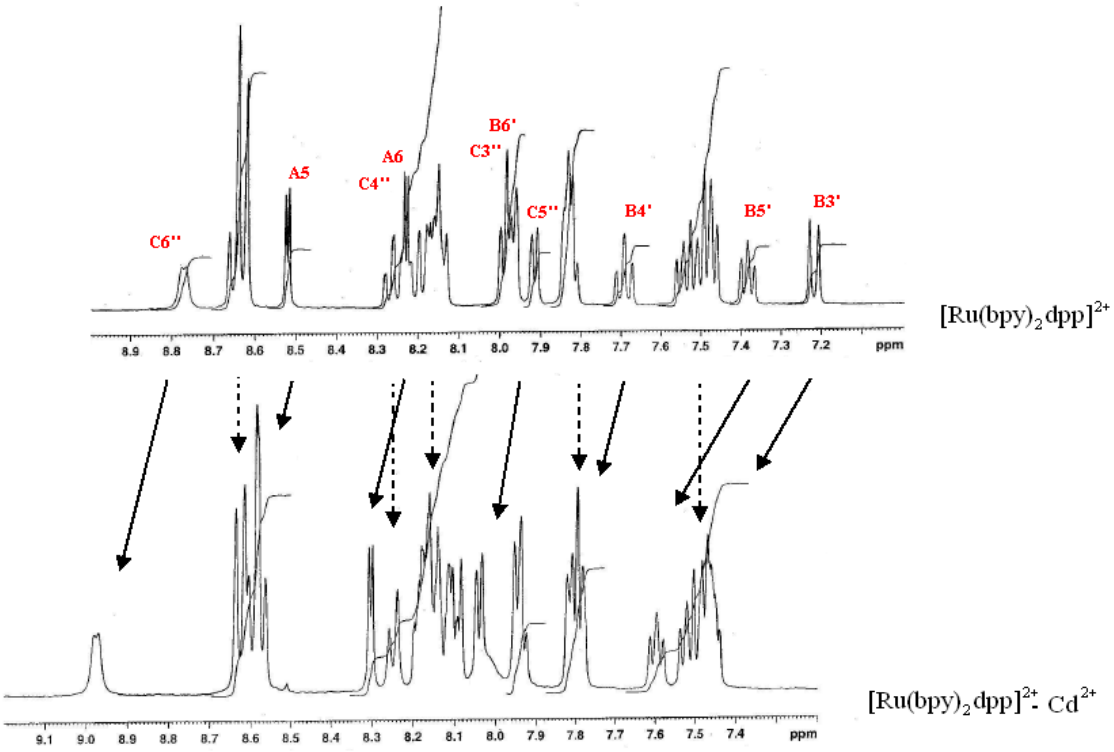

Figure 96. NMR shifts[65] upon coordination to Cd(II). Top NMR shows $[(bpy)_2Ru(dpp)]^{2+}$ alone. Bottom spectrum is for $[(bpy)_2Ru(dpp)]^{2+}$ and 2 M Cd^{2+}.

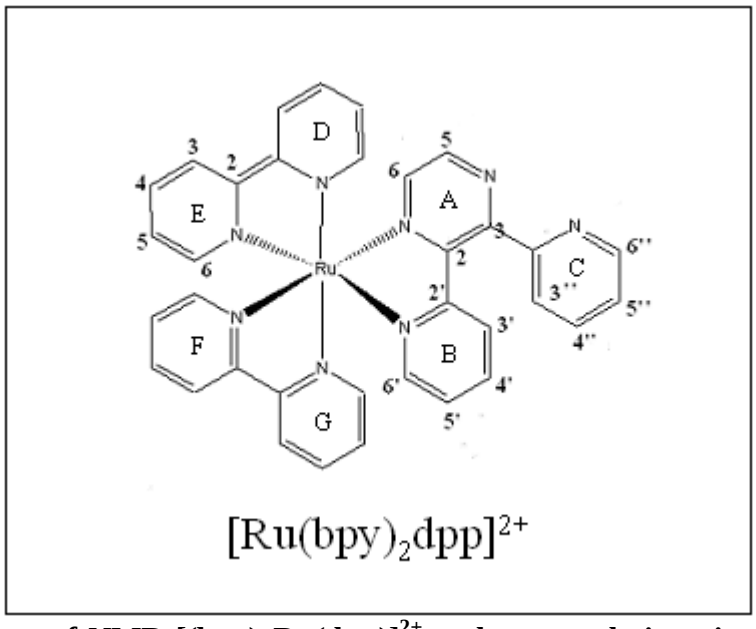

Figure 97. Structure of NMR $[(bpy)_2Ru(dpp)]^{2+}$ and proton designation as used in the discussion of related NMR spectra.

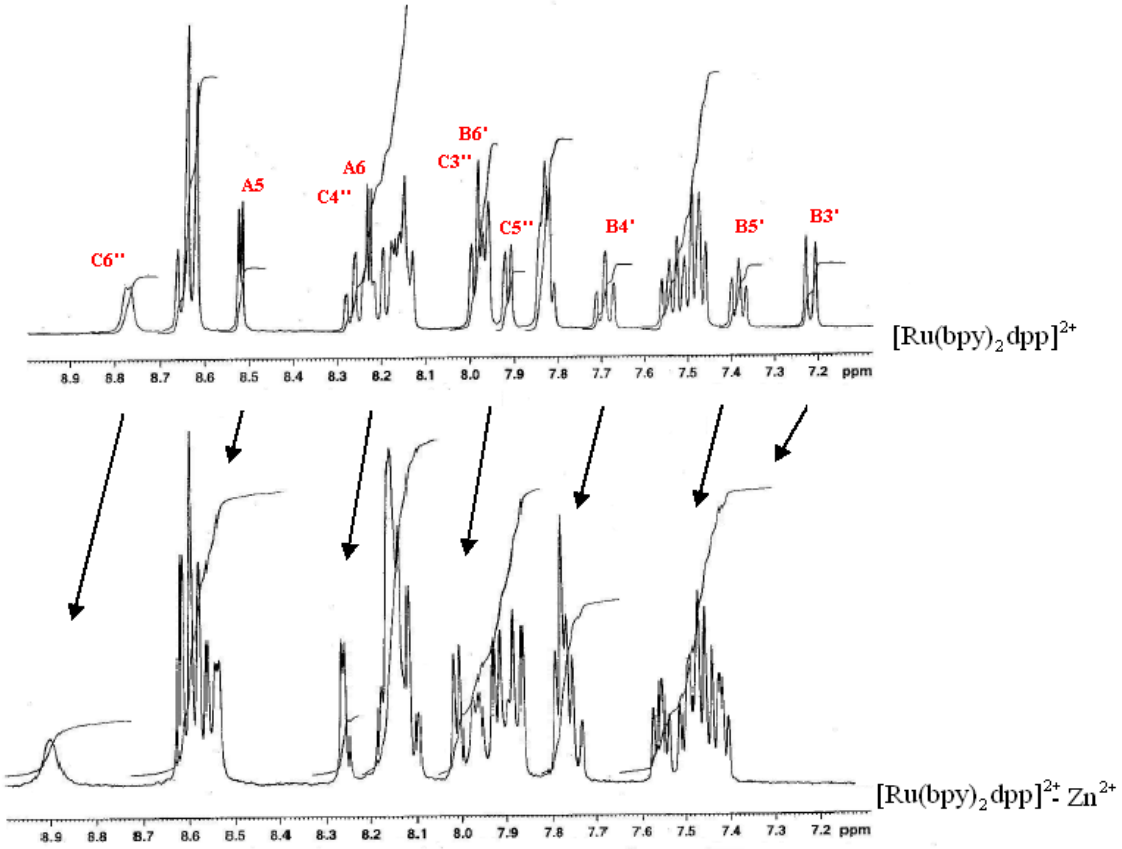

Figure 98. NMR shifts[65] upon coordination to Zn(II). Top: NMR of $[(bpy)_2Ru(dpp)]^{2+}$ and 0 M Zn^{2+}. Bottom: spectrum of $[(bpy)_2Ru(dpp)]^{2+}$ in 1.33 M Zn^{2+} solution.

Plots of the change in chemical shift versus the concentration of the d^{10} metal added yield very different values for the equilibrium constant if compared with the values obtained from the UV-Vis titration. The protons monitored for the Cd^{2+} titration are C6" and B3", chosen because they are easily identified in the complicated NMR. Their plots of change in chemical shift reach a limiting value and yield sigmoidal curves (Figure 99) that cannot be fit with equation (97). The two data sets normalized for percent change are nearly coincident with an equilibrium constant for association of about 1 M^{-1}.

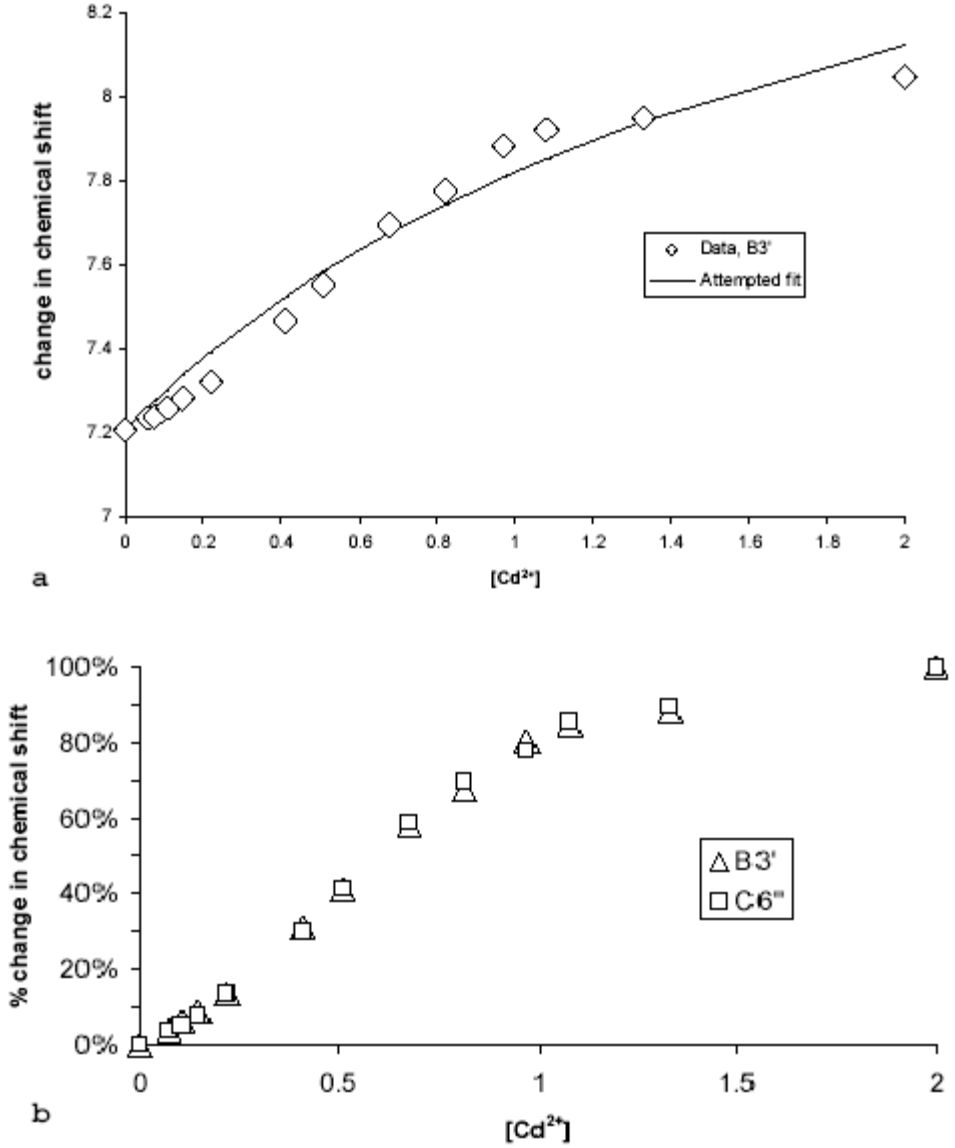

Figure 99. Change in chemical shifts[65] for proton B3' and C6'' upon coordination of Cd^{2+} to $[(bpy)_2Ru(dpp)]^{2+}$.

The same is observed for the Zn^{2+} titration: the plots of change in chemical shift for C6" and B3" yield a sigmoidal curve (Figure 100), with equilibrium constant for association of about 1 M^{-1}. Fits to equation (97) do not match the data.

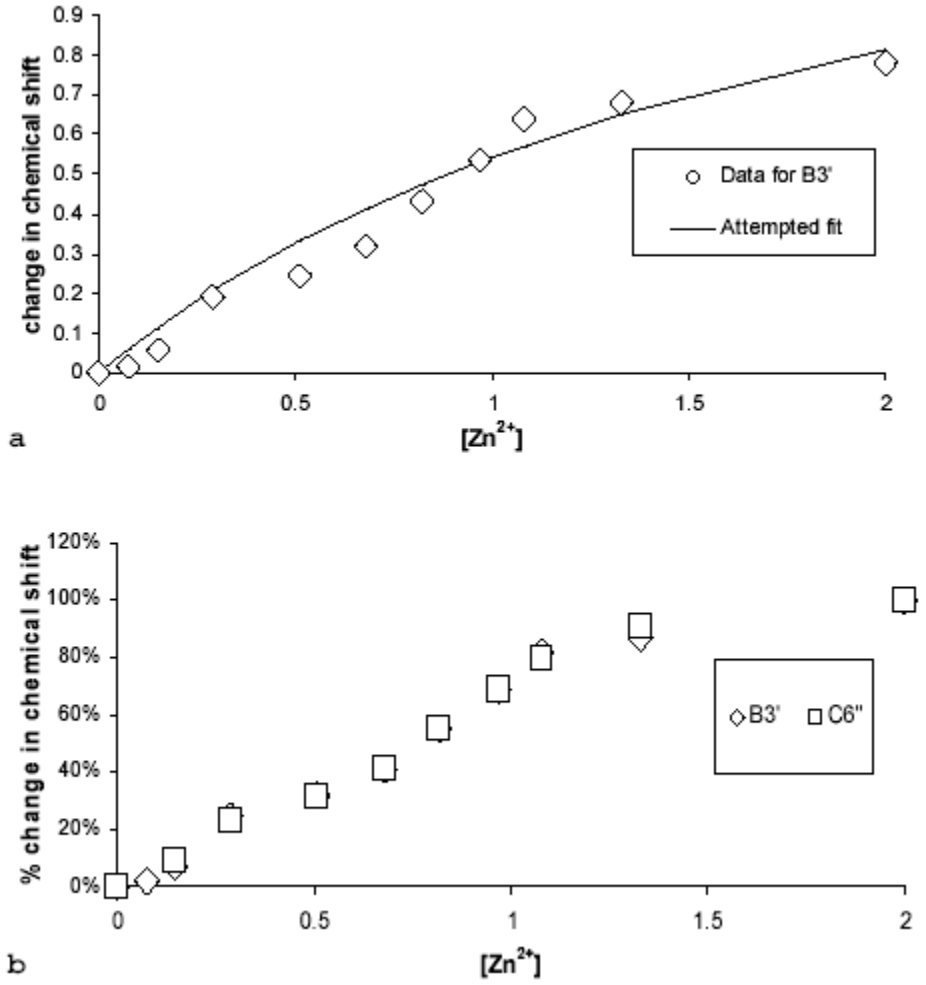

Figure 100. Change in chemical shifts[65] for proton B3' and C6'' upon coordination of Zn^{2+} to $[(bpy)_2Ru(dpp)]^{2+}$.

3.C.1.b. Excited-State Titration

The steady-state emission spectra of $[(bpy)_2Ru(dpp)]^{2+}$ at increasing concentrations of Cd^{2+} are shown in Figure 101. The emission intensity decreases sharply in the concentration range from 0 to 1 M, and the peak maximum shifts to the red. Further increases in the cadmium ion do not result in further quenching.

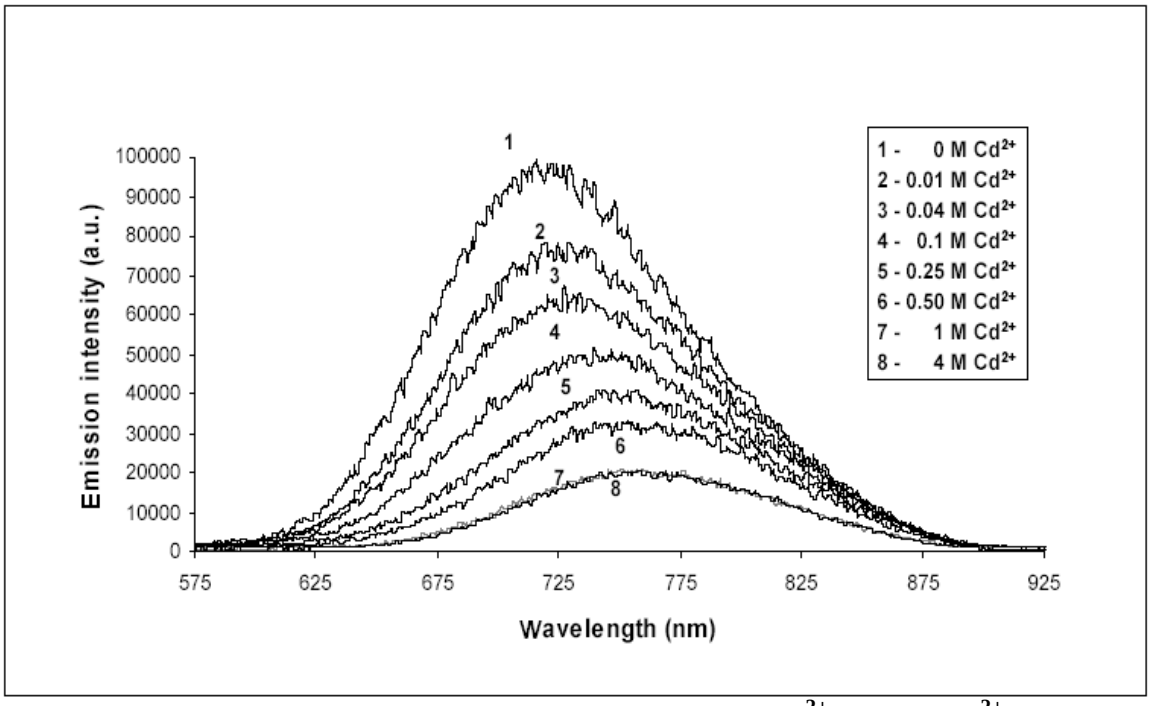

Figure 101. Luminescence titration of $[(bpy)_2Ru(dpp)]^{2+}$ with $[Cd^{2+}]$ at room temperature[65].

In the spectral region between 630- and 800-nm, the values of emission intensity monitored at a fixed wavelength and plotted as a function of $p[Cd^{2+}]$ reveal sigmoidal curves that can be fitted mathematically with Boltzmann equation. The example in Figure 102 shows the plot obtained using 650-nm monitoring wavelength. In the spectral region

where contributions from the rising emission are minimal, the 630- to 650-nm range, the titration curves show an inflection point at $p[Cd^{2+}] = 1.42 \pm 0.05$ which translates into an excited state equilibrium constant for association, K^*, of 26 ± 3 M^{-1}, assuming the lifetime of the two emitting species is comparable. At higher monitoring wavelength, the inflection point of the titration curve decreased steadily in value and appeared at higher initial metal concentrations (Figure 103).

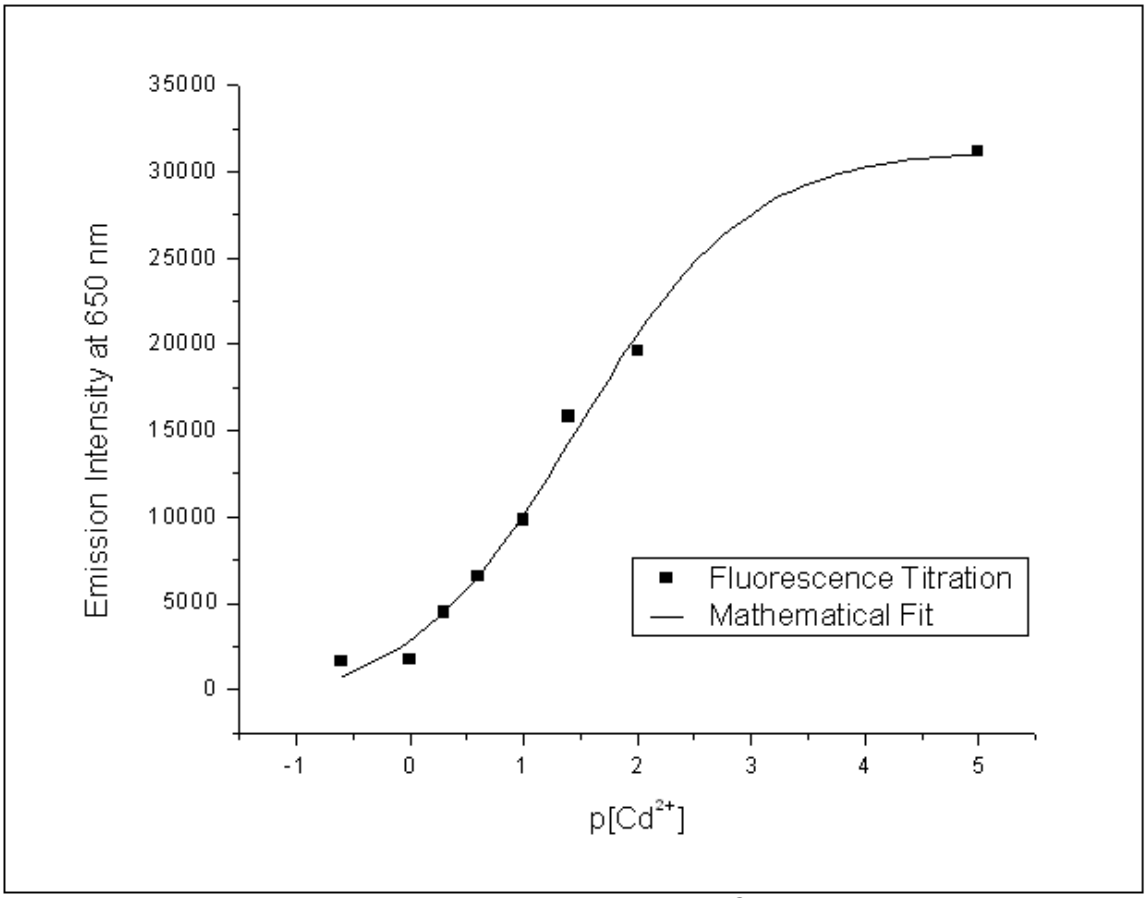

Figure 102. Emission intensities of $[(bpy)_2Ru(dpp)]^{2+}$ monitored at 650 nm and reported as a function of $-\log[Cd^{2+}]$.

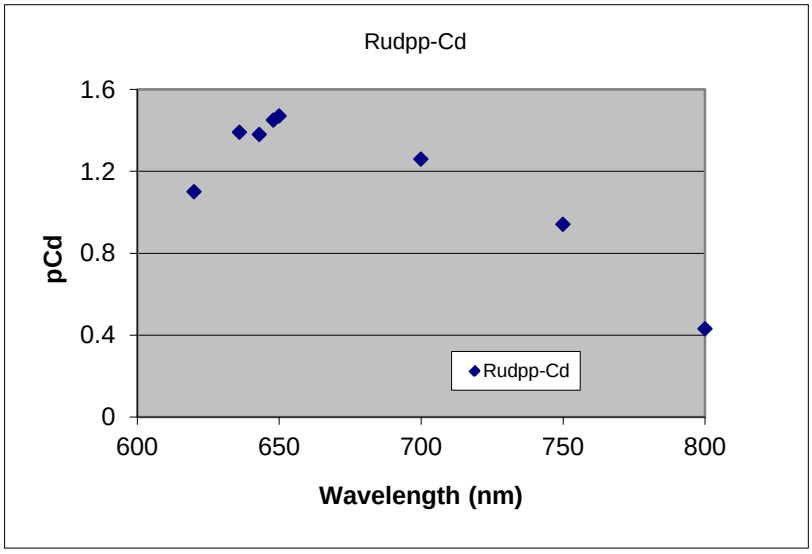

Figure 103. Inflection point of sigmoidal titration curves of $[(bpy)_2Ru(dpp)]^{2+}$ with $[Cd^{2+}]$ as a function of monitoring wavelength.

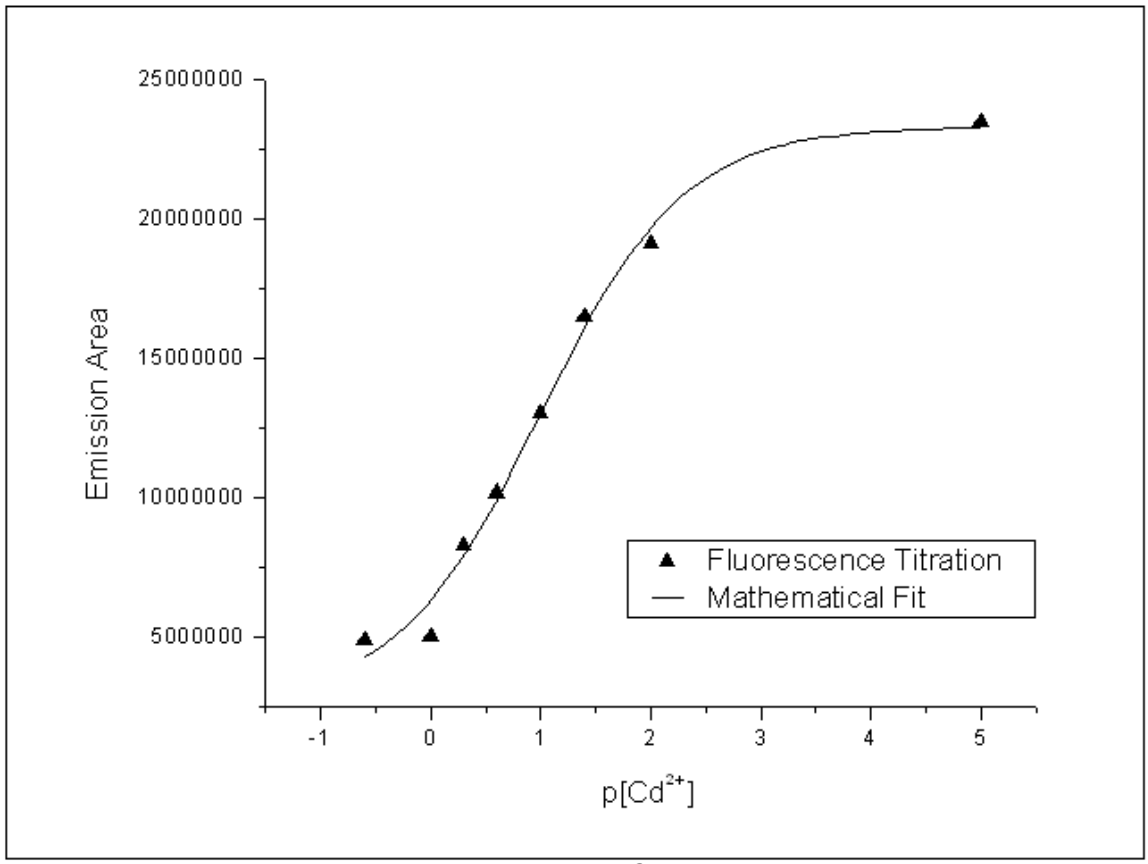

Figure 104. Emission area of $[(bpy)_2Ru(dpp)]^{2+}$ as a function of the negative log of $[Cd^{2+}]$.

The graph in Figure 104, obtained by plotting the areas under the emission curves versus p[Cd^{2+}] and thus including the contribution of the new emission, had an inflection point at p[Cd^{2+}] = 0.99 ± 0.02 which corresponds to a constant K^* of 9.8 ± 0.4 M^{-1}.

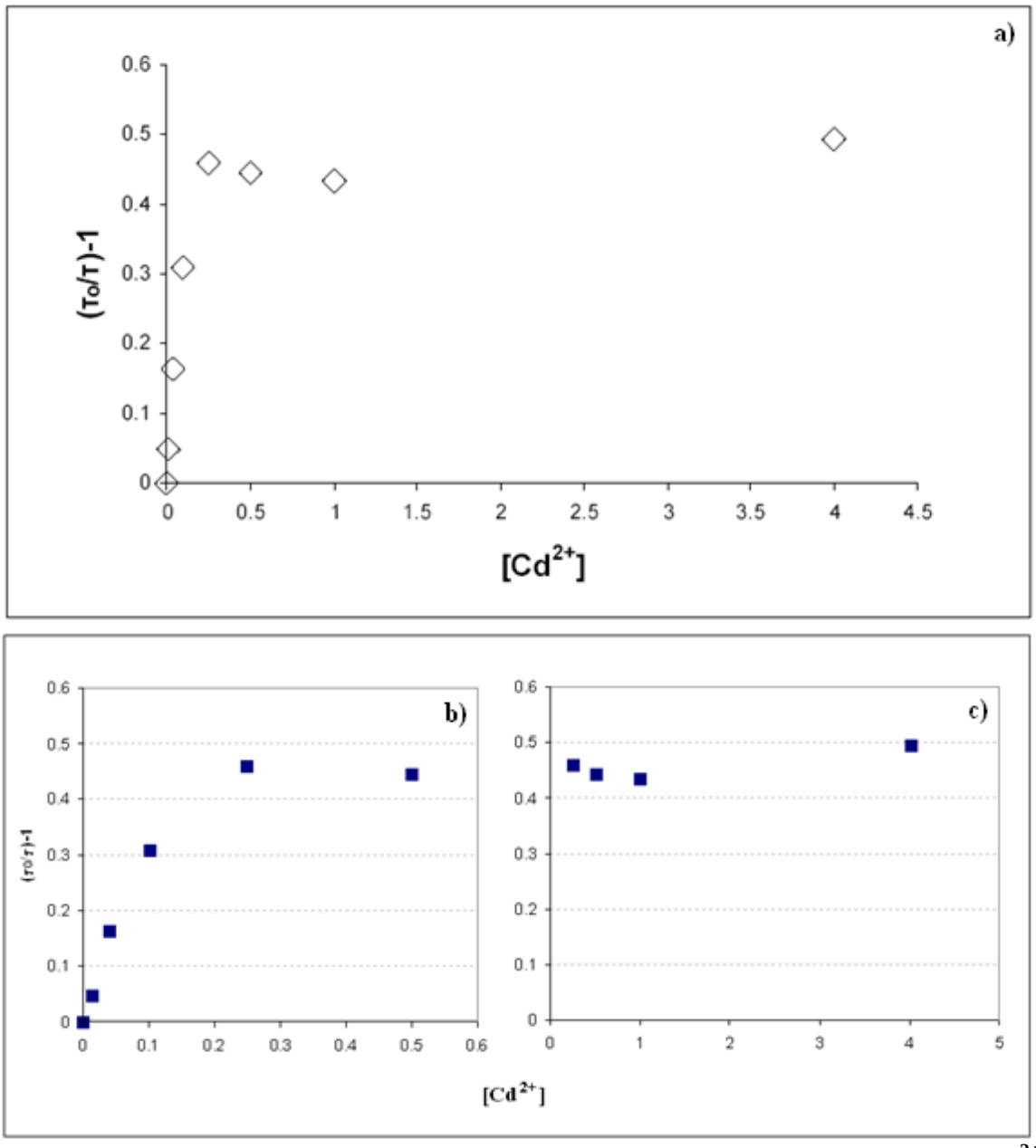

Figure 105. Stern-Volmer plots for the cadmium(II) titration of $[(bpy)_2Ru(dpp)]^{2+}$ over the full range of $[Cd^{2+}]$ concentration, 0.5 to 5M (a), and expanded plots of initial (b) and higher (c) cadmium concentrations.

The increased concentration of divalent cadmium ions has also the effect of quenching the lifetime of the $[(bpy)_2Ru(dpp)]^{2+}$ emission. The Stern-Volmer plot of the changing lifetime of the 700-nm emission, a plot of $[(\tau_o/\tau) - 1]$ vs. concentration (Figure 105), has two distinct regions: an initial portion with a linear dependence of the two variables and plateau at higher concentrations of Cd^{2+}. The Stern-Volmer plot of the changing emission intensity data monitored at 650 nm, a plot of $[(I_o/I) - 1]$ vs. concentration (Figure 106), shows a similar trend with negative deviations from linearity at higher $[Cd^{2+}]$, which will be discussed in further detail in the next chapter. The Stern-Volmer constants derived from the linear portion of the lifetime and intensity plots are K_{SV} (τ) = 3.24 ± 0.097 and K_{SV} (I) = 8.39 ± 0.10, respectively (Figure 107). Based on the Stern-Volmer data, approximately 39% of quenching occurs via a dynamic process.

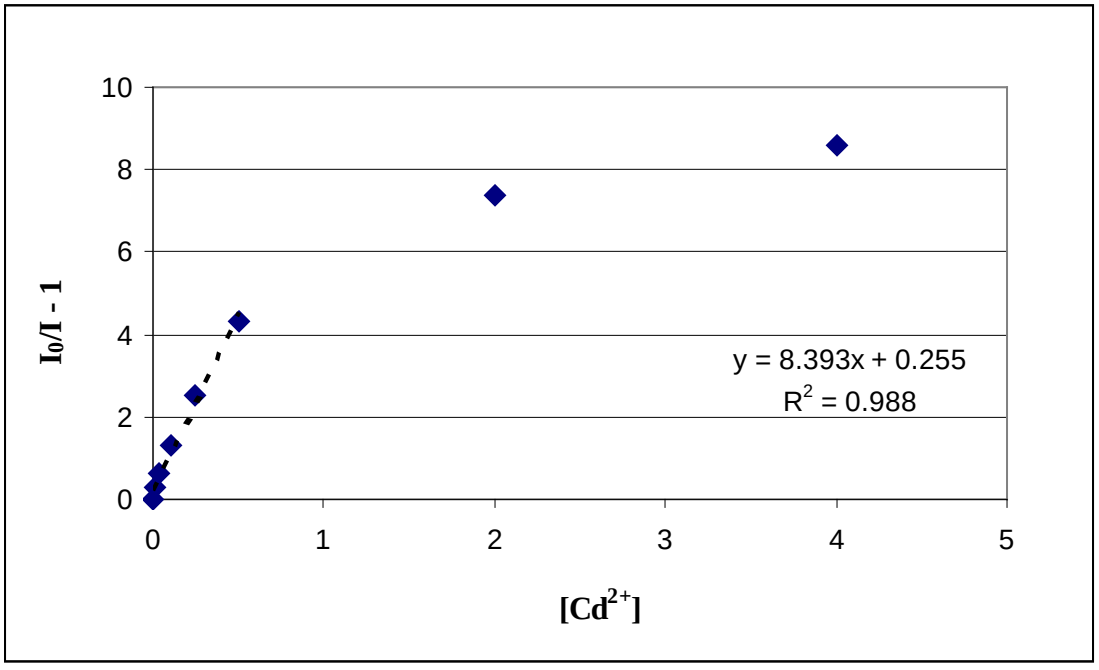

Figure 106. Stern-Volmer plot of emission intensity data for the cadmium(II) titration of $[(bpy)_2Ru(dpp)]^{2+}$. The initial portion of the plot has a linear trend (K_{SV} = 8.39).

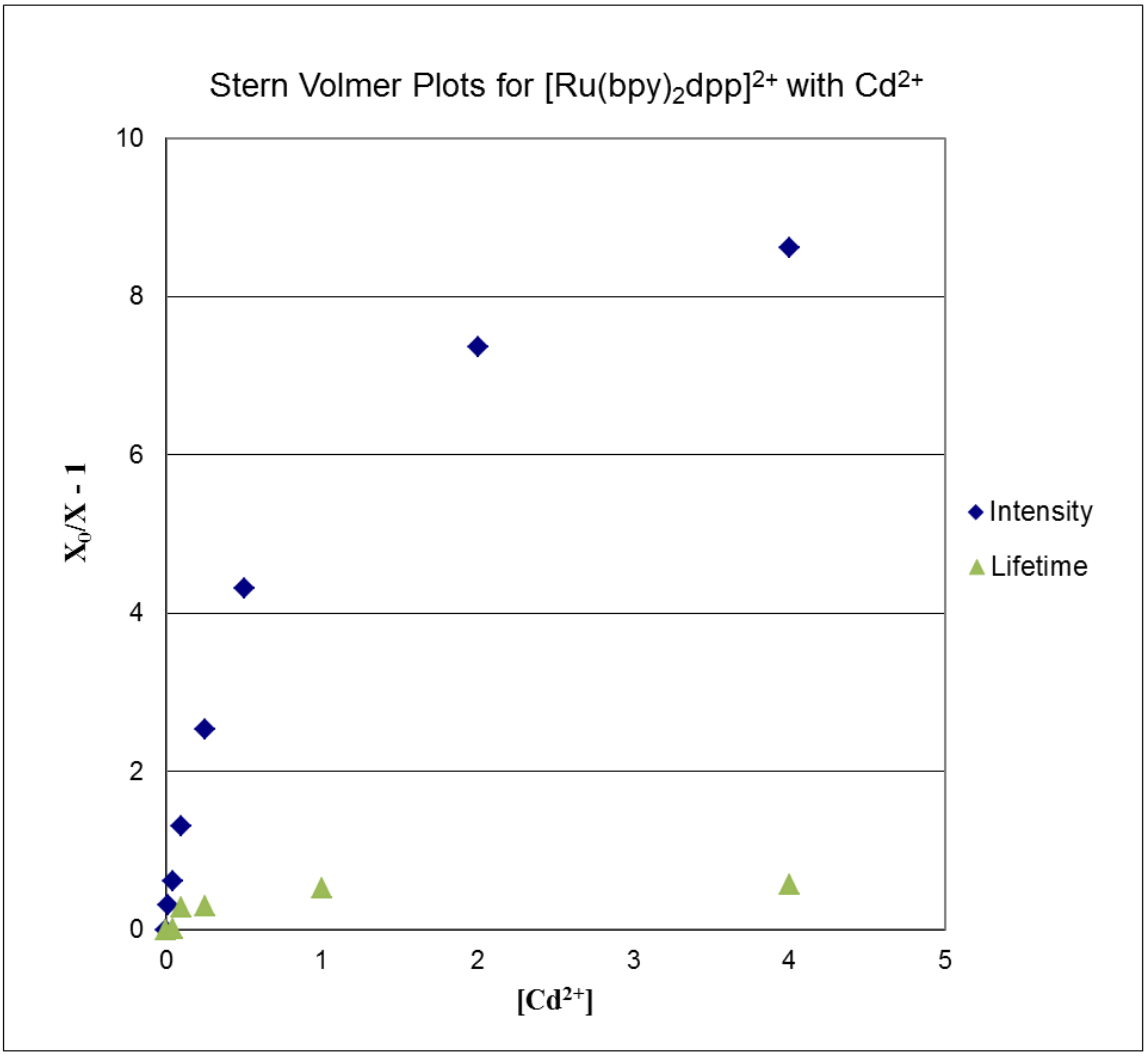

Figure 107. Comparison of the Stern-Volmer plots of emission intensity and lifetime data for the cadmium(II) titration of $[(bpy)_2Ru(dpp)]^{2+}$.

The Stern-Volmer plot constructed using the areas under the curve falls in between the traces obtained using lifetime and intensity data, with K_{SV} (A) = 4.86 ± 0.27 (Figure 108). The beginning part of the areas Stern-Volmer plot has the same K_{sv} value as the intensity plot. Ultimately, however, all three curves diverge.

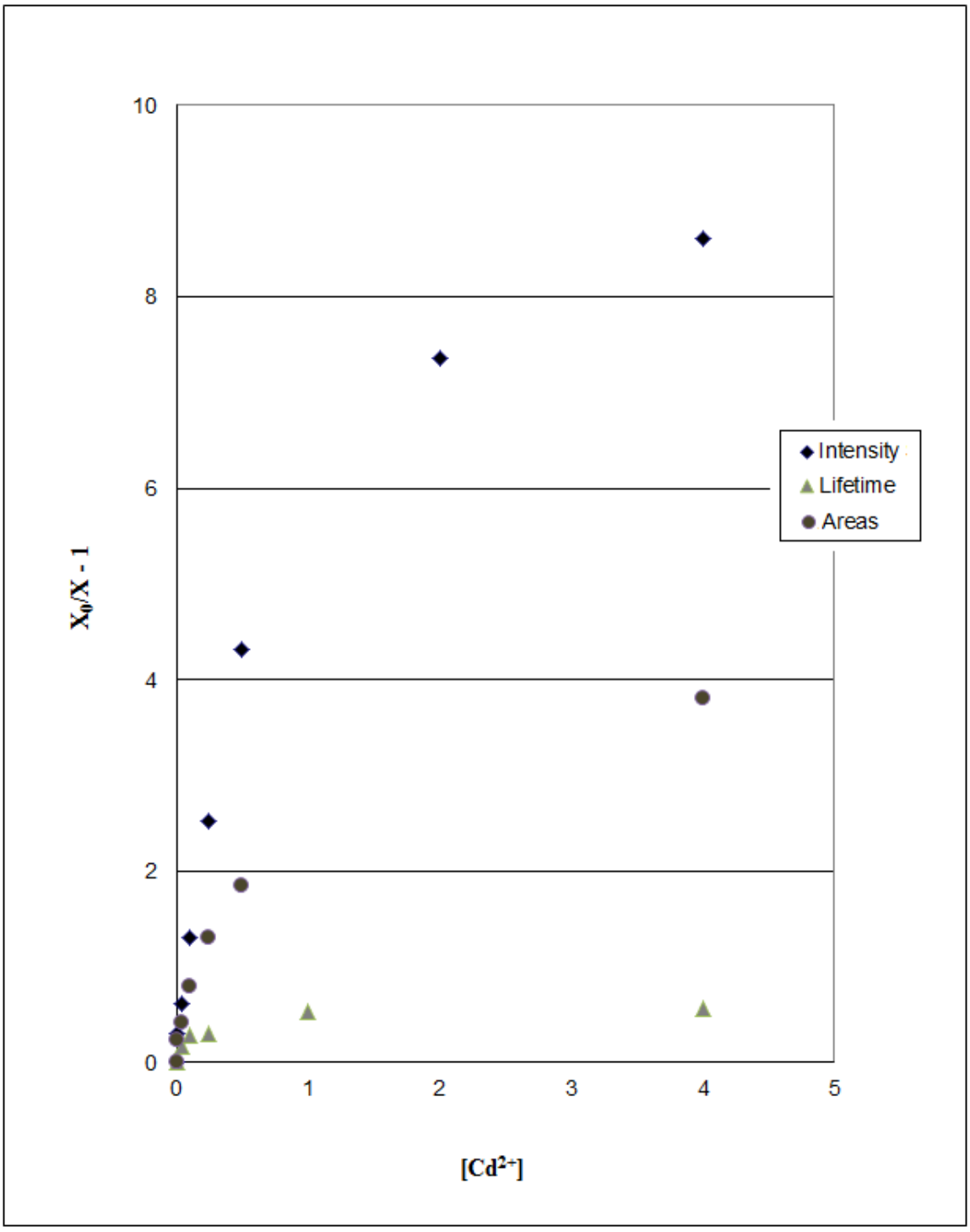

Figure 108. Comparison of the Stern-Volmer plots of emission intensity data, lifetimes and areas under the curve for the cadmium(II) titration of $[(bpy)_2Ru(dpp)]^{2+}$.

The steady-state emission spectra of $[(bpy)_2Ru(dpp)]^{2+}$ at increasing concentrations of Zn^{2+} are shown in Figure 109. Much like in the cadmium experiment, the emission intensity decreases sharply in the concentration range from 0 to 1 M, and the peak maximum shifts to the red.

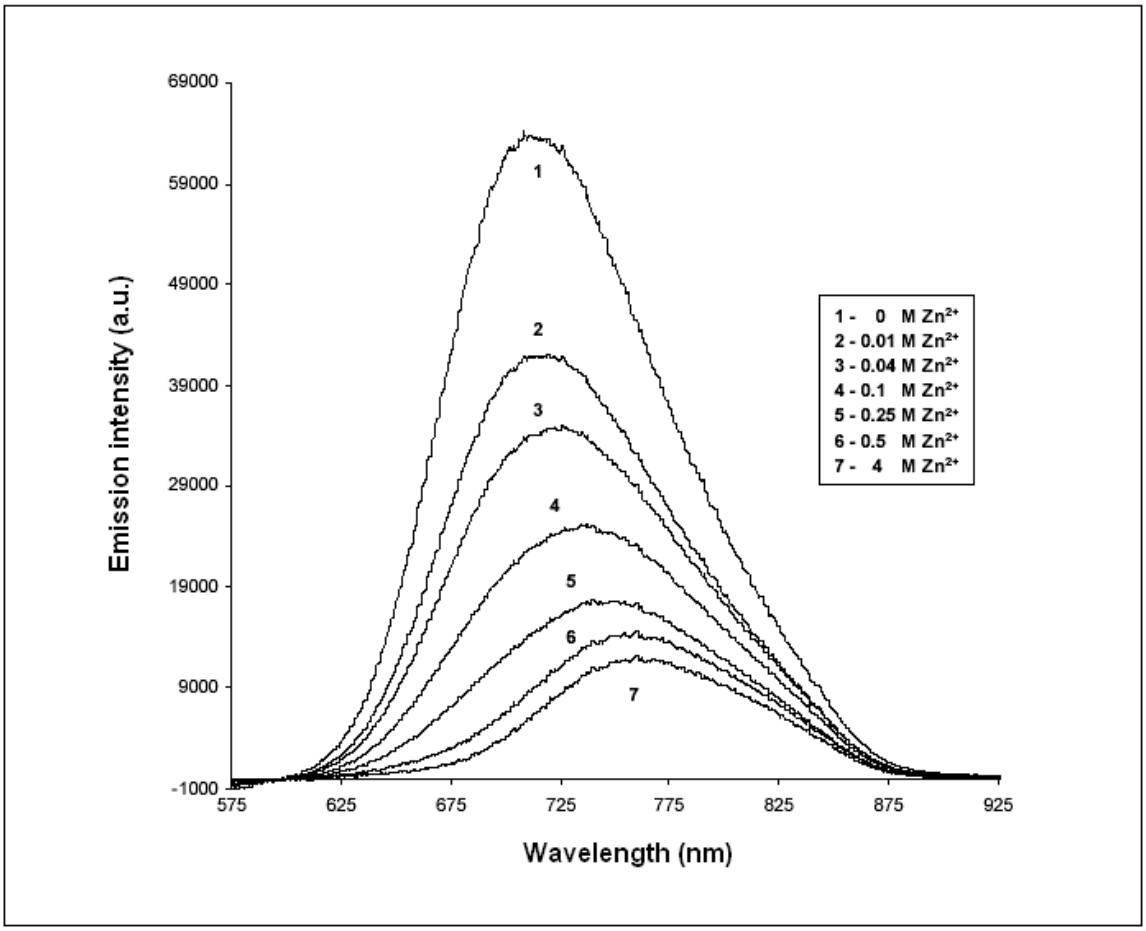

Figure 109. Luminescence titration of $[(bpy)_2Ru(dpp)]^{2+}$ with $[Zn^{2+}]$ at room temperature[65].

The titration curves obtained with monitoring wavelength in the spectral region where contributions from the rising emission are minimal are sigmoidal in shape (Figure 111) and can be fitted mathematically with Boltzmann equation. In the 620- to 680-nm range, all curves show an inflection point at $p[Zn^{2+}] = 1.48 \pm 0.02$ ($K^* = 30 \pm 1\ M^{-1}$). At

higher monitoring wavelengths, the inflection point decreases (Figure 110). The inflection point of the curve obtained by plotting the emission areas instead of the intensities (Figure 112) is also lower, at $p[Zn^{2+}] = 1.44 \pm 0.02$ which corresponds to into an excited state equilibrium constant for association, K^*, of 28 ± 1 M^{-1}, within experimental error of the intensity plot.

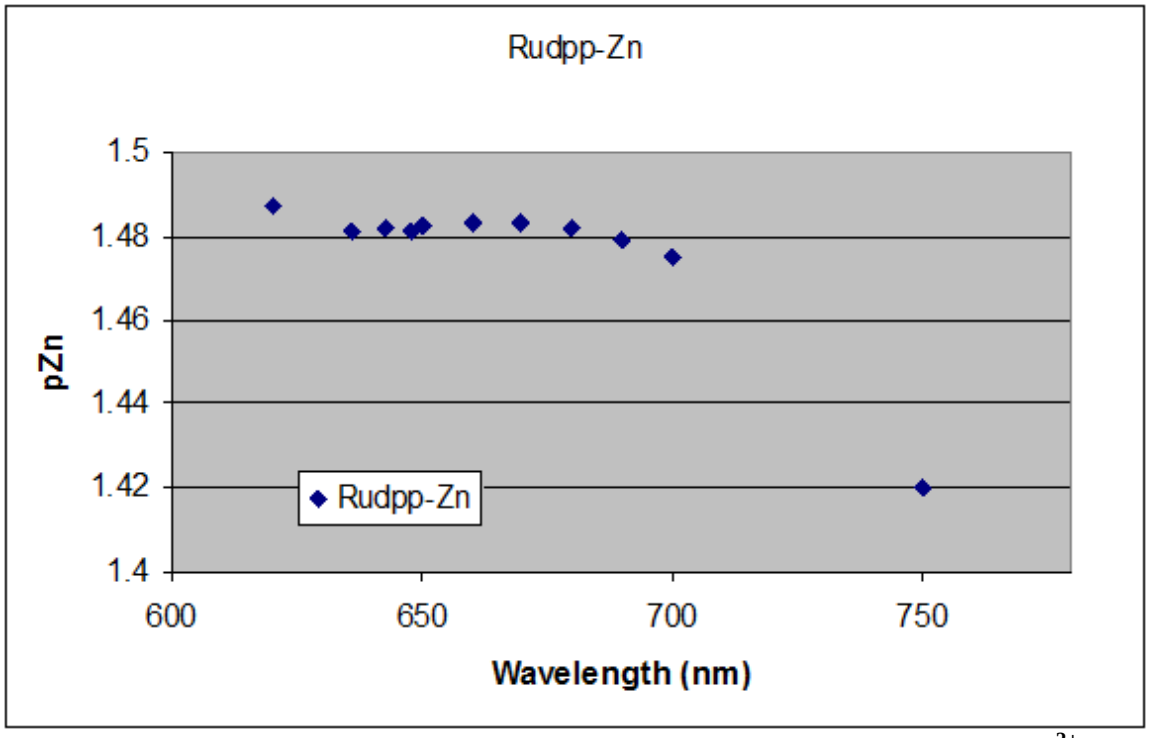

Figure 110. Inflection point of sigmoidal titration curves of $[(bpy)_2Ru(dpp)]^{2+}$ with $[Zn^{2+}]$ as a function of monitoring wavelength.

The lifetime of the $[(bpy)_2Ru(dpp)]^{2+}$ emission decreases at increasing concentrations of Zn^{2+} ions and reaches a limiting value of 54 ± 15 ns. The Stern-Volmer plot of the lifetimes, a plot of $[(\tau_o/\tau) - 1]$ vs. concentration (Figure 113), shows the same negative deviation seen in the titration with cadmium. The Stern-Volmer plot of the

changing emission intensity data monitored at 650 nm (Figure 114), also shows a similar trend with negative deviations from linearity at higher [Zn^{2+}]. The Stern-Volmer constants derived from the linear portion of the lifetime and intensity plots are K_{SV} (τ) = 5.93 ± 0.24 and K_{SV} (I) = 9.30 ± 0.32, respectively. The values suggest that more than half of the quenching (~ 64%) occurs by a dynamic process. In Figure 115, it can be seen that the Stern-Volmer plot obtained using the areas under the curve is almost identical to the one obtained using the emission intensities with K_{SV} (A) = 8.57 ± 0.36.

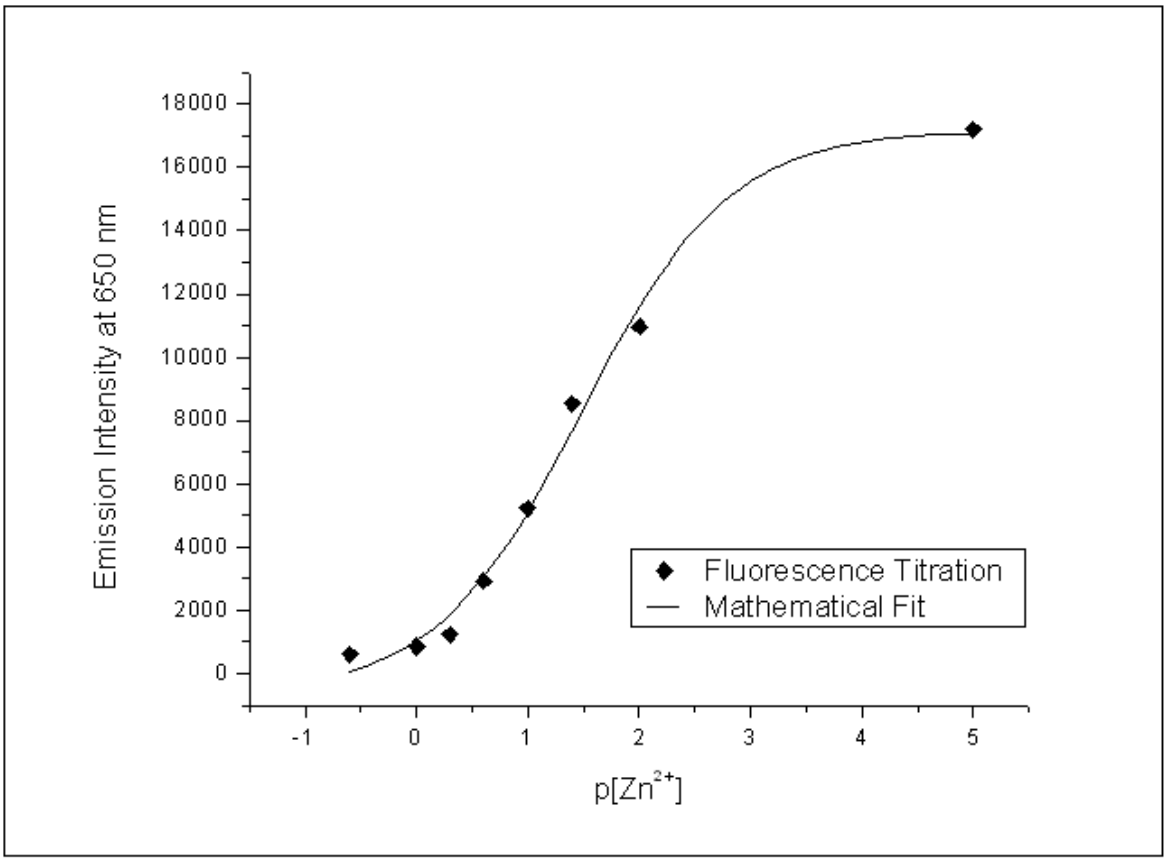

Figure 111. Emission intensities of $[(bpy)_2Ru(dpp)]^{2+}$ monitored at 650 nm and reported as a function of -log[Zn^{2+}].

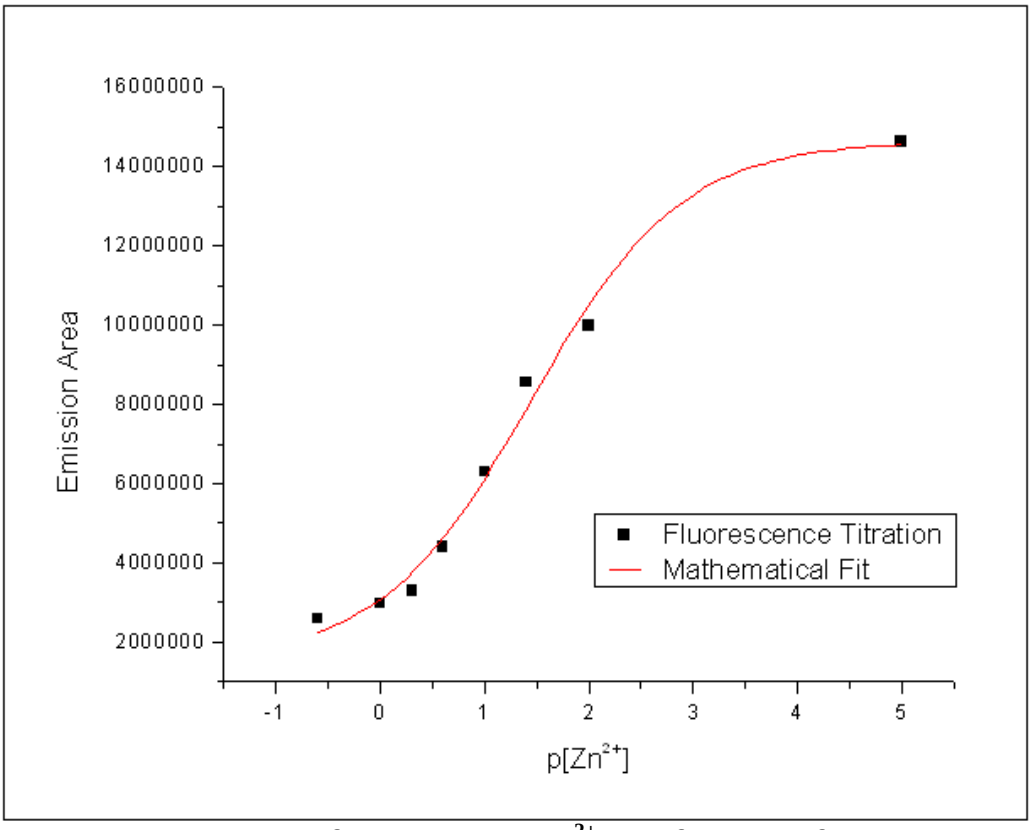

Figure 112. Emission area of $[(bpy)_2Ru(dpp)]^{2+}$ as a function of the negative log of $[Zn^{2+}]$.

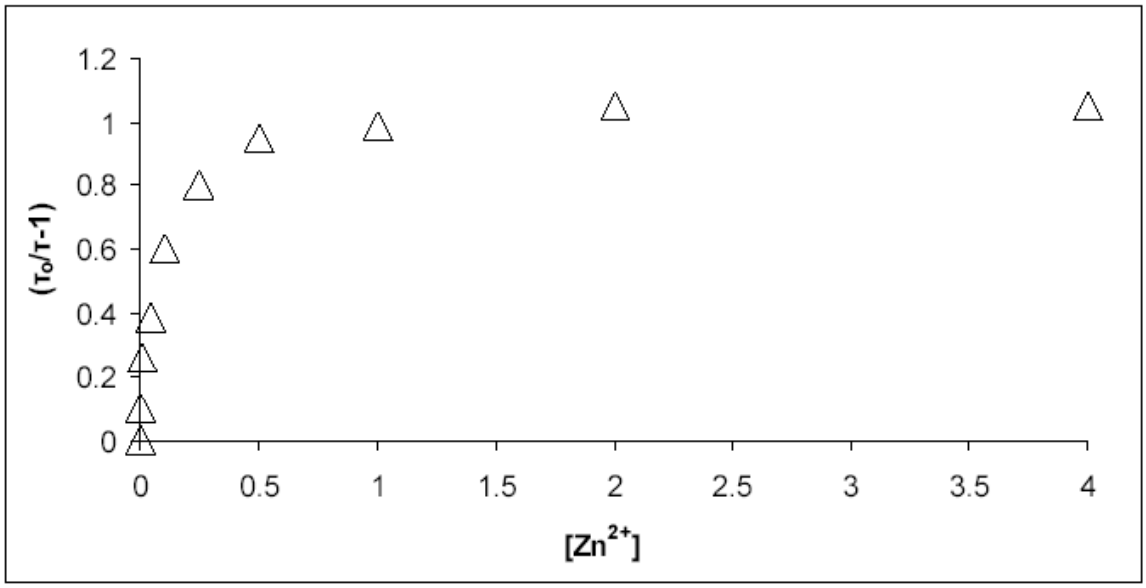

Figure 113. Stern-Volmer[65] plot for the zinc(II) titration of $[(bpy)_2Ru(dpp)]^{2+}$.

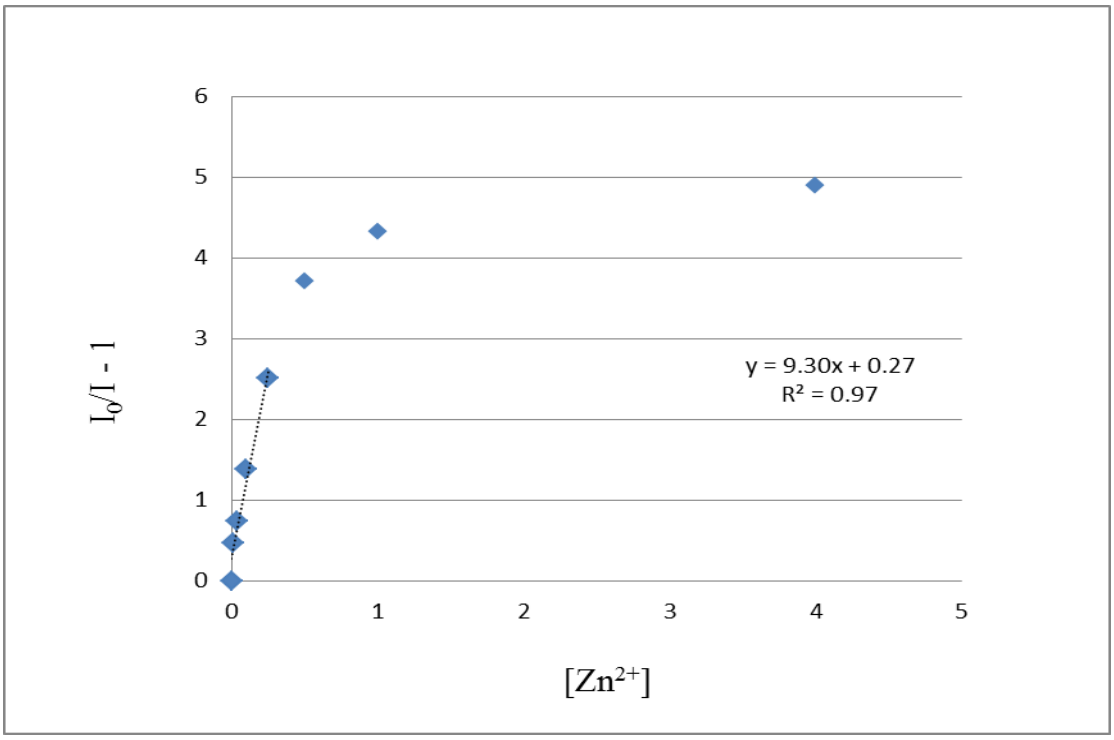

Figure 114. Stern-Volmer plot of emission intensity data for the zinc(II) titration of $[(bpy)_2Ru(dpp)]^{2+}$ (monitoring wavelength 650 nm). The initial portion of the plot has a linear trend (K_{SV} = 9.30).

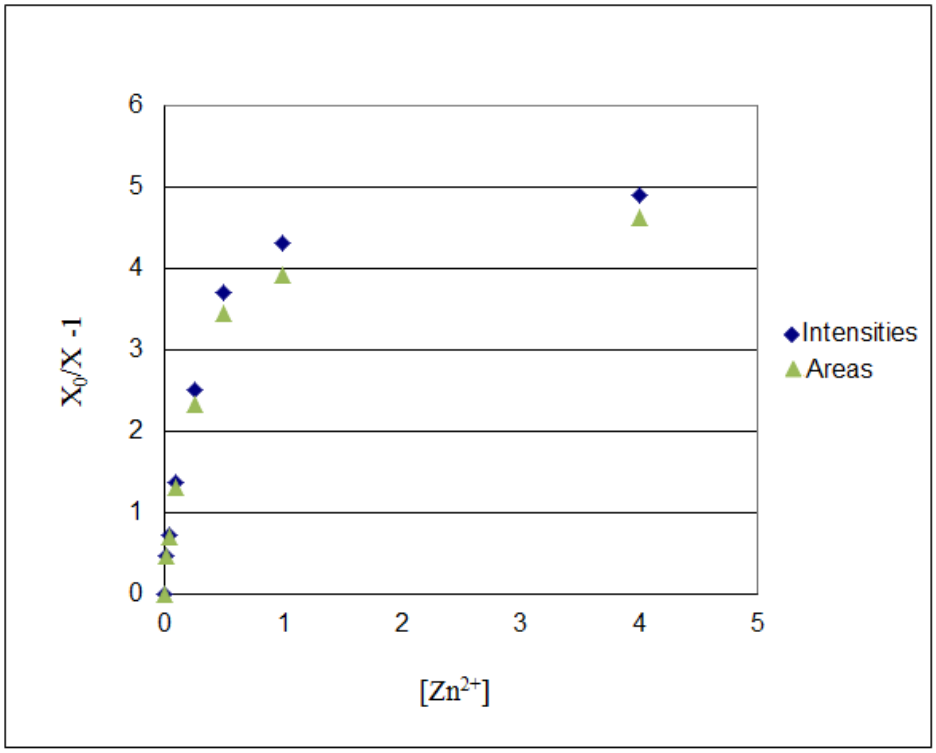

Figure 115. Stern-Volmer plots of emission intensity data and areas under the curve for the excited-state zinc(II) titration of $[(bpy)_2Ru(dpp)]^{2+}$.

3.C.2. Association of $[(bpy)_2Ru(pypz)]Cl_2$ with Zinc

The ruthenium complex was dissolved in a 5M $ZnCl_2$ aqueous solution to examine spectroscopically the effects of their interaction. The UV-Vis absorption spectrum of 3.6 x 10^{-5} M $[(bpy)_2Ru(pypz)]Cl_2$ in 5M $ZnCl_2$ taken at room temperature is presented in Figure 117. The spectra of 5M $ZnCl_2$ in water and 3.6 x 10^{-5} M $[(bpy)_2Ru(pypz)]Cl_2$ in water are also shown for comparison. The presence of the d^{10} metal cation affects the shape of the curve in the 400-500 nm region. A gaussian fit of the absorption spectrum of $[(bpy)_2Ru(pypz)]^{2+}$ with Zn^{2+} (Figure 116), highlights the new positions of the two MLCT absorptions and the individual contributions of each transition to the overall trace. The high energy bpy-centered MLCT transition blue-shifts to 422 nm from its original position around 430 nm while the pypz-centered transition moves to lower energy, from 476 to 488 nm, approximately by the same amount, 520 cm^{-1}.

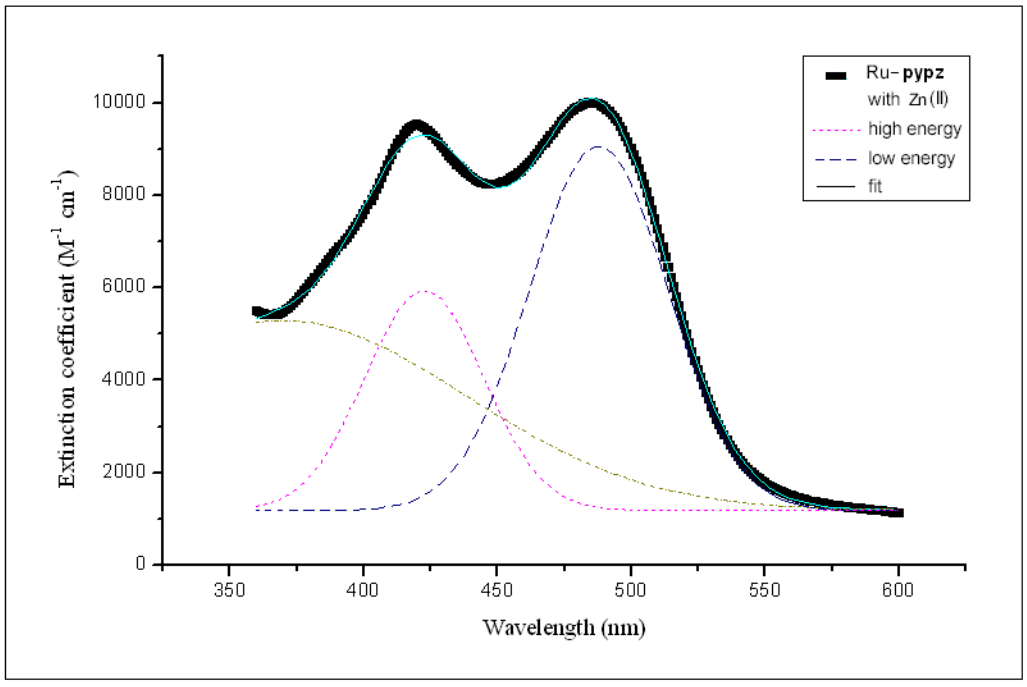

Figure 116. Gaussian fit of the UV-Vis MLCT spectral region of an aqueous solution containing 3.6 x 10^{-5} M $[(bpy)_2Ru(pypz)]^{2+}$ and 5M Zn^{2+}.

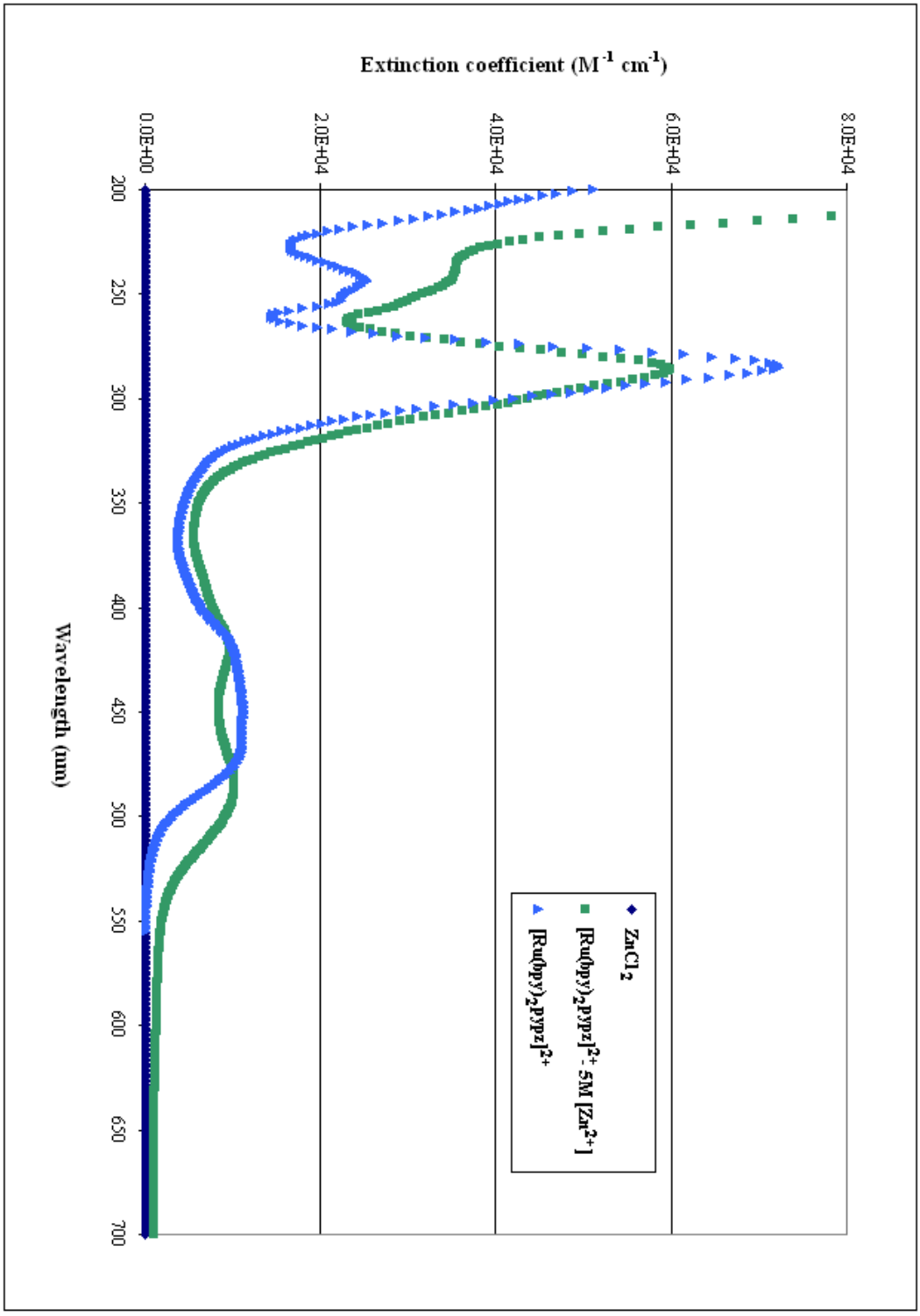

Figure 117. Room temperature UV-Vis absorption spectra of 5M $ZnCl_2$ in water, 3.6 x 10^{-5} M $[(bpy)_2Ru(pypz)]Cl_2$ in water, and 3.6 x 10^{-5} M $[(bpy)_2Ru(pypz)]Cl_2$ in 5M $ZnCl_2$.

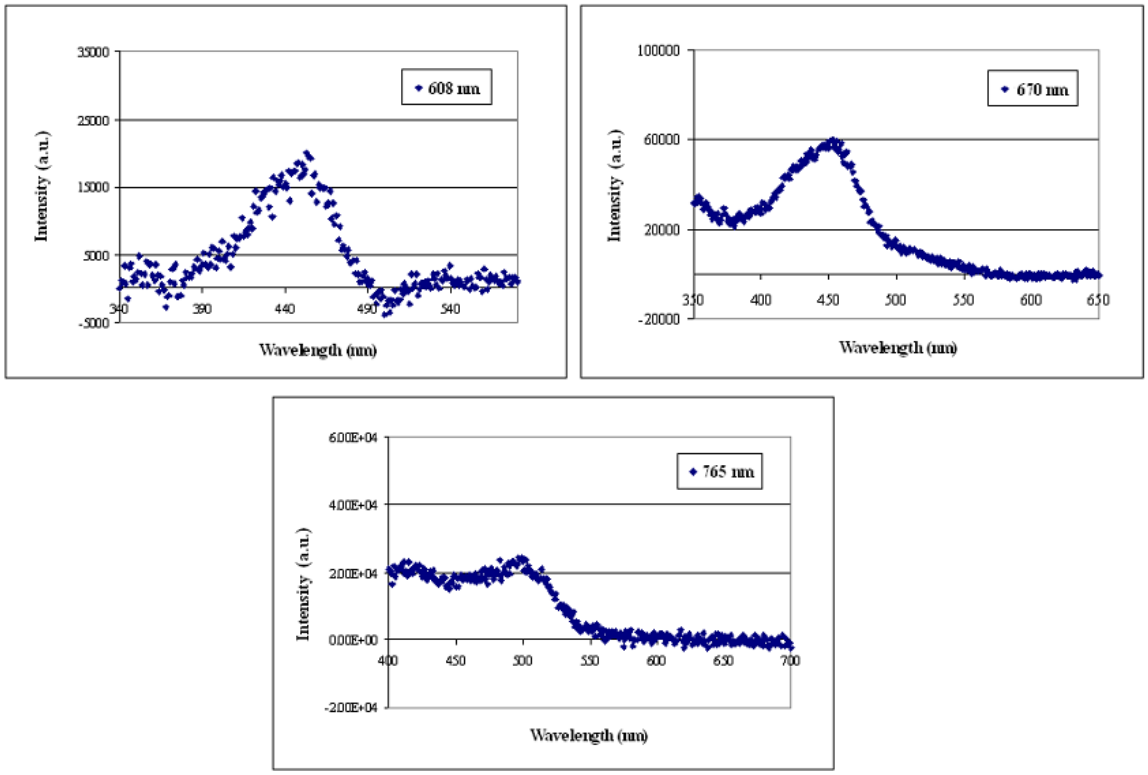

Figure 118. Corrected excitation spectra of 3.6 x 10^{-5} M $[(bpy)_2Ru(pypz)]Cl_2$ in 5M $ZnCl_2$ in water recorded at 608, 670 and 765 nm.

Three excitation spectra of 3.6 x 10^{-5} M $[(bpy)_2Ru(pypz)]Cl_2$ in 5M aqueous $ZnCl_2$ were recorded setting the emission at 608, 670 and 765 nm, respectively and corrected using the excitation spectrum of the background (Figure 118). At the shorter emission wavelength, the profile of the excitation spectra shows a single, slightly skewed, broad band centered around 450 nm, while the excitation spectrum obtained at 765 nm more closely mirrors the absorption spectrum with two bands contributing to the overall curve.

The emission spectrum was recorded using three different excitation wavelengths: 418, 450 and 490 nm (Figure 119). The Raman band of water is visible 3500 cm^{-1} from excitation. Corrected spectra without the Raman band (Figure 120) were obtained by

subtracting the emission spectrum of the background (Figure 121), a 5M aqueous solution of $ZnCl_2$, from that of the sample. More than one emission is observed and their intensity, not their position, appears to be dependent on the excitation wavelength. With shorter excitation wavelength, 418 nm for example, the 612-nm emission is predominant with a shoulder at 539 nm and a much less intense emission at 750 nm. With longer excitation wavelength, 490 nm, the 612-nm emission is partially quenched, and has approximately the same intensity as the 750-nm emission.

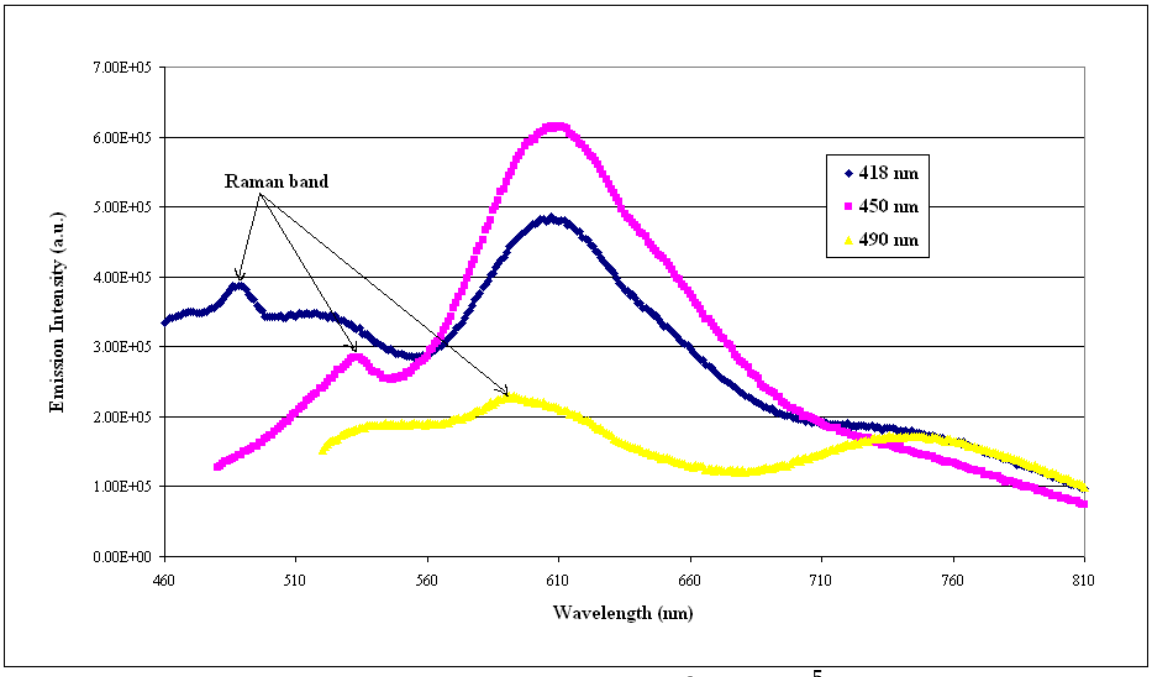

Figure 119. Room temperature emission spectra of 3.6 x 10^{-5} M $[(bpy)_2Ru(pypz)]Cl_2$ in 5M $ZnCl_2$ in water recorded using 418, 450 and 490 nm excitation wavelengths.

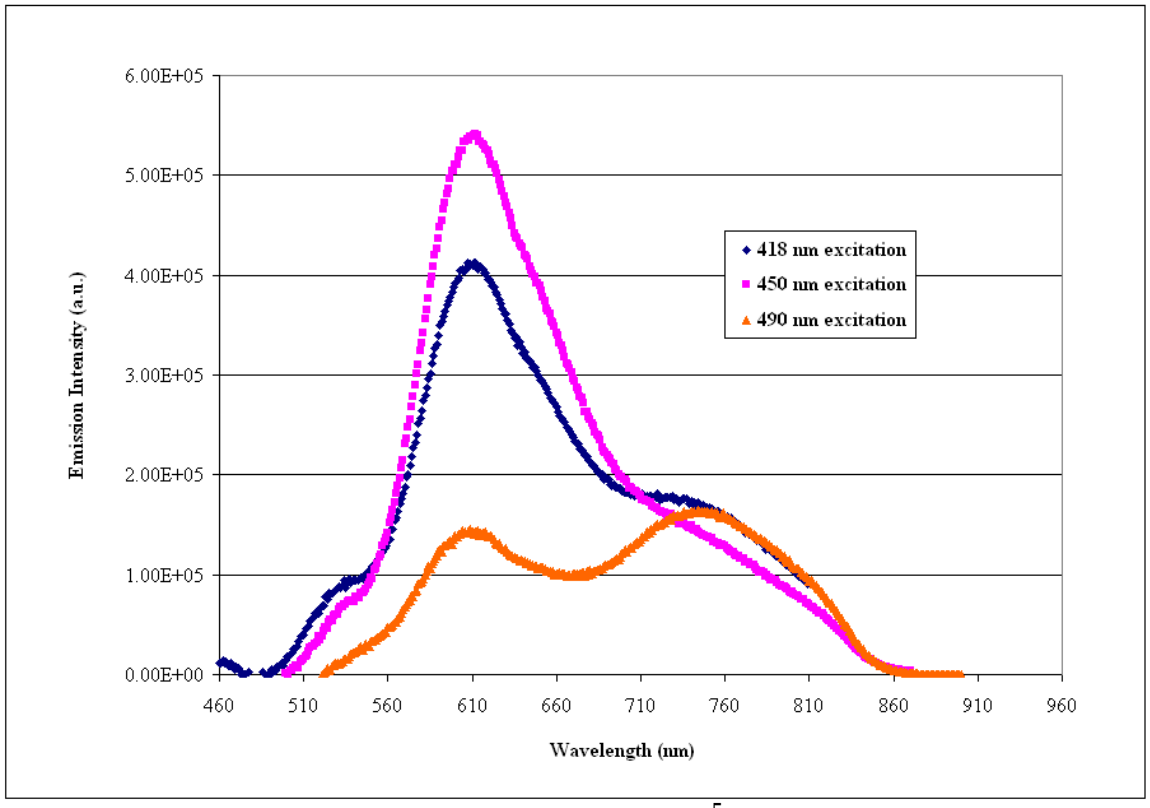

Figure 120. Corrected emission spectra of 3.6 x 10^{-5} M $[(bpy)_2Ru(pypz)]Cl_2$ in 5M $ZnCl_2$ in water recorded using 418, 450 and 490 nm excitation wavelengths.

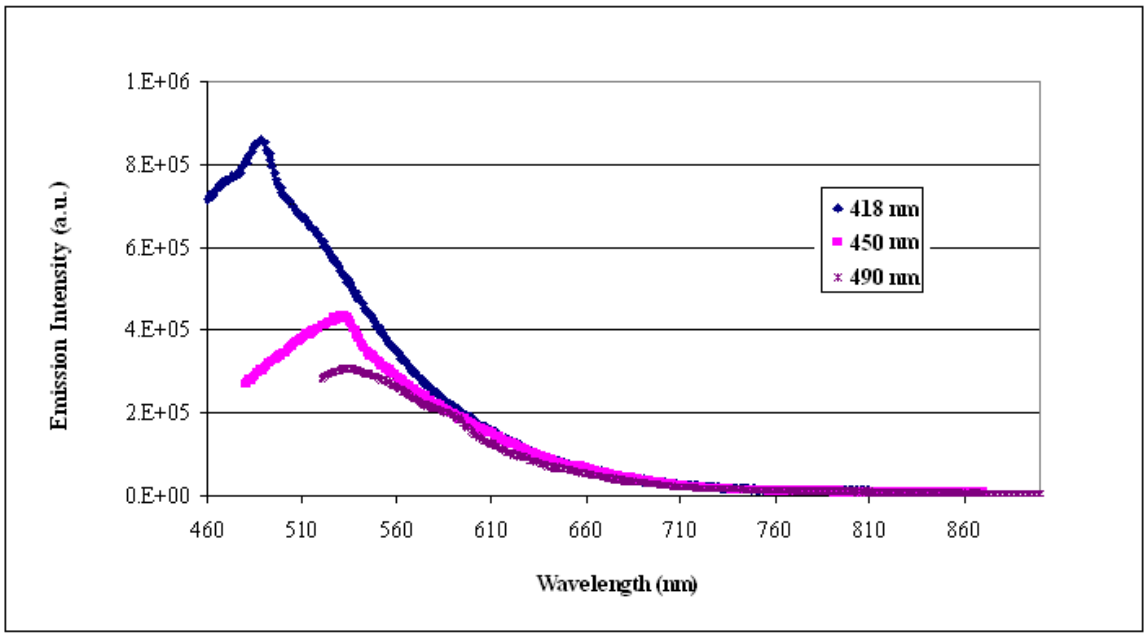

Figure 121. Background emission spectra of 5M $ZnCl_2$ in water recorded using 418, 450 and 490 nm excitation wavelengths.

Using gaussian functions, the skewed emission intensity profile centered at 750 nm can be resolved into two emissions centered at 737 and 803 nm, respectively (Figure 122).

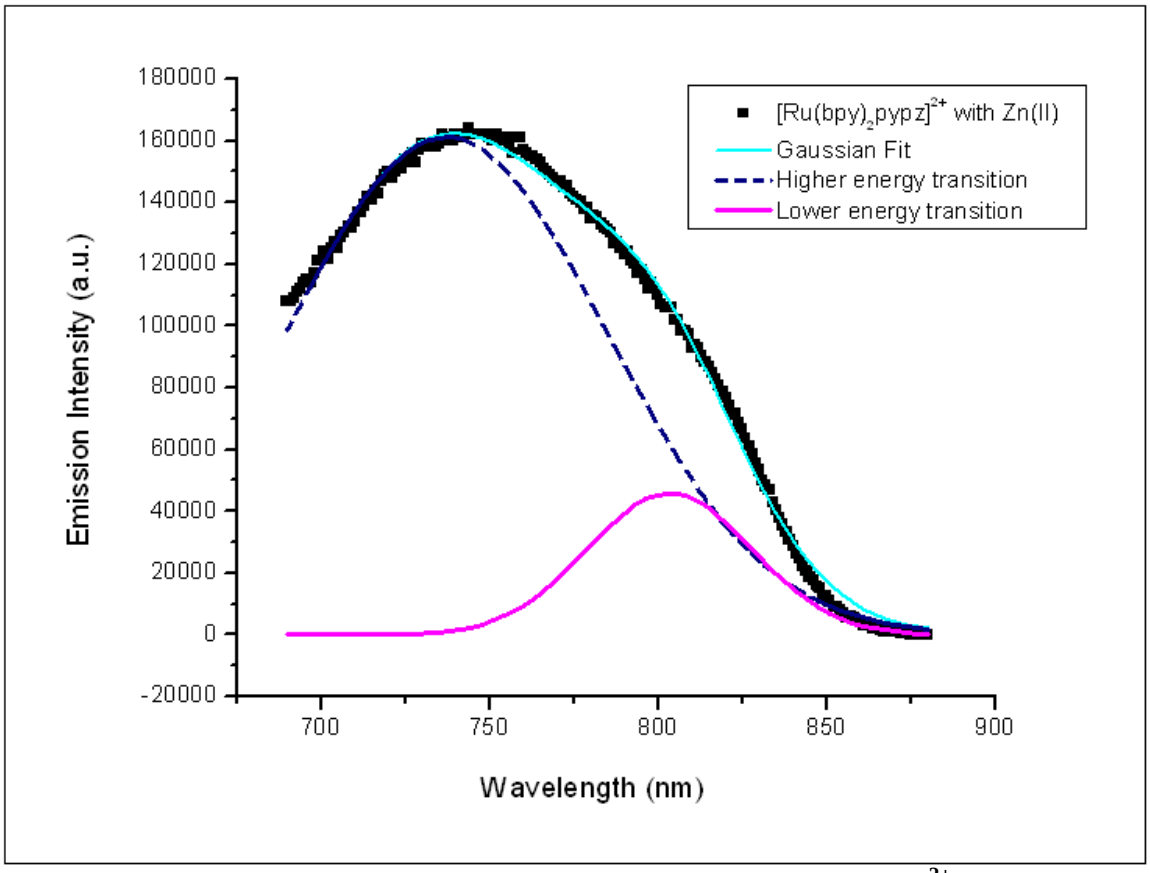

Figure 122. Gaussian fit of the 750-nm emission of $[(bpy)_2Ru(pypz)]^{2+}$ in 5 M $ZnCl_2$.

The average lifetimes of the 612-nm and 750-nm emissions are 320 ± 20 ns and 130 ± 8 ns. The time-resolved data modeled assuming a double-exponential decay could not distinguish between the two emissive components of the 750-nm band, suggesting that they have similar lifetimes.

3.C.2.a. Ground-State Titration

The $[(bpy)_2Ru(pypz)]Cl_2$ complex was titrated in a pH 3 buffer with zinc chloride solutions of concentrations ranging from 0 to 5.0 M. The absorption spectra recorded are shown in Figure 123. From 0 to 1.0 M $[Zn^{2+}]$ the changes in the MLCT region are minimal. Higher concentrations of the metal affect mainly the pypz-centered MLCT band. The change in absorbance monitored at 500 and 520 nm and plotted versus $-\log[Zn^{2+}]$ (Figure 124) yields only partial sigmoidal curves. The change in absorbance monitored versus $[Zn^{2+}]$ yields quasi-linear plots (Figure 125) and attempts to fit the data with equation (97), as previously done in the titration experiment with $[(bpy)_2Ru(dpp)]^{2+}$, lead to much less satisfactory results (Figure 126). Nonetheless, the equilibrium constant for association was extrapolated from the fit and found to be $6 \pm 1\ M^{-1}$.

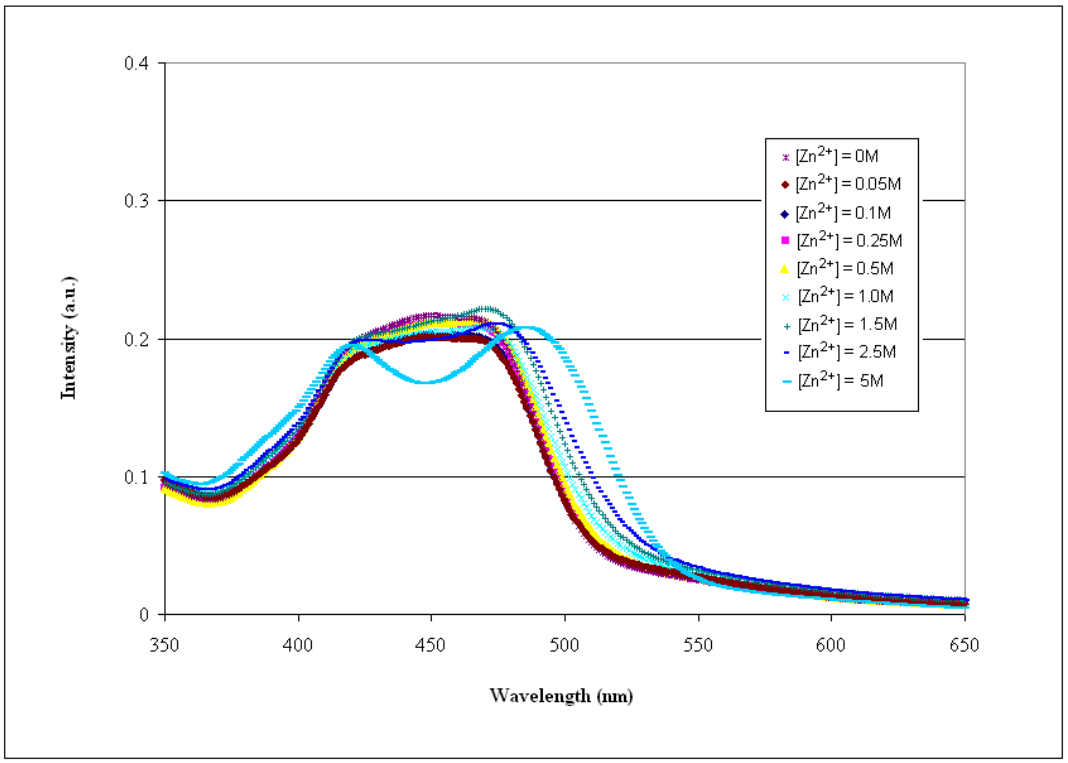

Figure 123. UV-Vis absorption spectra of room temperature solutions of $[(bpy)_2Ru(pypz)]Cl_2$ in pH 3 buffer at increasing Zn^{2+} concentrations.

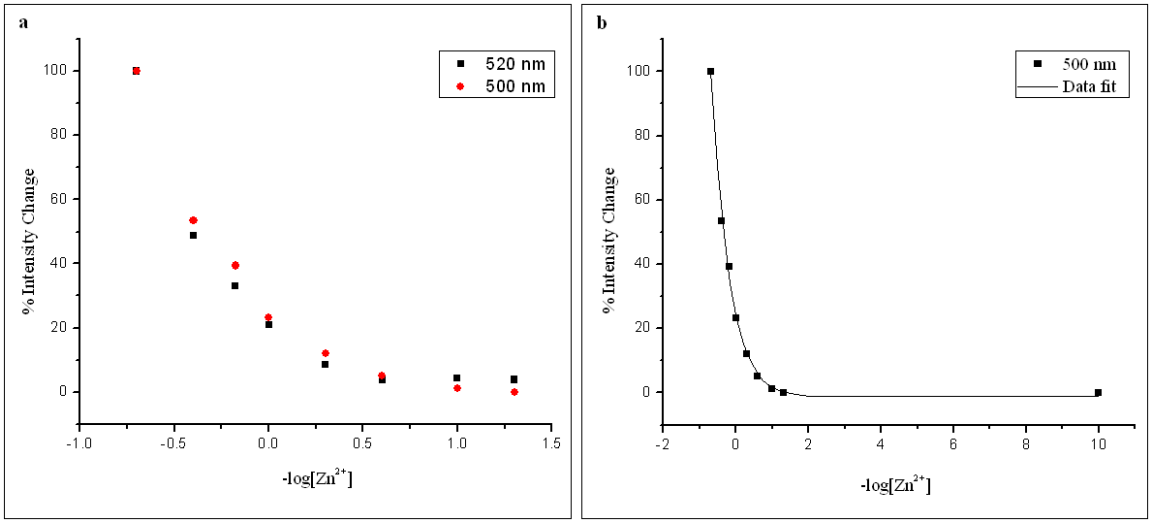

Figure 124. UV-Vis absorbance for room temperature solutions of $[(bpy)_2Ru(pypz)]Cl_2$ in pH 3 buffer as a function of $-log[Zn^{2+}]$ monitored at 500 and 520 nm (a), and sigmoidal data fit for the 500-nm plot (b).

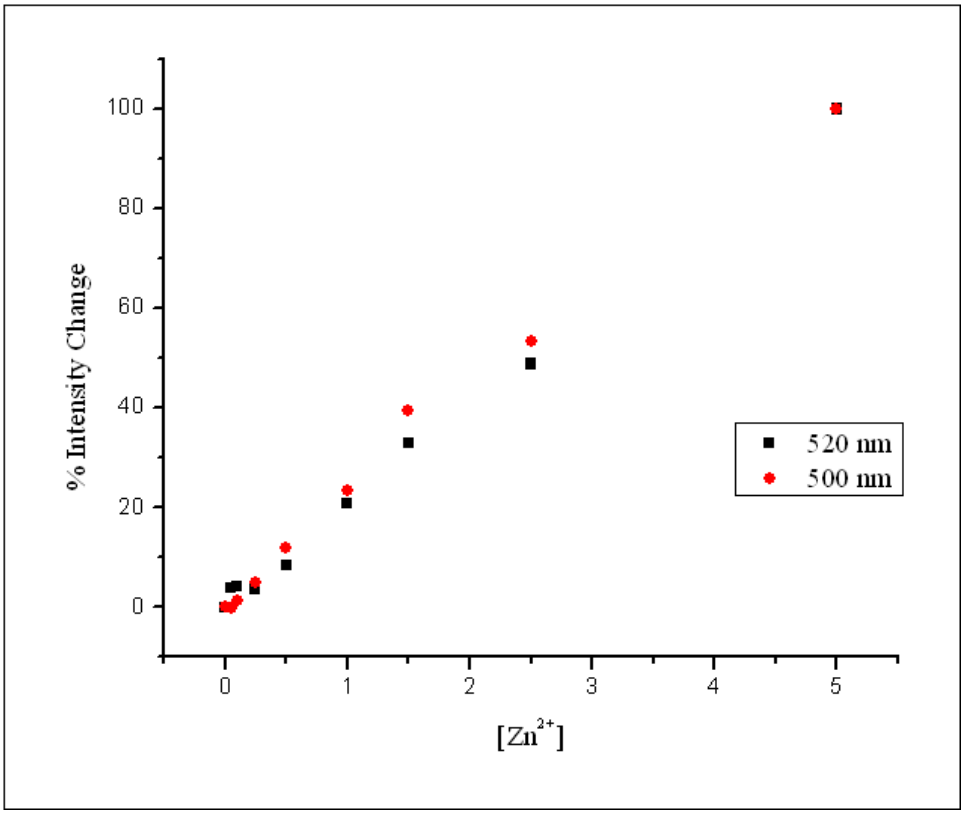

Figure 125. UV-Vis absorbance monitored at 500 and 520 nm, for room temperature solutions of $[(bpy)_2Ru(pypz)]Cl_2$ in pH 3 buffer at increasing Zn^{2+} concentrations.

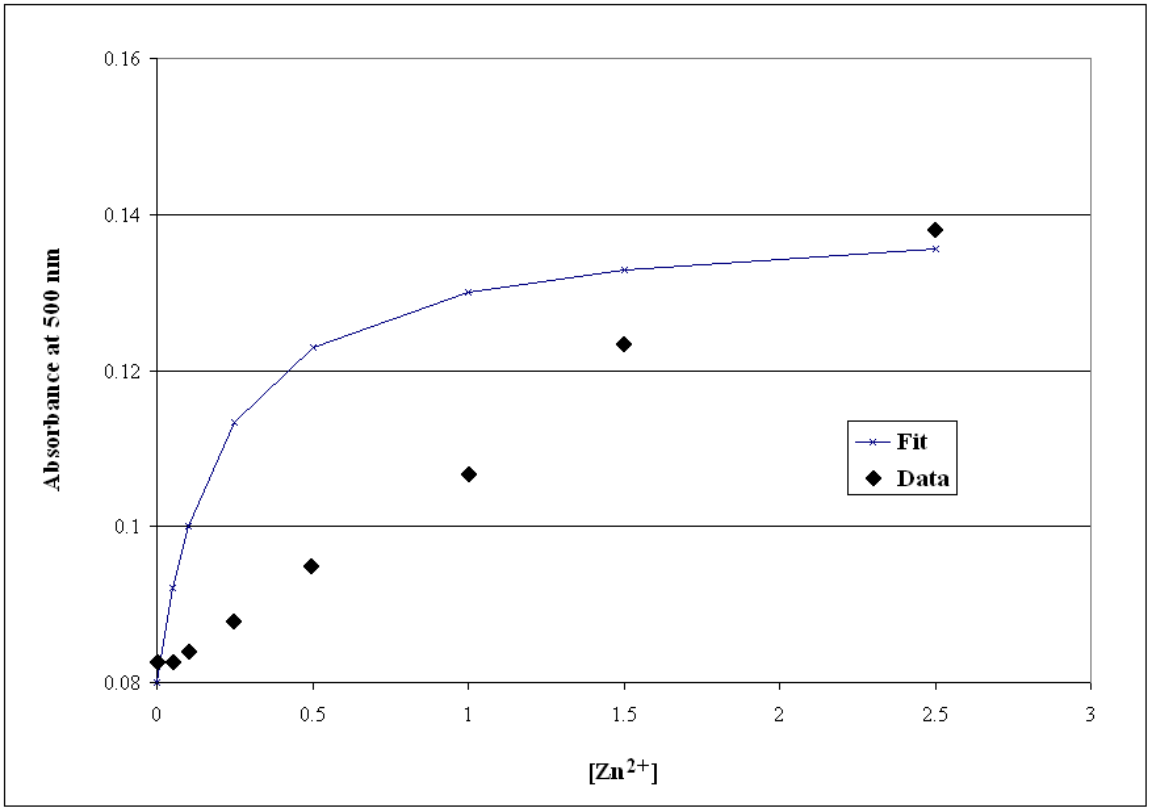

Figure 126. Fit using equation 97 of UV-Vis absorbance of $[(bpy)_2Ru(pypz)]Cl_2$ in pH 3 buffer at increasing Zn^{2+} concentrations monitored at 500 and 520 nm.

The ground state titration of $[(bpy)_2Ru(pypz)]Cl_2$ with zinc chloride solution was not performed using ^{1}H-NMR spectroscopy because viable NMR samples at pH 3 could not be obtained in the range of metal concentration where precipitation of the metal out of solution could be avoided.

3.C.2.b. Excited-State Titration

The titration in the excited state was carried out on $[(bpy)_2Ru(pypz)]Cl_2$ in pH 3 buffer solutions by exciting the samples with 400- and 420-nm light (Figures 127 and 128). Buffer 3 was chosen to avoid zinc precipitation out of solution. However, in pH 3 buffer solutions the $[(bpy)_2Ru(pypz)]Cl_2$ complex is 30% protonated and its emission intensity is quenched by approximately 80% compared to water as solvent (Figure 129). This represents a significant drawback, since it increases the error and uncertainty in all measurements and decreases the signal to noise ratio that may be achieved in all the samples, particularly the ones excited with the Nd-YAG laser, where the light source is pulsed. Furthermore, the titration is problematic due to the presence of the 610-nm emission, which is much more intense at pH 3 than it is at neutral pH, and overlaps with the 665-nm emission. Still, increasing the concentration of zinc from 0 to 5 M causes a detectable effect, in that it decreases the intensity of the emission centered at 665 nm, while the 610-nm emission remains unaffected and a new emission appears around 750 nm. The changes observed spectroscopically at several individual wavelengths in the 640- to 785-nm range, as well as the overall area under the curve, were plotted as a function of the negative logarithm of the zinc concentration (Figures 130 and 132).

Although all titration curves could be nicely fitted by the Boltzmann equation, no common inflection point was found. The value of the inflection point proved to be dependent on the monitoring wavelength: the longer the monitoring wavelength, the higher the inflection point value (Table 18, Figure 131).

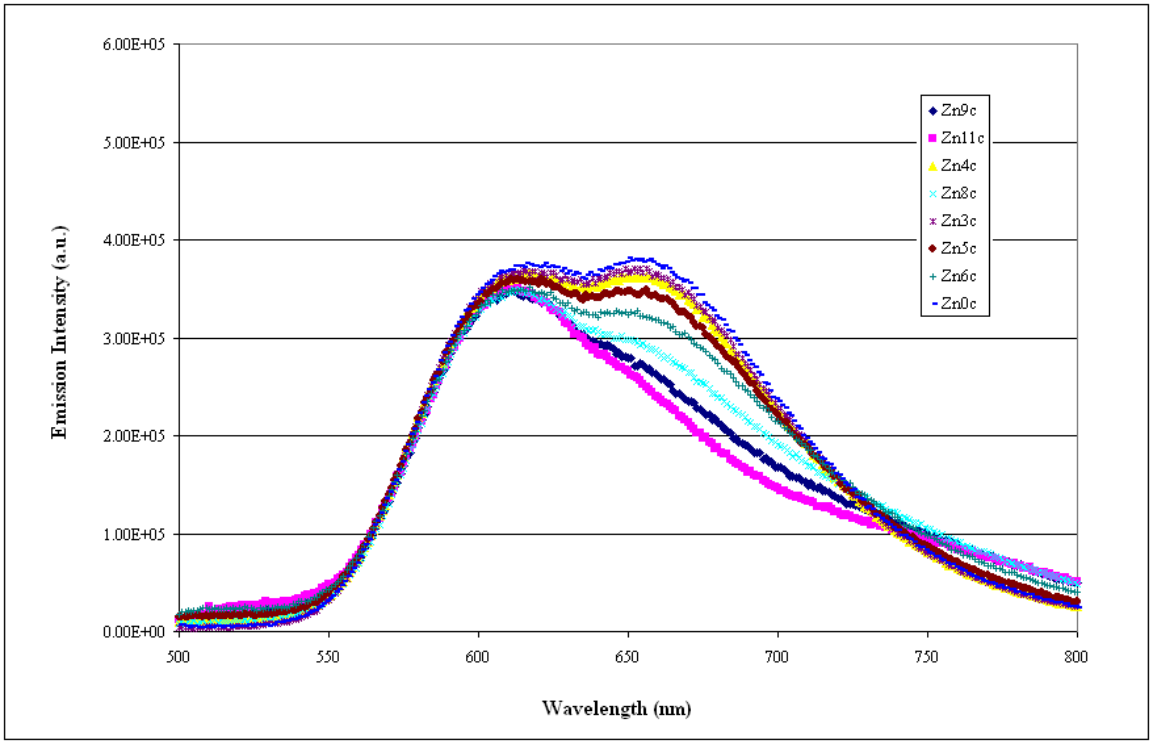

Figure 127. Corrected luminescence spectra of RT solutions of $[(bpy)_2Ru(pypz)]Cl_2$ in pH 3 buffer at increasing Zn^{2+} concentrations (λ_{ex} = 420 nm).

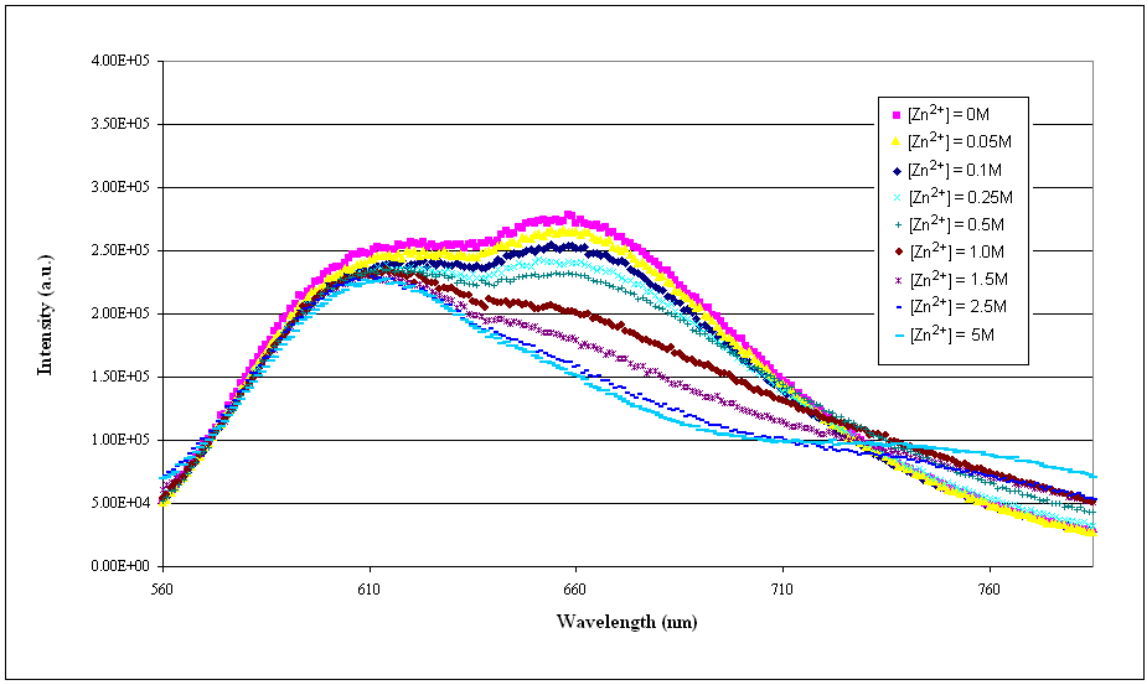

Figure 128. Corrected luminescence spectra of RT solutions of $[(bpy)_2Ru(pypz)]Cl_2$ in pH 3 buffer at increasing Zn^{2+} concentrations (λ_{ex} = 400 nm).

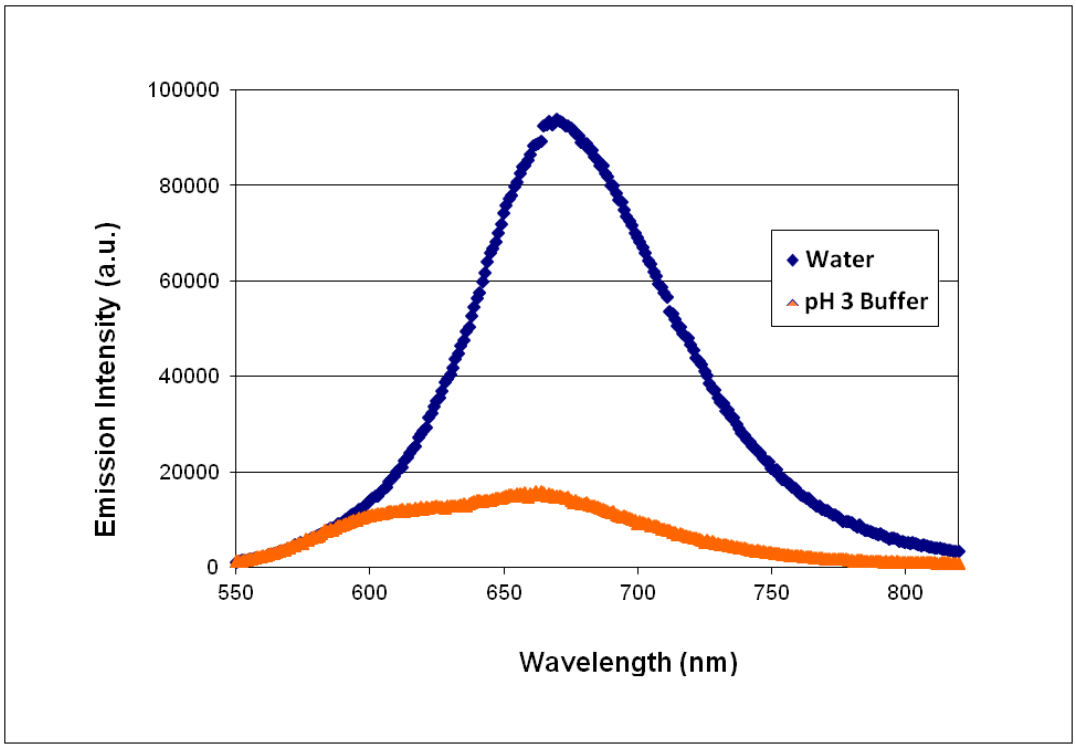

Figure 129. Effect of pH on the luminescence intensity of the 675-nm emission of $[(bpy)_2Ru(pypz)]Cl_2$ in water and in pH 3 buffer at room temperature.

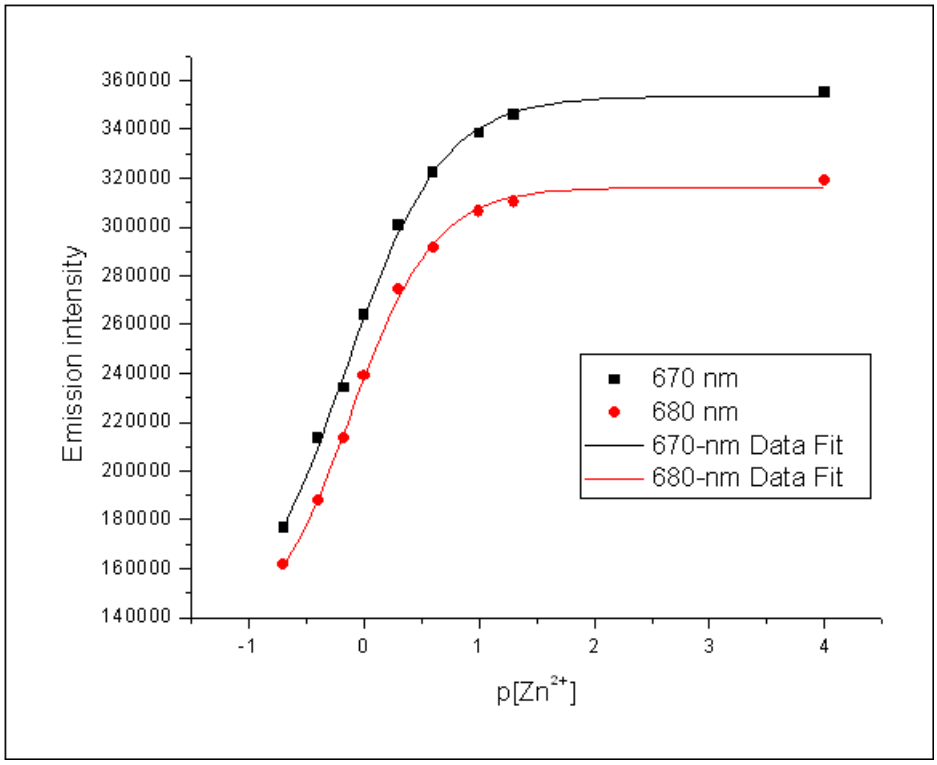

Figure 130. Emission intensity changes recorded with λ_{ex} = 420 nm and monitored at 670 and 680 nm for solutions of $[(bpy)_2Ru(pypz)]Cl_2$ in pH 3 buffer plotted versus pZn.

The inflection point of the titration plot obtained using the emission max of the 660-nm band as monitoring wavelength was found at $p[Zn^{2+}] = -0.30 \pm 0.01$ which corresponds to a K^* of $2.00 \pm 0.01\ M^{-1}$.

Table 18: Inflection points from excited-state titration curves of $[(bpy)_2Ru(pypz)]Cl_2$ in pH 3 buffer with Zn.

Monitoring wavelength	pKeq
630	-3.066
640	-1.186
650	-0.582
660	-0.302
670	-0.169
680	-0.122
685	-0.06
690	-0.047
785	-1.750

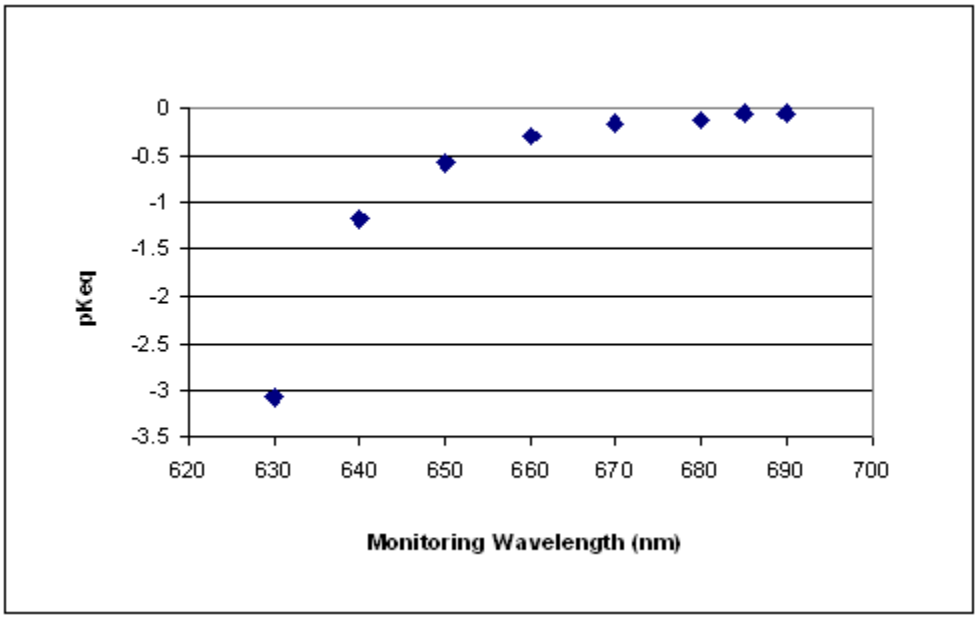

Figure 131. Inflection point trend according to the monitoring wavelength chosen for the excited-state titration of $[(bpy)_2Ru(pypz)]Cl_2$ in pH 3 buffer with Zn.

The inflection point of the curve obtained by plotting the emission areas instead of the intensities was found at $p[Zn^{2+}] = -0.13 \pm 0.08$ which corresponds to a K^* of $1.35 \pm 0.20\ M^{-1}$.

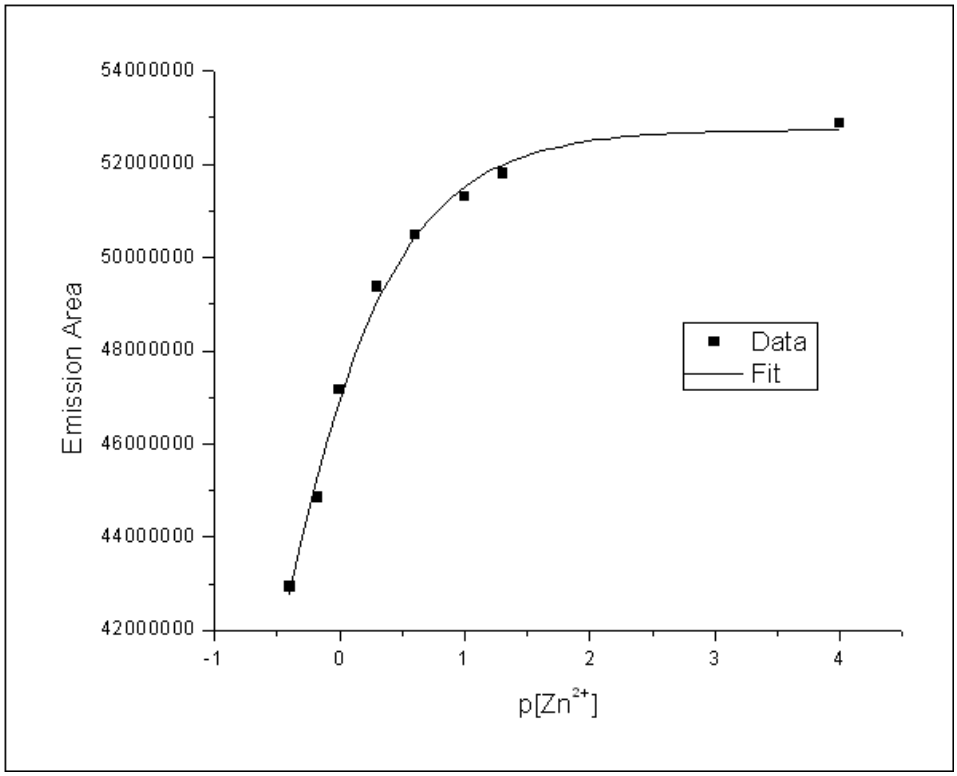

Figure 132. Emission changes recorded with λ_{ex} = 420 nm in area under the curve between 560-785 nm for solutions of $[(bpy)_2Ru(pypz)]Cl_2$ in pH 3 buffer plotted versus pZn.

At pH 3 with no zinc(II), the $[(bpy)_2Ru(pypz)]^{2+}$ complex exhibits initially an intense and short lived emission centered at 680 nm with lifetime of 26 ± 5 ns. As the intense emission decays, the less intense but longer lived emission centered at 620 nm may be observed (Figure 133). The lifetime of the 620-nm emission in buffer 3 solution is 400 ± 50 ns. At increasing concentrations of zinc ions, from 0 to 0.5 M $[Zn^{2+}]$, the intensity of the 680 nm emission decreases as does its lifetime, from 26 to 9 ns, while the

intensity and lifetime of the 620-nm emission remains unaltered (τ = 400 ns). Furthermore, a new red-shifted emission at 800 nm begins to appear (Figure 134), with lifetime of 70 ± 5 ns.

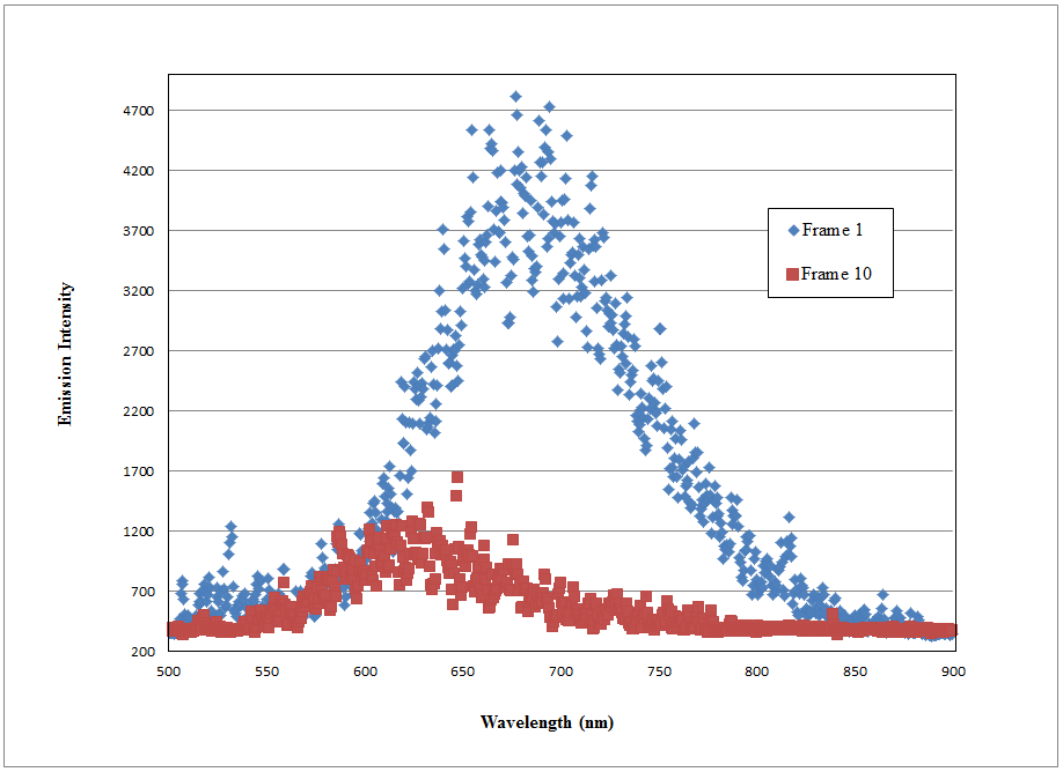

Figure 133. Time-resolved luminescence spectra, frame 1 and 10, of RT solutions of $[(bpy)_2Ru(pypz)]Cl_2$ in pH 3 buffer at 2 and 20 ns after the laser pulse, respectively.

At 1M $[Zn^{2+}]$, while steady state spectra still show the 680-nm emission as the predominant emission with no sign yet of a red-shifted band, in the time-resolved spectra the initial emission has shifted to 760 nm (Figure 135 a and b). The difference between the two spectra lies in the excitation wavelength, 420 nm for the steady state spectra and 532 nm for the time resolved data. According to the time-resolved spectra, the red-shifted emission has longer lifetime than the original 680-nm emission (Figure 136).

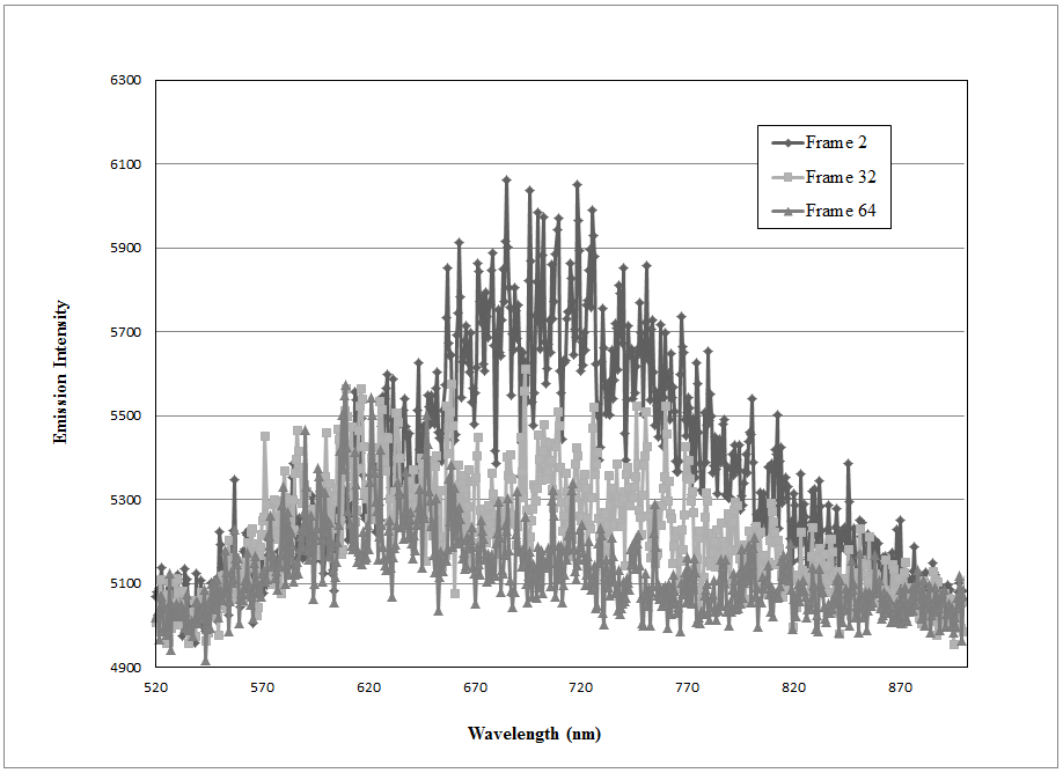

Figure 134. Time-resolved luminescence spectra, frames 2, 32 and 64, of RT solutions of $[(bpy)_2Ru(pypz)]Cl_2$ and 0.5 M $[Zn^{2+}]$ in pH 3 buffer at 4, 64 and 128 ns after the laser pulse, respectively.

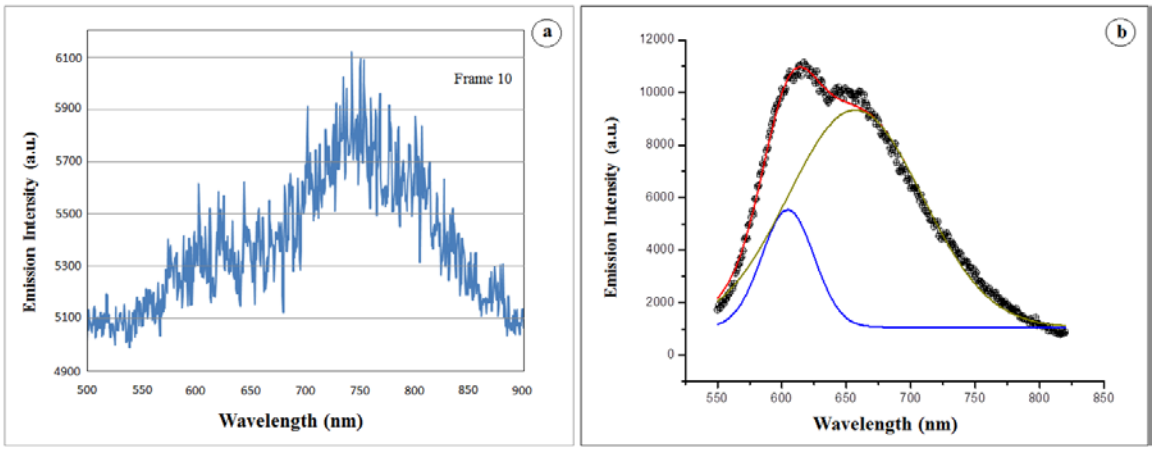

Figure 135. Time-resolved (a) and steady-state (b) luminescence spectra of RT solutions of $[(bpy)_2Ru(pypz)]Cl_2$ and 1 M $[Zn^{2+}]$ in pH 3 buffer obtained using λ_{exc} = 532 and 420-nm, respectively.

At this intermediate stage of the excited state zinc titration of $[(bpy)_2Ru(pypz)]^{2+}$, clearly establishing the lifetime of each emission contributing to the overall luminescence spectrum is challenging, as all bands overlap to some degree, either in the time domain or the wavelength domain. For the purpose of the Stern-Volmer plot determination, the lifetime of the 680-nm band were only considered for samples containing 0 to 0.5 M $[Zn^{2+}]$, excluding samples with concentration of Zn^{2+} of 1 M and above due to high uncertainty associated with the measurement.

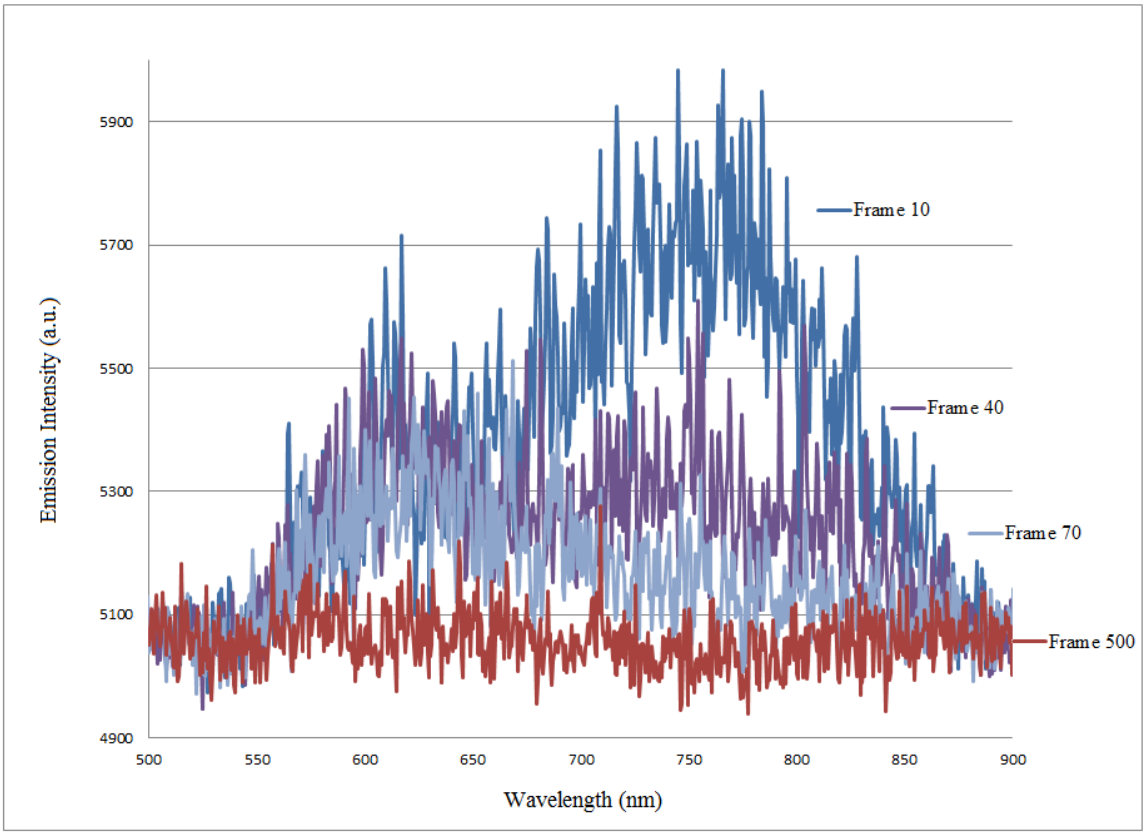

Figure 136. Time-resolved luminescence spectra, frames 10, 40, 70 and 500, of RT solutions of $[(bpy)_2Ru(pypz)]Cl_2$ and 1 M $[Zn^{2+}]$ in pH 3 buffer at 20, 80, 140 and 1000 ns after the laser pulse, respectively.

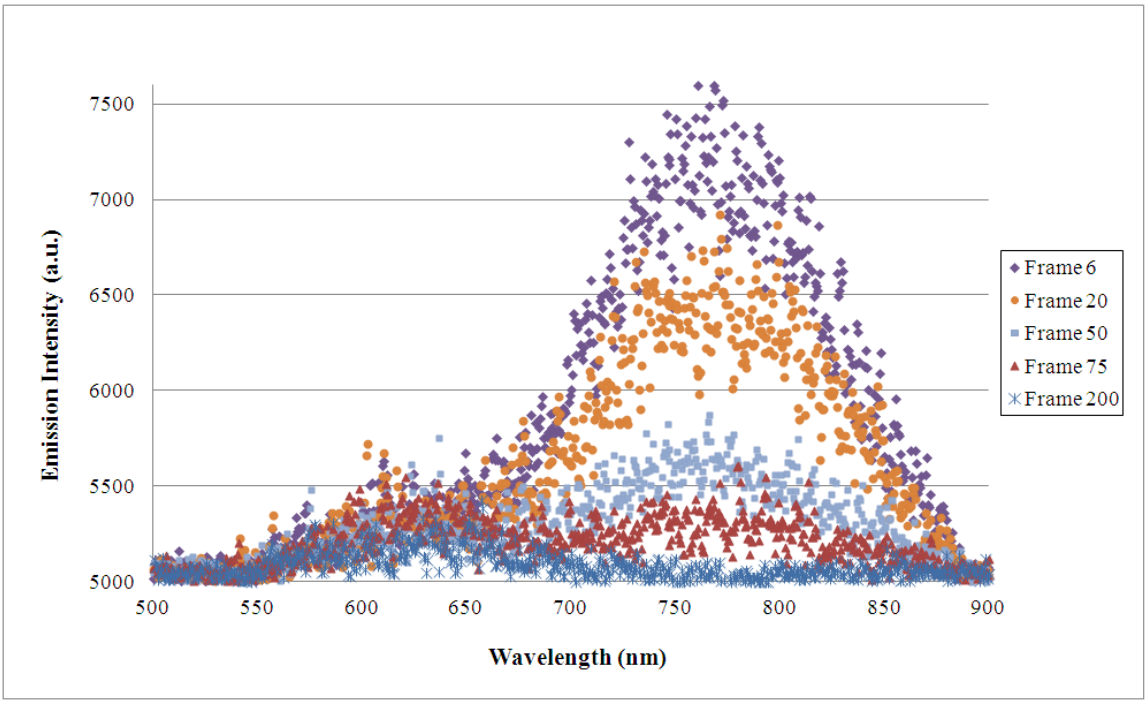

Figure 137. Time-resolved luminescence spectra, frames 6, 20, 50, 75 and 200 of RT sample of $[(bpy)_2Ru(pypz)]Cl_2$ and 4.5 M $[Zn^{2+}]$ in pH 3 buffer.

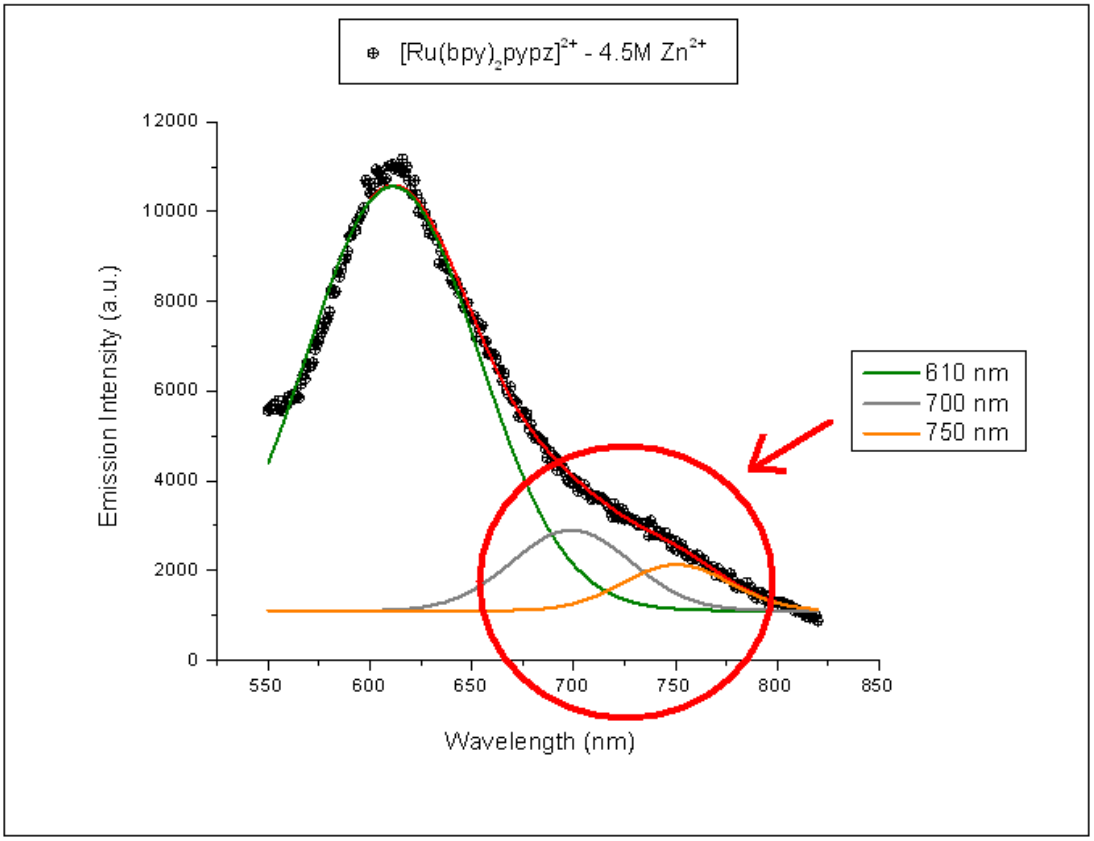

Figure 138. Steady state luminescence spectrum and resolved components of RT solution of $[(bpy)_2Ru(pypz)]Cl_2$ and 4.5 M $[Zn^{2+}]$ in pH 3 buffer.

Finally, at concentration of Zn^{2+} of 2M and above, time resolved spectra do not show sign of the 680-nm emission; instead, the dominant emission is centered at 760 nm and has lifetime of 70 ± 2 ns (Figure 137). The 620 nm emission is still present, and long lived (τ = 388 ± 20 ns). Again, there is a discrepancy with what is observed in steady state spectra (Figure 138). Steady state spectra do reveal the presence of a weak red-shifted emission and no 680-nm band, but the relative intensity of the 620-nm band and the emission past 700 nm is inverted compared to the time-resolved spectra, i.e. in the time-resolved spectra, the 760 nm emission at its max is more intense than the 620-nm band while in the steady-state spectrum, the predominant band is the 620-nm band. According to the deconvolution of the steady state spectrum carried out with Origin software, the red-shifted emission is composed of two emissions centered respectively at 700 and 750-nm. Lifetime calculations in that wavelength range shows that the lifetime decay at 700 and 750 nm corresponds to lifetimes of 85 ± 3 ns and 65 ± 1 ns, respectively.

The emission intensity quenching, obtained from steady-state data and due to increased concentrations of Zn^{2+}, results in an almost linear Stern-Volmer plot, as shown in Figure 139. The plot is much straighter than for $[(bpy)_2Ru(dpp)]^{2+}$, and never quite reaches a plateau, although it does show evidence of slight negative deviations at $[Zn^{2+}]$ higher than 1M. The Stern-Volmer plots obtained using different monitoring wavelength chosen in the spectral range near the maximum intensity of the 665-nm emission, does not affect the slope of each plot and the constants obtained in the first portion of each graph are identical: $K_{SV}(I) = 0.41 \pm 0.01\ M^{-1}$. The Stern-Volmer obtained using the integration values of the areas under the emission curves, has a more pronounced

negative deviation due to the difficulty of "removing" the individual contributions to the intensity value from the 610-nm emission and the growing 750-nm emission. The Stern-Volmer constant determined using only data from the first portion of the areas curve is: $K_{SV}(A)= 0.50 \pm 0.02\ M^{-1}$. The first portion of the two Stern-Volmer curves, from values of intensity and areas, are almost coincidental, as evidenced by the K_{SV} values within experimental error of each other. On the other hand, the Stern-Volmer obtained using lifetime data, yields a linear plot with a significantly different value of K_{SV}, $K_{SV}(\tau) = 3.776 \pm 0.055\ M^{-1}$.

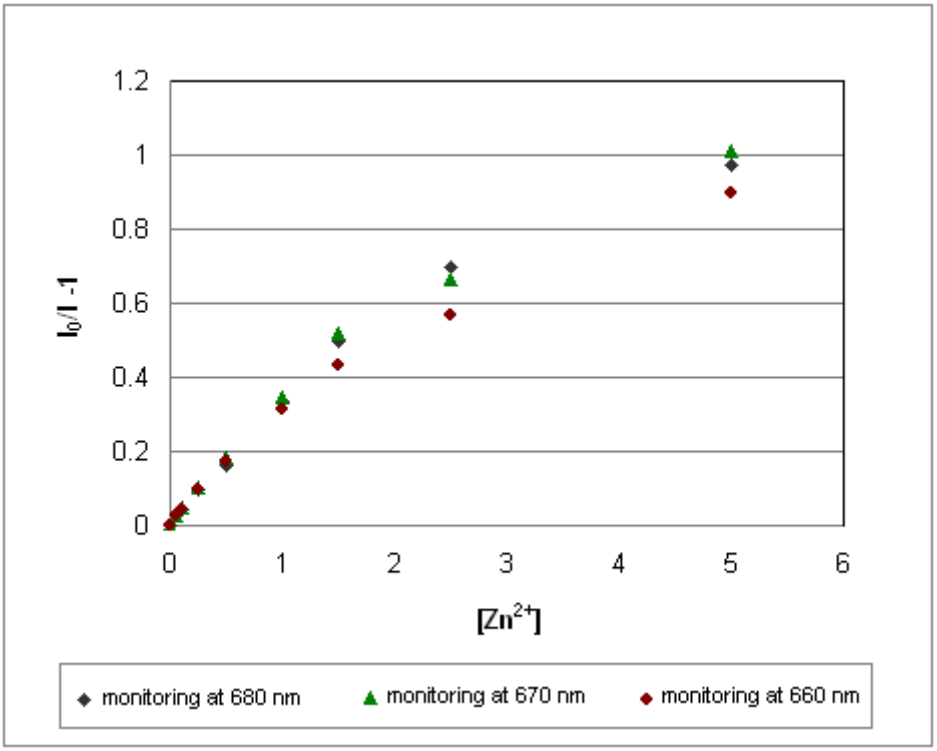

Figure 139. Stern-Volmer plot of emission intensity data monitored at 660, 670 and 680 nm for the excited-state titration of $[(bpy)_2Ru(pypz)]Cl_2$ in pH 3 buffer with Zn^{2+}, using 420 nm excitation wavelength.

The lifetime values, unlike the data for the intensity and area plots, were obtained from time-resolved spectra of $[(bpy)_2Ru(pypz)]^{2+}$, which do not match the steady-state spectra for peak position or intensity (vide supra). As a consequence, the lifetimes appear to decrease "much sooner", i. e. in samples with much lower concentrations of zinc ions, while the intensity and area values decrease at a lower rate, i.e. the Stern-Volmer incline is less than that for the lifetime Stern-Volmer plot and quenching appears to occur over a wider range of $[Zn^{2+}]$ (Figure 140).

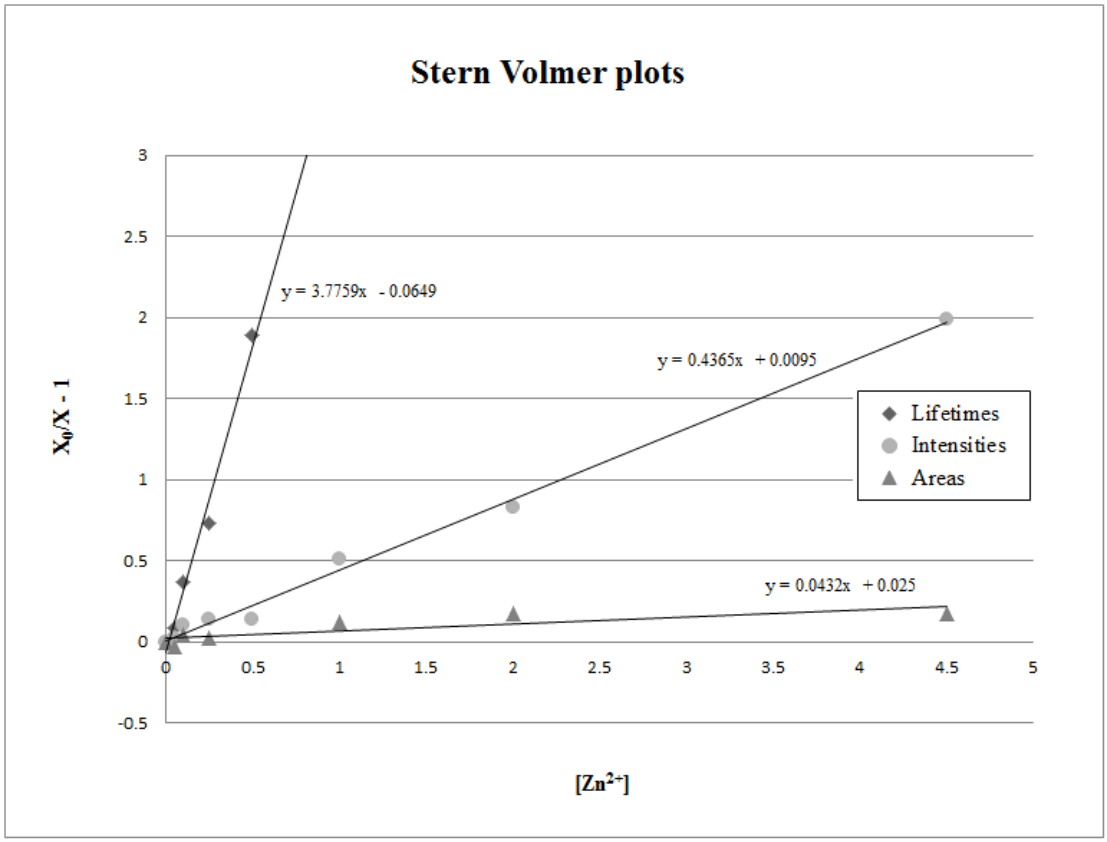

Figure 140. Stern-Volmer plots obtained from lifetime data, areas under the curve and emission intensity at 658 nm for RT solutions of $[(bpy)_2Ru(pypz)]Cl_2$ and increasing concentration of Zn^{2+} in pH 3 buffer.

3.D. Quantum Yield Determinations

Two series of compounds, the ruthenium(II)-dpp series and the ruthenium(II)-pypz series, were studied at chronologically separate periods of time using different absorption and emission spectrometers. All quantum yield measurements were made using the gradient method and relying on well-characterized reference compounds with known quantum yields at the temperature of interest. To maximize accuracy and ensure that operational parameters were the same throughout, emission and absorption spectra for reference samples were recorded on the same day as the spectra for analytes. The spectra were recorded again each time the quantum yield determination experiment was performed. The quantum yields of the ruthenium(II)-dpp series of compounds were determined using $[Ru(bpy)_3]^{2+}$, $[Ru(phen)_3]^{2+}$, and $[Os(bpy)_3]^{2+}$ as standards, while the quantum yields of the ruthenium(II)-pypz series were determined versus $[Ru(bpy)_3]^{2+}$ and $[(bpy)_2Ru(dpp)]^{2+}$.

3.D.1. Reference Compounds

The quantum yield for $[Ru(bpy)_3]^{2+}$ was taken to be 0.0429, as reported in the literature.[76,77,78,79] The quantum yield of $[Ru(phen)_3]^{2+}$ was determined to cross-standardize $[Ru(bpy)_3]^{2+}$ and assess the reliability of the method employed. The gradients from the graphs of absorbance versus emission obtained using the Fluorolog system (Figure 141) are $1.17 \pm 0.04 \times 10^8$ and $0.75 \pm 0.01 \times 10^8$ for $[Ru(phen)_3]^{2+}$ and $[Ru(bpy)_3]^{2+}$, respectively. Both instruments used, the Fluorolog system and the ICCD system, yielded nearly the same ratio of gradients, 1.556 vs 1.564, respectively. The value of quantum yield for $[Ru(phen)_3]^{2+}$ calculated using equation (83) and the

gradients, Φ_{em} = 0.0669 ± 0.002, is within experimental error of the published results, 0.05810[77] and 0.07212[80].

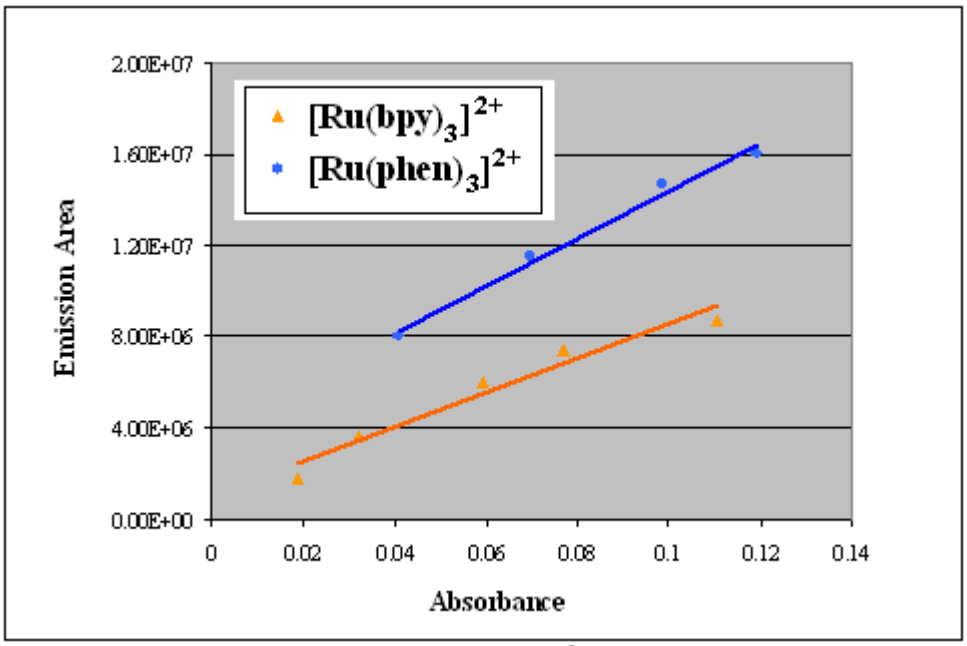

Figure 141. Cross-standardization of $[Ru(bpy)_3]^{2+}$ with the Fluorolog system using $[Ru(phen)_3]^{2+}$ as a reference[65].

The cross-standardization results suggest that the method is accurate and that $[Ru(bpy)_3]^{2+}$ can be confidently used to determine the quantum yield of emissions of other analytes emitting and absorbing in the same spectral regions.

3.D.2. $[Os(bpy)_3]^{2+}$

The published value of quantum yield for $[Os(bpy)_3]^{2+}$ in acetonitrile at room temperature is 0.005.[59] Repeated attempts to reproduce the literature result using $[Ru(bpy)_3]^{2+}$ as a reference, yielded Φ_{em} = 0.0015 ± 0.0002 and a gradient of 1.78 x 10^8 using the ICCD system. Given the discrepancy, tris(2,2'-bipyridine)osmium(II) was not used as a standard in the determination of the quantum yield of emission of

$[(bpy)_2Ru(dpp)]^{2+}$. The gradient was, however, compared to the gradient obtained for $[(bpy)_2Ru(dpp)]^{2+}$ in pH 7 buffer solution (Figure 142), and the ratio Grad(Os)/Grad(dpp) is 1.06: 1. The quantum yield for $[Os(bpy)_3]^{2+}$ calculated versus $[(bpy)_2Ru(dpp)]^{2+}$ using the ratio of the gradients, 1.06: 1, is 0.00215 ± 0.0003. The use of different solvents for osmium and ruthenium samples was accounted for by including the acetonitrile refractive index in the quantum yield calculation, while buffer solutions were considered, as an approximation, to have refractive index comparable to that of water.

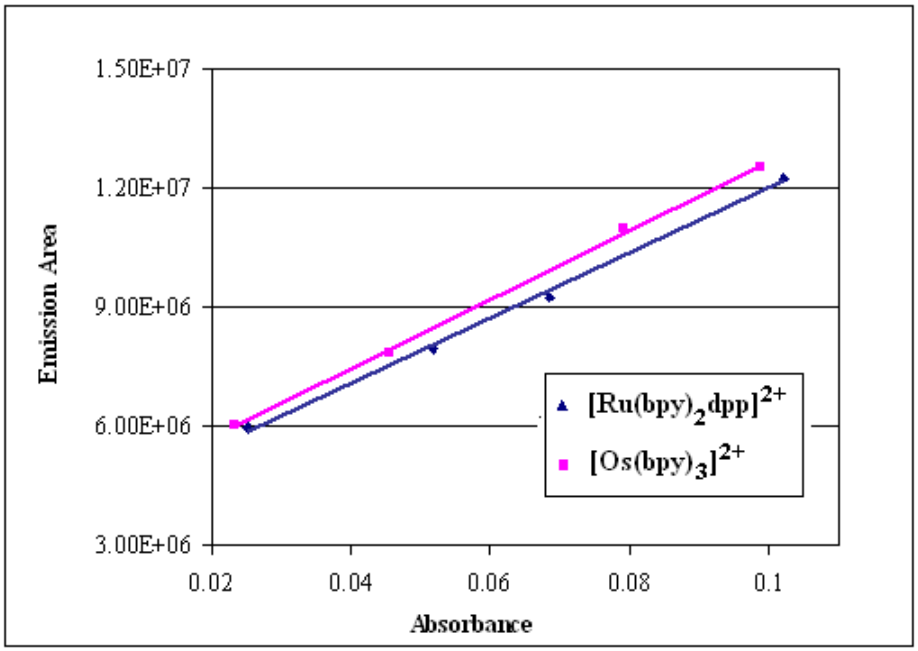

Figure 142. Comparison of the gradients for $[Os(bpy)_3]^{2+}$ in acetonitrile and $[(bpy)_2Ru(dpp)]^{2+}$ in pH 7 buffer obtained using the Argon/ICCD system[65].

3.D.3. $[Ru(bpy)_2dpp]^{2+}$

The quantum yield of emission of the complex in pH 7 buffer was determined using aqueous solutions of $[Ru(bpy)_3]^{2+}$ as standard. The linear fits of the integrated emission across the range of concentrations for the argon/ICCD system is shown in

Figure 143. The ratio of the slopes is 23.2:1 and the quantum yield calculated is Φ_{em} = 0.00198 ± 0.0002. The determination carried out with the Fluorolog system gave Φ_{em} = 0.00175 ± 0.0002.

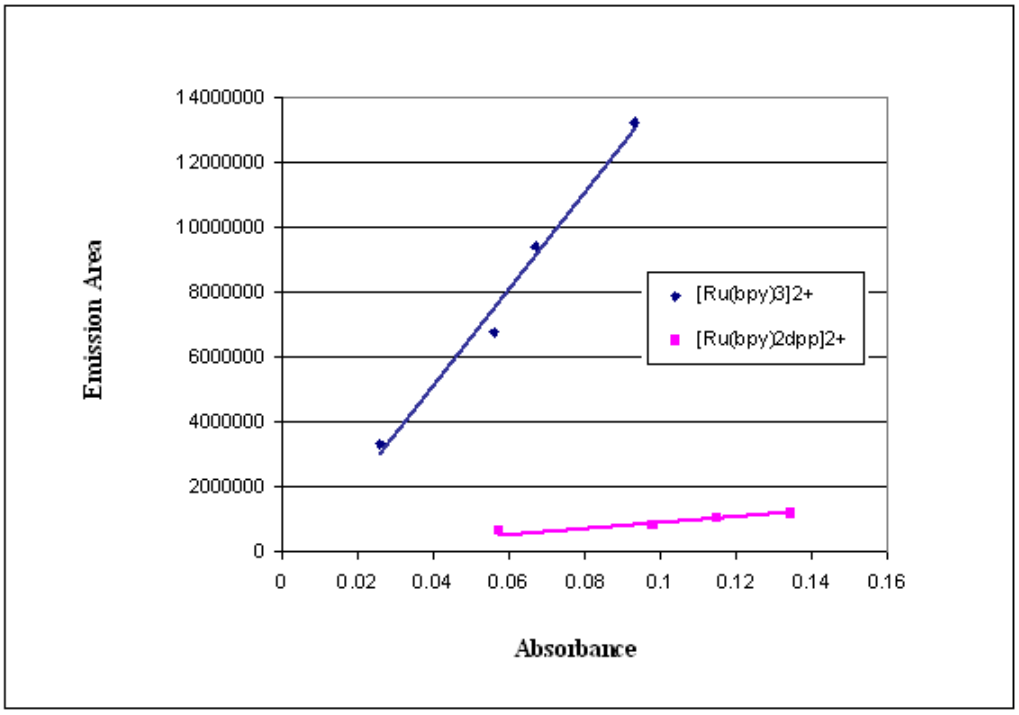

Figure 143. Plots of the integrated emissions of $[(bpy)_2Ru(dpp)]^{2+}$ in pH 7 buffer and $[Ru(bpy)_3]^{2+}$ in water obtained using the Argon/ICCD system versus their absorbance at 436 nm[65].

The quantum yield of $[Ru(bpy)_2dpp]^{2+}$ in water was also determined using $[Ru(bpy)_3]^{2+}$ as a standard. The UV-Vis spectra of standard and analyte solutions are reported in Figures 144 and 145. The steady-state emission spectra of both complexes (Figures 146 and 147) were recorded with the Fluoromax instrument using two excitation wavelengths for comparison, 436 nm and 450 nm, and all emission curves were integrated from 480 to 840 nm. Both sets of spectra and integrated emission areas give consistent results.

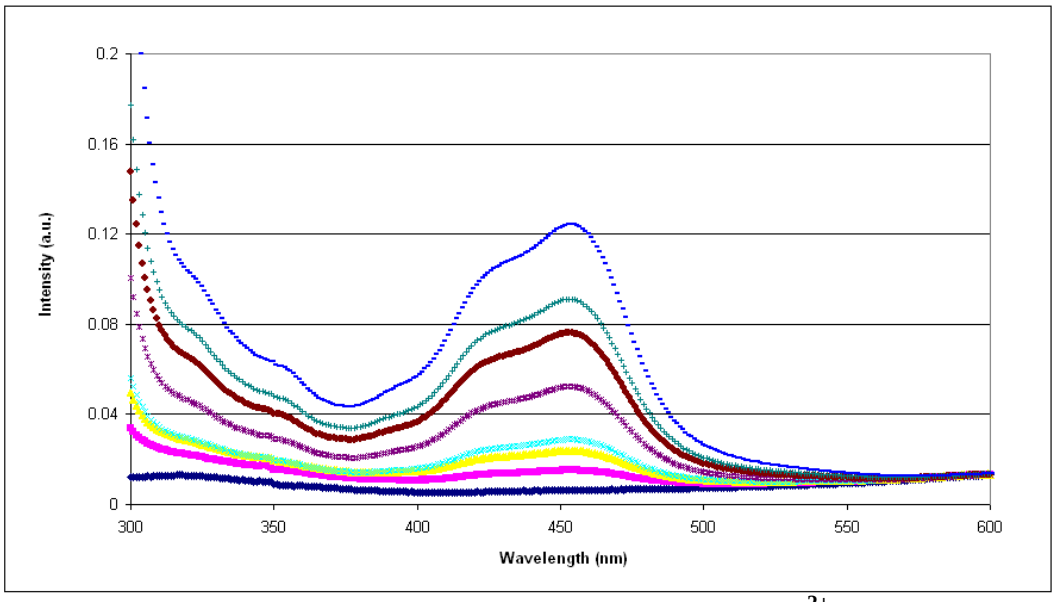

Figure 144. UV-Vis spectra of aqueous solutions of $[Ru(bpy)_3]^{2+}$ ranging from 0.02 to 0.13 in optical density for quantum yield determinations.

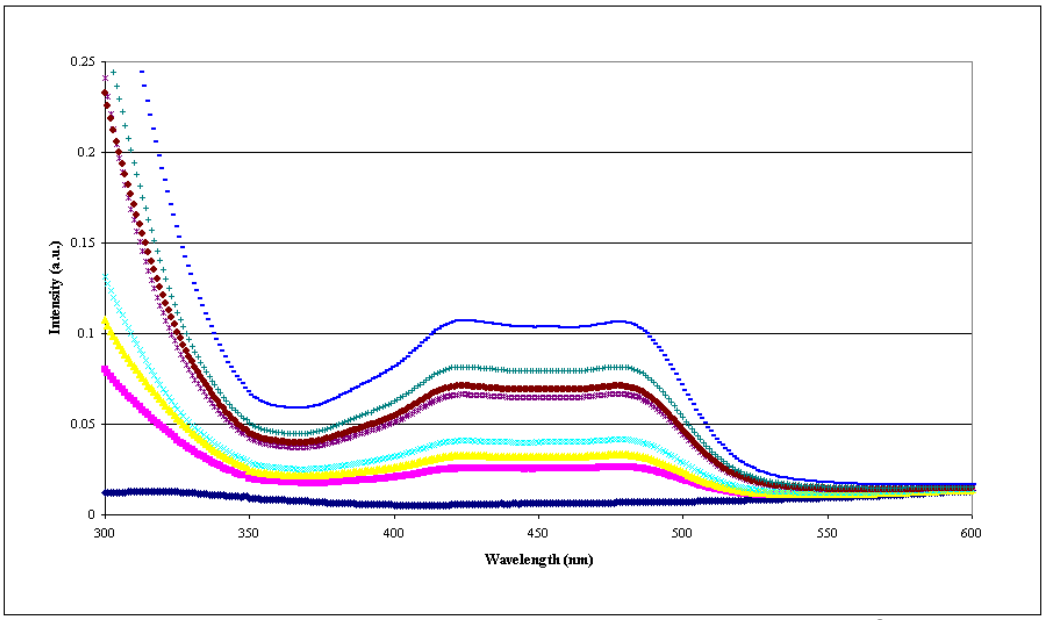

Figure 145. UV-Vis spectra of aqueous solutions of $[(bpy)_2Ru(dpp)]^{2+}$ ranging from 0.02 to 0.11 in optical density for quantum yield determinations.

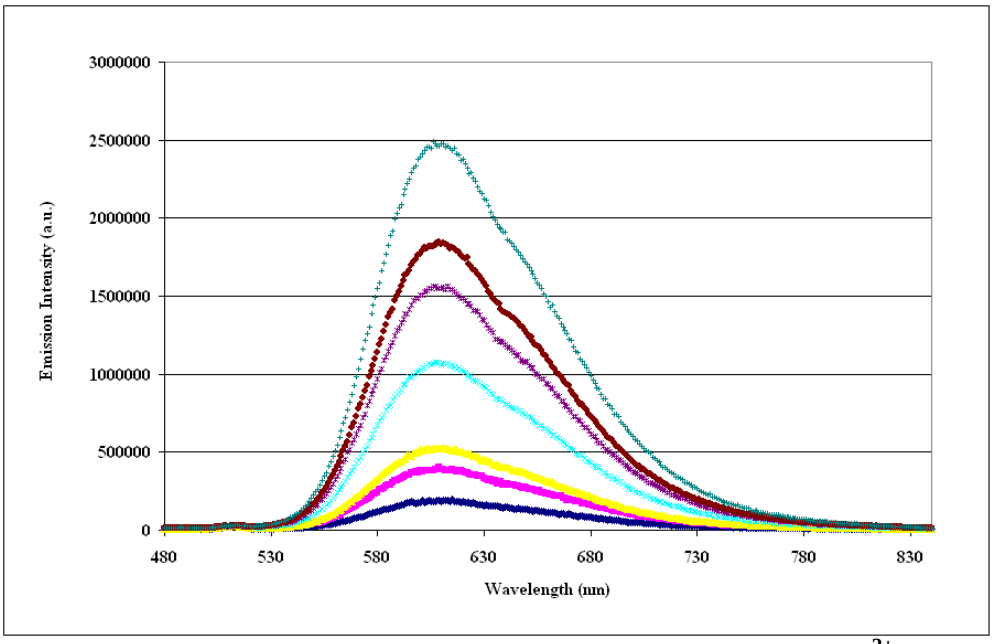

Figure 146. Steady-state emissions of aqueous solutions of $[Ru(bpy)_3]^{2+}$ for quantum yield determinations (λ_{exc} = 436 nm).

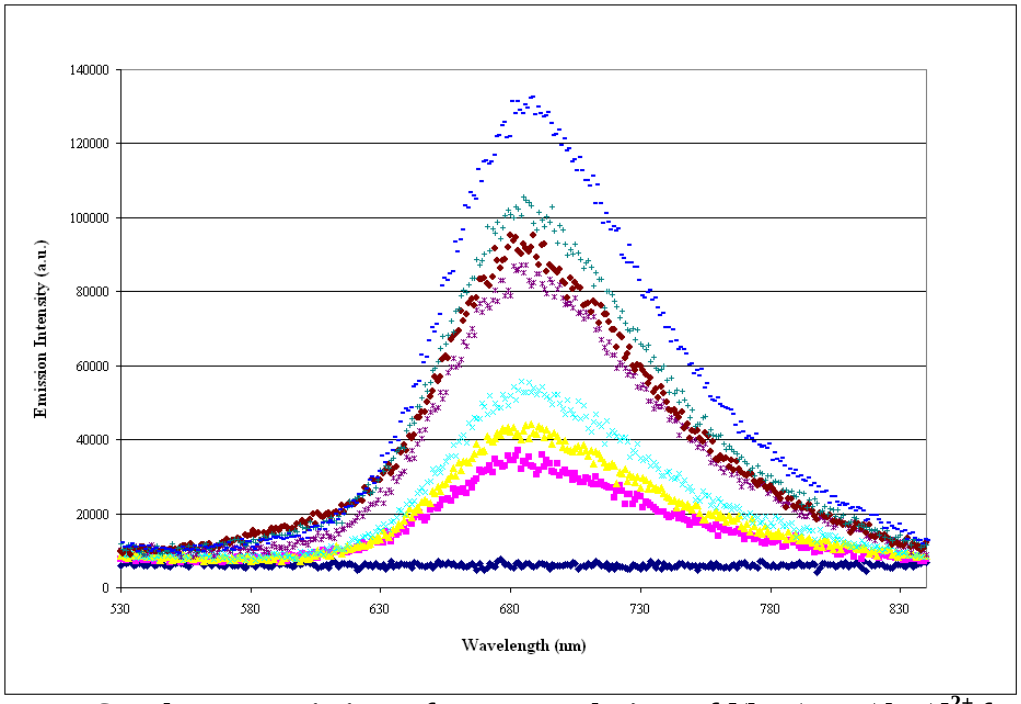

Figure 147. Steady-state emissions of aqueous solutions of $[(bpy)_2Ru(dpp)]^{2+}$ for quantum yield determinations (λ_{exc} = 436 nm).

The quantum yield of $[(bpy)_2Ru(dpp)]^{2+}$ was calculated to be 0.00265 ± 0.0005 using the published value for the quantum yield of $[Ru(bpy)_3]^{2+}$ as a reference. Figure 148 shows the gradients from the graphs of absorbance versus emission area. The ratio of the quantum yields is 15.3:1, slightly lower than the one calculated for $[(bpy)_2Ru(dpp)]^{2+}$ in buffered solution, 23.2:1.

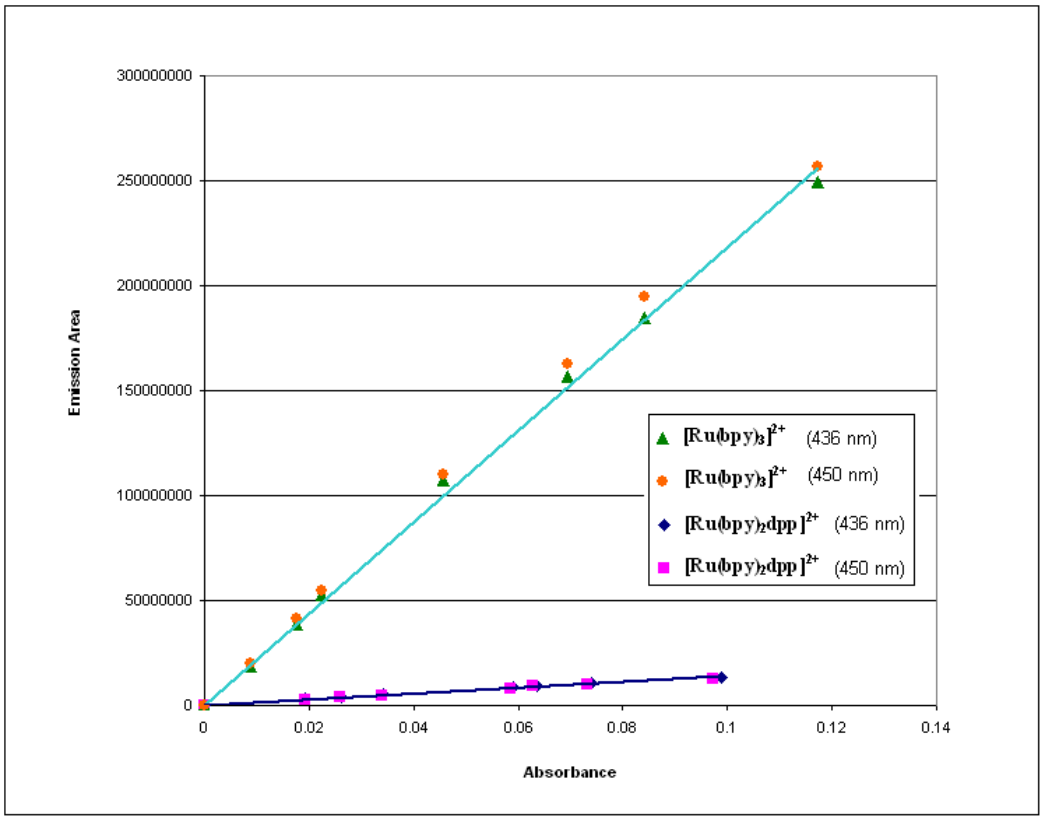

Figure 148. Emission areas of aqueous solutions of $[(bpy)_2Ru(dpp)]^{2+}$ and $[Ru(bpy)_3]^{2+}$ versus their absorbance at 436 and 450 nm.

The radiative and non-radiative rate constants, k_r and k_{nr}, were calculated from equations (25) and (28) using the quantum yield values obtained. For $[(bpy)_2Ru(dpp)]^{2+}$ in water, $k_r = 2.1 \pm 0.2 \times 10^4\ s^{-1}$ and $k_{nr} = 7.8 \times 10^6\ s^{-1}$. Assuming the lifetime of the complex in pH 7 buffer is the same as the one calculated in water, the radiative and non-

radiative rate constants of the complex in pH 7 buffer are $k_r = 1.5 \pm 0.2 \times 10^4\ s^{-1}$ and $k_{nr} = 7.8 \times 10^6\ s^{-1}$.

3.D.4. $[(bpy)_2Ru(dppH)]^{3+}$

The quantum yield determination of the emission from the mono-protonated form of the Ru-dpp complex proved challenging because of the vast difference in emissivity when compared to the standard and to the unprotonated complex itself. In order to maintain a high S/N ratio, the concentration of the samples had to be increased. As a consequence, the operational parameters (mainly the camera gain) had to be changed and the change had to be accounted for as well. Calibration of the camera gain (Figure 16, page 81) allowed correlation of the emission areas with the different camera gains: a change in the camera gain from 73 to 200 introduces a factor of 1:72 in the emission from species at different gain values.

Another problem arose in connection with the Raman band due to water, which appears at 570 nm, has intensity comparable to the intensity of the emission under investigation, and interferes with the integration of the emission (Figure 149).

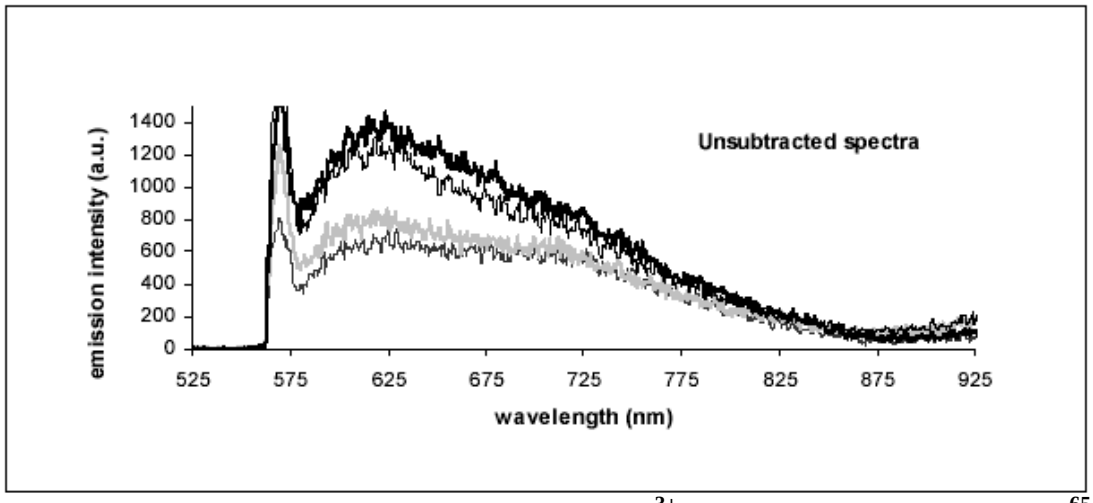

Figure 149. Emission spectra of $[(bpy)_2Ru(dppH)]^{3+}$ at increasing concentrations[65].

Simple mathematical subtraction of the background did not yield clean spectra so a template was constructed for the purpose of smoothing the curves and subtracting the Raman band (Figure 150).

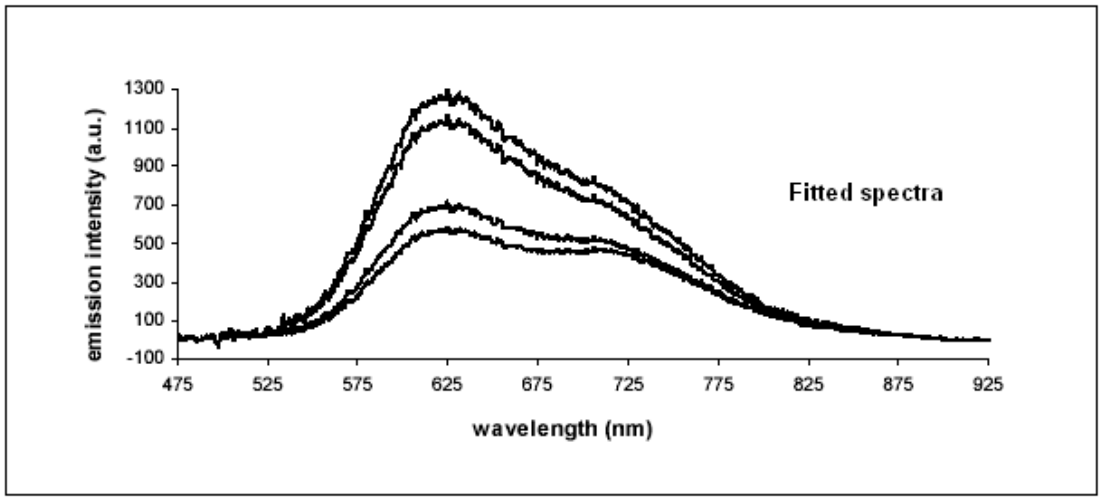

Figure 150. Fitted emission spectra of $[(bpy)_2Ru(dppH)]^{3+}$ complex[65].

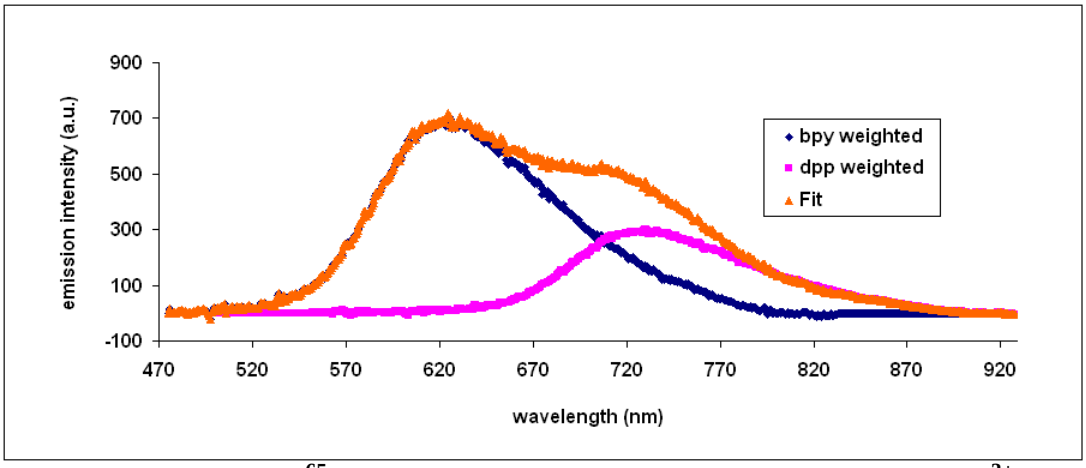

Figure 151. Gaussian fits[65] of the multiple emission from $[(bpy)_2Ru(dppH)]^{3+}$.

Finally the fact that two emissions appear concurrently made it difficult to establish the emission area from each emission. Two fitting templates centered at 624 nm and 730 nm, respectively, had to be used to calculate the individual contributions (Figure

151). The areas under the resolved fits were used for the relative quantum yield determination of each emission.

Relative to the unprotonated complex in pH 7 buffer, the quantum yield of the lower energy transition at 730 nm, which is presumably the transition associated with a LMCT emission from the dpp ligand, was estimated to be $4 \pm 1 \times 10^{-9}$. The quantum yield of the higher energy transition at 624 nm, also calculated relative to the unprotonated complex and assigned to the bpy ligands, was estimated to be $3 \pm 1 \times 10^{-8}$. The ratio of the gradients of the higher energy, 624-nm transition to the lower energy 730-nm one, calculated from the plots of absorbance versus emission area (Figure 152), is 7.56:1.

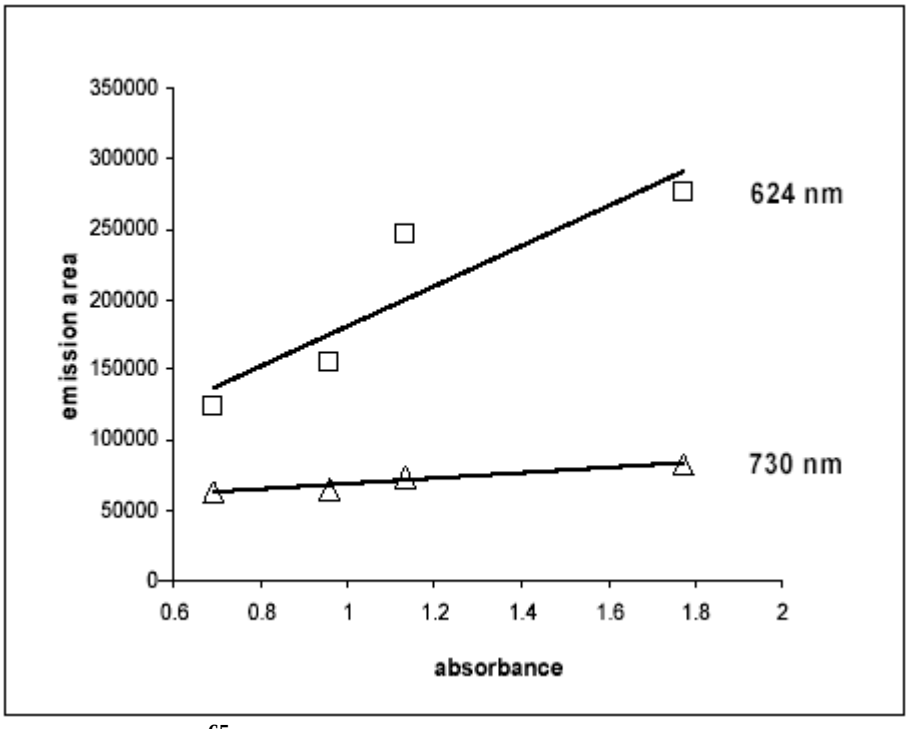

Figure 152. Gradients[65] for the two emissions from the monoprotonated complex $[(bpy)_2Ru(dppH)]^{3+}$.

3.D.5. $[(bpy)_2Ru(dpp)]^{2+}$- Zn^{2+} and $[(bpy)_2Ru(dpp)]^{2+}$- Cd^{2+}

The quantum yields of the presumed bimetallic complexes, $[(bpy)_2Ru(dpp\text{-}Zn)]^{4+}$ and $[(bpy)_2Ru(dpp\text{-}Cd)]^{4+}$ in pH=5 buffer solution were determined relative to $[(bpy)_2Ru(dpp)]^{2+}$ in pH 7 buffer. The emission spectra were recorded using the Nd-Yag/ICCD system and were integrated from 600 to 900 nm (Figures 153 and 154). As was the case for the mono-protonated $[(bpy)_2Ru(dppH)]^{3+}$, the camera gain had to be adjusted in order to increase the S/N ratio and obtain better spectra.

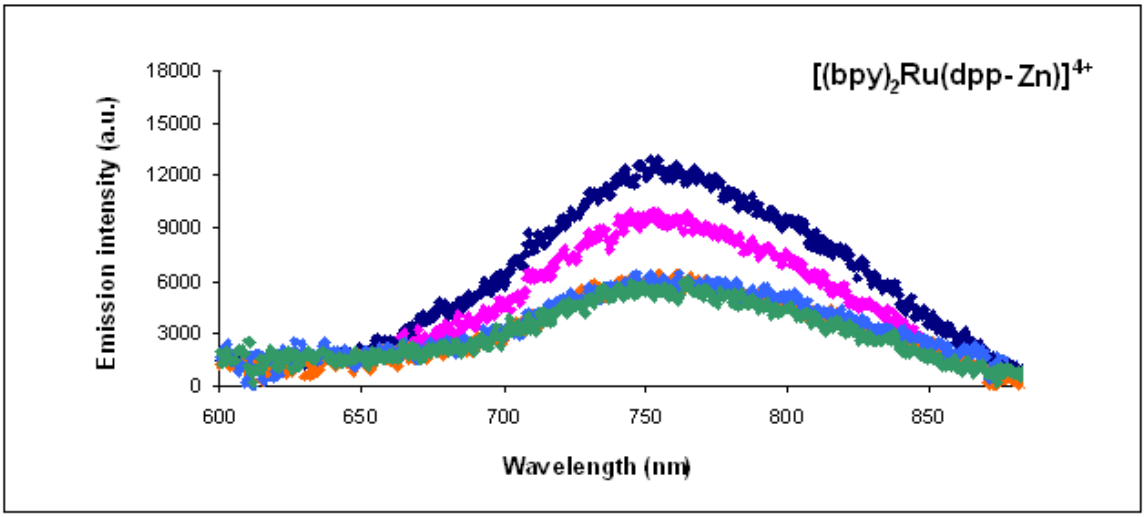

Figure 153. Emission spectra[65] of aqueous solutions of $[(bpy)_2Ru(dpp)]^{2+}$ and Zn^{2+}.

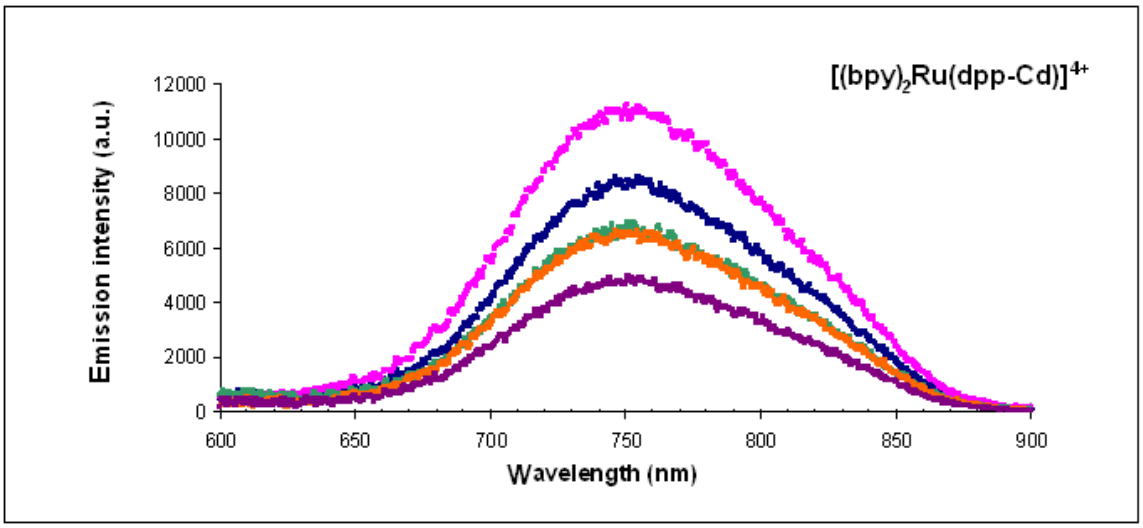

Figure 154. Emission spectra[65] of aqueous solutions of $[(bpy)_2Ru(dpp)]^{2+}$ and Cd^{2+}.

The linear fits of the integrated emission areas across the range of absorbances (concentration) for both bi-metallics relative to the uncoordinated complex are shown in Figures 155 to 157. The ratios of the slopes between $[(bpy)_2Ru(dpp)]^{2+}$ and $[(bpy)_2Ru(dpp\text{-}Zn)]^{4+}$ and between $[(bpy)_2Ru(dpp)]^{2+}$ and $[(bpy)_2Ru(dpp\text{-}Cd)]^{4+}$ are nearly identical: 7.06:1 and 7.62:1, respectively. It follows that the calculated quantum yield are also similar: 0.00026 ± 0.00003 for the presumed Ru-Zn complex and 0.00024 ± 0.00003 for Ru-Cd. From the quantum yield values, the radiative and non-radiative rate constants were calculated. The rate constants for $[(bpy)_2Ru(dpp\text{-}Zn)]^{4+}$ calculated using the lifetime value of 54 ns are: $k_r = 4.7 \pm 0.2 \times 10^3\ s^{-1}$ and $k_{nr} = 1.8 \times 10^7\ s^{-1}$. The rate constants for $[(bpy)_2Ru(dpp\text{-}Cd)]^{4+}$ calculated using the lifetime value of 63 ns are: $k_r = 3.8 \pm 0.2 \times 10^4\ s^{-1}$ and $k_{nr} = 1.6 \times 10^7\ s^{-1}$.

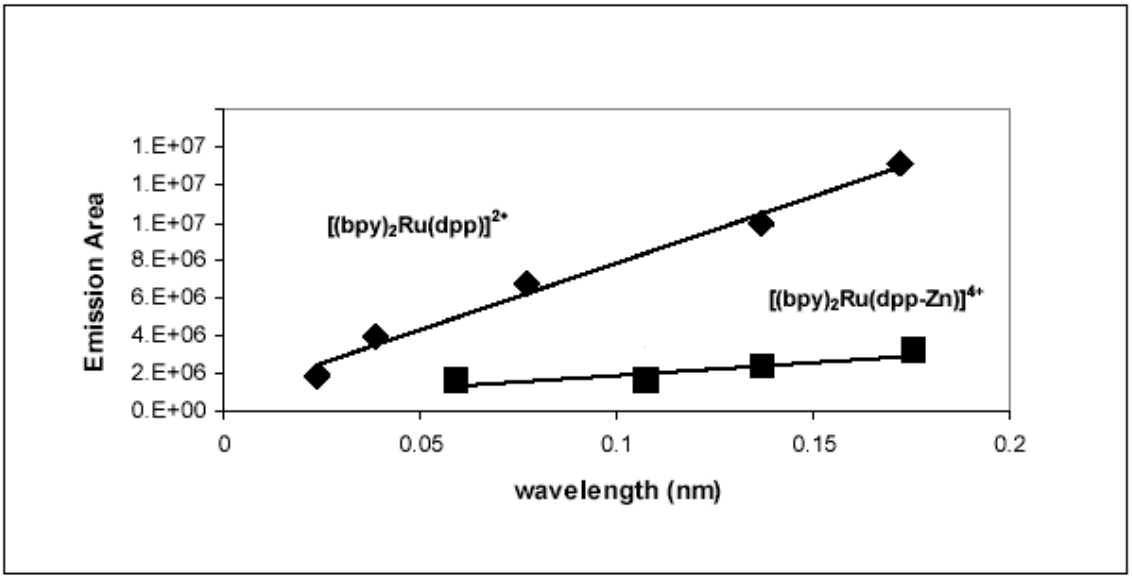

Figure 155. Emission areas of $[(bpy)_2Ru(dpp)]^{2+}$ and $[(bpy)_2Ru(dpp\text{-}Zn)]^{4+}$ versus their absorbance at 532 nm[65].

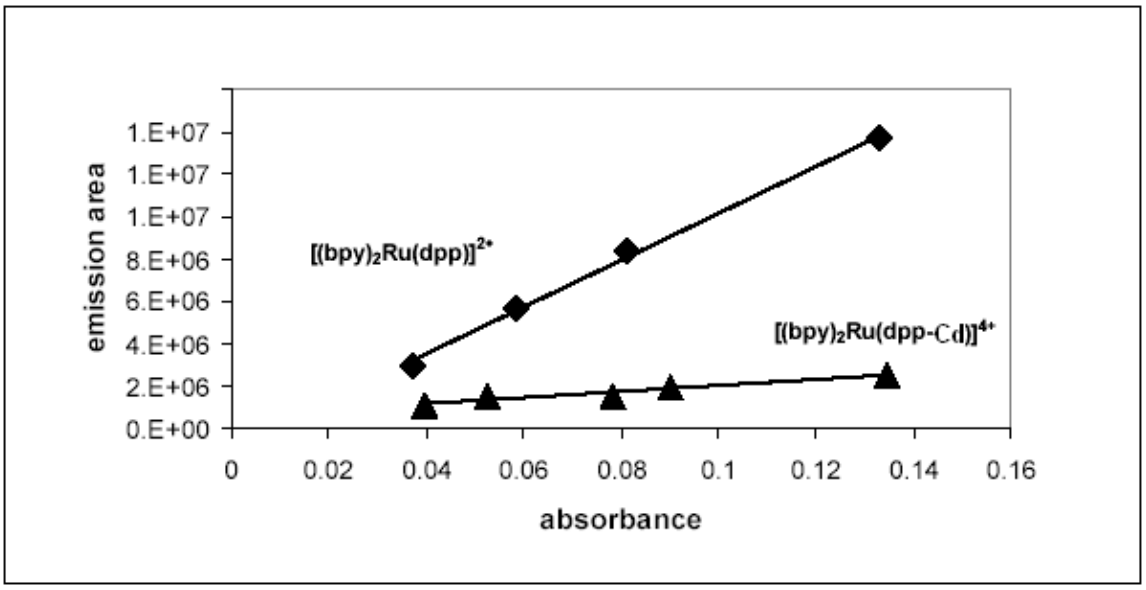

Figure 156. Emission areas of $[(bpy)_2Ru(dpp)]^{2+}$ and $[(bpy)_2Ru(dpp\text{-}Cd)]^{4+}$ versus their absorbance at 532 nm[65].

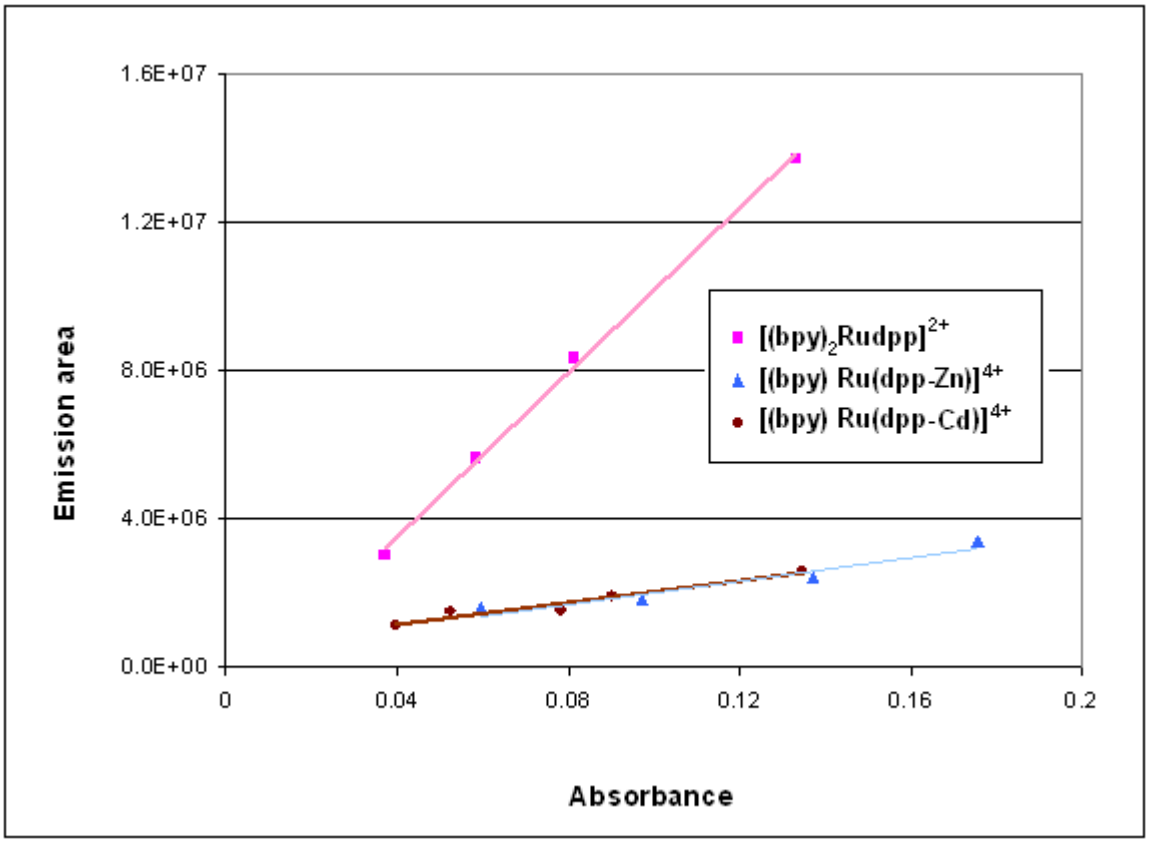

Figure 157. Emission areas of $[(bpy)_2Ru(dpp)]^{2+}$, $[(bpy)_2Ru(dpp\text{-}Zn)]^{4+}$ and $[(bpy)_2Ru(dpp\text{-}Cd)]^{4+}$ versus their absorbance at 532 nm.

3.D.6. $[Ru(bpy)_2pypz]^{2+}$

To determine the quantum yield of emission of $[(bpy)_2Ru(pypz)]^{2+}$ in water, aqueous solutions of $[(bpy)_2Ru(dpp)]^{2+}$ and $[Ru(bpy)_3]^{2+}$ were used as references and cross-references, respectively. The UV-Vis spectra and steady-state emission spectra of $[(bpy)_2Ru(pypz)]^{2+}$ solutions at increasing concentrations of the complex are reported in Figure 158 and 159. The emission spectra were recorded with the Fluoromax instrument using two excitation wavelengths for comparison, 436 nm and 450 nm, and all emission curves were integrated from 480 to 840 nm. Both sets of spectra and integrated emission areas give consistent results.

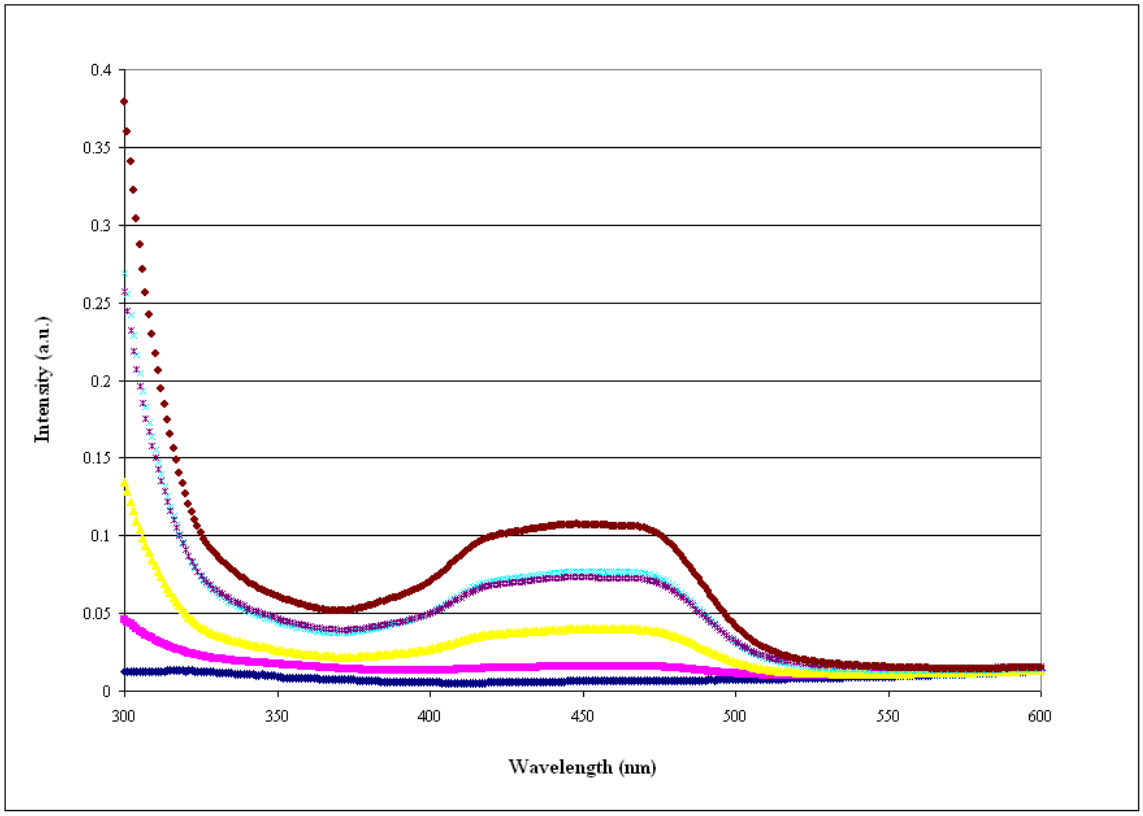

Figure 158. UV-Vis spectra of $[Ru(bpy)_2pypz]^{2+}$ in water at increasing concentrations of the complex.

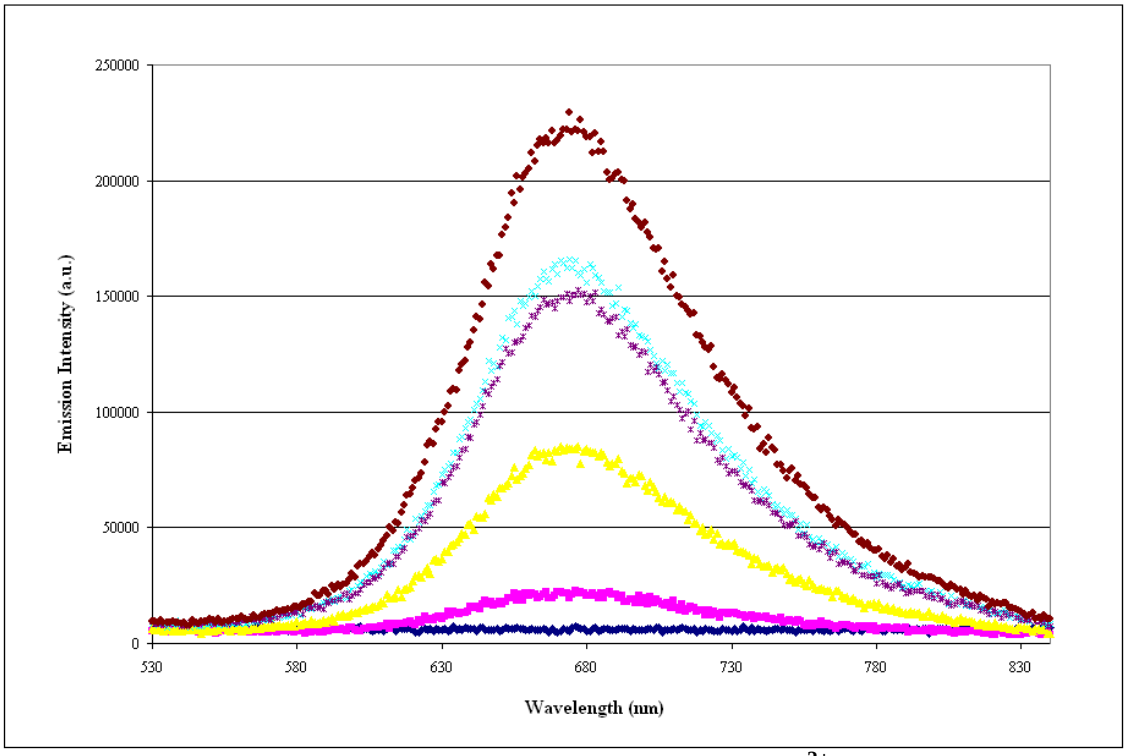

Figure 159. Steady-state emission spectra of $[Ru(bpy)_2pypz]^{2+}$ recorded with 436-nm excitation wavelength at increasing concentrations of the complex.

The ratios of the gradients, Grad(ref)/Grad(x), obtained from the graphs of absorbance versus emission area in Figure 160, are 1:1.64 for both the 436- and the 450-nm data sets. The quantum yield value calculated using the gradient ratio and the reference value for the $[(bpy)_2Ru(dpp)]^{2+}$ quantum yield is 0.0042 ± 0.0005; a factor of ten less than the quantum yield for $[Ru(bpy)_3]^{2+}$. From equations (25) and (28) and the lifetime value for $[Ru(bpy)_2pypz]^{2+}$ of 150 ns, the radiative and non-radiative rate constants calculated are: $k_r = 2.80 \pm 0.3 \times 10^4\ s^{-1}$ and $k_{nr} = 6.64 \times 10^6\ s^{-1}$.

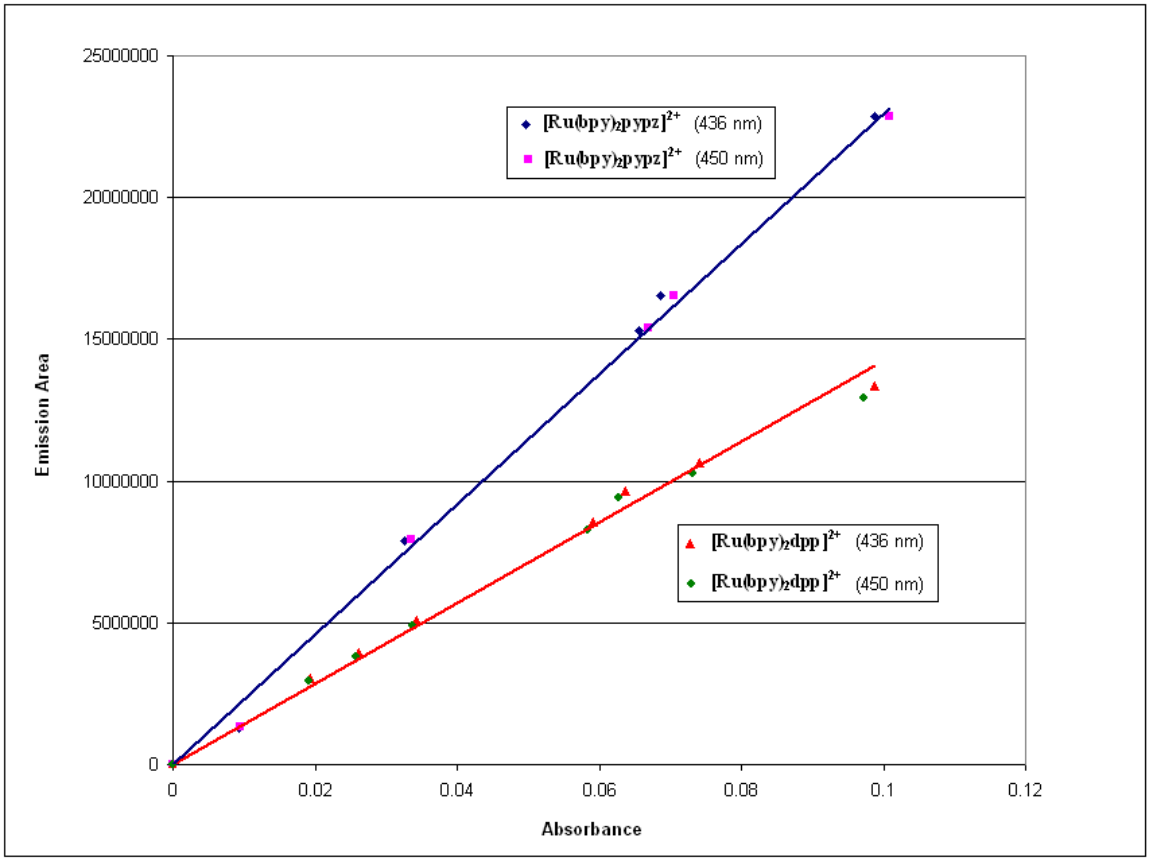

Figure 160. Graphs of emission area versus absorbance at 436 and 450 nm for $[(bpy)_2Ru(dpp)]^{2+}$ and $[Ru(bpy)_2pypz]^{2+}$.

3.D.7. $[(bpy)_2Ru(pypzH)]^{3+}$

The luminescence spectra of the complex $[(bpy)_2Ru(pypz)]^{2+}$ at increasing acidity showed no evidence of a red shift of the emission due to protonation at the pypz site, indication that the protonated species in not emissive. However, below pH 2 a new emission is observed centered at 610 nm. The quantum yield of the new emission at lower wavelength was determined in 5M sulfuric acid solutions with increasing concentrations of the ruthenium complex corresponding to values of absorbance ranging from 0.02 to 0.1 in optical density (the UV-Vis spectra are shown in Figure 161). The steady-state emission spectra were recorded on the Fluoromax-P spectrometer with 2µm

slit, and 436-nm (Figure 162) and 450-nm excitation. Emission areas were integrated from 545-830 nm. The integration was complicated by the presence of the Raman band of water at 514 nm (Figure 163). Although the Raman band itself falls outside the range of integration, the tail of the band and the background emission both contributed to a decrease in the signal to noise ratio at lower concentrations of the complex and larger uncertainty in the quantum yield value.

The gradient of the integrated emission across the range of concentrations was compared to the gradients obtained for aqueous solutions of $[(bpy)_2Ru(pypz)]^{2+}$, $[Ru(bpy)_3]^{2+}$ and $[(bpy)_2Ru(dpp)]^{2+}$. The ratios of the gradients, Grad(ref)/Grad(x), between $[(bpy)_2Ru(dpp)]^{2+}$ and $[(bpy)_2Ru(pypzH)]^{3+}$, Figure 164, are 5:1 and 4:1 for 436 and 450 nm, respectively. The quantum yield value calculated using the average of the gradient ratio and the reference value for the $[(bpy)_2Ru(dpp)]^{2+}$ quantum yield is 0.000696 ± 0.00005. The solvents' refractive indices, 1.33 for water at 20˚C and 1.44 for sulfuric acid solutions having density of 1.811 at the same temperature, were included in the calculation in accordance with equation (83). From equations (25) and (28) and the lifetime value of 400 ns for the 610-nm emission of $[(bpy)_2Ru(pypzH)]^{3+}$, the radiative and non-radiative rate constants calculated are: $k_r = 1.74 \pm 0.12 \times 10^3\ s^{-1}$ and $k_{nr} = 2.49 \times 10^6\ s^{-1}$.

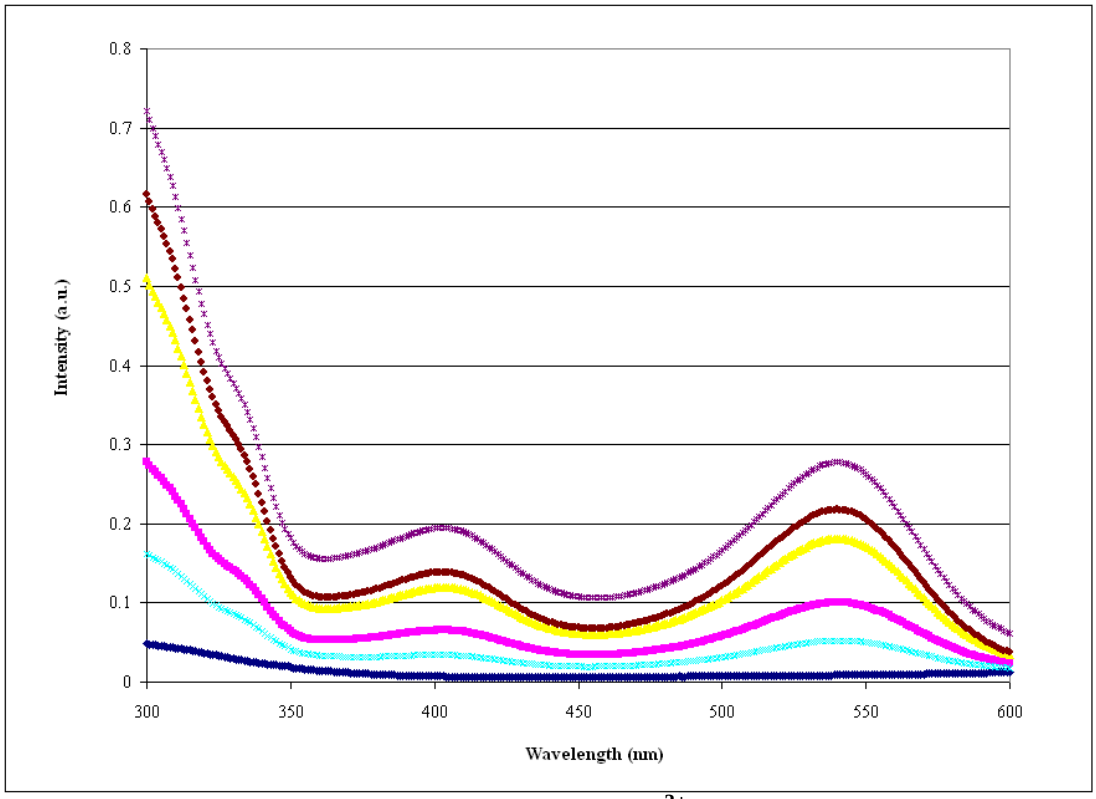

Figure 161. UV-Vis spectra of $[(bpy)_2Ru(pypzH)]^{3+}$ at increasing concentrations of the complex.

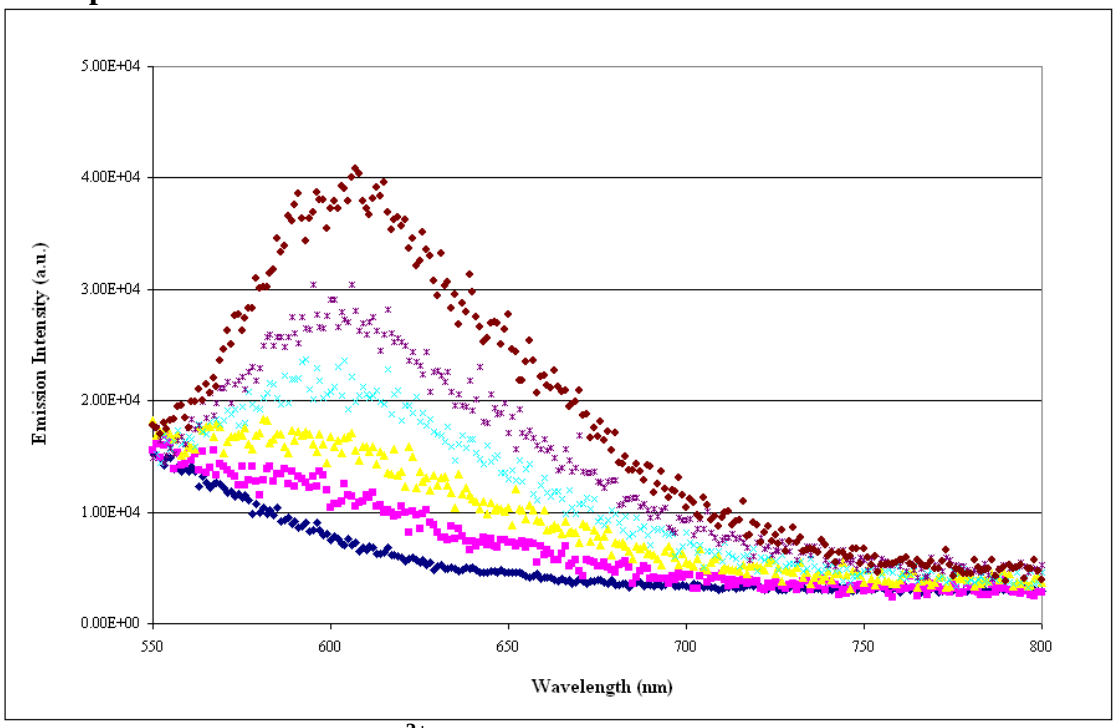

Figure 162. $[(bpy)_2Ru(pypzH)]^{3+}$ emissions obtained with 436-nm excitation at increasing concentrations for QY det.

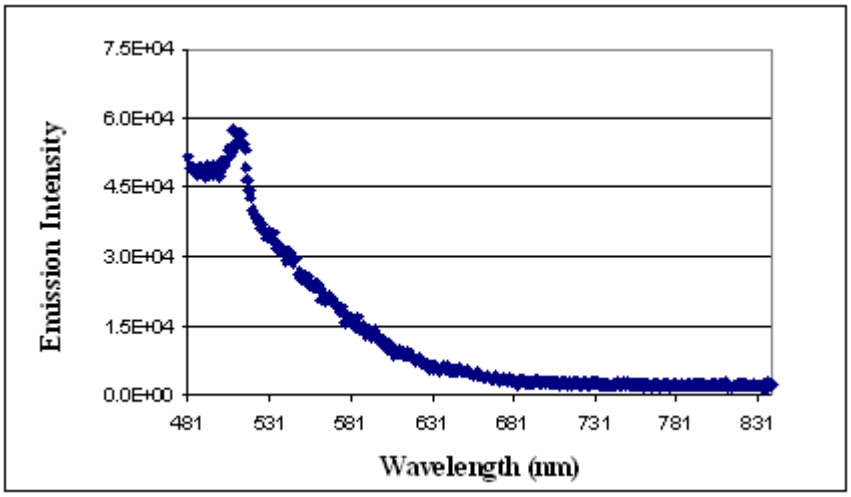

Figure 163. Background emission and Raman band of water from the 5M sulfuric acid solutions for the quantum yield determination of $[(bpy)_2Ru(pypzH)]^{3+}$ (λ_{exc} = 436 nm).

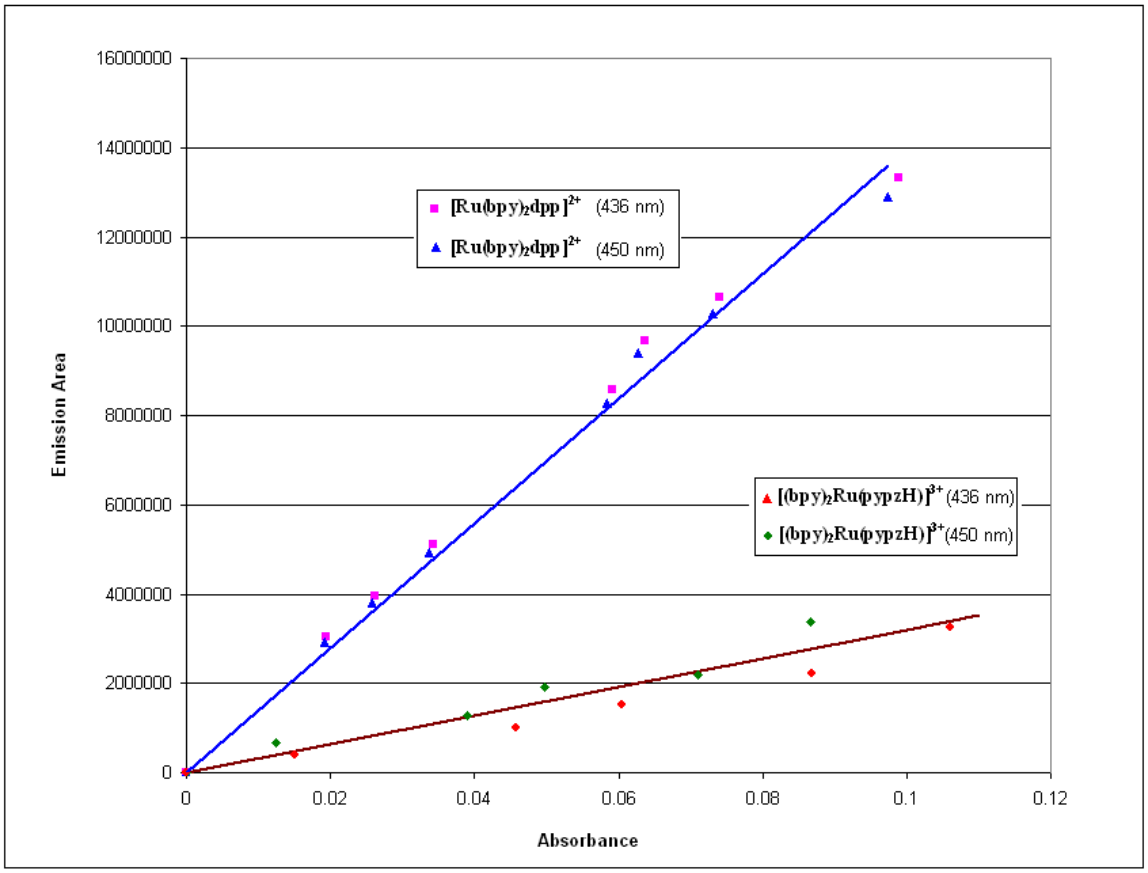

Figure 164. Graphs of emission area versus absorbance at 436 and 450 nm for $[(bpy)_2Ru(dpp)]^{2+}$ and $[(bpy)_2Ru(pypzH)]^{3+}$.

4. Discussion

4.A. Characterization

4.A.1. NMR of free ligands: pypz and dpp

The ^{1}H-NMR spectrum of 2-(2-pyridyl)pyrazine in $CDCl_3$ (Figure 25) shows seven signals in the aromatic region for each of the CH-groups present in the ligand. The assignment of each peak was facilitated by the comparison with the position of the NMR peaks in un-substituted pyridine and pyrazine molecules and symmetrical 2,2'-bipyridine (bpy) and 2,2'-bipyrazine (bpz).

Table 19: ^{1}H-NMR chemical shifts of free ligands.

H-position	py[81]	pz[82]	bpy	bpz[82]	pypz	dpp[83]
2	--	8.59 (s)	--	--	--	--
3	--	8.59 (s)	--	9.59 (s)	9.66 (s)	--
4	--	--	--	--	--	--
5	--	8.59 (s)	--	8.64 (d)	8.64 (d)	8.79
6	--	8.59 (s)	--	8.64 (d)	8.64 (d)	8.79
2'	8.62 (m)	--	--	--	--	--
3' (3'')	7.29 (m)	--	8.50 (d)	--	8.39 (d)	7.86 (d)
4' (4'')	7.68 (m)	--	7.66 (t)	--	7.88 (t)	7.91 (t)
5' (5'')	7.29 (m)	--	7.12 (t)	--	7.39 (t)	7.32 (t)
6' (6'')	8.62 (m)	--	8.59 (d)	--	8.75 (d)	8.25 (d)

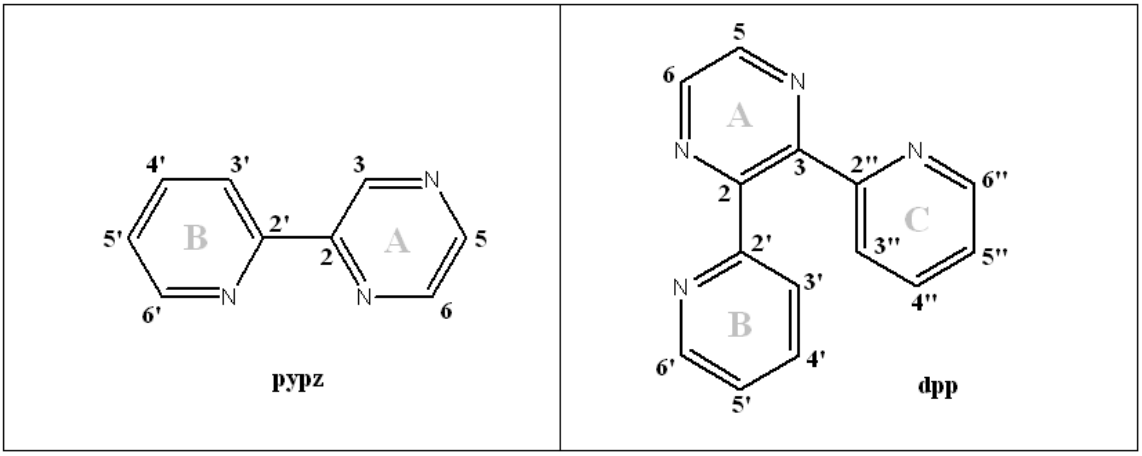

Figure 165. Structure and peak numbering for pypz and dpp ligands.

The protons on the pyrazyl ring of pypz fall in the same range as the protons in bpz. The singlet at lower field (9.66 ppm) is assigned to H-3 because it is strongly deshielded by the electron-withdrawing pyridyl ring in position 2. The doublet at 8.64 ppm corresponds to the nuclei H-5 and H-6 with an indirect coupling constant of 4.0 Hz. With the exception of H-3', all protons on the pyridyl ring of pypz move downfield compared to the corresponding protons on bpy. A combination of an inductive effect and a mesomeric effect may be responsible for the shift: the former operates through bonds, while the latter influences protons' shielding through resonance structures. The signals assigned to H-4' and H-5' split into triplets due to the coupling to the adjacent nuclei, while H-3' and H-6' form doublets by coupling with only one immediate neighbor (J(3'-4') = 4 Hz; J(5'-6') = 8 Hz).

The chemical shifts for the dpp molecule are listed in Table 19 to compare the protons belonging to the two aromatic rings (A & B in Figure 165) with and without the additional pyridyl ring (ring C). In dpp, the protons on the pyrazyl moiety are only slightly less shielded by the presence of the second electron-withdrawing substituent. Surprisingly, the protons most affected by the presence of the third ring (ring C in Figure 165) are those on the pyridyl portion of the molecule (ring B). According to crystallographic studies[84] by Peterson *et al.*, the pyridyl rings twist to minimize steric interactions within the molecule. The dihedral angle between the pyridyl rings and the pyrazine ring is 42.2°. Protons H-3' and H-6' are partially affected by the ring current originating from the other pyridyl ring and become more shielded, thus shifting upfield.

In the ^{13}C-NMR spectrum of pypz, Table 20, all the signals of the pyridyl ring fall in the range expected, coincident with the position of the carbon atoms in bipyridine. The

signals due to the carbons of the pyrizyl ring are more affected by the presence of the pyridyl ring and the effect is manifested in the different positions of C-2 and C-3 compared to the positions of analogous carbons on bipyrazine. The C-2 signal is shifted downfield by the inductive electron-withdrawing effect of the pyridyl substituent in position 2, whereas the C-3 signal is shifted upfield as a result of the change in charge distribution in the resonance structures.

Table 20: ^{13}C-NMR chemical shifts of several free ligands.

C-position	py[82]	pz[82]	bpy	bpz	pypz
2	--	145.22	--	149.55	151.5
3	--	145.22	--	145.26	143.7
4	--	--	--	--	--
5	--	145.22	--	143.78	144.8
6	--	145.22	--	143.66	143.9
2’	149.94	--	156.14	--	154.6
3’	123.75	--	121.00	--	121.8
4’	135.89	--	136.75	--	137.5
5’	123.75	--	123.63	--	124.8
6’	149.94	--	149.12	--	149.9

4.A.2. NMR of ruthenium complexes

Unlike the free ligands, the ^{1}H-NMR spectra of $[(bpy)_2Ru(dpp)]^{2+}$ and $[(bpy)_2Ru(pypz)]^{2+}$ were recorded in D_2O and the increased polarity is expected to have a slightly deshielding effect. The chemical shifts of the above-mentioned complexes and some tris-homoleptic ruthenium complexes are listed in Table 21 for reference. The presence of a heavy atom in the vicinity of a conjugated system has a general electron-withdrawing, inductive effect. Ruthenium is no exception and the chemical shifts of the

protons on the ligands are further shifted upfield as a result. Additionally, bidentate coordination brings ligands close and forces them to adopt a *cis* conformation.

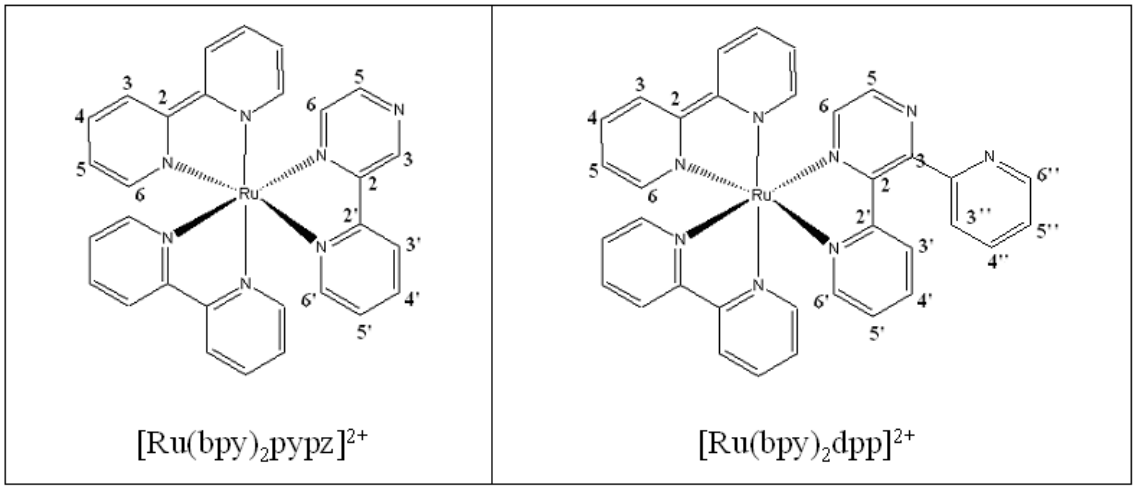

Figure 166: Structure and peak numbering for two ruthenium diimine complexes.

Table 21: 1H-NMR chemical shifts in ppm of Ru(II) diimine complexes.

H_n	$(L)_2Ru^{II}(dpp)$	$(L)_2Ru^{II}(pypz)$	$Ru^{II}(L)_3$	$Ru^{II}(dpp)_3$	$Ru^{II}(bpz)_3$
3 (bpy)	8.66	8.57	8.93	--	--
4 (bpy)	8.1 – 8.3	8.08	8.20	--	--
5 (bpy)	7.5 – 7.6	7.45	7.55	--	--
6 (bpy)	7.7 – 7.9	7.7-7.8	7.77	--	--
3	--	9.62	--	--	10.17
4	--	--	--	--	--
5	8.54	8.03	--	8.60	8.76
6	8.24	8.42	--	8.07	8.03
3’	7.22	8.7	--	7.26	10.17
4’	7.71	8.1	--	7.73	--
5’	7.40	7.48	--	7.42	8.76
6’	8.00	7.87	--	7.76	8.03
3’’	8.00	--	--	7.97	--
4’’	8.29	--	--	8.13	--
5’’	7.85	--	--	7.65	--
6’’	8.78	--	--	8.66	--

*L: bpy **Values for $[Ru(bpz)_3]^{2+}$ were determined in DMSO-d[82].

Protons in position 6 and 6’ in particular, reveal the indirect effect of the proximity of a cationic metal. Whether belonging to bpy, dpp or pypz, these protons are moved upfield by the ring current arising from their neighboring ligand[85]. The *cis* conformation, on the other hand, affects H-3 and H-3’ through Van der Waals deshielding interaction as evidenced by the downfield shift. The protons H-6’’ and H-3’’ on the uncoordinated pyridyl ring of dpp behave in quite the opposite way, as rotation along the C_2-$C_{3''}$ axis frees H-3’’ from possible steric interactions and moves H-6’’ away from any ring current.

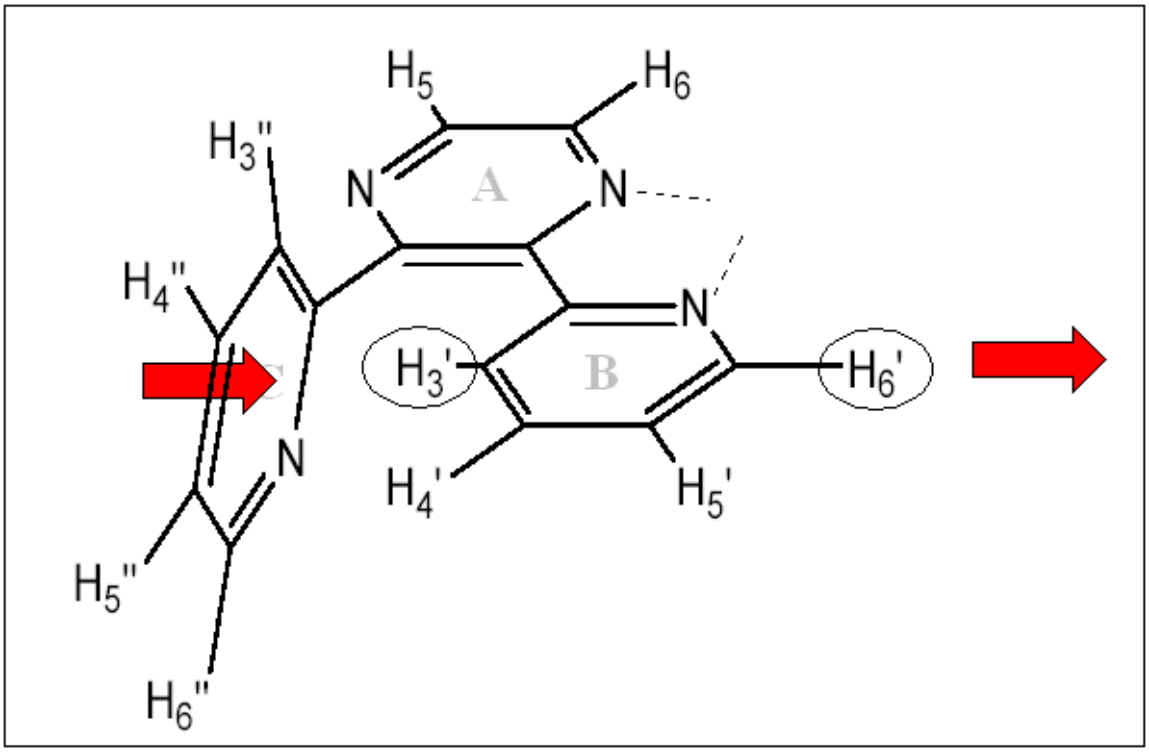

Figure 167: Ring current effect on dpp’s protons, H-3’ and H-6’, and on H-3’’ and H-6’’.

Aside from the common effects described above that coordination has on ligands, it is relevant to mention the important aspects in which the two complexes differ. In

$[(bpy)_2Ru(dpp)]^{2+}$, coordination forces the additional pyridyl ring to twist even further out of the plane and increases the ring current effect mentioned earlier (Figure 167). As a result, H-3' is shifted to higher fields upon coordination. The $[(bpy)_2Ru(pypz)]^{2+}$ complex is not impacted by the ring current of a third ring, hence the most relevant force responsible for the chemical shift of proton H-3' in this case is due to the deshielding Van der Waals interaction mentioned above, which shifts H-3' in the opposite direction, downfield. The presence of the third ring also affects the bpy ligands differently, rendering them non-equivalent. The chemical and magnetic likeness of H-5 and H-6 is removed in both complexes as the asymmetric ligand coordinates to ruthenium. However, in the Ru-pypz complex the proton in position 5 is the more shielded one and shifts upfield more than the proton in position 6, possibly because of the absence of the electron-withdrawing third ring.

4.A.3. Electronic Spectra

In depth analysis of the absorption spectra of $[(bpy)_2Ru(dpp)]^{2+}$ and $[(bpy)_2Ru(pypz)]^{2+}$ reveals overt similarities as well as a few distinctions. Both complexes absorb in the 200-300nm UV-region and 400-500nm visible range. Absorption maxima and extinction coefficients recorded at room temperature for homoleptic $Ru(LL')_3^{2+}$ and heteroleptic $Ru(LL)_2(LL')^{2+}$ divalent ruthenium complexes, along with the complexes in question, are reported in Table 22. The complexes were chosen for comparison based on the fact that they possess the same charge, the same or very similar geometries, the same electronic/ligand structure, and, except for $Ru(bpy)_3^{2+}$, nitrogen atoms with electron lone pairs on the periphery of the aromatic ligands. Many of

the conclusions that were drawn from studies concerning one or another of the complexes from the homologous series listed below apply to our complexes.

Table 22. Spectral data, λ_{max}, in nm and (log ε), for ruthenium diimine complexes.

Species	π-π^*	MLCT
$[Ru(bpz)_3]^{2+}$ [b, a]	241 (4.37), 295 (4.79)	266 (4.34), 343 (4.27), 415 (sh)[d], 443 (4.18)
$[Ru(bpy)_3]^{2+}$ [a]	238 (4.47), 250 (4.40), 285 (4.94)	323 (3.81), 345 (3.81), 430 (sh)[d], 452 (4.16)
$[Ru(bpm)_3]^{2+}$ [d]	252[e]	332, 360(sh), 418[e], 452
$[Ru(bpdz)_3]^{2+}$ [h]	266	344, 414, 444
$[Ru(dpp)_3]^{2+}$ [c]	295	428 (sh), 456
$[Ru(bpy)_2bpdz]^{2+}$ [h]	**240, 278**	**360(sh)[h], 410, 472**
$[Ru(bpy)_2bpz]^{2+}$ [d]	**242[e], 283[e]**	**343(sh)[e], 386(sh)[e], 403, 483**
$[Ru(bpy)_2bpm]^{2+}$ [c, d]	**240, 282**	**360[e], 416, 490(sh)**
$[Ru(bpy)_2dpp]^{2+}$ [f]	**244 (4.39), 284 (4.76)**	**432 (3.98), 487 (*3.66*[g] – 3.96)**
$[Ru(bpy)_2pypz]^{2+}$ [f]	**241 (4.37), 250 (4.34), 284 (4.82)**	**435 (4.04), 476 (*3.72*[g] – 4.04)**

[a] Reference 43. [b] Value measured in acetonitrile. [c] In water[62]. [d] in water[86]. [e] in ACN[87]. [f] in water (present work). [g] Estimate based on Gaussian de-convolution. [h] in water[88].

The higher-energy bands in the 200-300 nm UV region are reflective of the specific diimine ligands and are assigned as π-π^* transitions within the ligand rings. Table 23 reports the free ligands' absorption band values for comparison with the absorption values for the ligands coordinated to ruthenium(II). The bidentate diimine ligands compiled in Table 23 are very much alike in structure and composition hence it is not surprising that all the transitions fall at approximately the same wavelength. Solvent unchanged, the presence of two additional peripheral nitrogens in going from bpy to bpz does not seem to affect the position of the absorption maxima of the free ligands. Due to solubility differences, the absorption spectrum of the free dpp ligand was recorded in a

different solvent, acetonitrile, hence the attempt to highlight the effect that the presence of a third ring with two peripheral nitrogens has on the absoprtion spectrum, when compared to that of free bpy, is less conclusive. More significant, perhaps, is to observe that, when measured in the same medium, the UV bands for dpp coordinated to ruthenium fall in the same energy range as the bands for the other free and coordinated diimine ligands. The UV region of the spectrum is not considerably affected by coordination to the metal as much as it is dependent on the nature of the solvent and, as will be further discussed in the next chapter, on protonation.

Table 23. Spectral data, λ_{max} in nm and (log ε), for pluridentate diimine ligands.

Species	π-π^*
bpz[a]	227 (4.02), 288 (4.29)
bpy[a]	237 (3.87), 283 (4.01)
dpp[b]	247 (4.2), 318 (4.68)
pypz [c]	229 (3.98), 284 (4.17)

[a] Values measured in ethanol[43]. [b] Measured in acetonitrile[89]. [c] Measured in water (present work).

The absorption bands in the lower energy portion of the spectrum are sensitive to the identity of the metal, the surrounding ligands and the environment, particularly the solvent and pH. For their interpretation, a charge-transfer model is usually invoked[90] that assigns the lower-energy bands to transitions involving the promotion of an electron from a metal-centered π_M d orbital to a π^* ligand-localized orbital creating a "spatially isolated" excited state largely singlet in character.

According to the MLCT model and the work of Lytle[91], absorption of a photon creates a singlet charge-transfer state that, in less than 25 picoseconds, is converted into a

state with triplet character (^{3}MLCT) due to "extremely fast intersystem crossing and internal conversion processes". The large molar extinction coefficients, $\varepsilon \geq 10^4$ M^{-1} cm^{-1} ($\log \varepsilon \geq 4$), validate the idea that absorption occurs without a change in spin, while the relatively long lifetimes of the emissive states of most complexes (*vide infra*) support the consideration that the emissive state possesses a spin multiplicity different from that of the ground state and the state populated upon absorption. It is important to keep in mind, however, that for these systems, the magnitude of the high spin-orbit coupling of the ruthenium metal atom (Z = 44) is large and states cannot be adequately described with orbital configurations localized on a single ligand. Spin-orbit coupling also mixes singlets and triplets such that the spin quantum number S is not well defined. Consequently, the assignment of absorption and emission bands as well as the assignment of a different spin to the lowest emitting excited state is problematic, although it is generally agreed that the spin of the emissive state differs from that of the states populated on absorption.

In the visible region, all complexes listed in Table 22 have at least two electronic transitions, sometimes hidden under a single, broad, lopsided band envelope that is approximately Gaussian in shape. Clarifying that the use of pure spin labels is an oversimplification and that states are better described as a manifold of spin-orbit states rather than an individual one helps explain the experimental observation that homoleptic complexes that possess ligands of only one kind, each with identical π^* ligand-localized orbitals, display broad absorption maxima that appear to be the result of more than one closely-spaced absorption. For example, the spectrum of $Ru(bpy)_3^{2+}$ shows an absorption at 452 nm with a very distinct shoulder at 430 nm and the absorption spectrum of $Ru(bpz)_3^{2+}$ has a band at 443 nm with a prominent shoulder at 415 nm. Additionally, both

complexes display an absorption band at approximately 340 nm, which was identified in previous works as a $d\pi \rightarrow \pi_2^*$ transition. Gardner et al. seem to think that in the case of $Ru(bpdz)_3^{2+}$, where bpdz is the 3,3'-bipyridazine ligand, the absorptions around 344 and 444 nm are both ^{1}MLCT Ru→L transitions, with the shoulder at 414 nm identified as a vibrational sideband indicating distortion of one or more ligands. Hence, with three identical ligands, the authors suggest the possibility of having two MLCT transitions energetically distinct where the charge is transferred from the same ruthenium to two ligands, one of which is vibrationally distorted relative to the other. The details of why the energies differ are not clear and the authors failed to address that point. When an asymmetric ligand substitutes one of the ligands in a homoleptic complex, for example going from $Ru(bpy)_3^{2+}$ to $[Ru(bpy)_2pypz]^{2+}$ or $[Ru(bpy)_2dpp]^{2+}$, the electronic transitions separate from one another in energy so that they can be resolved. The absorption bands of $Ru(bpy)_3^{2+}$ at 452 nm and 430 nm were recorded at 473 and 410 nm in the heteroleptic $[Ru(bpy)_2bpz]^{2+}$ complex. Gardner et al. observed a similar widening of the absorption envelope in the electronic spectra of $Ru(bpdz)_3^{2+}$ and $[Ru(bpy)_2bpdz]^{2+}$. In going from $Ru(bpy)_3^{2+}$ to $[Ru(bpy)_2pypz]^{2+}$ or $[Ru(bpy)_2dpp]^{2+}$, two absorption bands emerge from the broad Gaussian centered at 450nm. Using resonance Raman spectroscopy, Strekas and coworkers[52] and Kincaid and coworkers[69] assigned the ligand termination of the MLCT absorptions, for the Ru-dpp and Ru-pypz complexes, respectively. At neutral pH, the higher energy MLCT band for $[(bpy)_2Ru(dpp)]^{2+}$ and $[(bpy)_2Ru(pypz)]^{2+}$ fall within experimental error of each other at wavelength of 432 ± 5 nm and 435 ± 5 nm, respectively, and are assigned to the electronic transition between $d(t_{2g})$ orbitals of the metal and the π^* orbitals of the bpy ligands. The fact that the position of the bpy-centered

MLCT transition does not vary significantly for $[(bpy)_2Ru(dpp)]^{2+}$ and $[(bpy)_2Ru(pypz)]^{2+}$ suggests that the ligand field strength at the metal is not affected by the nature of the asymmetric ligand. This seems reasonable since, in both pypz and dpp, the chelating portion of the ligand preserves a bpy-like coordination site structure. On the contrary, the position of the bpy-centered MLCT transition blue-shifts when both rings of the bipyridine ligand are modified by the acquisition of an additional nitrogen atom on the periphery of the ligand (Figure 168), as is the case for $[(bpy)_2Ru(bpdz)]^{2+}$, $[(bpy)_2Ru(bpm)]^{2+}$ and $[(bpy)_2Ru(bpz)]^{2+}$. This would suggest that, as the spacing increases between the bipyridine-like coordination site and the outer periphery of a ligand, the effect of the peripheral functionalities declines and *vice versa*. Alternatively, it could signal a decline in the electronic coupling within the diimine ligand. Either hypothesis is plausible albeit not confirmed.

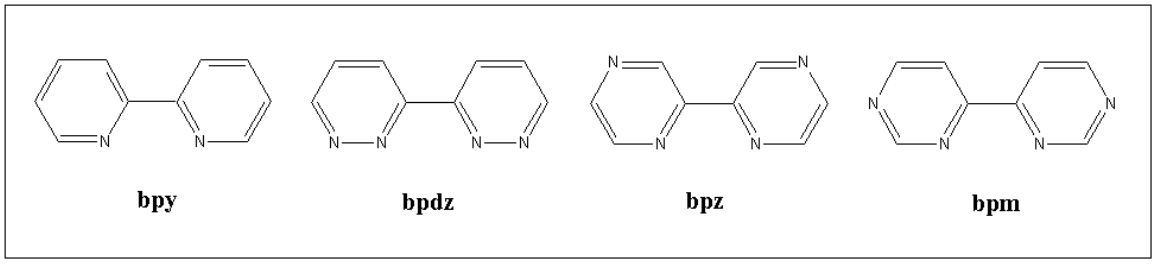

Figure 168. Molecular structure of four diimiine ligands: bpy, bpdz, bpz and bpm.

The position of the MLCT band to the asymmetric ligand is more likely dictated by the peripheral nitrogen atoms and dependent on the energy of the π^* orbitals of the dpp and pypz ligands. For all heteroleptic complexes listed in Table 22 the lower-energy MLCT band is red-shifted by just about 30 nm (a difference of approximately 0.17 eV or

1400 cm^{-1}) from the position it appears in the spectrum of $Ru(bpy)_3^{2+}$. The red shift is indicative of metal atoms becoming more readily oxidizable, since less energy is needed to reach the charge-transfer state with one electron on the ligand and an oxidized metal center. The fact that less energy was required to fill the π^* orbitals of that ligand suggests that the orbitals are stabilized compared to those of a complex with MLCT absorption at shorter wavelength. It also may mean that the ligand is a better π^* acceptor or a weaker base. Inasmuch as the dpp and pypz π^* orbitals are lower in energy than the π^* orbitals of the bpy counterpart, it is expected that the MLCT transitions terminating on dpp and pypz be centered at longer wavelength, at 487 ± 5 nm and 476 ± 5 nm, respectively. Compared to the dpp-localized charge-transfer energy level, the pypz-localized absorption is at higher energy by 5.88 x 10^{-2} eV, equivalent to approximately twice the vibrational energy at room temperature. As the electronegativity of ligand increases, the MLCT shifts to longer wavelengths, making the transition of the electron from metal to ligand energetically less demanding.

If the MLCT absorptions are viewed as distinct transitions to individual ligands, considerations can be drawn from their extinction coefficients. In both complexes, the extinction coefficients for MLCT (bpy), at a first glance, are of the same magnitude as the ε for MLCT to the asymmetric ligand. However, upon determination of the contribution from each component (Figures 19 and 30) it becomes apparent that the MLCT bands to pypz and dpp partially overlap with the tail of the transition to the bpy ligands and in reality have a lower ε, approximately half the coefficient for the transition to the bpy ligands. This reflects the 2:1 ratio of the number of each type of ligand in the complex. Each absorbance being additive, the MLCT band corresponding to the charge

transfer to two bipyridine ligands is twice as intense as the MLCT band corresponding to the transfer to one pypz or dpp ligand. This result suggests that the allowedness of MLCT transitions to different ligands is the same, as each ligand exhibits the same capability to accept charge. This contrasts with the findings by Zambrana[92] hinting that there is a difference in the ability of the ligands to absorb light whereas here, the 2:1 ratio implies comparable light absorbances.

Also, contrary to what Zambrana writes in his manuscript, the excitation spectrum recorded for $[Ru(bpy)_2dpp]^{2+}$ at neutral pH, *does* mirror the absorption spectrum (Figures 19 and 20). Likewise, the excitation spectrum for $[(bpy)_2Ru(pypz)]^{2+}$ at neutral pH mirrors its absorption spectrum. This finding has implications related to the quantum yield: it appears that quantum yield of emission when populating MLCT via bpy *is* same as when populating via dpp or pypz implying that no energy is lost during intersystem crossing.

While excitation seems to delocalize the charge over the entire ligand system, the fast internal conversion processes occurring right after absorption populates the lowest excited state, mainly triplet in character and localized over one ligand in particular. As suggested by the results of experiments on one-electron reduced Ru(II) diimine complexes[93], a simplified way of looking at the excited state is to see it as a Ru^{3+} metal center with an electron out on one of the ligands. For $[Ru(bpy)_2dpp]^{2+}$ and $[Ru(bpy)_2pypz]^{2+}$ emission could theoretically come from either the charge transfer from dpp or pypz to Ru or from bpy to Ru. According to Kasha's rule, out of several possible emitting states, emission usually derives from the lowest excited state only. In all

instances, it is indeed experimentally observed that, independent of the excitation wavelength, the predominant transition occurs from the MLCT state lowest in energy.

Table 24: Room temperature luminescence spectral data, λ_{max} in nm and (log ε), for ruthenium diimine complexes[43] in water, at neutral pH.

Species	Emission Max (nm)	Lifetimes (ns)
bpz	Not emissive	--------
bpy	Not emissive	--------
pypz	Not emissive	--------
$[Ru(bpdz)_3]^{2+}$	622	535
$[Ru(bpz)_3]^{2+}$ [a]	603	1040
$[Ru(bpy)_3]^{2+}$ [b]	625	620
$[Ru(dpp)_3]^{2+}$	647	185
$Ru(bpz)_2Cl_2$	Not emissive	--------
$Ru(bpy)_2Cl_2$	Not emissive	--------
$[Ru(bpy)_2bpdz]^{2+}$ [a]	**703**	**< 50**
$[Ru(bpy)_2bpz]^{2+}$ [a]	**690[c]**	N/A
$[Ru(bpy)_2bpm]^{2+}$ [a]	**680**	N/A
$[Ru(bpy)_2dpp]^{2+}$	**700**	**128**
$[Ru(bpy)_2pypz]^{2+}$	**675**	**150**

[a] Reference 94. [b] Reference 95. Previous data reported emission at 613 with a shoulder at 627 nm (lifetime 620 ns and quantum yield of 0.042). [c] Obtained in acetonitrile.

The luminescence spectra of Ru(II) diimine complexes in solution at 293 K show a broad, structure-less orange-yellow emission in the 600-700 nm region. Given the broadness of the emission bands, it is difficult to pinpoint the maximum with precision. In addition, different instruments show slightly shifted peak maxima (by ± 5 nm) due to their differing sensitivity in the near-infrared region. Ultimately, though, several measurements on the same instrument do provide consistent emission maxima so the shifts are attributed to subtle differences in instruments' calibration and detection systems

and are not considered significant. Spectra are better resolved in glassy solutions at low temp where vibrational progressions are apparent as well. The emission spectra of aqueous solutions of $[(bpy)_2Ru(pypz)]^{2+}$ and $[(bpy)_2Ru(dpp)]^{2+}$ obtained with 470 nm excitation, gives rise to luminescence at 675 and 700 nm, respectively (Figures 18 and 32). Since the pypz and dpp π^* orbitals in the above-mentioned complexes are lower in energy than those of bpy ligands, the transition giving rise to the emission is assigned to the charge transfer from the pypz or dpp ligand to the metal. A reason for the lower transition energy observed for $[(bpy)_2Ru(dpp)]^{2+}$ compared to $[(bpy)_2Ru(pypz)]^{2+}$ and $[Ru(bpy)_3]^{2+}$ may be found in the more extended ligand molecular backbone of dpp, which results in energetically closer levels for LC LUMO and MC HOMO. Emission maxima of similar complexes are listed in Table 24.

From the comparison of the two main categories of homoleptic and heteroleptic complexes it is readily apparent that the emission in heteroleptic complexes falls at longer wavelengths than the emission for homoleptic complexes. Independent of the identity of the ligand, all complexes with three identical ligands emit at higher energy, in the 600 to 640 nm range. Heteroleptic compounds with two bipyridines and an asymmetric ligand all emit from lower energy emissive excited π^* states, in the 675 to 700 nm range. Within the latter group of complexes, another trend is discernible, albeit less evident. Data in Table 24 indicate that the higher the number of uncoordinated nitrogens at the ligand's periphery, the longer the emission wavelength. The position of the emission maxima in the series of heteroleptic complexes is consistent with the model suggesting that increased electronegativity at the periphery of the asymmetric ligand in

the form of additional nitrogen atoms lowers the energy released by the ligand-to-metal deactivation.

Overall, based solely on the position of the emission peak maxima, while it is convincingly established that emission in this series of complexes originates from the lower lever π^* states and that the lowest level in heteroleptic complexes is mainly localized on the asymmetric ligand, it can be concluded that the emission wavelength and energy is more strongly dependent on the nature of the spectator ligands than it is on the nature of the asymmetric ligand itself. The complexes in Table 25 constitute a good example: the emissive state for all is localized on the bpz ligand. Nonetheless, the energy difference between the excited state and the ground state reached by radiative decay varies in accordance with the electronegativity of the other ligands coordinated to the metal: the higher the electronegativity of the "spectator" ligands, the lower the charge localized on the metal, the higher the energy of the emissive state. The increased number of electronegative ligands renders the excited state less stable, hence radiative emission from said state will correspond with a more energetically rich transition.

Table 25. Room temperature luminescence spectral data for the Ru/bpy/bpz series of complexes, in acetonitrile.

Series	Emission λ (nm)
$\mathbf{[Ru(bpy)_2(bpz)]^{2+}}$	690
$\mathbf{[Ru(bpy)(bpz)_2]^{2+}}$	650
$\mathbf{[Ru(bpz)_3]^{2+}}$	605

This remark challenges the theory that the position of the peak maxima is dependent chiefly on the identity of the ligand with the lowest π* energy level and suggests instead that the spectator ions and the symmetry of the complex have a bigger than expected impact on the absorption and emission energy states.

The MLCT excited states of $[Ru(bpy)_2dpp]^{2+}$ and $[Ru(bpy)_2pypz]^{2+}$ are emissive with lifetimes in room temperature aqueous solution of 128 and 150 ns, respectively. This is expected since the dpp ligand has an additional ring free to rotate and interact with the solvent, interaction that can more easily lead to radiationless deactivation hence shorten the average lifetime of the excited state molecules. Again, a marked difference between homoleptic and heteroleptic complexes should be noted: the lifetimes of homoleptic complexes is longer than the lifetime of heteroleptic ones. The complexes $[Ru(bpy)_3]^{2+}$ and $[Ru(bpdz)_3]^{2+}$ with lifetimes respectively of 620 and 535 ns exemplify this phenomenon, compared to $[Ru(bpy)_2bpdz]^{2+}$ with lifetime of less than 50 ns, shorter than the detection limit of the instrument. The substantial decrease in the lifetime of the excited complexes upon substitution of one of three ligands correlates with the decrease in the energy of the emissive state. As the energy of the emitting level decreases, it is possible that the more likely path to deactivation is a radiationless one. Alternatively, the decrease in emission may correlate with the disruption of the symmetry of the complex.

The lifetimes are not dependent on the wavelength at which the decay is followed. This is an additional indication that, for both complexes, only one state is responsible for the emission. Combining the data for lifetime and quantum yield, the radiative rates calculated for $[(bpy)_2Ru(dpp)]^{2+}$ and $[(bpy)_2Ru(pypz)]^{2+}$ are $2.1 \times 10^4\ s^{-1}$ and $2.8 \times 10^4\ s^{-1}$, respectively. The values are fairly close to each other and only about a

factor of three smaller than $[Ru(bpy)_3]^{2+}$, although $[(bpy)_2Ru(dpp)]^{2+}$ is 15 times less emissive than $[Ru(bpy)_3]^{2+}$, and $[(bpy)_2Ru(pypz)]^{2+}$ is 10 times less emissive. Also, it is not surprising that the k_{nr} for $[(bpy)_2Ru(pypz)]^{2+}$ is lower than for $[(bpy)_2Ru(dpp)]^{2+}$ since $[(bpy)_2Ru(dpp)]^{2+}$ has a more direct deactivation route to the solvent via a hydrogen bond between the nitrogen of the peripheral dpp pyridine and the water surrounding the molecule.

4.A.4. Electrochemistry

Cyclic voltammetry experiments on $[(bpy)_2Ru(pypz)]^{2+}$ dissolved in acetonitrile were performed at room temperature. Although the difference between the oxidation and reduction waves (Figure 39), 0.090 V, is slightly larger than the expected value, 0.059 V, the fact that the ratio of cathodic and anodic current, 0.93, is close to unity confirms that the process is reversible and justifies utilizing the $E_{1/2}$ value as the thermodynamic parameter, E^o, giving an indication of the energy level of the oxidized complex. Studies[87, 96] with other Ru(II) diimines that likewise exhibit reversible one electron oxidations and reductions, have also reported values of the peak separation differing from the theoretical value of 0.059 V. Oxidation of one of the diimine ligands in the range of potential scanned was ruled out since, according to the work of Crutchley and Lever[43], oxidation of diimine ligands occurs at more positive voltages (> 1.9 V), and coordination to the cationic Ru(II) ion shifts the oxidation potential to even higher voltages.

Combining the results from spectroscopy and electrochemistry, an energy level diagram can be drawn, showing the energy levels and reductive power of the excited species relative to the ground state (Figure 169).

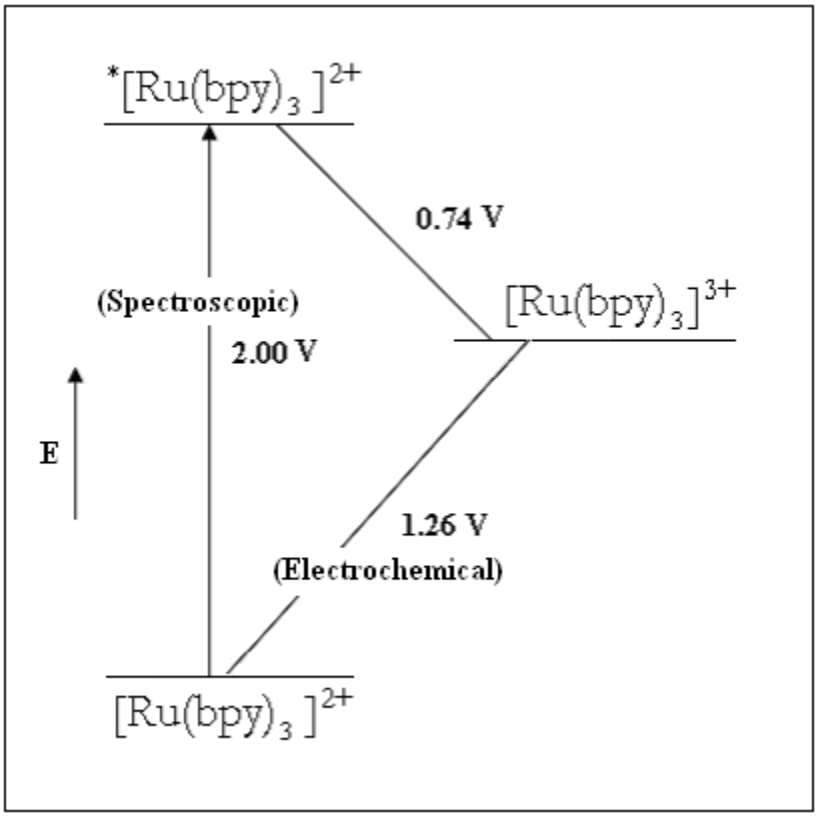

Figure 169: Schematic representation of the spectroscopic and ground state and excited state redox potentials for $[Ru(bpy)_3]^{2+}$.

The ground state redox potential for each redox pair is measured electrochemically, while the thermodynamic free energy of the excited state (ΔG^*), which represents the energy difference between the excited and ground state, is approximated by the wavelength maximum of the emission from the thermally equilibrated charge transfer state. Sometimes[97, 98] a correction for the entropy changes is introduced, but it is quite small compared to the energy gap and for the purpose of this discussion can be omitted. The likelihood that the excited state complex will undergo electron transfer (i.e. $^*[Ru(bpy)_2pypz]^{2+} \rightarrow [Ru(bpy)_2pypz]^{3+} + e^-$) in the presence of an oxidizing species is a quantity not directly measurable but the driving force for the process, which is often

taken as an indication of the likelihood of that process to occur, can be calculated, to a first approximation, from the difference between the excited state free energy and the ground state redox potential.

As Rillema and coworkers pointed out in their 1983 article, the values for the excited state potentials are lower limits since the luminescence energy contains a contribution from vibrational distortion between ground and excited states. Even so, excited state redox potentials of a complex are of pivotal significance in determining the photo-induced redox chemistry available to the molecule. From an energetic perspective, the excited-state specie, having higher energy content than the oxidized or reduced forms of the complex, will be a stronger oxidant and reductant than the ground state specie. This consideration does not take into account the kinetic aspects of redox reactions, which may be crucial in deciding whether the reaction will ultimately have time to happen. For electron transfer to be a competitive quenching process, the lifetime of the excited species has to be long enough to allow the molecules to come together and interact[a], and the rate of electron transfer has to be faster than the rate of relaxation. The driving force for electron transfer, i.e., the oxidation potential of the excited state, does not necessarily correlate with the rate of electron transfer, but in general, the higher the oxidation potential, the better reducing agent the complex is, and hence the wider the range of reagents that could possibly quench the emission by an electron transfer process. For comparison, the redox potentials of the Ru^{II}/Ru^{III} couples for various ruthenium complexes with similar bidentate polypyridyl ligands are listed in Table 8.

[a] Excited states need to have a minimum lifetime of 10^{-9} s to have a chance to be involved in encounters with other molecules[93].

Table 26: Room temperature electrochemical data for various Ru(II) complexes with bidentate polypyridyl ligands.

	Energy of the excited state (λ_{em})	Ground State Oxidation Potentials (V) $[ML]^{2+} \rightarrow [ML]^{3+} + e^-$	Excited state Oxidation Potentials (V) $^*[ML]^{2+} \rightarrow [ML]^{3+} + e^-$
$Ru(bpy)_2Cl_2$	Not emissive	-0.31[a]	n/a
$Ru(bpz)_2Cl_2$	Not emissive	-0.80[a]	n/a
$[Ru(bpy)_3](PF_6)_2$	2.00[b] (620), 2.016[c] (615)	-1.29 ± 0.05 [a,b,c,d,e,f]	0.74
$[Ru(bpz)_3](PF_6)_2$	2.033[c] (610), 2.019[g] (614)	-1.93 ± 0.05 [a,b,c,g]	0.049
$[Ru(dpp)_3]^{2+}$	1.916[g] (647)	-1.62[g]	0.296
$[Ru(bpy)_2(bpz)]^{2+}$	1.746[b] (710)	-1.49[b]	0.256
$[Ru(bpz)_2(bpy)]^{2+}$	1.896[b] (654)	-1.72[b]	0.176
$[Ru(bpy)_2dpp](ClO_4)_2$	1.77[h] (700)	-1.38 ± 0.13[d,g]	0.41 ± 0.07 [d,h]
$[Ru(dpp)_2bpy]^{2+}$	n/a	-1.51[g]	n/a
$[Ru(bpy)_2pypz]Cl_2$	1.84 (674)	-0.95[h]	0.89[h]

[a] SCE w/ TEAH[43]. [b] SSCE w/ TEAP. [c] SCE w/ TBAP[99]. [d] SCE w/ $TBABF_4$[100]. [e] SCE w/ Pt electrode, w/ $TBABF_4$ [71]. [f] SSCE w/ TBAH[101]. [g] SCE w/ $TBAPF_6$[73]. [h] current work.

The signs for redox potentials can be confusing as different sources may report those values following different conventions. In this manuscript, since the values are obtained from measures of spectral and reversible redox potentials, the convention used is to report the potentials for those half-reactions where the free energy of the reaction increases, as negative, whereas those in which the free energy decreases as positive. This is consistent with $\Delta G = -nFE$, and consistent with the diagrams (Figures 169 and 171) which present the respective redox changes as either increases or decreases in the free energy. For example, the oxidation potential for the half-reaction $^{*}[Ru(bpy)_3]^{2+} \rightarrow [Ru(bpy)_3]^{3+} + e^-$ in Figure 169, is reported as positive number in Table 26, meaning the half-reaction involves a decrease in free energy. The data show that, while the energy of emission remains fairly constant throughout the series varying over a small range from (1.8) to (2.1) eV, the ground state and excited state redox potentials vary widely as a function of the number of ligands substituted, with differences of up to 0.7 volts (see Table 27 below). It follows that the changes in the oxidation potential of the excited state, or conversely the driving force for electron transfer to a quencher, are a consequence of the changes in the oxidation potential of the ground state.

Table 27: Spectroscopic and ground and excited state oxidation potentials for two series of ruthenium(II) complexes.

Series 1	**$[Ru(bpy)_3]^{2+}$**	**$[Ru(bpy)_2(bpz)]^{2+}$**	**$[Ru(bpz)_2(bpy)]^{2+}$**	**$[Ru(bpy)_3]^{2+}$**
E_{GS}	**1.26**	**1.49**	**1.72**	**1.95**
$E(\lambda_{em})$	2.00	1.75	1.89	2.02
E_{ES}	0.74	0.26	0.176	0.05
Series 2	**$[Ru(bpy)_3]^{2+}$**	**$[Ru(bpy)_2(dpp)]^{2+}$**	**$[Ru(dpp)_2(bpy)]^{2+}$**	**$[Ru(dpp)_3]^{2+}$**
E_{GS}	**1.26**	**1.44**	**1.51**	**1.62**
$E(\lambda_{em})$	2.00	1.78	n/a	1.92
E_{ES}	0.74	0.34	n/a	0.296

At least two series can be extrapolated from the data in Table 27, series in which a linear trend in the values of redox potentials is apparent in going from a complex with three identical bidentate ligands (e.g. $[Ru(bpy)_3]^{2+}$) to another (e.g. $[Ru(bpz)_3]^{2+}$) by step-wise substitution of one ligand at a time: the absolute value of ground state oxidation potentials increase and excited state potentials decrease in the direction of increased number of more electronegative ligands. Figure 170 shows the linear correlation between the absolute values of ground state potential and the number of bpy ligands substituted with more electronegative analogues.

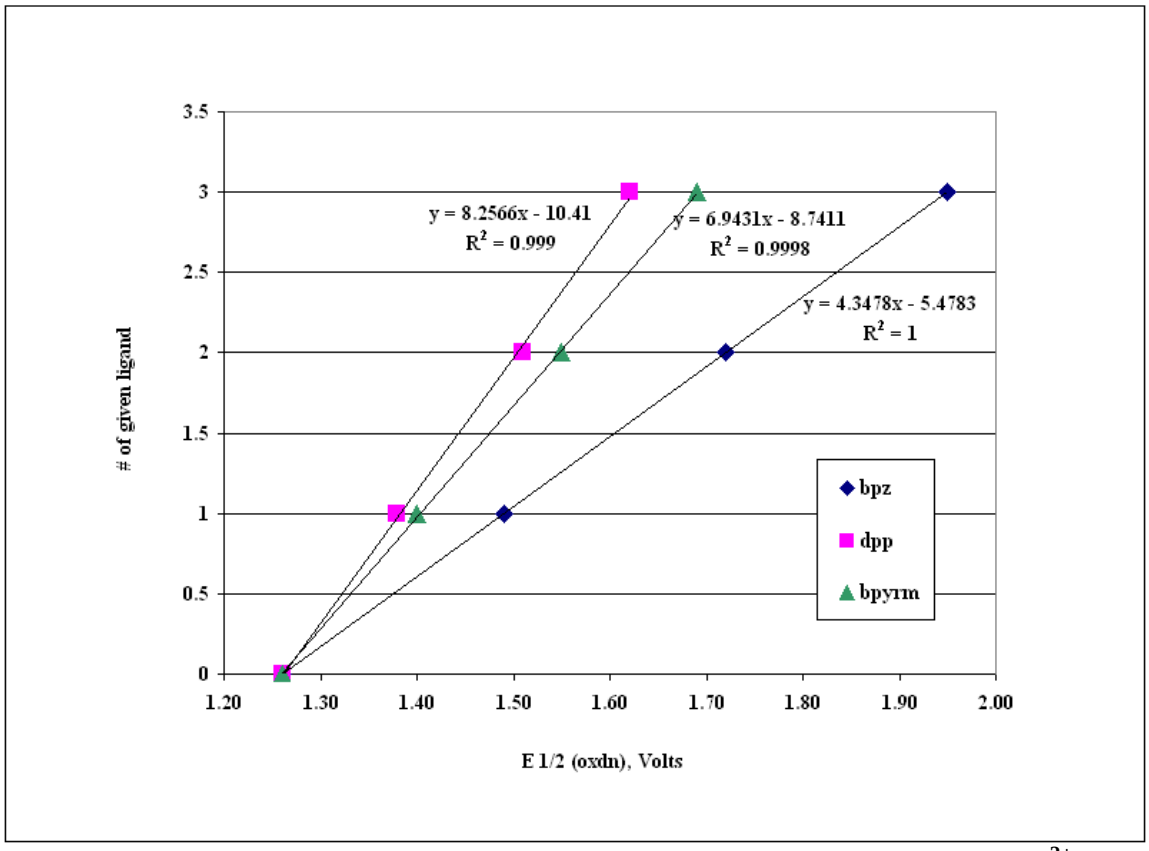

Figure 170: Ground State potentials for the oxidation of $[Ru(bpy)_{3-n}L_n]^{2+}$ as a function of n, the number of L ligands in the complex.

The trend-line with the smallest slope, the one generating the largest change in ground state potential, is the one corresponding to the most electronegative ligand as it substitutes bpy in the ruthenium complex. On the other hand, substitution of bpy with dpp causes the smallest change in ground state oxidation potential since the third ring on the dpp ligand is not electronically coupled with the metal and being far from it, has the least effect on it. It is, then, reasonable to conclude that electronegative ligands make the electron transfer from the metal center less favorable in the ground state by delocalizing the valence electrons over the ligand systems and rendering them "less available" for electron transfer. The same can be said about the excited state: oxidation of the excited state complex, i.e. $^{*}[RuL_{3-n}L'_{n}]^{2+} \rightarrow [RuL_{3-n}L'_{n}]^{3+} + e^{-}$, becomes less favorable when bpy is substituted with more electronegative ligands, which destabilize the positive charge on the metal and provides, upon excitation, a stronger force to keep the electron centered on the ligand. Following this reasoning, since pypz is a less electronegative ligand than dpp or bpz, substitution of bpy with the pypz ligand should have a smaller effect in lowering the oxidative power of either excited and ground state species, which translates in a smaller change in the ground state potential when compared to dpp or bpz, as is in fact observed.

Predictions based on the series below, would suggest that the ground state potential of $[Ru(bpy)_2pypz]^{2+}$ should fall close in value to 1.35 V. Hence, while it was expected to see the potential not increase much compared to the potential of $[Ru(bpy)_3]^{2+}$, it was unexpected to see it actually *decrease*. A lower potential suggests that $[Ru(bpy)_2pypz]^{3+}$ is more stable than the oxidized dpp or trisbipyridine analogues. Variations of the redox potential values could also reflect the change in solvation on

removing an electron from the complex. In contrast with coordinated bipyridine and the more elaborate diimines like dpp or ppz, the peripheral nitrogen of pypz is more exposed to the surrounding solvent and more susceptible to a reorganization of solvent molecules following oxidation, and the transfer of the electron to the quencher. Unfortunately there is no spectroscopic signature in which to test this hypothesis. Nonetheless, from the molecular orbital point of view, the changes in solvation could be indication that the HOMO of $[Ru(bpy)_2pypz]^{2+}$ is destabilized compared to the HOMO of $[Ru(bpy)_3]^{2+}$ and $[Ru(bpy)_2dpp]^{2+}$. In the case of $[Ru(bpy)_2pypz]^{2+}$, the excited state potential has the largest absolute value among all complexes listed in Table 27.

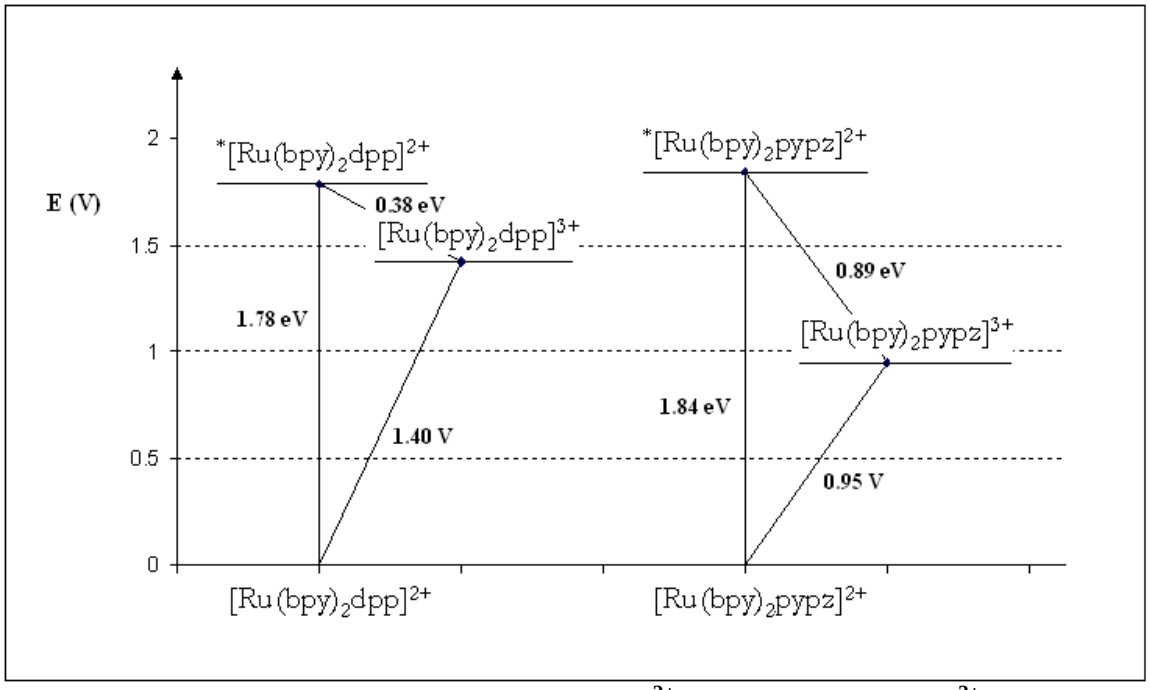

Figure 171: Redox potentials for $[Ru(bpy)_2dpp]^{2+}$ and $[Ru(bpy)_2pypz]^{2+}$.

According to the data, the driving force toward oxidation of the excited-state complex with one coordinated pypz ligand is larger than that of the analogue with one dpp ligand and more also than $[Ru(bpy)_3]^{2+}$. Figure 171 shows a side-by-side comparison of the energy diagrams for the two complexes.

Based exclusively on a comparison of the energy level of each species as it was determined from spectroscopic and electrochemical measurements, $[(bpy)_2Ru(pypz)]^{2+}$ is the better reducing agent in the ground state compared to the Ru complex with dpp as the asymmetric ligand, since its oxidized state lies at lower energy. In the excited state, the complex with pypz is energetically more disposed to undergo electron transfer than the complex with dpp since the energy driving the reaction is larger overall.

Possible reasons for the wider-than-expected change in potential for $[(bpy)_2Ru(pypz)]^{2+}$ may reflect differences in the extent of back bonding and/or solvation of the different oxidation states. Experimental parameters, such as solvent or nature of the counter-ion, may also contribute to increase the uncertainty associated with the excited state potential values. While the electrochemical measurements were performed on acetonitrile solutions, most of the spectrochemical data reported in Table 26 were recorded using aqueous solutions. No counter-ion effect was observed by Hitoshi Ishida when measuring the phosphorescence quantum yield and emission maximum for $[Ru(bpy)_3]^{2+}$. Still, the fact that different salts of the ruthenium diimine complexes were used to gather the data in Table 26, introduces some uncertainty in the conclusions that can be drawn from them. Even if the measurement was somehow skewed due to some unforeseen experimental error, the linear trends observed in other complexes with similar ligands as the ones in the series above, lead to the same conclusion that, compared to

$[(bpy)_2Ru(dpp)]^{2+}$, the better reducing agent in both ground and excited states is $[(bpy)_2Ru(pypz)]^{2+}$.

From a purely informational perspective, the electrochemical measurement provides more complete data on the complex, i.e. helps to characterize the complex fully. From an application perspective, it establishes the ranges of potential where the complex may undergo oxidation/reduction, in the ground- state, in conjunction with the emission energy. An advantageous potential, however, has proven in the past to be not a sufficient condition for the reduction to actually occur, as energy transfer and bonding may also happen as a result of the additional energy gained by the molecules. For instance, when $Ru(bpy)_3^{2+}$ is exposed to Fe(III), it undergoes redox reaction and no emission is observed, since Ru(III) is non-emissive. On the other hand, with silver(I), $Ru(bpy)_3^{2+}$ and other Ru(II) diimines have been shown to associate in the excited state via a type of interaction resulting in the formation of a new emissive species[27, 29, 102, 103, 104]. As part of this thesis work, the aim was to create conditions where exciplex formation is favorable, if not the only choice of metal-complex interaction. One way to achieve this is by selecting metals that do *not* undergo redox reaction with the ruthenium complexes under the chosen experimental settings, such as the divalent d^{10} metal ions Zn^{2+} and Cd^{2+}. If not for the fact that the cations are d^{10} systems, the electrochemical data warns us that the redox potential of $[(bpy)_2Ru(pypz)]^{2+}$ is such that, unlike $[(bpy)_2Ru(dpp)]^{2+}$ and $[Ru(bpy)_3]^{2+}$, a redox reaction with Zn^{2+} and Cd^{2+} could occur, assuming that the potential for the one electron reduction of Zn^{2+} and Cd^{2+} is less than or equal to the potential for the known two-electron reductions.

$Zn^{2+} + 2e^- \rightarrow Zn^0$ $\quad E^\circ = -0.76$ V

$Cd^{2+} + 2e^- \rightarrow Cd^0$ $\quad E^\circ = -0.40$ V

$^*[Ru(bpy)_2pypz]^{2+} \rightarrow [Ru(bpy)_2pypz]^{3+} + 1e^-$ $\quad E^\circ = +0.89$ V

$\Delta E^\circ > 0 \quad \Rightarrow \quad \Delta G^\circ < 0$

Simply based on the larger oxidation potential for $^*[Ru(bpy)_2pypz]^{2+}$ compared to $[(bpy)_2Ru(dpp)]^{2+}$ and $[Ru(bpy)_3]^{2+}$, it follows that more metals are likely to undergo *redox* reactions with $^*[Ru(bpy)_2pypz]^{2+}$ in the excited state rather than coordination or exciplex formation. Ultimately, however, it's not clear how the driving force for a reaction relates to the kinetics or the mode of reaction, i.e., what factors actually define the mechanism of the quenching reaction. Furthermore, oxidation potential has been shown[105] to change as a function of pH for similar ruthenium complexes, as the state of protonation is altered. So, if the goal is to promote excited state coordination over redox, then the key parameter to control is the pH of the solution and the change in acid-base properties of the complex going from the ground to the excited state rather than the redox properties. Further experiments would be needed to understand how the driving force of a reaction and its rate work before we can use this information in a systematic way.

4.B. Titrations

The pH titrations performed from pH 12 to Hammett acidity constant of –11 provide information on the acid-base properties of $[(bpy)_2Ru(dpp)](NO_3)_2$ and $[(bpy)_2Ru(pypz)]Cl_2$. Ground-state titrations established the range of pH in which each protonation takes place and offered evidence of *both* protonation steps for $[(bpy)_2Ru(dpp)^{2+}]$. NMR titrations confirmed that $[(bpy)_2Ru(dpp)^{2+}]$ undergoes acid-base reaction in the 1-3 pH range and helped identify the basic site involved. Excited-state titrations revealed interesting new emissions at low pH and cemented the notion that excitation may -and does-, at times, increase the basicity of the targeted complex.

Comparisons between ground- and excited-state titrations and between titrations of different complexes highlighted the complexity and fluidity of the system in the excited state and how difficult it is to model the behavior of each chelating site in the nanosecond and sub-nanosecond time domain.

4.B.1. Ground-State Titrations

4.B.1.a $[(bpy)_2Ru(dpp)]^{2+}$

Previous literature on ground state titrations of the complex does not report a protonation equilibrium in the pH range from neutral to zero. Researchers, at the time, concluded either that the first protonation of the complex could not be observed[52], or assigned it to the protonation step observable at much higher acidity[62]. Although the first protonation step was theorized to happen at pH ≅ 1-3, it was deemed not observable with the widely used UV-Visible spectroscopic techniques, until the NMR titration experiments described here. The pH titration carried out using NMR spectroscopy

conveys an average value of 1.52 ± 0.03 for the equilibrium constant of the first protonation process. Based on the changes in value of the chemical shifts, the protons most affected by the first protonation are identified as the ones on the uncoordinated pyridyl ring of the dpp ligand, protons that sterically interact with the protons on the pyrazine moiety as the free pyridine ring twists into planarity with the pyrazine portion of the ligand on protonation. Hence, the constant refers to the protonation of the free pyridyl nitrogen on the dpp ligand, designated N_{py} in the following reaction:

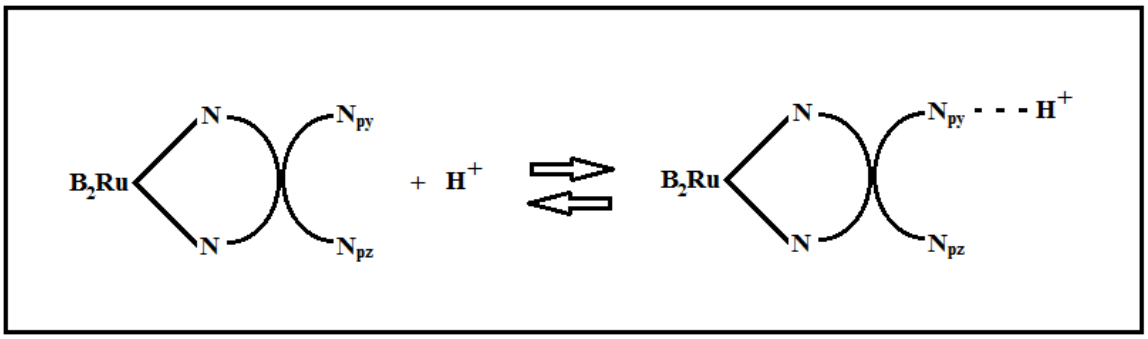

Figure 172: Schematic representation of the first protonation reaction of $[(bpy)_2Ru(dpp)]^{2+}$, where B = bpy.

UV-Visible spectral changes in the pH range from 7 to H_0 = -2 detected during the ground-state titration of $[(bpy)_2Ru(dpp)](NO_3)_2$ were originally attributed to ion pairing effects[52,62]. More sensitive instrumentation and careful analysis show that the changes in the first portion of the pH range fit a sigmoidal curve and, although surprisingly small, are consistent with a *first* protonation step. The optical changes yield a pK_{a_1} = 2.7 ± 0.1. Based on the ground state values of pK_a for free pyridine (5.25[43]) and pyrazine (0.73 ± 0.10, -6.25)[106] molecules, pyridines are more basic in the ground state and protonate at higher pH. Similarly, in the case of free diimine ligands, the bpy ligand gets protonated at higher pH, 4.45, than free bpz, 0.45[62] (Table 28). Consequently, in the

ruthenium(II) complex, the uncoordinated pyridyl nitrogen on dpp would also be expected to undergo protonation before the uncoordinated pyrazyl nitrogen. The protonation of the pyridyl nitrogen does not cause large changes in the absorption spectrum because the free pyridyl ring in coordinated dpp ligands is further away from the metal ion, structurally orthogonal to the remainder of the ligand, and presumably less coupled to the metal and the coordinated portion of the ligand. For the same reason, it is likely that the pK_a for the first protonation step may be close in value to that of the free dpp ligand[62] (pK_{a_1} (dpp) = 2.90), as turns out to be the case.

Table 28: First and second ground-state pK_a for free diimine ligands.

Free ligands	pK_{a1}	pK_{a2}
py	5.25[a]	----
pz	0.65[a]	-6.25[b]
bpy	4.45[a]	0.52[a]
bpz	0.45[a]	-1.35[a]
dpp	2.90[a]	0.80[a]

[a] Ref 62. [b] Ref 106.

Two conditions distinguish the titration methods: NMR analysis requires very high concentrations of the analyte to maintain high S/N ratios and as a consequence the ionic strength of the series of samples tested differs by at least three orders of magnitude from the samples examined by UV-visible spectroscopy. As solutions become more dilute, the percent of ionization of several acids has been shown to increase, thus increasing the value of the equilibrium constant. Furthermore, the differing responses of the absorption and NMR spectra could be related to the fact that the free pyridyl ring is relatively “uncoupled” from the MLCT system, with consequently minor changes in the

absorption, whereas the NMR will be quite sensitive to protonation because structurally addition of a proton causes, as observed, the twist of the free pyridine ring into planarity.

The UV-Vis titration establishes that the complex undergoes acid-base reactions at pH above zero in the ground state, while the NMR titration confirms that the first protonation is a site-selective process that occurs, as expected, at the nitrogen on the peripheral pyridyl ring and not at the other basic nitrogen on the pyrazyl ring of dpp (Figure 172 and 173). However, the two values of pK_{a1} measured differ, with the UV-Vis titration suggesting that $[(bpy)_2Ru(dpp)](NO_3)_2$ is a weaker acid than it is determined from NMR titration.

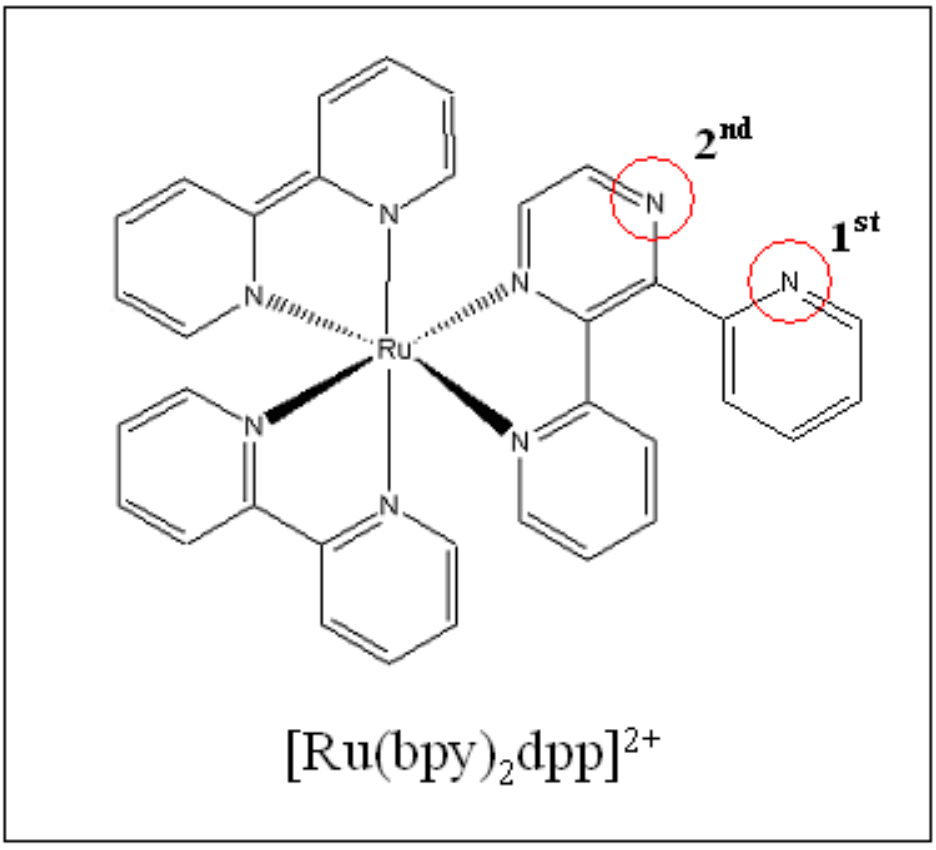

Figure 173: First and second protonation sites of $[(bpy)_2Ru(dpp)]^{2+}$.

Increasing $[H^+]$ beyond 2M by addition of aliquots of sulfuric acid dramatically transforms the profile of the absorption spectrum. The marked change in the absorption spectrum of the diprotonated species parallels the significant modifications in the structure. The sample's color transition from orange to purple is a consequence of the conversion of $[Ru(bpy)_2dppH]^{3+}$ to $[Ru(bpy)_2dppH_2]^{4+}$. Having established that the pyridyl nitrogen is already fully protonated at Ho = -2, the spectral changes that occur at higher acid concentration are now assigned to protonation to the pyrazinyl nitrogen on the dpp ligand, as was also suggested by Hosek et al.[52] The second pKa calculated here following the changes in absorbance at 450, 460 and 470 nm is somewhat lower than previously reported values[52]: -5.9 ± 0.1 instead of –4.9. This discrepancy was due to initial challenges in the preparation of solutions with negative Hammett acidity constants. The use of tables by Paul and Long[56] and by Hammett and Deyrup[57] helped to establish a standard procedure for the preparation of solutions with acidity that could be known up to two significant figures.

The pKa_2 for the complex is close to the value for the second protonation of free pyrazine[106], -6.25 and to the pKa of the last protonation of the 6th nitrogen on $[Ru(bpz)_3]^{2+}$, -6.7[107] . Such a low value of pKa can be accounted for since the changes are due to the second protonation; a protonation happening on a complex, $[Ru(bpy)_2dppH_{py}]^{3+}$, that already bears a +3 charge. In addition, the second protonation requires the disruption of the hydrogen bond between the proton bonded to the pyridyl nitrogen and interacting with the pyrazyl nitrogen. So overall, protonation is hindered for many reasons and the protonated complex is a much weaker base than originally established.

Protons have a high charge-to-mass ratio, thus placing two positive charges at the immine nitrogens is expected to significantly lower the energy gap of the MLCT terminating on the protonated ligand by lowering the ligand's π* orbital. Since the charge is transferred to the dpp ligand, the presence of positive charge there favors the charge transfer and since the transfer is primarily coupled to the pyrazine ligand, protonation of the pyrazinyl nitrogen is expected to lead to a red shift in the peak maximum of the MLCT terminating on the dpp ligand, as is in fact observed. The absorption maximum shifts from 480nm to 578 nm. The opposite shift is observed for MLCT bands terminating on the spectator ligands, bpy. As coordinated bipyridines feel the secondary inductive effect of charge being pulled away from the Ru(II) in favor of the protonated ligand, the transition from the metal to the bpy ligands requires more energy, thus blue-shifting the band max from 422 nm to 380 nm.

4.B.1.b $[(bpy)_2Ru(pypz)]^{2+}$

The most significant changes due to protonation are observed via UV-visible spectroscopy between pH 0 and H_0 -2. The complex has only one protonable site, so the titration is expected to reveal only one sigmoidal trace, and it does. The single sigmoidal curves (Figures 65 and 66, page 136) are indicative of a protonation step with an average pK_a value of -1.3 ± 0.2 for the equilibrium constant of the reaction. The value is within experimental error of the one found for the first protonation of $[(bpy)_2Ru(bpz)]^{2+}$ at room temperature[108], -1.6 ± 0.3. As anticipated, the slightly higher average pK_a value is attributed to the fact that the pypz ligand has only one basic protonable nitrogen, while bpz has two peripheral N-heteroatoms competing for the proton.

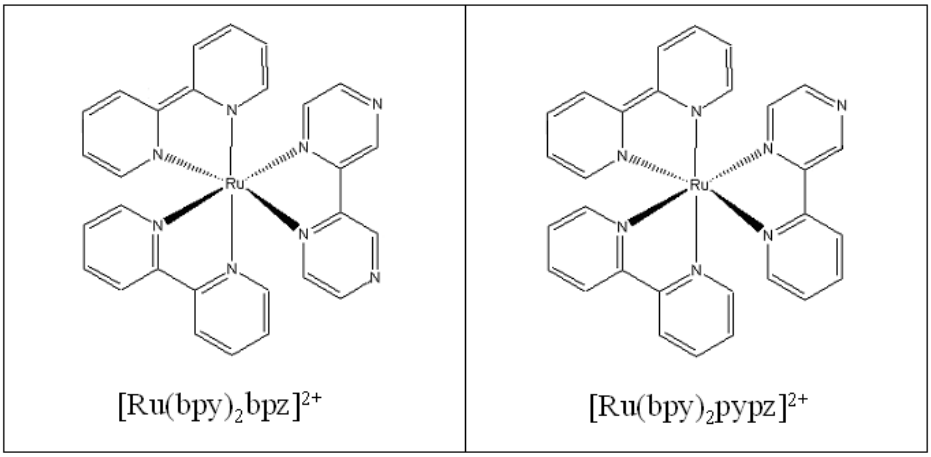

Figure 174: Structure of $[(bpy)_2Ru(bpz)]^{2+}$ and $[(bpy)_2Ru(pypz)]^{2+}$.

When titrating $[(bpy)_2Ru(pypz)]^{2+}$ with different acids, perchloric and sulfuric, a slight difference in the pK_a values (-1.22 vs –1.59) is observed and attributed to differences in the ionic strength of the samples (Figure 66). The difference is only noticeable in the ground state. In the excited state, samples prepared with perchloric acid protonate at the same pH as samples with sulfuric acid. The reason for this may be found in the different timescale of the two processes. In the ground state there is sufficient time for the system to come to equilibrium whereas in the excited state the titration happens faster and the system may not come to equilibrium. In other words, the solvent and the ions within the solvent have no time to significantly affect the equilibrium between protonated and unprotonated complex.

Different inflection points were also derived as a function of the monitoring wavelength for the titration (Table 15, page 137): the shorter the monitoring wavelength, the lower the equilibrium constant. This observation can be rephrased by saying that monitoring the changes in the UV-Vis spectrum at shorter wavelength results in a smaller, more negative, pK_a value. As the solution's pH is decreased it appears that, either the lower-energy MLCT transitions "respond" to the change in acidity before the

short-wavelength bpy-centered transition does (i.e. at higher pH), or that the MLCT to bpy is less sensitive to the change in pH. Since the absorption band at longer wavelength is centered on the ligand undergoing protonation, it is plausible, if not expected, that it may react first to the change in pH and undergo the biggest change in absorption intensity since the inductive effect of protonation of the pypz ligand reduces electron density at the Ru(II).

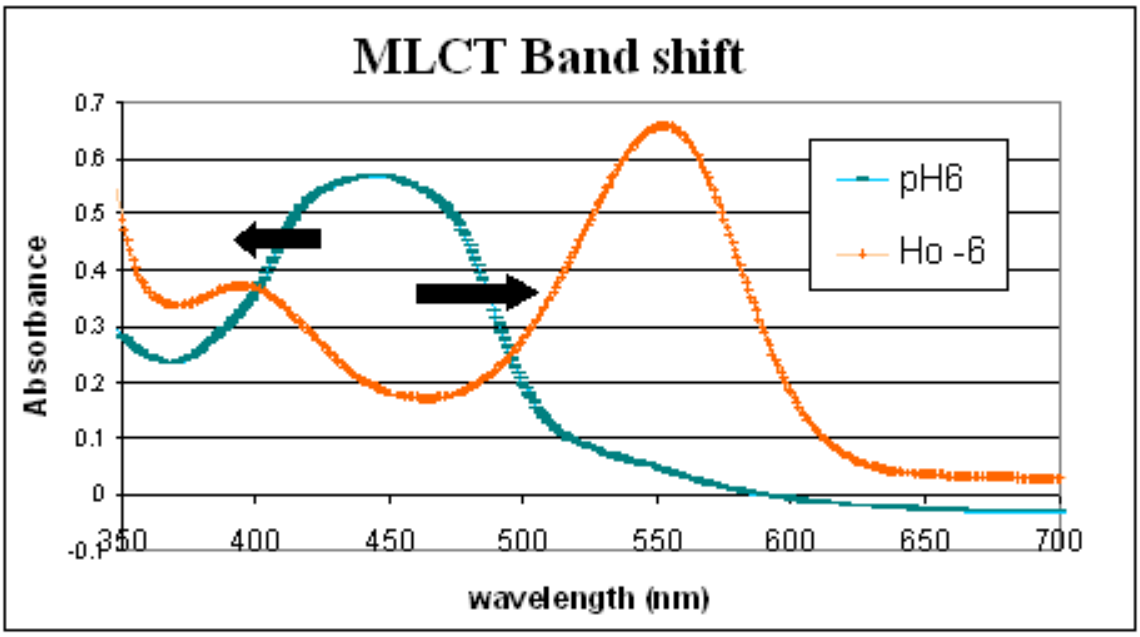

Figure 175: Red- and blue-shift of the $[(bpy)_2Ru(pypz)]^{2+}$ MLCT bands as a function of pH.

Similar to what was reported in the titration of $[Ru(bpy)_2dpp]^{2+}$, during the ground state acid titration of $[(bpy)_2Ru(pypz)]^{2+}$, the shift to the red experienced by the low energy MLCT band is a direct consequence of protonation (Figure 175). The presence of an additional positive charge on the pypz ligand reduces the energy required to transfer the electron to said ligand, hence reducing the energy of the corresponding MLCT transition. On the other hand, the bpy-localized higher energy MLCT band blue

shifts as a result of the secondary inductive effect of electron-withdrawal from the metal center as the charge on ruthenium itself moves toward the protonated ligand, pypz. To the extent that back-bonding is reduced, the MLCT(bpy) level is destabilized and the corresponding transition increases in energy. In other words, the inductive effect of protonation of the pypz ligand appears to:

1. Shift the MLCT to bpy to higher energy and,
2. by reducing electron density at the metal, reduce the hallowedness of the MLCT, i.e. the ε of the transition, thereby requiring higher acid concentration to see the net effect.

4.B.1.c Comparative analysis of ground-state titrations (dpp vs pypz)

The four ground state titrations are compiled in Figure 176 and the four pK_a values obtained can be schematically summarized as:

$$\mathbf{pK_a}(\text{dpp-N}_{pz}) < \mathbf{pK_a}(\text{pypz}) < \mathbf{pK_a}(\text{dpp-N}_{py}) \text{ from NMR} < \mathbf{pK_a}(\text{dpp-N}_{py}) \text{ from UV-Vis}$$

$$-5.9 > -1.3 > 1.52 > 2.7$$

As expected from the relative basicity of pyridine and pyrazine free ligands, as well as bypyridine and bipyrizine, the pyridyl nitrogen of $[(bpy)_2Ru(dpp)]^{2+}$ is a stronger base than the pyrazyl nitrogen of $[(bpy)_2Ru(dpp)]^{2+}$ and $[(bpy)_2Ru(pypz)]^{2+}$ and its protonation is observed in the pH 3 to 1 range. The pyrazyl nitrogen of $[(bpy)_2Ru(pypz)]^{2+}$ protonates next at Ho -1.3, as do other ruthenium complexes with at least one protonable N heteroatom on the ligand periphery (Table 29).

Table 29: Ground-state pK_as for ruthenium(II)-diimine complexes.

Ru-complexes	pK_{a1}	pK_{a2}
$[(bpy)_2Ru(pypz)]^{2+}$	-1.3[d]	----
$[(bpy)_2Ru(dpp)]^{2+}$	2.1[d]	-5.9[d]
$[(bpy)_2Ru(bpz)]^{2+}$	-1.6[c]	
$[(bpz)_2Ru(bpy)]^{2+}$	-2.4[c]	
$[(bpz)_2Ru(bpm)]^{2+}$	-1.6[c]	
$[Ru(bpy)(bpm)(bpz)]^{2+}$	-2.0[c]	
$[Ru(bpz)_3]^{2+}$	-2.2[a]	-3.0[b]

[a] Ref 62. [b] Ref 106. [c] Ref 108. [d] Present work. [e] bpm = 2,2-bipyrimidine.

Finally, the second and last protonation step of $[(bpy)_2Ru(dpp)]^{2+}$ occurs at Ho -5.9. This result is probably the most remarkable as it happens at much higher acidity than most peripheral nitrogens on diimine ligands coordinated to Ru(II).

The initial interest in the $[(bpy)_2Ru(pypz)]^{2+}$ complex stemmed from the desire to understand how the pyrazinyl nitrogen on the coordinated dpp would behave if the additional pyridyl ring on dpp was not present. It was speculated that, since the peripheral pyridyl ring is free to rotate away from the protonated pyrazinyl nitrogen, its effect on the latter nitrogen in the ground state would be essentially non-existent[53]. Measurements of the ground state pK_a value for the protonation of $[(bpy)_2Ru(pypz)]^{2+}$ prove that the basicity of the pyrazinyl nitrogen on the dpp ligand of $[(bpy)_2Ru(dpp)]^{2+}$ is significantly reduced (by over 4 orders of magnitude!) by the presence of the pyridyl ring and by the fact that protonation of the pyrazinyl nitrogen of dpp only happens in the ground state after first protonation has occurred. Hence it is a protonation of an already protonated +3 species increasing its charge to +4. This observation, together with the fact that protonation of the dpp ligand at the pyridyl ring is observed and occurs at higher pH than

initially assessed (between pH 4 and 1) means that previous interpretations of the proton quenching of $[(bpy)_2Ru(dpp)]^{2+}$ and the determination of the basicity enhancement of the protonable site upon excitation must be re-examined. Additionally, the presence of the mono-protonated form of $[(bpy)_2Ru(dpp)]^{2+}$ in solution in the pH 4 to 1 range means that, the unprotonated form of the complex in that range of acidity, is not the only form of the complex that can be excited, as initially concluded[52].

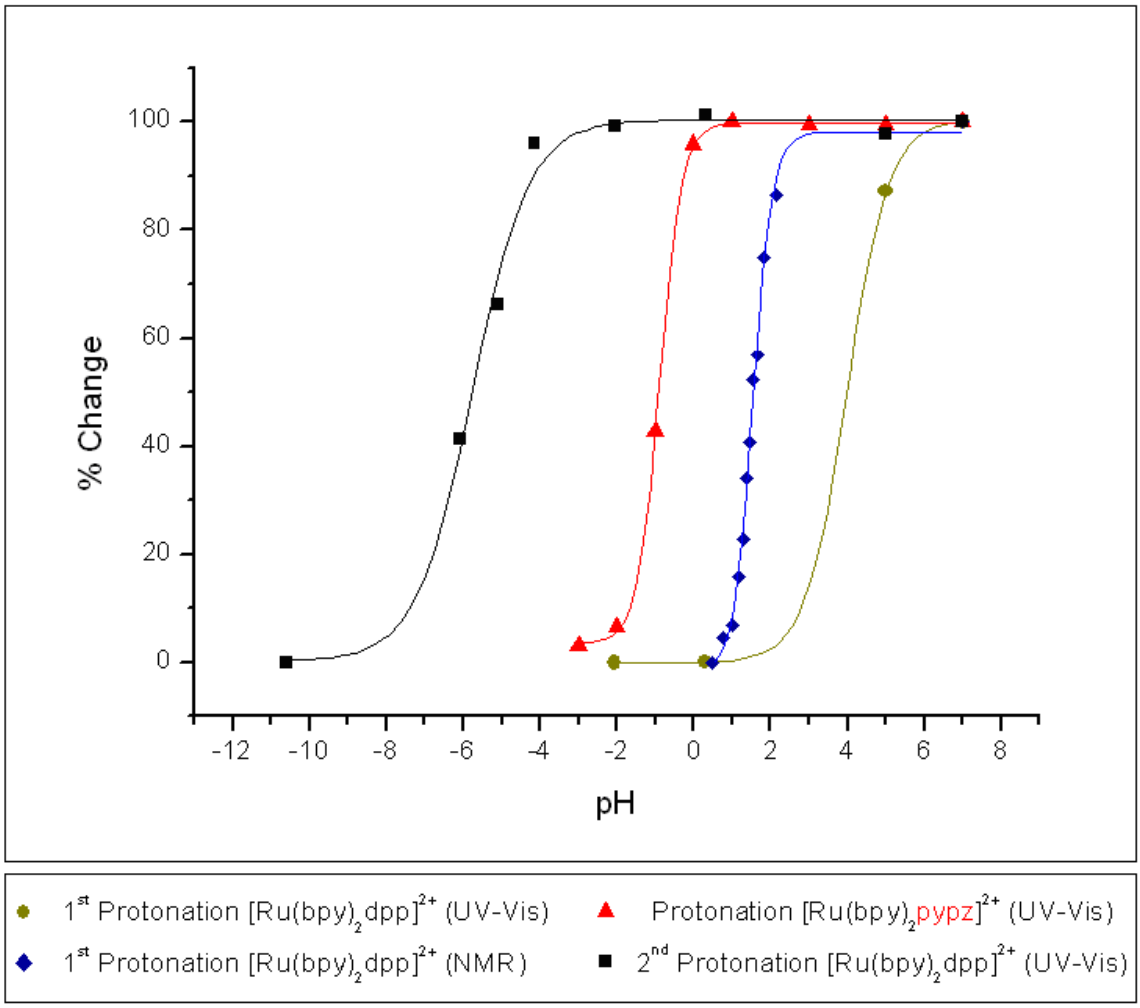

Figure 176: $[(bpy)_2Ru(dpp)]^{2+}$ and $[(bpy)_2Ru(pypz)]^{2+}$ ground-state acid-base titrations.

4.B.2. Excited-State Titrations

4.B.2.a $[(bpy)_2Ru(dpp)]^{2+}$

The acid-base behavior of the excited complex was examined in the pH equal to 8 to Ho equal to –2 acidity range by recording the steady-state and time-resolved luminescence spectra of the complex. Relevant parameters affected by the change in acidity are: transition energy and intensity, lifetime, quantum yield, areas under the 2D curves, and areas under the time-resolved 3D spectra. Kinetic constants and $pK_a^*(app)$ can be estimated by following the changes of the above parameters as a function of pH. A single exponential decay is observed in the 8 to 1 pH range. The values listed in Table 13 are within ± 0.2 units and the average value of pK_a^* obtained is 4.5. The equilibrium constant for protonation is "apparent" in view of the fact that it needs to be corrected for the differences in the excited-state lifetime of the protonated and unprotonated forms. Correction to the excited-state pKa is usually made using equation (64), if both forms are emissive and the lifetimes are known:

$$pK_a^* = pK_a^*(app) + \log(\tau_a/\tau_b) \qquad (64)$$

The $pK_a^*(app)$ is obtained from the inflection point of the luminescence titration curve while τ_a and τ_b are the lifetimes for the acid and the conjugate base forms of the complex, respectively[109]. Based on equation (64), if the lifetimes are of the same order of magnitude, the $pK_a^*(app)$ and the excited state pK_a^* are comparable. However, if the lifetime of the protonated species is much shorter than the lifetime of the unprotonated one, the reaction does not reach equilibrium and it will seem as if the complex is a better

base than it really is, because the protonated form will relax down and by Le Chatelier's Principle the reaction will shift toward formation of more excited-state protonated complex (Figure 177).

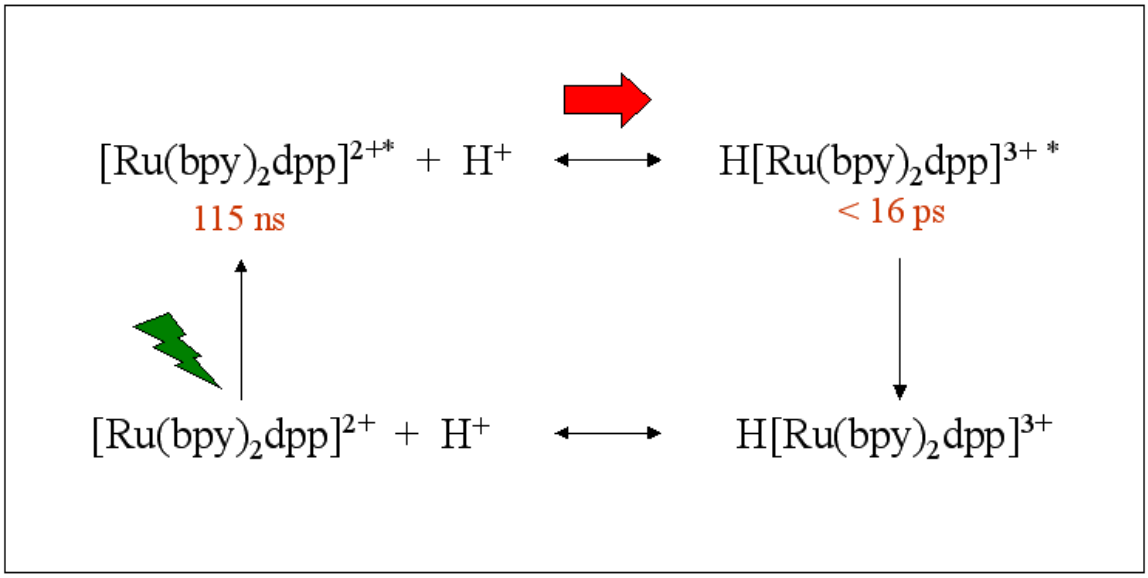

Figure 177: Schematic representation of Le Chatelier Principle applied to ground and excited-state protonation reactions of $[(bpy)_2Ru(dpp)]^{2+}$.

The emission from the monoprotonated form of the $[(bpy)_2Ru(dpp)]^{2+}$ decays within the lifetime of the exciting pulse hence its lifetime is, at most, as long as the pulse, 16 ps. Such a short lifetime renders the probability of reaching equilibrium extremely unlikely. The lifetime correction and other "corrections" to the apparent pK_a^* value, are not good ways to estimate the protonation constants of $[(bpy)_2Ru(dpp)]^{2+}$ because of the uncertainty inherent in the fact that the complex has two protonable sites and that protonation in the ground- and excited-state may not happen at the same site.

Two issues arise: determining the thermodynamically valid pK_a^*; and determining the change in basicity that the molecule as a whole experiences when in the excited state,

compared to that in the ground state. Both issues hinge on understanding what protonation equilibrium the molecule undergoes in the excited state. However, this may depend on the pH.

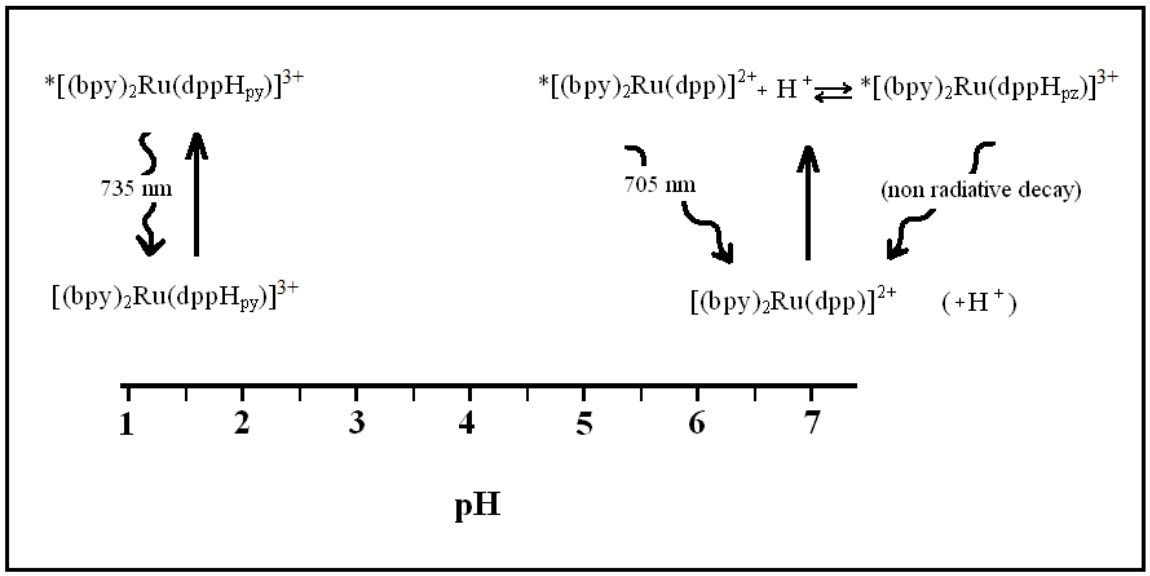

Figure 178: Diagram of ground and excited state protonation of $[(bpy)_2Ru(dpp)]^{2+}$.

According to the most plausible model proposed by Zambrana[53], the $[(bpy)_2Ru(dpp)]^{2+}$ complex protonates at the pyrazinyl nitrogen, H_{pz}, at neutral pH in the excited state and is protonated at the pyridyl nitrogen, H_{py}, at acidic pH in both ground and excited state (Figure 178). The luminescence quenching is thought to occur by protonation of the peripheral pyrazyl nitrogen of the dpp ligand regardless of pH. However, at pH 1, the protonated form of the complex with the proton bonded to the pyridyl nitrogen exists in the ground state and the data indicate it absorbs energy and emit at 735 nm. Several experimental observations support this thesis, including the results presented here about the protonation of the $[(bpy)_2Ru(pypz)]^{2+}$ complex which was examined in part to clarify the role of the peripheral dpp pyridine in the ground and excited state protonation:

1. Resonance Raman studies on $[(bpy)_2Ru(dpp)]^{2+}$ and $[(bpy)_2Ru(pypz)]^{2+}$ complexes, have revealed that the vibrations associated with the pyrazyl portion of the heteroleptic ligand are enhanced upon excitation. It was concluded that the pyrazyl nitrogen has increased electron density in the excited state and is therefore expected to be a better base than in the ground state.
2. No new emission is observed in the pH range 7-3 for aqueous solutions of either $[(bpy)_2Ru(dpp)]^{2+}$ and $[(bpy)_2Ru(pypz)]^{2+}$ complexes, suggesting that protonation at the pyrazyl nitrogen results in formation of a non-emissive species.
3. Given the fact that the pyridyl ring is more decoupled from the metal, emission at 735 nm is assigned to the $[(bpy)_2Ru(dpp)]^{2+}$ complex protonated at the pyridyl nitrogen. If the complex is protonated with a proton at the pyridyl ring, the occurrence of an emission –though with low quantum yield and short lifetime- is thought to reflect the reduced electronic coupling between the peripheral pyridine and the remainder of the complex. It is also possible that the emissive form of the protonated complex involves some degree of hydrogen-bonding, keeping both basic sites engaged and less capable of dissipating excitation to the solvent.

At intermediate pH, between 4 and 1, the $[(bpy)_2Ru(dpp)]^{2+}$ complex is partly protonated in the ground state. Therefore, in the excited state, protonation could theoretically be obtained through a number of different processes happening simultaneously:

- Protonation of the excited $^{*}[(bpy)_2Ru(dpp)]^{2+}$ complex at the pyrazyl nitrogen;
- Protonation at the pyridyl nitrogen in the ground state and subsequent excitation;
- Lastly, the observed protonation could be the result of the exchange of a proton from the pyridyl nitrogen to the pyrizyl nitrogen via intra-molecular hydrogen bond. It is possible that, the same first protonation that renders the pyrazinyl nitrogen of dpp a weaker base in the ground state, may contribute to favor the protonation of the pyrazyl site in the excited state. This could be the result of two concerted effects. First, a kinetic effect, where excitation inverts the relative basicity of the peripheral dpp nitrogens and bonding of the proton on the pyridyl nitrogen at acidic pH is followed by delivery of that proton to the pyrazinyl nitrogen upon excitation. Second, an energetic effect, where protonation of the dpp peripheral pyridyl nitrogen could reduce the electron density at the pyrazyl nitrogen thereby making the latter more receptive to the charge transferred on excitation.

The presence of two mono-protonated forms of the same complex in the excited state could account for the "gentle" sloping of the titration curve, since the protonation reaction followed via titration is not happening at a single basic site but involves instead two sites with changing relative basicity in the ground and excited state.

Now, going back to the issues about determination of the thermodynamic pK_a^{*} and the ΔpK_a, the only true excited state protonation equilibrium, if an equilibrium is in fact established, is envisioned to occur between the excited state unprotonated $^{*}[(bpy)_2Ru(dpp)]^{2+}$ and the excited state protonated $^{*}[(bpy)_2Ru(dppH_{pz})]^{3+}$ form. Since the complex protonated at the pyrazinyl nitrogen does NOT emit, the lifetime correction

previously applied by Zambrana, is no longer pertinent. Likewise, using the change in emission or absorption spectra as described for equation 49 is no longer possible. The emission spectra cannot be used because the protonated species in the excited state is different than in the ground state. The absorption spectra cannot be used because a clear band maximum cannot be localized as the changes in the MLCT for dpp are very small and subject to high uncertainty.

$$pKa^* = pKa + (2.86\ \Delta\nu)/(2.3\ RT) = pKa + (0.625\ \Delta\nu)/T \qquad (49)$$

As a consequence of the above considerations, it is not possible to calculate or extrapolate the thermodynamic pK_a^* from the spectra at hand. At most, an educated guess can be made of the increase in basicity of the pyrazinyl site of dpp by comparing the excited state pK_a^*(app) for $[(bpy)_2Ru(dpp)]^{2+}$ with the ground state pK_a of $[(bpy)_2Ru(pypz)]^{2+}$, since both protonations refer to the same kind of nitrogens:

$$\Delta pK_a = pK_a^*(app)\ [(bpy)_2Ru(dpp)]^{2+} - pK_a\ [(bpy)_2Ru(pypz)]^{2+} = 4.5 - (-1.3) = 5.8$$

In other words, assuming the peripheral dpp pyridine is not involved, population of the dpp localized MLCT state increases the basicity of the pyrazyl nitrogen by 5.8 or close to the original estimates of 6 orders of magnitude.

While only one pK_a^* (app) value was obtained with a certain degree of confidence, it can be inferred from the luminescence spectra that the second protonation also occurs at higher pH than observed in the ground state. Both protonations happen

sooner in the excited state, hence the basicity increases at both protonable sites upon excitation. Theoretically, with increased basicity at both sites, both pKa should be observed and a second pK_a^* (app) could be estimated from the decrease of the 735-nm emission. Even without conclusive data to calculate the exact value of pK_{a2}^* (app), based on when the 735-nm emission appears and disappears, the constant should have a value:

$$-0.5 \leq pK_{a2}^*(app) \leq 1$$

which is more than 5 orders of magnitude larger than the second protonation in the ground state. In the ground state, the second protonation occurs at acidity lower than H_0 -4. In the excited state both emissions, 700 and 730 nm, are quenched completely at H_0 -0.5, evidence that the double protonated, non-emissive species is formed.

We cannot attribute an exact value to the basicity enhancement brought on by excitation, but we can report that the direction of the change in pKa is consistent with the MLCT assignment (increased charge on the ligand increases the base strength).[110] The basicity of the pyrazinyl nitrogen on the dpp ligand DOES increase significantly upon excitation as does the pyrazinyl nitrogen on the pypz ligand of $[(bpy)_2Ru(pypz)]^{2+}$ (vide infra).

4.B.2.b $[(bpy)_2Ru(pypz)]^{2+}$

In the pH range, from 12 to 1, the emission intensity and lifetime of the $[(bpy)_2Ru(pypz)]^{2+}$ complex decrease with no change in the peak max position. Even in basic or neutral solutions where no protonated species can be detected via UV-Vis absorption, the luminescence is partly quenched. The parameters monitored as a function of pH were: lifetimes, intensity at 675 and 725 nm, and area under the emission curve

between 550 and 750 and they all displayed similar patterns of change. Two sigmoidal curves are obtained by plotting the parameters' change, one in the 12 to 7 pH range and one in the 6 to 0 pH range (Figure 179). The first, much steeper curve reflects a change that happens within 3 pH units, while the second more gradual slope depicts a change happening within twice as many pH units. The values of pH at midpoint of the breaks in the curves are, respectively, 7.7 and 2.7, estimated to within ± 0.2 units.

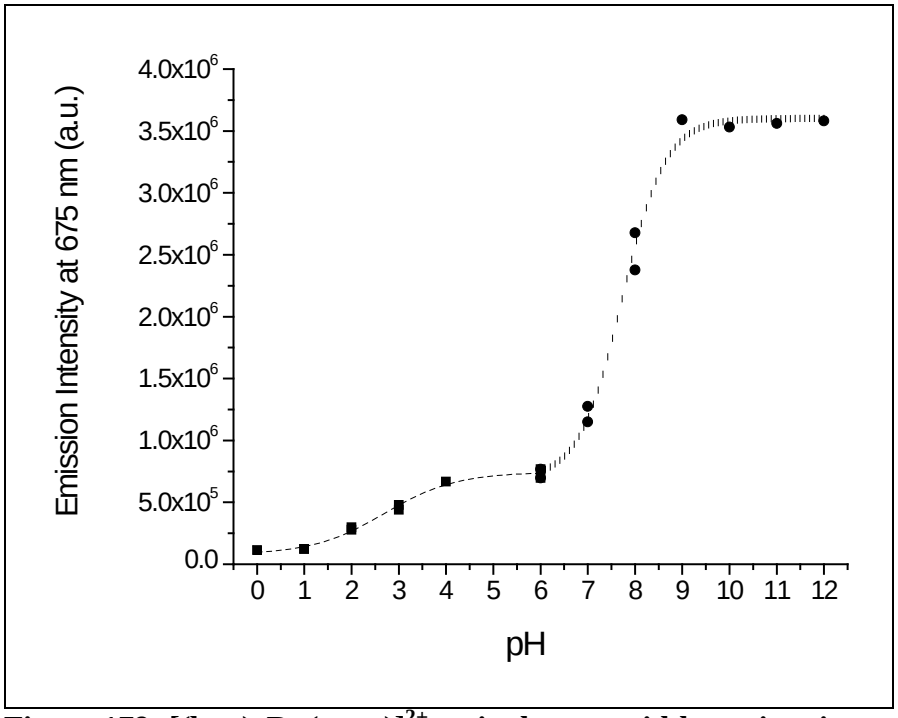

Figure 179: $[(bpy)_2Ru(pypz)]^{2+}$ excited-state acid-base titration.

Below pH 7, the emission quenching is due to protonation of the complex at the only available peripheral nitrogen of the pypz ligand and formation of the non emissive species $[(bpy)_2RupypzH]^{2+}$. The complex has only one basic site and, unlike the case of $[Ru(\mathbf{dpp})(bpy)_2]^{2+}$, there is no ambiguity as to where protonation occurs. The value of excited state pK_a obtained, $pK_a^*(app) = 2.7 \pm 0.2$ yields a ΔpK_a of 4, suggesting that the

complex is several orders of magnitude more basic in the excited state, than in the ground state. The change in pK_a for protonation in ground and excited states, from -1.3 to 2.7, is caused by electronic excitation, which rearranges the electron density within the complex. Since the lowest excited state of $[Ru(\mathbf{pypz})(bpy)_2]^{2+}$ is the "metal-to-pypz" charge transfer excited state, excitation increases electron density in the pypz ligand thereby increasing its basicity and protonation occurs at much higher pH than in the ground state. What seems to happen below pH 6 is the following: the neutral complex gets excited and, as a result, the basicity of the pyrazyl nitrogen increases many-fold allowing the complex to react with the proton. The protonated species in the excited state is formed and relaxes down to the ground state via radiationless decay, regenerating the unprotonated complex and the hydronium ion. The excited state pK_a value of 2.7 is well within the range of all the other values obtained in the past for similar complexes in comparable experimental conditions (Table 30).

Table 30: Ground and excited state pKa constants.

	pK_a (ground state)	pK_a (excited state) app
$\mathbf{[(bpy)_2Ru(pypz)]^{2+}}$	-1.3 ± 0.2[a]	2.7[a] (τ = 52ns)
$\mathbf{[(bpy)_2Ru(pypz)H]^{3+}}$		Non emissive
$\mathbf{[(bpy)_2Ru(bpz)]^{2+}}$	-1.6 ± 0.3[b]	2.80[b] (τ = 92ns)
$\mathbf{[(bpy)_2Ru(bpz)H]^{3+}}$		Emissive
$\mathbf{[Ru(bpz)_3]^{2+}}$	-2.2 ± 0.3[b]	3.30[b] (τ = 940ns)
$\mathbf{[Ru(bpz)_3H]^{3+}}$		(τ = 47ns)

[a] Current work. [b] Ref 62.

The change is due only in part to the increase of excited-state basicity and the pKa* is “apparent” because of the absence of a clear emission signal for the protonated species. The non-radiative relaxation process in the protonated species is so fast that emission cannot be observed and equilibrium is likely not established during the lifetime of the excited state. The lifetime correction cannot be applied but a Forster cycle analysis can provide an estimate of the excited pKa using the difference in absorption maxima of the fully protonated and deprotonated forms (in cm^{-1}):

$$pKa^{*} = pKa + (2.86\ \Delta\nu)/(2.3\ RT) = pKa + [0.625\ (\nu_1-\nu_2)]/T \quad (49)$$

where pKa* is the charge-transfer excited state pKa, pKa is the ground state pKa, ν_1 is the frequency in wavenumbers of the charge-transfer absorption maxima of the unprotonated form, and ν_2 is the frequency of the corresponding transition in the protonated form. The pKa^{*} value calculated using equation 49 is 4.7[a]. However, it has to be borne in mind that the $\Delta\nu$ does not necessarily accurately reflect the difference in free energy of the *relaxed* excited states and it does not account for changes in entropy between the ground state acidic and basic forms. Also, due to the intrinsic difficulty of obtaining a good approximation for the relative difference in the 0-0 transition energies, and the uncertainty in the estimated MLCT excited state energies, the K_a* value may vary by about 3 orders of magnitude, making the value derived unreliable.

[a] (476 nm/21008.4 cm^{-1}, 551 nm/18148.82 cm^{-1}, $\Delta\nu$ = 2859.58 cm^{-1})

Between pH 7 and 9, the lifetime and emission intensity increase rapidly and they are independent of further increase after pH 9. In general, three factors are responsible for excited state quenching: molecular oxygen, electron-transfer and protons. Molecular oxygen is excluded because all samples tested were degassed with N_2 or Ar for approximately 10 minutes before recording their spectra. Attributing these changes to electron transfer seems unlikely, mainly for the fact that emission intensity *increases* as the pH increases. Electron-transfer, whether in the excited state or in the ground state, yields either a Ru(III) or a reduced complex with the electron at the ligand or at the metal center. The absence of any report of emission from these species precludes the possibility that the increased emission is due to electron transfer. Proton transfer or reaction with the solvent is equally unlikely because no variation of the ground state UV-Vis spectrum is observed at pH 6-12, both in the MLCT region and the ligand centered absorption bands. The high energy bands centered on the ligands are affected by proton concentration below pH 2 but at neutral and basic pH the contour is un-altered and the band at 284 nm is identical to the band found at 284 nm in the spectrum of the free pypz ligand, thus suggesting that no structural change or change in the electronic distribution occurs at neutral pH. In addition, no concomitant change in emission peak maximum position is observed alongside the change in lifetime and emission intensity as the pH changes. Protons are present in low concentration at basic pH and are expected to protonate the complex at much higher acidity, which they do. It is not unlikely for ruthenium(II) complexes with pyrazine ligands to protonate in that region. For example, the excited state pKa* of pentaammineruthenium(II) complex of pyrazine has value 7.3, according to Rillema et al[87]. However, ruthenium(II) diimine complexes analogous to

$[(bpy)_2Ru(pypz)]^{2+}$ undergo protonation in the 6-9 pH range only when reduced using pulse radiolysis to the one-electron non-emissive $[L_2RuL^{\bullet+}]$ form[73]. It seems farfetched that the $[(bpy)_2Ru(pypz)]^{2+}$ complex could undergo reduction, in the excited state, in basic solution, and if it did, the emission would decrease and not increase. In conclusion, an increase in the radiative constant, k_r, is excluded since the constant is dependent on the chemical structure of the complex itself and, based on the spectroscopic evidence discussed above, the structure remains unaffected by the increase in pH. More likely, the reason for the more stable and longer-lived form of the complex in basic solution is attributable to a reduction in the non-radiative quenching rate, k_{nr}, which is dependent on the interactions of the complex with its surroundings (Equation 2). As the solvent shell around the molecule changes in basic solution, non-radiative decay processes such as intramolecular excited state deactivation and excited state decomposition as well as uni-molecular decay, may be less favored. Furthermore, the hydrogen bonds between the complex and the solvent that are responsible for vibrational loss of energy via non-radiative interactions may be hindered by the increased concentration of OH^- species in basic solutions.

$$A^* \xrightarrow{Knr} A + \Delta \qquad \text{Rate} = k_{nr}[A^*] \qquad (2)$$

While pinpointing exactly what causes the emission quenching is still very much an open challenge, the quantitative reversibility of both absorption and emission changes establishes that the interaction happens exclusively while the complex is in the excited

state and that the complex returns to its original composition and configuration as soon as it returns to the ground state.

4.B.3 Kinetics of proton quenching

In conjunction with the emission lifetime, Stern-Volmer plots can be constructed to determine experimentally the bimolecular rate constant (k_q) for the quenching of the excited state of ruthenium diimine complexes. If the quencher - in this case the proton- does not absorb the exciting and emitting light, the plots are linear as a function of the concentration of quencher and the proton encounter reaction is said to be "diffusion limited".[17] The constant k_q can be derived from the slope of the Stern-Volmer plot line, K_{SV}, using the relationship:

$$K_{SV} = k_q \tau_0 \qquad (101)$$

where τ_0 is the lifetime in the absence of a quencher.

Stern-Volmer applies when the excited molecule meets the quencher via a single-step irreversible reaction and is deactivated upon contact[17]. The Stern-Volmer plots obtained for $[(bpy)_2Ru(dpp)]^{2+}$ and $[(bpy)_2Ru(pypz)]^{2+}$ (Figure 57 and 80, respectively) show negative deviations from linearity. Attempts to fit the entire range of pH's examined were unsuccessful. In both cases, a fit is achieved only at high or low pH (Figure 58-59 and 81-82) but not at both, simultaneously, pointing to two distinctly different processes. In addition, the quenching of emission intensity and the quenching of excited-state lifetime do not yield coincident plots. Negative deviations and lack of coincidence are evidence that a more complex mechanism exists. This confirms the observations made while studying the excited-state acid-base titrations of $[(bpy)_2Ru(dpp)]^{2+}$ and

$[(bpy)_2Ru(pypz)]^{2+}$, and supports the idea that the interaction between the excited complexes and the proton is not a unique and continuous process over the 0 to 12 pH range.

In principle, many factors can contribute to deviations. As Hoffman et al. pointed out, there may be several reasons for "the kinetics of quenching to become more complex than expected from the S-V equations"[17]. In particular, the following factors may be at play in the case of the complexes studied herein:

1. Variations in ionic strength;
2. If two excited states of the substrate exist but only one is quenched;
3. Concomitant static quenching.

Ionic strength changes significantly as the acidity of the solution is increased. Attempts to keep ionic strength constant were met with the challenge of maintaining the analytes in solution and therefore abandoned since addition of significant amounts of electrolyte would cause precipitation of salts.

Existence of more than one excited state is possible, especially in the case of $[(bpy)_2Ru(dpp)]^{2+}$ where charge transfer to the ligand may lead to excess charge by the pyridyl nitrogen or pyrazyl nitrogen as well as to the bpy ligand. In general, quenching could occur following a variety of paths. "Experimental evidence in favor of a particular quenching process does not exclude the possibility that some fraction of the quenching acts occurs via a different mechanism". Hence, it is important to keep in mind that the experimentally obtained value of k_q is an overall rate constant representing the sum of the k_q values for all the possible individual deactivation pathways that are accessible to the excited complex.

Thirdly, static quenching does occur when protonation is established in the ground state, before excitation takes place. Pre-equilibrium is postulated at low pH for $[(bpy)_2Ru(dpp)]^{2+}$ where, based on the ground state protonation constant, over 80% of the complex is expected to be in the protonated form, $[(bpy)_2Ru(dppH_{py})]^{3+}$. No pre-equilibrium is proposed for $[(bpy)_2Ru(pypz)]^{2+}$ in the 0 to 12 pH range since the complex protonates in the ground state at much higher acidity.

Formation of an exciplex may also cause negative deviations from linearity as outlined by Hoffman[17]. If the quenching is expected to involve formation of an excited state complex between the excited species and the quencher, a contribution from the exciplex to the emission intensity under steady-state conditions should be taken into considerations and the plot of $\frac{I_1^0}{I_1}$ versus the concentration of quencher is not linear (Equation 94). The plot is expected to have negative deviation from linearity and reach a plateau for $[Q] \rightarrow \infty$. In the case of the $[(bpy)_2Ru(dpp)]^{2+}$ complex, an excited protonated form of the complex is probably formed at pH 5-7, "with redistribution of the electronic energy across the entire species"[17], and the deactivation constant is then the sum of the rate constant for all the possible deactivation pathways that are accessible to the excited complex (deactivation upon formation of a "precursor complex", non-radiative deactivation, deactivation after formation of a "successor complex"). However, the species is non emissive, so there is no direct evidence of its existence and the radiative pathway can be excluded. The only evidence of an emissive protonated species is for the $[(bpy)_2Ru(dpp)]^{2+}$ complex at pH 1 and the structure assigned to that species has a proton bonded to the pyridyl portion of the dpp ligand. We have no experimental

evidence for the formation of an emissive exciplex both for $[(bpy)_2Ru(dpp)]^{2+}$ at neutral pH and for $[(bpy)_2Ru(pypz)]^{2+}$ over the 0-11 range.

In view of the fact the two ruthenium complexes under study are structurally different enough to have the potential to establish distinct equilibria and undergo different reactions in different regions of pH, it is of interest to look in detail at how the interaction of each complex with the increasingly acidic solvent evolves as a function of the concentration of quencher, i.e. the proton.

4.B.3.a $[(bpy)_2Ru(dpp)]^{2+}$

Based on the observations made while studying the excited state protonation of $[(bpy)_2Ru(dpp)]^{2+}$, it was concluded that the complex is not undergoing one continuous phenomenon between pH 7 and 0. Rather two distinct occurrences happen. The complex has two protonable sites and it was proposed that the pyrazinyl site is "active" between pH 7 and 2, while the pyridyl site is involved in protonation at pH 1 and beyond. In the intermediate pH range, both basic sites may be competing for the proton and more complex mechanisms may be at play. This model is consistent with the trends observed when a Stern-Volmer model is applied and would explain why proposing one quenching mechanism doesn't work.

Table 31: Photophysical constants from the emission data fit.

$[(bpy)_2Ru(dpp)]^{2+}$	K_{SV} (M^{-1})	k_q ($s^{-1}M^{-1}$)
High pH (2-7)	3.4×10^6	2.7×10^{12}
Low pH (0-2)	1.174×10^3	1.0×10^{10}

It appears that, in the 2-to-7 pH range, quenching happens exclusively in the excited state, with no pre-equilibrium between the complex and the proton in the ground state. The extremely high values of K_{SV} and k_q suggest that the proton is a very efficient quencher and the rate of quenching is so fast as to exceed the diffusion rate of H^+ in water, 10^{12} $s^{-1}M^{-1}$. In this range of acidity, the negative deviation from linearity of the Stern-Volmer plot may be due to ionic strength effects. The absence of a detectable second emission or assuming two energetically coincident emissions, the singularity of the emission lifetime across the observed emission leads us to relegate a second emission pathway to a minor role and therefore not a major contributor to the negative deviation.

At low pH, static and dynamic quenching are both at play. Pre-equilibrium exists between the complex and the proton in the ground state. Quenching is less efficient, as implied by the lower values of K_{SV} and k_q, and the values are of the same order of magnitude as the values previously reported by Hosek et al., 737 M^{-1} and 5.5 x 10^9 $s^{-1}M^{-1}$, respectively. In this pH range, where the ground state equilibria indicate the presence of the unprotonated and protonated complex with the proton attached to the peripheral pyridyl dpp nitrogen, two quenching pathways can be envisioned. The first is the intermolecular, bimolecular, diffusional reaction between the unprotonated complex and the proton. The second is the intramolecular transfer of the proton from the peripheral pyridyl nitrogen to the peripheral pyrazinyl nitrogen. In fact, the latter intramolecular process is consistent with the large bimolecular rate constant.

Throughout the acidity scale, Stern-Volmer plots of Φ_0/Φ and τ_0/τ are not coincident for the proton quenching of $[(bpy)_2Ru(dpp)]^{2+}$. Treating protonation as an exciplex formation fits equation 87. When fitting is attempted, the equation fits well at

either neutral or very acidic pH values, suggesting that two quenching mechanisms are at play at the extremes of the tested pH range, but more complex than expected from Stern-Volmer equations are relevant in the intermediate range and they very likely involve exciplex formation.

4.B.3.b $[(bpy)_2Ru(pypz)]^{2+}$

Similar to $[(bpy)_2Ru(dpp)]^{2+}$, two quenching phenomena are observed for $[(bpy)_2Ru(pypz)]^{2+}$ in the pH ranges 9-6 and 5-2 (Figure 180).

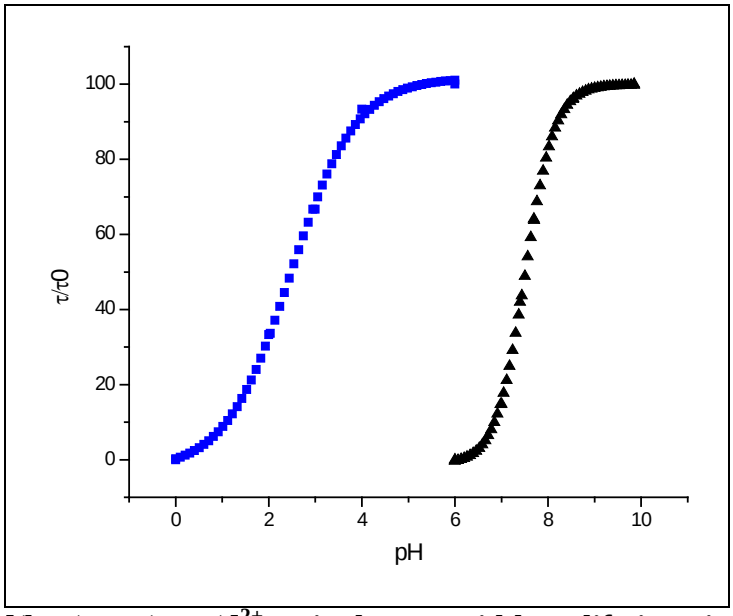

Figure 180: $[(bpy)_2Ru(pypz)]^{2+}$ excited-state acid-base lifetime titration.

The Stern-Volmer plots are linear at high pH (Figure 81), indication that the quencher inhibits the emission by a single reaction. On the other hand, at higher acidity the plots show negative deviations from linearity and the existence of a more complex mechanism must be invoked.

Table 32: Photophysical constants for proton quenching of $[(bpy)_2Ru(pypz)]^{2+}$.

$[(bpy)_2Ru(pypz)]^{2+}$	K_{SV} (M^{-1})	k_q ($s^{-1}M^{-1}$)
High pH (7-10) - (τ_0/τ plot)	2.3×10^7	1.3×10^{14}
High pH (7-10) - (I_0/I plot)	1.8×10^7	1.0×10^{14}
Low pH (2-6)	Not linear	Not linear

The lifetime and emission intensity Stern-Volmer plots do not deviate significantly from each other at high pH (Table 32). This suggests that a simple diffusional quenching model holds true and confirms the absence of static quenching and pre-equilibrium conditions. The kinetic constants obtained are extraordinarily high, comparable in order of magnitude to the constants determined at high pH for $[(bpy)_2Ru(dpp)]^{2+}$ and indicative of the presence of a very efficient quenching mechanism. Excited protonated species decay quickly and have less chance to exist for long in the excited state. H^+ is light and the bond it forms with the excited complex is a facile oscillator that can efficiently dissipate energy to the surroundings. However, at neutral and basic pH, free protons are not present in sufficient concentration to cause the observed changes in the emission spectra and measured lifetimes. More likely, the excited ruthenium diimine complex molecule, $^*M$, is held for a short period of time within a "solvent cage" that is different from the cage surrounding the molecule in the ground state. For example, whether in the ground state or in the excited state, all Ru(II) diimine examined in these experiment are cationic complexes. It would seem reasonable then to expect that a change in the solvent cage may occur on passing from the acidic to basic domain, where the increasing concentration of anionic OH^- may play a larger role in defining the composition of the surrounding solvent shell. If the composition of the solvent shell surrounding the cationic complex is becoming more anionic, then it may be

much more susceptible, i.e., require a large change in structure, to accommodate the change in electron distribution upon excitation and population of the dpp localized MLCT state.

In the lower pH range, negative deviations from linearity and lack of coincidence of the lifetime and emission plots are evidence of a more complex mechanism and suggest that protonation is not the only reaction that the excited complex molecules undergo. Based on visible absorption data, $[(bpy)_2Ru(pypz)]^{2+}$ is unprotonated in the pH range from 6 to 2. However, emission spectra tell a different story. In that range, excited state acid base reaction occurs at the pypz basic site and the complex is fully protonated in the excited state at pH 2. Exciplex formation is unlikely the reason for the negative deviation due to the absence of emission from the protonated complex. The lifetime of $^{*}[(bpy)_2Ru(pypzH)]^{3+}$ cannot be measured, but based on the absence of any detectable emission, it is assumed to be very short. The protonated complex does not live long enough to be emissive and equation 94 cannot be used to fit the data. On the other hand, a new emission at 610 nm ($\tau \approx 500$ns) becomes visible just around pH 2 and is more clearly discernible at even higher acidity (vide infra). The presence of another emission at 610 nm with relative intensity at pH 0 comparable to the intensity of the 675-nm emission at pH 4 could explain the non-linearity of the Stern-Volmer plot, together with the change in ionic strength of the solutions in going from almost neutral pH to a very acidic environment.

4.B.4. New emissions

4.B.4.a $[(bpy)_2Ru(dpp)]^{2+}$

A unique and unexpected feature was observed at acidic pH: the appearance of two concurrent and much-weaker emissions (620 and 730 nm), with sub-nanosecond lifetimes, starting at pH ≤ 1 and disappearing when $[H^+] \geq 2M$. The multiple emissions from the protonated form are negligible compared to the emission from the unprotonated complex, with a difference in quantum efficiency of 5 orders of magnitude or more: 10^{-8} and 10^{-9} for the 620- and 730-nm emission respectively, compared to 10^{-3} for the emission from the unprotonated form. This explains why previous reports[52] state that the emission of this complex "…is completely quenched below pH 1". Only when examined using enhanced detection systems, they may be observed and studied.

The protonated complex is considered to be the one absorbing the laser energy and decaying via double emission because, based on the pK_a calculated from NMR and UV-Vis experiments, over 90% of the complex is present in the protonated form at pH below 1. Additionally, all spectral changes can be quantitatively reversed by the addition of a base, so it is excluded that ligand substitution may have occurred in solution.

Unlike all the parent tris-analogues and the majority of other ruthenium(II) diimine complexes, where current spectral data indicate excitation populates quantitatively only one emissive state, absorption of energy by $[(bpy)_2Rudpp]^{2+}$ results in population of two emissive states with different emission characteristics. In the complexes described here, the detection of the two states is a consequence of the excited state acid base properties of the complex. The maximum intensity of the two emissions is recorded at pH 1; however, the 730-emission decreases in intensity between pH 1 and Ho –0.3, while the 620-peak stays the same in that range and then disappears at higher acidity (Figure 52). The acid dependence of the 730-nm emission is an indication that the

excited state involved has a protonable site; hence the emission is assigned to that from the mono-protonated dpp ligand since a vacant acid-base site remains at the peripheral pyrazine nitrogen. As the concentration of protons increases and the complex undergoes a second protonation, the 730-nm emission disappears indicating that the double-protonated form of the complex is non emissive. The fact that the 620-nm emission is not acid-dependent supports the theory that it is an emission centered on the bpy ligand, a ligand that cannot directly engage in a protonation reaction, at least within the range pH = 1 to H_o = -0.3.

Furthermore, the relative intensity of the two emissions is dependent on the excitation wavelength: the 620-nm peak becomes more intense when the λ_{exc} is shorter (458nm), while the 730-nm peak becomes more intense when the λ_{exc} is longer (514nm) (Figure 54). The excitation dependence suggests two emissive pathways: one that populates an emissive MLCT state localized on a bpy-Ru pair and the other localized on a dpp-Ru pair. The energy diagram of $[(bpy)_2Ru(dpp)H]^{3+}$ is reported in Figure 181: The solid lines represent energy absorption and the wavy lines represent radiative transitions.

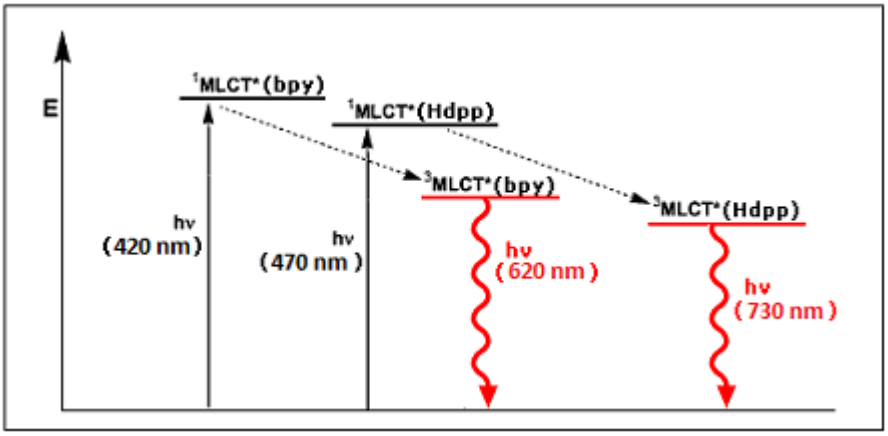

Figure 181: Energy level diagram of $[(bpy)_2Ru(dpp)H]^{3+}$.[111]

In a mixed-ligand complex, the MLCT excited state can, in principle, be located on any of the ligands and data seem to support the assumption that each peak corresponds to an emission localized on only one-type of ligand. With overlapping MLCT absorptions to the different ligands, the intensity of the emission assigned to each ligand reflects the amount of energy absorbed by each ligand. The higher the energy of the exciting beam, the more populated the bpy excited state will be, hence the intensity of the emission relative to such ligand will be high. Conversely, low-energy laser light mainly populates the dpp excited-state and the most intense emission will be centered at 730nm. For this reason, it was reputed unlikely that the 620nm emission may arise from ^{1}MLCT onto the dpp ligand, although the very short lifetime is consistent with an emissive state that is singlet in character. The possibility that contamination from $[Ru(bpy)_3]^{2+}$ could be responsible for the second emission was also considered and rejected, since the emission at 620-nm has a much shorter lifetime than the emission from the parent complex (less than 16 ps compared to 600 ns in room temperature aqueous solution). The diprotonated complex, $[(bpy)_2Ru(dpp)H_2]^{4+}$, is non-emissive and requires much higher acidity to be the prevailing species in solution and traces of the dimer $[(bpy)_2Ru]_2dpp^{4+}$ would have yielded a more red-shifted emission at 755 nm with lifetime in the nanosecond domain.

The findings reported challenge the basic tenet of photophysics of tris Ru(II) diimines stating that only one excited state, at most, luminesces or participates in a chemical process. Dual emission has been observed from Ru(II) diimine samples in the solid state and/or low temperature glassy matrices.[112,113,114,115] In such instances the multiple emission was thought to arise from a partitioning of energy between two states

with an energy separation larger than the available thermal energy. However, this cannot account for the emissions from $[(bpy)_2Rudpp]^{2+}$ since the two emissions are observed in room temperature aqueous solution. Alternatively, the "structured" emission was described as a vibrational progression due to emission from the 0-0, 0-1, 0-2…etc excited vibrational levels. The multiple emission described here occurs at room temperature, in aqueous solutions of the complex and rather than thermally, it becomes apparent when the solution's pH is changed. Other studies have reported multiple emission at room temperature from Ru(II) diimines, but they usually involve multi-nuclear complexes with spacially separated emissive sites[116,117] or involve emissions that are inter-ligand in character[118].

Since this emission and other multiple emissions from Ru(II) complexes of the general formula $Ru(bpy)_2L$ or $Ru(bpy)_2L_2$ all appear in the 600-620 nm region which is in the wavelength region of an MLCT emission localized on the bpy ligand, it is proposed that the 620-nm emission arises from a Ru-bpy localized MLCT state that decays competitively with the lower energy Ru-dpp localized emission from the protonated complex. The 620-nm emission may be the result of a perturbation of energy levels due to protonation; or it may exist at higher pH, but the very short lifetime, together with the low quantum yield of the emission relative to that from the Ru-dpp localized state may be the reason it is not visible. Without protonation of the parent molecule and the concurrent red shift and reduction in emissivity, the strong 705 nm emission completely masks the presence of any other underlying peak.

4.B.4.b $[(bpy)_2Ru(pypz)]^{2+}$

Despite the fact that protonation of the excited-state $[(bpy)_2Ru(pypz)]^{2+}$ complex results in formation of a non-emissive protonated form of the complex (*vide supra*) and emission quenching, a new emission with peak maximum centered at 610 ± 5 nm surprisingly appears in aqueous acidic solution of the complex at pH 2 and below (Figure 182). The observation was unexpected because the prevalent excited species in solution at pH 2 is the non-emissive protonated form of the complex, i.e. $[(bpy)_2Ru(pypz)H]^{3+}$ and none of the ligands possesses free nitrogens available for protonation. In addition, if the emission originated from the complex protonated at the pypz ligand, the band would be expected to appear red-shifted compared to the emission from the unprotonated complex.

Since the wavelength maximum of the 610-nm emission is very close to that of the parent analogue $Ru(bpy)_3^{2+}$, where the excited state is localized on an individual bpy ligand[119,120], the emission is assigned to an excited state localized on the bpy ligand.

It was also surprising to notice that the emission seems to become more intense as acidity of the solution is progressively increased (Figure 183), although further experiments are needed to unequivocally establish its acid dependence.

The possibility that the emission may arise from the background sulfuric acid solutions was considered and experimentally discounted. Absorption and emission spectra of the background solutions were recorded in the same range of acidity and solutions were found not to be emissive in the 600-nm region. Furthermore background samples do not absorb in the 400-500 nm range, range where the excitation wavelength was chosen.

The excitation spectra at decreasing pH show profiles that are all centered around the MLCT bands, thus reducing the possibility that some of the emission may arise from impurities. In addition, at decreasing pH and/or more negative H_0, the peak position does not shift following variations of the excitation wavelength, and the profile of the excitation spectrum narrows progressively. From a profile that clearly looks like the convolution of two gaussians, the spectrum changes into a single gaussian centered at 440nm (Figure 70). The maximum emission intensity is obtained when the complex is excited with light having wavelength in the 430-450 nm range, which is the range of excitation wavelengths observed in other Ru(II) diimine complexes, including $[Ru(bpy)_3]^{2+}$, and assigned to a transition localized on bpy ligands. This finding suggests that only one radiative pathway exists and only one MLCT with bpy-like characteristics is involved. Since the wavelength maximum of the 610-nm emission is very close to that of the parent analogue $Ru(bpy)_3^{2+}$, where the excited state is localized on an individual bpy ligand[119, 120], the emission is assigned to an excited MLCT state localized on the bpy ligand.

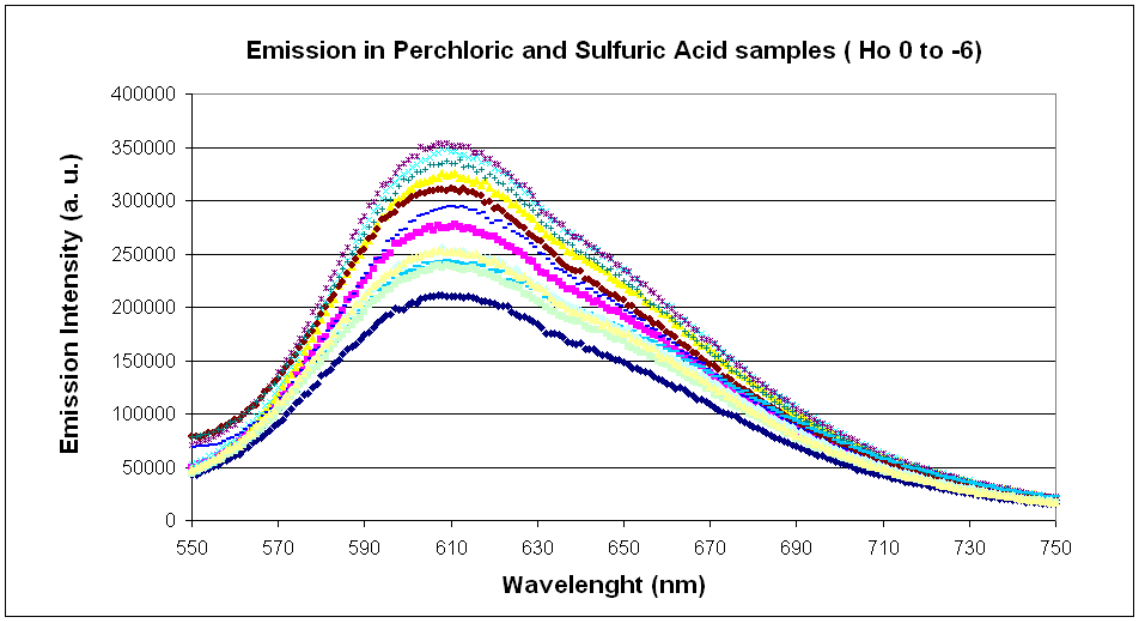

Figure 182. Emission of $[(bpy)_2Ru(pypz)]^{2+}$ in very acidic solution.

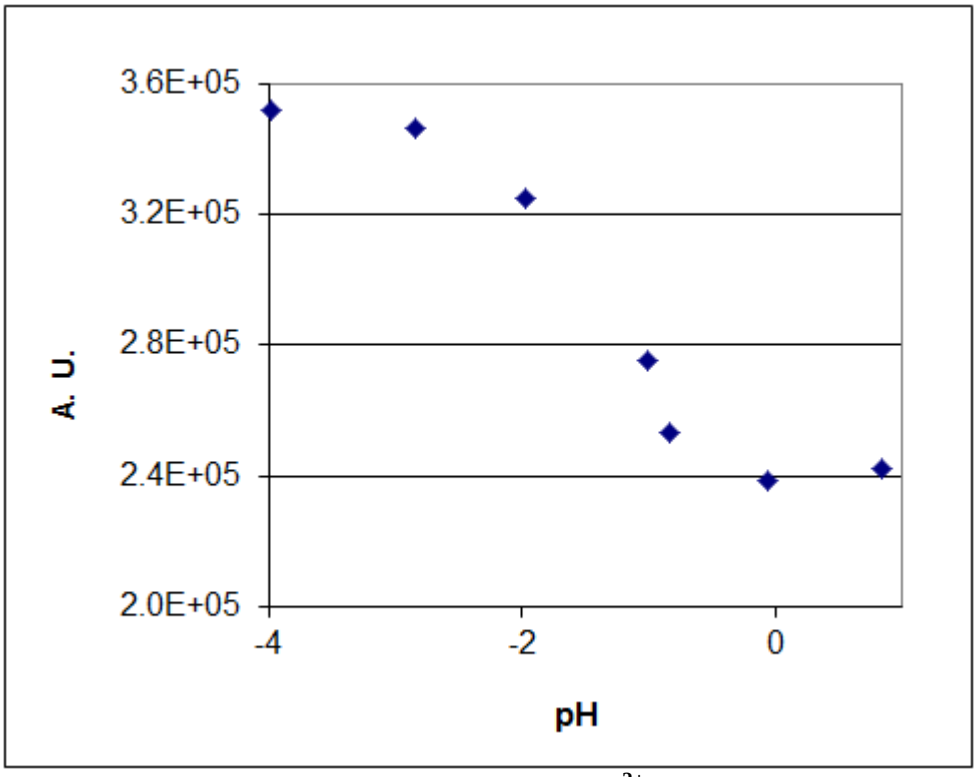

Figure 183. Emission intensity of $[(bpy)_2Ru(pypz)]^{2+}$ monitored at 610 nm as a function of acidity, from pH 1 to H_0 –4.

The similarity of the excitation spectrum (Figure 70) and emission lifetime, ~500 ns, relative to those of $[Ru(bpy)_3]^{2+}$ in room temperature aqueous solution raises the possibility that an impurity of $[Ru(bpy)_3]^{2+}$ may be present within the samples examined. While not individually conclusive, collectively the results of these experiments suggest this is not the cause. Firstly, looking at the way the complex was prepared, it seems unlikely that $[Ru(bpy)_3]^{2+}$ could be the side product in any step of the synthetic procedure since it was never added to the system and is not expected in a reaction where pypz is added to $(bpy)_2RuCl_2$. Secondly, as is the case for $[(bpy)_2Ru(dpp)]^{2+}$, all changes observed upon protonation are reversible. It is improbable that $[Ru(bpy)_3]^{2+}$ could form reversibly as a result of the change in the acidity of the solution. Thirdly, spectroscopic changes during titration give no indication of the presence of an impurity and are consistent with the pH change in the environment surrounding the complex. Lastly, luminescence spectra of $[Ru(bpy)_3]^{2+}$ recorded in concentrated sulfuric acid (Figure 166) reveal that the emission of the complex in very acidic solutions, i.e. under the conditions where the second emission from $[(bpy)_2Ru(pypz)]^{2+}$ is observed, is blue-shifted from its original 610-nm position at neutral pH and appears at 585 nm instead.

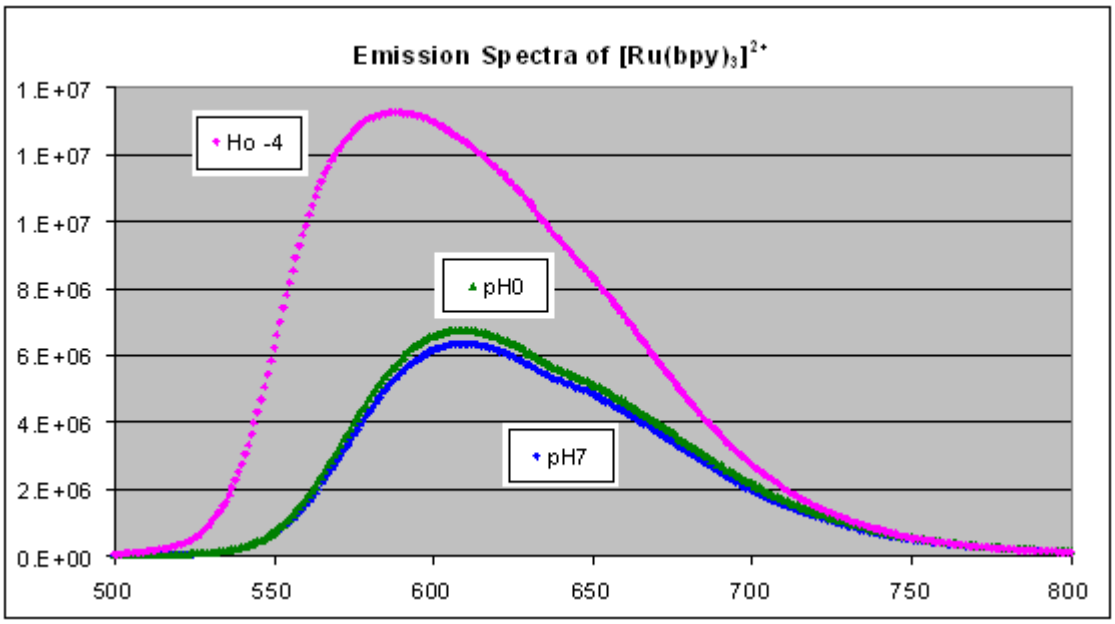

Figure 184. Emission spectra of $[Ru(bpy)_3]^{2+}$ from aqueous solution of differing acidity.

More likely, the new emission comes from a bpy-localized transition that is seen because the more dominant emission disappears as acidity is increased. Experimental data and the fact that a similar emission is observed in spectra of similarly acidic solutions of $[(bpy)_2Ru(dpp)]^{2+}$ supports the thesis that the 610-nm emission is not promoted by protonation but is present all along together with the 675-nm emission.

The emission at high acidity is less intense than the emission from the unprotonated parent, with a difference in quantum efficiency of approximately one order of magnitude: 10^{-4} for the 610-nm emission compared to 10^{-3} for the emission from the unprotonated form. The margin is not as wide as the difference found between protonated and unprotonated form of $[(bpy)_2Ru(dpp)]^{2+}$. The lifetime of the new emission is longer (~ 500ns)[b] than the lifetime of the neutral complex (150ns), suggesting the transition is

[b] The error provided by Igor software is too high to assess the lifetime (too much noise).

triplet in character and excluding the possibility that it may be a singlet ^{1}MLCT transition.

The 610-nm emission resembles closely that of the parent analogue $Ru(bpy)_3^{2+}$ in another respect: its behavior when H^+ concentration is increased beyond 1 M. While the 620-nm emission from solutions of $[(bpy)_2Ru(dpp)]^{2+}$ disappears at pH 0, the 610-nm emission observed from solutions of $[(bpy)_2Ru(pypz)]^{2+}$ persists in all solutions tested, up to the limit of acidity achievable. It is possible that no increase in emission intensity was observed for $[(bpy)_2Ru(dpp)]^{2+}$ because the emission is very short lived and there is no time for the bpy ligand to interact with the protons in solution or display its effect. On the other hand, solutions of $Ru(bpy)_3^{2+}$ in the negative Hammett acidity range (Figure 184) display the same trend of increased emission intensity as is observed for $[(bpy)_2Ru(pypz)]^{2+}$. A similar phenomenon (Figure 185) is also observed in the acid titration of $Ru(bpz)_3^{2+}$: after an initial quenching, emission is restored, and a new band centered around 610-620 nm reaches a maximum in concentrated sulfuric acid solution. The comparable behavior exhibited by complexes with conjugated phenyl rings and no protonable sites suggests that something else may be happening at very high acidity: the bpy ligand may interact with the protons in solution via the π-orbital system. This finding further supports the hypothesis that the emission is localized on bpy-type ligands.

4.C. Association of $[(bpy)_2Ru(dpp)]^{2+}$ and $[(bpy)_2Ru(pypz)]^{2+}$ with d^{10} metals

4.C.1. Ground state association

The changes in the absorption spectra (Figures 92, 94 and 123) suggest association of Cd^{2+}/Zn^{2+} with the dpp ligand in $[(bpy)_2Ru(dpp)]^{2+}$ and of Zn^{2+} with the pypz ligand in $[(bpy)_2Ru(pypz)]^{2+}$. As expected, the MLCT transition centered on the odd ligand is the most affected by the increase in d^{10} metal ion concentration, as it coordinates to the free immine sites of that ligand. The transition to dpp or pypz shifts to the red, suggesting that the MLCT state is stabilized by coordination, with increased stabilization for Ru-dpp due to chelate formation. For both complexes, the red-shift is, however, not as pronounced as in the case of protonation of $[(bpy)_2Ru(pypz)]^{2+}$, or the second protonation of $[(bpy)_2Ru(dpp)]^{2+}$. NMR spectra confirmed, in the case of the $[(bpy)_2Ru(dpp)]^{2+}$ complex, that coordination happens at the dpp ligand, since the protons most affected by coordination are the ones on the peripheral pyridyl ring and the pyrazyl ring of dpp.

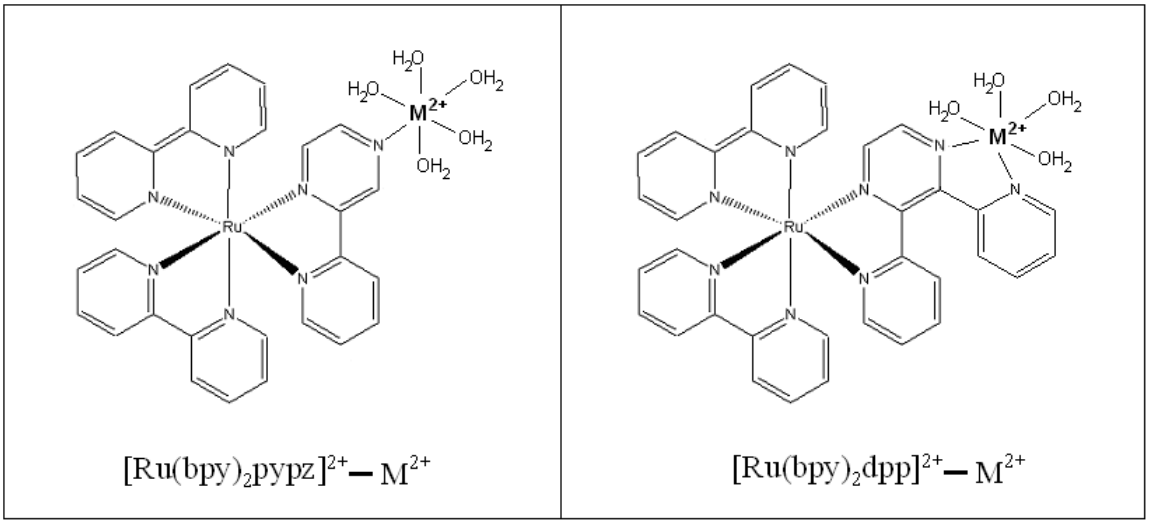

Figure 186. Theoretical structures of Ru-diimine complexes coordinated to aquated d^{10} metal ions.

Based on the molecular structure of $[(bpy)_2Ru(dpp)]^{2+}$ and the fact that Cd^{2+} and Zn^{2+} ions in solution are present in their aquated form, coordination is expected to lead to a bimetallic in which the "$[(bpy)_2Ru(dpp)]^{2+}$ ligand" acts as a bidentate ligand and coordinates to the Zn^{2+} (Figure 186). On the other hand, $[(bpy)_2Ru(pypz)]^{2+}$ possesses only one peripheral nitrogen available for coordination, hence coordination is limited to that single nitrogen. Nonetheless, with both complexes, coordination of the cationic metal ion reduces the energy of the acceptor orbital, shifting to lower energy the MLCT transition to that ligand.

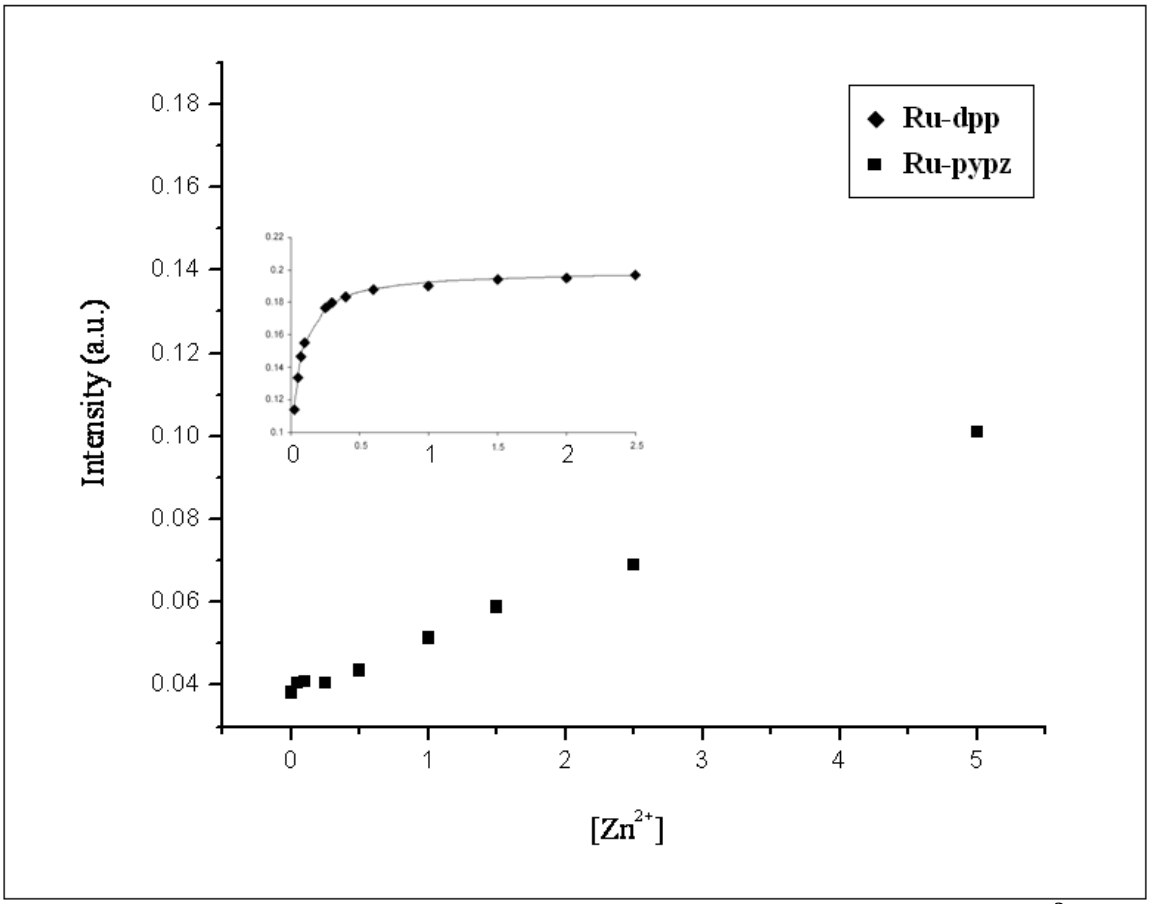

Figure 187. UV-Vis absorbance of room temperature $[(bpy)_2Ru(dpp)]^{2+}$ and $[(bpy)_2Ru(pypz)]^{2+}$ solutions with increasing $[Zn^{2+}]$ monitored at 520 nm.

Figure 187 illustrates the substantial differences in the UV-Vis titrations of bidentate $[(bpy)_2Ru(dpp)]^{2+}$ and monodentate $[(bpy)_2Ru(pypz)]^{2+}$ ligands. The biggest change for $[(bpy)_2Ru(dpp)]^{2+}$ in the ground- (and excited-state) titrations of the ruthenium complexes occurs with $[Zn^{2+}] \leq 0.5M$, whereas for $[(bpy)_2Ru(pypz)]^{2+}$ almost no change is observed at 0.5M $[Zn^{2+}]$ or below. The immediate implication is that the K_{eq} for the reaction:

$$[(bpy)_2Ru(dpp)]^{2+} + Zn^{2+} \leftrightarrows [(bpy)_2Rudpp{=}Zn]^{4+} \quad (102)$$

where =Zn indicates bidentate coordination, is significantly larger than the K_{eq} for the monodentate coordination of $[(bpy)_2Ru(pypz)]^{2+}$:

$$[(bpy)_2Ru(pypz)]^{2+} + Zn^{2+} \leftrightarrows [(bpy)_2Rupypz\text{-}Zn]^{4+} \quad (103)$$

indicated by –Zn. In fact, within the experimentally accessible range of $[Zn^{2+}]$, i.e. $\leq 5M$, the $[(bpy)_2Ru(pypz)]^{2+}$ system does not even appear to approach an equilibrium. Rather, the linear increase in absorbance with increasing $[Zn^{2+}]$ suggests that, even at 5M the concentration of Zn^{2+} is insufficient to form an equilibrium amount of the bimetallic. This difference in the value of K_{eq} may also be explained by remembering that the free pyridyl nitrogen on the dpp ligand is more basic in the ground state than the pyrazyl nitrogen of the dpp ligand, and by analogy, more basic than the pyrazyl nitrogen of the pypz ligand. Previous studies[42], have shown that the equilibrium constants for coordination of diimines increases linearly with the Brönsted basicity of the coordinating nitrogens. The higher basicity of the pyridyl nitrogen is evident by the fact that the first protonation of the $[(bpy)_2Ru(dpp)]^{2+}$ complex happens at much higher pH than the protonation of $[(bpy)_2Ru(pypz)]^{2+}$. It is plausible the coordination of $[(bpy)_2Ru(dpp)]^{2+}$ happens via a

two-step reaction with an initial coordination to the more basic peripheral pyridyl nitrogen and final chelate formation by coordination to the less basic peripheral pyrazyl nitrogen on the dpp ligand. On the other hand, $[(bpy)_2Ru(pypz)]^{2+}$ only has the less basic peripheral pyrazyl nitrogen on the pypz ligand and therefore the monodentate bimetallic is expected to be less stable, and in turn shorter lived, which prevents any buildup of $[(bpy)_2Rupypz\text{-}Zn]^{4+}$ bimetallic. The short ground-state lifetime of the bimetallic $[(bpy)_2Rupypz\text{-}Zn]^{4+}$ would account for the linear increase in absorbance at 520 nm with increasing $[Zn^{2+}]$ (Figure 187) which gives no indication that the system is approaching equilibrium.

The ground state titrations of $[(bpy)_2Ru(dpp)](NO_3)_2$ with zinc and cadmium performed using UV-Vis spectrometer gave good match between the experimental data and the fit using equation (104). The equilibrium constants obtained for coordination of the d^{10} metal to the peripheral N sites of the dpp ligand were 9 ± 2 and 15 ± 3 M^{-1} for Cd and Zn, respectively. The fit was not as good when titration was attempted using ^{1}H-NMR. The change in chemical shifts for protons B3' and C6" at increased concentration of the d^{10} metal ion, showed an almost linear trend that did not plateau. This is not uncommon[122] and could be due to the fact that chemical shifts of the protons respond to more than one concomitant factor. For instance, it can be explained in part by competing deshielding and shielding effects as the metal coordinates. Or perhaps, as Zambrana suggests[62], the sigmoidal fit implies consecutive rather than simultaneous equilibria involving more than one site, and is reminiscent of cooperative effects. Lastly, it is possible that the more dilute Ru(II) solutions used for UV-Vis spectra allow the reactants to reach equilibrium, while the more concentrated solution needed for NMR do not reach

the same equilibrium concentrations since an equilibrium constant, actually defined at infinite dilution, is dependent on the concentration of species used to measure its value.

In comparison to $[(bpy)_2Ru(dpp)]^{2+}$ (Figure 187), the ground state titration plot of $[(bpy)_2Ru(pypz)]^{2+}$ is markedly different and equation 97 (page 152) fails to reproduce the actual data (Figure 126, page 188). As shown in Figure 125 (page 187), the plotted curves do not reach a plateau, even at very high concentrations of the zinc cation, suggesting that within the accessible experimental conditions, i.e. $[Zn^{2+}] \leq 5M$, the reaction does not reach equilibrium. For this reason, the $\varepsilon_{Ru\text{-}M}$ and K_{eq} cannot be extrapolated from the two-parameter non-linear fit (equation 97, page 152) of the titration data. Hence, the constant obtained is only apparent and is, at best, an estimate of the order of magnitude for the equilibrium constant itself. Another way to rationalize the behavior is to invoke the existence of interception kinetics, where equation (103) can be re-written as the following two reactions:

$$[(bpy)_2Ru(pypz)]^{2+} + Zn^{2+} \xrightarrow{k_1} [(bpy)_2Rupypz\text{-}Zn]^{4+} \qquad (104)$$

$$[(bpy)_2Rupypz\text{-}Zn]^{4+} \xrightarrow{k_{-1}} [(bpy)_2Ru(pypz)]^{2+} + Zn^{2+} \qquad (105)$$

If the back reaction of 104 happens almost as quickly as 104 itself, $k_1 \approx k_{-1}$, the product of the first reaction, $[(bpy)_2Rupypz\text{-}Zn]^{4+}$, is expected to be extremely short-lived. Since the system is in steady-state conditions:

$$\frac{d[Ru-Zn]}{dt} = k_1\,[Ru][Zn^{2+}] - k_{-1}[Ru\text{-}Zn] \qquad (106)$$

and

$$0 = k_1 [Ru][Zn^{2+}] - k_{-1}[Ru\text{-}Zn] \quad (107)$$

where [Ru] and [Ru-Zn] are the concentrations of the free ruthenium complex and bimetallic species, respectively. Assuming [Ru] doesn't absorb at 520 nm, if the concentration of intermediate, [Ru-Zn], is proportional to the increase in absorbance at 520 nm, ΔA, and the concentration of short-lived product is directly proportional to the change in $[Zn^{2+}]$:

$$[Ru\text{-}Zn] = \frac{k_1}{k_{-1}} [Ru][Zn^{2+}] \quad (108)$$

it also follows that:

$$\Delta A \propto \frac{k_1}{k_{-1}} [Ru][Zn^{2+}] \quad (109)$$

The ΔA is observed to increase linearly with $[Zn^{2+}]$ ($R^2 = 0.997$) without any sign of a leveling off or plateau indicative of a system achieving a measurable equilibrium. Furthermore, the fact that an absorbance change is at all observed must imply that [Ru-Zn] has a finite lifetime sufficient for the change in absorbance to be recorded. Therefore, k_1 must be equal to, or at least, only slightly larger than k_{-1}.

The possibility that ionic strength effect may be responsible for the change in UV-Vis absorption spectra was considered, since the ionic strength of the ruthenium(II) solutions at increasing concentrations of Zn^{2+} could not be kept constant during the course of the titrations, lest formation of a precipitate would occur. However, based on previous work by Demas and coworkers[27] on the parent complex $Ru(bpy)_3^{2+}$, it was concluded that ionic strength while contributing in minimal way, cannot alone explain the spectral change observed.

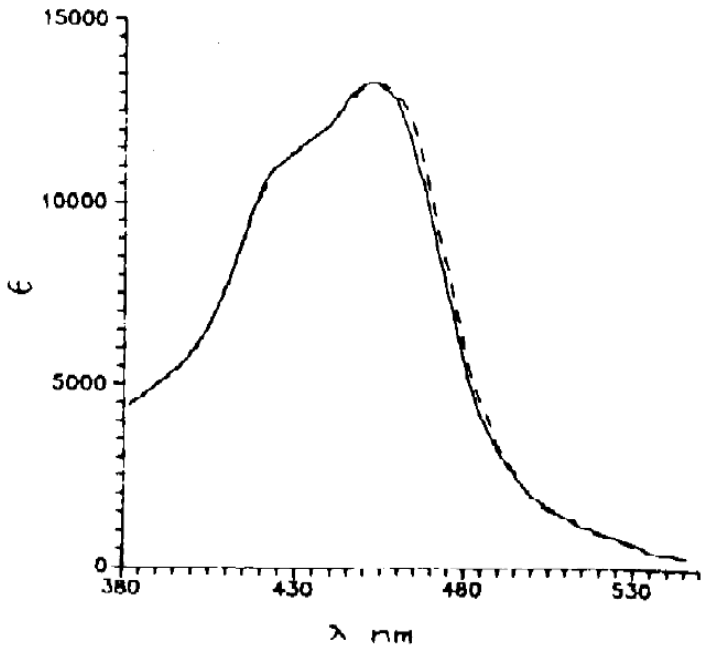

Figure 188. Absorption spectra of room temperature $[Ru(bpy)_3]^{2+}$ solutions in pure water (—), 3.0 M $LiNO_3$ and 1.5 M $AgNO_3$/1.5 M $LiNO_3$ (----)[27].

Demas *et al.*[27] recorded absorption spectra of $Ru(bpy)_3^{2+}$ in pure water, in 3 M $LiNO_3$ and in 1.5 M $LiNO_3$ –1.5 M $AgNO_3$ (Figure 188). The spectra in nitrate media were indistinguishable, while compared to the UV-Vis spectrum recorded in pure water, the lower energy MLCT transition exhibited a small 3-5 nm red-shift on the lower energy side of the absorption band. The ionic strength effect was significant enough to be observed, yet too small to shift the position of the absorption maximum. Quoting Meyer *et al.*[121], Demas' research group concluded that the red-shift was due to the presence of nitrate ions in solution and "…indicative of ion pairing between the Ru(II) complex and the NO_3^-…". However, the more substantial changes observed in the emission spectra upon titration with Ag^+, were attributed to the presence of a new emissive species, result

of the interaction between $Ru(bpy)_3^{2+}$ and Ag^+, and not due to ionic strength effects. Similarly, it is likely that ionic strength effects are contributing to the spectral changes observed here, but they are not, in themselves, significant enough to be the only cause. In the case of $Ru(bpy)_3^{2+}$ the only changes observed in the ground state are due to ionic strength effect because the complex has no free peripheral nitrogen available for coordination and it requires absorption of energy to excite an electron in order to promote a reaction between the ruthenium complex and the Ag^+ ions. On the other hand, the complexes under investigation here, do possess peripheral immine nitrogens available for coordination and, while ionic strength effects are still expected to occur, coordination is expected to occur as well and have a more significant impact in the spectral properties of the Ru(II) diimine.

The ground state titration of $[(bpy)_2Ru(dpp)]^{2+}$ was performed in solutions buffered at pH 5, while the titration of $[(bpy)_2Ru(pypz)]^{2+}$ was performed at pH 3 to avoid precipitation of zinc chloride out of solution. The $[(bpy)_2Ru(pypz)]^{2+}$ complex is unaffected by acidity in the range of pH between 8 and 1, so the presence of increased concentration of protons in the solution is not expected to have skewed the titration results and interfered with the reaction between the complex and the aquated zinc cations. For $[(bpy)_2Ru(dpp)]^{2+}$, the effect of increased acidity, i.e. pH = 5, as compared to neutral solution results is a reduced absorption in the corresponding dpp-centered MLCT. While the $[(bpy)_2Ru(dpp)]^{2+}$ complex is only partially protonated at pH 5, it should be born in mind that protons may potentially be competing with the zinc cations at pH 5, given the more basic nature of free pyridyl nitrogen on the dpp ligand compared to the pyrazyl nitrogen on the pypz ligand. For instance, at pH 0 the spectral change observed when the

concentration of zinc in solution goes from 0 to 2.5 M is barely noticeable (Figure 189), and likely due only to ionic strength effects. In contrast, at pH 5, the same increase in concentration of Zn^{2+} cations produces the maximum amount of bimetallic that can be formed when equilibrium (102) is established and a dramatic shift from 476 to 495 nm is observed in the dpp-centered MLCT band (Figure 94). This observation provides strong evidence that coordination of $[(bpy)_2Ru(dpp)]^{2+}$ to Zn^{2+} cations occurs via initial bonding to the more basic peripheral pyridyl nitrogen on the dpp ligand. If first protonation at that nitrogen has already occurred, coordination to Zn^{2+} will either not take place, or be severely retarded. Indirectly, this observation also confirms the assignment of first protonation of the $[(bpy)_2Ru(dpp)]^{2+}$ complex well above pH 0, contrary to what was initially suggested[62] due to the impossibility to experimentally detect signs of first protonation via UV-Vis spectroscopy.

When compared to the zinc titration of $[(bpy)_2Ru(pypz)]^{2+}$, the fact that the reaction between $[(bpy)_2Ru(dpp)]^{2+}$ and Zn^{2+} cannot take place when the complex has only the peripheral pyrazyl nitrogen free to coordinate, explains why $[(bpy)_2Ru(pypz)]^{2+}$ doesn't easily coordinate to Zn^{2+}. Not unlike the protonated form $[(bpy)_2Ru(dpp)H]^{3+}$, with the proton attached to the more basic peripheral pyridine nitrogen, $[(bpy)_2Ru(pypz)]^{2+}$ only has a pyrizyl nitrogen available for coordination. Lastly, these findings supports the hypothesis that, at pH 0, the peripheral pyrazyl nitrogen on the dpp ligand of $[(bpy)_2Ru(dpp)]^{2+}$ is not completely free to coordinate to other d^{10} metal ions in solution and is involved in some form of intra-molecular hydrogen bonding, i.e. the proton initially attached to the peripheral pyridyl nitrogen causes a rotation of the

peripheral dpp pyridine and becomes shared between the peripheral pyridyl nitrogen and the peripheral pyrazyl nitrogen.

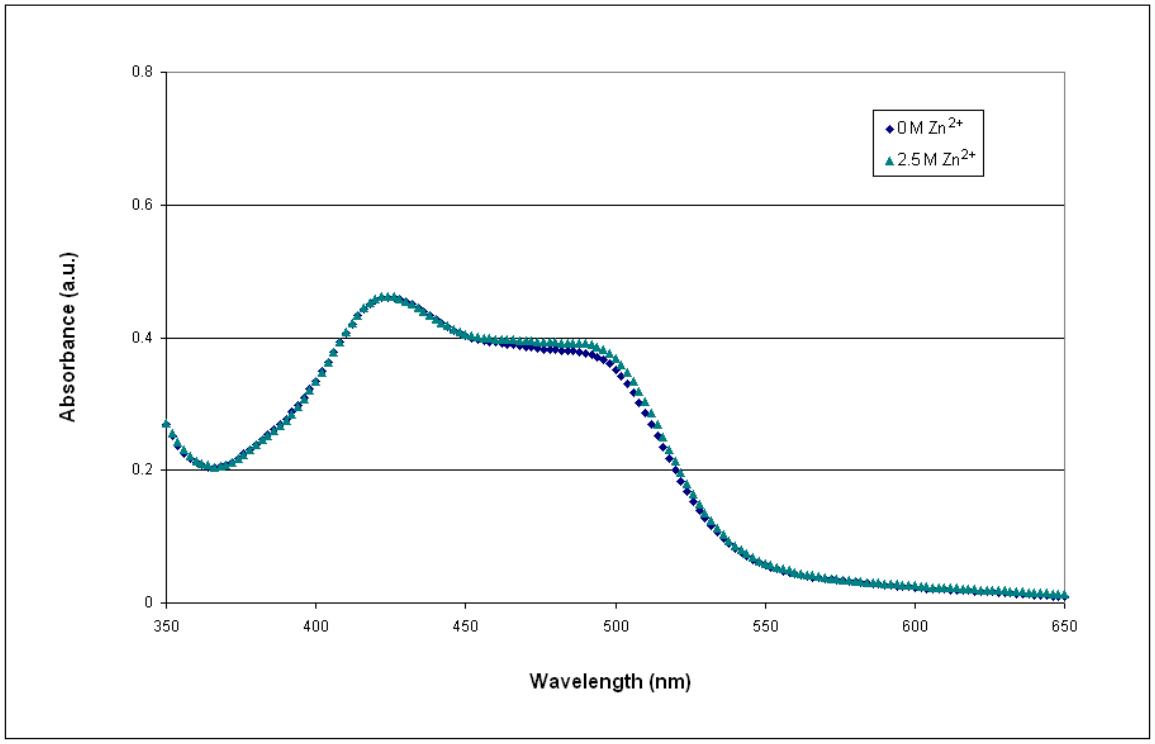

Figure 189. UV-Vis MLCT spectral region of room temperature aqueous solutions of 10^{-5} M $[(bpy)_2Ru(dpp)]^{2+}$ at pH 0 with 0 M and 2.5 M Zn^{2+}.

4.C.2. Excited state association

Excited-state titration of $[(bpy)_2Ru(pypz)]^{2+}$ with Zn^{2+} produces three distinct emissions which will be discussed separately (Figure 190). The 500- to 630-nm range, zone 1, contains the highest energy emission band, centered at 610 nm and a feature that was not observed in the $[(bpy)_2Ru(dpp)]^{2+}$ emission spectra. The middle spectral range, zone 2, contains the main emission band assigned to the MLCT transition to the pypz ligand and it is relevant to study the changes it undergoes, when compared to the parent band in the dpp complex. Lastly, the lower energy range, zone 3, is where a new emission begins to appear, evidence of the presence on an associative interaction between the complex and the Zn^{2+} ions added to the solution.

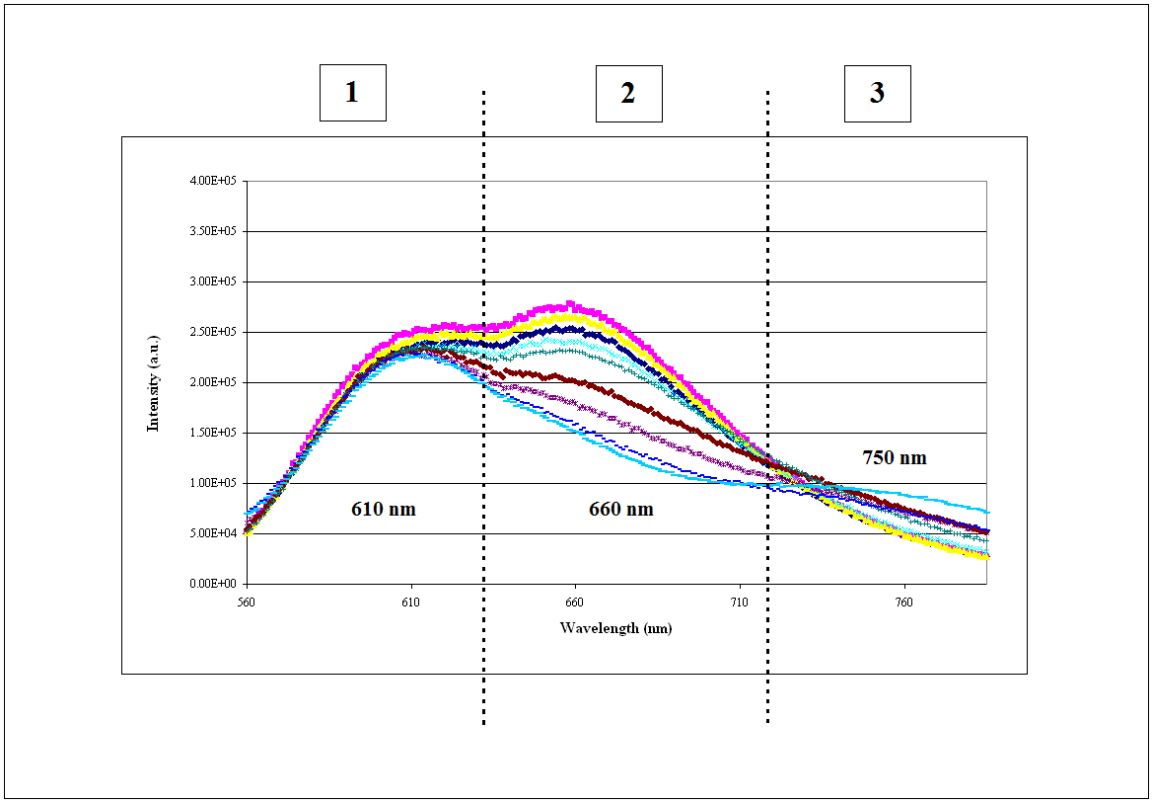

Figure 190. Three spectral regions of the luminescence titration spectra of $[(bpy)_2Ru(pypz)]Cl_2$ at increasing Zn^{2+} concentrations (λ_{ex} = 400 nm, pH 3).

4.C.2.a. 610-nm emission

Peculiar to the $[(bpy)_2Ru(pypz)]^{2+}$ complex, is the fact that an emission at 610 nm is visible in conjunction with the above-mentioned red-shifted 750-nm emission. The 610 nm emission is present before and after addition of Zn^{2+} because the solutions are buffered at pH 3: at this high acidity, 33% of the $[(bpy)_2Ru(pypz)]^{2+}$ complex is in the protonated form, hence not contributing to the overall emission intensity. Concurrently, the emission of the unprotonated $[(bpy)_2Ru(pypz)]^{2+}$ is significantly quenched by the proton compared to neutral solutions, rendering the 610-nm emission visible (Figure 129, page 191). When originally observed in acidic solutions of $[(bpy)_2Ru(pypz)]^{2+}$, the high energy emission was assigned to an MLCT transition centered on the bipyridine ligands. Both the emission's position and intensity remain unaffected by increasing concentrations of Zn^{2+} ions. Based on experiments by Zambrana, the emission of aqueous solutions of $Ru(bpy)_3^{2+}$ also remains unchanged in the presence of Zn^{2+} and Cd^{2+} ions. The absence of a metal ion-dependence for both complexes, $[(bpy)_2Ru(pypz)]^{2+}$ and $Ru(bpy)_3^{2+}$, is consistent with the assignment of the transition to a bpy-localized MLCT transition. In addition, it establishes that the Zn^{2+}, even though high concentrations of the ion are necessary for quenching, does not interact with the aromatic π systems of the bpy portion of the complex, and adds additional credence to the argument that the Zn^{2+} interacts exclusively with the pypz portion of the complex. The similarity to a Ru-bpy MLCT transition is further corroborated by the relatively long lifetime, ~400 ns, of the 610 nm emission recorded in the presence of 5M Zn^{2+} solution, which is similar to the lifetime of $Ru(bpy)_3^{2+}$ in room temperature aqueous solutions, 600ns. The excitation spectrum of $[(bpy)_2Ru(pypz)]^{2+}$ in 5 M $ZnCl_2$ corresponding to the change in emission intensity at

608 (Figure 118, page 182) shows only one absorption band centered at 440 nm. On the other hand, when the change in intensity is monitored at 765 nm, the excitation spectrum reveals a more familiar two-band contour, similar in shape to the absorption spectrum with MLCT bands at 420 and 500 nanometers. And, finally, the dependence on the excitation wavelength for the 610-nm emission (Figure 120, page 184) confirms that the emission originates from the excitation of the higher energy 440-nm MLCT band assigned to the bpy-localized charge transfer state because the intensity of the 610-nm emission is reduced by 73% when the excitation wavelength is changed from 450 to 490-nm light and moves into the pypz-localized MLCT absorption.

Since the experimental results support the idea that association of the divalent cations with the bipyridine ligands does not occur, we will focus our attention to the less energetic emissions that are affected by the presence of $[M^{2+}]$.

4.C.2.b. 660-nm emission

In view of the fact that these experiments on $[(bpy)_2Ru(pypz)]^{2+}$ were carried out to resolve the role of the pyridyl ring portion of the dpp ligand in coordination reactions, comparisons between $[(bpy)_2Ru(pypz)]^{2+}$ and $[(bpy)_2Ru(dpp)]^{2+}$ will be made throughout this discussion highlighting the many parallels and the few differences between the two complexes. For instance, as found with $[(bpy)_2Ru(dpp)]^{2+}$, increasing concentrations of d^{10} metals does affect the lower energy portion of both the absorption and emission spectra of $[(bpy)_2Ru(pypz)]^{2+}$. In the absorption spectrum of $[(bpy)_2Ru(pypz)]^{2+}$, a red shift is observed in the pypz-localized MLCT transition, Ru → pypz and a similar red-shift is also observed in the dpp-localized MLCT transition, Ru → dpp of

$[(bpy)_2Ru(dpp)]^{2+}$ at increasing $[M^{2+}]$. The shift in the absorption spectrum of $[(bpy)_2Ru(pypz)]^{2+}$ is accompanied by quenching of the original 660-nm pypz-localized emission from the ligand-to-metal transition down to the ground state, pypz → Ru and appearance of a new emission red-shifted from the position of the disappearing band. Similarly, the 680-nm emission of $[(bpy)_2Ru(dpp)]^{2+}$ due to the dpp → Ru LMCT transition is quenched and a new red-shifted emission begins to form. All transitions affected by the addition of Zn^{2+} ions to the solution, are assigned to the heteroleptic ligand in the complex. Generalizing to both complexes, the direction of the observed emission changes parallel the spectral changes detected in the ground-state titrations: the presence of positively-charged metal ions in the vicinity of the peripheral free nitrogens lowers the energy needed to transfer an electron to that portion of the ligand and, therefore, reduces the energy of the MLCT transitions involved, shifting all bands to the red. In addition to the intensity quenching, the presence of Zn^{2+} decreases the emission lifetime of the pypz localized MLCT state from 30 to 9 ns in the case of $[(bpy)_2Ru(pypz)]^{2+}$ and from 102 to 54 ns in the case of $[(bpy)_2Ru(dpp)]^{2+}$. None of these effects can be attributed simply to ionic strength effects, since, in the case of $[(bpy)_2Ru(pypz)]^{2+}$, the quenching selectively involves the pypz ligand-centered emission band and not the 610-nm emission band assigned to a bpy-centered transition. Furthermore, in the case of $[(bpy)_2Ru(dpp)]^{2+}$, the emission spectrum and lifetime are independent of $[Ca^{2+}]$ up to 5M. Indeed, experimental results are evidence that a new emissive bimetallic is formed between the $[(bpy)_2RuL]^{2+}$ complex and the d^{10} metal, and that the interaction happens at the heteroleptic ligand site of the molecule.

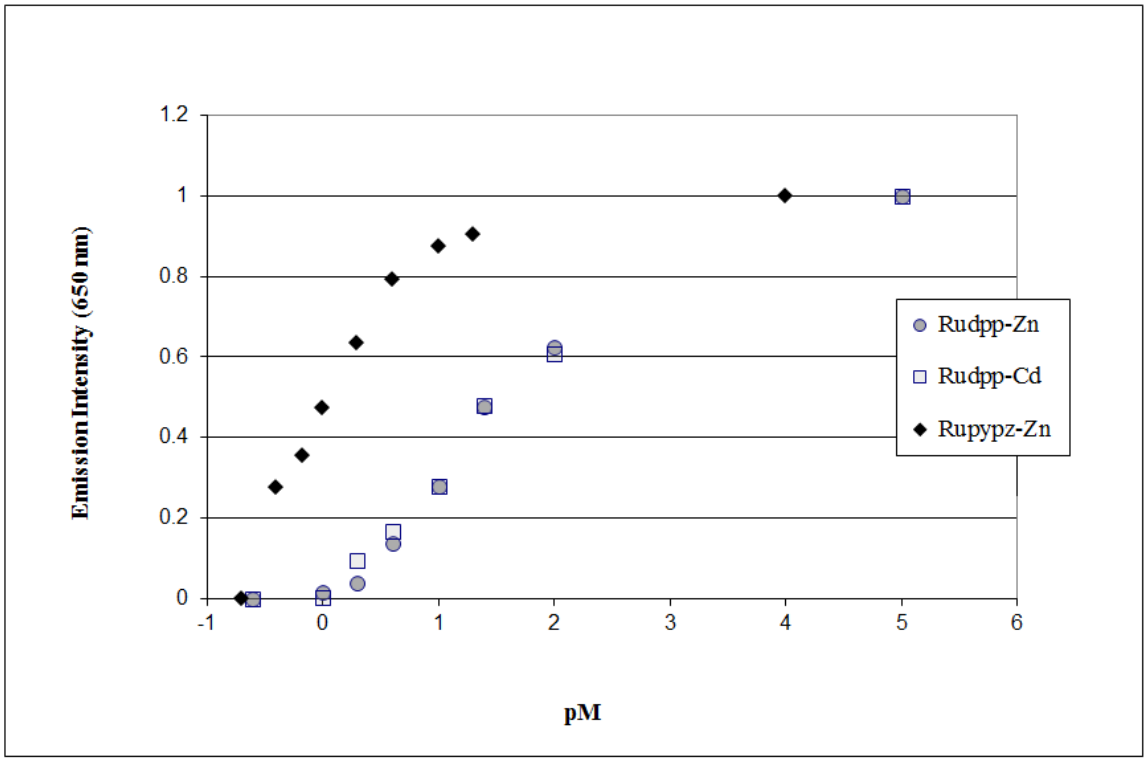

Figure 191. Comparison of excited state titrations of $[(bpy)_2Ru(dpp)]^{2+}$ and $[(bpy)_2Ru(pypz)]^{2+}$ with M^{2+} using steady-state emission intensity data monitored at 650 nm.

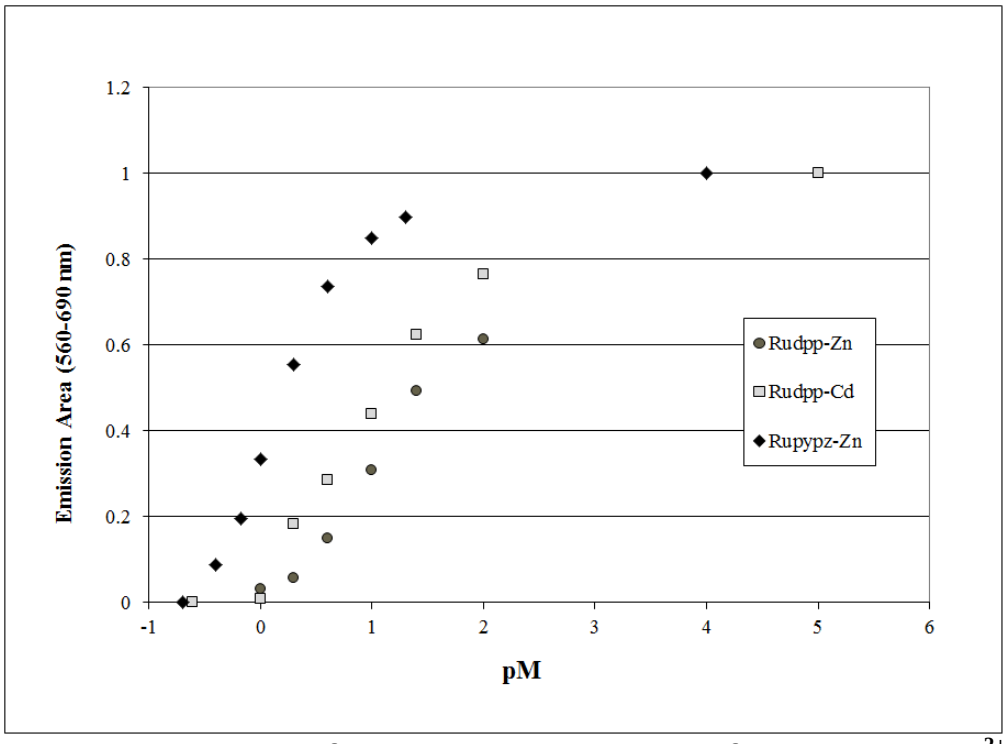

Figure 192. Comparison of excited state titrations of $[(bpy)_2Ru(dpp)]^{2+}$ and $[(bpy)_2Ru(pypz)]^{2+}$ with M^{2+} using integrated areas under the emission curves.

The changes in the emission spectrum of $[(bpy)_2Ru(dpp)]^{2+}$ described above are immediately apparent on addition of Zn^{2+} or Cd^{2+} and continue to progress up to $[M^{2+}]$ = 1M, independent of the type of d^{10} metal, Zn^{2+} or Cd^{2+}, used during the titration (Figure 191). Compared to $[(bpy)_2Ru(dpp)]^{2+}$, the complex $[(bpy)_2Ru(pypz)]^{2+}$ responds "more slowly" in the excited state to addition of Zn^{2+}, in the sense that higher concentrations of Zn^{2+} are required to observe a change in the excited state spectrum and gradual changes are observed over a wider range of concentrations ($0 < [Zn^{2+}] < 2M$), as seen in Figures 191 and 192. In the case of the $[(bpy)_2Ru(dpp)]^{2+}$ complex, the ground state interaction of M^{2+} with the ruthenium complex is postulated to occur via the pyridyl nitrogen of the dpp ligand (Figure 193), which is more basic than the pyrazyl nitrogen by close to five or six orders of magnitude. The complex $[(bpy)_2Ru(pypz)]^{2+}$ coordinates via a pyrazyl nitrogen which is less basic in the ground state than a pyridyl one hence a smaller response to addition of Zn^{2+} is to be expected.

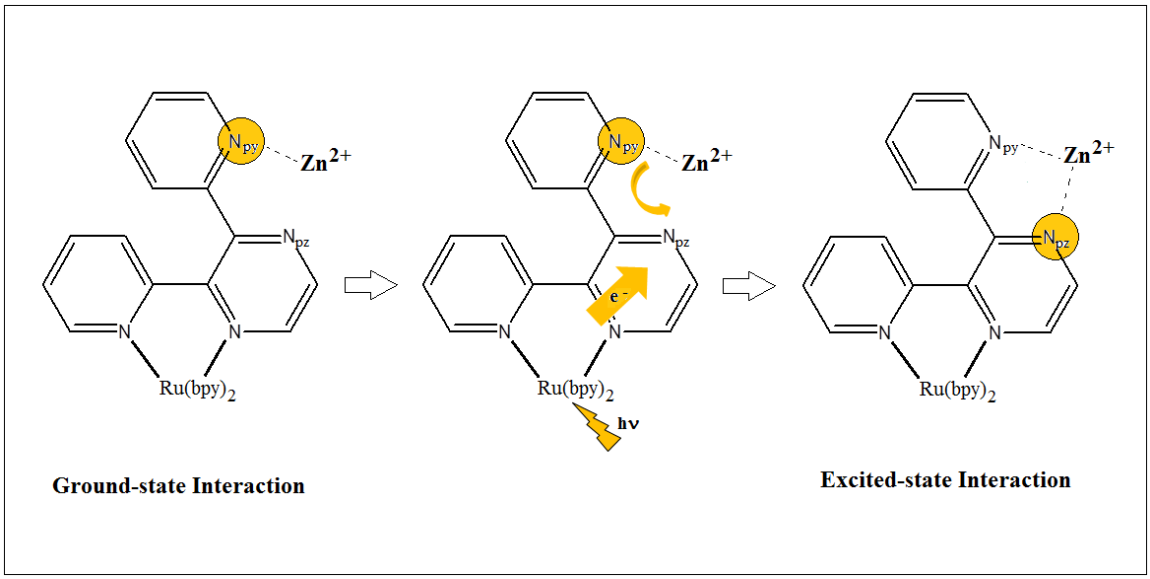

Figure 193. Schematic representation of the ground- and excited-state interaction between $[(bpy)_2Ru(dpp)]^{2+}$ and a d^{10} divalent metal cation, M^{2+}, and the basicity change undergone by the complex upon excitation.

The wide difference in basicity between the two nitrogens, pyridyl and pyrazyl, is expected based on the relative basicity of pyridine and pyrazine free ligand (pK_a(py) = 5.25; pK_a(pz) = 0.65)[62] and further evidence of it was gathered during the proton titration of the ground state of the $[(bpy)_2Ru(dpp)]^{2+}$ complex, where NMR spectra confirmed that the first protonation occurs at the uncoordinated pyridyl ring of the dpp ligand in the 1-3 pH range, while the second protonation involving the pyrazyl nitrogen only happens at very high acidity (H_0 ~ -6). Upon coordination to the pyridyl nitrogen, the subsequent rotation of the peripheral pyridyl ring of dpp evident from the downfield shift of its protons (C3", C4", C5", C6") in the NMR spectra (Figure 48, page 121) suggests an increased interaction with the pyrazyl nitrogen. However, we hesitate to call this "coordination" since the proton titration of the dpp complex shows that the dpp pyrazyl nitrogen is an extremely weak Brønsted base, and the equilibrium constant for coordination of a diimine increases linearly with the Brønsted basicity of the coordinating nitrogens[42]. What is clear, is that the metal interacts with the complex in the ground state and is held in the vicinity of the pyrazyl nitrogen. Upon excitation, the pyrazyl nitrogen becomes more basic by several orders of magnitude, as established in the acid titration of $[(bpy)_2Ru(dpp)]^{2+}$ by the changes observed in the dpp-localized MLCT transition of the complex. It is plausible to suspect that the Zn^{2+} ion, which appears to be already weakly interacting, or at least, based on the rotation of the pyridyl ring, in the vicinity of the pyrazyl nitrogen of dpp, is in a much better position to coordinate to the peripheral pyrazyl nitrogen when the $[(bpy)_2Ru(dpp)]^{2+}$ complex is excited. Population of the dpp-localized MLCT state shifts electron density to the peripheral dpp nitrogens, with the majority of the charge on the pyrazyl nitrogen, thereby dramatically increasing their

Brønsted basicity by more than five orders of magnitude. Analogous to what is observed in the ground state coordination of diimines, where the equilibrium constant for coordination increases linearly with the basicity of the coordinating nitrogens, the photo-induced increase in the basicity of the peripheral pyrazyl nitrogen leads to bidentate coordination (Figure 193). The accompanying rearrangement of the solvent, specifically the water molecules interacting with the dpp portion of $*[(bpy)_2Ru(dpp)]^{2+}$ and those coordinated to the zinc ions, leads to emission quenching. The initial interaction between the Zn^{2+} ions and the pyridyl nitrogen of dpp provides a rational for why the changes in the emission spectra of $[(bpy)_2Ru(dpp)]^{2+}$ are seen immediately upon addition of the metal ions, both in the ground- and in the excited-states. It also emphasizes the differences observed between the complexes, $[(bpy)_2Ru(dpp)]^{2+}$ and $[(bpy)_2Ru(pypz)]^{2+}$.

In the case of the $[(bpy)_2Ru(pypz)]^{2+}$ complex, proton titration of the complex shows (Figure 66, page 136) that the Brønsted basicity of the pypz peripheral nitrogen, while more basic than the peripheral pyrazyl nitrogen of dpp, is less basic by about 3 orders of magnitude than the pyridyl nitrogen of dpp (Figure 158, page 244). Consequently, the ground state interaction with Zn^{2+} ions is significantly less than that between the peripheral dpp pyridyl nitrogen of $[(bpy)_2Ru(dpp)]^{2+}$ and Zn^{2+} because the pypz ligand lacks the pyridyl nitrogen and can only coordinate via the much less basic pyrazyl nitrogen (Figure 194). The smaller quenching effect and slow rate of mono-dentate coordination in the ground state is probably also affected by solvent reorganization, i.e. the pyrazyl nitrogen is not sufficiently basic to displace water from the Zn^{2+} coordination shell. As a result, the reaction between $[(bpy)_2Ru(pypz)]^{2+}$ and

Zn^{2+} requires a higher concentration of zinc to shift the equilibrium sufficiently so that it can be observed spectroscopically.

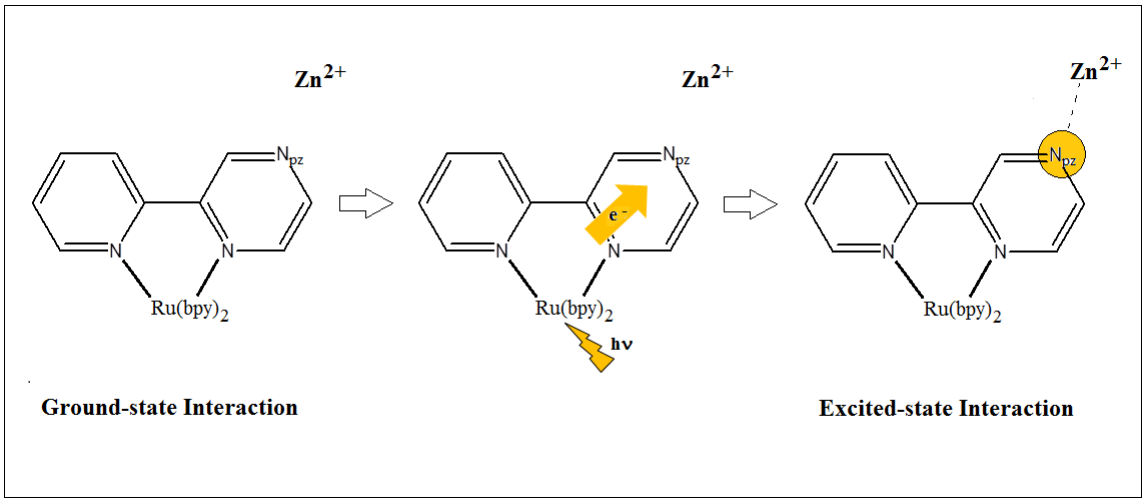

Figure 194. Schematic representation of the ground- and excited-state interaction between $[(bpy)_2Ru(pypz)]^{2+}$ and Zn^{2+}, and the basicity change undergone by the complex upon excitation.

Now, when comparing the ground- and excited-state titration of $[(bpy)_2Ru(pypz)]^{2+}$ with Zn^{2+}, while almost no change was observed in the ground state in the 0-1M range of zinc concentrations, the changes in the excited state are detectable immediately from the first addition of Zn^{2+}. This observation can be explained by the fact that the ruthenium-to-pypz charge transfer increases the electron density at the peripheral nitrogen of the pypz ligand rendering it more basic and, as a consequence, coordination at that nitrogen occurs more readily in the excited state than in the ground state (Figure 194). The higher *excited* state basicity of the peripheral pyrazyl nitrogen of pypz compared to its ground state basicity (see diagrams in Figures 193 and 194) is confirmed by protonation experiments (*vide supra*) that established that excitation increases the

basicity of the pyrazyl nitrogen of $[(bpy)_2Ru(pypz)]^{2+}$ by approximately 4 orders of magnitude ($\Delta pKa \approx 4$). In the case of coordination providing a numerical value for the extent to which the basicity is increased was challenging due to, in part, to the fact that ground state titration curves were only partially sigmoidal in shape and the midpoint for the titration could not be established with certainty.

Looking at the equilibrium constants listed in Table 33, it appears that the difference between ground- and excited-state coordination of the ruthenium(II) diimines complexes under investigation with d^{10} metals, is not significantly big and all the values found are within the same order of magnitude.

Table 33: Ground- and excited-state equilibrium constants for the coordination reaction between $[(bpy)_2Ru(dpp)]^{2+}$ or $[(bpy)_2Ru(pypz)]^{2+}$ and Zn^{2+} or Cd^{2+}.

	K^a	$K_{NMR}{}^a$	$K^*(E_i)^b$	$K^*(E_a)^b$	$K^*_{corr}(E_i)^c$
$[Ru(bpy)_2dpp]^{2+}$-Cd^{2+}	9 ± 2	1 ± 0.5	26 ± 3	9.8 ± 0.4	16.1
$[Ru(bpy)_2dpp]^{2+}$-Zn^{2+}	15 ± 3	1 ± 0.5	30 ± 1	28 ± 1	15.9
$[Ru(bpy)_2pypz]^{2+}$-Zn^{2+}	6 ± 1	-----	2.0 ± 0.5	1.4 ± 0.2	8.7

[a] Ground state eq. constants taken from changes in absorption and NMR spectra. [b] Excited state eq. constants extracted from emission spectra (E_i = emission intensity data; E_a = areas under the emission curves). [c] Excited state eq. constants after lifetime correction. [d] The unit for all listed constants is M^{-1}.

However, it must be kept in mind that the values, though listed as "equilibrium constants", may not be the actual equilibrium values. The source of the uncertainty stems from the fact that the excited-states of both reactants and products, having all lifetimes that are less than 200 ns, may or may not have had sufficient time to equilibrate. Experimental observation by Zambrana[53] that the excited state equilibrium constants measured for $[(bpy)_2Ru(dpp)]^{2+}$ are dependent on the initial concentration of metal

support the assumption that the system does not have time to equilibrate, as does the observation reported in the current work that, for both $[(bpy)_2Ru(dpp)]^{2+}$ and $[(bpy)_2Ru(pypz)]^{2+}$ complexes, the excited-state equilibrium constants also vary as a function of the wavelength of the monitoring light (Figure 103, 110 and 131). If the excited state does not have enough time to reach a time-independent ratio of coordinated and un-coordinated forms of the complex, then the measured equilibrium constant is expected to be a function of the excited state lifetimes[42]. As was the case for the excited-state acid-base study of coordination complexes by Hicks *et al.*[42], the word "equilibrium" is then intended to describe a ratio of coordinated and un-coordinated forms of the complex that is invariant within the lifetime of the species under a particular set of experimental conditions.

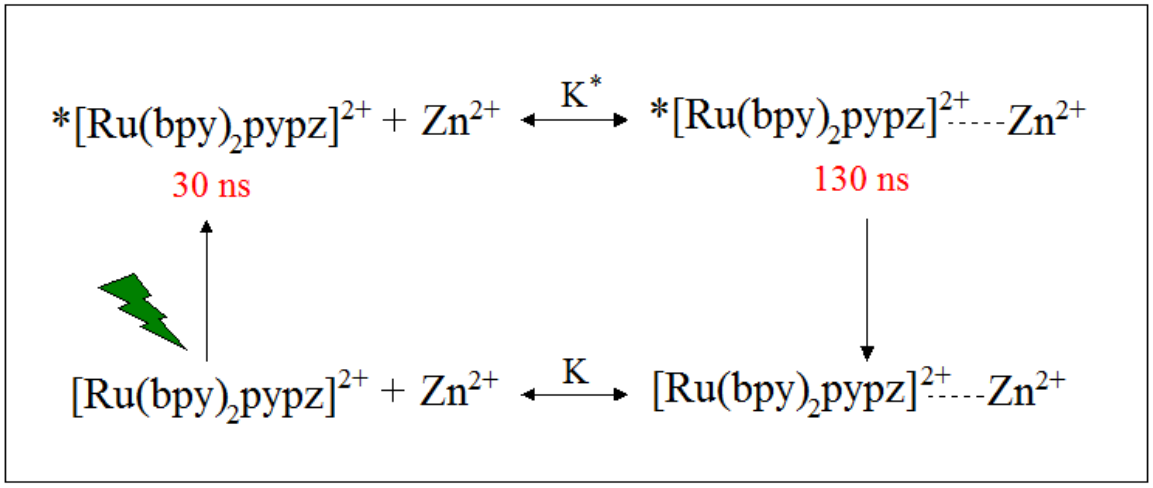

Figure 195. Schematic representation of the ground- and excited-state equilibria between $[(bpy)_2Ru(pypz)]^{2+}$ and Zn^{2+}.

To account for the fact that the lifetimes of the species involved -while comparable- are not identical, a lifetime correction may be applied, as suggested in the

literature (equation 64, page 39). The “rule”, according to Ireland and Wyatt, “is that the species of shorter lifetime produces a greater emission [intensity] than would be expected from the equilibrium concentrations, because its concentration is depleted more rapidly and is therefore replenished all the time from the longer-lived species in an attempt to maintain the equilibrium”[21]. Because the metallated species have lower lifetimes, the excited state equilibrium constants for $[(bpy)_2Ru(dpp)]^{2+}$, after correction, decrease from $K^*(E_i) = 26$ to 16.1 in the case of Cd^{2+} and from $K^*(E_i) = 30$ to 15.9 in the case of Zn^{2+}. The new values are in the vicinity of the values found by Zambrana[53] for the same complex but using a different data treatment. The corrected excited-state values are also in the vicinity of the ground-state equilibrium constants, suggesting that the ground-state interaction between species determines, to a significant extent, the interaction in the excited-state as well. In the case of $[(bpy)_2Ru(pypz)]^{2+}$ with Zn^{2+}, the lifetime of the coordinated species is actually longer than the lifetime of the parent complex, hence applying the lifetime correction increases the value of the equilibrium constant from $K^*(E_i) = 2$ to 8.7. Again, the correction brings the excited-state value within experimental error of the ground-state value of the equilibrium constant for $[(bpy)_2Ru(pypz)]^{2+}$.

In both ground- and excited-state, the value of the equilibrium constant is slightly larger for $[(bpy)_2Ru(dpp)]^{2+}$ than it is for $[(bpy)_2Ru(pypz)]^{2+}$, suggesting the reaction forms more product with dpp than with pypz. The logical conclusion is that the initial interaction in the ground state with the more basic pyridyl nitrogen promotes or facilitates the complex-metal interaction and the subsequent chelation has a stabilizing effect and contributes to produce a more stable Zn-Ru bimetallic.

The change in basicity upon excitation had a much more striking effect on the value of the equilibrium constant for protonation increasing its value by several orders of magnitude in the excited state, compared to the ground state. Yet, the protonated species are either non-emissive or have extremely short lifetime, while the products of association between ruthenium complexes and Zn^{2+} or Cd^{2+} are emissive with lifetimes of the same order of magnitude as the un-coordinated parent complex. This observation suggests that the nonradiative rate for protonation must be extremely large as the diffusion rate for protons is also much larger than that of any other ion in solution. The fact that protonated species are not emissive is probably more dependent on coupling to the solvent medium, rather than a function of the molecular and electronic structure of the emitter.

4.C.2.c. Stern-Volmer Plots

All Stern-Volmer plots presented herein, whether intensity, emission areas or lifetime, have an initial portion where the change in each is dependent on the concentration of the divalent ion added. After a certain concentration, 0.5 M Zn^{2+}, the curves for $[(bpy)_2Ru(dpp)]^{2+}$ approach or reach a plateau or "negative deviation" and become independent of $[M^{2+}]$. The Stern-Volmer intensity quenching plot for $[(bpy)_2Ru(pypz)]^{2+}$ remains essentially linear throughout the range of concentrations, which is consistent with the weak basicity of the pypz peripheral nitrogen. The plot obtained from integrated emission areas, on the other hand, shows negative deviations. This is attributed to contributions from other emissions, which affect the "true" value of the plotted areas. Finally, the Stern-Volmer lifetime quenching plot shows no curvature.

The linearity may be due to the fact that only the lifetime values in the initial range of Zn^{2+} concentrations could be calculated with a low margin of uncertainty and hence were the only values determined for the MLCT emission band centered on pypz. At higher concentrations, three emissions overlap, 610-, 660- and 750-nm and de-convoluting the triple exponential data results in lifetime values with large uncertainties.

All values of K_{SV} in Table 34 were obtained from the initial linear portion of each graph and the bimolecular rate constants of quenching, k_q, were derived from equation 101, using the same values of K_{SV} and the lifetimes in the absence of quencher. Since all Stern-Volmer plots for $[(bpy)_2Ru(dpp)]^{2+}$ are non-linear, while the plots for $[(bpy)_2Ru(pypz)]^{2+}$ are, for the most part, linear, the two sets of plots will be initially discussed separately and compared later.

Table 34: Quenching constants and Stern-Volmer constants for the bimolecular reaction between $*[(bpy)_2Ru(dpp)]^{2+}$ or $*[(bpy)_2Ru(pypz)]^{2+}$, and Cd^{2+} or Zn^{2+}.

	k_q (I)[a]	k_q (τ)[a]	K_{SV} (I)[b]	K_{SV} (A)[b]	K_{SV} (τ)[b]	τ_0 [c]
$[Ru(bpy)_2dpp]^{2+}$ -Cd^{2+}	8.23×10^7 $M^{-1} s^{-1}$	1.73×10^7 $M^{-1} s^{-1}$	8.39	4.86	1.763	102 ns
$[Ru(bpy)_2dpp]^{2+}$ -Zn^{2+}	9.12×10^7 $M^{-1} s^{-1}$	3.14×10^7 $M^{-1} s^{-1}$	9.30	8.57	3.20	102 ns
$[Ru(bpy)_2pypz]^{2+}$-Zn^{2+}	1.67×10^7 $M^{-1} s^{-1}$	1.26×10^8 $M^{-1} s^{-1}$	0.41	0.50	3.78	30 ns

[a] Quenching constants obtained using intensity data, $k_q(I)$, and lifetime data $k_q(\tau)$. [b] Stern-Volmer constants obtained using intensity data, $K_{SV}(I)$, lifetime data, $K_{SV}(\tau)$ and areas under the emission curves, $K_{SV}(A)$. [c] Lifetimes in the absence of a quencher.

The values obtained for the interaction of cadmium and zinc with $[(bpy)_2Ru(dpp)]^{2+}$ are within experimental error of each other and in the same range as

other quenching constant for ruthenium(II) diimines listed in reference 17. The fact that the intensity and lifetime plots are not coincident is indicative of the existence of a static component to the quenching phenomenon and pre-equilibrium conditions are usually involved in the excited state interaction. Based on the discrepancy in values of $K_{SV}(\tau)$ and $K_{SV}(I)$, it can be inferred that approximately 39% of quenching of $[(bpy)_2Ru(dpp)]^{2+}$ by Cd^{2+} ions occurs via a dynamic process, and more than half (~ 64%) in the case of $[(bpy)_2Ru(dpp)]^{2+}$ with Zn^{2+}. As the ruthenium portion of the adduct is excited, intramolecular interactions[17] within the ($^{*}[(bpy)_2Ru(dpp)]^{2+}$-$M^{2+}$) exciplex cause radiationless relaxation of the excited ruthenium molecule. Rephrased in terms of the extent of static quenching, in the metal-dependent range of concentrations where the Stern-Volmer plots are linear, the adduct formed in the ground state between $[(bpy)_2Ru(dpp)]^{2+}$ and Cd^{2+} ions contributes to the overall quenching of the emission from the excited $^{*}[(bpy)_2Ru(dpp)]^{2+}$ molecule more than does the adduct formed between $[(bpy)_2Ru(dpp)]^{2+}$ and zinc.

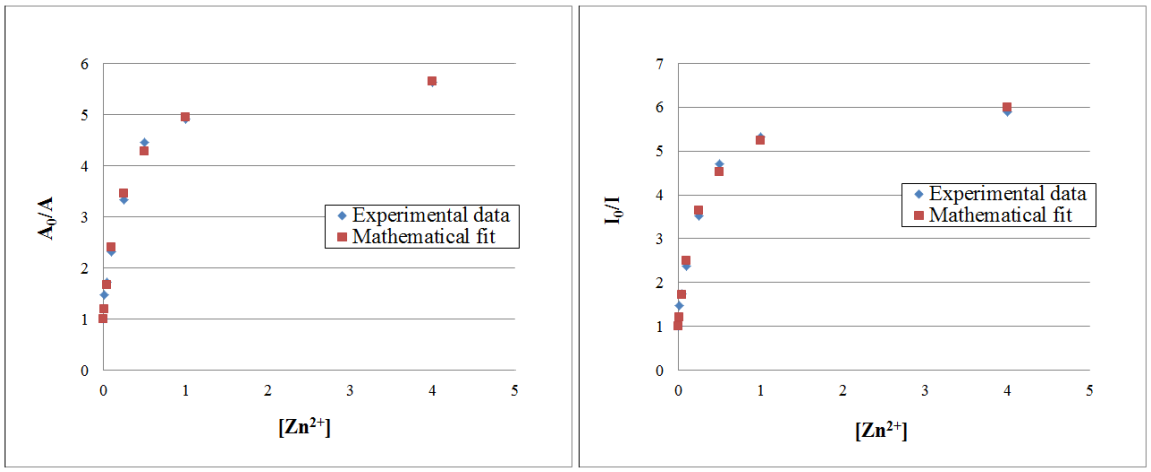

Figure 196: Area and intensity Stern-Volmer plots and data fits for quenching of $[(bpy)_2Ru(dpp)]^{2+}$ with Zn^{2+}.

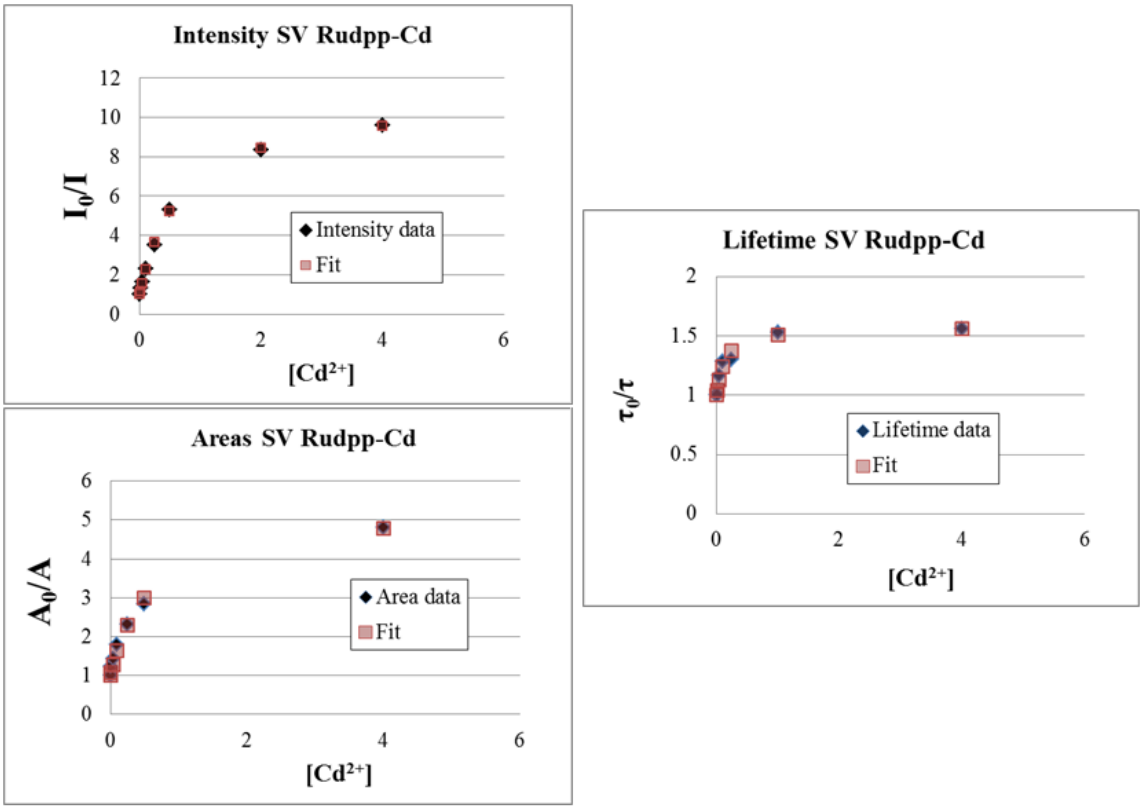

Figure 197: Area, intensity and lifetime Stern-Volmer plots and data fits for quenching of $[(bpy)_2Ru(dpp)]^{2+}$ with Cd^{2+}.

According to previous studies[17], the negative deviations at higher concentrations of divalent metal suggest that the interaction between M^{2+} ions and $[(bpy)_2Ru(dpp)]^{2+}$ may involve formation of an exciplex and, unlike protonation, the product of the excited-state reaction, between the two is emissive (λem = 752 nm for $[(bpy)_2Ru(dpp)]^{2+}$ with Zn^{2+} and λem = 745 nm for $[(bpy)_2Ru(dpp)]^{2+}$ with Cd^{2+}). In other words, the negative deviation is due to the overlap of the two emerging emissions with the 695-nm emission that is being quenched. Therefore, we can apply a modified form of equation 87, where $[H^+]$ in this case is $[M^{2+}]$ (Equation (110)), to the data and we can extrapolate the quenching constant, k_q , the rate constant for deactivation of the coordinated and un-

coordinated forms, k_0 and k_0", and γ, which represent the differential ratio of intensity between two emissive forms of ruthenium.

$$\frac{I_1^0}{I_1} = \frac{1 + \frac{k_q\,[M^{2+}]}{k_o}}{1 + \gamma\left(\frac{k_q[M^{2+}]}{k_0^{"}}\right)} \qquad (110)$$

The Stern-Volmer fits are presented in Figure 196 and 197 and the kinetic constants are listed in Table 35.

Table 35: Quenching constants, rate constant for deactivation and differential ratios for the bimolecular reaction between *[(bpy)$_2$Ru(dpp)]$^{2+}$ or *[(bpy)$_2$Ru(pypz)]$^{2+}$, and Cd^{2+} or Zn^{2+}.

Reaction w/ M^{2+}	**kq (A) (M^{-1} s^{-1})**	**k_0 (A) (s^{-1})**	**k_0" (A) (s^{-1})**	**ϒ (A)**
[Ru(bpy)$_2$pypz]$^{2+}$-Zn^{2+}	1.75E+07	1.08E+07	8.29E+08	62.8
[Ru(bpy)$_2$dpp]$^{2+}$-Zn^{2+}	4.69E+07	2.00E+06	9.37E+08	78.97
[Ru(bpy)$_2$dpp]$^{2+}$-Cd^{2+}	2.01E+07	2.20E+06	1.00E+09	85.4
Reaction w/ M^{2+}	**kq (I) M^{-1} s^{-1}**	**k_0 (I) (s^{-1})**	**k_0" (I) (s^{-1})**	**ϒ (I)**
[Ru(bpy)$_2$dpp]$^{2+}$-Zn^{2+}	4.75E+07	1.91E+06	9.38E+08	77.8
[Ru(bpy)$_2$dpp]$^{2+}$-Cd^{2+}	2.03E+07	1.27E+06	1.08E+09	76.7
Reaction w/ M^{2+}	**kq (τ) M^{-1} s^{-1}**	**k_0 (τ) (s^{-1})**	**k_0" (τ) (s^{-1})**	**ϒ (τ)**
[Ru(bpy)$_2$dpp]$^{2+}$-Cd^{2+}	3.62E+07	3.13E+06	5.45E+08	110.2

The values found are still in the same order of magnitude as the quenching constant extrapolated from the linear portion of the curves. The differential ratios give an idea of the extent of the overlap between emissions and it is reasonable that they may be close in value, since all emissions originating from similar states fall within 15-25 nm of each other. Also, the equation fits the plots in their entirety, unlike the case of protonation, where only the high or low pH range could be fitted at once. The rates of deactivation for the metallated forms of the complex are higher than the ones obtained for the parent complex, which confirms that the original ruthenium(II) complex is more stable than the product and parallels the lifetime values of each species.

In the case of the excited state interaction of $[(bpy)_2Ru(pypz)]^{2+}$ and Zn^{2+}, we can exclude pre-equilibrium association in the ground state based on the very low ground-state equilibrium constant and weak basicity of the pyrazyl nitrogen of pypz. The linearity of the intensity Stern-Volmer suggests that the interaction between the two reactants is a single-step diffusion process, as postulated above (Figure 194) and the standard Stern-Volmer equation can be used to fit the linear intensity and lifetime curves, and derive the values of the bimolecular quenching constants and the Stern-Volmer constants (Table 34). However, not much can be deduced from the fact that the lifetime and intensity quenching and the Stern-Volmer plots do not coincide. The Stern-Volmer plots for the excited state interaction of $[(bpy)_2Ru(pypz)]^{2+}$ and Zn^{2+} show a striking feature: the lifetime quenching plot yields a larger K_{SV} value than the intensity quenching plot (Table 34). This is hardly ever the case, because the lifetime plot is only supposed to account for dynamic quenching, while the intensity plot accounts for both static and dynamic quenching and usually has a larger value of K_{SV}. After in depth analysis of the

zinc titration emission spectra of $[(bpy)_2Ru(pypz)]^{2+}$, these findings are attributed to experimental data compilation and are not an inherent kinetic property of the $[(bpy)_2Ru(pypz)]^{2+}/Zn^{2+}$ system (i.e. type of reactions occurring and time-scale of each process). As reported in the result section, a discrepancy was found between the time-resolved and the steady-state emission spectra of $[(bpy)_2Ru(pypz)]^{2+}$ recorded on the same sample, at the same temperature, with the same concentration of d^{10} metal and obtained from measurements made only minutes apart from each other on different instruments (Figure 135). In the time-resolved spectra, the 660-nm emission was disappearing "sooner" (i.e. at lower concentrations of added $[Zn^{2+}]$), while the same sample under steady-state irradiation was still yielding an emission spectrum in which the dominant emission was the 660-nm band and there was still no sign of any new red-shifted emission at 750 nm. As a result, the parameters taken from time-resolved spectra (lifetimes), "seem" to change faster than the parameters (intensity or integration under the emission curve) extrapolated from the steady-state spectra. This is due to the fact that the emission originating from the pypz-localized MLCT state of $[(bpy)_2Ru(pypz)]^{2+}$ is extremely short-lived, less than 9 ns, at concentrations of Zn^{2+} equal or higher than 1M. Given the high levels of noise (Figure 136), it is plausible that the short-lived 660-nm emission may go undetected in the time-resolved luminescence spectra yet still be visible under steady state excitation. Another discrepancy observed between techniques was the relative intensity between the 610- and the 750-nm emission: The 610-nm emission is more intense when excited with 420-nm light while the 750-nm emission is undetected or hidden under the 660-nm emission in the same steady-state spectrum. On the other hand, the time-resolved spectrum reveals a much more intense 750-nm emission compared to

the 610-nm emission. This is not surprising based on earlier results outlining the effect of excitation wavelength on the intensity of the 610-nm band (Figure 120, page 184): when compared to 450-nm excitation wavelength, using 490-nm excitation wavelength, or higher, inverts the relative intensity of the 610- and 750-nm bands by decreasing the 610-nm intensity and increasing the 750-nm intensity. The use of different excitation wavelength, 532 nm in the time-resolved experiments (see Experimental Section) and 420 nm in the steady-state measurements is, in our opinion, the reason that the Stern-Volmer lifetime plot rises sharply while the intensity and area plots have lower slope values. This occurrence underscores the importance of taking into account the experimental parameters set for each experiment and paying attention to the type of information that each analytical technique can provide on the same sample. In this case, the intensity measurements made under steady-state conditions are more biased by the presence of other overlapping and hard-to-resolve emissions, while lifetime data are less susceptible to other emissions' lifetimes because the resolution of our instrument allows more separation between contributing emissions with lifetimes that differ by at least an order of magnitude and do not overlap completely.

Quoting Zambrana: "Clearly, there is associational quenching, but the critical question is whether or not there is a dynamic component to the quenching as well: Does data suggest that association is favored in the excited state?"[53] The answer, based on the mechanism suggested in Figure 193 and 194 would be yes for both, $[(bpy)_2Ru(dpp)]^{2+}$ and $[(bpy)_2Ru(pypz)]^{2+}$. However, comparison of the ground- and excited-state equilibrium constants (Table 33), would suggest that neither is favored. Further experiments would need to be carried out to confirm or disprove either statement. It is

plausible that the key factors are: having the metal already in the vicinity of the coordination site that will increase in basicity upon excitation, and having the possibility to form a chelate. The complex $[(bpy)_2Ru(pypz)]^{2+}$ lacks both and formation of a bimetallic does not seem significantly more favored by excitation.

Excited-state coordination for $[(bpy)_2Ru(pypz)]^{2+}$ seems to be diffusion limited and dependent on the concentration of Zn^{2+} in the immediate vicinity of the coordinating site, while in the case of $[(bpy)_2Ru(dpp)]^{2+}$, a pre-equilibrium between the complex and the divalent d^{10} metal is postulated to exist based on the structure of the complex and its ground state behavior.

4.C.2.d. New red-shifted emission peaks

The red-shifted emissions observed during the titration of $[(bpy)_2Ru(pypz)]^{2+}$ with Zn^{2+} and titration of $[(bpy)_2Ru(dpp)]^{2+}$ with Zn^{2+}/Cd^{2+} are broader and more asymmetrical in shape compared to the original emission and they can be fitted by the linear combination of two gaussian emissions with distinct lifetimes (Figure 198).

While it would be tempting to assign the two emissions to the mono- and bi-dentate form of the Ru complex, results obtained with $[(bpy)_2Ru(pypz)]^{2+}$, suggests otherwise. Both $[(bpy)_2Ru(pypz)]^{2+}$ and $[Ru(bpy)_3]^{2+}$, when mixed in solution with Zn^{2+} and Ag^{+}, respectively, exhibit a double emission red-shifted from the original peak max yet have no capability to form a bidentate[27]. Furthermore, $[(bpy)_2Ru(pypz)H]^{3+}$ does not emit and yet the double emission is visible in $[(bpy)_2Ru(pypz)]^{2+}$ solutions buffered at pH 3 with high concentrations of Zn^{2+}. Hence, based on this experimental observation, while a small percentage of the ruthenium complexes present in solution exists in the

protonated form, it may be concluded that the protonated form of the free complex is not responsible for said emission.

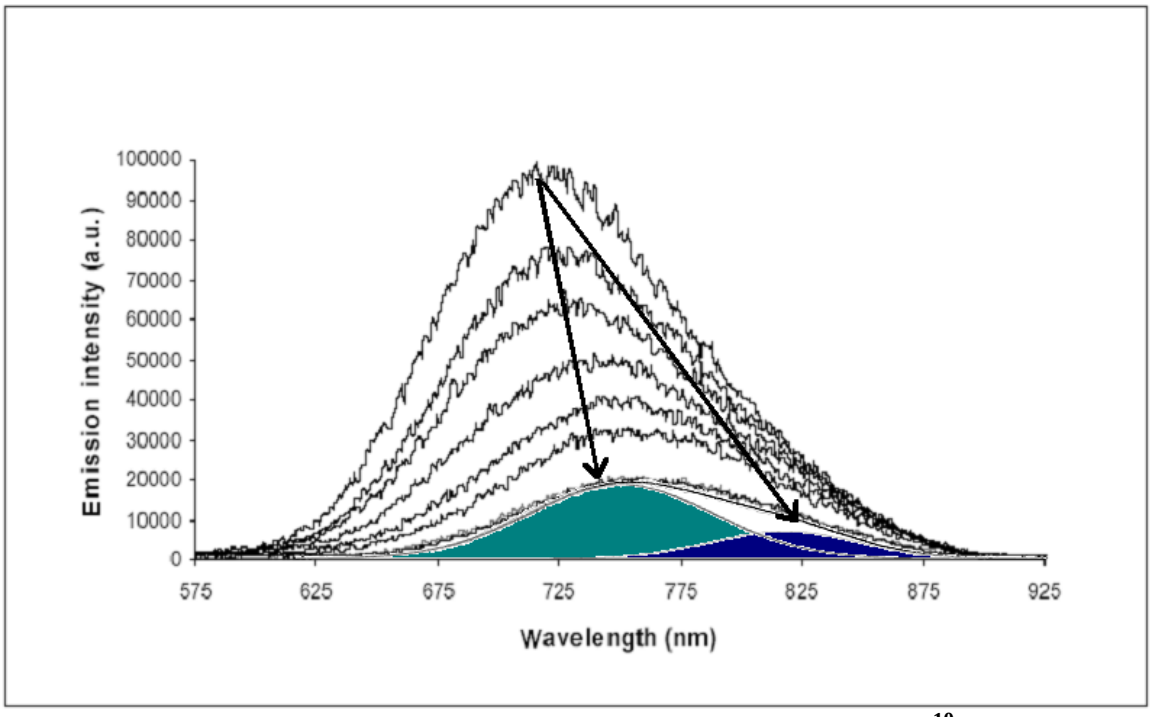

Figure 198. Example of the effect of increasing concentrations of d^{10} metals on the emission of Ru(II) diimine complexes.

According to the review article on $Ru(bpy)_3^{2+}$ by Balzani and Campagna, the multiple emission from $Ru(bpy)_3^{2+}$ originates from a set of 3 closely spaced levels (ΔE = 10 and 61 cm^{-1}) in thermal equilibrium[47]. It's clear that the energy levels involved are MLCT in nature, but there's still debate as to whether they can be described by a spin quantum number and whether the promoted electron resides in a single bpy ligand or in a delocalized π^* orbital. The fact that the MLCT bands observed in the UV-Vis spectrum of $[(bpy)_2Ru(pypz)]^{2+}$ move apart as the zinc(II) concentration is increased, is consistent with the idea that the MLCT levels of the $[(bpy)_2Ru(pypz)]^{2+}$ complex are not coincident

and become even more distinguishable as more zinc is added. Hence, more than one emission could result depending on the ligand that the relaxing electron was transferred to. The fact that the excitation spectrum for $[(bpy)_2Ru(pypz)]^{2+}$ in 5 M $ZnCl_2$ recorded at 765 nm closely resembles the absorption spectrum (Figure 114), confirms that all MLCT bands in the 422 to 488-nm range contribute to the emission observed at 750 nm. Following this reasoning, the multiple emissions described herein could arise from the three MLCT levels that split further and become more distinguishable. This, however, is not consistent with the calculated ΔE between the two emission components (> 1000 cm^{-1} for all three titrations). More likely, they reflect emission from $[(bpy)_2Ru(pypz)]^{2+}$ (or $[(bpy)_2Ru(dpp)]^{2+}$) species exhibiting different levels of interaction with M^{2+}. For example, one could be a direct interaction between the pypz nitrogen and Zn^{2+}, i.e., equivalent to or very similar to formal coordination. Assuming the ruthenium(II) complex in question were to interact with all the species in solution, if the metal in solution is present in equilibrium with its conjugated acid and base:

$$Zn(H_2O)_n^{2+} \leftrightarrows Zn(H_2O)_{n-1}OH^{+} + H^{+}$$

the excited ruthenium complex, $*[(bpy)_2RuL]^{2+}$, could potentially form excited-state exciplexes with differing composition:

$$*[(bpy)_2RuL]^{2+} \text{ --- } Zn(H_2O)_n^{2+}$$

$$*[(bpy)_2RuL]^{2+} \text{ --- } Zn(H_2O)_{n-1}OH^{+}$$

and the two emissions would be experimentally observed as a result. The possibility that the ruthenium complex may interact via the hydrogen of one of the waters of hydration surrounding the Zn^{2+} ion and form an emissive excited state species with formula $*[(bpy)_2RuL]^{2+}\text{---}H_2O\text{-}Zn(H_2O)_{n-1}^{2+}$ was considered and discarded because the

experimental results obtained during protonation studies of $[(bpy)_2Ru(dpp)]^{2+}$ and $[(bpy)_2Ru(pypz)]^{2+}$ showed that protonation of the peripheral pyrazine nitrogen leads to emission quenching and radiationless decay. Further experiments will be needed to resolve the matter and clarify the mechanisms involved.

5. Conclusions

The differences and similarities in the properties of $[(bpy)_2Ru(pypz)]^{2+}$ and $[Ru(bpy)_2dpp]^{2+}$ in the same environment were used to highlight the peculiar behavior of the acid-base sites of each complex upon excitation and their role in coordination and protonation reactions.

5.A. Acid-Base Chemistry

The pypz analogue of the dpp ligand was synthesized, and used to prepare the mixed ligand complex of ruthenium(II), $[Ru(bpy)_2pypz]^{2+}$, in an effort to identify –by comparison- the sequence of protonation steps at the peripheral dpp nitrogens in the ground and excited states of $[(bpy)_2Ru(dpp)^{2+}]$, and quantify the magnitude of the photo-induced change in acid-base properties at each of the sites. The pypz ligand, identical in almost every respect to dpp except for the absence of the free pyridyl ring, was the ideal candidate to elucidate how the pyrazinyl nitrogen on the coordinated dpp would behave if the additional pyridyl ring on dpp was not present. Through pH titrations performed from pH 12 to Hammett acidity constant of –11 it was possible to establish the range of pH in which the protonation steps for *both* $[(bpy)_2Ru(dpp)^{2+}]$ and $[Ru(bpy)_2pypz]^{2+}$ take place. As expected from the relative basicity of pyridine and pyrazine free ligands, as well as bypyridine and bipyrizine, the pyridyl nitrogen of $[(bpy)_2Ru(dpp)]^{2+}$ is a stronger base than the pyrazyl nitrogen of $[(bpy)_2Ru(dpp)]^{2+}$ and $[(bpy)_2Ru(pypz)]^{2+}$. The UV-Vis titration was used for the first time to confirm that $[(bpy)_2Ru(dpp)^{2+}]$ undergoes its first acid-base reaction in the 1-3 pH range and the NMR titration helped identify the imine site at which it occurs (pyridyl site). The pyrazyl nitrogen of $[(bpy)_2Ru(pypz)]^{2+}$

protonates next (H_o -1.3) and finally, the second and last protonation step of $[(bpy)_2Ru(dpp)]^{2+}$ occurs at H_o -5.9 (Figure 148). This latter result is probably the most remarkable as it happens at much higher acidity than most peripheral nitrogens on diimine ligands coordinated to Ru(II).

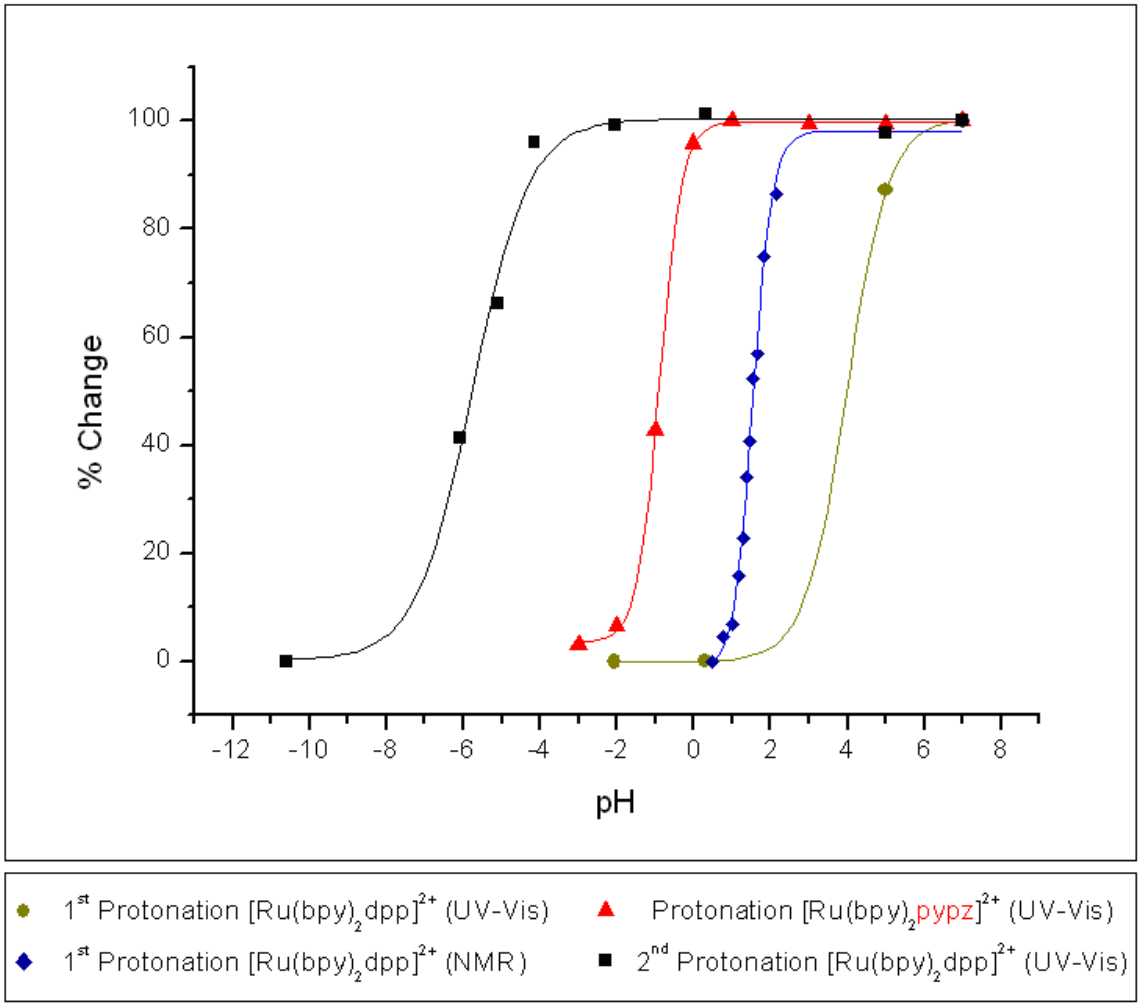

Figure 148: $[(bpy)_2Ru(dpp)]^{2+}$ and $[(bpy)_2Ru(pypz)]^{2+}$ ground-state acid-base titrations.

Measurements of the ground state pK_a value for the protonation of $[(bpy)_2Ru(pypz)]^{2+}$ prove that the basicity of the pyrazinyl nitrogen on the dpp ligand of

$[(bpy)_2Ru(dpp)]^{2+}$ is significantly reduced (by over 4 orders of magnitude!) by the presence of the pyridyl ring and by the fact that protonation of the pyrazinyl nitrogen of dpp only happens in the ground state after first protonation has occurred (Figure 148). Speculations[53] that, the peripheral pyridyl ring might not affect the pyrazinyl nitrogen in the ground state because of the ability of the pyridyl ring to rotate away from the protonated pyrazyl nitrogen, are refuted.

The basicity enhancement of the protonable sites of $[(bpy)_2Ru(dpp)]^{2+}$ upon excitation was re-examined in light of the new protonation values determined during the course of this work. It was concluded that, in the excited state, it is not possible to calculate or extrapolate the thermodynamic pK_a^* spectroscopically. At most, an educated guess can be made of the increase in basicity of the pyrazinyl site of dpp by comparing the excited state pK_a^*(app) for $[(bpy)_2Ru(dpp)]^{2+}$ with the ground state pK_a of $[(bpy)_2Ru(pypz)]^{2+}$, since both protonations refer to the same kind of nitrogens. Assuming the peripheral dpp pyridine is not involved, population of the dpp localized MLCT state increases the basicity of the pyrazyl nitrogen on $[(bpy)_2Ru(dpp)]^{2+}$ by 5.8, close to the original estimates of 6 orders of magnitude. The second pK_a^* (app) is calculated to be more than 5 orders of magnitude larger than the second protonation in the ground state. Though we cannot attribute an exact value to the basicity enhancement brought on by excitation, we can report that both protonations of $[(bpy)_2Ru(dpp)]^{2+}$ happen at higher pH in the excited state, and the direction of the change in pKa is consistent with the MLCT assignment (increased charge on the ligand increases the base strength at both protonable dpp sites upon excitation).

A striking feature was observed during protonation of $[(bpy)_2Ru(pypz)]^{2+}$ complex that is unrelated to dpp and has yet to be fully understood. In addition to protonation at the only available peripheral nitrogen of the pypz ligand occurring at pH 2.7 with formation of the non-emissive species $[(bpy)_2RupypzH]^{2+}$, it was observed that, between pH 7 and 9, the lifetime and emission intensity of $[(bpy)_2Ru(pypz)]^{2+}$ increase rapidly and they are independent of further increases beyond a pH of 9. The quantitative reversibility of both absorption and emission changes establishes that the interaction happens exclusively while the complex is in the excited state. The complex returns to its original composition and configuration as soon as it returns to the ground state and no structural change or change in the electronic distribution within the molecule occurs in that pH range. Pinpointing the causes of the emission increase is still an open challenge. However, the likely reason for the more stable and longer-lived form of the complex in basic solution, in our opinion, is the reduction in the non-radiative quenching rate, k_{nr}, which is dependent on the interactions of the complex with its surroundings. As the solvent shell around the cationic complex changes in basic solution, non-radiative decay processes may be less favored and the hydrogen bonds between the complex and the solvent that are responsible for vibrational loss of energy via non-radiative interactions may be hindered by the increased concentration of OH^- species in basic solutions.

Observations made while studying the excited-state acid-base titrations of $[(bpy)_2Ru(dpp)]^{2+}$ and $[(bpy)_2Ru(pypz)]^{2+}$ support the idea that the interaction between the excited complexes and the proton is not a unique and continuous process over the 0 to 12 pH range.

Finally, a new blu-shifted emission was discovered at acidic pH as a result of protonation experiments at room temperature. The emission, centered at 610 nm, had not been observed before in either complex and its detection was particularly unexpected for $[(bpy)_2Ru(pypz)]^{2+}$ because none of the ligands of the complex possess free nitrogens available for protonation at high acidity and the protonated form of the complex is not emissive. In the case of $[(bpy)_2Ru(pypz)]^{2+}$, the transition is triplet in character and the possibility that it may be a singlet ^{1}MLCT transition is excluded because the lifetime of the new emission is longer (~ 500ns) than the lifetime of the neutral complex (150ns). The emission is assigned to an excited MLCT state localized on the bpy ligand that is seen because the more dominant 675-nm emission disappears as acidity is increased.

Unlike all the parent tris-analogues and the majority of other ruthenium(II) diimine complexes, where excitation populates quantitatively only one emissive state, absorption of energy by $[(bpy)_2Rudpp]^{2+}$ at high acidity results in population of two emissive states with different emission characteristics, one centered around 610 nm and the other red-shifted around 730 nm, even though protonation at the pyrazyl nitrogen of either $[(bpy)_2Ru(dpp)]^{2+}$ or $[(bpy)_2Ru(pypz)]^{2+}$ complexes, results in formation of a non-emissive species. Findings suggest that the emissions come from different Ru(II)-ligand pairs. Experimental data and the fact that a similar emission is observed in spectra of similarly acidic solutions of $[(bpy)_2Ru(dpp)]^{2+}$ supports the thesis that the 610-nm emission is not promoted by protonation but is present all along together with the 675-nm emission, although the increased intensity at higher acidity may be due to an enhanced interaction of the bpy ligand with the protons in solution via the π-orbital system.

In the case of $[(bpy)_2Ru(dpp)]^{2+}$, the acid dependence of the 730-nm emission is an indication that the excited state involved has a protonable site; hence the emission is assigned to that from the mono-protonated dpp ligand since a vacant acid-base site remains at the peripheral pyrazine nitrogen. As the concentration of protons increases and the complex undergoes a second protonation, the 730-nm emission disappears indicating that the double-protonated form of the complex is non-emissive. The fact that the 620-nm emission is not acid-dependent supports the assignment that it is an emission centered on the bpy ligand, a ligand that cannot directly engage in a protonation reaction.

5.B. Coordination

Coordination experiments performed using the mixed ligand complex of ruthenium(II), $[Ru(bpy)_2pypz]^{2+}$, have been carried out to probe the role of the chelate effect in excited-state coordination reactions of $[(bpy)_2Ru(dpp)^{2+}]$ with d^{10} metal ions such as Zn(II). Results suggest that both complexes, $[(bpy)_2Ru(dpp)]^{2+}$ and $[Ru(bpy)_2pypz]^{2+}$, interact with d^{10} metal cations, and form emissive bimetallics which can be observed spectroscopically but are not stable enough thermodynamically to be isolated. For $[Ru(bpy)_2pypz]^{2+}$, the linear increase in absorbance with increasing $[Zn^{2+}]$ suggests that, even at 5M the concentration of Zn^{2+} is insufficient to form an equilibrium amount of the bimetallic. For $[(bpy)_2Ru(dpp)]^{2+}$, coordination happens via the imine nitrogens of the dpp ligand, which were identified as the “active site” for association via NMR. The ground-state titration curves’ deviation from the expected shape implies consecutive rather than simultaneous equilibria involving more than one site, and is reminiscent of cooperative effects. Data gathered in the experiments point to

coordination of $[(bpy)_2Ru(dpp)]^{2+}$ via a two-step reaction with an initial coordination to the more basic peripheral pyridyl nitrogen and subsequent intramolecular interaction with the less basic peripheral pyrazyl nitrogen on the dpp ligand. On the other hand, $[(bpy)_2Ru(pypz)]^{2+}$ has only the less basic peripheral pyrazyl nitrogen on the pypz ligand and therefore the monodentate bimetallic is expected to be less stable, preventing any buildup of $[(bpy)_2Rupypz\text{-}Zn]^{4+}$. The observation that coordination of $[(bpy)_2Ru(dpp)]^{2+}$ to Zn^{2+} will either not take place, or be severely retarded if first protonation at that nitrogen has already occurred (i.e. at pH 0), is additional proof that coordination of $[(bpy)_2Ru(dpp)]^{2+}$ to Zn^{2+} cations initiates via bonding to the more basic peripheral pyridyl nitrogen. Indirectly, this observation also confirms the assignment of first protonation of the $[(bpy)_2Ru(dpp)]^{2+}$ complex well above pH 0, contrary to what was initially suggested[62]. When compared to the zinc titration of $[(bpy)_2Ru(pypz)]^{2+}$, the fact that the reaction between $[(bpy)_2Ru(dpp)]^{2+}$ and Zn^{2+} cannot take place when the complex has only the peripheral pyrazyl nitrogen free to coordinate, is consistent with the fact that $[(bpy)_2Ru(pypz)]^{2+}$ does not easily coordinate to Zn^{2+}.

Excited-state titration of $[(bpy)_2Ru(pypz)]^{2+}$ with Zn^{2+} produces three distinct emissions: the high energy band at 610 nm not observed in the $[(bpy)_2Ru(dpp)]^{2+}$ emission spectra, the main emission quenched by addition of Zn^{2+} and assigned to the MLCT transition to the pypz ligand, and a new emission (or multiple emissions) centered at 750 nm, evidence of the presence on an associative interaction between the complex and the Zn^{2+} ions added to the solution.

The 610-nm emission is peculiar to the $[(bpy)_2Ru(pypz)]^{2+}$ complex and visible in conjunction with the above-mentioned red-shifted 750-nm emission. The absence of a

metal ion-dependence for both the emission's position and intensity is consistent with the assignment of the transition to a bpy-localized MLCT transition. In addition, it establishes that Zn^{2+} interacts exclusively with the pypz portion of the complex and does not interact with the aromatic π systems of the bpy portion of the complex.

The red-shifted emissions around 750 nm, observed during the titration of $[(bpy)_2Ru(pypz)]^{2+}$ with Zn^{2+} and titration of $[(bpy)_2Ru(dpp)]^{2+}$ with Zn^{2+}/Cd^{2+}, are broader and more asymmetrical in shape compared to the original emission and they can be fitted by the linear combination of two gaussian emissions with distinct lifetimes. Though not completely excluded, the interpretation here is that the multiple emissions are not due to mono- and bi-dentate forms or protonated forms of the ruthenium complex. More likely, they reflect emission from $[(bpy)_2Ru(pypz)]^{2+}$ (or $[(bpy)_2Ru(dpp)]^{2+}$) species exhibiting different levels of interaction with M^{2+} or interactions with different $Zn(H_2O)_n^{2+}$ species.

Finally, changes to the main 660-nm emission were studied to derive kinetic and thermodynamic conclusions regarding the coordination mechanisms applicable to either or both complexes. Unlike what is observed in the ground state, quenching of the main 660-nm emission occurs immediately upon addition of the metal ions for both complexes. The presence of a pre-existing ground-state interaction between the Zn^{2+} ions and the pyridyl nitrogen of dpp before excitation occurs, gives a slight advantage to $[(bpy)_2Ru(dpp)]^{2+}$, but both complexes benefit from the increased basicity of their peripheral pyrazyl nitrogens. The higher *excited* state basicity of the peripheral pyrazyl nitrogen of pypz compared to its ground state basicity is confirmed by protonation

experiments that established that excitation increases the basicity of the pyrazyl nitrogen of $[(bpy)_2Ru(pypz)]^{2+}$ by approximately 4 orders of magnitude ($\Delta pKa \approx 4$).

The difference in stability between ground- and excited-state coordination of the ruthenium(II) diimines complexes with the d^{10} metal ions, is not that large and all the equilibrium constants found for both ground and excited state are within the same order of magnitude. In both states, the value of the equilibrium constant is slightly larger for $[(bpy)_2Ru(dpp)]^{2+}$ than it is for $[(bpy)_2Ru(pypz)]^{2+}$, suggesting the reaction forms more product with dpp than with pypz. The logical conclusion is that the initial interaction in the ground state with the more basic pyridyl nitrogen promotes or facilitates the complex-metal interaction and the subsequent chelation has a stabilizing effect and contributes to produce a more stable Zn-Ru bimetallic. As the ruthenium portion of the adduct is excited, intramolecular interactions[17] within the ($^{*}[(bpy)_2Ru(dpp)]^{2+}$-$M^{2+}$) exciplex cause radiationless relaxation of the excited ruthenium molecule.

Stern-Volmer analyses for both complexes show negative deviation due to the overlap of the two emerging 750-nm emissions with the 670- (or 690-nm) emission that is being quenched. The fact that the intensity and lifetime plots are not coincident is indicative of the existence of a static component to the quenching phenomenon and pre-equilibrium conditions are usually involved in the excited state interaction. In the case of the excited state interaction of $[(bpy)_2Ru(pypz)]^{2+}$ and Zn^{2+}, we can exclude pre-equilibrium association in the ground state based on the very low ground-state equilibrium constant and weak basicity of the pyrazyl nitrogen of pypz. Excited-state coordination for $[(bpy)_2Ru(pypz)]^{2+}$ seems to be diffusion limited and dependent on the concentration of Zn^{2+} in the immediate vicinity of the coordinating site, while in the case

of $[(bpy)_2Ru(dpp)]^{2+}$, a pre-equilibrium between the complex and the divalent d^{10} metal is postulated to exist based on the structure of the complex and its ground state behavior.

References

(1) Roda, A., *The Discovery of Luminescence: The Bolognian Stone,* International Conference on Bioluminescence and Chemiluminescence, 1998.

(2) McCarroll, M. E., Warner, I. M., Agbaria, R. A., "Electronic Absorption and Luminescence: Introduction", *Encyclopedia of Analytical Chemistry*, 2006.

(3) Hoffman, M. Z., *J. Chem. Ed*., 60, **1983**, 784.

(4) Ciamician, G., *Science*, 36, **1912**, 385-394.

(5) Roth, H. D., *Pure Appl. Chem.*, 73, **2001**, 395-403.

(6) a) Stryer, L., Haugland, R. P., *Proc. Natl. Acad. Sci. U.S.A.*, 58, **1967**, 719; b) Stryer, L., *Annu. Rev. Biochem.*, 47, **1978**, 819; c) Birks, J. B., *Photophysics od Aromatic Molecules*, Wiley (Interscience), New York, **1970**; d) Bennett, R.G., *J. Chem. Phys.*, 41, **1964**, 3037; e) Zimmerman, H. E., Goldman, T. D., Hirzel, T. K., Schmidt, S. P., *J. Org. Chem.*, 45, **1980**, 3933.

(7) Choi, J. D., Fugate, R. D., Song, P.-S., *J. Am. Chem., Soc.*, 102, **1980**, 5293.

(8) http://en.wikipedia.org/wiki/Franck-Condon_Principle.

(9) Kasha, M., *Faraday Soc. Disc*., No 9, **1950**, 14.

(10) Crosby, G. A., *Journal of Chem. Ed.*, 60, 1983, 793.

(11) Porter, G. B., *J. Chem. Ed.*, 60, **1983**, 785-790.

(12) Weller, A., *Prog. React. Kinet.* 1, **1961**, 189-214.

(13) Turro, N. J., *Modern Molecular Photochemistry*, University Science Books, Sausalito, CA, Ch. 8, **1991,** 232-295.

(14) Stern, O., Volmer, M., *Physik. Z.*, 20, **1919**, 183.

(15) Wagner, P. J., *Creation and Detection of the Excited State*, Vol. I, Part A, New York, **1971**, 173.

(16) Balzani, V., Moggi, L., Manfrin, M. F., Bolletta, F., Laurence, G. S., *Coord. Chem. Rev.*, 15, **1975**, 321.

(17) Hoffman, M. Z., Bolletta, F., Moggi, L., Hug, G. L., *J. Phys. Chem. Ref. Data*, 18, **1989**, 219-543.

(18) Weber, K., *Z. Physik. Chem. (Leipzig)*, B 15, **1931**, 18.

(19) Förster, T., *Z. Elektrochem.*, 54, **1950**, 42.

(20) Förster, T., *Z. Elektrochem.*, 54, **1950**, 531.

(21) Ireland, J. F., Wyatt, P. A. H., *Advances in Physical Organic Chemistry*, 12, **1976**, 131-221.

(22) Weller, A., *Z. Elektrochem.*, 56, **1952**, 662.

(23) Weller, A., *Z. Elektrochem.*, 58, **1954**, 849.

(24) Parker, C. A., *Photoluminescence of solutions*, Elsevier Publishing Company, **1968,** 328-344.

(25) Horváth A., Stevenson K. L., *Coord. Chem. Rev.* 153, **1995**, 57-82.

(26) Hoshino, M., Seki, H., Shizuka, H., *J. Phys. Chem.*, 89, **1985**, 470.

(27) Ayala, N. P., Demas, J. N., DeGraff, B. A., *J. Am. Chem. Soc.*, 110, **1988**, 1523-1529.

(28) Tsubomura, T., Igarashi, O., Morita, M., *Chem. Lett.*, 21, **1992**, 385.

(29) Chandrasekaran, K., Foreman, T. K., Whitten, D. G., *Nouveau Journal de Chimie*, 5, **1981**, 275

(30) Crosby, G. A., Klassen, D. M., *J. Chem. Phys.*, 43, **1965**, 1498.

(31) Crosby, G. A., Watts, R. J., Carstens, D. H. W., *Science*, 170, **1970**, 1195.

(32) Gafney, H. D., Adamson, A. W., *J. Am. Chem. Soc.*, 94, **1972**, 8238.

(33) Balzani, V., Sabbatini, N., *J. Am. Chem. Soc.*, 94, **1972**, 7587.

(34) Endicott, J. F., Natarajan, P., *J. Phys. Chem.*, 77, **1973**, 971.

(35) Sutin, N., Navon, G., *Inorg. Chem.*, 13, **1974**, 2159.

(36) Meyer, T. J., Bock, C. R., Whitten, D. G., *J. Am. Chem. Soc.*, 96, **1974**, 4710.

(37) Sutin, N., Creutz, C., *Proc. Natl. Acad. Sci. USA*, 72, **1975**, 2858.

(38) Xu, W., McDonough, R. C. III, Langsdorf, B., Demas, J. N., DeGraff, B. A., *Anal. Chem.*, 66, **1994**, 4133-4141.

(39) Sutin, N., Creutz, C., *J. Chem. Educ.*, 60, **1983**, 809.

(40) Balzani, V., Scandola, F., *Supramolecular Photochemistry*, Ellis Horwood, Chichester, UK, **1991**.

(41) Meyer, T. J., *Acc. Chem. Res.*, 22, **1989**, 163-170.

(42) Gafney, H. D., Hicks, C., Ye, G., Levi, C., Gonzales, M., Rutenburg, I., Fan, J., Helmy, R., Kassis, A., *Coord. Chem. Rev.*, 211, **2001**, 207-222.

(43) Crutchley, R. J., Lever, A. B. P., *Inorg. Chem.*, 21, **1982**, 2276-2282.

(44) Goodwin, H. A., Lions, F. *J. Am. Chem. Soc*., 81, **1959**, 6415-6422.

(45) Elderfield R. C., "*Heterocyclic Compounds*," Vol. VI, John Wiley and Sons, Inc., New York, NY, **1957**, 400.

(46) Braunstein C. H., Baker D. A., Strekas T. C., Gafney H. D., *Inorg. Chem.*, 23, **1984,** 857-864.

(47) Balzani, V., Baudin, H. B., Davidsson, J., Serroni, S., Juris, A., Campagna, S., Hammarstrom, L., *J. Phys. Chem. A.*, 106, **2002**, 4312.

(48) Kirchhoff, J. R., Kirschbaum, K., *Polyhedron*, 17, **1998**, 4033.

(49) Denti G., Campagna S., Serroni S., Ciano M., Balzani V., *J. Am. Chem. Soc*., 114, **1992**, 2944-2950.

(50) Gafney, H. D., Hicks, C., Dougherty, T., Rutenburg, I., Fan, J., Maletta, A., *J. Am..Chem. Soc.*, 120, **1998**, 4226-4227.

(51) Gafney, H. D., Hicks, C., Rutenburg, I., Fan, J., *Coord. Chem. Rev.*, 171, **1998**, 71-84.

(52) Strekas, T. C., Gafney, H. D., Hosek, W., Tysoe, S. A., Baker, A. D., *Inorg. Chem.*, 28, **1989**, 1228-1231.

(53) Zambrana J. L. Jr., *Doctoral Dissertation*, Graduate Center of the CUNY, **2007**.

(54) Nakabayashi, Y.; Omayu, A.; Yagi, S.; Nakamura, K.; Motonaka, J. *Analytical Sciences*, 17, **2001**, 945.

(55) Berghian, C.; Plé, N.; Darabantu, M.; Turck, A. *Tetraehedron*, 61, **2005**, 9637.

(56) Paul, M. A.; Long, F. A. *Am. Soc. Testing Materials, Spec. Tech. Publ.*, 190, **1956**, 1-38.

(57) Hammett, L. P.; Deyrup, A. J. *J. Am. Chem. Soc.*, 54, **1932**, 2721-2739.

(58) Williams, A. T. R.; Winfield, S. A.; Miller, J. N. *Analyst*, 108, **1983**, 1067.

(59) Johnson, S. R.; Westmoreland, T. D.; Caspar, J. V.; Barqawi, K. R.; Meyer, T. J. *Inorg. Chem.*, 27, **1988**, 3195.

(60) Zambrana J. L. Jr., *Doctoral Dissertation*, Graduate Center of the CUNY, **2007**, 187.

(61) Zambrana J. L. Jr., *Doctoral Dissertation*, Graduate Center of the CUNY, **2007**, 81-100.

(62) Kalyanasundaram, K., Nazeeruddin, M. K., *Inorg Chem.*, 28, **1989**, 4251-4259.

(63) Ferrari, M. B., Fava, G. G., Pelosi, G., Predieri, G., Vignali, C., Denti, G., Serroni, S., *Inor. Chim. Acta*, 275-276, **1998**, 320-326.

(64) Brewer, K. J., Murphy, W. R., Spurlin, S. R., Petersen, J. D., *Inorg. Chem.*, 25, **1986**, 882.

(65) Data gathered in collaboration with Dr. J. L. Jr Zambrana.

(66) Burstall, F.H.; Dwyer, F.P.; Gyarfas, E.C. *J. Chem Soc*, **1950**, 953.

(67) Pankuch, B. J., Lacky, D. E., Crosby, G. A., *J. Phys. Chem.*, 84, **1980**, 2061-2067.

(68) Nazeeruddin, M. K., Kalyanasundaram, K., *Chem. Phys. Let.*, 158, **1989**, 42-50.

(69) Kincaid, J. R., Danzer, G. D., Golus, J. A., *J. Am. Chem. Soc.*, 115, **1993**, 8643-8648.

(70) Nicholson, R.S., *Anal. Chem.*, 37, **1965**, 1351.

(71) Bard, A.J., Tokel-Takvoryan, N.E., Hemingway, R.E., *J. Am. Chem. Soc.*, 95, **1973**, 6582-6589.

(72) Rillema, D. P., Jones, D. S., Levy, H. A., *J. Chem. Soc., Chem. Comm.*, **1979**, 849.

(73) Anderson, P. A., Anderson, R. F., Furue M., Junk, P. C., Keene, R. F., Patterson, B. T., Yeomans, B. D., *Inorg. Chem.*, 39, **2000**, 2721-2728.

(74) Rutherford, T.J., Pellegrini, P. A., Aldrich-Wright, J., Junk, P. C., Keene, F. R., *Eur. J. Inorg. Chem.*, **1998**, 1677.

(75) Zambrana J. L. Jr., *Doctoral Dissertation*, Graduate Center of the CUNY, **2007**, 143-146.

(76) Van Houten, J., Watts, R. J., *J. Am. Chem. Soc.*, 98, **1976**, 4853.

(77) Nakamaru, K., *Bull. Chem. Soc. Jpn.*, 55, **1982**, 2697.

(78) Johansen, O., Launikonis, A., Mau, A. W. H., Sasse, W. H. F., *Aust. J. Chem.*, 33, **1980**, 1643.

(79) McClanahan, S. F., Dallinger, R. F., Holler, F. J., Kincaid, J. R., *J. Am. Chem. Soc.*, 107, **1985**, 4853.

(80) Kawanishi, Y., Kitamura, N., Kim, Y., Tazuke, S., Riken, Q., *Sci. Papers I.P.C.R.*, 78, **1984**, 212.

(81) Gottlieb, H. E., Kotlyar, V., Nudelman, A., *J. Org. Chem.*, 62, **1997**, 7512-7515.

(82) AIST: RIO-DB Spectral database for organic compounds SDBS.

(83) Zambrana J. L. Jr., *Doctoral Dissertation*, Graduate Center of the CUNY, **2007**, 231.

(84) Huang, N. T., Pennington, W. T., Peterson, J. D., *Acta Crystallogr., Sect. A: Found. Crystallogr.* C47, **1991**, 2011.

(85) Birchall, J. D., O'Donoghue, T. D., Wood, J. R., *Inorg. Chim. Acta*, 37, **1979**, L461.

(86) D'Angelantonio, M., Mulazzani, Q. G., Venturi, M., Ciano, M., Hoffman, M. Z.; *J. Phys. Chem.*, 95, **1991**, 5121-5129.

(87) Rillema, D. P., Allen, G., Meyer, T. J., Conrad, D., *Inorg Chem.* **1983**, 22, 1617-1622.

(88) Gardner, J. S., Strommen, D. P., Szulbinski, W. S., Su, H., Kincaid, J. R., *J. Phys. Chem. A*, **2003**, 107, 351-357.

(89) Campagna, S., Denti, G., De Rosa, G., Sabatino, L., Ciano, M., Balzani, V., *Inorg. Chem.*, 28, **1989**, 2565-2570.

(90) Durham, B., Caspar, J. V., Nagle, J. K., Meyer, T. J., *J. Am. Chem. Soc.*, 104, **1982**, 4803-4810.

(91) Lytle, F. E., Hercules, D. M., *J. Am. Chem. Soc*., 91, **1969**, 253

(92) Zambrana J. L. Jr., *Doctoral Dissertation*, Graduate Center of the CUNY, **2007**, 225.

(93) Bradley, P. G., Kress, N., Hornberger, B. A., Dallinger, R. F., Woodruff, W. H., *J. Am. Chem. Soc*., 103, **1981**, 7441-7446.

(94) Juris, A., Barigelletti, F., Campagna, S., Belser, P., Von Zelewsky, A., *Coord. Chem. Rev.*, 84, **1988**, 85-277.

(95) Hitoshi Ishida, *"Re-evaluation of phosphorescence quantum yields ruthenium(II) tris(bipyridine) complex"*, Topical session at the 18th International Symposium on the Photochemistry and Photophysics of Coordination Compounds, 2009.

(96) Nicholson, RS, Shain I., *Anal. Chem.* 36, **1964**, 705.

(97) Navon, G., Sutin, N., *Inorg Chem*, 13, **1974**, 2976.

(98) Bock, C. R.; Meyer, T. J., Whitten, D. G.; *J. Am. Chem. Soc.*, 97, **1975**, 2909.

(99) Nieuwenhuis, H. A., Haasnoot, J. G., Hage, R., Reedijk, J., Snoeck, T. L., Stufkens, D. J., Vos, J. G., *Inorg Chem*, 30, **1991**, 48-54.

(100) Fucks Y., Lofters S., Dieter, T., Shi W., Morgan R., Strekas, T. C., Gafney, H. D., Baker, A. D., *J. Am. Chem. Soc*., 109, **1987**, 2691-2697.

(101) Johnson, E. C., Sullivan, B. P., Salmon, D. J., Adeyemi, S. A., Meyer, T. J., *Inorg Chem*, 17, **1978**, 2211-2215.

(102) Foreman, T. K., Bonhalla, J. B. S., Whitten, D. G., *J. Phys. Chem.*, 86, **1982**, 3436.

(103) Lever, A. B. P., Seymour, P., Auburn, P. R., *Inorg. Chim. Acta*, 145, **1988**, 43.

(104) Shinozaki, K., Kaizu, Y., Hirai, H., Kobayashi, H., *Inorg. Chem.*, 28, **1989**, 3675.

(105) Masaaki, H., Tomoaki, A., Kenji, K., Shinichi, Y., *Inorg Chem*, 30, **1991**, 3843-3849.

(106) Brignell, P. J., Johnson, C. D., Katritzky, A. R., Shakir, N., Tarhan, H. O., Walker, G., *J. Chem. Soc. B*, **1967**, 1233-1235.

(107) Crutchley, R. J., Lever, A. B. P., Kress, N., *J. Am. Chem. Soc.*, 105, **1983**, 1170-1178.

(108) Rugge, A., Clark, C. D., Hoffman, M. Z., Rillema, D. P., *Inorganica Chimica Acta*, 279, **1998**, 200-205.

(109) Hage, R., Haasnoot, J.G., Nieuwenhuis, H. A., Reedijk, J., Wang, R., *J. Chem. Soc. Dalton Trans.*, **1991**, 3271.

(110) Giordano, P. J., Bock, C. R., Wrighton, M. S., Interrante, L. V., Williams, R. F. X., *J. Am. Chem. Soc.*, 99, **1977**, 3187-3189.

(111) Zambrana, J. L., Ferloni, E. X., Colis, J. C., Gafney, H. D.; *Inorg Chem.*, **2008**, 47, 2-4.

(112) Keyes, T.E.; O'Connor, C. M.; Vos, J. G.; *Chem. Commun.* **1998**, 889.

(113) Keyes, T.E.; O'Connor, C. M.; O'Dwyer, U.; Coates, C. G.; Callaghan, P.; McGarvey, J. J.; Vos, J. G. *J. Phys. Chem. A,* 103, **1999**, 8915-8920.

(114) Blakley, R. L.; DeArmond, M. K.; *J. Am. Chem. Soc.*, 109, **1987**, 4895-4901.

(115) Taffarel, E.; Chirayil, S.; kim, W. Y.; Thummel, R. P.; Schmehl, R. H., *Inorg. Chem.*, 35, **1996**, 2127-2131.

(116) Glazer, E. C.; Magde, D.; Tor, Y., *J. Am. Chem. Soc.*, 127, **2005**, 4190-4192.

(117) Cavazzini, M.; Pastorelli, P.; Quici, S.; Loiseau, F.; Campagna, S., *Chem. Comm.* **2005**, 5266.

(118) Song, L.; Feng, J.; Wang, X.; Yu, J.; Hou, Y.; Xie, P.; Zhang, B.; Xiang, J.; Ai, X.; Zhang, J., *Inorg. Chem.*, 42, **2003**, 3393-3395.

(119) Li, C.; Hoffman, M. Z., *Inorg. Chem.*, 37, **1998**, 830-832.

(120) Dallinger, R. F.; Woodruff, W., *J. Am. Chem. Soc.*, 101, **1979**, 4391-4393.

(121) Vining. J.; Caspar, J.V.; Meyer, T. J., *J. Phys. Chem.*, 89, **1985,** 1055.

(122) Bryant, G. M.; Fergusson, J. E., *Aust. J. Chem.*, 24, **1971**, 441.